PROCEEDINGS ON THE SYMPOSIUM ON

ELECTRON AND ION BEAM SCIENCE AND TECHNOLOGY

NINTH INTERNATIONAL CONFERENCE

Edited by

Robert Bakish

Bakish Materials Corporation
Englewood, New Jersey

and

Fairleigh Dickinson University
Teaneck, New Jersey

ELECTRONICS AND ELECTROTHERMICS AND METALLURGY DIVISIONS

Proceedings Volume 80-6

THE ELECTROCHEMICAL SOCIETY, INC., 10 South Main St., Pennington, NJ 08534

R Bakish
personal copy

PROCEEDINGS ON THE SYMPOSIUM ON

ELECTRON AND ION BEAM SCIENCE AND TECHNOLOGY

NINTH INTERNATIONAL CONFERENCE

Edited by

Robert Bakish

Bakish Materials Corporation
Englewood, New Jersey

and

Fairleigh Dickinson University
Teaneck, New Jersey

ELECTRONICS AND ELECTROTHERMICS AND METALLURGY DIVISIONS

Proceedings Volume 80-6

THE ELECTROCHEMICAL SOCIETY, INC., 10 South Main St., Pennington, NJ 08534

Library of Congress Catalog Card Number 71-120300
Printed in the United States of America

PREFACE

Almost by habit now as this is the ninth time, I rearranged the order of the papers presented at the International Electron and Ion Bean Science and Technology Conference in the hope to make its record a more coherent volume. Regretfully, those of you who attended the conference will note that these proceedings do not contain all the papers which were presented at the conference. Despite the fact that I extended the deadline for manuscript submission from April to July, a number of contributors to the conference still failed to meet it. As one of the objectives of any conference including this one is to share the information presented in it promptly to those unable to attend the conference, no further delay was possible. While I indeed regret that we do not have all the papers presented in St. Louis, this incomplete volume published on time is better than a complete conference record published two years after the event. We are dealing with a rapidly changing technology and timely publication is of the essence.

Now as to the content of the proceedings. After the paper on the educational challenge of submicron technology, I have grouped the material in six sections. The first section contains a variety of papers dealing with electron optics, system fundamentals and cathode materials and design. The second section in the proceedings contains sixteen papers on lithographic systems and related-to-them topics. These systems are certain to play an ever increasing importance in the manufacture of integrated electronic devices of both today and tomorrow. The one micron line width capabilities, the objective of yesterday, is certainly to be replaced in devices with linewidths in the submicron range before too long. The third section contains the papers dealing with a subject which was not even on the horizon three conferences ago and which is assuming increasing importance in this technology. It is the topic of proximity effects and some seven papers dealing with various aspects of the subject are grouped here. The fourth section deals with the very important topic of resists. It is indeed unfortunate that Mike Hatzakis, who presented the invited review paper on this subject was unable to submit his most valuable review of the subject matter for our proceedings. Resists remain one of the important areas needing further development, as progress here holds one of the keys to increased device production rates and decreased costs.

The next section, the fifth, contains the papers dealing with a topic which is also becoming an integral part of today's IC manufacturing technology, i.e., X-Ray lithography. I am grateful to Hank Smith who did manage to submit his paper despite a most arduous work and travel schedule.

The last and concluding section contains papers dealing with what can be best expressed as various topics with the ion beam, though not exclusively as the common denominator. We have papers on ion etching, ion milling, ion implantation and also two papers dealing with electron beams. The first of these presents work on a gun for annealing of ion implanted materials and the second dealing with a topic which at earlier conference had occupied as much as a third of its proceedings, i.e., high power electron guns.

In summary, it is my belief that this volume, the record of the ninth International Electron and Ion Bean Science and Technology Conference, conveys a realistic image of the state-of-the-art of this technology as 1980 comes to a close, a technology distinguished by an existing dynamism and great future.

Robert Bakish
Englewood, N. J.
August 20, 1980

ACKNOWLEDGMENT

The conference chairman wishes to express his sincere thanks to all who made this conference a reality. The roster includes: 1) the authors whose papers are included in these proceedings; 2) the members of the conference committee listed here - F. Benesowski, A. E. Jenkins, L. Habraken, W. W. Smeltzer, W. C. Nixon, M. Boston, M. van Ardenne, M. Allais, G. Slodzian, L. A. Fontijn, S. Namba, C. Hayashi, E. Bas, W. Barwicz, G. Molenstedt, H. Bohlen, N. A. Olshanski and B. Paton; 3) conference sessions chairmen and cochairmen; K. Amboss, G. Brewer, J. Trotel, D. Keyser, J. S. Greeneich, M. Hatzakis, C. G. Wilkins, K. Pickar, D. Mattox, R. Seliger, T. Sakurai, A. Wittkower and R. L. Lubena; 4) the headquarters staff who participated in organizing the event and the publication of the proceedings with special thanks to Donna Kimberlin and Sarah Kilfoyle; 5) last but not least to my wife Ellen, who always patiently puts up with the endless number of projects with which I have the habit of getting involved.

TABLE OF CONTENTS

INTRODUCTORY REMARKS

Ladies and Gentlemen:

It gives me great pleasure to welcome you today in St. Louis on the occasion of the 9th International Electron and Ion Beam Science and Technology Conference. For some of us in the field a second decade of involvement here is coming to an end, while for others this might well be the introduction to this truly exciting technology. It is a technology with far reaching implications not only for all of us here, but also for countless others outside the confines of this hall. As one who got involved with this technology early in its state of development, one must say that the achievements have surpassed even the fondest dreams of optimists among us. Electron beam technology involves a wide range of applications of electron beams, and I will briefly review accomplishments in the more important areas of applications.

Let us first look at the applications of thermal electron beams in melting and refining, for that is where I was introduced into the field in 1959 while working on a 10kW furnace. The almost completed 8 megawatt furnace, capable of casting 100 ton steel ingots is indeed covering some distance and shows the exciting growth and progress which has taken place here. As I am making this presentation, discussions are in progress for the installation of additional megawatt size melting and refining furnaces both here and abroad.

Today this technology appears to be on the verge of a new resurgence under the pressures of energy conservation and environmental protection. Electron beam melting and refining installations enjoy the distinction of the highest efficiency of power conversion in the industry with efficiencies well above 95% and they are certainly the cleanest melting plants. These advantages which are of particular importance in today's conjuncture exclude even mention of all the very advantages of electron beam melting and refining which originally were responsible for the commercial introduction of the technique in metallurgy in 1958.

The modest seeds of electron beam welding contemporary to that 1959 furnace have so mushroomed today that virtually no car which anyone of you drives or plane on which you fly leaves its manufacturer without at least some input by electron beam welders. There would have been no nuclear power plants without it, or for that matter would there have been any satellites and important space missions. The critical-for-the-survival (of some individuals) pacemaker has been a notable application as have been the areas of highly complex mechanical and electromechanical components and systems; all of which could not have

been produced if it were not for the capabilities of electron beam welders.

Evaporation is another success story for the electron beam. Here refractory metals, materials for high temperature and corrosion protection, diverse metals for thin film circuitry, coatings for optical filters, aluminum coating of steel for sardine cans and of most recent date even apparently zinc coating of steel for galvanic protection in competition with electroplating are all areas where electron beam power is making important contributions.

While it has not matched the above mantioned applications in growth, electron beam micromachining, another important application has had its own achievements from the trimming of thin film resistors through the manufacture of cooled jet engine blades, and scores of other applications,including the newest, the annealing ion implanted semi conductors.

We must look next at the nonthermal beams in electron beam lithographic processes and the products of their achievements in microprocessors and computers. This technology would be truly inconceivable without the contribution of electron beams and their truly outstanding capabilities.

In fact the largest number of papers in our meeting here in St. Louis will deal with nonthermal applications of electron beams. As a consequence of work in this domain of application systems for manufacturing functional structures with line widths in the submicron range are becoming a reality.

The importance and anticipated growth here and the industry's demand for trained personnel lead to the formation of The Submicron Technology Center at Cornell University, the first of its kind in the world.

We are indeed fortunate to have my friend of many years, Tom Everhart, and a long term pioneer of this technology, address us shortly and tell us more about this task.

X-Ray lithography, a technique which was pioneered by another friend of many years, Hank Smith, and who will review it later this morning, is also coming on its own. Along with electron beam lithography it too would not have been possible without the electron beam which generates the X-Rays. This technique is assuming increasing importance in the manufacture of some type of IC's.

The electron and X-Ray sensitive resists which will be

reviewed by Mike Hatzakis, also an early pioneer and friend, have been an integral part of progress here to date and will influence progress tomorrow.

The ion beam has been the alternate pillar to our conference and has had a growing importance in a diversity of areas. Ion beams have been responsible for important technological advances though the growth of their applications has not been as pronounced as those of the application of electron beams. It is my belief that we are entering a new period where we will see a much wider scope of the application of ion beams and that ion beams also will become an important part of manufacturing technology. Ion propulsion was an important application when this conference started, but we hear little about work in this field today. Ion implantation which followed today is strong and growing rapidly. For some time now we are seeing development of ion beam processes for micro structure fabrication. In fact some of the individuals who were responsible for the development and building of the ion engines of yesterday, an important achievement of ion beam technology,are now busy redirecting their skills to these new ion beam applications in the electronics field. We have a separate plasma meeting running simultaneously here in St. Louis, and in the opinion of some, those papers could well have been scheduled under the umbrella of this conference because of its relation with ion beams.

In closing let me say that when this conference started 18 years ago we had a fairly even distribution of papers in all domains of electron beam and ion beam studies and applications. Time has helped solve some of the problems and challenges and created new ones, and as a consequence we see a notable departure from the early balanced distribution of reported material at this conference. In a free enterprise the effort and investment needed to support it are guided by future potential. Today much of the work reported on our conference is supported by those who see its tremendous potential in service to man's need to manage the information explosion through micro processors and computers. It is indeed exciting to know that you the scientists, engineers and managers working in this field have made in the past and will continue to make in the future major contributions to simplify man's means to generate,store and retrieve information, perhaps one of the most important keys to progress.

I hope that you will find our 9th Electron and Ion Beam Science and Technology Conference well organized, and that it will meet your expectations. Please accept the Society's and my thanks for selecting this forum to share the fruits of your work.

Robert Bakish,
St. Louis, May 12, 1980

Submicron Technology - An Educational Door to the Future

T. E. Everhart
College of Engineering
Cornell University
Ithaca, New York 14853

In previous talks before this conference, I have appeared as an engineer and scientist, speaking about scanning electron microscopy, or electron interactions with matter. Today I come as an educator, to discuss an important opportunity I believe higher education should seize if humankind is to advance in knowledge as rapidly as it should. Therefore, I come with no slides, no graphs, and no carefully reasoned analysis of experiments, but merely with observations about what is happening in electron and ion beam science and technology, what is happening in related fields of endeavor, what is liable to happen in the future, and what implications these events have for those of us engaged in engineering higher education today.

First, let me observe that for many years, science was the driving force behind technology. During the last 10-20 years, perhaps longer, the improvements in technology have been essential for much of scientific advancement. Technology has produced crystals of material of unprecedented purity. We have learned to process these single crystals to make electronic integrated circuits that are both powerful and economic. We have used these electron devices to measure parameters of interest to science

(and to technology), such as the mobility of Na atoms through glass (SiO_2), the number of interface states at a SiO_2-Si interface, etc. The integrated circuits have led to cheaper computers, which have in turn led to scientific studies that were impractical only a decade or so ago. Today we can say that in solid-state materials, science and technology proceed hand in hand, and technology is as important to science as science is to technology. The case can also be made for other areas of science.

Secondly, as man extends his ability to observe smaller dimensions of either space or time, he increases his understanding of the material world. In 1958, we could observe dimensions of about 10-20Å in the transmission electron microscopes then commercially available, and no scanning electron microscopes (SEM) were for sale. In a university-built scanning electron microscope at Cambridge, we could get 200 Å resolution on a solid object. Today, we can get $\sim$ 2Å resolution of thin objects in either a transmission electron microscope (TEM) or scanning transmission electron microscope (STEM), and $\sim$ 30-50Å resolution in a scanning electron microscope of certain opaque objects. Many commercial instruments of all three kinds are available. Because the scanning electron microscope observes opaque or solid objects, its observations relate well to the macroscopic world. The transmission electron microscope and scanning transmission electron microscope help observe the really microscopic world - the world where quantum

mechanics is necessary to explain what we see and how it behaves.

Third, I would observe that hand-in-hand with our ability to observe, our ability to fabricate smaller structures has improved. In 1955, no one used electron beams extensively to fabricate anything. In the early 1960's, conferences on electron and ion beam science and technology mentioned the possibility of fabrication, but more was said about electron beam welding and milling.

In the 1970's, not only was the fabrication of small objects using electron beam technology explored, but instruments were developed for electron beam fabrication: EBES at Bell Labs, and its commercial offspring, MEBES; VS-1, EL-1, EL-2, at IBM, the TI instruments, etc., and newer instruments are being discussed in this conference. Today, electron-beam fabricated masks are standard in many integrated circuit companies and laboratories, and some direct-writing is being done. Much of the fabrication is at 1 μm and above, but some is at smaller dimensions, and it is in the submicron size range that we need pioneering - where innovation of a very fundamental kind is needed, and will very likely come.

On a different subject, let me observe that over the post-war years, but certainly over the last 25 years, education has become more specialized. We teach more now than we did then. Some fundamental senior courses are now junior courses; some of the graduate curriculum has moved to the senior year. Some students

come to college much better educated in high school - and some do not. As knowledge of circuits has increased, we have tended to teach more courses on circuits - the same can be said for devices, for materials, etc. Graduates have become more specialized, especially PhD graduates.

However, at this point in time there are significant pressures toward building a broader education, where different disciplines can interact in a synergistic way. Consider the field of electrical engineering. The integrated circuit is an important part of that field today. To understand integrated circuits, one must know solid-state devices such as the field-effect transistor, the junction field-effect transistor, the bipolar transistor, the metal-oxide-semiconductor transistor, etc. To make these devices, one must understand the rudiments of materials, of processing, such as resist exposure, development, etching, doping, diffusion, ion-implantation, annealing, oxidation, etc. To make circuits, we must understand how devices interact; to make large scale integrated circuits, we must understand systems design, which during the last decade or so has been mathematically based (as opposed to physics-based). Thus the student of integrated circuits must know the fundamental of mathematics, physics, chemistry, material science, and electrical engineering, and must be able to use knowledge of most of these fields concurrently to understand and to solve problems of design of new integrated circuits.

In summary, complexity requires more broadly based knowledge to deal with it, and the student of today probably should learn more than any one professor knows or can teach!

Why do I discuss integrated circuits in the above paragraphs, since they are after all somewhat removed from Electron and Ion Beam Science and Technology? These integrated circuits are, by and large, the driving force behind the attendance of most of the participants in this symposium. Advances in electron and ion beam science and technology have been fueled by our desire for better integrated circuits. More precise positioning, improved deflection of beams with much less defocusing, brighter cathodes, more clever lens and deflection design, the Scanning Auger Microprobe, etc. have resulted, as have better ion sources, better knowledge of range-energy relationship for ions, ion backscattering, secondary ion mass spectrometry for analysis, etc.

Having made these observations, I note that you in U. S. industry want to hire more students who know electron and ion beam technology as well as other technologies, and that U. S. higher education is <u>not</u> producing sufficient numbers of students for you. In addition, there is, as usual, much discussion about the education today's students should receive for tomorrow's technology. At this point, I should like to reveal some of my own biases, and the reasons for them.

First, entering freshmen will graduate and enter the work force in four years if they leave with a bachelor's degree, in 5 or 6 years if they leave with a MS, and in 7-10 years, if they leave with a PhD. There is a substantial time-lag between entry time and leave-time. In a fast-changing world, that means we have to teach a good fraction of fundamentals that will be helpful no matter what happens in science and technology, and our specialized knowledge had better be aimed a few years hence, and not be based on what industry needed a few years ago. Insight, courage, and a little faith are needed to teach such subject matter, and to start research based on what some call "such speculations".

In answer to those of you who feel these ideas are too far out, let me give an example with which I have had some experience. In 1961, the integrated circuit was being discussed, and there was great controversy about it. Some predicted yields would never be good enough to make integrated circuits economic. Others said better performance would always come from discrete devices connected together in circuits, because there would be fewer constraints on the design of each device. Others said integrated circuits would always be too expensive, etc. At this time, a group of three professors at the University of California at Berkeley decided that integrated circuits were the wave of the future, and that at least one university should teach something about them. One professor, Don Pederson, was interested in circuit design, and saw integrated

circuits as a challenge to circuit design. A second professor, Paul Morton, was interested in computers, and saw integrated circuits as possible components of computers, and the third professor, who was younger, believed that people working with integrated circuits would need new tools to observe them, physically and electrically, and had faith that scanning electron microscopes might have some role to play in that observation process. So, in 1961, with questioning looks from peers, these three faculty members proposed a University integrated circuits lab to design, to fabricate, and to test integrated circuits. A considerable number of leaders in both education and industry have come from that laboratory, and subsequently similar laboratories were founded at other universities. These laboratories have helped produce educated graduates who could step in and make a contribution to the integrated circuits industry. Even so, industry had to train many people, and all entering professionals had much to learn.

It is now almost twenty years later. Technology and science, hand in hand, advance even more rapidly today. Industry needs, or soon will need, more and more people who understand the technology necessary to produce one micron and smaller structures for electronics - and for many other purposes not yet fully understood. But chemistry, physics and other scientific disciplines will certainly benefit from such technology.

We who are trying to build submicron structures do not know all the ramifications of our work, just as the early workers in integrated circuits could not (and did not) predict the total ramifications of their work. We do suspect that we are at the periphery of a new realm of fabrication intellectually, a realm where we leave the macroscopic world, and enter over into the edges of the microscopic world, where we leave classical physics and chemistry, and deal much more with quantum physics and chemistry. At one micron wavelength, we are in the infra-red regime, and shorter wavelengths take us into the visible; the corresponding photon energies are 1.2eV and above, considerably greater than many molecular bonding energies, bandgap energies in common semiconductors, etc.

We at universities need more interaction with those of you in industry who have thought deeply about this realm, who have developed approaches to work in the submicron era, who may see more clearly than we do the ultimate impact of such technology. We need to develop both a theoretical base and experimental expertise, so our students will leave the university with both theoretical knowledge and practical knowledge in some area of this technology. We need excellent students to enter this field - and excellent professors to teach them. We would welcome experts from industry to come and share their knowledge with us for a few months - or for a year. I learned semiconductor technology from a lecturer

from Fairchild many years ago, who came to Berkeley to teach graduate students (and a few faculty) from some notes he had developed. Andy Grove later published the notes into a book, and still later accepted the even greater challenge of management of the fast moving integrated circuit technology at Intel. Of course, if you come to a university and teach a course for us, we cannot guarantee you will become the president of a company like Intel - but it probably won't hold you back!

In summary, Electron, Ion and Photon Beam Technology have an important part to play as we move from fabrication in the macroscopic world of a few microns and up, into the microscopic world of submicron structures. We are opening up new frontiers. We do not know for sure what lies on the other side of the mountains ahead. We have explored the natural structures in the regime to some extent, but we cannot visualize what the region will look like with manmade structures, anymore than the Indians who sold Manhattan Island for $16 worth of beads over 300 years ago could have visualized Manhattan Island today. We were in a similar position with integrated circuits only two decades ago, and the developments have exceeded the most optomistic projections I heard then.

In order that this field move forward expeditiously, industry and academia must work together. We have students anxious to work

on new ideas - these new ideas do not have to be a product two years from now; industry has people who understand the opportunities and the limitations of microfabrication; some of you can suggest important ideas which we should explore - some of you can provide fundamental knowledge and insights to our students (and faculty), so we do the best possible job for you in educating students.

By working together, and with support from research funding agencies of the U. S. government, we can explore this new world of submicron dimensions, we can build structures and devices that will improve our knowledge of both science and technology, that will perform tasks only dreamed about today, and will ultimately benefit all humankind.

It is not often that a group of people stand at the edge of a frontier. It perhaps is even rarer that they realize it. We have a fantastic opportunity for exploration of a new dimensional era. We should seize it and move forward with haste. Such a journey will be exciting, exhilirating, fruitful I am sure, and also fun. Papers spread throughout this symposium will give you more details about our progress into the submicron world - they deserve your attention, your applause, and should stimulate your thought and action.

Section 1.

Electron Optics, System Fundamentals and

Cathode Materials and Design.

A SIMPLIFIED SPOT-SHAPING METHOD FOR E-BEAM MACHINES

W. Knauer and W. Perkins
Hughes Research Laboratories
3011 Malibu Canyon Rd.
Malibu, CA 90265

ABSTRACT

An electron-beam column is described that provides spot-shaping capability with only three lenses. The spot shape is varied by the familiar technique in which two square apertures are made to overlap electron-optically. In contrast to earlier column configurations where the two apertures were interspaced by an imaging lens, both apertures of the present approach are placed so close together that they shadow each other directly. A compact deflection system is mounted between both apertures for spot-shape control. The electron-optical performance achievable with such a column is comparable to that of earlier described spot-shaping systems. With a Cambridge Mk IIa column, variable spots ranging in size from 0.3 μm x 0.3 μm to 1 μm x 1 μm, with an edge resolution of 0.1 μm, and with a current density of 30 A/cm^2 have been generated.

INTRODUCTION

The writing speed of conventional E-beam systems, in which the demagnified image of a thermionic electron source serves as the writing spot, is inadequate for sub-micron circuit fabrication purposes. It is estimated that the throughput of such systems is limited to 0.1 - 0.2 wafer-levels per hour for four inch diameter wafers with 0.5 μm minimum feature size and with a resist sensitivity of 10^{-5} $Coulomb/cm^2$. This limit derives from the finite brightness of thermionic emitters, from the circular and diffused shape of Gaussian spots, and from spot increases due to spherical aberrations in the final lens.

Several alternative column configurations offer higher submicron performance potentials; however, a price must be paid in each case. One approach under consideration is based upon the exceptionally high brightness of field emitters.[1-4] By imaging the virtual source of such an emitter into the target plane, a spot of very high current density can be generated. In concept, this approach is very attractive since it requires only one or two lenses. However, realization is made difficult by several physical and technological constraints. First, the spot current density must reach values of several thousand A/cm^2 in order that fabrication rates of several wafer-levels per hour (4 inch wafers, 0.5 μm minimum features size, 10^{-5} $Coulomb/cm^2$ resist sensitivity) can be achieved. At such high current densities chromatic lens aberrations restrict the image distance to about 3-5 cm[5]. This restriction, in turn, limits the size of the scanfield and necessitates dynamic distortion and aberration corrections. Second, the positional stability of the emitter tip must be very high. Under imaging conditions which provide maximum spot current density, the source must be held within a few hundred Angstroems. Otherwise, the writing spot wanders over distances which exceed its own diameter. Third, exposing resist with a sensitivity of 10^{-5} $Coulombs/cm^2$ at current densities of several thousand A/cm^2 leads to spot dwell times in the nanosecond range. Therefore, the deflection system must be able to handle GHz signals. The sum total of these constraints and requirements places a rather heavy burden upon the developer of a Gaussian field emitter system.

A second approach to high-speed, sub-micron E-beam lithography is to use shaped spots. Several investigators have shown that variable shaped spots with good edge resolution can increase the writing speed potential dramatically [6, 7]. In fact, for minimum feature sizes of

1-2 μm, this approach has been proven in an actual production environment[8].

Extension of the spot-shaping technique to sub-micron levels must be accompanied by a reduction in beam aperture, in order that chromatic and spherical aberrations be prevented from blurring the spot edge. For 0.5 μm minimum feature size, this constraint is expected to limit throughput rates to less than ten wafer-levels per hour (same specifications as above) with sources of about 3.10^5 A/cm^2 sr brightness.

A drawback of the spot-shaping method is the complexity of its electron-optics. As described by the originators of this approach[6,7], spot-shaping columns consist of 5-6 lenses and 2-4 sets of beam alignment coils. Two of the lenses provide variable aperture imaging, while the remaining lenses serve to demagnify and project the shaped spot into the target plane. Alignment coils are required since misalignment results in loss of the beam (unlike in Gaussian systems, where the spot is displaced only).

SPOT-SHAPING METHOD

Here, a modified variable aperture-imaging technique is described which requires fewer lenses and alignment coils without compromise in performance. This improvement is achieved through two, basically independent modifications. First, instead of separating the two shaping apertures by an imaging lens, both apertures are placed close together, with just enough space in between to permit insertion of a compact beam deflection unit. This modification eliminates the need for one lens. Second, the deflecting unit displaces the beam laterally, rather than to direct it off-axis, as in conventional shaping systems. This method eliminates a second lens, one which normally redirects the beam parallel to the axis. At the same time, the double deflection

feature of the present approach can serve also to align the beam.

For a more detailed description of this shaping method, a modified Cambridge Mk IIa column is considered (see Figure 1). A tungsten hairpin generates beams with a brightness of about 10^5 A/cm^{2}sr at 20 kV and with a virtual source (cross-over diameter) of approximately 50 μm. The first lens serves as a condenser which illuminates the two square apertures. The distance between source and apertures and the size of the apertures is chosen such that only the uniformly bright core of the beam ($\cong 10^{-3}$ rad) can pass through both apertures. The focal length of the condenser is adjusted to project a magnified image of the virtual source into the aperture plane of the final lens. A round final-lens aperture serves to limit aberrations to below 0.1 μm and to select spot-forming rays from a well-defined center region of the cross-over. This latter feature assures that small alignment changes do not affect the uniformity of spot illumination.

The square beam leaving the first shaped aperture is deflected by a ferrite-core double deflector (see Figure 2). Depending upon the degree of deflection, a larger or smaller portion of the square beam passes through the second aperture. The resulting variable shaped beam is demagnified by the second and third lenses and imaged into the target plane. Since the two shaping apertures are located at different distances from the target plane, both cannot be imaged sharply at the same time. An intermediate focusing plane must be chosen which leads to some edge blurring. As shown in Figure 3 the aperture edges are imaged as if they were diffused lines of about 2 μm width. In the target plane, where a 100:1 demagnified image is created, edge blurring amounts to about 100 Å. This is well below the edge resolution desired in most applications. Deflection aberrations

associated with the dual deflectors are even smaller since beam aperture and beam deflection angles are small.

Tests of this concept were performed in a modified Mk IIa column. A spot-shaping unit was inserted into the throat of the condenser lens and two sets of alignment coils were added (only one of these was needed). Spot-shape measurements were performed by scanning the spot across a tungsten wire target and by recording the secondary currents derived from the wire. Figure 4 shows results thus obtained.

The quality of the spot in the test column was determined by spherical rather than chromatic aberrations because of the low source brightness. Under these circumstances current density j and spot-edge resolution d are related by

$$j = \pi\beta\left(\frac{2d}{C_s}\right)^{2/3}$$

With a brightness β of 10^5 A/cm^{2}sr, a spherical aberration coefficient C_s of the final lens of 20 cm[9]), and for a desired edge resolution d of 10^{-5} cm one is led to an expected current density limit of 32 A/cm^2 which is closer to the measured value of 30 A/cm^2 than expected.

CONCLUSIONS

A simplified spot-shaping technique has been investigated which performs as well as conventional shaping methods. All electron-optical components used in shaping and varying the shape of the spot are combined into a single, compact unit. In some cases, this unit can directly be retrofitted into existing source-imaging lithography machines. Spot current density and spot edge resolution measured in a converted Cambridge Mk IIa column suggest that this method is well suited for high-speed, sub-micron lithography.

REFERENCES

1. D. Kern, D. Kurz, and R. Speidel, Optik 52, 61 (1978)
2. L. Veneklasen and J. Wiesner 8th International Conf. on Electron and Ion Beam Science and Technology, Seattle (1978)
3. H. P. Kuo and B. Siegel, 8th International Conf. on Electron and Ion Beam Science and Technology, Seattle (1978)
4. J. E. Wolfe, 15th Symposium on Electron, Ion and Photon Beam Technology, Boston (1979)
5. W. Knauer, 15th Symposium on Electron, Ion and Photon Beam Technology, Boston (1979)
6. M. G. R. Thomson, R. J. Collier, and D. R. Herriott J. Vac. Sci. Technol. 15, 891 (1978)
7. H. C. Pfeiffer J. Vac Sci Tech. 15, 887 (1978)
8. G. J. Giuffre, J. F. Marquis, H. C. Pfeiffer, W. Stickel 15th Symposium on Electron, Ion and Photon Beam Technology, Boston (1979)
9. J. P. Martin and D. Geisler, Optik 36, 322 (1972)

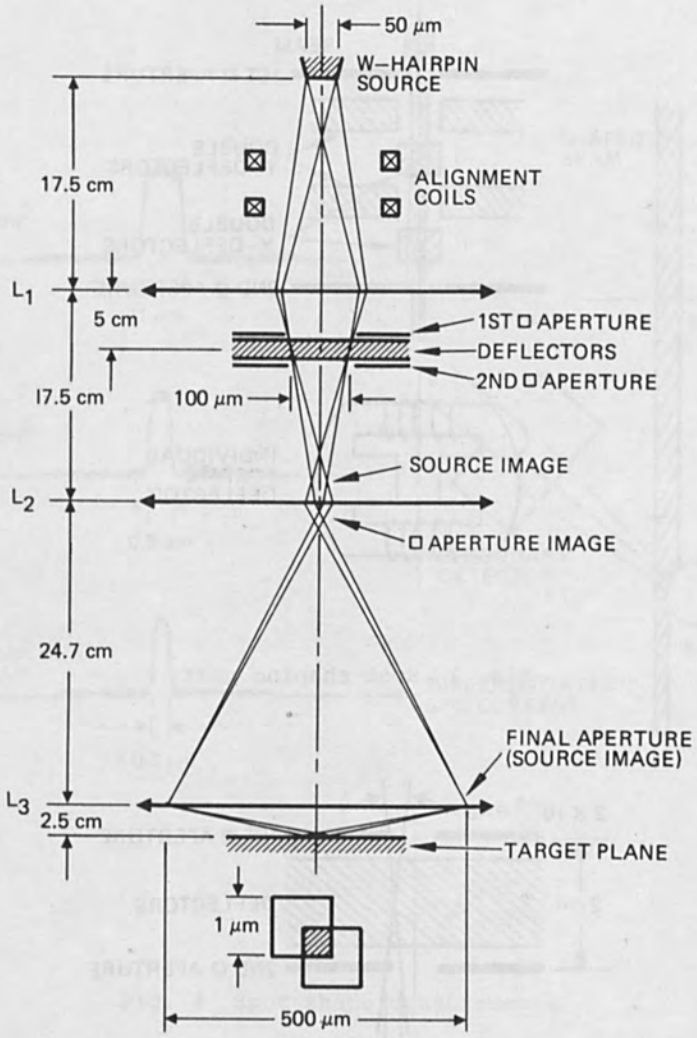

Fig. 1 Three-lens column (Cambridte MK IIa, modified for spot shaping)

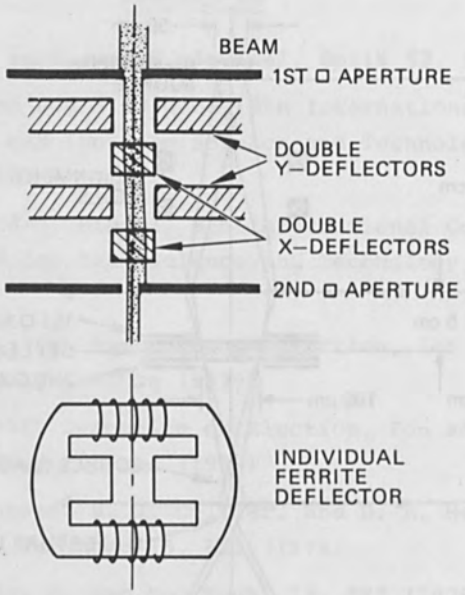

Fig. 2 Spot shaping unit

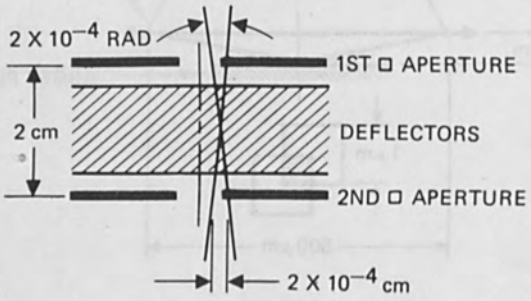

Fig. 3 Image blurring associated with Spot Shaper

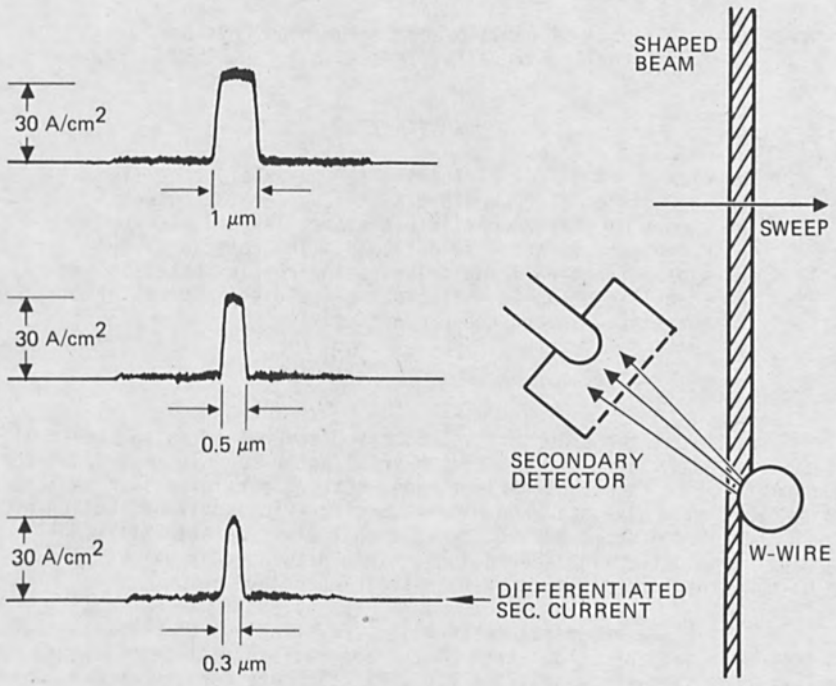

Fig. 4 Spot shape measurements

ABERRATIONS IN ELECTROSTATIC OPTICS FOR CHARGED PROBE FORMING SYSTEMS

Hajime Ohiwa*
National Research and Resource Facility for Submicron Structures
and
School of Applied and Engineering Physics
Cornell University, Ithaca, N.Y. 14853

ABSTRACT

Numerical methods for evaluating the paraxial properties and aberrations of probe forming systems are discussed. The theory of charged particle trajectories and electromagnetic field calculation is outlined. The rotational symmetry of deflection is described using complex notation and the so-called octupole deflector is analyzed in terms of its rotational invariance properties.

I. Introduction.

Electrostatic scanning systems offer several advantages over magnetic scanning systems. They have a faster scanning speed and the capability to focus and deflect heavy charged particles such as ions. However, they have not been widely used for wide-angle deflection of finely focused beams because conventional electrostatic deflectors have large deflection aberrations. This drawback can be overcome by using octupole deflectors such as those described below.

First, the numerical integration (ray-tracing) of paraxial trajectories and the calculation of the aberrations will be discussed. Then, the symmetry conditions for deflection are derived by using complex notation. Finally, the voltage distribution of electrostatic deflector electrodes is Fourier-analyzed by using these symmetry conditions.

II. Numerical Integration of the Paraxial Trajectories and Calculation of the Aberrations.

The optical properties of charged probe scanning systems can be determined by specifying the electric and/or magnetic scalar potential of the focusing and deflection fields. Assume that the optical axis is straight and that the z-axis is aligned with the optical axis. Then the potential $\phi(r,\theta,z)$ throughout the scanning system can

*On leave from Toyohashi University of Technology, Toyohashi, 440 Japan.

be described by the potential distribution on the axis [1];

$$\phi(r,\theta,z) = \sum_{m=0}^{\infty} \sum_{\ell=0}^{\infty} \frac{(-1)^{\ell} r^{2\ell+m} \left\{ \Phi_{cm}^{(2\ell)}(z) \cos(m\theta) + \Phi_{sm}^{(2\ell)}(z) \sin(m\theta) \right\}}{4^{\ell} \cdot (\ell!) \cdot (m+1)(m+2) \cdots (m+\ell)} \tag{1}$$

because the potential must satisfy the Laplace equation. Hence, if $\Phi_{cm}(z)$ and $\Phi_{sm}(z)$ are known, the optical properties of the system can be calculated by solving the trajectory equations for charged particles;

$$\begin{aligned} &\left[(\phi\ (1 + \varepsilon\phi))^{\frac{1}{2}} (1 + w'\bar{w}')^{-\frac{1}{2}} w' \right]' \\ &= -\tfrac{1}{2}\ (1 + 2\ \varepsilon\phi)(1 + w'\bar{w}')^{\frac{1}{2}} (\phi\ (1 + \varepsilon\phi))^{-\frac{1}{2}}\ E_w \\ &+ j\eta(w'B_z - B_w) \end{aligned} \tag{2}$$

where $w = x + jy$, $E_w = E_x + jE_y$ and $B_w = B_x + jB_y$ denote trajectory, electric field and magnetic flux density respectively in complex form, the bars on the variables indicate complex conjugate, the primes indicate differentiation with respect to z and ϕ is the electrostatic potential [2].

The paraxial properties of the system are found by neglecting all terms higher than first-order in w and w' in the trajectory equation (2). The first-order chromatic aberrations are obtained as perturbations caused by a small change in the acceleration voltage of the paraxial equations. The third order geometrical aberrations are also obtained by treating the third-order terms as perturbations to the first-order trajectory equations. These optical properties are obtained by integrating the paraxial and perturbation equations.

The integration of perturbations or aberrations can be done both analytically and numerically. The conventional method uses analytical integration to obtain the aberration coefficients because of the following reasons:

1) Integration of skew rays can be avoided.
2) Higher-order derivatives of the potential can be eliminated by partial integration.
3) Some insight for reducing aberrations can be obtained from the integral form expressions.

The first reason was meaningful some thirty years ago when no high speed digital computers were available. Now, the skew rays can easily be integrated thanks to the computer.

The second reason is important because measurement of the potential or its calculation by finite difference or finite element methods give only a numerical value for the potential and do not give the derivatives of the potential. Numerical differentiation which is known to be an inaccurate process must be used. However, recent developments in the integral equation formulation for potential problems (for example, the charge density method for the electrostatic case [3]) have enabled the higher-order derivatives to be calculated as well as the potential itself. Experimentally obtained potential distributions could also be expressed as a superposition of some appropriate analytical functions by using a nonlinear least squares fitting technique. This technique has recently been improved so much in terms of error analysis that it could be used not only for fitting parameters but also for choosing the most appropriate model quantitatively among the possible models by using the Akaike's Information Criterion [4]. Therefore, the importance of the second reason seems to have diminished.

The third reason is still important for gaining some insight into the system to be designed. However, it is necessary to carry out an extensive amount of algebraic manipulations for obtaining the integral form aberration formulas. When the system becomes complicated, such manipulations are so extremely troublesome that they must be carried out by a computer [2].

Here, we adopt the method of numerically integrating the aberrations and the paraxial trajectories with an assumed analytical expression for the field. It should be noted that in order to avoid the cancellation error of the subtraction, the aberrations or the analytically evaluated differences between the perturbed and the paraxial trajectories are directly integrated over the whole trajectories and that they are not evaluated by taking the numerical differences of both trajectories at the image plane. The reasons for our adoption are as follows. First, algebraic manipulations for deriving the necessary equations are kept to a minimum which implies that typographical errors in coding the program are minimized and that further generalizations to include both magnetic and electrostatic lenses and deflectors and various other optical components such as dynamic aberration corrections can easily be carried out. Second, the qualitative dependence of the optical properties on the physical or geometrical parameters of the system can be obtained even if some analytical expressions are used for describing the fields. As is described above, these qualitative results could become quantitative by relating them to computationally or experimentally obtained potential distributions by nonlinear least squares fitting. Third, although intuitive insights from the integral form aberration formulas are very useful, some numerical optimization technique is needed for optimizing system parameters with respect to optical properties. As such techniques have been developed [5], intuitive insights may not be needed, or, at least, their importance

is decreased.

The details of the equations for the optical properties of a magnetic scanning system are already known [6]. The electrostatic case can be treated in the same manner and shall be described elsewhere.

III. The Rotational Symmetry of the Deflection Potential.

Denote the potential expression (1) in a complex form so that symmetry condition of the system can be easily recognized;

$$\phi(w,\bar{w},z) = \sum_{m=o}^{\infty} \sum_{\ell=o}^{\infty} \frac{(-1)^{\ell}(w\bar{w})^{\ell}}{4^{\ell} \cdot (\ell!)(m+1)(m+2)\cdots(m+\ell)} \left\{ \frac{w^m + \bar{w}^m}{2} \Phi_{cm}^{(2\ell)}(z) + \frac{w^m - \bar{w}^m}{2j} \Phi_{sm}^{(2\ell)}(z) \right\} \tag{3}$$

For round lenses, the potential is axially-symmetric, and an arbitrary rotation of position from w to $w \cdot \exp(j\delta)$ should keep the potential constant. This condition is satisfied only by those terms of m = o. Hence, round lenses are described by those terms.

For a deflector oriented in the x-axis direction, the potential must satisfy the following condition known as two-fold symmetry because of the shape of the deflector [7];

$$\begin{cases} \phi(\bar{w},w,z) = \phi(w,\bar{w},z) , \\ \phi(-\bar{w},-w,z) = -\phi(w,\bar{w},z) . \end{cases} \tag{4}$$

Hence, a deflector potential includes only the odd m terms in (3).

As is easily seen from the discussion of the previous section, the terms with m > 4 are negligible unless aberrations higher than third-order are required. Therefore, only those terms of m = o, 1, and 3 are of interest to us.

Next, consider a deflector whose potential includes only m = 1 terms and which is rotated with respect to the x-axis by an angle γ. The potential is expressed as;

$$\phi_H(w,\bar{w},z) = \sum_{\ell=0}^{\infty} \frac{(w\bar{w})^{\ell}\, \phi_1^{(2\ell)}(z)}{4^{\ell}(\ell!)\cdot 2\cdot\cdots\cdot(\ell+1)} \left\{ \frac{w+\bar{w}}{2} \cos(\gamma) + \frac{w-\bar{w}}{2j} \sin(\gamma) \right\} \quad (5)$$

where the subscript H denotes horizontal deflection. For two-dimensional deflection, a vertical deflector is required as well. Let us assume that the vertical deflector is the same as a horizontal deflector rotated through $\pi/2$. Then, its potential is expressed as;

$$\phi_V(w,\bar{w},z) = \phi_H(-jw,j\bar{w},z) \quad . \quad (6)$$

Denote the deflection current or voltage applied to horizontal and vertical deflectors by X and Y, or W in a complex form, and the horizontal deflector potential by;

$$\phi_H(z) = \phi_1(z)(\cos(\gamma) + j\cdot\sin(\gamma)) \quad . \quad (7)$$

Then, the whole deflector potential is expressed as;

$$\begin{aligned} \phi_L(W,\bar{W},w,\bar{w},z) &= X\phi_H + Y\phi_V \\ &= \sum_{\ell=0}^{\infty} \frac{(w\bar{w})^{\ell}}{2\cdot 4^{\ell}\cdot(\ell!)\cdot 2\cdot\cdots\cdot(\ell+1)} \left\{ W\bar{w}\phi_H^{(2\ell)}(z) + \bar{W}w\bar{\phi}_H^{(2\ell)}(z) \right\} \quad . \end{aligned} \quad (8)$$

The importance of this linear deflection potential is that ϕ_L is invariant for the rotational transformations of deflection W into $W\cdot\exp(j\delta)$ and of trajectory w into $w\cdot\exp(j\delta)$, where δ is an arbitrary angle [8,9]. Hence, the above linear deflector potential is said to be a rotationally invariant deflector potential. Further extension of this invariant property to a scanning system with dynamic correctors is described in [9].

As was shown above, a deflector includes in general not only m = 1 but also other odd terms as well. The corresponding expressions for those m = 2k + 1 terms are;

$$\begin{aligned} &\phi_L(W,\bar{W},w,\bar{w},z) \\ &= \sum_{k=0}^{\infty} \sum_{\ell=0}^{\infty} \frac{(-1)^{\ell}(w\bar{w})^{\ell}\, F_{k,\ell}}{4^{\ell}\cdot(\ell!)(2k+2)(2k+3)\cdot\cdots\cdot(2k+\ell+1)} \quad , \end{aligned} \quad (9)$$

where,

$$F_{k,\ell} = \frac{1}{2}\left[w^{2k+1}\ \bar{\Phi}^{(2\ell)}_{2k+1}(z)\ \bar{W} + \bar{w}^{2k+1}\ \Phi^{(2\ell)}_{2k+1}(z)\ W\right] \quad \text{for even } k \ , \tag{10}$$

$$= \frac{1}{2}\left[w^{2k+1}\ \bar{\Phi}^{(2\ell)}_{2k+1}(z)\ W + \bar{w}^{2k+1}\ \Phi^{(2\ell)}_{2k+1}(z)\ \bar{W}\right] \quad \text{for odd } k \ .$$

Note that $\Phi_{2k+1}(z)$ are complex as ϕ_H is defined in (7).

As is seen from (9) and (10), for the m = 3 and 5 terms, a rotational transformation is invariant only for $\delta = \pi/2$. Hence, these components in a deflector yield the so-called four-fold aberrations, whereas the m = 1 component yields the round-lens-type aberrations [6,10]. Although the previous work was for magnetic scanning systems, this result holds for a general system in which magnetic and/or electrostatic components are included, because the argument is based on the invariant conditions of the scalar potential.

In addition, these m = 3 and 5 components do not contribute to the paraxial properties because the lowest term in W and w are fourth- and sixth-order respectively in (9) and (10). Therefore, it is desirable to eliminate these components from the deflector so as to eliminate the four-fold aberrations. Indeed, such a deflector is called a cosine-distributed deflector and is widely used for magnetic deflection. However, such deflectors were not used for electrostatic deflection until the so-called octupole deflector was introduced [11]. In the next section, we shall Fourier-analyze the electrostatic deflector construction so as to clarify the advantages of the octupole deflector.

IV. Fourier-Analysis of Electrostatic Deflectors.

First consider the voltage distribution of a conventional electrostatic deflector in which dipole electrodes are placed on the x-axis for horizontal deflection and another set of dipole electrodes are placed on the y-axis for vertical deflection. It is apparent from the comparison of the voltage distributions of horizontal deflection (X = 1 and Y = o) and diagonal deflection ($X = Y = 1/\sqrt{2}$) shown in Fig. 1 that the shape of the deflection fields for these two cases are different. This means that conventional electrostatic deflectors do not satisfy the condition of rotational invariance, and their potential includes the m = 3 and/or 5 components.

Next, let us consider a so-called octupole deflector in which

another pair of dipole electrodes is placed in both of the diagonal directions in addition to the conventional deflector electrodes and the deflection voltages of X, $(X + Y)/\sqrt{2}$, Y, $(-X + Y)/\sqrt{2}$ are applied to each of the dipoles in the counter-clockwise azimuthal direction from the x-axis. Then, as is shown in Fig. 2, the potentials are of the same shape for both the horizontal and diagonal deflections provided that all of the dipole electrodes are of the identical shape. This means that the system satisfies the eight-fold symmetry condition which holds for the m = 7 and 9 components as is seen from (9) and (10). Therefore, those components of m = 3 and 5 are eliminated from the octupole deflector, because, if they were to exist, they would satisfy four-fold rather than eight-fold symmetry condition and the field shapes for horizontal and diagonal deflection would be different. Hence, the octupole deflector can be regarded as cosine-distributed as far as the third- and fifth-order aberrations are concerned.

The octupole deflector proposed by Kelly [11] is realized by rotating our deflector through $\pi/8$ and by changing the applied voltages. The above argument holds for Kelly's deflector as well.

V. Conclusion.

The voltage distribution of an octupole deflector has been Fourier-analyzed using a discussion of its rotational symmetry properties. The whole potential is determined by the geometry of the electrodes, and then their Fourier-components are of primary importance because they are directly related to the aberrations. Some designers may worry about the end effect of the finite-length deflector, because a uniform field is only realized in an infinitely long cosine-distributed deflector and a cosine-distributed deflector yields non-uniform fields at both ends. However, the finite extent of the deflector is relatively unimportant because the uniform field is not directly related to the aberrations. Indeed, they can be evaluated with the end effects included once the potential functions on the axis are obtained. The important point of the Fourier-analysis technique described in this paper is that it reduces a three-dimensional problem into a number of two-dimensional problems and that the number in our case is small.

It should also be noted here that the condition of rotational invariance is satisfied for a system comprising round lenses and cosine-distributed deflectors. Hence, the deflector electrodes can be used as focusing electrodes by giving all of them a bias voltage which is different from that of other focusing electrodes.

ACKNOWLEDGMENTS

The author would like to express his sincere gratitude to Prof. B. M. Siegel for giving him the opportunity to do this research and for stimulating discussions and to members of his laboratory, in particular, to Dr. E. J. Kirkland for stimulating discussions and the revision of English. This work has been supported by NSF Grant No. 77-09688 through the National Research and Resource Facility for Submicron Structures at Cornell University.

REFERENCES

[1] W. Glaser, Grundlagen der Electronenoptik (Springer, Wien, 1952) p.102.
[2] T. Soma, Optik Vol.49, pp.255-262 (1977).
[3] E. Harting and F. H. Read, Electrostatic Lenses (Elsevier, Amsterdam, 1976), pp.32-34.
[4] T. Nakagawa, Y. Oyanagi and H. Ohiwa, Tenth Int. Symp. Math. Program, (Montreal, 1979).
[5] H. Ohiwa, J. Inst. Maths. Applics., Vol.21, pp.189-196 (1978).
[6] H. Ohiwa, J. Phys. D: Appl. Phys., Vol.10, pp.1437-1449 (1977).
[7] J. Kaashoek, Phillips. Res. Rept. Suppl., Vol.11, pp.1-114 (1968).
[8] H. Ohiwa, E. Goto and A. Ono, Electron. Commun. in Japan, Vol.54-B, pp.44-51 (1971).
[9] E. Goto and T. Soma, Optik Vol.48, pp.255-270 (1977).
[10] E. Munro, Optik Vol.39, pp.450-466 (1974).
[11] J. Kelly, Adv. Electron. Electron Phys. Vol.43, pp.43-133 (1977).

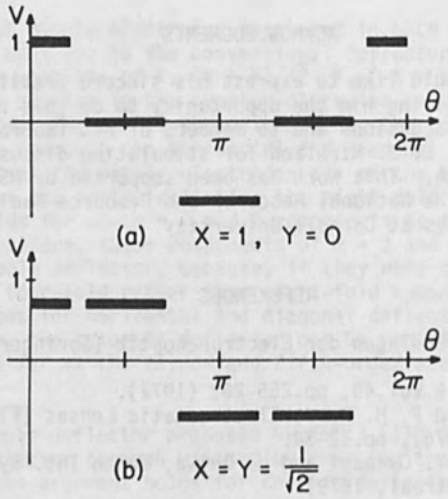

Fig. 1. Voltage distributions of a conventional deflector with the applied voltage of X and Y.

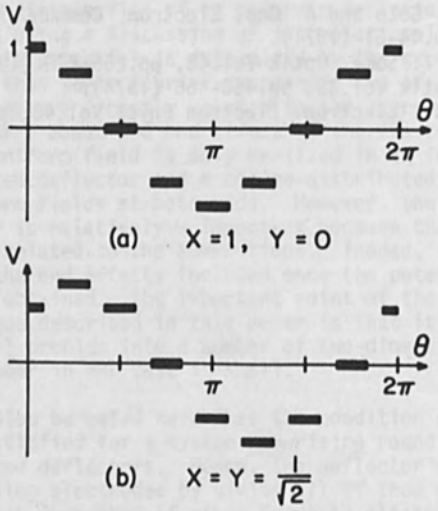

Fig. 2. Voltage distributions of an octupole deflector with the applied voltage of X and Y.

DESIGN OF EDDY CURRENT COMPENSATING HIGH SPEED TOROIDAL DEFLECTION YOKES

M. A. Sturans and H. C. Pfeiffer
IBM Corporation, Data Systems Division
East Fishkill Facility, Hopewell Junction, N.Y. 12533

Abstract

A toroidal yoke for an electron beam lithography system is compensated for deflection placement errors that normally result from eddy currents and induction currents generated within the coil windings as well as driver settling time and parasitic coupling. Compensation is achieved through a unique winding technique and the addition of passive conductive material (for controlled eddy current generation) along the outer periphery of the yoke. Both theoretical and experimental results are presented. Agreement is shown to be very good in a specific E-Beam lithography system.

Introduction

The magnetic fields used in probe forming lithography systems to deflect the electron beam over the exposure field are dynamic in nature, i.e., changes in the deflection coil driving input signals are required for each predetermined movement of the electron beam. The varying magnetic fields also generate eddy currents in any conductive material surrounding the coils. The eddy currents, in turn, cause undesired fields which adversely affect the beam motion in time and space, primarily by exerting drag on the beam. In view of the precision and speed of beam deflection required for successful electron beam lithography, the eddy currents present a major problem in achieving satisfactory beam control.

Ferrite materials which suppress eddy currents because of their high electrical resistivity are frequently used to shield deflection yokes from the bulk metal of the neighboring electron lens. This approach has been successfully employed even in the case where the deflection yoke is positioned inside the final lens between the pole pieces. (1)

Other compensation techniques proposed by Wardly (2 - 4) employ a second auxiliary deflection coil surrounding the first, the current of which produces a field partially opposing the deflection field, but practically completely neutralizing the eddy-current-induced error.

In electron beam lithography systems covering large exposure fields with low resistance, low inductance deflection yokes for low power consumption and fast response, eddy currents within the winding

structure itself cannot be ignored. In this situation, neither of the above referenced techiques can fully compensate the eddy current effect. In addition, driver current settling time and parasitic coupling within the yoke will further affect the beam movement.

By careful design of the yoke windings, the intrinsic eddy currents can be minimized. The remaining magnetic deflection settling time (including yoke driver and parasitic coupling) can be compensated by positioning passive conductive material of specific dimensions in critical locations of a toroidal yoke. Two basic concepts exploited by this technique are: 1) Toroidal wound deflection yokes generate opposing fields near the inside and outside of the windings, and thereby also produce opposing eddy currents; 2) Conductive sheets can be dimensioned to generate eddy currents of given amplitude and time constant.

Eddy Currents in Conductive Sheets

The differential equation which governs eddy currents in a conductive media can be written: (5)

$$\nabla^2 I(x,y,z,t) = \sigma\mu_o \frac{\partial I}{\partial t}(x,y,z,t)$$

Where I = induced current (eddy current)
σ = conductivity
μ_o = permeability

For the simple geometry shown in Fig. 1, the solution to the differential equation can be written as:

$$I = \sum_{\ell mn} C_{\ell mn} \sin \frac{\ell\pi x}{w} \sin \frac{m\pi y}{h} \cos \frac{n\pi z}{(K\delta d)} 1/2 \; e^{-\lambda_{\ell mn}\tau}$$

Where δ = skin depth = $\left(\frac{2}{\sigma\omega\mu_o}\right)$ 1/2

K = empirical constant, and

$$\text{time constant} = \tau = \frac{1}{\lambda_{\ell mn}} = \frac{\sigma\mu_o}{\pi^2\left(\frac{\ell^2}{w^2} + \frac{m^2}{h^2} + \frac{n^2}{K\delta d}\right)}$$

We are interested primarily in the term that has the longest time constant, i.e.: when $\ell = m = n = 1$.

Hence: $$\tau = \frac{\sigma\mu_o}{\pi^2 \left(\frac{1}{w^2} + \frac{1}{h^2} + \frac{1}{K\delta d}\right)}$$

Figure 2 shows a plot of this equation for copper sheets of fixed height (h) as a function of width (w) and various thicknesses (d). Along with the theoretical values are curves of experimental data obtained by positioning the copper sheets next to a magnetic deflection yoke (free of intrinsic eddy current) in an electron beam system and measuring the settling time of the beam movement produced by a step function deflection current input. The discrepancy between the theory and experiment is primarily due to the fact that the calculation was based on planar geometry with uniform incident field while in the experiment the copper sheets were wrapped around the outer diameter of the yoke, hence creating angular dependency and non-uniform incident fields. The important characteristic to derive from this graph is that the time constant becomes constant after the height (h) exceeds the width (w). At the point where h = w, the induced eddy currents have reached their maximum diameter (Larmour diameter) and hence their largest time constant. Further increase of the width of the sheet only increases their magnitude, not the time constant. Thus we have the freedom to vary the amplitude and time constant of eddy currents independently.

Compensation of Toroidal Yokes

In the development of modern electron beam lithography systems, the demands for larger deflection fields, higher accuracy and speed are continually increasing. This necessitates ever larger deflection yokes with bulkier conductors in order to decrease the inductance, preferably with rectangular cross section, to achieve high accuracy of wire placement. The use of larger conductors introduces non-negligible eddy current effects. In addition, driver settling time and internal coupling of the yoke windings, previously considered negligible, now impose a limitation on system performance.

In order to minimize the intrinsic eddy current effect, the coils of a toroidal yoke were wound with five parallel conductors. In this configuration eddy currents are minimized, but prohibitive induction currents are generated between adjacent coils, even when the unexcited coil is open-circuited. Figure 3 shows a single layer from two adjacent coils, as well as the geometry of their magnetic fields and induced currents. The induced current in the non-excited winding circulates primarily in the outside wires of each layer (since they enclose the larger amount of flux), and produces a magnetic field with a prohibitive time constant L/R. Each layer of the coil will contribute to the total field strength; the net result will be the sum of all the layers, and finally the sum of all the coils.

It can be argued that the ultimate solution to induction and eddy current elimination is to use very fine braided or twisted wire such that eddy currents are negligible and induction currents are cancelled. Two major problems prohibit this solution. The most serious problem is that placement accuracy is lost, resulting in deflection distortion and aberrations, and the second is that the probability of two adjacent wires shorting together is very great--which would create detrimental internal current loops and destroy deflection accuracy.

The solution to the induction current problem, using parallel conductors, is to invert the wire sequence of approximately half the layers in each coil, as shown in Fig. 4. In this way the deflection field remains unaltered, but the induction currents are cancelled. In practice, the inner windings of a coil are smaller; hence, their field strength is less than that produced by the outer windings. The ratio for cancellation, therefore, is not 1:1; instead the wire sequence reversal should be made near the physical center of the total length of wire in each coil.

The remaining magnetic deflection settling time (drag) due to eddy currents, parasitic coupling, and yoke driver settling, can be practically eliminated by introducing additional eddy currents of opposite polarity and the careful tailoring of their time constants.

Figure 5 depicts the configuration of currents and fields which may support a better understanding of the eddy current effects and the countermeasures that can be implemented in a toroidal yoke. Eddy currents (giving rise to fields always opposing the originating fields) generated by the current I_i close to the beam exert a drag on the beam motion, while those of equally strong, but more remote current I_o, aid the beam deflection--however, less effectively. Enhancement of the eddy currents of I_o by placing conductive material in the vicinity of the outer windings will result in the cancellation of the eddy current effects of I_i and I_o on the beam.

Figure 6 shows the physical placement of the compensating conductive sheets on a toroidal yoke depicted with only one pair of windings on each axis for simplicity. It is important to note that the sheets are not only positioned in the proximity of the outer windings, but also centered on the axis orthogonal to the deflection axis. Therefore, the compensating sheets for the X-deflection are positioned on the Y-axis, and vice-versa. The explanation for this can be easily seen by considering the magnetic field distribution, see Fig. 7. To gain the maximum effect of the outer windings on the conductive sheets, they must be placed in the area where the incidence angle approaches 90^{o}; hence, the orthogonal axis position is the most desirable. For reasons of field symmetry and uniformity, the sheets should be centered on the axis.

The apparent simplicity of this approach is quite deceptive, because no simple solution exists for practical implementation. The eddy currents not only have to be compensated in space (amplitude), but also in time. By considering the time constant equation plotted in Fig. 2, it can be seen that such tailoring is possible. In a practical system one would first measure the total deflection settling time constant (including eddy current, driver settling and coupling) and then from a similar graph as Fig. 2 choose the proper dimensions of the compensating conductive sheets.

Experimental Results

The described compensation method has been implemented in a practical lithography system and produced very satisfactory results. Initial experiments were performed outside the E-beam column by applying a known current step to the deflection yoke and sensing the field produced in the yoke center by means of a low inductance search coil. By positioning copper compensating foils of various dimensions on the outer periphery of the yoke, the eddy current compensation technique was confirmed. Figure 8 shows scope traces of the current input and deflection field settling times at various stages of compensation. It is important to note that overcompensation can be achieved.

Higher accuracy experiments on the compensating technique were performed using the E-beam column itself as an oscilloscope. The experimental method for deflecting the beam is shown in Fig. 9. The point of the experiment is to measure how fast the magnetically deflected beam reaches its destination. In order to obtain a pictorial representation of the magnetic deflection speed, the beam is simultaneously deflected electrostatically in the orthogonal direction. Electrostatic deflection is used because it is inherently very fast and does not introduce additional eddy currents. In addition, time markers are imposed by blanking and unblanking the beam at precisely known time intervals.

The ideal circumstance would be for the magnetic deflection to occur along the line perpendicular to the electrostatic trace, and to instantaneously strike the target point. The actual beam traces are shown in Fig. 10 in various states of compensation. The traces were obtained by electron-optically magnifying the image onto a phosphor screen (6) and then using a TV camera to obtain the photographs. It should be noted that, for reference, the ideal trace is included in each case, obtained by setting the magnetic deflection to zero. Figure 10A illustrates beam lag introduced by the deflection coil without compensation. By placing too much compensating material around the coil, the opposite effect can be achieved (Fig. 10B), where the beam overshoots the target point and then gradually returns. In the properly compensated state (Fig. 10C), the beam is deflected immediately very close to the target point. Some error was deliberately left in Fig. 10C so that the two traces could be distinguished.

Summary

It has been shown that detrimental electron beam settling times produced by intrinsic eddy currents, driver settling, and parasitic coupling in a toroidal magnetic deflection system can be significantly reduced by a unique winding technique and the critical placement of passive conductive material within the active field lines. A theoretical calculation of a simplified model has shown good accuracy in predicting the physical dimensions and electrical characteristics of the compensating material. The technique has been implemented in a practical electron beam lithography system.

Acknowledgment

The authors are indebted to Douglas Cullum for his valuable contributions in the efforts to minimize yoke intrinsic induction currents and to Alain Gheeraert for performing many of the experiments that were required to verify eddy current compensation technique.

References

1) H. C. Pfeiffer, "New Imaging and Deflection Concept for Probe-Forming Microfabrication Systems," J. Vac. Sci. Technol., Vol. 12, No. 6, p. 1170, 1975.

2) G. A. Wardly, "Correction of Eddy Current Errors in Electron Beam Deflection," J. Appl. Phys., Vol. 44, No. 8, p. 3766, August 1973.

3) G. A. Wardly, "Eddy-Current Compensating Deflection Yokes," J. Appl. Phys., Vol. 44, No. 12, p. 5607, December 1973.

4) G. A. Wardly, "Design Study of Toroidal Deflection Yokes with Eddy-Current Compensation," J. Appl. Phys., Vol. 45, No. 5, p. 2316, May 1974.

5) W. R. Smythe, "Static and Dynamic Electricity," (McGraw-Hill New York, 1950), Chaps. 7 and 11.

6) H. C. Pfeiffer and K. H. Loeffler, "A High Current Square Spot Probe for Micro Pattern Generation," 7th Int. Conf. on Electron Microscopy (Grenoble, France), p. 63, 1970.

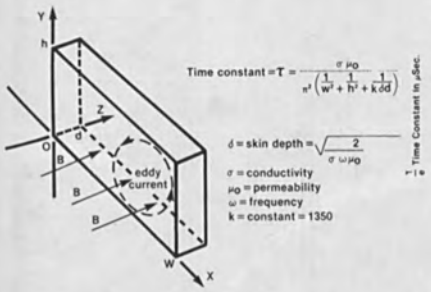

Fig. 1. Eddy current time constant model.

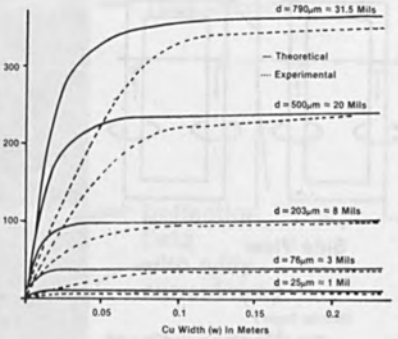

Fig. 2. Time constant solutions for copper sheet.

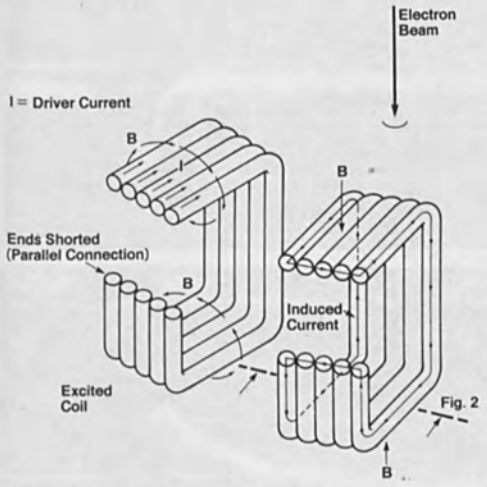

Fig. 3. Two adjacent windings of a toroidal yoke.

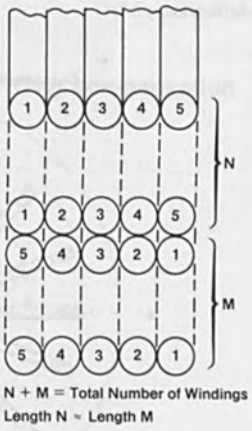

Fig. 4. Winding inversion for cancellation of induction currents.

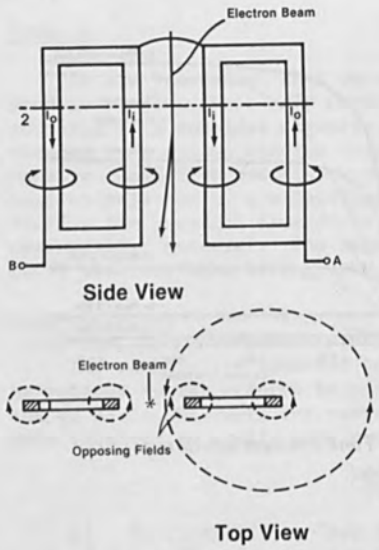

Fig. 5. Magnetic field lines for toroidal deflection yoke.

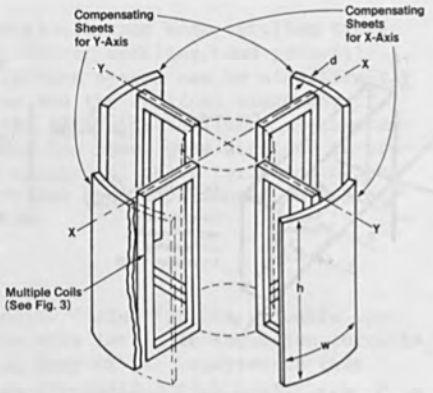

Fig. 6. Toroidal deflection yoke with compensating sheets.

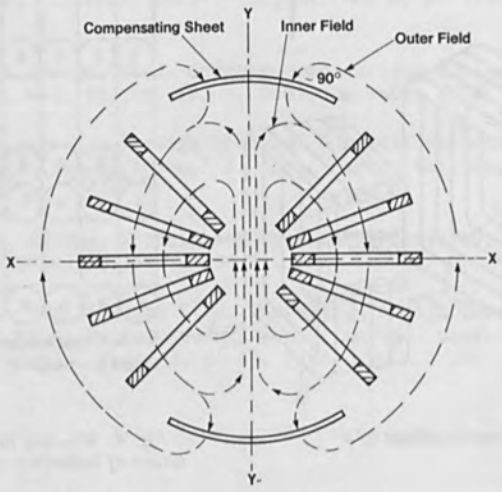

Fig. 7. Complete set of x-deflection windings and associated compensating sheets.

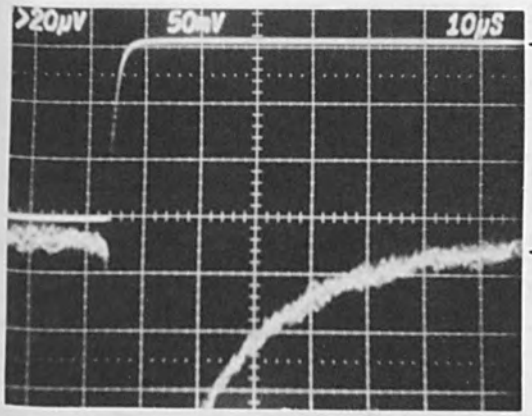

← Yoke current

← Deflection field with eddy current drag

No compensation

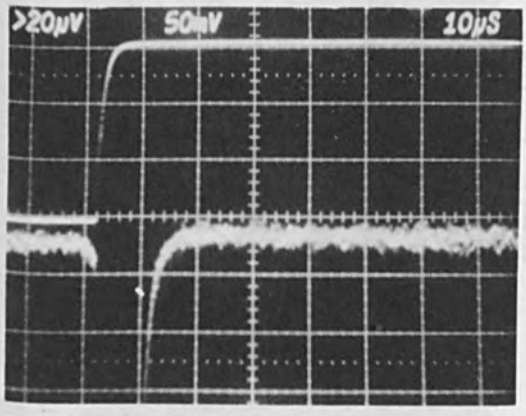

Over compensation

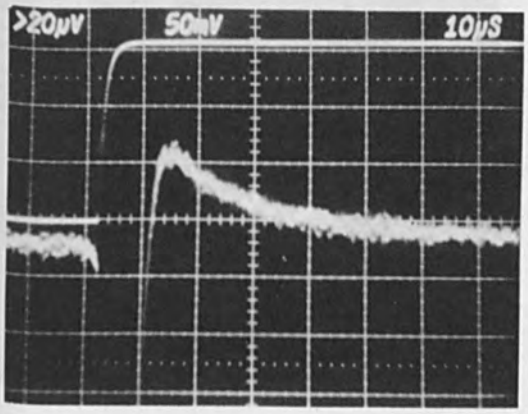

Proper compensation

Fig. 8. Scope traces showing deflection field settling times.

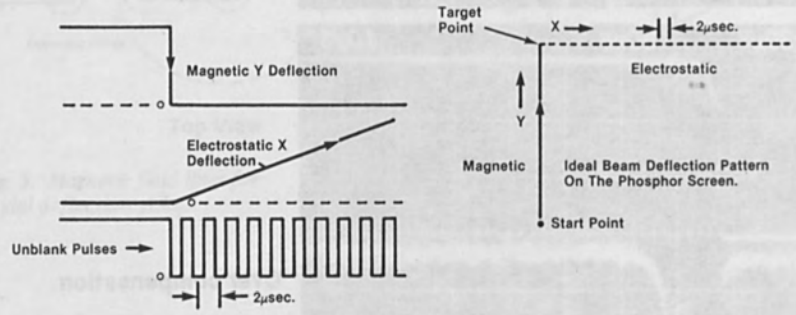

Fig. 9. Experimental method to measure magnetic deflection time.

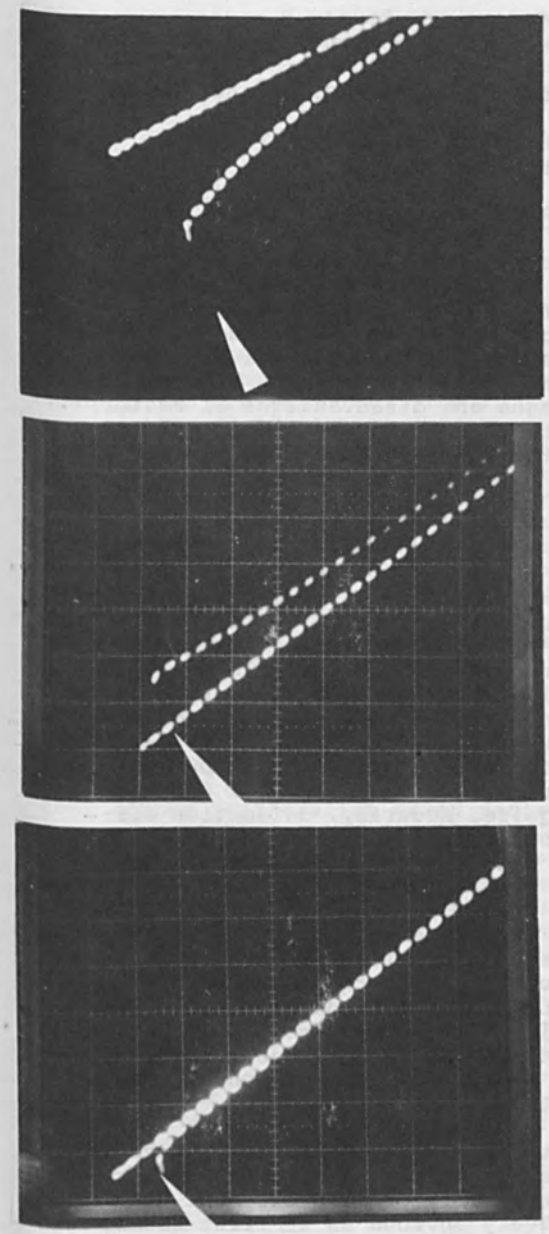

(A)

No compensation
800μm step

Scale: 8 dots = 75μm
2μs dot to dot
(Same in all 3 photos)

(B)

Over compensation
2500μm step

(C)

Proper compensation
2500μm step

Fig. 10. E-beam traces showing effects of compensating foil on beam settling time.

ELECTRON BEAM DEFLECTION; THEORETICAL AND PRACTICAL LIMITS OF PERFORMANCE

O. C. Woodard, C. T. Ho

IBM Data Systems Division - East Fishkill
Hopewell Junction, NY 12533

ABSTRACT

Electron-Beam lithography systems are ultimately limited in accuracy by the performance of the analog deflection systems. To achieve the desired pattern accuracy, tradeoffs must be made which limit field sizes and writing speeds. In this paper, the analog error sources are examined theoretically, and practical ways of minimizing these errors are presented. The advantages and disadvantages of raster, vector, and other deflection techniques are given. Practical results are given for the EL-1 and EL-2 Electron-Beam Systems.

INTRODUCTION

Electron-Beam lithography is rapidly moving from the laboratory to the manufacturing floor (1). Performance parameters, in addition to its long recognized ability to draw fine lines, are required to make it a viable manufacturing tool. To effectively utilize its resolution capabilities, long term accuracy must be added to allow overlay of patterns written days or weeks before. The utilization of more than one system (for manufacturing throughput requirements) imposes the added requirement of tool compatibility. To achieve the required accuracy, deflection circuit nonlinearity, noise, and drift must be very low and a fast and accurate means of calibration and its verification provided.

Throughput is a prime requirement to keep manufacturing costs low. Direct wafer writing applications require higher throughputs for economic justification than mask writing applications. High throughput implies high writing speeds which require wideband analog deflection circuits. The classic analog circuit bandwidth/accuracy tradeoff is a major consideration in the design of high throughput, high accuracy Electron-Beam systems.

There are many considerations in the design of Electron-Beam systems. However, the deflection techniques used are the basis for overall system architecture. The best technique to use is not intuitively abvious as it first seems.

Impacts on other parts of the system must be studied thoroughly to achieve the desired performance. This paper examines design considerations and constraints that dictate the deflection design chosen and some problems of implementation.

DEFLECTION CIRCUIT REQUIREMENTS

The integrated circuit designer is concerned primarily with the lateral dimensional specifications of lithography tools: field size (chip size), minimum linewidths which can be reliably fabricated, line width tolerances, and pattern-to-pattern overlay errors. To achieve projected levels of integration for the near future, field sizes between five and ten millimeters containing pattern features down to 1μm are required. The ability to write a 1μm line over a 10mm field with linewidth control, placement accuracy, and pattern overlay suitable for fabricating 1μm sized integrated circuit devices may be expressed as 10,000 fabricated lines per field. EL-1 and EL-2 (5) write 2,000 and 4,000 fabricated lines-per-field respectively. To reach 10,000 lines, improvements are required in both the electron optics and the deflection electronics. It is unlikely that one E-Beam system can satisfy all IC designer's requirements for resolution and field size. The capability to write large chip patterns by several fields stitched together by XY table moves should be considered.

Another area of prime concern is tool interchangeability and long term accuracy. Long term stability of the deflection system combined with the ability to frequently calibrate to a standard reference is a necessity (2). The four corner registration makes deflection system stability less of a concern since linear errors are corrected by this technique (3). Nonlinear errors must be corrected for tool-to-tool overlay, but their magnitudes do not drift as rapidly as linear errors. Unregistered writing operations should include a strategy for frequent corrections of linear terms and occasional correction on nonlinear errors.

Integrated circuit manufacturers are concerned primarily with exposure costs. This translates directly to tool costs and throughputs. Since E-Beam tool costs are high, throughput is of major concern. The time required to write a wafer or mask consists of mechanical handling time, registration time, writing time, and XY stage moves between fields. EL-1 is a completely automated tool where handling time, etc. have been reduced to approximately equal the writing time (4); its throughput is 10 wafers per hour. Significant throughput gains can best be made by reducing all significant time components (1). Writing time can be

reduced by decreasing exposure time - using more sensitive resist or higher beam current density. It can also be decreased by reducing the number of spots in the field using larger variable shaped spots (5) or by eliminating unwritten spots (vector scanning) wasted by the raster scanning over blank areas.

Thus range, speed, and accuracy are the three basic requirements of the deflection circuits. The problems and tradeoffs to achieve these requirements are discussed below.

DEFLECTION CIRCUIT PERFORMANCE LIMITS

Figure 1 represents a basic deflection circuit. The object is to force a predetermined current through the deflection yoke winding to deflect the beam to the desired position. The amplifier drives current through the yoke proportional to its input voltage, using the voltage developed across the sense resistor in series with the yoke as negative feedback. The deflection voltage at the amplifier input is produced by a digital to analog converter (DAC) which consists of a number of switchable current sources with relative binary values. The summed current of the selected current sources produces the desired deflection voltage by flowing through a scaling resistor or capacitor. A resistor produces voltage steps as required for a vector system. A capacitor produced voltage sweeps as required for a raster scanning system.

Current sources can be designed to be stable within five parts per million (ppm), resistors to one ppm and capacitors to about five ppm over a small temperature range. Eighteen bit DAC's with a resolution of 1:256,000 and 16 bit accuracy (16 ppm) are available. Amplifier offset stability, which affects field position, can be held to within 1 ppm of full scale. Gain stability, which affects field size, is essentially the stability of the sense resistor and the amplifier feedback resistors.

Table 1 lists EL-2 errors predicted from component specifications after periodic LEARN calibrations have removed initial errors and long term drifts. Cooling air temperature for the circuits is maintained within 0.5°C.

Deflection speed is limited by the bandwidth of the deflection amplifier which must be narrow enough to suppress the noise produced by the DAC's, resistors, and the amplifier itself. A major source of white noise is the shot noise of the current sources. Figure 2 illustrates the shot noise contribution to deflection errors as a function of

bandwidth and current source value. The diagonals are lines of constant noise. Higher current source values are desirable for low noise since the noise increases as the half power of the current. However, design considerations for stability and DAC component matching limit maximum current values. The operating point for EL-1 and EL-2 is 10ma at 200kHz bandwidth, which limits the noise to ± 10 ppm or about ± 0.1μm. Deflection noise measurements on EL-1 and EL-2 systems are close to theoretical values.

DUAL CHANNEL DEFLECTION TECHNIQUES

Dual channel deflection (6) provides writing speed and accuracy which cannot be achieved with a single channel.

The deflection waveform required for the EL-2 raster system to step the beam across the writing field is a staircase (6). Total time per spot is 460 nsec. Of this, 42 nsec. is allowed for stepping, blanking, and applying positional offsets. The remainder is utilized for exposure.

The deflection driver bandwidth necessary to accommodate the 42 nsec. stepping and settling time between spots is 15 MHz. The deflection also has to be able to cover the maximum field size of 8mm. Deflection circuits with a range of 8mm and a bandwidth of 15 MHz would also introduce over 1μm of positional noise to the beam, which is not acceptable.

Since noise passed by an amplifier is proportional to the half power of its bandwidth, noise can be reduced to an acceptable 0.1μm at the expense of reducing the bandwidth to 200kHz. However, such an amplifier will not pass the 460 nsec. steps without severe distortion, so the stepping rate must be reduced accordingly. This means throughput is reduced to about one wafer per hour. Therefore, with single channel deflection, accuracy and speed cannot be achieved simultaneously.

In EL-2, this accuracy/speed tradeoff dilemma is solved by using dual channel deflection (Figure 3). The magnetic deflection/channel provides the 8mm range and the electric deflection provides the speed.

With this combination, it is possible to use a magnetic deflection driver with a bandwidth of only 200kHz and noise levels under 0.1μm. The electric deflection provides the 15 MHz bandwidth necessary for high speed stepping and positional offsets. It only requires a 25μm range so its relatively low signal-to-noise ratio does not add appreciable noise to the beam position. This dual channel concept

makes possible a field size of 8mm, a 460 nsec/spot (or faster) stepping rate, and a positional beam noise of only 0.1μm.

RASTER/VECTOR TRADEOFFS

The choice of a deflection system depends on many factors. The repeating raster deflection pattern makes it relatively easy to measure errors and correct them as the LEARN technique (2) does for EL-1 and EL-2. Transient errors caused by electronics, eddy current, hysteresis, etc. are all corrected as well as the linear deflection errors. Dual channel deflection solves the noise problem for both raster and vector. Raster system throughput is independent of pattern coverage as the whole field is scanned. A vector system needs only scan the written areas, but the time required to make the jumps between pattern features becomes large for complex patterns. In a shaped-spot, raster system spot depletion can occur for complex patterns where the number of spots required in a given area exceeds the number available. A vector system utilizes as many spots as required before moving to the next pattern element. Vector systems have an inherently simpler data format which defines pattern elements as dimensional geometric shapes at a given field location. This makes it easier to utilize hardware for expansion of pattern data from shape definitions to individual spot definitions required to generate deflection control signals.

Throughput depends on pattern parameters and the capabilities of the electron optics, as well as the deflection system specifications. The throughput advantages of shaped-spot systems with dual channel deflection systems have been shown (7). To compare raster and vector scanning fairly, we analyzed systems with computer simulations of writing using actual pattern data. The comparison results were very dependent on pattern complexity and coverage. A simplified analysis of the effect of pattern complexity can be shown by using a checkerboard pattern which covers the writing field. Reducing the size of the squares results in their number increasing while the pattern coverage remains constant.

Consider raster and vector systems utilizing shaped spot optics, dual channel deflections, and comparable in every way except for the deflection technique. Table 2 lists the parameters used for the analysis. The independent variable used is the number of pattern elements (checkerboard squares). As the number (N) increases, their size and

spacing decrease as the square root of N. The actual writing time remains constant for both raster and vector, since the area to be written remains constant. However, the total vector step time (T) increases as shown by the equation of Table 2, even though the steps get smaller.

The curve of Figure 4 shows that for small numbers of pattern elements, the vector system is faster because the raster system wastes half its scan time. As the number of elements increases, the total vector time eventually exceeds the raster time. For this simple checkerboard case, the crossover point is at 100,000. If the pattern coverage were reduced to 25%, the crossover moves up to 160,000. The conclusion drawn from this analysis is that for high levels of integration, such as 128 or 256kbit memory chips, the raster system may be faster. However, an analysis using the actual patterns involved should be done.

SOME PRACTICAL CONSIDERATIONS

The deflection yoke must handle the bandwidth required to achieve the desired deflection speed (8). To first order, the deflection yoke windings are considered inductors. However, parasitic capacitances of the windings cause some difficult drive problems. Parallel and series resonances are a serious problem if they occur at frequencies within the bandwidth required to achieve the desired deflection speed. The phase shifts and peaks which occur at the resonance points make it difficult to stabilize the amplifier feedback loop which controls yoke current. Compensation techniques which stabilize the amplifier, such as damping resistors across the windings, do not solve the basic problem of controlling the current through the yoke at high frequencies. The only practical solution is to design the yoke for resonant frequencies above the highest deflection frequency of interest. Another problem is capacitive and inductive coupling between windings. X and Y deflection amplifiers are coupled together, creating other difficult stability and control problems.

Eddy currents can produce undesirable deflection transients. Dynamic magnetic fields produced by the yoke induce eddy current transients into nearby conductive materials. These eddy currents produce fields which oppose the yoke deflection fields, causing deflection errors. Eddy current transients can last for many microseconds, making it impossible to position the beam quickly to a desired location. The use of low-conductivity magnetic materials for lens parts and for yoke shielding is a key solution. Another is the replacement of solid conductive parts with plated insulators.

Eddy currents within the yoke windings themselves are reduced by making the cross-sectional area of individual conductors small (stranded wire) or by using compensation techniques (8).

System wiring, grounding, and shielding must be designed for minimum position and amplitude noise on the beam. The same practices used for high quality instrumentation apply to the deflection and other sensitive circuits. The physical layout of the systems and routing of cables must minimize pickup of unwanted signals. Ground current coupling is minimized by single point grounding and the use of optical isolators between the digital and analog portions of the system. High frequency ground loops closed by inductive and capacitive coupling must be considered as well as the physical ground wire connections.

Temperature control of sensitive components is required to achieve the required long term stabilities for overlay of patterns on wafers and mask writing. In EL-1 and EL-2 a temperature control unit is used which maintains the temperature of the analog unit to $\pm$ 0.5°C. Periodic calibrations are still required to remove long-term drifts.

EL-1/EL-2 SYSTEM RESULTS

Table 3 shows EL-2 performance results consistent with deflection design predictions. The nonlinearity errors of the deflection circuits and yoke combined were $\pm$ 8μm. After calibration by the LEARN technique the deflection error was reduced to 0.2μm, which is the total of reference grid errors and uncorrectable beam noise of $\pm$ 0.1μm. Pattern placement errors of $\pm$ 0.25μm include the deflection error after calibration, beam shaping, and offset. Overlay test results of $\pm$ 0.6μm are close to the predicted overlay found by combining the registration error with the deflection errors.

Figure 5 is a plot of overlay errors measured on a wafer written by an EL-1 machine. The four plots represent the four corners of each 5mm chip where overlay was measured. All 86 chips on the wafer were measured and errors were plotted. In this case, all errors are within $\pm$ 0.4μm. The scatter of the points, which gives a good indication of random deflection noise, is 0.17μm, 3 sigma. The mean of the errors, indicated by offsets in the groupings of parts, illustrates drifts and registration errors.

SUMMARY

Reliable prediction of deflection circuit performance at the design stage is required because reliable test results are not available until an Electron-Beam system is operational. Major engineering changes at that point would be costly since the deflection technique affects the whole system architecture. Rigorous application of basic design principles and deflection technique analysis including simulation of pattern writing using real pattern data can optimize system design and reliably predict performance. Good engineering practices and careful attention to detail in implementation will minimize eddy current transients, electromagnetic interference, and other error sources which are not as predictable. EL-1 and EL-2 systems have demonstrated performance equal to or better than their predicted specifications.

REFERENCES

(1) R. D. Moore, "E-Beam Direct Writing in Manufacturing," Proc. Ninth International Conf. Electron and Ion Beam Sci. and Technology, May 11-16, 1980, St. Louis, MO.

(2) M. S. Michail, "Automatic Correction and Monitoring of Deflection Distortion In Electron-Beam Lithography Manufacturing Systems," Proc. of Microcircuit Engineering 1978, Cambridge, England, Cambridge Univ. Pres. 1980, pp. 563-573.

(3) D. E. Davis, R. D. Moore, M. C. Williams, and O. C. Woodard, "Automatic Registration in an Electron-Beam Lithographic System," IBM J. Res. Develop, Vol. 21, p. 498, (1977)

(4) H. S. Yourke and E. V. Weber, "A High-Throughput Scanning Electron-Beam Lithography Syste, EL1, for Semiconductor Manufacture: General Description," Tech. Digest, IEDM, Washington, DC, 1976, p. 431.

(5) E. V. Weber and R. D. Moore, "EL2: A Variable Shaped Spot, E-Beam Lithographic Tool," Proc. 15th Symposium on Electron, Ion, and Photon Beam Technology, May 30, 1979, Boston, MA.

(6) O. C. Woodard, C. T. Ho, M. S. Michail, A. W. Muir, M. C. Williams, "Variable Spot Shape Control Electronics," Ibid.

(7) W. Stickel and H. C. Pfeiffer, "Optics of a Variable Shaped Electron Beam Column," Proc. of Eighth International Conf. on Electron and Ion Beam Sci. & Tech., May 22, 1979, Seattle, Washington, p. 32.

(8) M. A. Sturans and H. C. Pfeiffer, "Design of Compensating High Speed Toroidal Deflection Yokes," Proc. Ninth International Conf. on Electron and Ion Beam Sci. and Technology, May 11 - 16, 1980, St. Louis, Missouri.

TABLE 1

EL-2 Electronic Error Sources

Amplifier and DAC Offset	± 3 ppm
Resistors and Capacitors	± 4 "
Amplifier and DAC Nonlinear Errors	± 1 "
Current Source Shot Noise	± 10 "
Resistor Thermal Noise	± 1 "
Amplifier Input Noise	± 2 "
Digital Resolution	± 2 "
Calibration Accuracy	± 4 "
TOTAL (Root of summed squares)	± 12 ppm

TABLE 2

Raster/Vector Writing Time

(Dual Channel Deflection)

Field Size	8 mm
Variable Spot Size	0 - 4 μm
Spot Time	225 nsec.
Pattern Coverage (Checkerboard)	50%
Number of Pattern Elements	N
Magnetic Deflection Bandwidth	200 KHz
Electric Deflection Bandwidth	15 MHz
Spots in Raster Field	4×10^6
Total Vector Step Time (Settle to .05 μm)	$T = N\left(\frac{0.16}{200\ \text{KHz}}\right)\text{Log}\left(\frac{8\text{mm}}{.05\ \mu\text{m}\sqrt{N}}\right)$

TABLE 3

EL-2 Performance

Field Size	8 mm
Deflection Error Before Calibration	8 μm
Deflection Error After Calibration	0.2 μm
Positional Beam Noise	0.1 μm
Total Pattern Placement Error	0.25 μm
Registration Error	0.3 μm
Predicted Overlay	0.53 μm
Overlay Test Results	0.6 μm

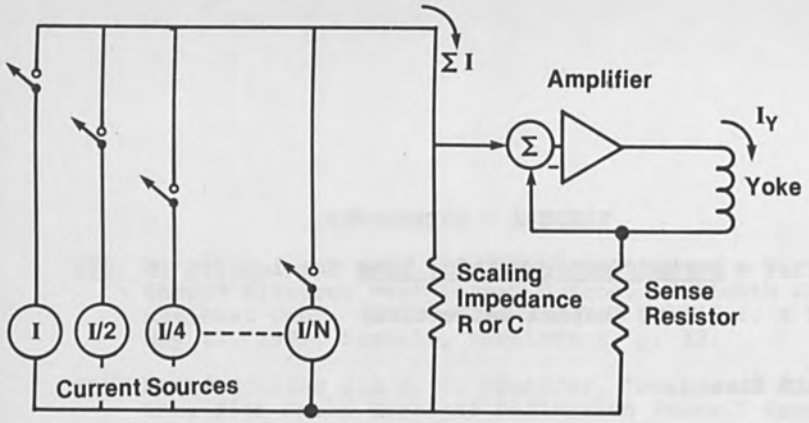

Fig. 1 Basic Deflection Circuit

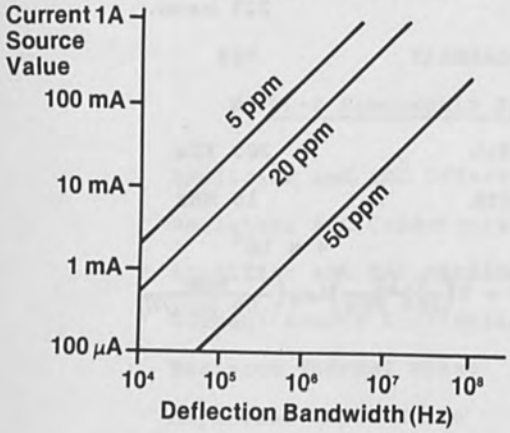

Fig. 2 Shot Noise vs. Bandwidth & Value

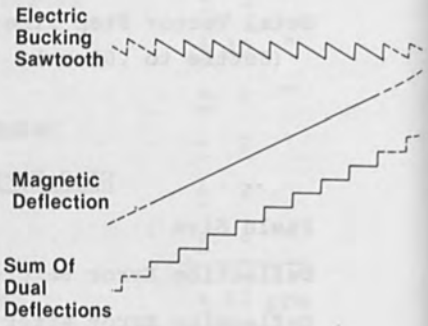

Magnetic Deflection	
Range	8 mm
Speed	200 KHz Bandwidth
Noise ($\sqrt{\text{speed}}$)	0.1 μm
Electric Deflection	
Range	25 μm
Speed	15 MHz Bandwidth (17 Wafers/
Noise	0.02 μm
Total	
Range	8 mm
Speed	15 MHz (10.5 Wafers/Hr.)
Noise	0.1 μm

Fig. 3 Dual Channels Deflection

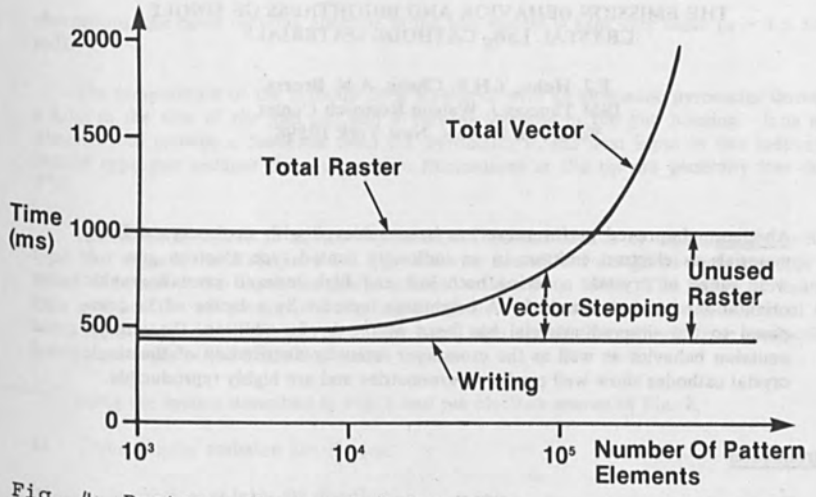

Fig. 4 Raster - Vector Writing Time

Overlay Error Summary		
Direction /Corner	(Micrometers) Mean	3σ
X0	−0.11	0.16
X1	−0.03	0.13
X2	−0.03	0.19
X3	−0.09	0.17
Y0	0.29	0.12
Y1	0.19	0.13
Y2	0.01	0.15
Y3	0.12	0.16

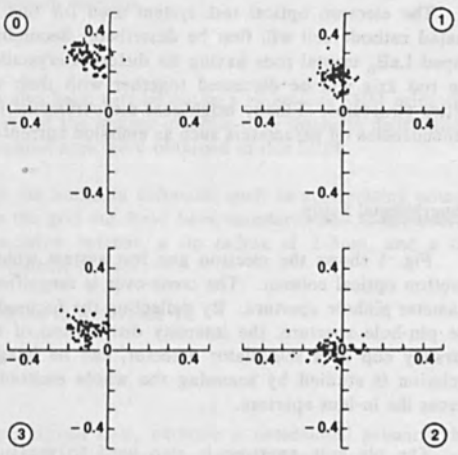

Fig. 5 EL-1 Overlay Data

THE EMISSION BEHAVIOR AND BRIGHTNESS OF SINGLE CRYSTAL LaB_6 CATHODE MATERIALS

F.J. Hohn, T.H.P. Chang, A.N. Broers
IBM Thomas J. Watson Research Center
Yorktown Heights, New York 10598

Abstract: Improved performance has been achieved with single crystal LaB_6 materials as electron emitters in an indirectly heated type electron gun. A wide range of crystals covering both low and high indexed crystallographic orientations has been studied. A brightness increase by a factor of 3x compared to the sintered material has been attained. In addition, the angular emission behavior as well as the cross-over intensity distribution of the single crystal cathodes show well predicted symmetries and are highly reproducible.

Introduction

Electron beam systems such as SEM's or electron beam lithography tools require a highly reliable electron source of high brightness, high stability and long life. Recently the use of single crystal LaB_6 as a cathode material has attracted a great deal of attention[1,2]. This paper will discuss the emission behavior of this type of electron emitter in a thermionic triode electron gun.

The electron optical test system used for this study and the low power indirectly heated cathode cell will first be described. Secondly the emission behavior of conically tipped LaB_6 crystal rods having six different crystallographic orientations with respect to the rod axis will be discussed together with their relationship to their crystallographic lattice structures. Finally brightness measurements for the various orientations and their dependencies on parameters such as emission current and temperature will be presented.

Experimental Setup

Fig. 1 shows the electron gun test system which consists of a one lens magnifying electron optical column. The cross-over is magnified 7.7 times into the plane of a 5μm diameter pinhole aperture. By deflecting the focused beam using deflection coils C_2 over the pin-hole aperture, the intensity distribution of the cross-over, collected by either a Faraday cup or a scintillator detector, can be imaged on a CRT screen. The angular emission is studied by scanning the whole emitted beam with the deflection coils C_1 across the in-lens aperture.

The pin-hole aperture is also used to measure the brightness by the following relationship:

$$\text{Brightness} = \frac{I_c}{A \times \pi \alpha^2}$$

where I_c (Amp) is the current collected through the pin-hole aperture, A (cm^2) is the area of the pin-hole aperture, and α (radian) is the beam semi-convergent angle as defined by the in-lens aperture. In order to minimize errors that may be introduced by the lens

aberrations, the beam defining aperture in the test system is kept very small ($\alpha \sim 1 \times 10^{-5}$ rad).

The temperature of the cathode tip is measured with an automatic pyrometer through a hole in the side of the gun cell and a viewing window in the gun housing. It is not necessary to provide a feedback from the pyrometer to the heat input in this indirectly heated type gun because the temperature fluctuations at the tip are generally less than 5°C.

The electron source in all the experiments reported here is of an indirectly heated type first reported in Reference 4. Fig. 2 shows a modified design of such a source in which the total power input has been reduced to less than 15W. The indirectly heated type gun has the advantage of being highly stable - the cathode rod with a conical tip being rigidly held in a collett type holder - and also avoids the cathode from contacting foreign materials at the high temperature region.

Using the system described in Fig. 1 and the electron source of Fig. 2,

a) the angular emission distribution

b) the cross-over intensity distribution

c) the cathode tip temperature

d) the on axis brightness of the cathode, and

e) the brightness for different emission currents

has been investigated.

Comparative measurements have also been carried out in a three-lens SEM using the technique described in Broers[3]. Several of the images of cross-over intensity distribution and angular emission distribution presented here were obtained in this SEM.

Parameters which can also affect the emission behavior, such as accelerating potential, tip radius, tip position relative to the grid etc. have been standardized. Comparative data are based on 20kV, 200μA emission current, a tip radius of 2-3μm, and a tip placement of 0.2mm underneath the Wehnelt surface.

Part of the results have been reported in Reference 10.

Work Function and Lattice Structure

The emission behavior of a single crystal LaB_6 cathode is determined primarily by two parameters: the work function and the lattice structure of the crystal plane. Data on work function have been published for different crystal orientations. A wide spread of values for the same crystal plane have been measured. This is probably caused by the presence of different amounts of impurities and/or crystal defects. Of the low indexed crystals, the <100> plane appears to have the lowest work function value <2.1 to 2.4eV>[5,6,7] followed by <110> planes and <111> planes with values of approximately 2.6eV[4] and 3.0eV[4], respectively. Sintered materials can be represented by a statistical mean value from the various randomly oriented crystal particles and a value in the range of 2.5eV to 2.9eV[8] has been suggested.

To have a better understanding of the emission behavior, it is also important to analyze the lattice structure. The LaB_6 lattice is formed by two interpenetrating cubic lattices containing six atoms of Boron to one atom of Lanthanum, as shown in Fig. 3. Depending on the direction one views into this lattice, different symmetries will occur: the <110> orientation, the <111> orientation, and the <100> orientation will show a two-fold, three-fold, and four-fold symmetry, respectively. The <210> orientation will have a mirroring symmetry and higher indexed orientations should be without obvious symmetry.

Experimental Results

Sintered vs. Single Crystal Material

Fig. 4 gives general comparison of a sintered cathode to a single crystal cathode. Fig. 4a (top) shows an SEM image of a typical sintered cathode and the corresponding angular emission and cross-over distribution are shown directly below. It can be seen that the angular emission consists of a number of randomly distributed lobes of varying intensities. These lobes are believed to be caused partly by roughness on the cathode surface and partly by presence of crystal particles of random orientations in the tip region as shown by the SEM image. The cross-over intensity at the operating temperature of 1800K is generally round and Gaussian in distribution. But non circularity has also been observed in some cases which is undesirable for probe forming systems.

As a comparison to the sintered material, the SEM image of a single crystal, <100>, cathode is shown in Fig. 4b (top). Because of the homogeneity of the single crystal material, the surface of the cone is smooth and without any irregularities. It can also be seen in Fig. 4b that both the angular emission and cross-over distributions are much better defined as compared to the sintered cathodes. The angular emission is generally more uniform in the intensity distribution with the highest intensity in the center. The cross-over is always round and of Gaussian intensity distribution. The diameter which can vary slightly depending on the actual radius of the tip used is typically less than 10μm at 20kV accelerating potential. In addition, the emission behavior of the single crystal materials is accurately reproducible whereas the emission behavior of the sintered material can vary from cathode to cathode. For a given sintered cathode, the location of the lobes can also vary slowly with time.

A comparison of brightness between single crystal material and the sintered material will be discussed in the following section entitled Brightness.

Emission Behavior of Different Crystal Orientations

The performance of LaB_6 cathodes using single crystal materials of different orientations has been studied experimentally. It has been pointed out earlier that the different crystal planes can have different modes of symmetry. Experimental results show that a dependency exists between the emission behavior and the lattice structure.

<110> Crystal Orientation: In Fig. 5 the cross-over intensity distribution and the angular emission pattern of a cathode with <110> orientation are shown. It can be seen that a two-fold symmetry is apparent in both cases. This is in agreement with the two-fold symmetry of the lattice structure. At low temperatures, the cross-over distribution shows a ring type structure consisting of two symmetrical intensity segments. With increasing temperatures, the two segments shrink concentrically, and at a temperature of about 1800K, a single round spot is formed. This single cross-over has a Gaussian

intensity distribution. A two-fold symmetrical pattern has also been observed for the angular emission of the <110> cathode. This is more apparent at low temperatures. By increasing the temperature, the angular emission gradually merges towards the axis with the peak intensity at the center.

<111> Crystal Orientation: In Fig. 6 the cross-over intensity distribution and the angular emission of a <111> oriented single crystal are shown. A three-fold symmetry is clearly observed which is again in agreement with the symmetry of the lattice structure. At low temperatures, a ring cross-over is formed. With increasing temperatures, the diameter of the ring shrinks concentrically, and at about 1780K, a single spot of 7μm diameter and of Gaussian intensity distribution is formed. The angular emission has a three-fold symmetry distribution and has its intensity maximum in the center. This high intensity should be on the optical axis when cathode and anode are correctly aligned.

<100> Crystal Orientation: Cross-over and angular emission distribution of <100> orientation is shown in Fig. 7 and 8, respectively. Fig. 7 shows the cross-over distributions at different temperatures. A four-fold symmetry is observed in this case which is again in accordance with the lattice symmetry. At low temperatures a ring is formed consisting of four symmetrical side intensities. At higher temperatures (1620K), an additional spot occurs in the center of the ring. This spot also contains the four-fold symmetry when magnified as shown in the lower left hand corner of Fig. 7. At about 1780K, the ring shrinks into a single spot with a diameter of less than 8μm and Gaussian intensity in distribution.

The angular emission of this <100> oriented crystal at different temperature is shown in Fig. 8. The four-fold symmetry is maintained over the temperature range shown, and the total angle of emission decreases with increasing temperature. The center portion becomes more and more intense and at 1780K, a fairly uniform distribution is achieved. It is important to point out that in order to observe the symmetrical pattern of emission shown in this diagram, it is necessary to accurately align the cathode rod axis within $\pm$ 2° in the correct crystallographic orientation.

Brightness Measurements

Brightness measurements have been carried out for single crystal cathodes of six different orientations. Fig. 9 shows the brightness vs. tip temperature for three low indexed single crystal cathodes (<100>, <110>, <111>) and a sintered cathode. All measurements are done at a standard beam potential of 20kV and an emission current of 200μA. It should be pointed out that the brightness values of sintered LaB_6 cathodes can vary considerably depending on the particles which happen to form the tip (see also sintered vs. single crystal material).

In all cases, the brightness increases with increase of temperature. At temperatures higher than 1800K, the curves begin to flatten out towards a saturation value. This flattening of the brightness curves indicates that the performance of the gun in this temperature region is becoming increasingly space charge limited. The work function values listed earlier are represented in the brightness curves of Fig. 9 as follows: the lowest work function (100) crystal plane results in the highest brightness, and the highest work function (111) plane results in lowest brightness values. A brightness value of approximately 3 x 10^6Amp/cm^2.ster. has been measured for the <100> crystal which represents a factor of 3x improvement over a typical sintered cathode.

Fig. 10 shows results of cathodes with higher indexed crystal orientations (<210>, <311>, <321>). It can be seen that a similar brightness vs. temperature characteristic

as shown in Fig. 9 is also obtained. In this group, the <321> orientation has been found to be comparable in brightness to the <100> orientation. So far no value for the work function of this high indexed plane has been reported. The two other orientations - <210> and <311> - gave lower brightness values, and the slope of the curves falls more rapidly at low temperatures.

Using <321> oriented cathode material, brightness vs. temperature measurements have been performed for four values of emission currents as shown in Fig. 11. The results indicate that the brightness at a given temperature increases with increasing emission currents. In addition, the temperatures at which the brightness begins to flatten out increases with increasing emission currents.

An arrow is introduced at each curve to indicate the point at which a single cross-over is formed. This takes place at different temperatures for the different emission currents. For normal operation, it is generally not necessary to operate the gun at a temperature beyond the points indicated by the arrows. Thus one can adjust the temperature of the LaB_6 cathode in accordance with the desired brightness value. This avoids overheating the cathode at low brightness operation, hence increases the cathode lifetime. The curves eventually level off at higher temperatures than those indicated by the arrows. One therefore assumes that at these points, the electron emission of the gun is still only partially space charge limited.

The general behavior of the brightness vs. tip temperature at different emission currents as shown in Fig. 11 has also been obtained for other crystal orientations. All brightness values measured, of course, are influenced by the exact tip geometry and also by rod axis deviations off the correct crystal orientations.

Conclusion

LaB_6 single crystals of <100>, <110>, <111>, <210>, <311>, and <321> orientations have been studied as an emitter in a thermionic electron gun. Measurements on cross-over, angular emission and brightness for these crystals have been performed.

As expected from the LaB_6 lattice structures, the occurrences of two, three, four-fold, and mirroring symmetries in angular emission and cross-over intensity distributions are observed in <110>, <111>, <100>, and <210> oriented single crystals, respectively. These distributions are accurately reproducible and give a much higher degree of homogeneity at higher temperatures as compared to sintered materials. For 20kV and 200μA emission current at about 1800K, a single cross-over is formed which is approximately round, of 7μm diameter, and has Gaussian intensity distribution.

Since the tip radius of the cone can be repeatedly produced in the range of 2-3μm, brightness values for a given orientation can be accurately reproduced. Repeatedly the highest brightness was measured for the <100> orientation, and a value of $3 \times 10^6 A/cm^2$ sterad have been achieved. This represents an increase of a factor of about three compared to the sintered material. Though the other single crystals studied gave brightness values higher than the sintered material, they are generally below that of the <100> orientation. Therefore, the preferable LaB_6 cathode material is a single crystal of the <100> orientation.

Depending on the required electron gun brightness, an optimum temperature can be set to form a single cross-over. The point at which this is formed depends on the

emission current used, and higher brightness can be achieved by increasing both the temperature and the emission currents.

REFERENCES

1. P.H. Schmidt et al., Appl. Phys. Lett., 29, (400) 1979.
2. C. Oshima, M. Aono et al., J. Appl. Phys., 51, (1201) 1980.
3. A.N. Broers, J. Vac. Sci. Technol., 16, (1692) 1979.
4. A.N. Broers, J. Appl. Phys., 4, (1991) 1967.
5. L.W. Swanson, T. Dickinson, Appl. Phys. Lett., 28, (578) 1976.
6. M. Aono et al., J. Appl. Phys., 50, (7) 1979.
7. H. Yamanchi et al., Appl. Phys. Lett., 29, (638) 1976.
8. H. Ahmed, A.N. Broers, J. Appl. Phys., 43, (2185) 1972, further ref. therein.
9. C. Oshima et al., J. Appl. Phys., 48, (3925) 1977.
10. F.J. Hohn, T.H.P. Chang, A.N. Broers, Proc. Confer. on Microcirc. Engin., Aachen, 1979.

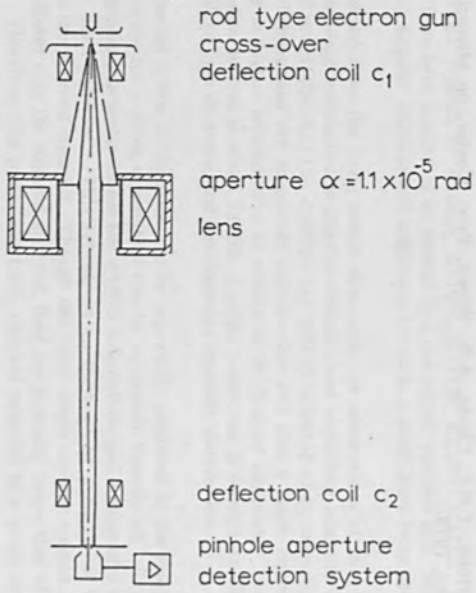

Fig.1: Experimental arrangement for electron gun testing

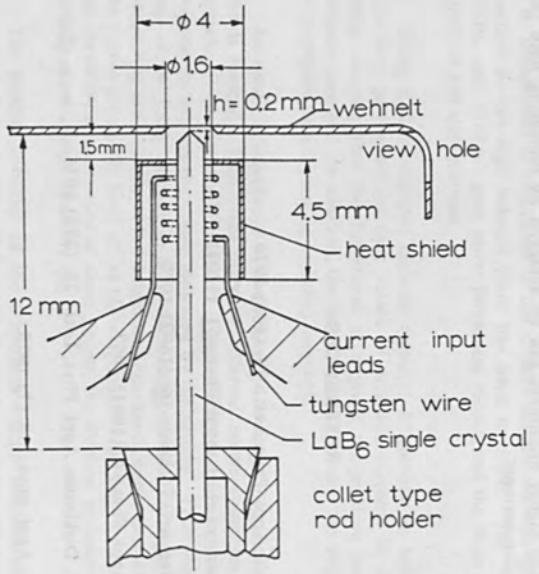

Fig.2: Cross section of indirect heated type LaB_6 gun for low power input

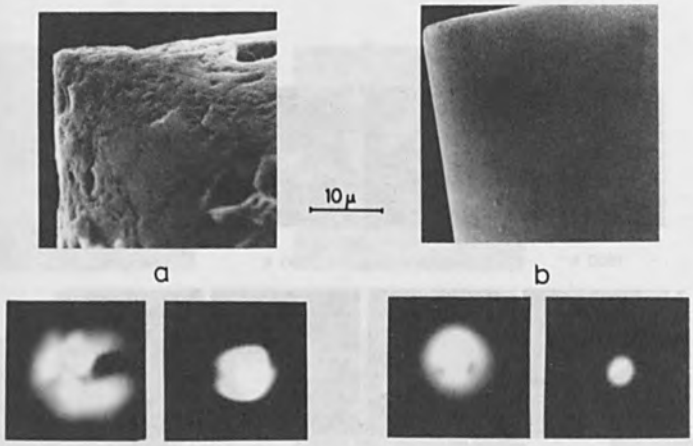

Fig.3: Angular emission and cross-over distribution for a) sintered LaB_6, b) <100> oriented single crystal cathode

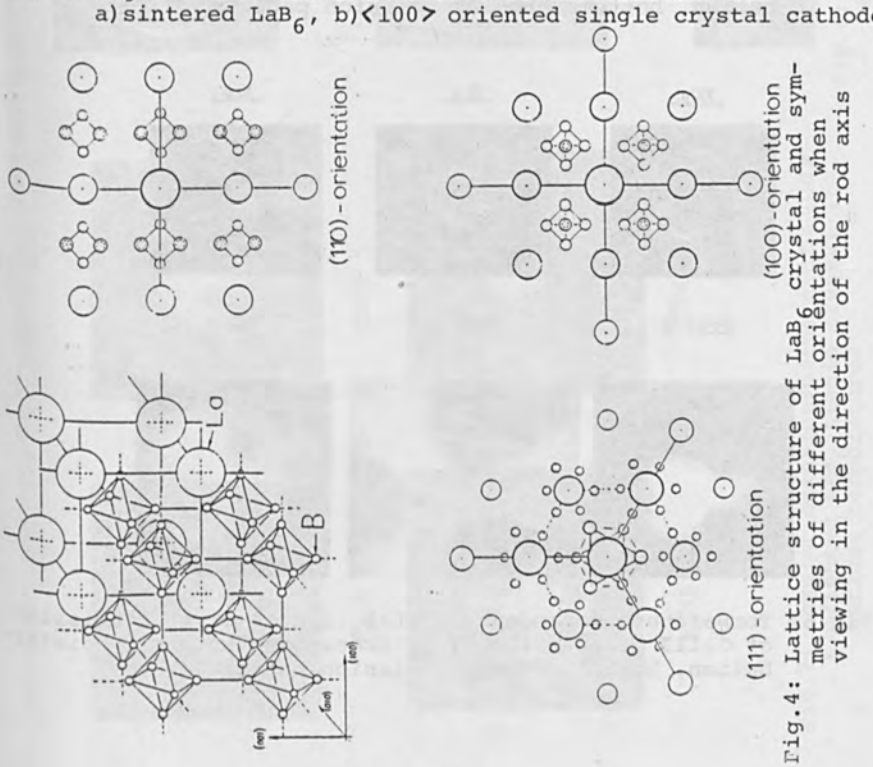

Fig.4: Lattice structure of LaB_6 crystal and symmetries of different orientations when viewing in the direction of the rod axis

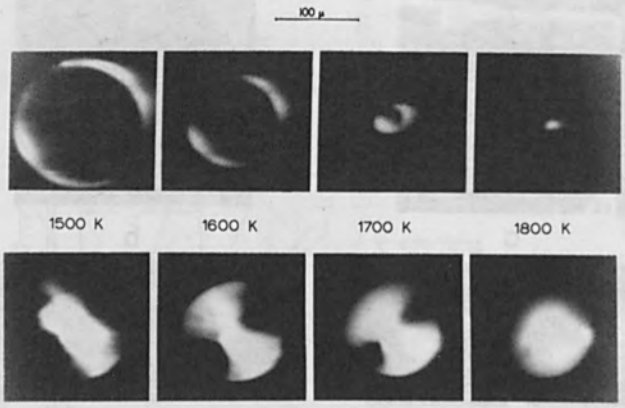

Fig.5: Temperature dependence of LaB_6 single crystal emission of <110> orientation. Top: Cross-over intensity distribution, bottom: angular emission pattern

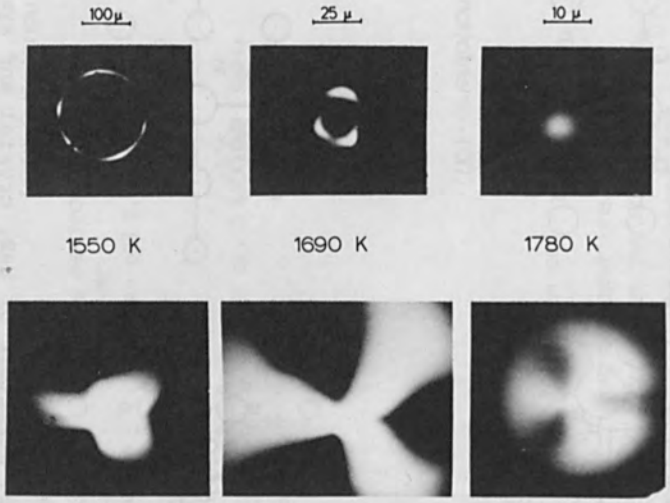

Fig.6: Temperature dependence of LaB_6 single crystal emission of <111> orientation. Top: Cross-over intensity distribution, bottom: angular emission pattern

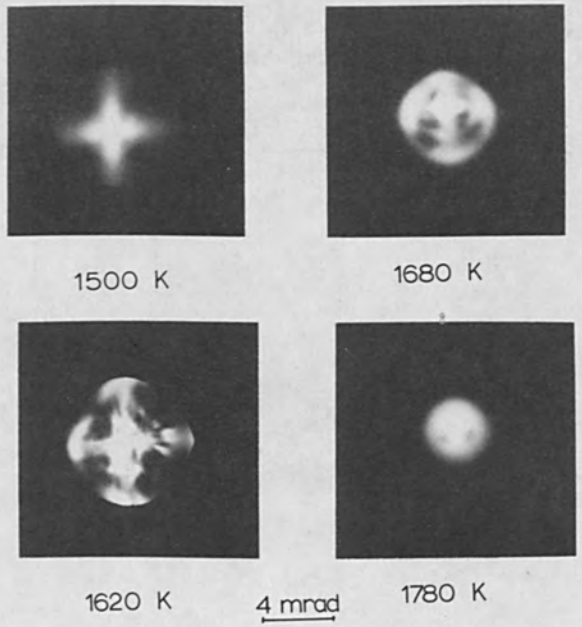

Fig.7: Angular emission pattern of <100> oriented LaB_6 single crystal at various temperatures

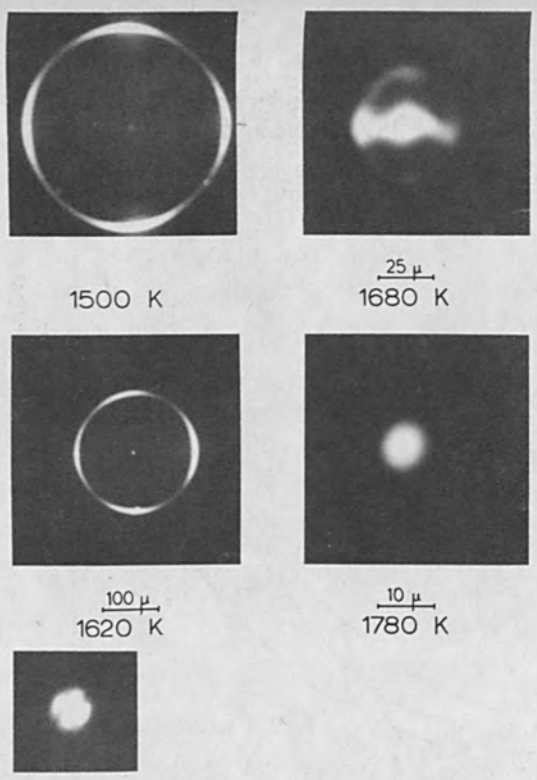

Fig.8: Cross-over intensity distribution of <100> oriented LaB_6 single crystal at various temperatures

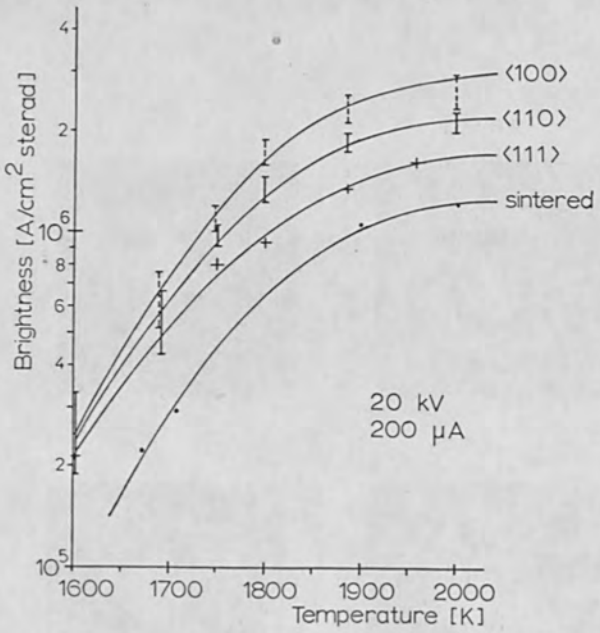

Fig.9: Brightness vs. tip temperature measured from various LaB_6 single crystal- and asintered cathode

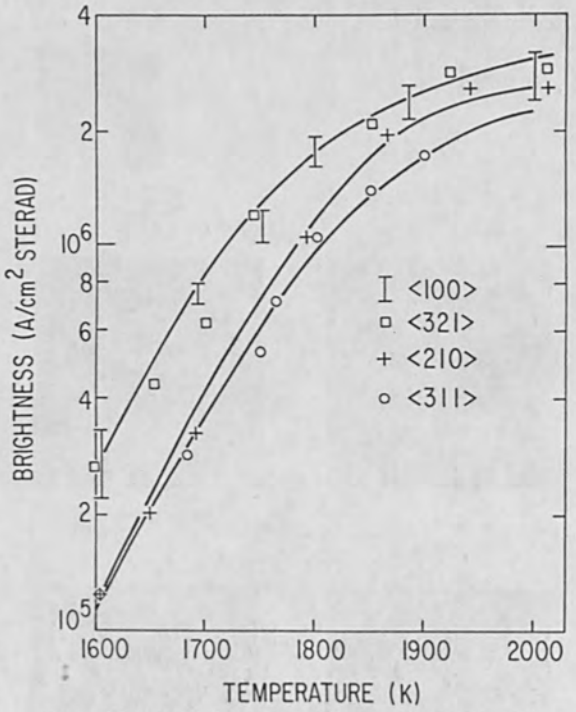

Fig.10: Brightness vs. tip temperature from LaB_6 single crystal cathodes of different orientations

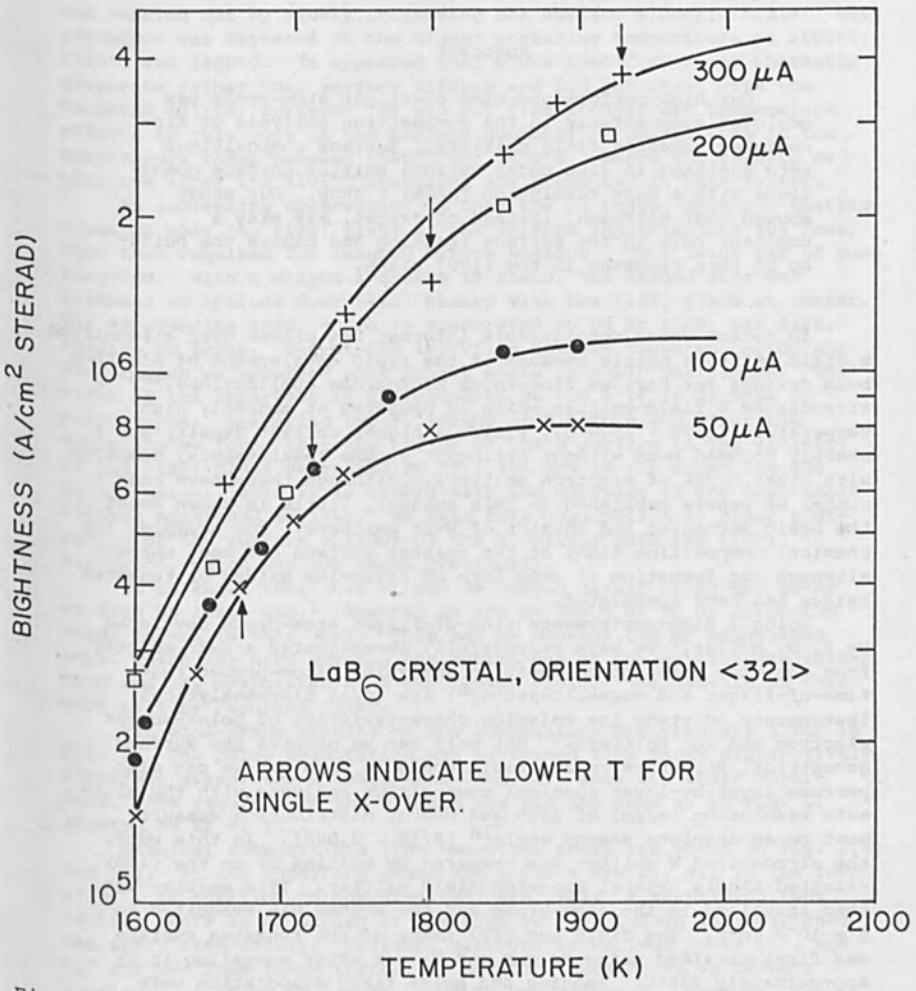

Fig. 11: Brightness vs. tip temperature for different total emission currents

TIME-OF-FLIGHT ATOM-PROBE STUDY OF A W-Zr FIELD EMITTER

Toshio Sakurai and Y. Kuk
Department of Physics
The Pennsylvania State University
University Park, PA 16802 USA

Abstract

Our high-performance time-of-flight atom-probe was employed successfully in the composition analysis of zirconiated tungsten field emitters. Surface compositions were analyzed in situ under various emitter surface conditions with a mass resolution ($m/\Delta m$) $\gtrsim$ 2000. Our study showed that nitrogen, instead of oxygen, may play a dominant role in the surface reaction and causes the build-up of pure tungsten in the (100) plane.

In recent years considerable interest has arisen over zirconiated W field emitters mainly because of the rapid development of electron beam devices for various fine-focus microprobe applications.[1-6] A zirconiated W field emitter which is operated at modestly high temperature (1100 ~ 1500°C), yields a higher current density and a sharply focused beam without stringent vacuum requirements, compared with other types of electron emitters. Although there have been a number of papers published on this subject, little is known about the basic mechanism and physics of W-Zr emitters. For example, the chemical composition right at the emitter surface has been unknown although the formation of some form of zirconium oxides or tungsten oxides has been speculated.

Using a high-performance time-of-flight atom-probe developed by E. W. Müller,[7] we have successfully investigated a W-Zr emitter from the view point of composition analysis. Atom-probes (both time-of-flight and magnetic-sector[8]) are ideal microanalytical instruments to study the emission characteristics of point-source electron and ion emitters.[9] Not only can we observe the surface geometrical structure on an atomic scale in situ but we can also perform layer-by-layer chemical composition analyses with the ultimate resolution ($m/\Delta m$) of 2000 and energy distribution measurement on an absolute energy scale[10] ($E/\Delta E$ ~ 2,000). In this work, the zirconiated W emitter was prepared by coating Zr on the <100> oriented single crystal tungsten field emitter. This emitter was then installed in the atom-probe and the system was evacuated to 5×10^{-9} Torr. The field ion (FI) image of the tungsten surface was first obtained using He gas and H_2 gas after annealing it at approximately 900°C. Imaging and pulse field evaporation were carried out at 78 K emitter temperature. Annealing at 900°C is low enough not to cause the diffusion of Zr. The pulse-field evaporation

of this surface yielded only tungsten atoms in form of W^{3+} and W^{4+}. No Zr signals were found from this original surface. Figure 1 is the histogram of signals. Many He^+ signals from this surface are due to He adsorbed on the clean W surface as reported previously.[10]

This emitter was subsequently heated in vacuum (1×10^{-8} Torr) at 1000°C for five minutes and the surface composition analysis was carried out by slowly increasing the surface electric field. This procedure was repeated at the higher annealing temperature at 1100°C, 1200°C and 1400°C. It appeared that above 1500°C Zr atoms thermally evaporate rather than surface diffuse and did not react with the tungsten emitter surface. We did not find significant temperature effects in this work on the surface geometry or composition in the temperature range between 1000°C and 1400°C. Hence the results we obtained after the 1100°C annealing are presented in this letter.

An increasing observation is that the FI image, upon the heating, appeared near the (100) plane at the voltage approximately 30% lower than that required for imaging before heating. This image was of pure tungsten. With a slight increase in field, the imaged area was extended to include four (110) planes with the (100) plane at center. The surrounding area, which is speculated to be Zr rich, was dark, showing no image. And at the interface between tungsten region and dark region we observed many bright spots randomly positioned. The width of the interface is estimated to be ~50 Å ($\pm$ 20 Å) from Fi micrographs. Comparing two Fi images of W before and after the annealing we found that the radius of the W surface in the vicinity of the (100) plane decreased by 25 ~ 30% due to the annealing and Zr diffusion. This is in accord with the decrease of the best image voltage mentioned earlier. We take this observation as clear indication of the surface buildup of the W emitter into the (100) direction, which was not known previously.

It is known that pure Zr can be imaged nicely using Ne, He-He or even He image gas.[1] However we see no image of Zr or zirconium oxide layers in this work. This may be because the Zr associated layer which may have covered the entire cap of the emitter was rather thin and was evaporated at a much lower field. The details of this work will be reported later.

The atom-probe results on the composition analyses are given in Fig. 2. The pulse evaporation was performed from three distinctively different areas; the W image area, the dark area and their interface. The result from the W image are was the same as in Fig. 1, showing no Zr at all.

Chemical compositions from two other areas are shown in Fig. 2(a) and (b). At the interface there are quite a few Zr, all in the form of Zr^+, in addition to tungsten (W^{3+} and W^{4+}). A surprising fact is that there is no oxygen in any form at all, though its existence was speculated widely. Instead, nitrogen in various forms (N^+, and N_2^+ and WN^{3+})was found there. At the dark area which we thought consisted of thick Zr layers, some Zr was detected. However, the dominant species was again nitrogen, many as a pure element, N_2^+ and N^+, and some as tungsten nitride (WN^{2+} and WN^{3+}) and zirconium nitride (ZrN^+ and ZrN_2^+). The composition change across the interface was

studied and shown in Fig. 3. It is striking that the abundance of Zr is not more than 2% even in the Zr rich region (dark area) while the amount of nitrogen reaches almost 70%. This nitrogen must have been trapped from the ambient gas phase by a thin Zr layer.

In order to ascertain this unexpected result, two additional annealings were performed each at 1100°C for 10 minutes in the presence of oxygen (3×10^{-6} Torr) and nitrogen (6×10^{-6} Torr), respectively. In the case of oxygen exposure, we have indeed found some oxygen in the form of O^+_2 and O^+, ArO_2^+ and ZrO^+, and WO^{3+}. These amount to approximately 40% of the total signals. Many (~75%) of them were zirconium oxides, and pure oxygen was a relatively rare species (~6%). However the rest of the signals (~60%) were found to be associated with nirogen, although a small amount of signals were W^{3+} and Zr^+ (~6% each). Among the signals associated with nitrogen, approximately 65% were pure nitrogen, N_2^+ and N^+, and the rest were ZrN^+ and WN^{2+}.

When this emitter surface was exposed to nitrogen during the annealing, we found no oxygen associated signals at all. More than 65% were N^+_2 and N^+ while there were some nitrogen compounds, such as ZrN^+ (~4%) and WN^{2+} (~18%) and a small amount of (~5%) of pure Zr^+ and W^{3+}. In both cases, the buildup of the (100) surface, mentioned earlier in this letter, was observed. It seems evident based on these results that nitrogen, instead of oxygen, plays a most important role for a zirconiated W emitter. Because of the qualitative nature of the present data, it is rather difficult to pinpoint the underlying mechanism of the buildup. We, however, suggest that a large amount of nitrogen trapped by thin Zr films on the W emitter react with the tungsten substrate and prompts the buildup towards the cap of the emitter. This, in return, enhances the effective surface electric field and thus higher electrons emission. This mechanism is not contradictory with the field emission characteristics reported in the past. The stability and long lifetime of the W-Zr emitter are likely due to the continuous replenishment of the W buildup due to high temperature and field during the electron emission mode.

This work was partially supported by a grant from Exxon Research and Engineering Company.

REFERENCES

1. J. J. Carroll and A. J. Melmed, Surf. Sci. 58, 601 (1976).
2. J. E. Wolfe, J. Vac. Sci. Technol. 12, 1169 (1975).
3. L. A. Fontign, J. Vac. Sci. Technol. 15, 1053 (1978).
4. L. W. Swanson and N. A. Martin, J. Appl. Phys. 46, 2029 (1975).
5. F. Okuyama, Surf. Sci. 43, 293 (1974).
6. L. W. Swanson, J. Vac. Sci. Technol. 12, 1229 (1975).
7. E. W. Müller, CRC Critical Reviews in Solid State Sciences 6, 85 (1976).
8. R. J. Culbertson and T. Sakurai, J. Vac. Sci. Technol. 15, 1752 (1978).

9. T. Sakurai, R. J. Culbertson and G. Robertson, Appl. Phys. Lett. 31, 11 (1979); T. Sakurai, CRC Critical Reviews in Materials Science.
10. R. J. Culbertson, T. Sakurai and G. H. Robertson, Phys. Rev. B19 4427 (1979).

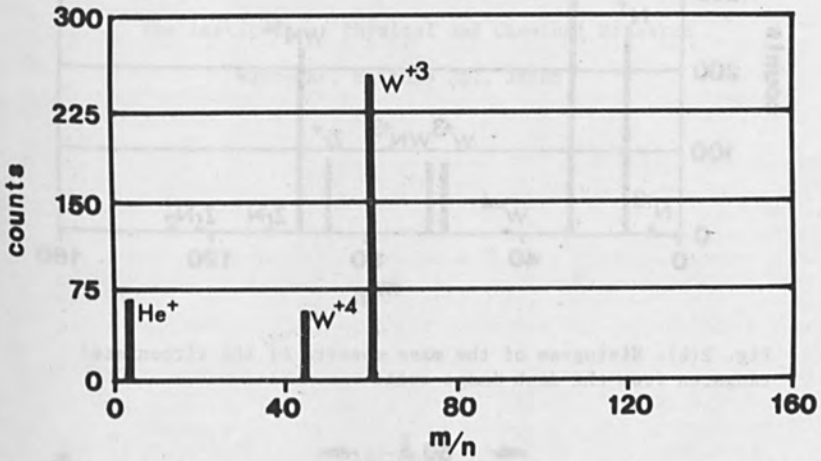

Fig. 1. Histogram of the mass spectra of tungsten with ZrH_2 before heating.

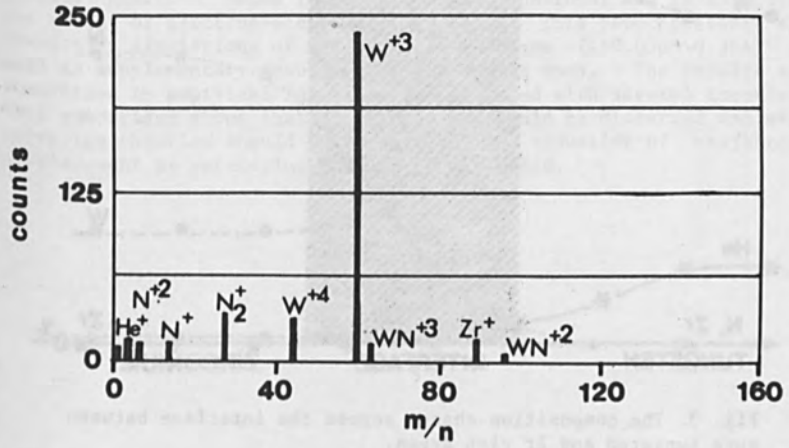

Fig. 2(a). Histogram of the mass spectra of the zirconiated tungsten from the interface area.

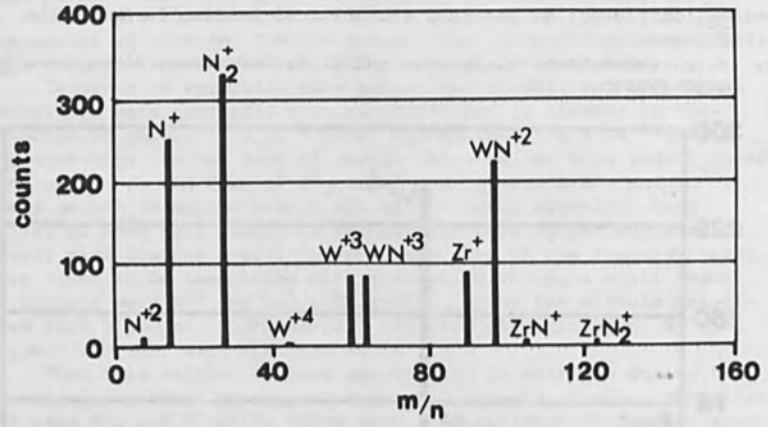

Fig. 2(b). Histogram of the mass spectra of the zirconiated tungsten from the dark image area.

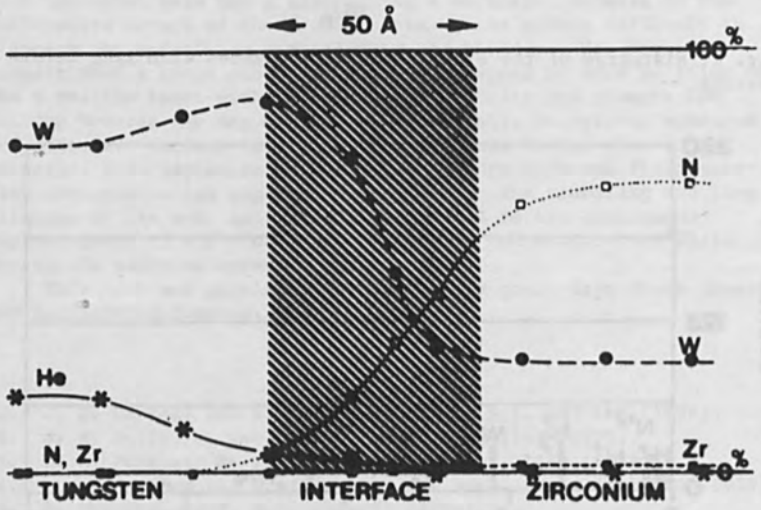

Fig. 3. The composition change across the interface between pure tungsten and Zr rich areas.

EFFECT OF ELECTRON-ELECTRON INTERACTION IN COMPUTER SIMULATION

Tateaki Sasaki

The Institute of Physical and Chemical Research

Wako-shi, Saitama 351, Japan

ABSTRACT

At the conference on VLSI held at CALTEC in January of 1979, the present author reported some results of computer simulations of high density electron beams (beam current $I \simeq 0.5\mu A \sim 10\mu A$) and investigated the effect of electron-electron interaction. This paper presents the results of simulations of medium density beams ($I \simeq 0.03\mu A \sim 0.3\mu A$) as well as supplementary results to the previous ones. The results are summarized in empirical formulas and compared with several theories. This comparison shows that some theories should be discarded and even surviving theories should be improved. The reduction of trajectory displacement by refocusing is also investigated.

§1. Introduction

In 1954, Boersch revealed that the energy distribution of electrons in electron beams was broadened [1]. This effect, which is called the Boersch effect, brought many researchers' attention to the Coulomb interaction among beam electrons. This interaction is often called the electron-electron interaction. The studies before 1970, which were summarized in [2] by Zimmermann, were concerned mainly in broadening of energy distribution, and were motivated by an academic interest in the effect of electron-electron interaction.

Recent development of electron exposure systems for LSI and VLSI fabrication made researchers revisit the electron-electron interaction. According to Loeffler and Hudgin [3], the electron-electron interaction causes a trajectory displacement Δr, an energy change ΔE, and an angular change $\Delta\alpha$ for each beam electron. These effects are negligible for many electron probe systems such as electron microscopes because of a small beam current. A large beam current is, however, a key to attain a high exposure speed in many electron exposure systems. Some systems using large beam currents are described in [4], [5], [6], [7], and Pffeiffer surveyed such systems in [8]. In such a system, the electron-electron interaction is never negligible. In particular, the trajectory displacement is often a serious problem.

Many theoretical attempts have been made to analyze the effect of electron-electron interaction [2], [9], [10], [11], [12]. These studies treated electron beams forming crossovers because crossovers are formed in most practical beams. However, there are two factors which make theoretical analysis quite difficult: one is that the problem ia a many-body problem and the other is that actual beam geometries are quite complicated. These reasons stimulate us to simulate phenomena by computers and study the effect computationally. In fact, such studies are quite popular in plasma physics, etc.

The number of computational studies of the electron-electron interaction is quite few at present. Except for a work of the present author [13], the author knows only the works of Loeffler [10] and Loeffler and Hudgin [3]. Their works cannot, however, be considered as performing computer simulations, although they used a computer to estimate the effect of stochastic Coulomb interaction among beam electrons. On the other hand, in [13], the electrons were traced with a small time step from a gun to a screen. This work made the author recognize the usefulness of computers in studying the electron-electron interaction.

This paper has two aims. One is to present the results of simulations of medium density beams as well as some results which supplement the previous results of simulations. The other is to compare several theoretical formulas with our empirical formulas. This comparison will show that some formulas should be rejected and even surviving formulas should be refined further.

§2. Survey of the simulation method

The non-relativistic equation of motion of the i-th electron in a group of electrons being acted by an external force $\mathbf{F}_{ext}$ is

$$(1) \qquad m_e \ddot{\mathbf{r}}_i = \mathbf{F}_{ext} + \frac{e^2}{4\pi\varepsilon_0} \sum_{j\neq i} \frac{\mathbf{r}_i - \mathbf{r}_j}{|\mathbf{r}_i - \mathbf{r}_j|^3}, \quad i=1,2,3,\cdots,$$

where m_e is the electron mass, and $\mathbf{r}_j$ is the coordinate vector of the j-th electron. The second term in the right hand side represents the electron-electron interaction. Our problem is to determine the electron trajectories by using the above equation of motion.

Since we are interested in electron beams forming crossovers, we assume the $\mathbf{F}_{ext}$ is caused by a uniform coaxial magnetic field $\mathbf{H}=(0,0,H)$ acting as a focusing field. Electrons emitted randomly from an electron gun and accelerated to an average velocity $\bar{\mathbf{v}}=(0,0,\bar{v})$ are focused by this field with a focal length

$$(2) \qquad f = \frac{\pi m_e \bar{v}}{eH}.$$

Furthermore, the electrons are assumed to have a Maxwellian energy distribution with a temperature T at the first crossover just in front of the gun. We simulate only round beams having random electron distributions at the first crossover. Figure 1 illustrates typical beam geometries considered in our simulations.

The motions of electrons emitted are traced by a time step $(L/\bar{v})/n$, where L is the beam length and n is the number of total time steps which are necessary to move an electron from the gun to the screen. A typical value of n is 1000. At every time step, the motion of each electron is first determined analytically by using the focusing magnetic field and then corrected by calculating Coulomb forces between the electron and the nearest 2m electrons. A typical value of m is 50. Thus, we are treating the electron-electron interaction as a perturbation. The unperturbed trajectory is the one determined by $\mathbf{F}_{ext}$.

When an electron reaches the screen, we compare the electron motion with its unperturbed motion and calculate the trajectory displacement $\Delta\mathbf{r}$ and the energy change ΔE. Since we are simulating motions of many electrons emitted randomly, we can obtain distributions of the trajectory displacement and the energy change. These distributions allow us to calculate the average trajectory displacement $\langle|\Delta\mathbf{r}|\rangle$ and the average energy change $\langle|\Delta E|\rangle$ as well as their variances $\sqrt{\langle|\Delta\mathbf{r}|^2\rangle}$ and $\sqrt{\langle|\Delta E|^2\rangle}$. The accuracy of these quantities are estimated to be about 5%. Figures 2.1 and 2.2 show examples of distributions of $\langle|\Delta\mathbf{r}|\rangle$ and $\langle|\Delta E|\rangle$. For details of our simulation method, see [13]. Note that $\langle|\Delta\mathbf{r}|\rangle$ and $\langle|\Delta E|\rangle$ are quantities used in most theories but they have slight differences from experimentally measured quantities $\Delta r_{1/2}$ and $\Delta E_{1/2}$.

§3. Results of simulations

We characterize an electron beam by the beam length L, the beam current I, the acceleration voltage V, the beam radius r_c at the first crossover, the beam semi-angle α at the first crossover, and the cathode temperature T. The average trajectory displacement $<|\Delta \mathbf{r}|>$ and the average energy change $<|\Delta E|>$ are functions in these parameters as well as the focal length f.

Since we have six beam parameters, to obtain full dependences of $<|\Delta \mathbf{r}|>$ and $<|\Delta E|>$ on these parameters will require an impractically large number of simulations. Therefore, only separate dependences on the beam parameters are obtained. That is, we set a "standard" value for every beam parameter and perform simulations by changing each beam parameter and fixing the others to the standard values.

In the previous work, we chose the standard parameter values as L=30cm, I=2μA, V=20kV, r_c=10μm, α=2mrad., T=2500°K, and changed these parameters in the ranges 5cm≦L≦50cm, 0.5μA≦I≦10μA, 5kV≦V≦100kV, 5μm≦r_c≦20μm, 1mrad.≦α≦10mrad., 500°K≦T≦2500°K, by setting f to 5cm. Figures 2.1 and 2.2 show distributions of $<|\Delta \mathbf{r}|>$ and $<|\Delta E|>$ obtained in our simulation for the above standard parameter values. Note that the variances of these distributions are slightly smaller than the corresponding averages, respectively.

The results of previous simulations are summarized in

$$<|\Delta \mathbf{r}|> \propto LIV^{-4/3}(r_1+r_c)^{-1/5}(\alpha_1+\alpha)^{-3/4}T^{-1/10} \quad \text{for } \alpha<5\text{mrad.}, \tag{3}$$

$$<|\Delta E|> \propto L^{1/2}I^{1/2}V^{0}(r_2+r_c)^{-1/3}(\alpha_2+\alpha)^{-2/5}T^{0} \quad \text{for } \alpha<5\text{mrad.} \tag{4}$$

The $<|\Delta \mathbf{r}|>$ and $<|\Delta E|>$ go to constant values as α increases above 5mrad. The values of $<|\Delta \mathbf{r}|>$ and $<|\Delta E|>$ are 1.1μm and 1.0eV, respectively, for the standard parameter values. Since we have fitted a simple fractional power curve to the dependence on each beam parameter, the powers given in the above formulas are not so accurate. Note that, even if we increase the aperture radius, the electron beam does not spread so much above $\sqrt{2kT/m_e}/\bar{v}$ (k is the Boltzmann constant). The dull α-dependences of $<|\Delta \mathbf{r}|>$ and $<|\Delta E|>$ for α>5mrad. can be explained by this fact.

Let us briefly mention on the values of r_1, r_2, α_1, and α_2 in the above formulas. Although the results of previous simulations indicate finiteness of $<|\Delta \mathbf{r}|>$ and $<|\Delta E|>$ at r_c=0 or α=0, they are not enough to determine the values of r_1, etc. We, hence, simulated electron beams by decreasing r_c or α to 0.3μm and 0.1mrad., respectively, and by fixing the other beam parameters to the standard values. The results show that $<|\Delta \mathbf{r}|>$ and $<|\Delta E|>$ seem to become 1.25μm and 2.0eV as $r_c \to 0$ and 3.1μm and 1.8eV as $\alpha \to 0$, respectively, and that $r_1 \simeq$5μm, $r_2 \simeq$1μm, $\alpha_1 \simeq$0.5mrad., and $\alpha_2 \simeq$0.8mrad.

The above results tell us clearly that such high density beams as have the standard parameter values cannot be used for VLSI fabrication systems which require a resolution of as small as 0.1μm. In order to reduce the effect of electron-electron interaction, we changed standard parameter values for L, I, and r_c as L=10cm, I=0.1μA, and r_c=1.0μm. Other parameters are not changed, i.e., V=20kV, α=2mrad., T=2500°K, and f=5cm. With these standard parameter values, simulations were made by changing I, r_c, and α in the ranges $0.03\mu A \leqq I \leqq 0.3\mu A$, $0.3\mu m \leqq r_c \leqq 3\mu m$, and $0.5mrad. \leqq \alpha \leqq 5mrad.$

The results of simulations are summarized in

$$(5) \qquad \langle|\Delta \mathbf{r}|\rangle \propto I r_c^0 (\alpha_1' + \alpha)^{-2/3}, \qquad \alpha_1' \simeq 0.4mrad.,$$

$$(6) \qquad \langle|\Delta E|\rangle \propto I^{1/2} (r_2' + r_c)^{-1/3} (\alpha_2' + \alpha)^{-3/7}, \qquad r_2' < 0.3\mu m,\ \alpha_2' < 0.4mrad.$$

The values of r_2' and α_2' are unclear from the parameter ranges investigated. The values of $\langle|\Delta \mathbf{r}|\rangle$ and $\langle|\Delta E|\rangle$ are about 0.034μm and 0.20eV, respectively, for the new standard parameter values. These values are sufficiently small, and we can well use such beams as have new standard parameter values for VLSI fabrication systems.

It should be noted that the exponents of r_c or α in (5) and (6) are not the same as those in (3) and (4), showing that complete expressions of $\langle|\Delta \mathbf{r}|\rangle$ and $\langle|\Delta E|\rangle$ cannot be expressed by functions factorized into each beam parameter. Figures 3.1 and 3.2 show, respectively, the dependences of the trajectory displacement and the energy change on the beam current. Other beam parameters are fixed to the new standard values. Note that the variances $\sqrt{\langle|\Delta \mathbf{r}|^2\rangle}$ and $\sqrt{\langle|\Delta E|^2\rangle}$ are slightly greater than the averages $\langle|\Delta \mathbf{r}|\rangle$ and $\langle|\Delta E|\rangle$, respectively. Comparing figure 2 with figures 3.1 and 3.2, we find that the distributions of the trajectory displacement and the energy change are broadened by decreasing I or r_c.

We also simulated a number of beams in which the focal length f was changed with the relation L=2f fixed. Other beam parameters were fixed to new standard parameter values. The f was changed within $2cm \leqq f \leqq 7cm$. The results are summarized in

$$(7) \qquad \langle|\Delta \mathbf{r}|\rangle \propto f^{2/3}, \qquad (L=2f),$$

$$(8) \qquad \langle|\Delta E|\rangle \propto f^{0}, \qquad (L=2f).$$

These empirical formulas indicate that the energy change is caused mainly at crossovers while the trajectory is displaced during the whole electron movement. Therefore, if a beam forms more than one crossover as shown by Fig.2.1, the electron energy will be changed stochastically by a constant amount on an average at each crossover, and $\langle|\Delta E|\rangle$ will be proportional to $\sqrt{n_c}$, where n_c is the number of crossovers. The $\sqrt{L}$ behavior of formula (4) should be interpreted in this way.

§4. Comparison with theories

Several persons derived theoretical formulas for $<|\Delta r|>$ and $<|\Delta E|>$ for beams forming crossovers. We consider in this paper three theories: one is by Loeffler and Hudgin [3], [10], the second is by Crewe [11], and the last is by Goto [12]. The theoretical formulas to be presented below are for beams which are focused by a thin lens. In spite of the difference in beam focusing between the above theories and our simulations, there is no essential difference in beam geometries. Therefore, our results may be compared with the theoretical formulas.

We distinguish formulas of Loeffler and Hudgin, of Crewe, and of Goto by suffices L, C, and G, respectively. Their formulas with numerical coefficients omitted are

$$(9) \qquad <|\Delta r|>_L \propto \Gamma(\lambda\alpha L)/V\alpha r_c \quad \text{and} \quad <|\Delta E|>_L \propto \Omega(\lambda r_c)/\alpha r_c,$$

$$(10) \qquad <|\Delta r|>_C \propto LI/\alpha V^{3/2} \quad \text{and} \quad <|\Delta E|>_C \propto (I/\beta)/(\alpha+10^{-9}\pi I^2/\beta^6\alpha^3),$$

$$(11) \qquad <|\Delta r|>_G \propto LI/\alpha V^{3/2},$$

where $\lambda=\sqrt{m_e/2e^3}(I/\sqrt{V})$ is the average axial density of electrons, $\beta=\bar{v}/c$ is the average electron velocity in the unit of light velocity c, and Γ and Ω are dimensionless functions. The $\Gamma(x)$ and $\Omega(x)$ behave, respectively, as $x^{7/8}$ and $x^{2/3}$ for $x\gtrsim 1$, and as x^1 and $x^{2.9}$ for $x\lesssim 0.2$. The beams we have simulated correspond to the case $x\gtrsim 1$. The formula (9) may, therefore, be expressed as

$$(9') \qquad \begin{aligned} <|\Delta r|>_L &\propto L^{7/8} I^{7/8} V^{-3/2} r_c^{-1} \alpha^{-1/8}, \\ <|\Delta E|>_L &\propto L^{0} I^{2/3} V^{-1/3} r_c^{-1/3} \alpha^{-1}. \end{aligned}$$

We first compare the above theoretical formulas for $<|\Delta r|>$ with our empirical formulas (3) and (5). We can see that dependences on L, I, and V are almost consistent with each other. We can, however, find some discrepancies on the dependences on r_c and α, although the formulas of Crewe and Goto are not so inconsistent with our empirical formulas.

In deriving formulas (10) and (11), Crewe and Goto approximated the force due to the electron-electron interaction by an averaged force (cf. $\mathbf{F}_{av}$ to be given in the next section). Obviously, this approximation is valid only when the beam radius is much greater than λ^{-1}, the average axial distance between two neighboring electrons. The λ^{-1} has the value 6.524μm and 130.5μm for I=2μA and I=0.1μA, respectively. Therefore, approximating the electron-electron interaction by an averaged force is allowed only for such high density beams, as have the old standard parameter values, and even for which the approximation is not valid at crossovers. Nevertheless, our results indicate that the approximation is valid to a considerable extent even for lower density beams.

Let us next consider the energy change $<|\Delta E|>$. As we have noted in section 3, the $\sqrt{L}$ factor in our empirical formula (4) should be interpreted as $\sqrt{n_c}$ with n_c the number of crossovers. Therefore, there is no inconsistency between the theories and the results of our simulations on the dependence on L. As for the dependences on other beam parameters, we can see remarkable discrepancies between theoretical formulas and our empirical formulas. Since the discrepancies are so large, the formulas of both Loeffler and Crewe for $<|\Delta E|>$ should be discarded. On the other hand, the I-dependence of (4) is the same as that of Zimmermann's formula based on a statistical mechanical treatment [2]. Pffeiffer also observed the same behavior in his experiment [14].

§5. Effect of refocusing

We have seen that the trajectory displacement is a serious problem for using high density beams in VLSI fabrication systems. Our next concern is, hence, how much the trajectory displacement can be reduced by a dynamic mechanism. The electric force acting on a beam electron due to the electron-electron interaction may be divided into two parts:

$$\mathbb{F}_{ee} = \mathbb{F}_{av} + \mathbb{F}_{loc}. \tag{12}$$

Here, $\mathbb{F}_{av}$ is an averaged force, which may be viewed as is calculated by treating the electron beam as a charged fluid, and $\mathbb{F}_{loc}$ is a local force due to the particle nature of electrons. The $\mathbb{F}_{loc}$ may sometimes be quite strong but is effective only in a range of $2\lambda^{-1}\sim 3\lambda^{-1}$.

If the density of the beam is radially uniform, the effect of $\mathbb{F}_{av}$ for the trajectory displacement appears, in the first approximation, only as a stretch of the focal length. This stretch can be observed in Fig.2.1 as that the distribution is nearly symmetric w.r.t. the peak. Denoting the electron density at the axial coordinate z by $\rho(z)$, the focal length stretch Δf of magnetically focused beams is given by

$$\Delta f = \frac{m_e}{4\varepsilon e}\,\frac{1}{H^2}\int_0^{2f}\rho(z)\,dz. \tag{13}$$

We can, therefore, eliminate the effect of $\mathbb{F}_{av}$ by refocusing.

Figure 4 shows an effect of refocusing for high density beams, and Fig.5 shows a distribution of the trajectory displacement after refocusing for the beam having the old standard parameter values. Comparing Fig.5 with Fig.2.1, we can see the effect of $\mathbb{F}_{av}$ is well eliminated. The effect of $\mathbb{F}_{loc}$ is, however, quite large even for high density beams. For medium density beams, which are more useful for actual VLSI fabrication, the refocusing mechanism is almost ineffective: the effect of $\mathbb{F}_{loc}$ is much larger than that of $\mathbb{F}_{av}$ for such beams. Since $\mathbb{F}_{loc}$ is determined by only relative positions of neighboring electrons and hence its effect is completely stochastic, we have no means to control it.

References

[1] H.Boersch, Z.Phys. 139, p.115 (1954).
[2] B.Zimmermann, Adv. Electronics & Electron Physics 29, Academic Press, 1970, p.257.
[3] K.H.Loeffler & R.H.Hudgin, Proc. 7th Int. Congress on Electron Microscopy, Grenoble, p.67 (1970).
[4] J.Trotel, J. Vac. Sci. Technol. 15, p.872 (1978).
[5] E.Goto, T.Soma & M.Idesawa, J. Vac. Sci. Technol. 15, p.883 (1978).
[6] H.C.Pfeiffer, J. Vac. Sci. Technol. 15, p.887 (1978).
[7] M.G.R.Thomson, R.J.Collier & D.R.Herriott, J. Vac. Sci. Technol. 15, p.891 (1978).
[8] H.C.Pfeiffer, IEEE Trans. Electron Devices ED-26, p.663 (1979).
[9] J.R.Schwarz, RCA Review 18, p.3 (1957); see also A.B.El-Kareh & J.C.J.El-Kareh, Electron Beams, Lenses, and Optics, Vol.2, Academic Press, 1970, ch.13.
[10] K.H.Loeffler, Z. Angew. Phys. 27, p.145 (1069).
[11] A.V.Crewe, Optik 50, p.205 (1978); ibid. 52, p.337 (1978/79).
[12] E.Goto, T.Soma, M.Idesawa & T.Sasaki, Proc. 8th Int. Conf. on Electron & Ion Beam Sci. & Technol., Seattle, p.135 (1978). This paper presents only the final formula.
[13] T.Sasaki, Proc. VLSI Conf. at CALTEC, Pasadena, p.125 (1979).
[14] H.C.Pfeiffer, Rec. 11th Symp. on Electron, Ion & Laser Beam Technol., San Francisco, p.239 (1971).

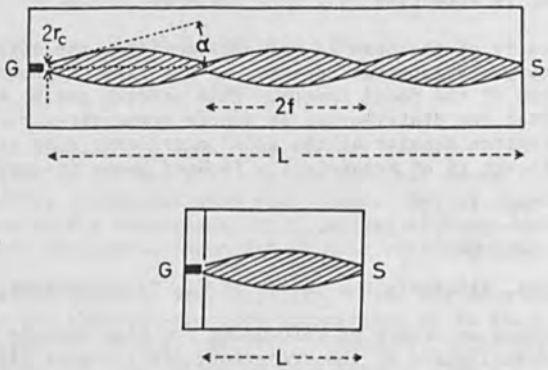

Fig.1. Illustration of typical beam geometries simulated: the upper for high density beams (I∿2μA) and the lower for medium density beams (I∿ 0.1μA). The electrons are focused by a uniform coaxial magnetic field.

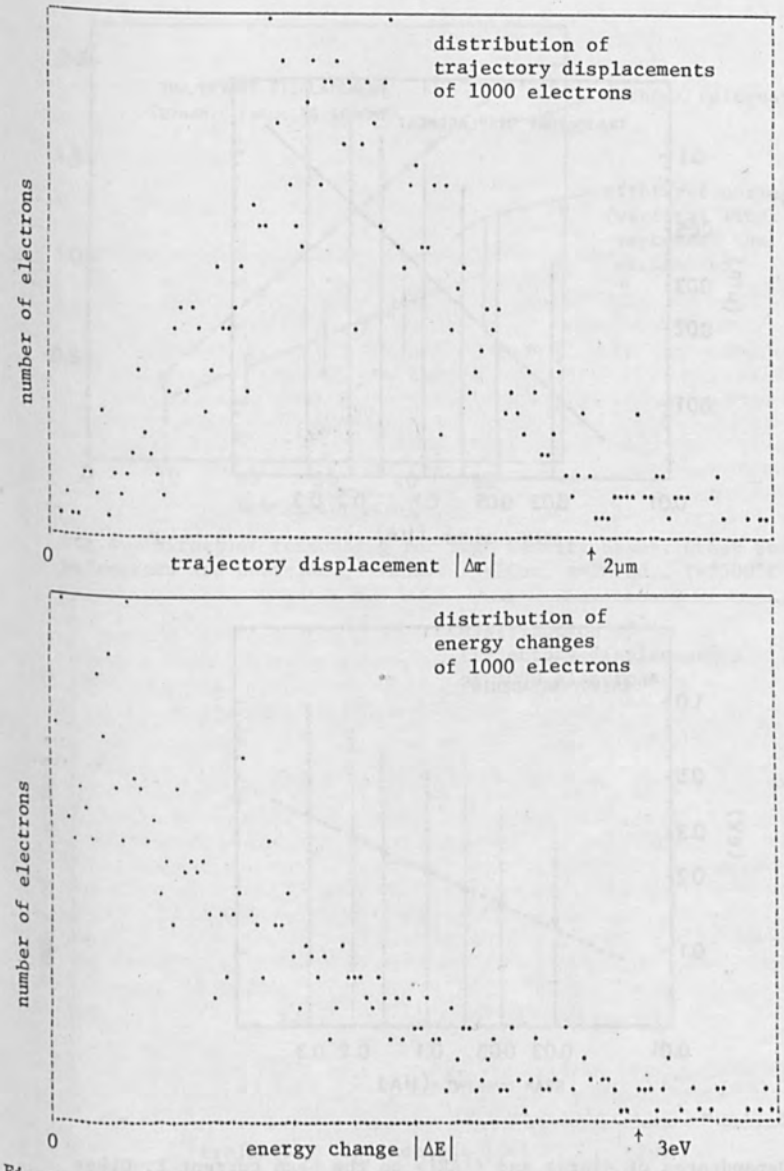

Fig.2. Distributions of trajectory displacements and energy changes for a beam of L=6f=30cm, I=2μA, V=20kV, r_c=10μm, α=2mrad., T=2500°K.

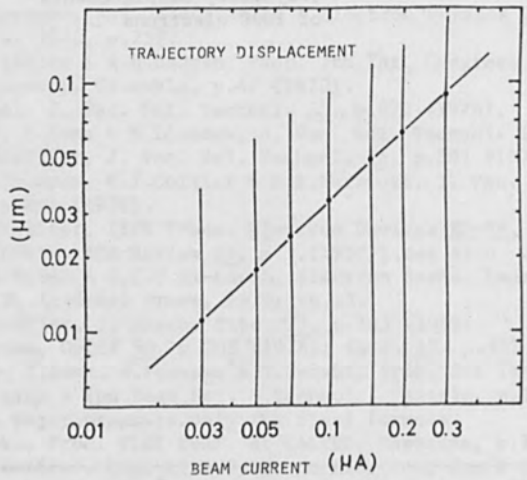

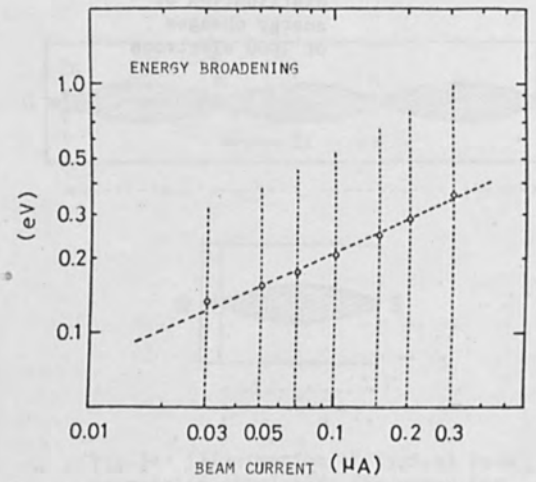

Fig.3. Dependences of $<|\Delta r|>$ and $<|\Delta E|>$ on the beam current I. Other beam parameters are L=2f=10cm, V=20kV, r_c=1μm, α=2mrad., T=2500°K. Vertical lines (both solid and dotted lines) represent the variances.

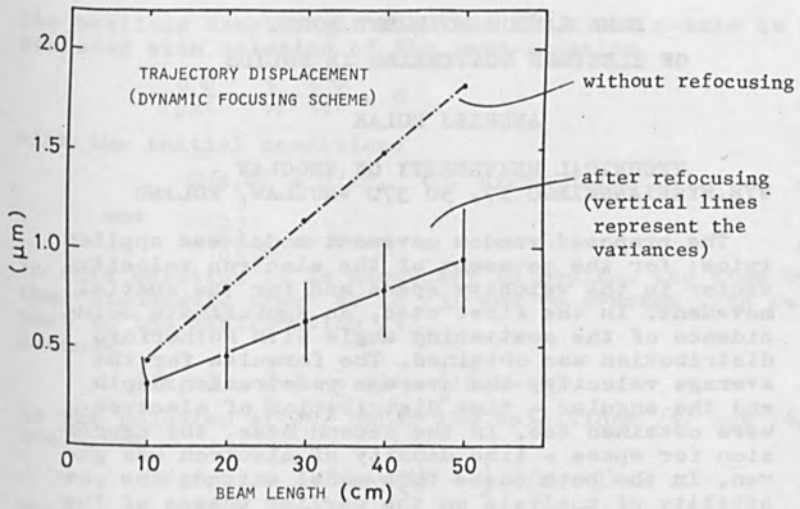

Fig.4. Effect of refocusing for high density beams. Other beam parameters are L=6f=30cm, V=20kV, r_c=10μm, α=2mrad., T=2500°K.

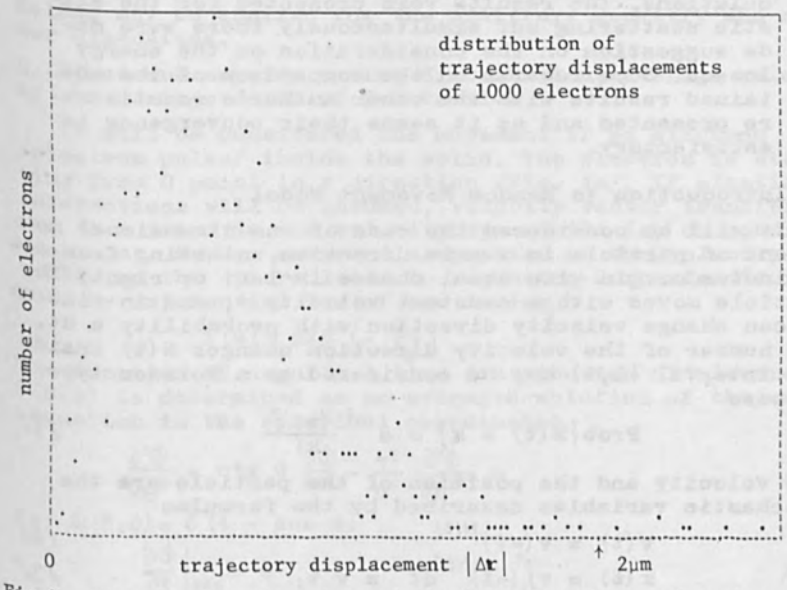

Fig.5. Distribution of trajectory displacements after refocusing. This distribution is obtained by the distribution shown in Fig.2.1.

SOME RANDOM MOVEMENT MODEL OF ELECTRON SCATTERING IN SOLIDS

ANDRZEJ MULAK

TECHNICAL UNIVERSITY OF WROCŁAW
WYB.WYSPIANSKIEGO 27, 50 370 WROCŁAW, POLAND

The proposed random movement model was applied twice: for the movement of the electron velocity vector in the velocity space and for the spatial movement. In the first case, an approximate coincidence of the scattering angle with Rutherford distribution was obtained. The formulae for the average velocity, the average penetration depth and the angular - time distribution of electron were obtained too. In the second case, the expression for space - time density of electron was given. In the both cases this model extends the possibility of analysis on the carlier phases of the scattering not subjected to the diffusion model and permits in a wide range on the analytical calculations. The results vere presented for the elastic scattering but simultaneously there were made suggestion on the consideration on the energy losses. Some remarks on the comparison of the obtained results with the other author's results were presented and as it seems their convergence is satisfactory.

1. Introduction to Random Movement Model

It will be considered the case of one-dimensional movement of particle in x-axis direction, starting from coordinates origin with equal chance in left or right. The particle moves with a constant velocity v, and in time dt it can change velocity direction with probability a dt. The number of the velocity direction changes N(t) inside the interval (0,t) may be considered as a Poisson type process

$$\mathrm{Prob}\{N(t) = k\} = e^{-at}\frac{(at)^k}{k!} \qquad /1/$$

The velocity and the position of the particle are the stochastic variables described by the formulae

$$v(t) = v(-1)^{N(t)} \qquad /2/$$

$$x(t) = v\int_0^t (-1)^{N(\tau)}d\tau = v\,t_s \qquad /3/$$

The integral t_s in /3/ may be called "the stochastic time". As follows from considerations presented in (1),

the particle density distribution $F(x,t)$ on x-axis is associated with solution of the wave-equation

$$\frac{\partial^2\phi}{\partial x^2} - \frac{1}{v^2}\frac{\partial^2\phi}{\partial t^2} = 0 \qquad /4/$$

with the initial conditions

$$\phi(x,0) = \delta(x), \quad \delta \text{ - Dirac delta} \qquad /5/$$

and

$$\left.\frac{\partial\phi}{\partial t}\right|_{t=0} = 0 \qquad /6/$$

In this solution it is necessary to peplace the time by the "stochastic time" as in /3/ and to average with respect to the distribution /1/.
Because

$$\phi(x,t) = \frac{1}{2}\delta(x+vt) + \frac{1}{2}\delta(x-vt) \qquad /7/$$

is the solution of /4/ under the conditions /5/ and /6/, therefore

$$F(x,t) = \frac{1}{2}\langle\delta(x+vt_\zeta)\rangle + \frac{1}{2}\langle\delta(x-vt_\zeta)\rangle \qquad /8/$$

where $\langle\rangle$ means an averaging over /1/.

This model becomes the diffusion model when $a\to\infty$, $v\to\infty$ and $2a/v^2 \to 1/D$ (D - diffusion coefficient). This method may be applied for the arbitrary geometry and number dimensions.

2. Electrons angular - time distribution, average velocity and average depth of penetration

It will be considered the movement of an electron /electron pulse/ inside the solid. The electron is starting from 0 point in x direction /Fig. 1a/. If elastic interactions will be assumed, velocity vector transferred to A point in the velocity space will lay on sphere v = const. Random movement assumption of the velocity vector on the sphere leads to replacing Rutherford's formula by exponential law of scattering

$$f(\theta) \sim \exp\left(-\frac{\theta}{\theta_0}\right) \qquad /9/$$

The function of angular - time distribution of electron $F(\theta,t)$ is determined as an averaged solution of the wave-equation in the spherical coordinates

$$\frac{\partial^2\phi}{\partial\theta^2} + \operatorname{ctg}\theta\frac{\partial\phi}{\partial\theta} - \frac{v^2}{u^2}\frac{\partial^2\phi}{\partial t^2} = 0 \qquad /10/$$

for $\phi(\theta,0) = \delta(1 - \cos\theta)$ /11/

$$\left.\frac{\partial\phi}{\partial t}\right|_{t=0} = 0 \qquad /12/$$

In this case

$$\phi(\theta,t) = \sum_{n=0}^{\infty} \frac{2n+1}{4\pi} P_n(\cos\theta) \cos\sqrt{n(n+1)}\frac{u}{v} t \qquad /13/$$

where $P_n(x)$ - Legendre's polynomial

$$u = av\theta_0 \qquad /14/$$

The function $\langle\cos\sqrt{n(n+1)}\frac{u}{v} t\rangle$ can be determined by expanding the cosine into power series and applying the Laplace's transforms (1) to the stochastic time moments

$$\mathcal{L}\{t_S^{2k}\} = \frac{(2k)!}{s^{k+1}(s+2a)^k} \qquad /15/$$

It will be obtained the following expression for angular--time distribution

$$F(\theta,t) = \sum_{n=0}^{\infty} \frac{2n+1}{4\pi} P_n(\cos\theta)\, e^{-at}\left[\mathrm{ch}\,\chi_n t + \frac{a}{\chi_n}\,\mathrm{sh}\,\chi_n t\right] \qquad /16/$$

$$\chi_n^2 = a^2 - n(n+1)\frac{u^2}{v^2}$$

/for $\chi_n^2<0$, $\mathrm{ch}\,\chi_n t = \cos|\chi_n|t$ etc./

The dependence /16/ may not be applied for $t < \frac{1}{a}$ /then $\theta < \theta_0$/, because the model introduces the false movement of unscattered electron on the velocity sphere.

The average velocity and the average penetration depth can be determined as

$$\bar{v}_x = v\langle\cos\theta\rangle = v\, e^{-at}\left[\mathrm{ch}\,\chi t + \frac{a}{\chi}\,\mathrm{sh}\,\chi t\right] \qquad /17/$$

$$\chi^2 = a^2 - \frac{u^2}{v^2}$$

For $\theta_0^2 \leqslant 0,1$

$$\bar{v}_x \approx v\, e^{-\beta t}\ , \quad \beta = \frac{u^2}{2av^2} \qquad /18/$$

$$\bar{x} \approx \frac{v}{\beta}\left(1 - e^{-\beta t}\right) \qquad /19/$$

$$x_D = \bar{x}(\infty) = \frac{v}{\beta} = \frac{2av^3}{u^2} \qquad /20/$$

Analogically to /17/ the simple dependences for $\overline{v_x^2}$ etc. can be obtained

E.g.

$$\overline{v_x^2} = \frac{v^2}{2}\left[1 + e^{-at}\left(\mathrm{ch}\,\chi' t + \frac{a}{\chi'}\,\mathrm{sh}\,\chi' t\right)\right] \qquad /21/$$

$$\chi'^2 = a^2 - 4\frac{u^2}{v^2}$$

3. Separation of electron movement on drift and isotropic random movement.

As follows from Fig. 1 velocity of the random movement is given by

$$v_R^2(\theta) = v^2 + \bar{v}_x^2 - 2v\,\bar{v}_x\cos\theta \qquad /22/$$

$$v_{R\min} = v - \bar{v}_x\ , \quad v_{R\max} = v + \bar{v}_x \qquad /23/$$

Velocity $v_R > v$ has a formal character. It is connected with the introduction of the random movement origin. For $t > 1/\beta$ the movement may be treated as isotropic

$$v_R(\theta) \approx \bar{v}_R = v \qquad /24/$$

Taking into consideration $v_R(\theta)$ instead of v, an analysis could be extended on the earlier phases of scattering.

4. Electron density distribution

An effective method of calculation of the density distributions is given by using the differential equation for the Laplace transform of the density function. In the one-dimensional case (1)

$$\frac{d^2f}{dx^2} - \frac{s(s+2a)}{v^2} f - \frac{s+2a}{v^2} F(x,0) = 0 \qquad /25/$$

where $f(x,s) = \mathcal{L}\{F(x,t)\}$.
An application of /25/ to the problem described in p.1 gives

$$F(x,t) = 0, \quad t < \frac{|x|}{v}$$

$$= \frac{ae^{-at}}{2v}\left[I_0(\xi) + \frac{at}{\xi} I_1(\xi)\right] +$$

$$+ \frac{e^{-at}}{2}\left[\delta(x-vt) + \delta(x+vt)\right], \quad t > \frac{|x|}{v} \qquad /26/$$

where I_0, I_1 - modified Bessel functions

$$\xi^2 = a^2\left(t^2 - \frac{x^2}{v^2}\right)$$

It may be verified, that for the three-dimensional case the equation /8/ replaces the equation

$$G(\varrho,t) = \frac{1}{4\pi\varrho} \left\langle \frac{\partial\delta}{\partial\varrho} (vt_s - \varrho) \right\rangle \qquad /27/$$

from where, after taking account of /26/

$$G(\varrho,t) = 0, \quad t \leq \frac{\varrho}{v}$$

$$= \frac{ae^{-at}}{4\pi v\varrho}\left[I_1(\xi) + \frac{at}{\xi} I_2(\xi)\right] +$$

$$+ \frac{e^{-at}}{4\pi\varrho^2} \delta(\varrho - vt), \quad t > \frac{\varrho}{v} \qquad /28/$$

For continuous particles injection and for exponential disappearance law with the average life-time $\tau = 1/\delta$

$$G(\varrho) = \int_0^\infty e^{-\delta t} G(\varrho, t)\,dt = \frac{a+b}{4\pi v^2\varrho} e^{-\frac{\varrho}{v}\sqrt{b^2-a^2}} \qquad /29/$$

where $b = a+\delta$

$$\int_0^\infty G(\varrho)\, 4\pi\varrho^2\, d\varrho = \tau \qquad /30/$$

The drift in /28/ can be taken into consideration by an introduction of $G(r,x,t)$, $\varrho^2 = r^2 + (x-\bar{x})^2$ and the correction the term containing Dirac's delta /the unscattered electrons will be found in this case at the same point/.

5. Consideration of energy loss

In the case of the energy losses, the average values of v, a, θ_0 will change in time and appear spread of their distributions. In the first step of approximation, it becomes necessary to choose the average values obtained when distributions of these values and their changes in(0,t) time interval, are taken into account. A more precise electron density distribution may be obtained by the superposition e.g. the two random movements with various v and a taken with weights dependent on time.

6. Comparison with experimental results

Formula for maximal average depth of penetration for elastic scattering /20/ may be transformed to form

$$x_D = 2 \cdot \frac{1}{\theta_0^2} \cdot \frac{v}{a} = 2 \cdot \frac{1}{\theta_0^2} \cdot \lambda_{\pi/2} \qquad /31/$$

where $\lambda_{\pi/2}$ - average way on which takes place the velocity direction change by $\pi/2$. It results from definition of the parameter a for random movement on the grate. The parameter a is associated with the ensemble of collisions giving the resultant change of the velocity direction equal $\pi/2$.

The angle dispersion according to Rutherford distribution is $\theta_m/2$, where (3):

$$\theta_m^2 = \left(\frac{1.12}{0.885}\right)^2 \frac{e^4}{\hbar^2} \frac{Z^{2/3}}{v^2} \qquad /32/$$

$/\theta_m^2 = 4\beta_i$, β_i - screening parameter /

The dispersion of the sum of the scattering angles lying on the different planes $(\theta_1 + \theta_2 + \ldots + \theta_n)^{1/2}$ may be evaluated on the basis of the central limit theorem as been equal to $\sqrt{n}\,\theta_m/2$. To obtain the angular deviation equal to $\pi/2$, number of the collision should be equal on average

$$n = \frac{\pi^2}{\theta_m^2} \qquad /33/$$

If the average distance between the points of the successive collisions is l /being of the order of the lattice constant/, then

$$\lambda_{\pi/2} = nl = \frac{\pi^2 l}{\theta_m^2} \qquad /34/$$

Because $\theta_0 \approx \theta_m$ it follows from /31/ and /32/ that

$$x_D = \frac{2\pi^2 l}{\theta_m^4} \qquad /35/$$

hence in the face of /32/ we have

$$x_D \sim \frac{v^4}{Z^{4/3}} \qquad /36/$$

This result approximately is in accordance with the well-known Kanaya - Okayama equation (2), where

$$x_D \sim \frac{v^{10/3}}{Z^{8/9} + 0.187 Z^{14/9}} \qquad /37/$$

In addition, the density distribution /29/ was compared with the results of Monte Carlo experiment by Matsukawa, Murata and Shimizu (3). In the zones placed between the two planes parallel to the beam axis, marked on the graph, number of the trajectories were computed /two-sidedly/ and compared with the values calculated from /29/. For facility the theoretical curve was traced by the boundary points. Author tested also the distribution /29/ in which $1/\varrho$ was replaced by $1/\varrho^2$. This distribution arises from the approximate model. The consistance with results obtained by the Monte Carlo method.is equally good in both the cases. The exponent of ϱ is not critical.

REFERENCES

(1) M.Kac, Some Stochastic Problems in Physics and Math., Magnolia Petroleum Co, Dallas /1956/

(2) K.Kanaya, S.Okayama, J. Phys. D: Appl. Phys., Vol.5, /1972/

(3) T.Matsukawa, K.Murata, R.Shimizu, Phys. Status Solidi B, Vol. 55 nr 1, p. 371-83 /1973/

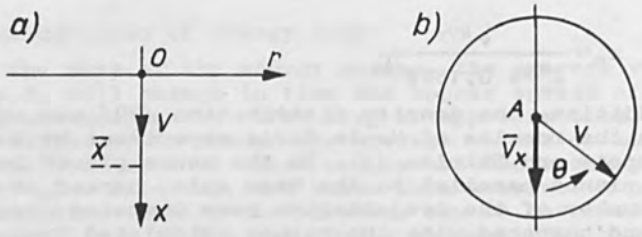

Fig. 1 Electron scattering
a/ coordinates, b/ velocity space

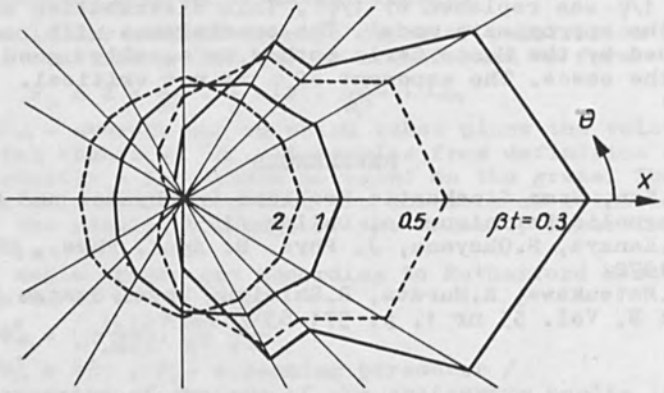

Fig. 2 Electrons angular - time distribution
(schematic, for approximation n ≤ 6).

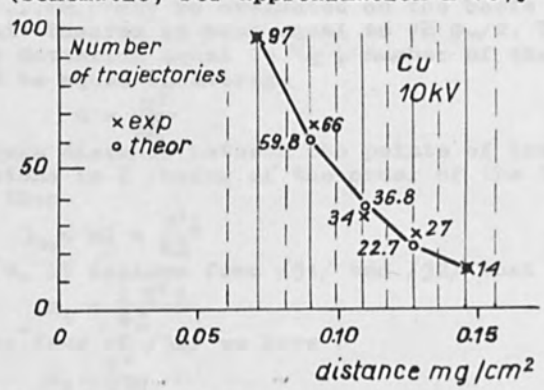

Fig. 3 Comparison of formula /29/ with
Monte Carlo experiment /3/.

Section 2.

Electron Beam Lithography Systems

and Related Topics.

DESIGN OF A HIGH PERFROMANCE VARIABLE-SHAPED E-BEAM MACHINE

E. Goto, T. Soma, M. Idesawa and T. Sasaki

The Institute of Physical and Chemical Research
Wako-shi Saitama 351 Japan

ABSTRACT

Multi-lens and multi-deflector electron beam focus deflection systm is described, which is to be applied to a pracrical shaped-beam exposure system for microfabrication. Based upon the MOL (Moving Objective Lens) concept, the system is of in-lens-deflector configuration, and consists of magnetic focusing lens with multiple of electrostatic deflectors and with dynamic correction coils. The system parameters are chosen such that the aberrations linear in deflection (coma, transverse-chromatic, and landing error) are canceled without dynamic correction, and those non-linear in deflection are minimized, allowing easier correction of remaining significant aberrations by dynamic means. The results of optimized design calculation include the typical case of 5 mm square, 5 mrad semi-aperture beam and 10 mm square scan field with aberrations less than 0.2 μm.

INTRODUCTION

In previous papers [1,2], it was shown numerically that a high performance focus-deflection system for shaped beam could be realized without dynamic corrections. Based upon the MOL concept, the systems considered are of in-lens configuration and consist of magnetic focusing lens with multiple of either magnetic or electrostatic deflectors placed in the lens-field. The width, the relative intensity and the rotational as well as axial positions of each deflector are optimized so that the wider scan field is obtained with minimum aberrations.

To realized an aberration free system there will be a design choice between the systems with increased number of deflectors but without dynamic correction and that with less number of deflectors but with dynamic correction. Since there exist some difficulties in fabricating the electron beam system with sufficient accuracy to the design calculation, it is a common practice to incorporate in the system the correction means to dynamically correct the aberrations caused by unpredictable mechanical or material defect as well as those due to non-Gaussian field distribution. With increasing availability of high performance analog and digital circuit element such

as digital to analog converters or digital and analog multipliers, which are to be used in the correction circuits, many systems presently manufactured use a complex correction scheme for eliminating such aberrations as distortions, astigmatisms and field curvatures.

With these background in mind, this paper deals with the design calculation for variable shaped electron beam focus-deflection systems. We introduce a new design procedure of, first eliminating the aberrations linear in deflection by adjusting the relative intensities and the rotational postions of deflectors, and then minimizing the non-linear parts which are to be dynamically corrected. It is already known that the deflection induced coma [3] or deflection induced transverse chromatic aberration [4] can be eliminated in the two-deflector system by choosing appropriate value for mutual intensity and rotational position. From the consideration of the number of freedom in deflection system, these results can be generalized as in the following statement that all the deflection induced aberrations linear in deflection (coma, transverse chromatic and error in vertical landing) can be eliminated simultaneously by using four deflectors.

ELIMINATION OF DEFLECTION-INDUCED ABERRATIONS LINEAR IN DEFLECTION

The aberration formulas for the focus-deflection system having rotational invariant property is given in [5,6]. Of these aberrations the deflection-induced coma and the deflection-induced transverse chromatic aberration are linear in γ or deflection. The landing angle from the normal, which can be considered as an aberration in the normal landing wishing system, is also linear in γ. Using the notation given in [5], these aberrations are represented as

$$\left.\begin{array}{ll} K_L \alpha\gamma & \text{(coma length)} \\ K_T\ \gamma\ \Delta V/V & \text{(chromatic)} \\ K_V\ \gamma & \text{(landing error).} \end{array}\right\} \qquad (1)$$

Consider the problem of eliminating these aberrations simultaneously. Since these aberrations are all complex having x and y components there are six functions in total, which are to be eliminated. The freedom or the independent parameters for the deflection system necessary to eliminate these aberrations are six in number. Taking the intensity and the rotational position of the deflector as the independent parameters, four deflectors are needed to obtain six independent parameters, since the relative intensity and the relative rotational positions are significant for such multi-deflector system.

To obtain the value of these parameters for a given configuration, first calculate four sets of aberration coefficients K_{Li}, K_{Ti}, K_{Vi} $(i = 1,2,3,4)$ for the system with each one deflector is ex-

cited and positioned at reference angular position. Figure 1 shows schematically the c-trajectory [5] $c_i(z)$ for each system to calculate the aberrations; then solve the following linear simultaneous equation with complex coefficients,

$$\begin{bmatrix} K_{L1} & K_{L2} & K_{L3} & K_{L4} \\ K_{T1} & K_{T2} & K_{T3} & K_{T4} \\ K_{V1} & K_{V2} & K_{V3} & K_{V4} \\ 1 & 1 & 1 & 1 \end{bmatrix} \begin{bmatrix} W_1 \\ W_2 \\ W_3 \\ W_4 \end{bmatrix} = \begin{bmatrix} 0 \\ 0 \\ 0 \\ 1 \end{bmatrix} \tag{2}$$

to obtain the mixing weight W_i for c-trajectory as,

$$c(z) = \sum_{i=1}^{4} W_i \, c_i(z), \tag{3}$$

from which to calculate aberrations for the system with K_L, K_T and K_V eliminated. In eq. (2), zero in right hand side column-vector signifies the condition that each aberration must be canceled, while one in that signifies the normalization condition for W_i.

SYSTEM CONFIGURATION AND ABERRATION CALCULATION

Figure 2 shows the system considered from the practical view point. It consists of two magnetic focusing lens L_1 and L_2; L_1 is the demagnifying lens whose object plane z_o is supposed to be the second aperture plane for variable shaping, and L_2 is the 1 to 1 projection lens whose image plane z_s is supposed to be the target on which the shaped beam is scanned. Inside these lenses four deflectors D_1, D_2, D_3 and D_4, with different radius and length, are placed forming in-lens-deflector configuration; further, the dynamic focus coil C_F and the stigmator coil C_S are placed, as shown, to correct field curvature K_F and astigmatism K_A, respectively. Dynamic correction for distortion K_D is to be performed by superposing correction signal to the normal deflection signal.

The method of calculation taking into account the size of the object is given in [1,2]. The axial potential functions for focusing lens, deflector and stigmator used for numerical calculation are given as follows,

$$\left.\begin{aligned} \phi'_F(z) &= F_0(z;\, A_F,\, R_F,\, P_F,\, L_F) && \text{(focus)} \\ \phi_G(z) &= F_0(z;\, A_G,\, R_G,\, P_G,\, L_G) && \text{(dynamic focus)} \\ \phi_P(z) &= F_1(z;\, A_P,\, R_P,\, P_P,\, L_P)\, e^{iT_P} && \text{(deflection)} \\ \phi_Q(z) &= F_2(z;\, A_Q,\, R_Q,\, P_Q,\, L_Q) e^{2iT_Q} && \text{(dynamic stigmator)} \\ \phi_R(z) &= F_1(z;\, A_R,\, R_R,\, P_R,\, L_R)\, e^{iT_R} && \text{(dynamic distortion)} \end{aligned}\right\} \tag{4}$$

where

$$F_i(z;\ A_x,\ R_x,\ P_x,\ L_x) = \frac{A_x}{R_x}\ \{\ \frac{1}{2}\ \tanh\left(\omega_i\ \frac{z + L_x - P_x}{R_x}\right) - \frac{1}{2}\ \tanh\left(\omega_i\ \frac{z - L_x - P_x}{R_x}\right)\} \qquad (5)$$

with parameters having the following significance,

A_x : amplitude

R_x : radius

P_x : position

L_x : length

T_x : angle

as shown in Fig. 3, where subscript x represent F, G, P, Q or R. The numerical coefficients ω_i are given as [7],

$$\left.\begin{aligned} \omega_0 &= 1.3262 \\ \omega_1 &= 1.7758 \\ \omega_2 &= 1.0598. \end{aligned}\right\} \qquad (6)$$

RESULT OF OPTIMIZED CALCULATION

Table 1 shows one of the result of optimized design calculation together with the system parameters considered. The interaction aberration is calculated using the formula given in [8]. Experimental work based upon these design is under way and the result will be published elsewhere.

ACKNOWLEDGMENTS

The authors would like to thank Toshinori Goto and Teruo Someya of Japan Electron Optics Laboratory Ltd., for their helpful discussion regarding the practical system.

REFERENCES

[1] E.Goto, T.Soma and M.Idesawa, J. Vac. Sci. Technol.,15(1978)883.
[2] T.Soma, Optik,53(1979)281.
[3] H.Hhiwa, Thesis Univ. Tokyo,(1970).
[4] W.Stickel and H.C.Pfeiffer, Proc. 8th Intl. Conf. Electron Ion Beam Sci. Technol.,(1978)32.
[5] E.Goto and T.Soma, Optik,48(1977)255.
[6] T.Soma, Optik,49(1977)255
[7] T.Soma, J. Info. Proc. Soc. Jpn.,14(1973)218.
[8] E.Goto, T.Soma, M.Idesawa and T.Sasaki, Proc. 8th Intl. Conf. Electron Ion Beam Sci. Technol.,(1978)32.

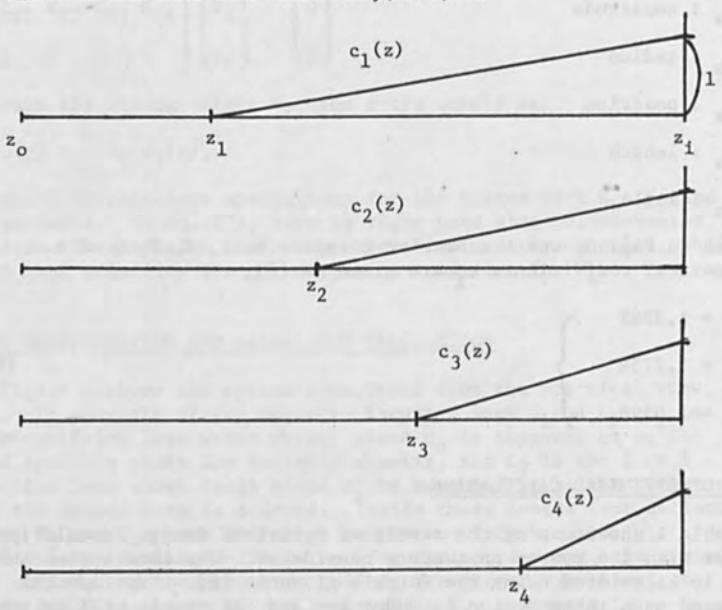

Fig. 1 c-trajectories

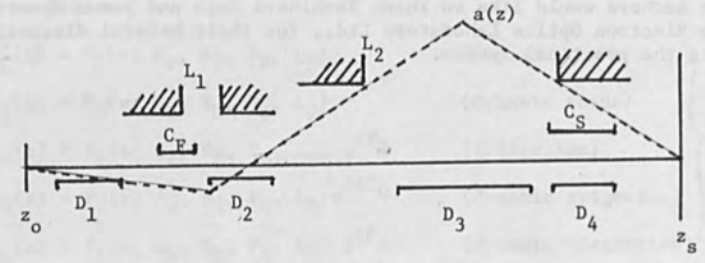

Fig. 2 System configuration

Table 1 Design specifications

Focusing lens :	number	2
	type	magnetic
	magnification	L_1 : 1/3
		L_2 : 1/1
Deflector :	number	4
	type	electrostatic
	maximum voltage applied	D_1 : 604 V
		D_2 : 301 V
		D_3 : 1055 V
		D_4 : 497 V
Accelerating voltage		V : 20 kV
Object to image distance		L : 250 mm
Semi-aperture angle		α : 5 mrad
Beam size		β : 5 μm sq
Scan field		γ : 10 mm sq
Voltage variation		$\Delta V/V : 10^{-4}$
Aberration :	geometrical uncorrected	K_D : 31.0 μm
	geometrical corrected	κ_{d4} : 0.18 μm
	interaction	0.17 μm at 1 μA

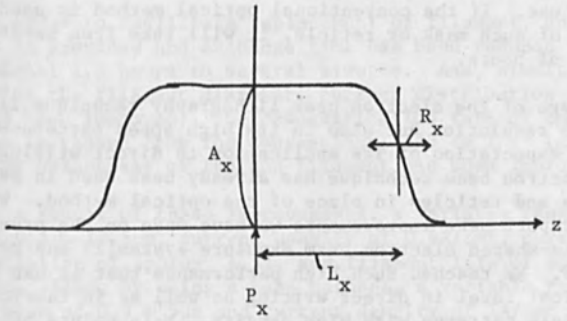

Fig. 3 Axial function

ADVANCED PERFORMANCE OF THE VARIABLE-SHAPED BEAM ELECTRON LITHOGRAPHY SYSTEM JBX-6A

N. Goto, T. Someya, K. Tanaka, M. Takeuchi and S. Miyauchi
JEOL Ltd., Nakagami, Akishima, Tokyo 196, Japan
G. Cogswell
JEOL (U.S.A.) INC., Peabody, Mass. 01960, U.S.A.

Abstract

By adding new functions of direct writing and reticle writing to the previously reported variable-shaped electron beam lithography system [1][2][3] and, simultaneously, by improving the system with regard to the data transfer speed and the current density, we succeeded to obtain a shot cycle of 2 ∿ 3.5μsec. Also, by increasing the accuracy of the D-A converter, we obtained an overall pattern accuracy of 0.2μm (3σ). Furthermore, with the aid of a newly developed automatic substrate loading system, we succeeded to produce software which fully automatically performs the entire processes of pattern exposure from substrate exchange to completion of exposure. It has been verified, as a result of these improvements, that a 1μ lithography can now be exposed on a 5 inches plate in about 15 minutes.

1. Introduction

In semi-conductor industries, production of masks by using electron beam is now becoming routine while the importance of the electron beam technique in the reticle fabrication is increasing. In a trend of high integration of pattern density in various IC devices, the conventional optical method becoming uneconomical because it takes an enormously long time to write a pattern. Nowadays, 2μm lighography is in practical use. If the conventional optical method is used to write a pattern of such mask or reticle, it will take from several hours to scores of hours.

The advantage of the electron beam lithography technique lies not only in its high resolution but also in its high speed pattern writing capability. In expectation of its application to direct writing in furture, the electron beam technique has already been used in pattern writing of masks and reticles in place of the optical method. We should like to report here improvements we have made on the previously reported variable-shaped electron beam exposure system[2] and results we have obtained. We reached such high performance that it can be used on a practical level in direct writing as well as in fabrication of mask and reticle patterns with high density. Main points of the

improvements are as described below.

In order to increase exposure speed, data transfer was made high speed, beam current density and speed of stage movement were increased, an automatic substrate loading system has been developed, and a new filament exchange mechanism was added for facilitating the operation. Furthermore, software which full automatically performs all processing for pattern exposure including substrate set-up and adjustment of electron optical system has been developed. R.A.S. (reliability, availability and serviceability) have also been improved and a technique of data compression has been included in the system, too. Details of the respective points and their results are described below. Regarding direct writing, details will be reported in another session of this conference.

A part of this improvement work, development of a high speed data transfer system, was carried out under the guidence of the Cooperative Laboratories VLSI Technology Research Association.

2. Hardware

Figure 1 shows an external view of the JBX-6A system. Three power supply racks included in the system are not shown in the picture. In Figs. 3 and 4, main performance specifications and a block diagram of the improved exposure system are shown.

2-1 Electron Optical Column

As previously reported, in the variable-shaped beam lithography system[4][5], a rectangle electron beam is formed, and while changing the area of the rectangle beam, the respective rectangle elements of a pattern are exposed in one shot. The principle of the optical pattern generator is used here, replacing the optical correspondence by the electron beam deflection technique.

In order to facilitate replacement of filament, an exchange sub-chamber is provided and exchange time has been reduced from the conventional 1.5 hours to several minutes. And, simultaneously, by increasing the filament diameter, current distribution of the shaped beam has been improved. The demagnification rate of the shaped beam has been increased from the conventional 1/5 to $1/7 \sim 1/10$ and at the same time brightness of the gun filament has been improved.

As a result of these improvements, a variable range of the shaped beam of $0.5 \sim 12.5\mu m$, current density of $0.4A/cm^2$, current distribution variation of approx. 1.5%, and filament life of approx. 500H were obtained. Also, by using a LaB_6 cathode, a variable range of the shaped beam of $0.5 \sim 5\mu m$ and current density of $1A/cm^2$ were obtained. Furthermore, a special attention was paid to maintenance. A sub-

chamber is provided so that parts in the column which require cleaning or replacement can now be easily dismounted or remounted without disassembling the column itself.

2-2 Stage Mechanism and Automatic Loading System

A stage of the step and repeat type having a movable distance of 2mm was used. In order to conform to the recent trend of using a large wafer for exposure, the driving range was taken as large as 135mm × 110mm so that mask plates of up to 5 inches square can be used. Also, in order to make high speed pattern exposure possible, a ferrofruidic seal was used as transmission feedthrough of the motive power to the exposure chamber and low-friction torque in high vacuum was introduced. As a laser interferometer for controlling the shift amount of the stage, the HP 5501 system was employed. The shift was measured with an accuracy of $\lambda/32$ by using the laser interferometer, and deviation from the assigned value was fed back to correct the electron beam position. As a result of the above, a stage driving speed of 0.35sec/2mm was obtained.

In order to increase the reliability and throughput of the system as production system, an automatic loading system was developed and applied to the system. Twelve cassettes are loaded in a batch type and each cassette is exposed according to the schedule data that designates exposure procedure like kinds of pattern, chip layout, pitch, etc. Termination of vacuum curing time after exposure is indicated by a lamp and it can be read with your eyes and also by computer. Furthermore, various types of interlocks, both in software and hardware, have been provided for assuring safe operation of the system all the time. A picture showing an external view of the electron optical column equipped with the abovementioned automatic loading system is given in Fig. 2. Time required for exchanging a cassette is about 30 seconds.

2-3 Evacuation System

When exposing a fine pattern, contamination in the electron optical column delicately affects the exposure results. We have decreased the partial pressure of hydrocarbons in the column as much as possible for preventing contamination, by using a completely clean vacuum system as well as by increasing the degree of vacuum.

As shown in Fig. 4, the JBX-6A is provided with a large capacity sputter ion pump and a turbo-molecular pump. The exposure chamber is evacuated by using the sputter ion pump of 400ℓ/s as main pump, while the electron optical column is evacuated by using the 110ℓ/s ion pump so as to prolong the life time of a tungsten filament. The filament exchange chamber, auto-loader chamber in which 12 cassettes are loaded and shaping aperture exchange chambers, all of which are separated by the air lock system from other parts, are connected to another evacuation system. After being evacuated rapidly up to 1×10^{-5}Torr vacuum,

the evacuation system is switched over to the ion-pump. The roughing system was independently designed and the ideal of clean and high vacuum is strictly kept. With this evacuation system, vacuum below 10^{-7}Torr is obtained in the electron gun chamber, and in the exposure chamber approximately 10^{-7}Torr is obtained.

2-4 Cross-wire Beam Detection System

In the variable-shaped beam method, measurement control of the size, position, rotation, etc. of the rectangle beam is the most important factor in enhancing pattern accuracy. The JBX-6A is provided with both software and hardware for automatically adjusting the beam size, position, rotation, etc., using a beam detector comprising a cross-wire and a Faraday cup. The items practically adjusted are: (1) beam position, (2) beam dimension, (3) scanning amplitude, (4) scanning direction, (5) scanning distortion, (6) beam edge sharpness (focusing), (7) beam direction, etc.

The derivative waveform of the current signal detected by the Faraday cup is obtained by processing the signal while scanning the rectangle beam perpendicularly to the wire. The clock frequency used is 110KHz, and the scanning step and scanning width are 0.025μm and 30μm, respectively. The wire position is measured by the laser interferometer with an accuracy of 0.01μm in order to use as reference of measurement. Waveforms of the signals at various stages of signal processing in the beam detector system and a histogram showing distribution of measured beam position are given in Fig. 5. Since, usually, the position or dimension of the beam is obtained as an arithmetic average of 20 $\sim$ 30 measurements, it can be said from the results on the histogram of measurements that the measurement accuracy of beam position is better than 0.01μm.

2-5 High Speed Data Transfer System and Data Compression

The newly developed high speed data transfer system is schematically shown in Fig. 6. Data converted into the assigned format is usually stored in a magnetic tape. Prior to exposure, the data is transferred to and stored in the 90MB disc under the CPU control. Although it depends on the data amount, the usually required transfer time is from several to sixteen minutes. (If exposure data were stored in the disc in advance, this transfer time is not needed.) After the substrate is set up and the assigned scheduled data is read in the 128KB CPU memory, the data is transferred from the disc to the data memory. The time required for it is approximately 10μsec. per pattern data.

During exposure, the data controls the electron beam from the data memory via each controller, without passing through the CPU. The times required by the controllers for performing their respective functions during exposure are shown in Fig. 6 (a), (b) and (c). If these are simply added up, their sum will be 1.8μsec. However, the

actual time required is much shorter than this, because HDTC has registers R_1 and R_2 and during exposure of previous data the next data can be transferred up to R_1. Thus, the transfer speed of approximately 1μsec. per pattern data is actually obtained. The shot cycle, approximately 3.5μsec., can be obtained by adding the shot time 2.5μsec. to the transfer time 1μsec. Functions of the respective controllers are shown in Fig. 6 *1) and *2).

Although in the variable-shaped beam method the substrate can be shot by a beam of any shape and any size between 0.5 ∿ 12.5μm, frequently, in practice, a fixed shape pattern is repeatedly used to form an exposure pattern. If high integration of patterns progresses and the number of exposure patterns reaches several millions or over, the memory capacity required for storing these patterns increases, prolonging the data conversion time and reading time. Paying attention to the fact that the same exposure pattern is frequently repeated, we employed the method in which data is processed in groups (namely, data is compressed). while assigning the pattern shape, repetition pitch and repetition times for repeatedly used patterns and which expands the compressed data to the original size in VHSC during the exposure. Although the degree of data compression attainable depends on the nature of exposure patterns, usually compression of one third to one several tenths is possible.

2-6 Software

The program system of the JBX-6A is shown in Fig. 7-1). Data of the PG3000 (or PG3600) format is converted to exposure format data by using the "CONV" program and actual exposure is carried out by using the "EXPC" program. Data of the CALCOMP format should be, first, converted to "JEOL format" data by using the "PLOT" program, then it can be converted to exposure format data by using the "CONV" program. The program system includes a check program for checking the operation of the respective components of the hardware system, too. A block diagram of the "CONV" program and its main functions are shown in Fig. 7-2). The "CONV" program not only converts data of various formats to exposure format data but also has capabilities of resizing and shot-time modulation for proximity correction, and other functions of scaling, making a mirror image, reversing NEGA-POSI, etc.

The "EXPC" program automatically controls the exposure device and executes the automatic exposure. A block diagram of the "EXPC" program and subroutines for adjusting the exposure device are shown in Fig. 7-3). Main functions of the "EXPC" program are: 1) automatic exchange of 12 substrates in the automatic loader, 2) scheduling the exposure to be executed by designating the type of exposure, kinds of patterns, arrangement of patterns, character exposure, shot time, stage shift sequence, etc., 3) "MNTE" automatic measurements and adjustments of the operating functions of electron optical system components, including automatic adjustments of the scanning width (GNRTO), rectangular beam size (P.G.R. PGR), deflection distortion

(DISMES, DISCHEK), automatic measurement of the electron beam current with automatic control of the shot-time, designation of control parameters for various automatic adjustments (PRWIRE, PRBE, PRCHNG, PRMRI), etc.; 4) executing automatic and successive exposures by feeding 12 substrates sequentially according to the scheduler; 5) print-out of a rearranged exposure condition list or its storage into a specified memory after the exposure, and so on.

3. Exposure Results and Throughput

As a result of the above-mentioned inprovements, the throughput has been drastically improved. In Fig. 8, the throughput in mask making under various conditions is shown. Although the throughput largely depends on the pattern density and plate size, the average time is 5 $\sim$ 16 minutes. With regard to the reticle fabrication, the time required for an exposure of 100mm square is approximately 18 minutes. In Fig. 9, some examples of exposure of resists patterns (PGMA, approx. 4000Å) are shown. With regard to the oblique line exposure as shown in Fig. 9-3, the smoothness of line edges has been drastically improved after improvement of the software. Finally, it has been confirmed that the overall accuracy of exposure pattern is 0.2μm ($\pm 3\sigma$).

Acknowledgement

We should like to express our sincere gratitude to people in the Cooperative Laboratories VLSI Technology Research Association for their guidence and cooperation, especially in the improvement of the high speed data transfer system.

References

(1) E. Goto, T. Soma and M. Idesawa, J. Vac. Sci. Technol., 15, 883 (1978).
(2) G. Cogswell, S. Miyauch, K. Tanaka and N. Goto, Proc. 8th Symp. Electron and Ion Beam Science and Technology, 117 (1978).
(3) Y. Tarui, IEDM, 2 (1977).
(4) H.C. Pfeiffer, J. Vac. Sci. Technol., 15, 887 (1978).
(5) E.V. Weber and R.D. Moore, 15th Symp. Electron, Ion and Photon Beam Technology, F-3 (1979).

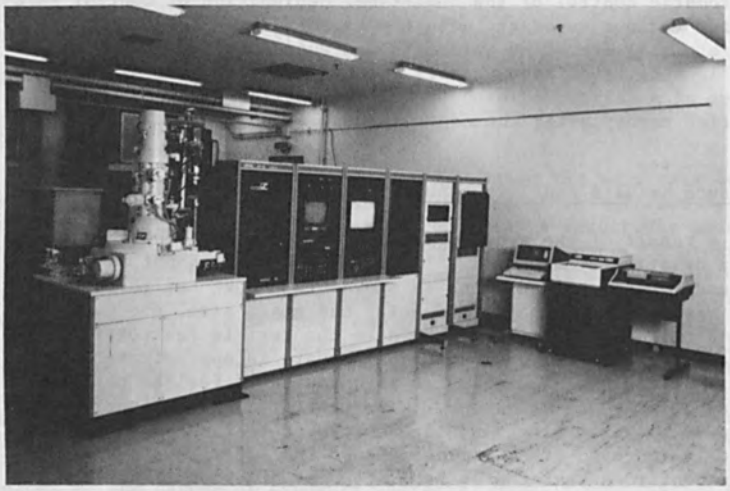

Fig. 1. General view of JBX-6A.

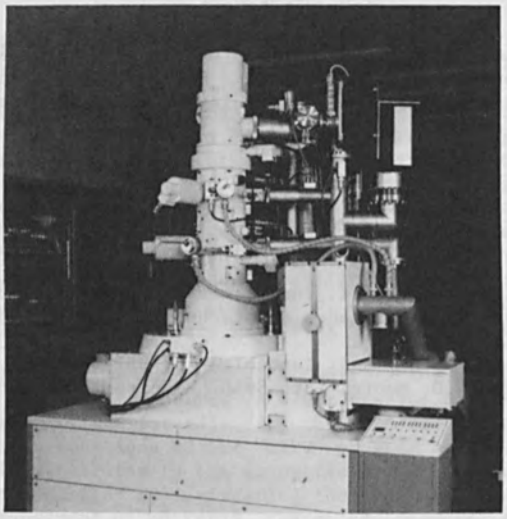

Fig. 2. Electron optical column equipped with automatic loading system.

1.	Electron Optical Column	
	Electron optics:	Variable shaped rectangle beam.
	Electron gun:	Tungsten filament, 20 kV. Subchamber for filament exchange.
	Beam size:	0.5 μm ∿ 12.5 μm with 0.05 μm step.
	Beam current:	0.4 A/cm^2, 0.625 μA (max.)
	Scanning field:	Variable field (2 m x 2 mm max.)
2.	Data Transfer	
	Beam shaping DAC:	9 bits (response: ∿ 800 ns).
	Beam position DAC:	17 bits (1/2 LSB, response: ∿ 850 ns).
	Shot cycle:	∿ 3.5 μs including a shot time of 2.5 μs (minimum shot cycle: ∿ 1.5 μs).
3.	Data Compression:	Employed.
4.	Work Stage	
	Work stage size:	5 x 5 inches for plate (max.) 4 inches dia. for wafer (max.)
	Positioning:	0.01 μm with electron beam and laser interferometer system.
	Driving speed:	∿ 0.3 s/2 mm, ∿11 mm/s (max.)
	Automatic loader:	12 pieces/1 magazine.
5.	Vacuum System:	Automatic clean vacuum system.
	Sputter ion pump:	110 ℓ/s, 450 ℓ/s.
	Turbo molecular pump:	450 ℓ/s.
6.	Computer System:	CPU (JEC-9808)
	Magnetic disk:	90 MB.
	Magnetic tape:	800 BPI, 1600 BPI, 2400 ft.
	IC memory:	128 KB and 1.5 ∿ 9 MB.
7.	Software	
	Input data:	PG 3000, Calcomp 900, JEOL format.
	Program:	CONV (data conversion). EXPC (exposure control). MONITOR, EBXULT, TSE 980, CHECK (miscellaneous).

Fig. 3. Principal specifications of JBX-6A.

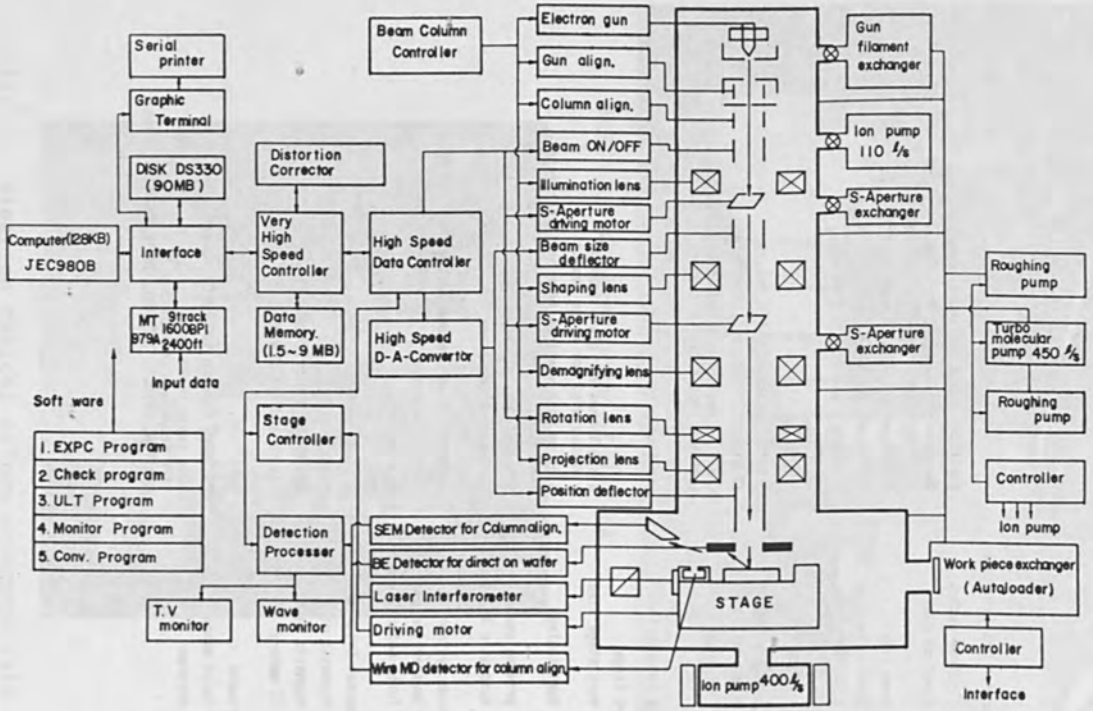

Fig. 4. System block diagram of JBX-6A.

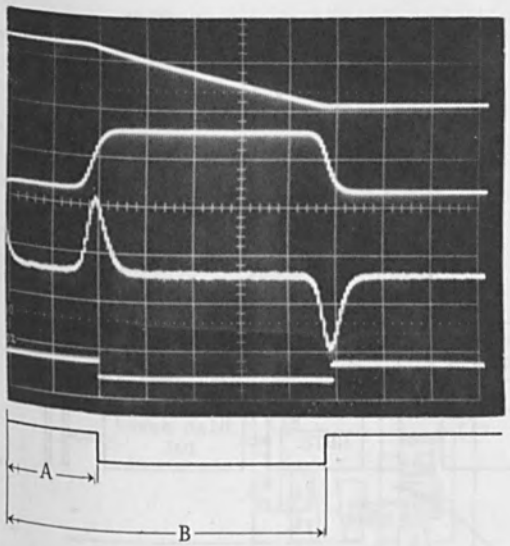


```
                                        300-500/B
                                AVERAGE                  1144.42
                                NUMBER OF DATA           100
                                STANDARD DEVIATION       σ=0.86(Point)
Point          0         10        20        30        40
      +---------+---------+---------+---------+---------+------.
<1139   0  +
 1139   0  +
 1140   0  +
 1141   0  +
 1142   0  +
 1143  13  +*************
 1144  44  +*******************************************
 1145  31  +*******************************
 1146  12  +************
 1147   0  +
 1148   0  +
 1149   0  +
>1149   0  +                                  0.025μm/1 Point
```

Fig. 5. Signal waveform and histogram for measurement of beam position (with wire detector).

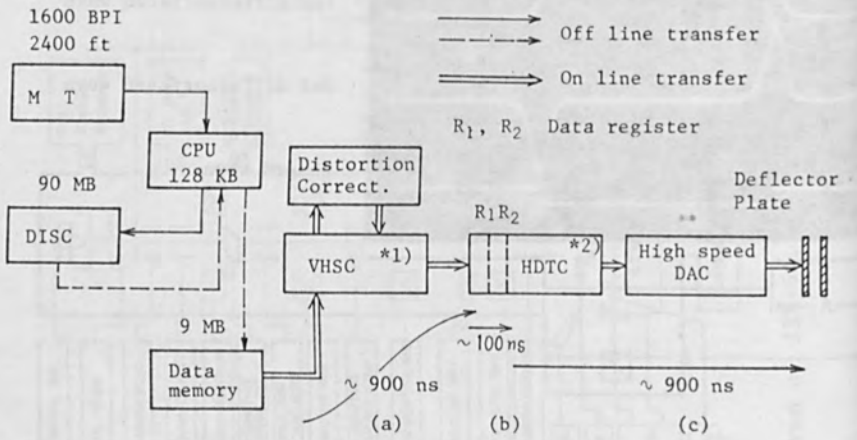

* 1) Main Functions of VHSC.

1. Correction of distortion.
2. Control for subfield shift step.
3. Parallel processing of signals.
4. Pipe line control.
5. Simultaneous processing for data and command.
6. Data compression.

* 2) Main Functions of HDTC.

1. Control for shot time.
2. Generation of rectangle and trapezoid patterns.
3. Signal provision for EOS control system.
4. Status check for respective control units.
5. Scan. generation for measuring system.
6. Counter for measuring system.

Fig. 6. High speed data transfer system.

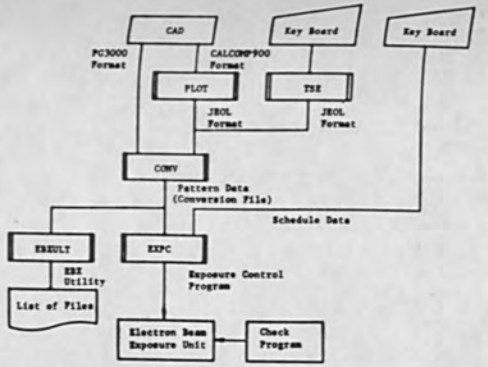

1) Outline of Software

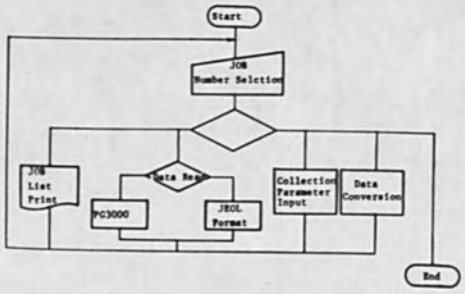

2) Block Diagram of Conversion Program (CONV)

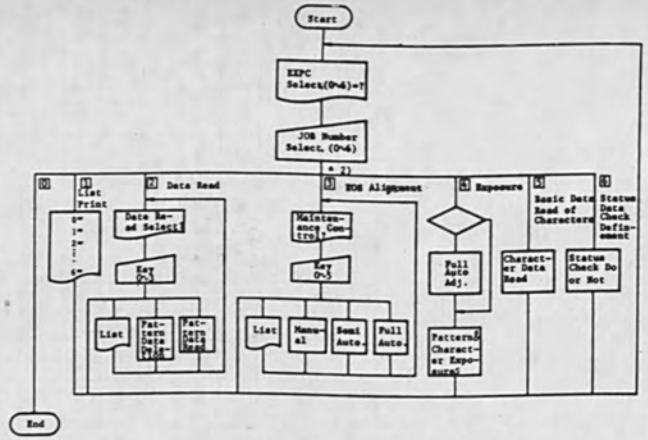

3) Block Diagram of Exposure Control Program (EXPC)

* 1) Main Functions of CONV

1) Data conversion (→ Expc format)
2) Bias
3) Unit transformation (inch→mill.)
4) Scaling
5) Mirror image
6) Maximum Slit width
7) Elimination of multi. exposure
8) Resize
9) Mega-Posi

* 2) Subroutines for EOS Adjustments

STGINI	MDWIRE
GHRTO	HEIGHT
POS	PRWIPE
GAIN	PRCHNG
ROT	XQWDSQ
PGR	RATIO
DISMES	GAINW
DISCHK	WRITING
FOCUS	PRBE
ERRINE	MDBE
PTSET	PRMRI

Fig. 7. Software

	1 μm lithography				2 μm lithography				4 μm lithography			
Plate size	5"		4"		5"		4"		5"		4"	
Chip size (mm□)	10	6	10	6	10	6	10	6	10	6	10	6
N. of chips	52	148	24	80	52	148	24	80	52	148	24	80
N. of shots/chip	2×10^6	6×10^5	2×10^6	6×10^5	7.5×10^5	2.5×10^5	7.5×10^5	2.5×10^5	3×10^5	1×10^5	3×10^5	1×10^5
Shot cycle	3.5 μsec. (Shot time 2.5 μsec.)											
1) Exposure time (sec.)	364	311	168	168	136	129	63	70	55	52	25	28
2) Stage shift (sec.)	497	525	229	284	497	525	229	284	497	525	229	284
3) MNTE (sec.)	30 ∿ 120											
4) Plate exchange (sec.)	30											
Cycle time for mask making (min.)	15.9	15.4	8.1	9.0	12.1	12.4	6.4	7.4	10.7	11.1	5.7	6.7
Pattern density (KRAM)	10^3	256	10^3	256	256	64	256	64	64	16	64	16

Notes. 1. Time required for MNTE is assumed to be 60 sec.
2. Only rectangle patterns are included.
3. Resist sensitivity : 1×10^{-6} C/cm^2
4. Cycle time for mask making : (1) + (2) + (3) + (4)

Fig. 8. Throughput in mask making.

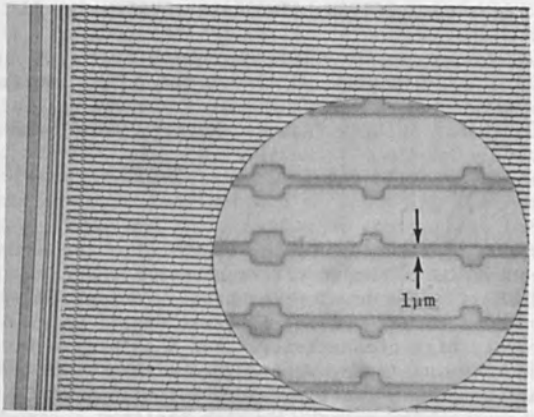

1. 1M bit RAM pattern with 1 μm line width.

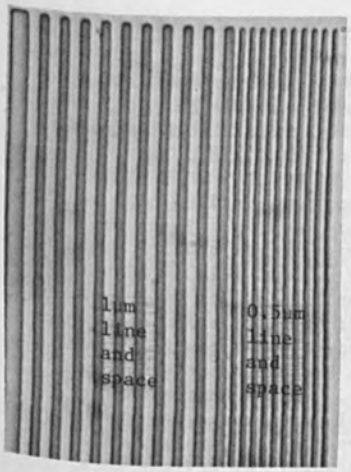

2. Submicron line pattern.

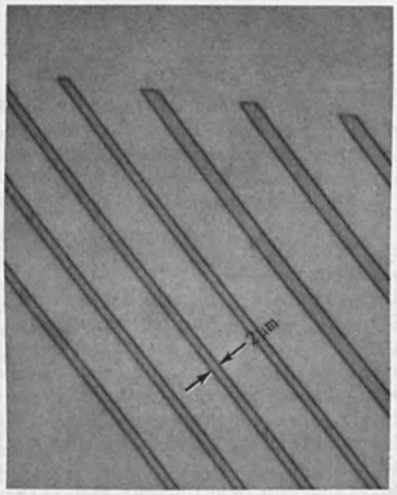

3. Oblique line pattern.

Fig. 9. Examples of exposure patterns.

DEVELOPMENT OF DIRECT WRITING EXPOSURE TECHNIQUE WITH THE ELECTRON LITHOGRAPHY SYSTEM JBX-6A

N. Goto, T. Someya, T. Yuasa, K. Tanaka and S. Miyauchi
JEOL Ltd., Nakagami, Akishima, Tokyo 196, Japan
G. Cogswell
JEOL (U.S.A.) INC., Peabody, Mass. 01960, U.S.A.

Abstract

By adding a direct writing function to the previously developed variable shaped electron beam lithography system JBX-6A(1)(2)(3), we developed a production-purpose electron beam direct writing exposure system which offers an extremely high productivity. For a chip size larger than the scanning field, we executed direct writing by use of a mark detection function and a measuring system based on a laser interferometer. We also realized a throughput of 10 to 20 minutes by introducing an automatic wafer loading system, automatic electron beam alignment system, higher speed data transfer system, etc. In addition, we proved that the overlay accuracy was 0.2μm (3σ).

1. Introduction

Successful fabrication of a 256K RAM by electron beam lithography(4), proven feasibility of fabrication of a 1M RAM(5), etc. are only a few examples of the recent extensively published advances in fabrication of VLSI by electron beam direct writing(6).

The advantages of electron beam lithography include high resolution, flexibility and high speed of pattern writing. These advantages have already made possible practical fabrication of quality masks for LSI and reticles and are expected to play a vital role in direct writing as well. The direct writing technique, as you well know, is believed to play the most significant part in fabrication of submicron devices in the future. Recent device production statistics reveal the growing trend toward a greater variety in smaller quantities, endorsing the importance of the technique. In the semiconductor industry stepping up the pace of technical development, on the other hand, the semiconductor manufacturers have greater interest in completing the development and trial manufacture of devices in a shorter period. The flexibility or ease of pattern correction, a major advantage of electron beam direct writing, seems to fully meet the requirement. From these points of view, we added a practical direct writing function to the JBX-6A system.

Direct writing, needless to say, is done by putting specific

registration marks on a wafer and exposing several to more than 10 layers of patterns on the basis of the marks. When the chip size is larger than the scanning field size, it is not desirable to put marks in a pattern. For this reason, we developed methods which, under this condition, make possible direct writing without deteriorating the accuracy. Although there are various methods that would serve the purpose, we adopted two methods. One is what we call the "wafer mark reference method" (Fig. 1, 1-a), whereas the other is what we call the "chip mark reference method" (Fig. 1, 1-b). Both of the methods feature a combination of the function of detecting the marks on a wafer by electron beam and the function of controlling the movement of the stage by a laser interferometer. In the case of a chip smaller than the scanning field in size, exposure is performed by detecting the four registration marks put on the corners of the chip as shown in Fig. 1, 2.

This paper describes the direct writing technique and its overall performance, including its methods, mark detection system, exposure process, throughput, etc. In completing the development of the writing technique, we owe a great debt of gratitude to the Electrical Communication Laboratory (NTT) and the Cooperative Laboratories VLSI Technology Research Association for their valuable suggestions and guidance.

2. Method of Direct Writing

An example of mark layout on a wafer is shown in Fig. 1. To allow for automatic mark detection by software, the registration marks must be set within predetermined permissible limits on the laser reference axes of the stage. Before a wafer is set on the stage, prealignment of the following two points must be accomplished.

a) P mark position: Set for less than 1mm with respect to the specified value (software specified value) on the laser reference axes. In this case, the mechanical accuracy is ±0.2mm. No alignment function is provided. Only verification is performed.
b) P mark cross line direction (or $\overrightarrow{PQ}$ direction): Set for less than 0.1^0 with respect to the laser reference axes. In this case, a mechanical alignment function is provided.

After the prealignment, the wafer is set on the stage. Under either of the methods, mark detection is executed fully automatically by software as the exposure is carried out. Marks can be made on the wafer surface by the "0 LEVEL" exposure based on the ordinary electron beam mask exposure technique, although they can also be made by optical means.

2-1 Wafer mark reference method

The layout of registration marks on a wafer is shown in Fig. 1,

1-a. Under this method, it is a prerequisite that the expansion rate of the wafer before and after each process is equal. Therefore, the distance ratios $|ef|/|PQ|$ and $|eg|/|RS|$ are constant. First the positions P, Q, R and S on the laser reference axes and the directions $\overrightarrow{PQ}$ and $\overrightarrow{RS}$ are found by use of the mark detection technique. Next the stage is moved to the 1st field (c_1-1) of the 1st chip to detect the marks e, f and g. On the basis of the marks the distances ef and eg with respect to the deflector and the position e are found to determine the deflector gain and scanning starting position. The scanning directions of the deflector are always fixed in the directions $\overrightarrow{PQ}$ and $\overrightarrow{RS}$.

After exposure of the 1st field in this manner, the stage is moved to the 2nd field. Let the values specified at the time of mark fabrication be $|e_of_o|$ ($|e_og_o|$) and $|PoQ_o|$ ($|RoSo|$) and let the value measured at the time of the nth layer exposure be $|PnQn|$ ($|RnSn|$), and the movement of the stage is given by $|e_of_o|/|PoQo| \times |PnQn|$ ($|e_og_o|/|RoSo| \times |RnSn|$). The directions of stage movement with respect to the axes x and y respectively coincide with the directions $\overrightarrow{PnQn}$ and $\overrightarrow{RnSn}$. After movement of the stage, the 2nd field is exposed under the same deflector conditions as for the 1st field. In this manner all fields are exposed one after another until exposure of the whole chip is completed.

This method makes possible exposure of a chip size larger than the field size, does not require marks to be put in the chip, does not necessitate wasteful movement of the stage at the time of exposure of chips for performing mark detection, and eliminates the effects of electron beam drift and wafer height variation, as the mark position and deflector gain are measured for each chip.

2-2 Chip mark reference method

The mark layout on a wafer is shown in Fig. 1, 1-b. This method can be effectively used for a wafer involving irregular distortions before and after the wafer process. Thus $|ef|/|PQ|$, $|eg|/|RS|$ = Constant, and exposure performed only on the basis of chip marks e, f and g. All of the deflector gain, rotation and scanning starting position and stage moving direction and movement are determined on the basis of the marks e, f and g. First, at the location of the P mark, the P mark position concerning the laser reference axes is obtained (prealignment) and the stage moved to the center of the 1st field of the 1st chip (c_1-1 in Fig. 1, 1-b). At this place the marks e, f and g are detected to find the position of e, distances and directions of ef and eg with respect to the deflector. On the basis of the measurements the scanning starting position (S), deflector gain (A) and deflector rotation (R) are determined.

Then, the stage movement and moving direction are determined. When the stage movement and moving direction are determined, the positions of e, f and g must be measured under the same condition to

prevent effects of deflector characteristics on detection of the marks e, f and g. When e, f and g are to be measured, therefore, the position of e is measured at c_1-1 in Fig. 1, 1-b for example. Next, the stage is shifted to move f to the position of e and measure the position of f. Then, g is moved to the position of e to measure the position of g. In this manner the distances ($|ef|$, $|eg|$) and directions ($\vec{ef}$, $\vec{eg}$) of ef and eg with respect to the laser reference axes are found to determine the movement (L) and moving direction (D) of the stage from the 1st to 2nd field. On the basis of the scanning starting position (S), deflector gain (A) and deflector rotation (R) found as described above, the 1st field is exposed, and then the stage is moved to the 2nd field according to the movement (L) and moving direction (D). Exposure of the 2nd field is performed under the same deflector condition as for the 1st field. In this manner all fields are exposed one after another until exposure of the entire chip is exposed.

This method makes possible exposure of a chip size larger than the field size, does not cause deterioration of accuracy even with irregular distortions and warp in the wafer process, and eliminates the effects of beam drift and wafer height variation, as the mark position and deflector gain are measured for each chip.

2-3 Four-point mark method

The mark layout on a wafer is shown in Fig. 1, 2. This is a method suited for exposure of a chip size smaller than the field size. First, at the location of the P mark, the P mark position concerning the laser reference axes is found (prealignment), and the stage moved to the 1st chip (c_1 in Fig. 1, 2). Exposure is performed by detecting the marks e, f, g and h put at the four corners of the chip and determining the scanning starting position, deflector gain and deflector rotation with respect to the deflector.

This method offers the advantages that the exposure accuracy does not depend on the accuracy of the laser interferometer system and that the method is free from the effects of beam drift, wafer height variation, wafer distortion, etc., as the deflector gain and the scanning starting position are determined on each chip.

3. Detection and measuring system

In direct writing, the mark detection functions (7) (8) (9) are the most important elements. It is desirable that the mark positions for the electron beam be measured accurately and in a short time.

Normally, through use of P-N junction, accurate mark positions are obtained by running a scanning beam across the marks on the wafer and measuring the back-scattered electron intensity variations. The

mark shape (Fig. 2, 3) may be either depressed or raised shape. It is desirable that the mark width be more than several μm and the mark depth be more than 5,000Å. As for the beam shape, a 1μm × 12.5μm shaped slit beam is used. We do not correlate the slit beam width (Bw) and mark width (Mw). The sweep width and scanning speed by the deflector are respectively 20 to 30μm and 0.5μsec/step (0.025μm), and detection performed by 10 to 20 forward and backward scannings. Therefore, the measuring time per mark is 20 to 50msec. Normally, under the wafer mark reference method, the time required for mark detection per chip, including the measuring time, calculation time, etc., is less than several 100msec. The mark position is obtained by averaging four data items, A and B obtained by forward scanning and C and D obtained by backward scanning (Fig. 2, 1).

Fig. 2 shows the block diagram of the signal processing system, photograph of the P-N junction and diagram of relation between marks and signals. Fig. 3 shows a photograph of signal waves under forward scanning in various parts of the signal processing system and a histogram showing the dispersion of the "A" counter measurements. The mark positions are obtained by arithmetically averaging the measurements, and the measurement accuracy is less than 0.01μm. However, since the minimum correction unit is 0.025μm, the position accuracy by mark detection is 0.025μm.

4. Exposure procedure

Actual exposure is performed fully automatically by the exposure control program (EXPC). The software is discussed in detail under a separate theme at this conference. For direct writing, a program consisting of two subroutines, "WSETING" for detecting the wafer marks and "GAINW" for detecting each chip mark, and "schedule data" specifying various mark positions, added to an ordinary mask exposure program is used. Direct writing of each method can be done by changing the "assignments" of the schedule program.

The exposure procedure for direct writing and the average required time are shown in Fig. 4. The exposure data and schedule data specifying the chip arrangement, pitch of chip, mark position, type of pattern, etc. can be loaded in advance in the data memory (to be presented at this conference) and CPU memory during the evacuation period.

5. Throughput and exposure results

As previously stated, the most important part of direct writing is to increase the throughput. Fig. 5 shows the throughput time for the wafer mark reference method of the direct writing technique we developed at this time. The exposure cycle per wafer, required for fabrication of a 10mm square chip, from 1μm lithography of 4-inch

wafer to 4μm lighography of 3-inch wafer, is 19 to 7 minutes, although it depends largely on the number of patterns, chip size, pattern detail, etc. Exposure of a 2-inch wafer can be made in 5 to 4 minutes.

Figs. 6 and 7 show the exposure results. Fig. 6 shows a test pattern of verniers around the field showing the accuracy of overlay exposure. I and II respectively indicate the 1st and 2nd layer patterns. The four verniers on the field boundaries show the stitching accuracy at the corners of the 2mm scanning field at the time of the 1st layer pattern exposure. The verniers are displaced 0.1μm from each other. This photograph shows that the overlay accuracy, including the stitching accuracy, is less than ±0.2μm. Fig. 7 is a photograph of a 1μm square through hole pattern exposed and etched as the 1st layer pattern and a 1μm width circuit pattern overlaid and developed as the 2nd layer pattern.

6. Conclusion

The direct writing method for a chip size larger than the field size, its throughput and exposure accuracy have been described. To realize a production machine for direct writing, the throughput must be further increased, but we are convinced that a sufficient level of performance to meet the recent trends toward higher pattern density integration, greater variety in smaller quantities and shorter turn-around time could be achieved.

Acknowledgement

The authors are indebted to Dr. H. Katsuragi and Dr. T. Ogawa, Electrical Communication Laboratory (NTT), for their guidance and cooperation in the development of the direct writing techniques.

References

(1) E. Goto, T. Soma and M. Idesawa, J. Vac. Sci. Technol., 15, 883 (1978)
(2) G. Cogswell, S. Miyauchi, K. Tanaka and N. Goto, Proc. 8th Symp. Electron and Ion Beam Science and Technology, 117 (1978)
(3) H. Katsuragi, The Journal of the Institute of Electronics and Communication Engineers of Japan, 61(8), 884 (1978)
(4) T. Mano, K. Takeya, T. Watanabe, K. Kiuchi, T. Ogawa and K. Hirata, A High-Performance 256K RAM Fabricated with Molybdenum-Polysilicon Technology, ISSCC, San Francisco (1980)
(5) Cooperative Laboratories VLSI Technology Research Association, in private communication
(6) E.V. Weber and R.D. Moore, 15th Symp. Electron, Ion and photon Beam Technology, F-3 (1979)
(7) A.D. Wilson, T.H.P. Chang and A. Kern, J. Vac. Sci. Technol., 12,

1240 (1975)
(8) D.E. Davis, R.D. Moore, M.C. Williams and O.C. Woodard, IBM J. Res. Develop., 21, 498 (1977)
(9) W. Stickel, J. Vac. Sci. Technol., 15(3), 901 (1978)

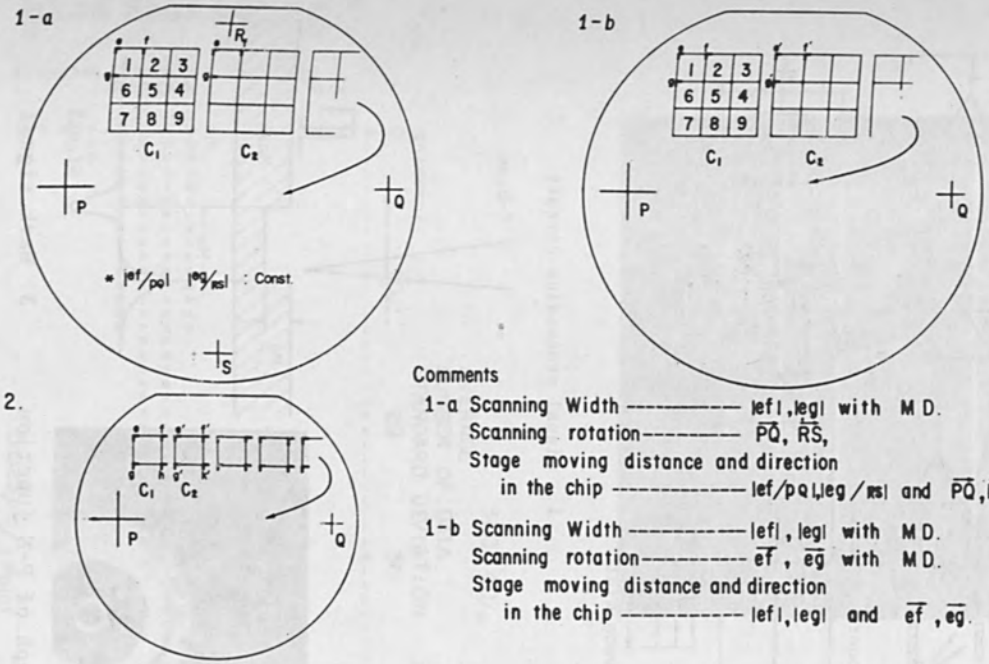

Fig. 1. Exposure methods for direct writing.

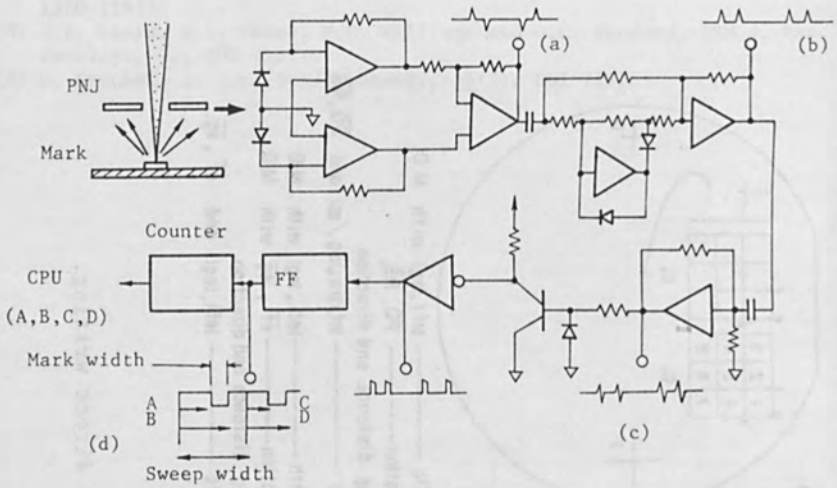

1. Signal processing circuit

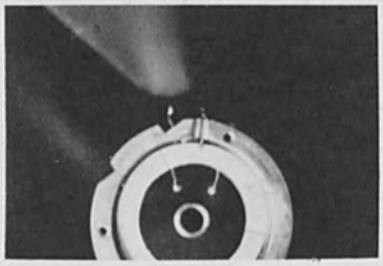

2. Photograph of P-N junction

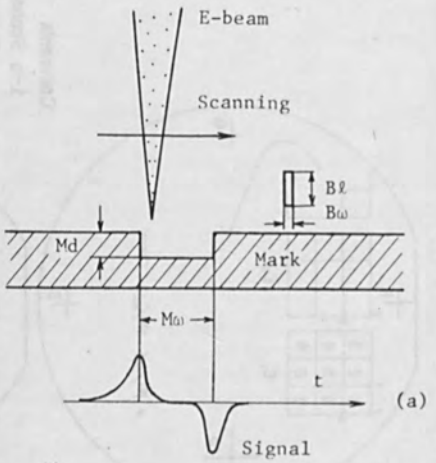

3. Mark signal

Fig. 2. Method of mark detection.

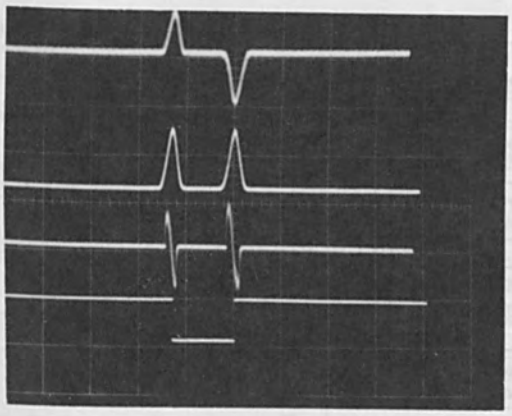

(a)

(b)

(c)

(d)

500 - 40/A

AVERAGE	2315.47
NUMBER OF DATA	100
STANDARD DEVIATION	σ=0.99(Point)

```
                0          10          20          30          40
Point           +----------+----------+----------+----------+
< 2310    0     +
  2310    0     +
  2311    0     +
  2312    0     +
  2313    1     +*
  2314   14     +**************
  2315   40     +****************************************
  2316   29     +****************************
  2317   14     +**************
  2318    2     +**
  2319    0     +
  2320    0     +
> 2320    0     +
```

0.025μm/1 Point

Fig. 3. Signal waveform and histogram for measurement of beam position.

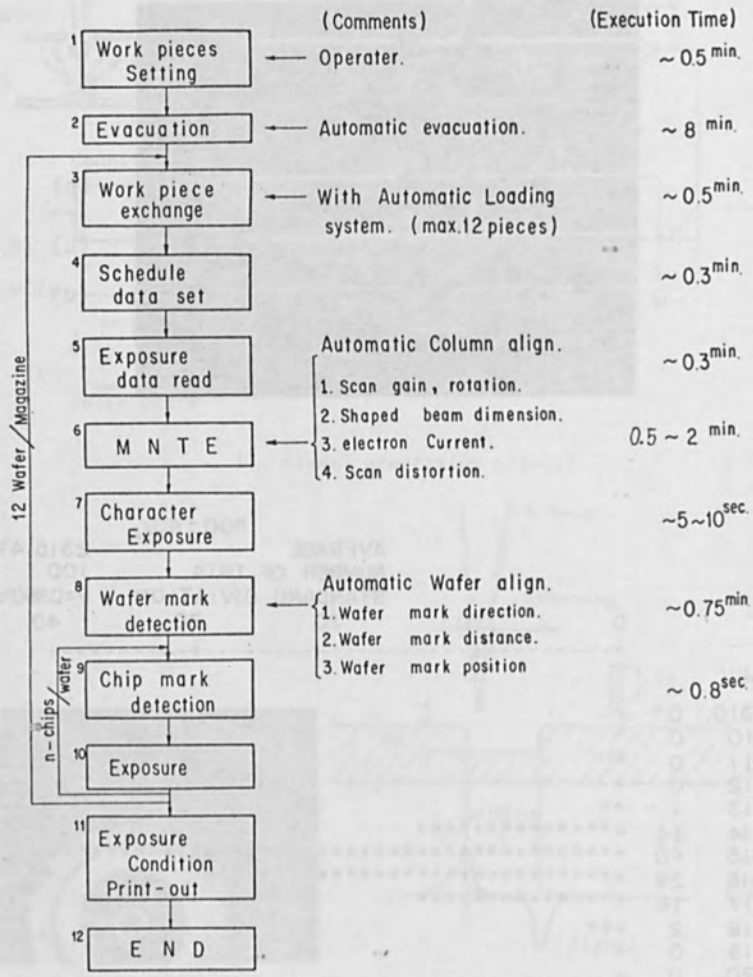

Fig. 4. Exposure procedure for direct writing.

	1 μm lithography				2 μm lithography				4 μm lithography			
Wafer size	4" dia.		3" dia.		4" dia.		3" dia.		4" dia.		3" dia.	
Chip size (mm□)	10	6	10	6	10	6	10	6	10	6	10	6
N. of chips	52	148	24	80	52	148	24	80	52	148	24	80
N. of Shots/Chip	2×10^6	6×10^5	2×10^6	6×10^5	7.5×10^5	2.5×10^5	7.5×10^5	2.5×10^5	3×10^5	1×10^5	3×10^5	1×10^5
Shot cycle	3.5 μsec. (Shot time 2.5 μsec.)											
1) Exposure time (sec.)	364	311	168	168	136	129	63	70	55	52	25	28
2) Stage shift (sec.)	497	525	229	284	497	525	229	284	497	525	229	284
3) MNTE(Auto. align. of column) (sec.)	30 ~ 120											
4) MD (sec.)	52	148	24	80	52	148	24	80	52	148	24	80
5) WSETING (sec.)	40											
6) Wafer exchange (sec.)	30											
Cycle time on wafer (min.)	17.4	18.6	9.2	11.0	13.6	15.5	7.4	9.4	12.2	14.3	6.8	8.7
Pattern density (KRAM)	10^3	256	10^3	256	256	64	256	64	64	16	64	16

Notes:
1. Wafer mark reference method is used.
2. Time required for MNTE is assumed to be 60 sec.
3. Only rectangle patterns are included.
4. Resist sensitivity : 1×10^{-6} C/cm^2
5. Cycle time on wafer : (1) + (2) + (3) + (4) + (5) + (6).

Fig. 5. Throughput in direct writing.

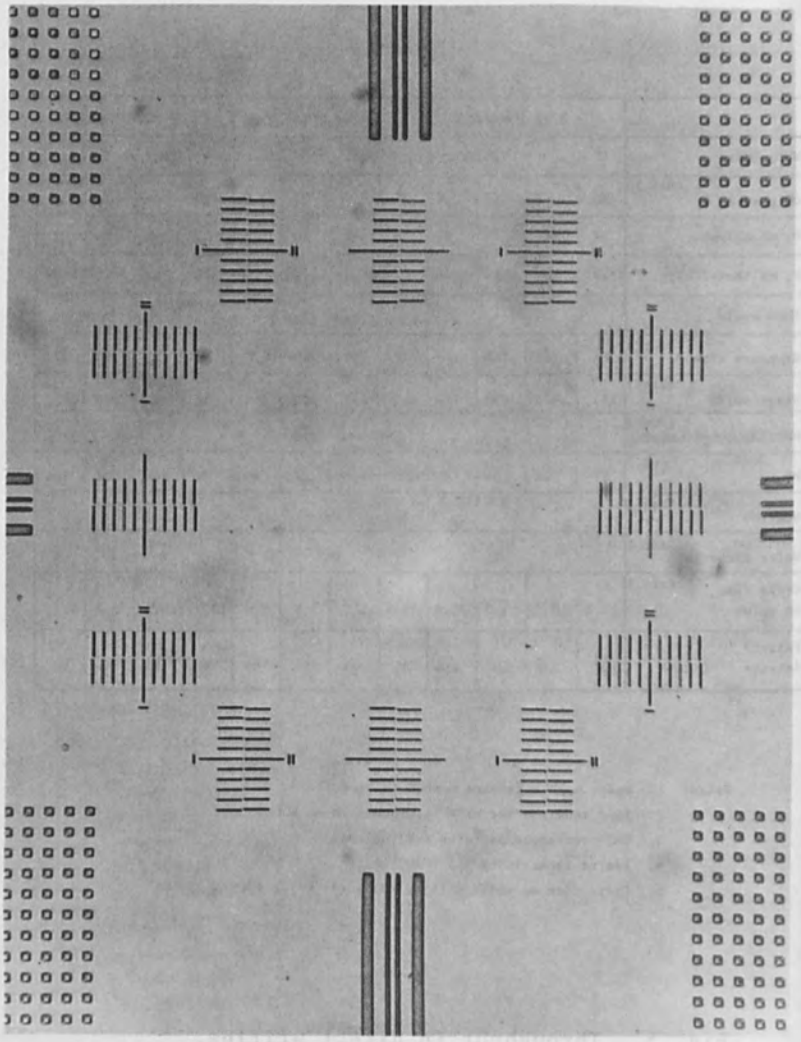

Fig. 6. Vernier test pattern showing overlay and stitching accuracies of less than +0.2μm.

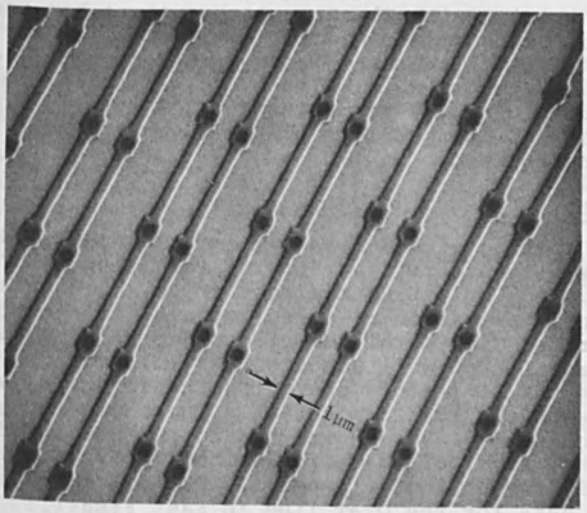

Fig. 7. SEM photograph of overlay exposure pattern. 1st layer etched through hole pattern is overlaid with 2nd layer circuit resist pattern.

E-BEAM DIRECT WRITING IN MANUFACTURING

R. D. Moore

IBM Data Systems Division - East Fishkill
Hopewell Junction, NY 12533

ABSTRACT

Direct writing with Electron Beam systems has been used to manufacture semi-conductor devices at IBM for over five years. Some of the experience gained from this application will be discussed in this paper. Additional manufacturing applications of E-Beam direct write systems are considered. Some of the problems that may develop with their use are also reviewed.

INTRODUCTION

Direct writing with E-Beam systems has been used primarily in semi-conductor laboratories for advanced product development. The only E-Beam direct write, high volume manufacturing application revealed to date has been the Quick Turnaround Time (QTAT) Manufacturing Line operating at IBM's plant in Hopewell Junction, NY (1, 2, 5). Presently there are six EL-1 tools operating in QTAT-type manufacturing lines in the IBM Corporation. The operating experience with these tools has shown them to be equal, and in some respects, superior to optical lithography equipment from a manufacturing tool viewpoint. Table 1 contains EL-1 performance data for the QTAT line in East Fishkill.

Several factors are developing that could move E-Beam direct write lithography into large-scale applications of semi-conductor manufacturing in the near future. First, significant systems advances have been reported over the past few years, making E-Beam direct write a more competitive technology. Second, the evolution toward micron and sub-micron dimensions has moved lithography requirements to the limits of optical technology. E-Beam direct write is the lithography technique most likely to replace optics. Thirdly, selective use of direct write allows for "personalization" of masterslice wafers, giving an "open part number set" to prospective users. This open part number set is rapidly available to the user and has proven to be invaluable in computer development (2).

The introduction of E-Beam direct write into manufacturing applications places demands on the E-Beam system that either do not exist, or are not as severe in laboratory applications. Some of these considerations are:

1. System throughput requirements
2. Pattern data handling
3. System to system compatibility
4. System stability
5. System RAS

SYSTEM THROUGHPUT REQUIREMENTS

If E-Beam direct write lithography is to compete with optical and other lithographic techniques, the basic system throughput must be competitive. This means that for 1.5μ product, the system throughput must be in the range of 25 (3 in.) wafers per hour. The highest reported throughputs for direct write systems are those of the EL-1 and EL-2 systems at about 10 wafers per hour (1, 3).

Electron optics advances (4) and system advances reported over the past few years have moved E-Beam system technology to where a 25 wafer per hour system is achievable, and a 50 wafer per hour system is conceivable.

Table 2 shows throughput performance parameters. Tables 3 and 4 illustrate possible system performance changes that would increase direct write throughput, with indications of possible approaches that could be used to achieve this.

Table 2 lists the throughput parameters for EL-1. For the 2.5μ lithography product being run on EL-1, the throughput is 10 wafers per hour. Wafer handling is done serially, registration computations are made in the S/370, and raster scan is used.

Table 3 lists system performance parameters that have been reported recently. These parameters are for direct writing 1.5μ product. Vector scan coupled with variable shaped spot is assumed. Registration is improved via dedicated analog circuitry. A system utilizing these approaches would be capable of 25 wafers per hour.

Table 4 shows the performance levels possible in a near term (2 - 3 years) system. Assumed in these estimates are some enhancements reported to be in development (4). Character projection and faster resist performance are assumed as well as batch loading of wafers. Wafer size assumed in all cases is 82mm.

PATTERN DATA HANDLING

A high-throughput, direct write E-Beam system used for semi-conductor manufacture places two primary demands on its pattern data management system. First, it must be capable of rapidly storing and locating part number data as required. Once located, it must supply that data to the beam control electronics in real time so that data supply does not limit system throughput.

System DP architecture must be developed in conjunction with the imaging and deflection subsystems. EL-1 uses high speed disks and a data compaction technique to insure data transfer does not limit system performance on the QTAT line.

In EL-1, up to four IBM 3330 disk drives can be used, allowing on-line storage of up to 5000 part numbers at 250 kilo-bytes per part number. Use of raster scan results in peak data rates during writing of up to 8 Megabytes per second. High speed custom logic and pattern buffering are used to handle these peak data loads.

Future requirements of 25 to 50 wafers per hour with more complex product patterns will increase the data management problems. Vector scan techniques, shaped beam techniques, more efficient data compaction, and large high speed on-line memories will be used to insure data management remains a "background" systems operation.

Figure 1 is a block diagram of a pattern data subsystem for an E-Beam tool. The pattern library stores all part number data and can use either tape or disk storage. The main processor and the high speed digital system must store and manage the data for a day's production. The output of the digital system is a high performance bus that drives the analog system and, in turn, the writing beam.

Table 5 lists some key data management related parameters for EL-1 applications and future requirements. The high speed bus between the digital and analog subsystems is a key design challenge for any future high throughput manufacturing tool. One design approach being considered is the use of a large capacity memory in the digital subsystem capable of storing the total data required for writing a wafer. Another approach is to develop more efficient data compaction techniques to reduce the peak data rates.

SYSTEM-TO-SYSTEM COMPATIBILITY

E-Beam systems used in an efficient manufacturing line should be designed to be compatible with other lithography tools, both optical and E-Beam, in that line.

The movement to 1μ product manufacturing will result in mixed lithography tooling where tight tolerance levels will be written by E-Beams and non-critical levels by optical lithography.

There are two proven E-Beam System techniques that will be invaluable in optimizing overlay in these mixed technology lines. The four-corner field registration and the "LEARN" field calibration scheme have been used successfully in both EL-1 and EL-2 to accomplish this (6).

The LEARN technique is used to virtually eliminate any electron-optic or other field deflection distortions in the EL-1 and EL-2 systems. The LEARN corrected field for each system is absolutely accurate to less than 30 ppm. The field-corrected systems are, therefore, identical and E-Beam to E-Beam compatibility is achieved.

Optical to E-Beam compatibility can be achieved in one of two ways. In the situation where optical field distortion is limited to displacement, magnification, and trapezoidal errors, the four-corner registration technique can be used to achieve the desired overlay. This type of optical distortion has been found with reflective full-field systems. This type of correction is illustrated in Figure 2.

Where the optical distortions are more complex, as in step and repeat reduction systems, it is necessary to use both four-corner registration and a modified LEARN system to achieve overlay. By accurately plotting lens distortion and modifying the LEARN field, it is possible to emulate the optical distortion in the E-Beam field. Four-corner registration is then used as before to achieve the final E-Beam to optical overlay. Figure 3 shows a typical 10:1 reduction system field error that could be corrected with LEARN.

SYSTEM STABILITY

System stability objectives are, for the most part, determined by product and process requirements. Field stability limits are determined by product overlay specifications. These specifications will determine the accuracy and frequency requirements of the calibration (LEARN) operation. Beam current stability and beam shape stability are determined by the lithography process. Electronic methods must be employed to measure and correct beam parameters to required levels. Experience has shown that beam stability can be achieved only with the use of real time servo-type corrections on most beam parameters. Reliability, Availability, and Serviceability (RAS) data for the electron-optics subsystems of EL-1 illustrates the value of the "Servo" type correction systems. Mean time to failure (MTF) for the column, gun, and associated hardware is in excess of 400 hours. Shown in Figure 4 is a schematic of the beam servo system used in EL-1.

SYSTEM RAS

As with any manufacturing tool, a direct write, E-Beam system operating in a semi-conductor line must have a RAS plan that allows for up time to be 80% or greater of available time. That target has been shown to be reasonable with a system designed with an RAS plan as part of the basic design objectives (7). Table 6 lists some recent EL-1 system RAS data.

Overall, our experience with Electron-Beam lithography tooling in IBM has been very encouraging. When all factors are considered, E-Beams become competitive with other lithography in the sub-2μ region.

REFERENCES

(1) E.V. Weber and H.S. Yourke, "Scanning Electron-Beam System Turns Out IC Wafers Fast," Electronics, November 10, 1977.

(2) H.W. Curtis, "Integrated Circuit Design, Production and Packaging for System/38," IBM System/38 Technical Developments, p. 11 (1978).

(3) R.D. Moore and E.V. Weber, "EL2: Variable Shaped Spot E-Beam Lithographic Tool," 15th Symp. on Electron, Ion and Photon Beam Technology, May 29 - June 1, 1979, Boston, Mass.

(4) H.C. Pfeiffer, "Recent Advances in Electron-Beam Lithography for the High-Volume Production of VLSI Devices," IEEE Trans. El. Dev. ED-26, p.663, (1979).

(5) Ning-Gau Wu, "The Design and Operation of a Highly Automated Semi-conductor Production Line," ISSCC 80, (2/80) San Francisco, Cal.

(6) H. Engelke, J.F. Loughran, M.S. Michail, and P.M. Ryan, "Correction of Nonlinear Deflection Distortion in a Direct Exposure Electron-Beam System," IBM J. of Res. and Development, (11/88) p.506.

(7) R.D. Moore, "Reliability, Availability, and Service-ability of Direct Wafer Exposure Electron Beam Systems," in Proc. Int. Conf. on Microlithography, (1977) Paris, France.

TABLE 1

1979 EL-1 Performance (3 Systems)

Wafer Exposures = 65,723

Different Field Sizes = 7 (129 Mils to 240 Mils)

Different Master Slices = 11

Raw System Throughput = 10 W/Hr.

Part Numbers in Residence ≈ 2,400

System Availability = 95% for 2-Shift Operation

TABLE 2

Wafer Write Times

Operation	EL1 (1974)	
	Time (Sec.)	Approach
T_L Wafer Load	15.0	Serial
T_{WR} Wafer Registration	2.0	Software (S/370)
T_{FR} Field Registration	0.3	Software (S/370)
T_{FW} Field Write	1.0	Raster $50\ A/cm^2$ $10\mu C/Resist\ cm^2$
T_{FM} Field Move	0.5	Servo Control
T_{UL} Wafer Unload	10.0	Serial

For 150, 5mm fields/wafer @ 2.5μ design @ 30% Dense wiring

Throughput ≈ 10 w/hr.

TABLE 3

Wafer Write Times

Operation	With Today's Technology	
	Time (Sec.)	Approach
T_L Wafer Load	10.0	Serial
T_{WR} Wafer Registration	1.0	Hardware
T_{FR} Field Registration	0.1	Hardware
T_{FW} Field Write	1.0	VSS (EL-2) VECTOR (VS) $10\mu C$ (Resist) cm^2
T_{FM} Field Move	0.2	Improved Servo (EL-2)
T_{UL} Wafer Unload	5.0	Serial

For 100, 6.5mm fields/wafer @ 1.5μ design @ 30% Dense wiring

Throughput ≈ 25 w/hr.

TABLE 4

Wafer Write Times

Operation	With Near Term Improvements	
	Time (Sec.)	Approach
T_L Wafer Load	2.0	Batch Loading
T_{WR} Wafer Registration	1.0	Hardware
T_{FR} Field Registration	0.05	Hardware
T_{FW} Field Write	0.5	VSS Character Projection VECTOR 1-5μC/cm^2 Resist
T_{FM} Field Move	0.1	Write during ring out
T_{UL} Wafer Unload	2.0	Batch Loading

For 100, 6.5mm fields/wafer @ 1.5μ design @ 30% Dense wiring

Throughput ≈ 52 w/hr.

TABLE 5

Data Volumes/Rates for Direct Write E-Beam

	EL1	Future Requirements
Line Width	2.0 - 2.5μ	1μ - 1.5μ
Data Volume/Chip	250k Bytes-500k Bytes	1MByte-2MBytes
Throughput	10 W/Hr.	50 W/Hr.
Time/Chip	2.0 sec.	.65 sec.
Field Data Rate to Analog	.1-.2MBytes/sec.	2.0-4.0MBytes/sec.
Peak Data to Analog	8MBytes/sec.	20 - 40MBytes/sec.

TABLE 6

EL-1 RAS (1979)

Average for three EL-1 tools:

MTF	33.5 Hrs.
MTR	1.81 Hrs.
Availability	95%

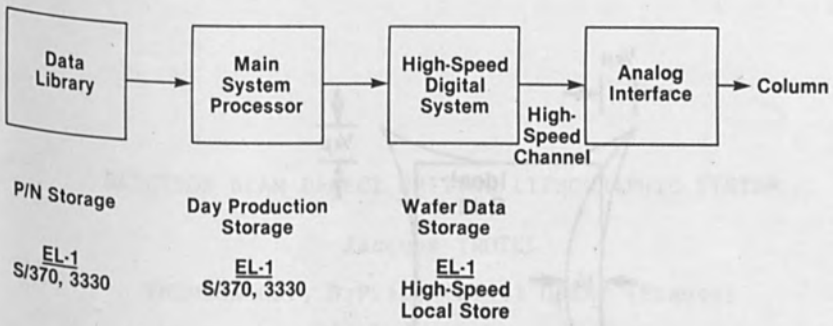

Fig. 1 Pattern Data Processing

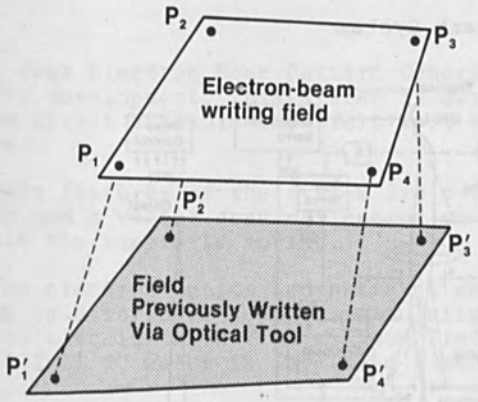

Fig. 2 Field Registration Compensation for Optical Field Distortion

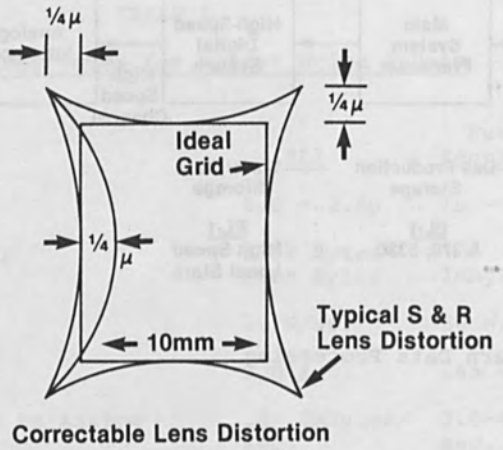

Fig. 3 Step & Repeat System

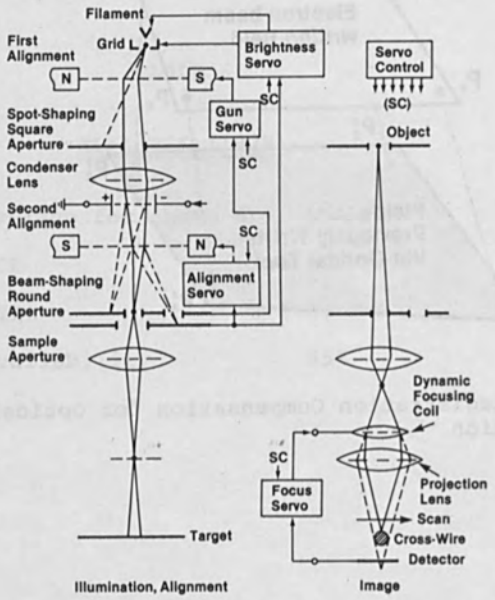

Fig. 4 Servo Systems Controlling Beam Illumination, Alignment, and Image

ELECTRON BEAM DIRECT WRITING LITHOGRAPHIC SYSTEM

Jacques TROTEL

THOMSON-CSF, B.P.10 - 91401 ORSAY (France)

Abstract

A fast Electron Beam Pattern Generator (FEPG) is under development, this system is designed to make E. Beam direct exposure of wafers fast enough for production.

Main features of the system are a variable shape beam and a vector scan deflection on a small area while the sample is moving.

The electron optics and patterns delineation strategy is described. Computer simulation shows that typical circuits with 1 µm minimum linewidth can be drawn on a full 3" wafer in less than 5 minutes.

ELECTRON BEAM DIRECT WRITING LITHOGRAPHIC SYSTEM

Jacques TROTEL

THOMSON-CSF, B.P.10 - 91401 ORSAY (France)

A fast Electron Beam Pattern Generator (FEPG) is under development in our laboratory. The main specifications of the system are as follows :

Wafer size	:	up to 6"
Throughput	:	10 3" wafers/hour
Minimum linewidth	:	1 µm for maximum throughput

The system has the capability to make 0.3 µm minimum linewidth at a lower throughput.

The Electron optics uses the variable shape beam concept [1].

Figure 1 gives its principle :

The cross-over of a tungsten hairpin filament gun is magnified and imaged on an aperture A_1 which has at least one right angle.

The aperture A_1 is imaged at scale one on an aperture A_2 similar to A_1 by a nearly confocal doublet L_2 and L_3 .

The intersection of A_2 and the image of A_1 forms a rectangle, the dimensions of this rectangle can be changed by a deflector D_1.

This rectangle is demagnified and imaged on the sample by the final lens L_4 , its position over the sample can be changed by the deflector D_2.

Main specific features of the electron optics are :

- Critical illumination scheme, that is to say illumination of the apertures by the cross-over image, Usually the illumination is of the Kohler illumination type, in which the image of the cross-over is on the entrance pupil of the last lens.

  We found that is was easier to get an homogeneous and reproducible illumination with the critical illumination type.

- Short focal length of the last lens L_4 . The lens L_4 has a 15 mm focal length. With such a short focal length we get :

  · Low spherical and chromatic aberrations.

  · High demagnification : 10 to 1 demagnification can be obtained with only one lens.

  · Low sensitivity to spurious electric and magnetic fields : Due to the short path of the beam, drift of the beam is strongly reduced.

The main drawback of that short focal length is high deflection aberration coefficient, so the deflection field has to be limited to 0.16 x 0.16 mm^2.

Due to the small deflection field it would be too much time consuming to step the table and to stop it when the beam is writing, so writing is done while the table is moving.

The movement of the table is illustrated on figure 2 : The pattern of each chip is divided into 0.16 mm width stripes. The same stripe in each chip is written while the table has a meander like movement illustrated by the solid line, then the next adjacent stripe is written by moving the table according to the dotted meander line.

Deflection of the beam is of the vector scan type, but it has to take into account the movement of the table in the y direction. Figure 3 shows the principle of the y deflection only :

On the upper right hand side is an example of a pattern to be written, comprising five rectangles R_1 to R_5 ; each rectangle is supposed to be smaller than the maximum dimension of the beam, so each rectangle is made by a single exposure and the time to make it is constant to a first approximation.

On the left hand side are several time diagrams :

On coordinates (y,t) : The solid line Y_T gives the movement of the sample compared to the optical axis of the electron optic column, the movement is assumed to be at constant speed although it is not mandatory.

The dotted line Y_R gives the movement of the beam compared to the sample, this movement has some plateaus whose length is given by the time necessary to expose the rectangles.

On coordinates (Y_B,t) is the representation of the deflection, that is the movement of the beam compared to the optical axis of the electron optic column.

On coordinates (B,t) is the time diagram of the intensity of the beam.

On coordinates (E,t) is an error signal which occurs when the amplitude of the deflection of the beam exceeds a given value.

It can easily been understood that curve (Y_B,t) is obtained by substracting curve (Y_T,t) from curve (Y_R,t).

Curve (Y_T,t) is given in digital form by the output of an interferometer which monitors the movement of the table driven at constant speed by a D.C. motor.

The plateaus of curve (Y_R,t) are given by the output of a memory containing the description of the pattern to be drawn, with the rectangles ordered according to their y value. The read signal of that memory is derived from the (B,t) curve.

Curve (Y_B,t) is then obtained by making in real time the difference between the output of the interferometer and the output of the memory. The result of that difference is clipped so as not to exceed the deflection limits.

To get the maximum speed, the table must move as fast as possible without being in the situation where the deflection which would be necessary exceeds the maximum amplitude of the deflector.

The maximum speed depends on the time to make a rectangle and on the density of rectangles.

Some computer simulations have been made to get an evaluation of that maximum speed.

The simulation has been done on an actual integrated circuit and on circuits which where deduced from it by reducing the geometry by 2 and 4 and stitching these reduced circuits to get 5 mm x 5 mm and 10 mm x 10 mm chip sizes.

In all cases, the maximum dimension of the beam is 10 µm x 10 µm and the time to make a rectangle 1 µs.

From table I it can be seen that for the most complex stripe of the most complex level. The maximum speed of the table is 14 $cm.s^{-1}$ for a 1.25 µm minimum linewidth circuit.

For a 3" wafer with 37 chips 10 mm x 10 mm the time to write a wafer would be in the worst case less than 5 minutes.

References

[1] - J. Trotel

Dynamic Beam Shaping
J. Vac. Sci. Technol. 15(3), pp.872-873 (May/June 1978)

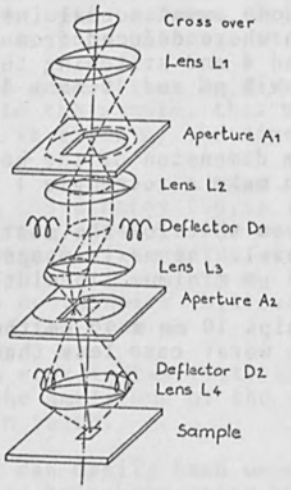

Fig.1 - Principle of the electron optics

Fig.2 - Movement of the sample

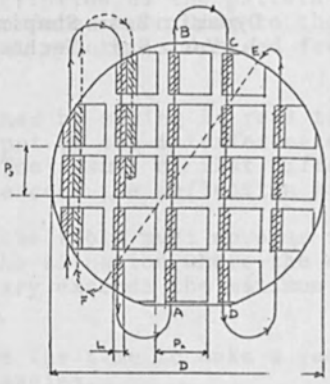

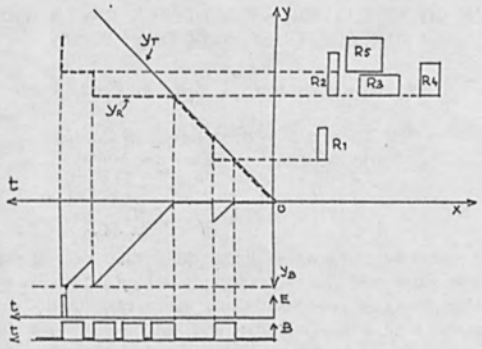

Fig.3 - Deflection of the beam in the direction of the movement of the table.

TABLE I - TABLE SPEED COMPUTER SIMULATION

CHIP SIZE (mm x mm)	5 x 5	5 x 5	10 x 10
NUMBER OF TRANSISTORS	5.050	21.000	323.200
MINIMUM LINEWIDTH (µm)	5	2.5	1.25
MAX.NUMBER OF RECTANGLES/STRIPE			47.000
MAXIMUM SPEED (Cm/s)	57	29	14

STITCHING WITH OVERLAY IN DIRECT WAFER WRITING USING SCANNING ELECTRON BEAM

A.D. Wilson, A. Kern, J. Kirk and C. Dooly

IBM Thomas J. Watson Research Center
Yorktown Heights, New York 10598

Abstract: Exposure of chips whose linear dimensions exceed that of a single electron beam written field can be made by stitching of smaller fields into the required size chip. This has been done using two methods: stitching by registration marks within the chip area and stitching by laser interferometer control. In the first method, because of the use of registration marks within the pattern area to stitch the subfields into a large chip, two sequentially written pattern levels are automatically registered to one another. In the laser interferometer method, registration marks are located in kerf area of the chip and not within the body of the chip, and sequentially written pattern levels are not necessarily "registered" unless a special registration operation is executed at each chip location. This paper discusses the registration question in laser interferometer controlled stitching and describes a software and hardware system to achieve such overlay.

Introduction

Fabrication of chips composed of several stitched subfields with overlay to similarly written previous levels is the topic of this paper. The IBM Research Center Vector Scan Electron Beam System[1] has been programmed and used to evaluate the problems in doing accurate overlay of stitched patterns.

There are two main applications of stitched and overlayed patterns: The first is the fabrication of micron and submicron VLSI working devices over fields significantly larger than that possible by writing single field patterns. In this first application, it is assumed that the total device, consisting of several pattern levels, would be generated by electron beam direct-write lithography[2] because the fine line-width and overlay requirements can only be met by direct-write techniques. The second main application is the direct-write of electron beam generated patterns whose line-widths are compatible with those printed by conventional optical systems such as 1X projection, step-and-repeat or contact. This is a plausible case in early product development when prototype devices are fabricated by electron beam methods for rapid evaluation of a design. This occurs because of the combination of quick turn around time and process control associated with the direct write process and not the fine line capability of the electron beam systems.

Technique

It has been previously demonstrated that a vector scan system can accurately "stitch" a pattern on a substrate such as a silicon wafer or chrome mask plate.[3] In the non-

overlayed case of stitching, the electron beam system is adjusted so that the stitched fields are a specific size and written with no apparent orthogonality, size, rotation or offset errors. In the vector scan systems developed at our laboratory (VSI (1)) a calibration sequence is executed to force the deflection system to generate a properly adjusted pattern. The X-Y stage is then moved under laser interferometer control a distance to which the deflection field was calibrated, and thus a properly stitched single level pattern is written.

For the case of stitching with overlay to a pattern previously written on the substrate, some additional requirements must be met. These are that the pattern to be overlayed must be sized and registered to that already on the substrate, usually a wafer. Conventional four mark registration[4] to marks on the wafer chip is not really feasible because of the potentially large size of the stitched chip and the limited field size of the electron beam system. What is needed is then a different "registration" approach designed for overlay of stitched patterns. The technique developed for the VSI system is largely a software one; however, it utilizes the full system including the laser controlled stage and registration signal processor.

It is essential that the wafer have at least three and preferably four fiducial marks located on the periphery. These marks are used to determine both the relative size of the wafer in X and Y directions and also the general location and rotation of the wafer with respect to the X-Y stage-laser interferometer measuring system. Expected chip locations in stage coordinates are determined from the fiducial mark location.

The first step in stitched-overlay is to determine the orientation, size, orthogonality, etc. of the wafer. This is accomplished by moving the X-Y stage so that the aforementioned fiducial marks can be located by a "registration" type beam-scan at the center of the electron beam field. The fiducial marks are located in terms of the laser interferometer system coordinates, and if four marks are used, correction terms are generated in software for the X-Y stage as follows*

$$X_s = aX_w + bY_w + cX_wY_w + d$$

$$Y_s = eY_w + fX_w + gY_wX_w + h \qquad (1)$$

where subscript "s" refers to X-Y stage coordinates and subscript "w" refers to wafer coordinates.

From a measurement of the wafer fiducials the X-Y stage motion is scaled to the appropriate size ("a" and "e" coefficients), and the X-Y stage is moved chip to chip along the wafer axis determined by the above coordinate linear transformations as depicted in Figure 1. The X-Y stage is commanded to the first chip site. Each chip site has four chip marks located as shown in Figure 2, around the boundary of the chip. Again these marks are likely to be too far apart for them to be located by a conventional four-mark registration sequence, and thus the X-Y stage is moved to the first anticipated chip mark location (specified in VSI system with respect to the chip center location) and note that this stage motion is along the "wafer axis" direction. The chip "registration or

* If only three marks are used, then the product term coefficients, "c" and "g", are undetermined and as such are set to zero.

fiducial" mark is located, as well as the other three, by simple beam scans at the column center. The laser interferometer is used to measure the locations of the marks. From these measurements, the chip rotation, size, orthogonality, etc. are determined.

Having determined the correct overall size of the chip as well as its angular orientation relative to the wafer axis, a calibration sequence is executed to force the deflection field to the correct size, rotation, etc., for the pending field stitching. The pattern is then effectively registered to the previously written level even though the previous level's total field size far exceeds the scan field size of the electron beam. Shown in Figure 2 is the stitching of a four by four array of subfields to form a large chip. During stitching, the X-Y stage is moved according to the Equation 1 where the coefficients "a through h" include not only the wafer correction parameters but also those of the chip, including rotation. The X-Y stage is thus moved within the chip along the chip axes defined by the chip marks. At the end of the last subfield in the chip the X-Y stage is moved to the next chip according to Equation 1, but now only the wafer correction parameters are in the coefficients "a through h", and the entire process repeats with the chip marks being located, the field calibrated and registered, and the stitched pattern written.

A key to the technique discussed here is the extensive use of the electron beam and laser interferometer to "map" the full wafer as well as each individual chip site. The interferometer system, coupled with a relatively small beam scan, provides accurate information on the location of the wafer and chip marks. The stitching subfields are then properly oriented and sized, and the X-Y stage, with its interferometer control, is moved to the correct locations to locate chip marks and write the stitched patterns. As long as the wafer or substrate is reasonably flat, there does not seem to be a limitation on the size of a stitched and overlayed chip that can be written.

Results

To evaluate overlay in stitched patterns, several conventional optical chrome mask plates were written on the VSI system with a significant amount of intentional chip rotation ($\pm$ 1.5 x 10^{-3} radian) introduced at various chip sites. The chip marks were separated 7.5mm, a distance greater than the system can deflect the beam. These masks were copied onto wafers by conventional contact printing and by 1X projection methods. Registration marks for the wafer and chip were thus transferred to silicon wafers. These wafers were then processed and returned to the electron beam system. A test pattern was generated which allows the evaluation of stitching between level 1 in adjacent subfields, level 2 in adjacent subfields, and between level 1 and level 2 in adjacent subfields. It is the latter case that is a measure of overlay in stitching. Also measured was level 1 to level 2 within the same subfield. A simple representation of the test pattern is shown in Figure 3. The test pattern consists of 20 0.11 micron sensitive verniers per subfield.

The first pattern level was written as a four by four stitched vernier test pattern with three separate and different chip rotation angles established by prewritten marks on the wafers. The system automatically "registered" the stitched first level to the wafer, and then the wafer was removed from the system and the resist was processed. At a later time, the wafer was reinserted into the system, and it was oriented differently (small angular rotation) from the previous level. The wafer was again "registered" for the second stitched level, and that level was written automatically.

The exposed wafer was processed, and the errors in stitching recorded by a) verniers that measure level 1 to level 2 in one subfield, and b) verniers that measure level 1 to level 2 of adjacent subfields in X and Y directions. The nominal field size for the stitching is 1.66mm.

An example of some overlay stitching results is shown in Figure 4, as number of sample measurements vs observed error in units of the vernier, 0.11 micron. It is concluded from the observed results that it is possible to have good overlay in stitched patterns. Three sigma values for X and Y errors are 0.20 micron. Note that this is the three sigma error for the stitching or joining of a line crossing a subfield boundary where one side of it was written as the first level, and the other side as a second level after the wafer had been processed and returned to the system.

Factors Contributing to Stitching Errors

Errors in stitching due to non-flatness of substrate over the region of the stitched pattern are likely to be the major error in overlayed stitched patterns. For a simple deflection system the field size error introduced in the stitched pattern due to displacement along the axis of the column, ΔZ, of the substrate is

$$X = \frac{\Delta Z \times W \times 2}{f}$$

where W is the deflection distance from the center of the column to the stitching boundary, f is the focal lenghth of the final lens, and X is the observed field size stitching error. The factor 2 arises because each subfield will have the basic field size error and two adjacent fields will thus have an observed gap or overlay equal to twice the single field amount. For the system used in these experiments the focal length was 50mm, and the field size is 1.66mm and thus the out-of-flatness error expected is about 0.05 micron per micron out-of-flatness if a simple deflection system analysis is used. However, VSI uses a specially designed double deflection system optimized for low deflection aberrations and thus the non-flatness errors are considerably less than the formula of the above because the electron beam angle is nearly perpendicular to the plane of the substrate. (This simple analysis assumes the system is not automatically adjusting for changes in sample height within the chip area as subfields are written.) As an example of "typical" wafer non-flatness, Figure 5 shows a 57mm diameter wafer chucked at three points for insertion into the electron beam system. (Each fringe corresponds to .32 micron.)

Unless some exotic methods such as electrostatic chucking[5] is employed in an electron beam system, it is doubtful that wafer non-flatness can be ignored for stitched patterns and particularly for overlayed stitched patterns. Wafer height sensors with either mechanical or electrical or software ΔZ compensation does not totally solve the flatness-error problem because of the continuous nature of the wafer surface (sloped surface). For the wafer of Figure 5, it could be expected that a stitching error of about .1 micron would occur at some places in the test pattern used for this study.

Some other potential sources of stitching errors are basic electron beam field distortions, estimated to be no more than 0.05 micron for the 1.66mm field size used here.[4] This could add a .1 micron stitching error the the fabricated patterns, (0.05 from each field); however, it seems to be somewhat less than this 0.1 micron figure. Another

source of error is the detection of chip "registration marks" and the subsequent calculation of chip rotation, etc. For the operating conditions under which those tests were conducted, the resolution at mark detection time was 0.07 micron. Lastly, the field size was set with a potential quantization error of 0.06 micron. If it is assumed that the following errors could be reasonably expected for the experiment discussed here;

ΔZ effect = 0.1 micron
field distortion = 0.05 micron
field size quantization = 0.05 micron
registration error mark detections = 0.07 micron

then an "expected" error of 0.14 micron in overlay stitching can be expected. This is close to the error observed in test wafers monitored with precision vernier patterns.

Conclusions

Stitched and overlayed patterns can be made on vector scan type electron beam systems with expected errors on the order of 0.25 micron for stitching fields of about 2mm or less. Attention must be given to the flatness of the substrate if no flatness correction is implemented in the system. Even with flatness correction, changes in slope of the wafer surface must be considered. Very large chips can be made by this technique and good overlay achieved.

Acknowledgements

The authors wish to acknowledge the valuable assistance of H. Voelker, T. Donohue, D. Webb, and D. Long in operating the VSI electron beam system, test pattern generation and wafer processing and helpful suggestions and discussions with T. H. P. Chang.

REFERENCES

1. T.H.P. Chang, A.D. Wilson, A.J. Speth, C.H. Ting, "Vector-Scan I an Automated Electron Beam System for High Resolution Lithography", Proc. of the Symposium on Electron and Ion Beam Sci. and Technol., Ed., R. Bakish, (1976), p. 392.

2. W.D. Grobman, H.E. Luhn, T.P. Donohue, A.J. Speth, A.D. Wilson, M. Hatzakis, T.H.P. Chang, 1μm Mosfet VLSI Technology: Part VI Electron Beam Lithography, IEEE Jour. Solid State Circuits, Vol. SC-14, No. 2, April 1979, p. 282.

3. A.D. Wilson, T.W. Studwell, G. Folchi, A. Kern, and H. Voelker, "A Comparison of Pattern Stitching by Subfield Registration and Laser Interferometer Servo Control", Proc. of the Symposium on Electron and Ion Beam Sci. and Tech., 8th Int. Conf., Ed., R. Bakish, 78-5 (1978), p. 198.

4. T.H.P. Chang and R. Viswanathan, "Deflection Distortion in Scanning Electron-Beam Systems", Proc. of the 14th Symposium on Electron, Ion and Photon Beam Technology, Eds., G.L. Varnell and J.L. Bartelt, (Palo Alto, CA, May 25-27, 1977), p. 878.

5. G. Wardly, "Flatness, Contrast, and Resolution Considerations of Cathode Project Microfabrication Systems", J. Vac. Sci. Tech., Vol. 12, No. 6, Nov/Dec. 1975, p. 1313.

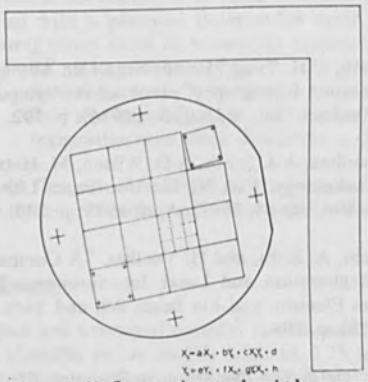

Fig. 1 Wafer oriented with respect to laser interferometer mirror and illustrating wafer fiducial and chip registration marks.

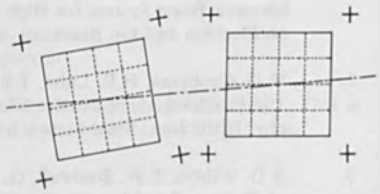

Fig. 2 Two chips illustrated with registration marks oriented differently relative to wafer axis. Stitch subfield boundaries indicated by dashed lines.

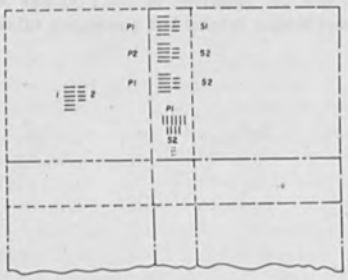

Fig. 3 Illustration of overlay-stitching test vernier pattern showing primary and secondary verniers for X and Y measurements of stitching between adjacent subfields: levels 1-1, 2-2, and 1-2 and overlay of level 1-2 within a subfield.

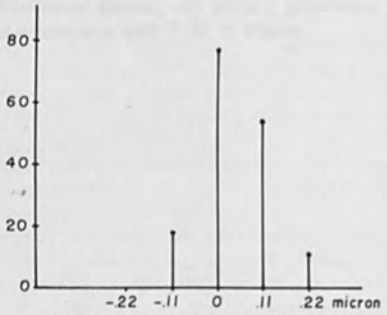

Fig. 4 Overlay stitching errors between subfields for two pattern levels.

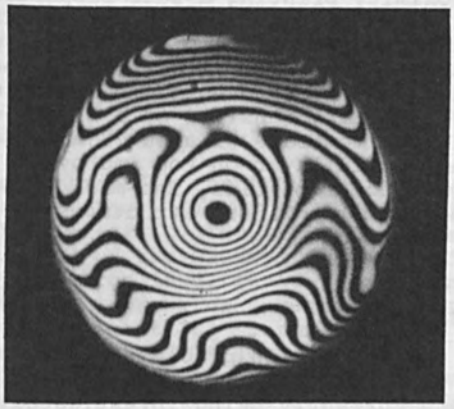

Fig. 5 Fifty seven mm diameter wafer showing non-flatness of wafer. Each fringe (bright to bright) corresponds to 0.32 micron.

FABRICATION TECHNIQUE FOR ELECTRON BEAM TRANSMISSION MASKS

J. Greschner, H. Bohlen, H. Engelke,
P. Nehmiz
IBM Deutschland
German Manufacturing Technology Center
D 7032 Sindelfingen, Germany

ABSTRACT

Electron beam proximity printing is an extension of optical proximity or off-contact printing. It opens up the possibility of replicating micron and submicron structures directly on wafers with high speed. One basic difference to optical off-contact printing is the mask. For electron beam proximity printing a self-supporting mask with physical holes is required. This paper describes a new mask fabrication process where all critical etching processes are achieved by very precise reactive ion etching. The mask consists of a single crystal silicon membrane of about 2 µm thickness and a gold layer on top improving the beam-stopping properties. The mask has chip size and contains finest structures of 0.3 µm width.

INTRODUCTION

To overcome the resolution problems of optical proximity printers in semiconductor lithography three alternative approaches are currently being investigated: X-Ray printing (1), ion beam printing (2) and electron beam printing (3). All these methods use much shorter wavelengths than optical methods and therefore have the capability of printing submicron patterns.
Electron beam proximity printing has three major advantages which, in the other techniques, are missing or exist to a lesser extend. These are: 1. Short exposure time. 2. Easy registration techniques for mask and wafer, since the same beam of the same radiation can be used for registration and exposure. 3. An electronic alignment technique permitting rapid positional correction of the x-y table stepping the wafer under the mask (3,7).
These potential advantages make electron beam proximity

printing a promising candidate for submicron lithography. Consequently the need was raised for transmission masks with submicron structures and with geometrical precision fullfilling adequate overlay requirements.
Electron beam transmission masks must have physical holes at transparent areas since electrons interact strongly with matter. The inherent mask stencil problem is solved by distributing the mask pattern in a set of two complementary masks which are sequentially printed.
The transmission masks described in this paper have a high mechanical stability and a good thermal conductivity. Nevertheless for achieving optimum overlay we restricted the mask dimensions to a chip size and planned printing of patterns on any sized wafer in a step and repeat mode. The size of the largest masks which we fabricated so far was about 12 x 12 mm^2.
The same masks have also been used successfully in ion beam proximity printing (2).
We succeeded to make masks with submicron patterns by employing a new fabrication process which is superior to the one described earlier (4).
This paper will describe the new process, its differences compared to the formerly used process and the achieved results.

MASK FABRICATION PROCESS

Fig. 1 shows schematically the fabrication steps.
The mask substrate (Fig. 1a)) is a 0.2 mm silicon wafer having a (100) orientation. The wafer is polished on both sides. The backside of the wafer is covered with a 1 µm thick SiO_2 layer. Boron is diffused into the polished frontside of the silicon wafer substrate to a surface concentration of at least 10^{20} boron atoms/cm^3. This boron diffusion has two effects. It acts as an etch stop for the bulk-etching of the wafer and thus defines the resulting mask thickness. A p-n-junction at 3.8 µm depth leads to a mask thickness of about 2 µm. Furthermore, the boron concentration causes a tensile stress in the finished mask resulting in a delayed mask bending when the later mask foil is warmed up in its rigid cool silicon frame.
In the next process step (Fig. 1b)) one or several windows of chip size are opened in the backside SiO_2 layer by means of conventional photolithography and HF wet etching. Through these windows the bulk-etching will be carried out through the wafer later on.
The boron doped frontside of the wafer substrate is then covered with a 0.8 µm thick SiO_2 layer in a low temperature process (also Fig. 1b)). The SiO_2 surface is coated with a 0.5 µm thick electron beam resist layer. Patterns

with geometries above 1 µm were exposed by means of optical contact printing. The submicron patterns on our mask substrates were exposed in a Vector Scan System at the IBM T.J. Watson Research Center, Yorktown Heights. The resist patterns must have vertical profiles, to guarantee an accurate linewidth transfer during the following reactive ion etching (RIE) processes.
The resist pattern acts as a mask for the first RIE process (Fig. 1c)). This process was carried out in a diode type reactor with the wafer substrates held on the powered cathode. CF_4 or similar gases were used for this etching step. The resist etch rate is essentially lower than the SiO_2 etch rate. This leads to SiO_2 walls which are exactly vertical and do not indicate a noticeable lateral etching. This newly introduced RIE process step is superior to the gold ion etching process which was formerly used in the old process (4). In the new mask fabrication process the gold deposition becomes the last process step.
After this RIE process the remaining resist is removed in an O_2 plasma. As a result shows Fig. 2 a SEM micrograph of a SiO_2 pattern about 0.8 µm thick.
In the following step (Fig. 1d)) the patterned SiO_2 layer is used as a mask in a second RIE process to transfer the pattern about 2 µm deep into the boron doped silicon. This process uses an Ar/Cl_2 plasma and is described in detail by H.B. Pogge et al (5). In this second RIE process the directional etching again results in vertical silicon walls without a noticeable lateral etching.
Fig. 3 shows a SEM micrograph of a silicon pattern with an etch depth of about 2 µm.
The silicon wafer substrate is then thinned (Fig. 1e)) through the SiO_2 window on the backside by a wet preferential anisotropic etching process (6). The etching solution consists of ethylene diamene, pyrocatechol and water.
The resulting single crystal boron doped silicon membrane is about 2 µm thick.
After removing the residual SiO_2 layers the patterned silicon membrane is covered by a 0.2 - 0.8 µm thick gold layer which is required to stop on electron beam up to energies of about 25 keV.

EXPERIMENTAL RESULTS

A set of two complementary masks fabricated in the described manner is shown in the SEM micrograph of Fig. 4. The size of the larger areas containing test patterns with submicron structures, is (6 x 6) mm^2. The other two smaller areas serve for registration purposes.
The smallest structures which we have fabricated so far are shown in the SEM micrograph of Fig. 5. The 0.3 µm wide

silicon bars are 50 µm long and 2 µm thick. They have absolutely vertical walls.
Due to the crystalline structure of the supporting silicon the masks have an excellent mechanical stability. This is demonstrated in the SEM micrographs of Figs. 6 a), b). The total area in Fig. 6 b) is about (200 x 150) µm² in size. The patterns of Figs. 7 a), b) were exposed in a EB Vector Scan Tool as mentioned above. The very acute corners seen in Fig. 7 together with the 0.5 µm lines clearly demonstrate the high resolutions of the Vector Scan System and the subsequent mask fabrication process.

ACKNOWLEDGEMENTS

The authors are indebted to acknowledge the contributions of K. Asch, G. Kraus and W. Recktenwald (IBM GMTC and Plant Sindelfingen), H.J. Trumpp (IBM Development Laboratories in Boeblingen), H.B. Pogge and J. Lechaton (IBM East Fishkill), W.D. Grobmann, H. Luhn and T. Donohue (IBM T.J. Watson Research Center, Yorktown Heights).

REFERENCES

(1) H.I. Smith et al,
J. Vac. Sci. Technol., Vol. 10, 913 (1973)

(2) R. Speidel, U. Behringer,
Proceedings Microcircuit Engineering'79
Sept. 79, Aachen

(3) H. Bohlen, J. Greschner, W. Kulcke,
and P. Nehmiz,
8th Int. Conf. Electron and Ion Beam
Science and Technology, Seattle 1978

(4) H. Bohlen, J. Greschner, and P. Nehmiz,
8th Int. Conf. Electron and Ion Beam
Science and Technology, Seattle 1978

(5) H.B. Pogge, J.S. Lechaton, and P.J. Burkhardt,
4th Symp. on Sol. State Dev. Technol.,
Munich 1979

(6) R.M. Finne, and D.K. Klein,
J. Electrochem. Soc. 114, 965 (1967)

(7) H. Bohlen, J. Greschner, J. Keyser,
W. Kulcke, and P. Nehmiz,
this issue

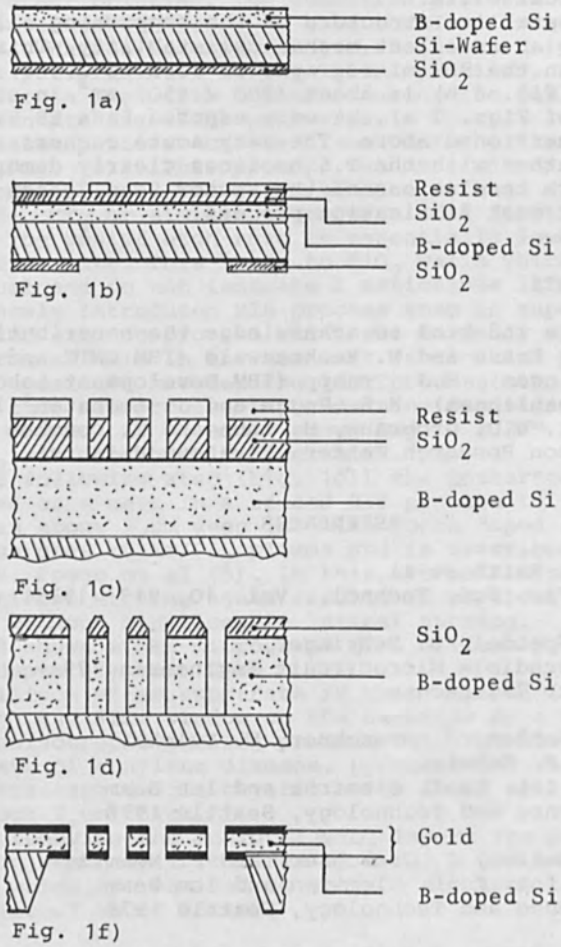

Fig. 1 Mask fabrication scheme

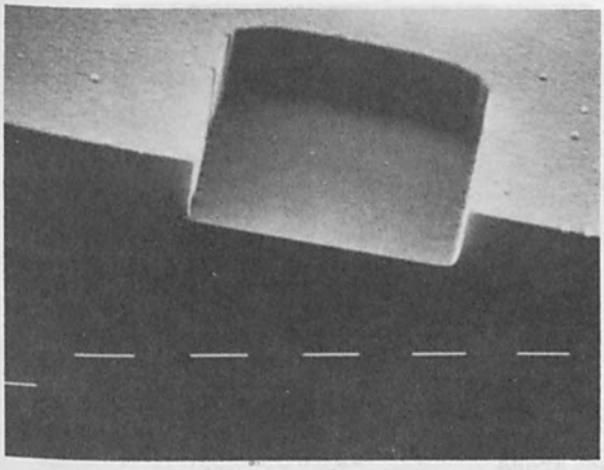

Fig. 2 SEM micrograph of a pattern detail etched into 1 μm SiO_2

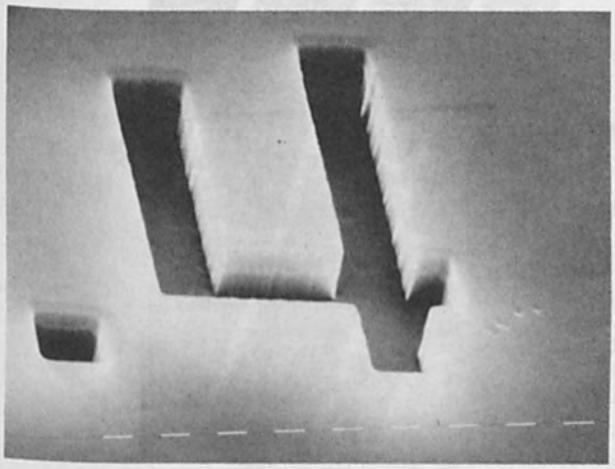

Fig. 3 SEM micrograph of a pattern detail etched 2 μm deep into the B-doped silicon

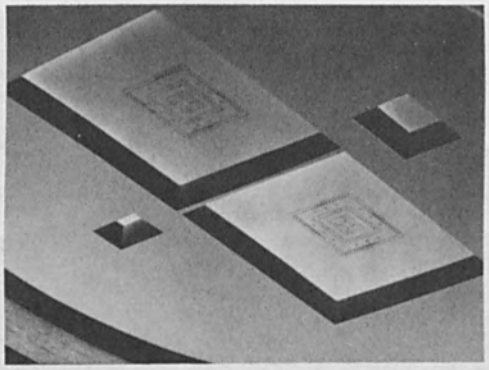

Fig. 4 SEM micrograph of a set of two "complementary masks" with registration areas

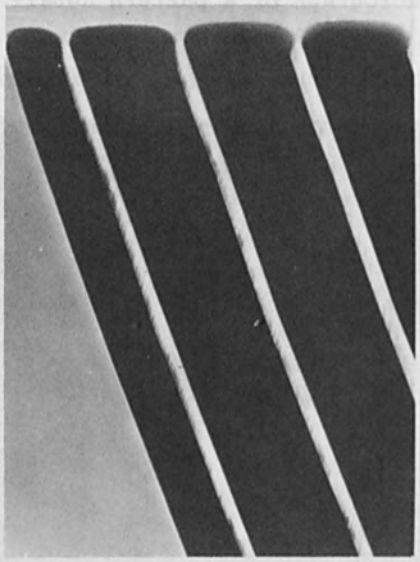

Fig. 5 SEM micrograph of a mask detail; 0.3 µm wide silicon bars, 2 µm thick, 50 µm long

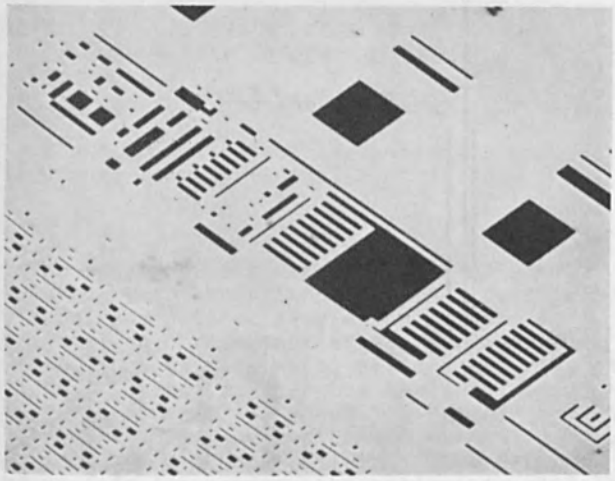

Fig. 6a) SEM micrograph of an EB silicon mask

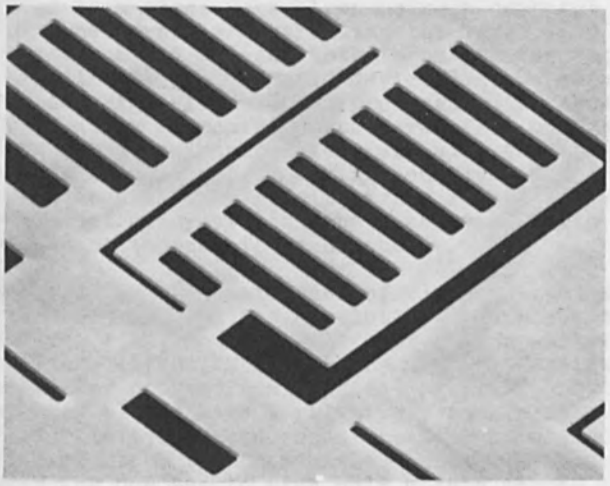

Fig. 6b) Mask detail with an area of about (200 x 150) μm^2

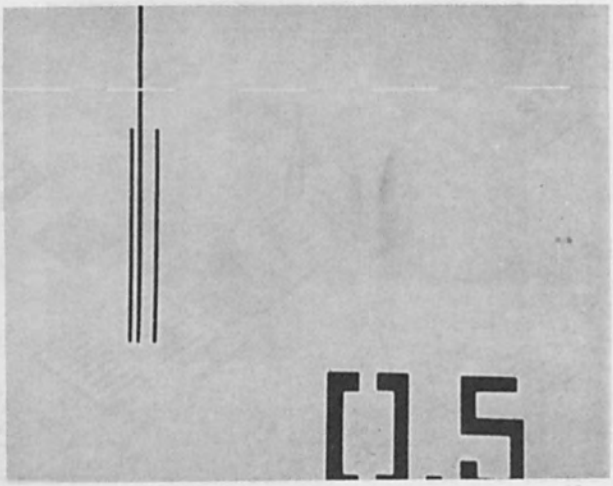

Fig. 7a) Part of an EB silicon mask
0.5 µm lines

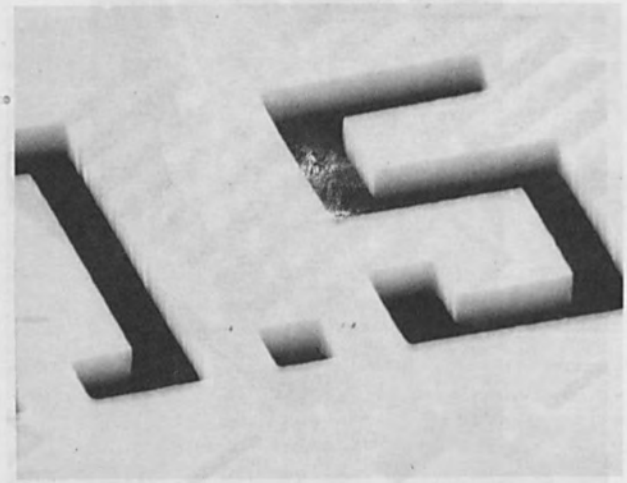

Fig. 7b) Part of a silicon mask;
pattern generated by a Vector-Scan
System; line width: 2.5 µm

FABRICATION OF CHROME MASK BY USING AN ELECTRON BEAM EXPOSURE SYSTEM

Qiu Pei-yong and Wang Jian-kun

Shandong College of Engineering,
Jinan, People's Republic of China.

ABSTRACT

The electron beam exposure system SDS-1, developed by author's laboratory and configured for submicron pattern generation is used to fabricate the chrome mask of semi-conductor devices, such as microwave, SAW and LSI circuit devices. The paper describes the fabrication and technical process, and shows the exposing results of lines with various widths and spaces ranging from 0.5 micron in the pattern. When the chip size exceeds 4mm square, the pattern is stitched by subfield to compose a larger chip with laser interferometer.

INTRODUCTION

Electron beam exposure systems using a computer to generate the patterns by controlling the deflection of the electron beam and a laser interferometer for registration are attractive for rapid device design, mask fabrication, and high yield device processing, because they permit delineation microcircuit patterns from computer data. These electron beam systems are also advantageous for high frequency and high packing density microcircuit fabrication, because they permit higher resolution and better alignment accuracy than that achievable with conventional photolithographic techniques.

Mask making is the basic task of electron beam exposure system SDS-1, When the resolution requirements are only moderate, i.e., the line width of device patterns larger than one micron, SDS-1 can be used to fabricate chrome masks for conventional optical printing. Owing to chrome mask blanks have a relatively smooth, flat surfaces, a relatively thin resist coating is needed. The processing steps for fabricating chrome masks are also simple for one has to etch only a thin chrome layer. The system has used to fabricate the chrome masks of simi-conductor devices, such as microwave SAW and LSI circuit devices.

SYSTEM CHARATERISTICS

The SDS-1 system characteristics have been reported elsewhere(4)., therefore only those characteristics which are important to fabricate chrome masks will be discussed here.

The maximum field size of system is 4 mm square and is also can reduce to 2 mm square and 1 mm square, depending on chip size and resolution requirement. The digital to analog convertion is performed by a 14 bit D/A converter for each axis, defining the beam position in X and Y axes respectively. That means it is composed of 16384 spots in both X and Y axes. For the chip size either on area larger than 4 mm square, or more than 16384 spots to describe the pattern, several fields must be stitched together to compose the chip. The exposure time for each spot can be adjusted from 2 microseconds to several tens microseconds, depending upon the resolution requirement and resist sensitivity.

The pattern data are stored in the memory of SK-2 computer. The basic shape of pattern is rectangle described by 4 words one each for X-position, Y-position, X-size, Y-size and their increments if necessary. On account of the storage capacity of a computer is not sufficient to describe a complicated chip design, the fifth word is used as arraying feature of pattern generator. With the arraying feature, a repeated shape is described only once; and this shape is repeated by specifying only in distance (X and/or Y direction) and number of times to be removed. By using this arraying feature, the amount of pattern data can be greatly reduced.

MASK MAKING

There are two different types in application of EBES to make the mask. One is to make 1X mask directly, and the other is to make 5X reduction mask reticles.

In 1X mask making one of the important factor is the pattern registration. In order to improve the step and repeating accuracy, a closed loop pattern registering system is developed. The two axes laser interferometer is mounted on the X-Y table and is used to determine the X and Y moving distance of the workstage. The sensitivity of the laser interferometer is one impulse equivalent to 0.079 micron. ($\lambda/8$). The stage location errors is corrected by deflecting the electron beam electronically to the intended location. The micrograph of two cross marks

for inspecting registering accuracy is shown in Fig. (1)

In order to inspect registering accuracy of the mask. two cross marks registering method is applied. In the first time at the side of each chip, a hollow cross mark is drawn. Then the X-Y table is steping and repeating for every chip controlled by laser interferometer. After patterns and hollow cross marks have been drawn on all the chip, the workstage is driven to the initial position of first chip controlled by laser interferometer. A solid cross is drawn, then step and repeating in the same manner. The mask will be inspected. If all the solid cross marks are just living in the hollow cross marks, that means the registering accuracy is sufficient, otherwise the mask can not be used.

To achieve accurate pattern delineation, it is there fore necessary to apply some method of exposure adjustment to compensate for the proximity effect. One such method is to vary the scanning speed of each pattern element. In order to determine the exposure dosage, the exposure results of lines with various widths and gaps, ranging from 0.5 micron is shown in Fig.(2) and (3). The experiments explain this method is suitable for our system.

We also use the system to make the 5X reduction mask reticles. If the chip size larger than 4 mm square,several fields must be stitched together to compose the chip. In this case all processes including pattern seperation,selection and stitching are controlled by computer automatically. In 5X mask making, one of the difficulty is to decrease the field distortion. Since the contribution of the deflection coil is not ideal, the pincushion distortion is existed in the pattern, and it may be measured by field stitching experiments. Although the distorsion in 4mm square field size only 2-3 microns, but in stitching it will greatly decrease the quality of the pattern.

In order to decrease the field distorsion, three approaches may be adopted. One is by hardware, but it needs high performance devices. The other is by software but the storage capacity of computer must be large enough and the calculating speed of the computer must be so fast. The third approach is to decrease the field size to be stitched This approach is comparatively simple but the total time for mask making will be increased. We have used the third approah to make the 5X reduction mask reticles with beam current 20 na, chip size 16x20 mm 30% pattern area, The time will exceed 10 minutes.

PROCESSING AND MATERIALS

The process used in electron-beam mask fabrication are similar to those used in conventional photolithographic practice;i.e., resist caating, prebake, exposure, developing, postbake, etching and stripping.(for negtive resist). The total processing time, excluding electron-beam exposure and inspection, is about 1 hour.

Resist is one of the important material in processing. It's suitability for use in the EBES, whether positive or negative, depends on its (1) sensitivity- customarily measured in electron charge deposited per unite area. (2) Resolution- indicated by the minimun line width that can be developed in resist layer of a given thickness. (3) Compatbility with fabrication process- including the resistance to chemcal etching, adhension to the substrate, temperature stability of the resist image and so on.

Some different kinds of resists have been tried and listed in Tab.1. In general negative resists have higher sensitivity, and the positive resists are with better compatibility and higher resolution.

Tab.1.

Material	Type	Sensitivity (c/cm^2)	Resolution (micron)	Compatbility
J-2 (Chow-Tung)	Neg.	$5x10^{-6}$	0.5	good
Wuxi-3	Neg.	$6x10^{-6}$	0.7	fair
AZ-1350 Shipley	Pos.	$5x10^{-5}$	0.5	good
PMMA Wuxi	Pos.	$5x10^{-5}$	0.7	fair

We also have tried the ion mill as drying etching method for substractive processes. Evidently the resistance to ion etching is not same for different kinds of resists. By test, better result is got from Az-1350.

Owing to the larger depth of focus of EBES, the substrates without the requirement of special flattening techniques. The chrome layer of the substrates must be so uniform and the thickness must be suitable to the geometric size of the pattern. The standard chrome layer approximately 800Å thick has been used to produce submicron feature size.

RESULTS

Chrome mask fabrication is now for experiment. Some results with photomicrographs is shown in the following figures. It contains: Two cross marks for inspecting the registering accuracy; photomicrograph of equal line width and spacing group, photomicrograph of equal line width and different spacings for "proximity effect" test. Mask of diode matrix with several hundred thousands units made by fieid stitching method; Mask of LSI circuit devices and SAW devices.

AKNOWLEDGEMENT

The author's gratefully acknowledge the technical contributions of Lee Xiang, Gao Wen-hong, Wang Shao-jun, Lee Chuan-lin, Zhao Jin-lei, Chang Hong-sun, Lee Pen-kong, and all the members of the electrn-beam laboratory.

REFERENCES

1. C.H.Ting, R.L.Anderson, D.Y.Saiki, and A.J.Kraft. J.Vac. Sci.Technol. 15(3), May/June 1978 p.948.
2. T.H.P.Chang, M.Hatzakis, A.D.Wilson, and A.N.Broers. Electronics May 12 1977 p.90-98.
3. R.F.W.Pease, J.P.Ballantyne, R.C.Henderson, A.M. Voshchenkov and L.D.Yau. IEEE Trans. Elec. Dev. Vol. ED-22 No.7, July 1975.
4. Qiu Pei-yong and Wang Jian-kun. Proceedings of 15th symposium on Electron, ion and Photon Beam Technology. 1979.
5. J.Trotel and G. Pircher. Japanese J. of Applied Physics. Vol.16 (1977) Supplement 16-1 pp57-60.
6. F.S.Ozdemir, W.E. Perkins, R.Yim, and E.D.Wolf. J.Vac. Sci. Technol. Vol. 10 NO.6 Nov/Dec. 1973.

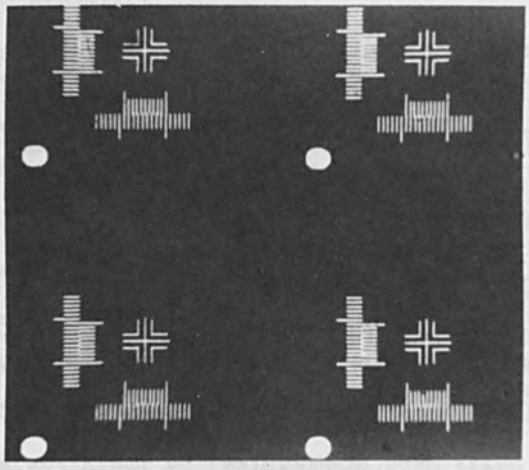

Fig. 1. Two cross marks for inspecting the registering accuracy. Measureing accuracy 0.2 micron.

Fig. 2. Effect of different spacings on line width in microns. a.o.5line o.5 gap. b. o.5 line 1.o gap. c. 0.5 line, 1.5 gap.

a. b.

Fig. 3. Photomicrograph of equal line and spacing in micron. a. 0.75 line and gap. b. 1.0 line and gap.

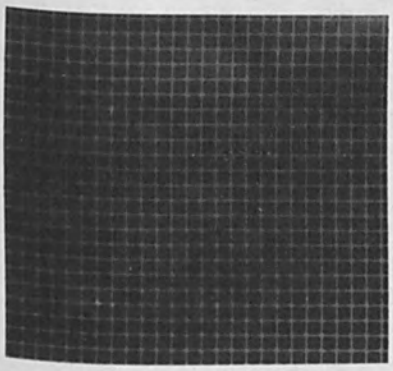

Fig. 4. Mask of diode matrix made by field stitching method. Size of squre 16 microns.

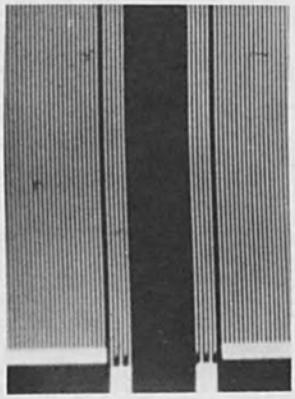

Fig. 5. Mask of SAW devices. 1 micron line 1 micron gap.

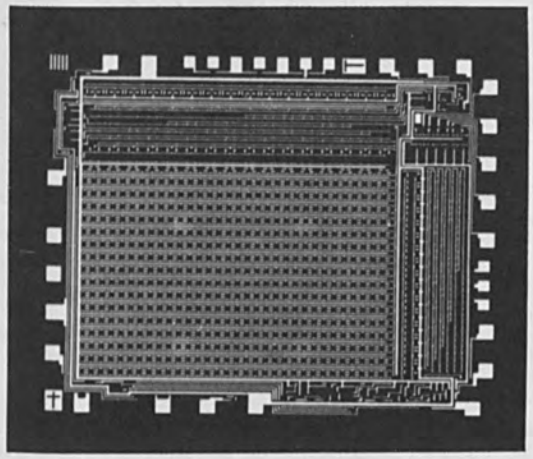

Fig. 6. Mask of large scale integral circuit.

AUTOMATED ELECTRON BEAM PULSER FOR SEMICONDUCTOR PROCESSING

Roger G. Little, Robert A. Kiesling, and Stephen N. Bunker
Spire Corporation, Bedford, Massachusetts 01730

ABSTRACT

A high current (6 kA), low mean energy (30 keV), short pulse (40 ns) electron beam machine has been developed for semiconductor thermal processing applications. This apparatus utilizes a cast solid dielectric, coaxial energy store configured vertically. The energy store is d.c. charged to 100 kV and then discharged upon command into a field/plasma emission diode. The anode of the diode consists of a transmitting mesh structure through which the electron beam can propagate and impinge upon a semiconductor specimen for transient thermal processing. The system incorporates a semiconductor handling end station consisting of a 12 wafer cassette which is loaded through a vacuum interlock. Each wafer is then automatically positioned upon command into the pulsing station where fluences from 0.1 - 10 joules per cm^2 are available over varying areas. The energy store of the pulser is charged in less than a few seconds such that rep-rate pulsing for a range of process applications is possible.

The ability to process semiconductor surfaces with a thermal transient while the bulk material remains at or near room temperature, allows novel device fabrication processes to be used. Transient irradiation processing utilizing pulsed electron beams has been applied to regrowth or modification of semiconductor and conductor films, generation of controlled interactions between materials and annealing of ion implantation damage (1-4). Pulsed electron beam annealing (PEBA) can be applied to processing compound semiconductors such as GaAs and InP. Gallium arsenide has been pulse electron beam annealed without the nitride caps customarily used to prevent molecular dissociation during high temperature furnace processing (5).

The electron beams used for pulsed processing differ from those used in lithography or scanning electron microscopy in that the pulsed beams are characterized by a large working area, submicrosecond duration and high intensity. Typical 2-inch-diameter PEBA beams have currents in kiloampere range with pulse widths on the order of

40 nanoseconds. Continuing efforts to achieve low cost, high throughput automated production equipment for solar cell processing have resulted in the development of an automated electron beam research machine called the SPI-PULSE 300, which is shown in Fig. 1.

This paper presents a description of the design and operational features of this new research tool.

APPARATUS

The electron beam processor, shown pictorially in Fig. 2, has the major following components: the electron beam pulse generator and the vacuum processing station with its sample transport.

The pulse generator consists of a 122-cm-long, 24-cm-diameter solid dielectric coaxial transmission line charged with an oil-immersed 100 kV DC power supply. The HV supply charges the 3 nanofarad energy store via a high voltage cable which terminates at the energy store through a 300 megohm high voltage isolation resistor. This resistor protects the HV power supply from surges during pulser operation. The aluminum pressure vessel is pressurized up to 100 PSIG with a dielectric gas to retard corona and increase the voltage hold-off between the energy store and ground. The energy stored in the transmission line is discharged through an electropneumatic switch to the tube cap of a vacuum field/plasma emission diode.

The field emission diode is comprised of a fine grained carbon cathode up to 5 cm in diameter, and a 77 percent transparent tungsten mesh anode. This mesh allows the electrons emitted from the cathode to propagate through to the wafer being processed. The diode is mounted on the lower cover of the pressure vessel and is composed of a tube cap, insulator rings, cathode shank, and the cathode and anode assembly. An upper insulator isolates the tube cap and cathode shank from ground and also is the pressure interface between the pressurized energy store and the vacuum process chamber housing the diode. The lower section of the diode is an integral assembly easily detached from the cathode shank and removed from the process chamber for servicing or adjustment. This assembly has a second insulator which supports the cathode and maintains close parallelism with the anode plane. The anode-to-cathode (A-K) gap is set by inserting spacers of various thicknesses between the cathode and cathode shank. In the same manner, spacers are used to adjust the sample-to-anode distance.

Samples to be processed by the SPI-PULSE 300 are loaded one above the other in a 12-carrier, vertically constructed cassette. Each sample is placed in an individual aluminum carrier with a recess that accepts 76 mm diameter wafers. Other geometries are processed riding on graphite or silicon which serves as the sample support in the carrier. Even though 76 mm diameter wafers can be transported, the maximum cathode diameter designed for processing with this machine is 50 mm. A schematic drawing illustrating the operation of the process chamber and transport is shown in Fig. 3.

After the loaded cassette is placed in the lock chamber, stepwise valve sequencing is controlled by sensors and relays coupled to digital logic. The process chamber uses a cryogenic vacuum pump to reach pressure levels in the low 10^{-6} to 10^{-7} torr range. A pneumatically driven transport arm draws the carrier into position in the process chamber for pulsing. After triggering the beam discharge, the energy store recharges within 3 seconds to full voltage and is then ready for the next phase. Upon completion of the pulse, the transport arm returns the carrier to the cassette, and the next carrier is moved into position. The transfer/processing/transfer sequence continues until all 12 samples have been processed. An automatic vent cycle is then initiated to facilitate sample removal. With single shot pulsing, this processing system can yield throughputs of 60 wafers per hour.

From the control console the operator sets the charging voltage and triggers the discharge of the energy store after initiating the automatic sequence of the valves and mechanics associated with the sample transport and processing. The overall integration of the system elements is shown in the block diagram of Fig. 4.

THEORY OF OPERATION

The heating of a sample's surface depends upon the electron energy spectrum, the total fluence in the beam, and the pulse width. There is an additional dependence on the pulse shape as a function of time and the angle of incidence. In qualitative terms, increasing the pulse width allows deposited thermal energy to diffuse into the bulk of the sample, lowering the surface temperature (for constant fluence) and reducing the thermal gradient. The surface temperature will be approximately proportional to the total fluence, neglecting a change in phase such as melting, as long as the pulse width is short. For very short pulse widths which are less than the characteristic thermal diffusion time for depths of penetration considered, the

average electron energy will control the near-surface temperature profile and depth-dose of energy deposited in the material.

The four quantities, electron energy, fluence, pulse width, and total beam energy, are dependent variables. This means that they cannot be varied separately, independently of the other variables, by adjusting any one machine parameter. The independent, separately adjustable parameters of the SPI-PULSE 300 are: charging voltage, cathode radius, cathode-anode gap, sample-anode distance and optionally, anode transparency and applied magnetic field. Each of these independent adjustable variables alter the depedent qualities of the electron beam.

The pulse generator has the equivalent circuit of a series R-L-C combination, where R is the combined resistance of all conductors and the arc in the switch, L is the combined inductance of the switch and transmission line, and C is the capacitance of the dielectric coaxial transmission line and energy store. Because the impedance of the diode, in series with the generator, changes in time, the circuit equations need to be solved by numerical techniques. Transmission line equations are not appropriate due to the large value of L. The energy stored in the capacitor is $1/2\ CV^2$, where V is the charging voltage. The maximum energy at 100 kV is about 15 joules. Most of this energy can be extracted from the diode except when early gap closure is desirable to lower the mean electron energy.

The current produced in the diode is space-charge limited and behaves according to the Child-Langmuir relation:

$$I = \frac{8\pi}{9\sqrt{2}} \frac{\varepsilon_o e}{\mu_o m c^2} \left(\frac{r}{d}\right)^2 V^{3/2}$$

$$= 2.33 \times 10^{-6} \left(\frac{r}{d}\right)^2 V^{3/2} \text{ amperes}$$

where: r = cathode radius (cm)
d = diode gap (cm)
V = applied voltage (volts)

This equation holds only when the diode is fully emitting. At the start of the pulse, electron emission is confined to the corners of the crosshatched pattern on the

cathode. Microscopic carbon grains carry the current and are rapidly heated to the vaporization point at the high applied electronic field strength. The small grains explode and form a carbon plasma. The large electron beam current is emitted from this plasma, which expands to cover the whole diode area. Contamination from the carbon plasma is below 10^{12} ions/cm^2 at the sample. As the plasma drifts from the cathode towards the anode, the effective cathode-anode gap is reduced at a near constant rate of approximately 2.5 cm/μs. The gap reduction causes the diode impedance to change in time through its dependence upon d.

The anode, when bombarded by the intense electron beam, may also form a plasma which drifts toward the cathode and closes the gap at a rapid rate. The gap closing emanating from the anode only occurs at fluences in excess of 1 joule per cm^2. The spacing between the wires of the anode mesh should be less than half the cathode-anode gap so that the diode resembles a planar configuration. Anode transparency can be increased but at the expense of anode lifetime. The reduction in current density by a denser anode mesh can vary the fluence on samples without changing the electron energy spectrum, provided that the charging voltage, cathode-anode gap, and anode material are not changed. The effect is only approximately linear, since the reduction in beam current also affects self-focusing.

The electron beam current can exceed 1 kA, depending upon diode impedance and charging voltage. At this level self-interactions between charges in the beam dominate propagation of the current. Electrostatic repulsion tends to improve the beam uniformity, since density perturbations may be unstable. Uniformity also improves with increasing the sample-to-anode spacing or drift distance. To the extent that the cathode-anode and sample-anode spacings are smaller than the beam radius, the current may also be considered to be propagating between large parallel conducting plates. Here, the self-magnetic field of the beam causes focusing when the radial electric field is reduced by the presence of near, conducting planes. Since the radial electric field is affected by the spacing between conductive plates, the self-focusing effect can be varied by changing the sample to anode distance. At large spacings, the electron beam tends to expand radially to the outer chamber walls, reducing the fluence on the sample despite focusing effects.

An axial magnetic field can be applied perpendicularly to the cathode-anode gap by an optional solenoid and low-carbon-steel cathode holder. The steel pole pieces help

a uniform field in the critical region. At roughly 1 kilogauss, the Larmor radius of electrons at 10 to 50 keV is less than 1 cm. At this point the self-focusing effect is inhibited because electrons tending to pinch inward are held to axial orbits. This magnet can be used to control focusing of the beam in conjunction with varying the sample-anode distance. It represents another variable, but since it serves a duplicate function it is considered an option.

Summarizing what has been discussed: (1) The total beam energy and fluence increase approximately as the square of the charging voltage. (2) The diode impedance depends upon the square of the ratio, cathode radius/cathode-anode gap, and upon the square-root of the applied voltage. Therefore, increasing both the cathode radius and the cathode-anode gap proportionately can be used to vary the fluence with a minor change in other parameters. Increasing the diode impedance will increase the average electron energy and decrease the beam current. The total beam energy and fluence will vary, depending on the matching of the load (diode) to the generator impedance. (3) Decreasing the cathode-anode gap, or allowing the gas pressure in the diode to rise above 2×10^{-4} torr, will shorten the pulse width. (4) Varying the sample-anode distance can adjust the self-focusing of intense electron beams and propagation efficiency. It varies the fluence but not the electron energy. (5) Reducing the transparency of the anode will reduce the beam current at constant electron energy but will also affect focusing so that the fluence is not directly proportional to this quantity. (6) Similarly, an optional magnetic field applied parallel to the axis will also affect focusing but not electron energy.

BEAM DATA AND DIAGNOSTICS

In order to optimize the electron beam generator's operating parameters, experimental data was taken using carbon calorimetry in conjunction with calibrated voltage and current monitors.

The current monitor used was a 13 milliohm coaxial resistive shunt made from a large number of resistors wired in parallel and secured to the outside rim of the cathode insulator support housing. During the pulse discharge, this monitor with its 300 megahertz response time measures the displacement current produced by the electron beam in the diode. Readouts in kiloamperes per volt were obtained with a Tektronix 7834 storage oscilloscope.

The voltage monitor used was a 7 nanofarad coaxial capacitive divider made from Mylar and attached with conductive epoxy to the wall of the vacuum chamber transition sleeve opposite the cathode shank. The output from this voltage monitor, with its frequency response of 300 megahertz is the accelerating potential on the cathode shank, which is essentially equivalent to the electron beam voltage. Readouts in kilovolts per volt were obtained with a Tektronix Type 519 oscilloscope.

Voltage and current data were acquired for cathode diameters of 25, 38 and 50 mm at various charging voltages and A-K gaps. Representative voltage and current monitor output data for the 25 mm diameter cathode and an anode-cathode gap of 1.25 mm fired at a 100 kV charging voltage is shown in Fig. 5. The upper two curves illustrate the typical shape and amplitude for a sequence of shots fired at the full 100 kV charging voltage. The nominal pulse width (FWHM) was 40 nanoseconds and was found to be independent of cathode diameter for the three sizes studied.

The third curve in Fig. 5 presents the computed electron energy spectra generated by the Spire computer code called EBSPEC. The validity of this code has been confirmed with time resolved magnetic spectroscopy. Given the accelerating voltages and total current as a function of time for an electron beam, EBSPEC calculates the beam energy spectrum or the charge delivered per unit energy interval. Electrons are produced at all energies up to a distinct maximum with a mean energy at almost two-thirds of the maximum. This is consistent with the peak of the current emission occuring near the peak of the voltage on the diode, as shown in the upper curves in Fig. 5. The mean energy was computed to be 33.6 keV with the total energy in the beam of 8.1 joules. This value for the total energy content of the beam represents about 50 percent of the energy stored in the liner. Values between 50 and 60 percent were found to be typical depending on diode geometry. However, a very small anode-cathode gap would have a much lower transmission efficiency, which is sometimes desirable to lower the mean energy of the beam. The lower energy components are important in heating a wafer surface.

The fluence of the beam in joules per cm^2 was measured by a calorimeter made of high-density, fine-grained graphite. The choice of graphite was dictated by the need to prevent spalling at high fluences, which would change the calibration. The calorimeter was located perpendicular to the beam axis and in the same plane normally occupied by the wafer to be processed. During the beam pulse, the front surface of the

carbon disk becomes heated. At equilibrium the measured temperature is proportional to the fluence. Isolating the calorimeter thermally also isloated it electrically from ground. Therefore the current impinging upon it during the pulse was shunted to ground. The thermocouple output was measured by a Keithly Model 160 B high-input impedance d.c. voltmeter and displayed on a Gould 110 chart recorder. At a 100 kV charging voltage for the 25 mm cathode, with the A-K gap set at 1.25 mm and an anode to calorimeter spacing of 3 mm, the average fluence was measured to be 2.18 joules per cm^2. For other diode geometries and beam voltages, fluences varied over the range of 0.1 to 10 joules per cm^2.

SUMMARY

The availability of the SPI-PULSE 300 electron beam processor for laboratory research and development applications, should encourage efforts to incorporate pulsed electron beam technology into standard automated semiconductor processes as well as offer a new and unique method for VLSI and compound semiconductor device fabrication.

ACKNOWLEDGMENTS

The authors wish to thank P.J. Barber, A.C. Greenwald and M.N. Horenstein of Spire Corporation for their technical contributions during the SPI-PULSE 300 development program.

REFERENCES

1. S.S. Lau, W.F. Tseng, M.A. Nicolet, J.W. Mayer, J.A. Minnucci, and A.R. Kirkpatrick, Appl. Phys. Lett., 33 (3), 235 (1978).

2. A.C. Greenwald, A.R. Kirkpatrick, R.G. Little, J.A. Minnucci, J. Appl. Phys., 50 (2), 783 (1979).

3. R.L. Mozzi, W. Fabian, F.J. Pickorski, Appl. Phys. Lett., 35, 337 (1979).

4. A.C. Greenwald and R.G. Little, Solid State Tech., 22 (4), 143 (1979).

5. J. Tandon and F.H. Eisen, AIP Conf. Proc., 50, 616 (1978).

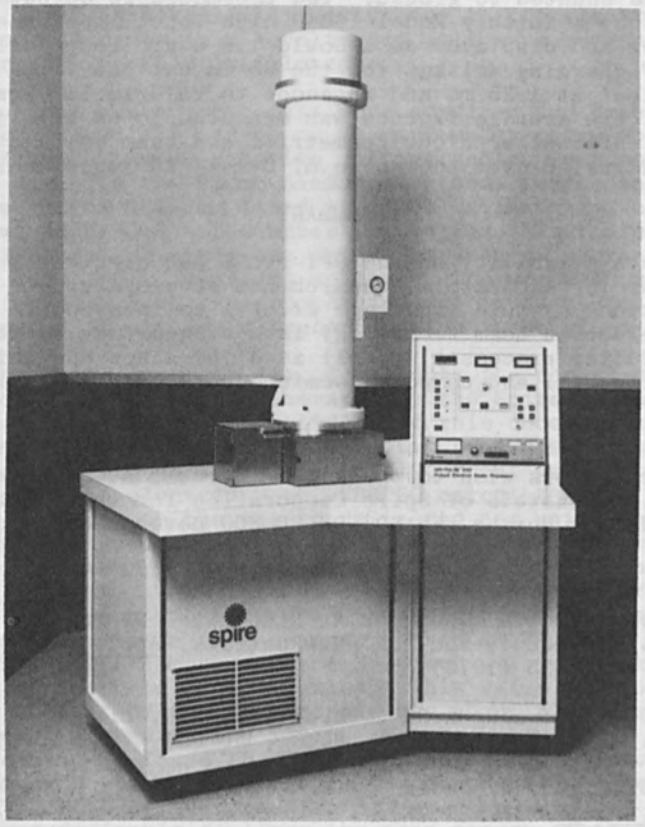

Fig. 1. Research electron beam pulser.

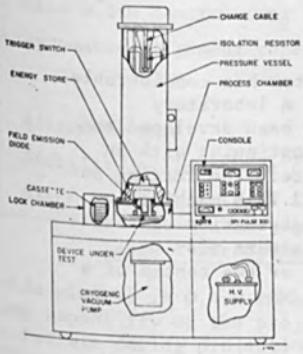

Fig. 2. SPI-PULSE 300 pictorial.

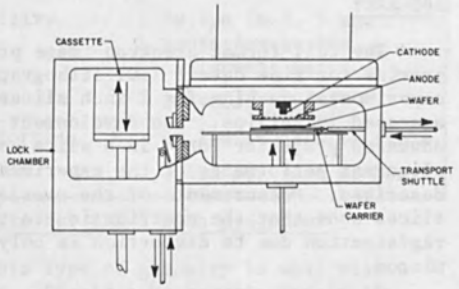

Fig. 3. Vacuum process chamber and transport schematic.

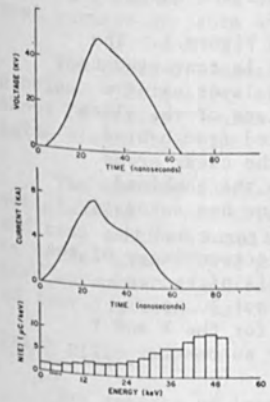

Fig. 5. SPI-PULSE 300 diode output data and computed electron energy spectra.

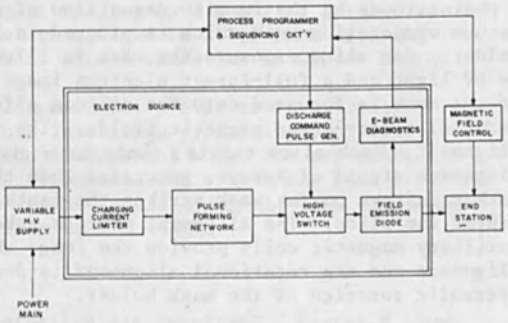

Fig. 4. System block diagram of electron beam processor.

PERFORMANCE OF THE 2 INCH ELECTRON IMAGE PROJECTOR

C.E. Fuller, P.A. Gould, R.J. Tree and D.J. Vinton
Philips Research Laboratories, Redhill, Surrey RH1 5HA, England

ABSTRACT

The full-format electron image projector has considerable promise for fine detail I.C. lithography. A laboratory experimental machine for 2 inch slices has been developed and assessed in Philips. The development is continuing with an advanced projector for 4 inch slice exposure. The imaging and alignment performance of the experimental 2 inch machine is described. Measurements of the overlay registration on device slices show that the contribution to the pattern mis-registration due to distortion is only one or two tenths of a micron.

INTRODUCTION

Philips Research Laboratories has been actively engaged in the development of electron image projectors for some time (1,2). Four similar experimental machines for 2 inch slice lithography have been in use in different parts of European Philips for the past few years and this paper gives a brief description of the performance and assessment of this laboratory projector. The machine development is continuing with an advanced machine for 4 inch slice exposure (3).

A schematic of the image chamber is shown in Figure 1. The projector uses a chromium-on-silica mask and this is converted to a photocathode by the in situ deposition of a CsI layer using a vacuum evaporation unit which is plugged-in in place of the slice holder. For slice exposure the mask is illuminated from behind by UV light and a full-format electron image of the clear areas of the mask is focussed onto the silicon slice by the combined parallel electric and magnetic fields. The machine has automatic alignment. Each slice carries tantalum marker patterns and the alignment signal of X-rays, generated when the electron image of the marker pattern on the mask strikes the tantalum, is picked-up behind the slice. The alignment process takes about 10 secs. Auxiliary magnetic coils provide the image shift for the X and Y alignment and the rotational alignment is done by automatic hydraulic rotation of the mask holder.

Table 1 gives the basic operational data for the projector.

RESOLUTION, DEPTH OF FOCUS AND MACHINE ALIGNMENT

The machine can resolve lines a few tenths of a micron wide but device patterns are of more direct interest and Figure 2 shows a I^2L isolation wall pattern for a shift-register circuit with 1μm

Resolution/pattern capability	0.5μm lines
Depth of focus	75μm
Line width control over the slice	±5% for 1μm windows
Automatic alignment repeatability	±0.1μm in X, Y and rotation at the alignment marks
Alignment time	10 secs.
Stability of image-field distortion	±0.2μm at edge of field
Slice bow distortion	0.4μm per 10μm of bow

Table 1 Performance data for the 2 inch projector

wide windows in 0.4μm PMMA. This type of geometry is well within the capability of the projector. Electron backscattering in the substrate during projection exposure can cause pattern distortion. These effects are now well understood. Projection masks are normally made with an E/B pattern generator and corrections for back-scattering proximity effects in projection exposure can be made by adjusting pattern sizes, and possibly shapes, in the mask design and mask making processes. This has been done quite successfully for device geometries down to 0.7 to 0.8μm. No correction was made in the mask used for the 1μm pattern in Figure 2. Some distortion is appearing but this is due to electron backscattering both in the mask pattern exposure and in the slice exposure.

The depth of focus is around 75μm and defocussing is not a problem. The quality of pattern imaging on a non-flat surface is shown in Figure 3 which shows 1μm windows in 0.4μm PMMA crossing oxide ridges 1μm high. There is little variation in window width.

The machine automatic alignment has proved to be entirely satisfactory in use through our laboratory processing programme. In addition to the XY and rotational alignment where the repeatability is better than ±0.1μm in each component, the system has been provided with automatic magnification control - all using the same two areas of tantalum oxide marker pattern on the slice.

IMAGE DISTORTION

Two aspects of image distortion are important. Figure 4 shows the component of image plane distortion obtained by measuring the image displacement over the area of a slice when the magnetic field is reversed - without slice alignment. The main cause of the distortion is non-uniformity of the electric field which can arise from slice bow and the chamber construction, but this pattern was obtained using a flat slice and the main origin of this distortion is the slice holder itself. The slice is located about 300μm

behind the face of the slice holder resulting in an annular step in the image plane. Of course, with automatic X, Y and rotational alignment, this distortion pattern is registered with the alignment marks on the slice which removes overall variations in placement and any uniform rotation. The non-linear component of the pattern is shown in Figure 5. The variations from the reference grid are less than 5μm to within about 2mm of the slice holder edge. These distortions are not very significant providing the distortion pattern remains the same at each exposure. This mainly requires that the slice and its holder are accurately relocated in the chamber for each exposure.

Our experience shows that the distortion of the field is very repeatable, any errors are in the region of tenths of a micron but there is obviously considerable scope for improving the uniformity and so reducing the possibility of overlay misregistration due to unintended changes in the slice holder or chamber either due to wear or strain.

The second important image distortion is due to slice bow. The slice is the anode of the image system. A non-flat slice will give transverse components of electric field and consequent image distortion. This is potentially more serious than chamber distortion because the slice bow can change by 20-40μm, for a 2 inch slice, in a normal bipolar fabrication process. The sensitivity of the overlay registration accuracy to a change of bow between aligned exposures is about 1μm for a bow change of 25μm without magnification control, and we expect about half this value if magnification control is used.

This residual problem can be solved in more than one way. The change of bow throughout our I^2L process is shown in Figure 6. Also shown is the variation of the difference of the oxide thicknesses on the back and front of the slice, and a high degree of correlation is apparent. We find that the fabrication process can be modified to reduce the difference in oxide thickness on the back and front of the slice and so reduce the change of bow through the process, from about 30μm, to less than 8μm. This gives a device misregistration of about 0.3μm which is tolerable for 2μm geometries. For finer geometries the slice can be flattened at each exposure stage by using an electrostatic chuck (2, 4). We have not used the chuck so far in our slice processing work; prototype chucks have shown that the misregistration due to bow distortion can be reduced to a very low value. The electrostatic chuck is being incorporated in the larger machines.

SLICE PROCESSING

An important part of the assessment of the 2 inch projector has been the development and use of a fabrication process

incorporating electron-projection lithography, for small I^2L circuit arrays. Figure 7 shows a detail of a 100 gate serial transfer array. The finest detail is the collector contact window 1.5μm in the resist and 2μm in the finished device and the isolation wall 1μm wide in the resist - the width that is seen in the Figure is the extent of the side diffusion of the phosphorus layer. Excellent device characteristics are obtained. Figure 8 shows that the initial low transistor gain is brought up to the full expected value by the normal metallisation anneal. The improvement in gain is due to the removal of the damage caused by the electron exposure of the metallisation pattern and we can see this in the top diagram. Here the gain has been increased from its initial value by a short anneal at 350°C. The gain falls again after the slice has been given a repeat electron exposure and again the damage can be removed.

The laboratory processing of I^2L arrays has shown the potential of the projection lithography and the associated alignment system and marker technology for devices and ICs with 1 and 1.5μm features in the resist.

OVERLAY REGISTRATION

The fabrication work has been supplemented by direct measurement of a key feature of the lithography; the control on the pattern overlay registration. We find that the machine itself is capable of lithography into the sub-micron pattern feature region. Figure 9 shows the distribution of the misregistration for two pattern layers, the isolation and base layers, measured on electrical monitors on the finished device slice. The average misregistration between the two layers is three tenths of a micron but values up to 1μm are present. This diagram does not directly show the machine capability. The contributions to this misregistration can be in machine alignment, pattern placement errors on the two masks, and image distortion due to slice bow and changes in the machine itself.

The machine alignment error for each slice can be estimated by averaging the measured misregistration on the monitors surrounding the alignment markers.

Figure 10 shows the misregistration vectors measured on two completed device slices for the same pair of mask layers. It is clear that there is a common element to the misregistration even though the slices were processed at an interval of 6 months. We have identified this common pattern as due to pattern placement errors on the masks used for the two exposures. An accurate vector distribution of the relative pattern placement errors for these two masks can be obtained by averaging measured misregistration vectors at each chip site for a number of slices.

The common mask error together with the particular value of machine alignment error may be extracted from the measured vector distributions for each slice to give a residual error distribution. Figure 11 shows the residual for the device slice whose measured overall misregistration error is shown in Figure 9. This diagram, together with the machine alignment of ±0.1μm in XY and rotation, illustrates the machine performance for these two device layers. The residual errors which include misregistration due to changes in slice bow - in this case reduced by process modifications - and non-reproducible image distortions in the projector, are less than two tenths of a micron overall.

The conclusion is that the measured overlay misregistration mainly comes from errors on the masks and the main contribution from the machine is one or two tenths of a micron due to the alignment process. At this stage our attention is directed at improved masks and control on the processing to fully utilise the capability of the machine.

REFERENCES

(1) J.P. Scott, Solid State Tech. 43 (May 77).

(2) C.E. Fuller, P.A. Gould and D.J. Vinton, Proc. Sym. Electron and Ion Beam Sci. and Tech. 8th Intl. Conf. 108 (1978).

(3) R. Ward, 15th Sym. Electron, Ion and Photon Beam Tech. Boston (May 1979).

(4) W.R. Livesay. J. Vac. Sci. Tech. 15 (3) 1022 (May/June 1978).

CEF/SPC
30.4.80.

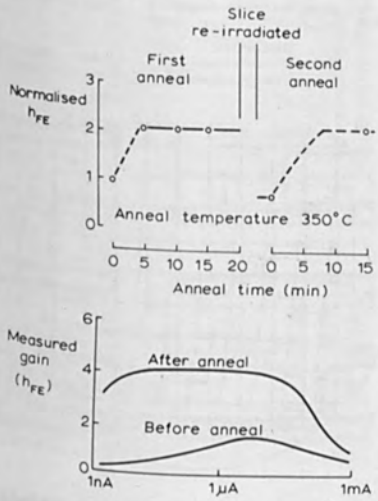

Figure 8. Effect of anneal and re-exposure on h_{FE}

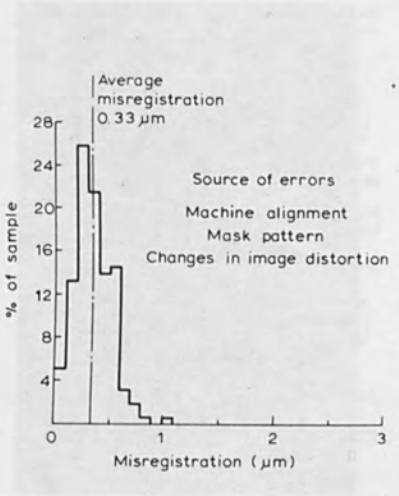

Figure 9. Isolation-base misregistration

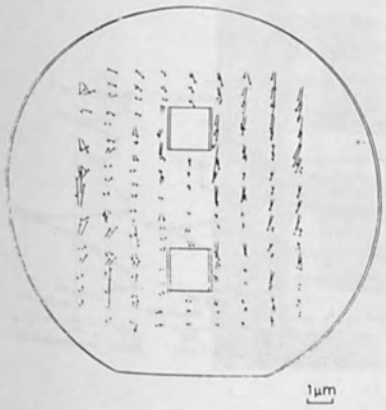

Figure 10. Superimposed misregistration for two slices

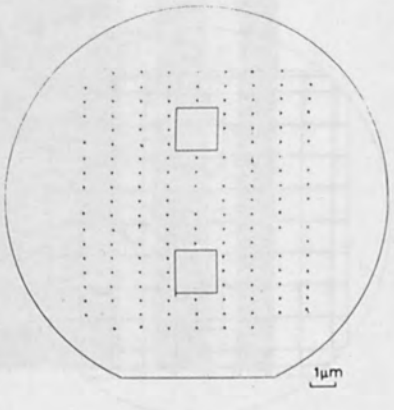

Figure 11. Residual isolation-base misregistration

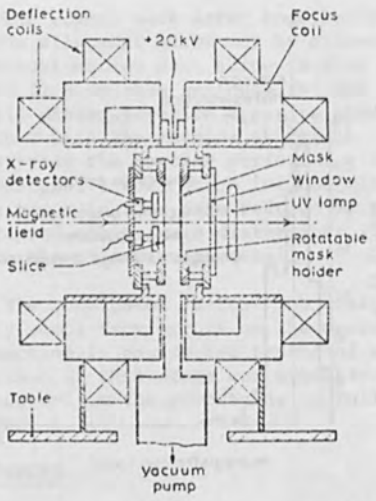

Figure 1. Schematic of Projector

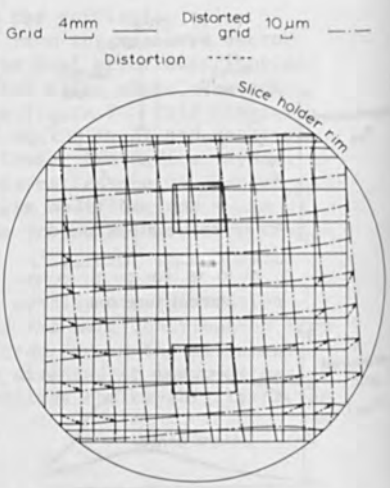

Figure 4. Measured image-plane distortion

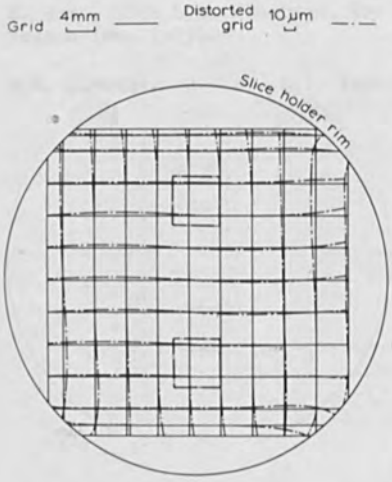

Figure 5. Non-linear component of distortion

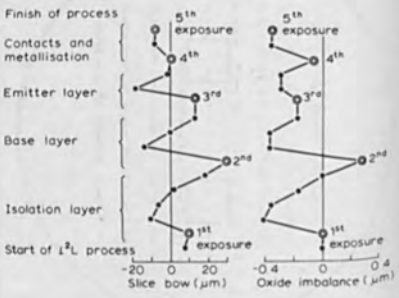

Figure 6. Variation of bow and oxide thickness in I^2L process.

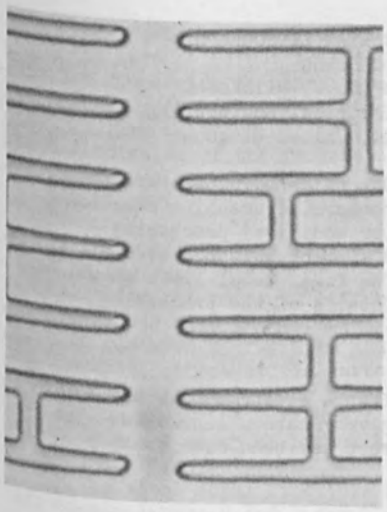

Figure 2. 1μm isolation pattern in resist

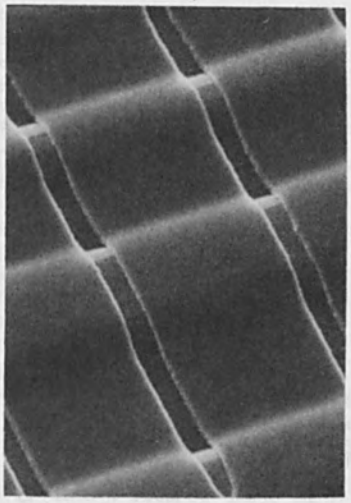

Figure 3. 1μm pattern over 1μm ridges

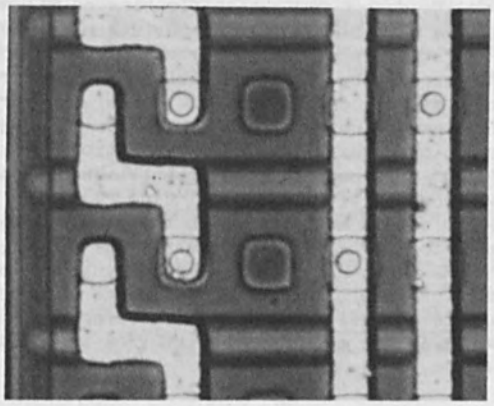

Figure 7. Detail of 100 gate serial-transfer array

VERY HIGH RESOLUTION ELECTRON BEAM LITHOGRAPHY USING LIFT-OFF PROCESSING

S.P. Beaumont, T. Tamamura and C.D.W. Wilkinson
Department of Electronics and Electrical Engineering,
The University, Glasgow G12 8QQ, United Kingdom.

20nm metals lines in Pt/Pd 20nm thick have been written on thin carbon substrates using a commercial scanning electron microscope and employing lift-off (or additive) processing. The lines in resist appear U shaped sloping outwards even at high exposures. The linewidth of the final metal lines shows a marked dependence on exposure. Details of the processing procedure are given.

The aim of this work is to establish a electron beam and X-ray lithographic system capable of printing very narrow lines (sub 25nm) on solid substrates. Substantial progress has been made towards achieving this aim.

In order to make a mask by electron beam exposure with linewidths of less than 0.1nm, it is necessary to avoid multiple electron scattering events in the resist and back scattering from the substrate by employing a thin layer of resist and a thin membrane substrate. A 30nm thick film of carbon is arc evaporated onto a microscope cover slip and a 50nm thick film of PMMA dissolved in MiBk is spin-coated onto the carbon. The glass is then dissolved away in hot hydrofluoric acid, leaving the carbon and resist floating on the acid. After transferring the thin films onto the surface of a water bath the carbon and resist are picked up on a transmission microscope grid. The resist is exposed by the 8nm diameter electron probe of a Philips PSEM 500 under microprocessor control. After exposure the resist is developed for three minutes in 1:3 MiBk:IPA. This relatively weak developer solution gives better edge resolution but requires a dosage of $5 \times 10^{-4} C/cm^2$ for complete development. The developed pattern in resist is over-coated with 20:80 Palladium-Platinium alloy. Lift-off is then used to obtain metal lines on the carbon substrate. The procedure used for lift-off is to immerse the specimen in a non-solvent for PMMA (methanol) and to inject a strong solvent (methyl ethyl ketone) into the liquid using a syringe directed at the film. We refer to this process as 'shooting'. Using shooting we have been able to clear away the metal and resist from isolated areas as small as 0.07 by 0.1μm.

Using the lift-off technique lines have been written in 20nm thick Pt/Pd which are less than 20nm wide. A pattern of characters with linewidth of about 25nm and with four characters to the micron has also been written. The advantages of using lift-off rather than etching as we see it are:-

a wider choice of metal as no etching technique has to be found

no electron scattering from a high Z metal layer during exposure
no need to adjust resist thickness for relative etch rate.

The minimum centre to centre spacing between 20nm wide lines which can be successfully lift off is about 50nm. This result is in accord with the experimental findings of Broers et al (1), and in disagreement with simulation of the process using Monte Carlo methods to estimate the distribution of electrons in the resist after exposure and a string model (2) to simulate the development process.

Insight into this failure to write very closely spaced lines has been gained from studies of exposed and developed specimens after metalisation but prior to lift-off. The profile of the lines in such specimens has been interpreted from bright field conventional transmission electron micrographs and it is found that the resist profile is U-shaped, narrow at the carbon surface, and wider at the top of the resist with walls which slope upwards and outwards in a width of 10-15nm on each side. Figure 1 shows such a resist line of total width 66nm and width at bottom 48nm.

The final metal linewidth after lift-off depends markedly on the exposure. Figure 2 and 3 shows a series of lines in which the width has increased from 16nm to 36nm with a two fold increase in dosage. The beam is stepped by 5nm between successive point exposures; the numbers by each line in Figs. 2 and 3 refer to the dwell time of the beam (in μsec) at each point.

To make useful devices on solid substrates it is intended to X-ray contact print, employing the electron beam written, Pt/Pd pattern as an X-ray mask. The recent report by Flanders et al[3] of 17 nm lines printed using Carbon K_α radiation encourages the belief that a complete lithographic system of 20nm or better minimum linewidth is possible.

REFERENCES

1) A.N. Broers, J.M. Harper and W.W. Molzen. Appl. Phys. Letts. 33, 392-393 (1978)
2) Jewett, R.E., Hagouel P.I., Neureuther A.R. and Van Duzer T. Polymer Eng. Sci. 17, 381-383 1977.
3) Flanders D.C. Appl. Phys. Letts. 36, (1), 93-96 1980.

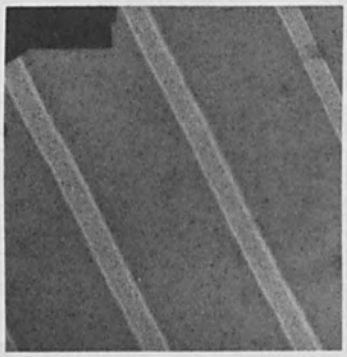

Fig. 1
Lines written by 8nm diameter electron beam after metallisation and prior to lift-off. Line on substrate is 48nm wide: walls of resist are approximately 10nm wide.

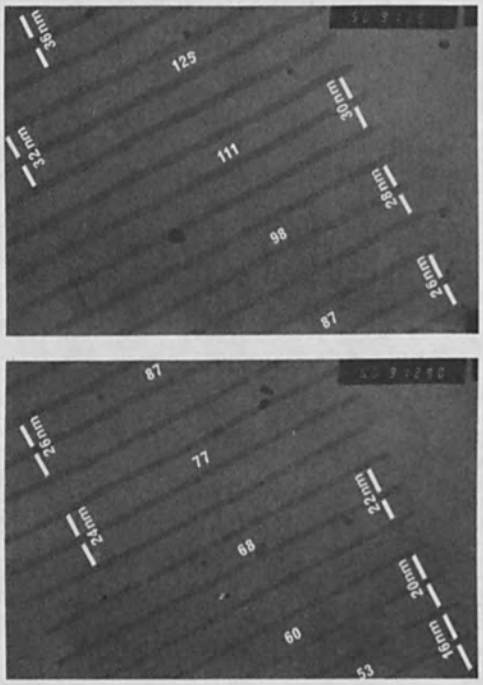

Figs. 2 & 3
Lines written by 8nm diameter electron beam after lift-off. Lines exposed with increasing dose as indicated by dwell times by each line. Linewidth increases from 16nm to 36nm when exposure increased by a factor of 2.4

LIMITATIONS DUE TO ELECTRON SCATTERING IN ELECTRON BEAM LITHOGRAPHY

I. Adesida and T.E. Everhart
National Submicron Facility
and
College of Engineering
Cornell University, Ithaca, New York 14853

ABSTRACT

A Monte Carlo method based on the continuous slowing down approximation was used to calculate the spatial distribution of electron energy dissipation in a very thin resist film on different thicknesses of silicon substrates. The distributions were then fitted with Gaussian functions. The Gaussian parameters obtained provided a measure of the impact of electron scattering on electron beam lithography. Approximate agreement between theory and experiment was found.

I. Introduction

For a consistent realization of submicron size features in electron beam lithography (EBL), the basic resolution limitations in EBL must be understood. Some basic limitations such as those due to electron sources and the spherical aberration of electron probe systems have been examined by Crewe (1). The most fundamental limitations are those due to electron scattering of incident electrons in the exposed sample (thin electron-sensitive resist flim on a substrate). Electron scattering limits the lateral resolution of isolated lithographic patterns - intra proximity effect, and also determines the spacings between adjacent lithographic patterns - inter proximity effect (2-5). Various methods of minimizing or correcting proximity effects have previously been explored, and usually, these methods involve an appropriate adjustment of factors such as incident electron energy, incident exposure dosage, substrate and resist thicknesses (5-8). A specific example that has been shown to reduce electron scattering, and thereby minimize proximity effects, is the use of very thin resist films on very thin substrates and higher incident electron energies (6,7). The use of this combination has produced the smallest lithographic patterns achieved to date with conventional EBL (6). Electron beam lithography on thin substrates have also been used to achieve the smallest working devices (Josephson junction) to date (9). Other novel devices that should benefit from these fabrication guidelines are thin-film optical and surface acoustic wave devices.

In the present work, we have used the approach of Chang (4) to further study the reduction of electron scattering, and in particular electron backscattering, as a function of substrate thickness and incident electron energy. In this approach, an analytic method (2) or a Monte Carlo (MC) method (3,7,13) is first used to calculate the spatial distribution of the energy dissipated by fast incident electrons in a material, and thereafter, the distribution is fitted with Gaussian functions. We have used a Monte Carlo (MC) method to calculate the spatial distribution of electron energy dissipation in a limiting thickness of polymethyl methacrylate (PMMA) film on various thicknesses of silicon substrates. The calculations were performed for a number of incident electron energies, and the calculated energy distributions were then fitted with Gaussian functions as stated above. The Gaussian parameters obtained are discussed and compared with experiment.

II. Proximity Function

Chang (4) has shown that the contribution to the electron energy dissipated in materials by either forward scattered electrons or backward scattered electrons can be represented by a Gaussian distribution. Following Grobman and Speth (10), the sum of Gaussians, otherwise called the proximity function, for PMMA on silicon can be written as

$$f(r) = \frac{1}{\pi(1+\eta_E)} \left[\frac{1}{\beta_f^2} \exp\left(\frac{-r^2}{\beta_f^2}\right) + \frac{\eta_E}{\beta_b^2} \exp\left(\frac{-r^2}{\beta_b^2}\right)\right] \qquad (1)$$

where β_f and β_b are the full width at half maximum of the forward and backward scattered components. The third parameter η_E is interpreted as a measure of the contribution to the proximity function due to backward scattered electrons, compared to that due to the forward scattered electrons. A compendium of the Gaussian parameters β_f, β_b, and η_E for thick PMMA films on thick substrates has recently been reported (11). A proximity effect correction algorithm based on the use of these parameters has also been reported (12).

Investigation of the Gaussian parameters for a 1000 Å PMMA film on various thicknesses of silicon substrates have been performed. Calculations of energy deposition were carried out using the conventional MC model which is based on the continuous slowing approximation. The details of this MC model, and in general the details of they physics of electron scattering in solids applicable to the work done here, are available in literature (3,13). However, it is pertinent to point out that forward scattered electrons were defined in our calculations as those electrons with a total scattering angle of $\theta \leq \pi/2$, while backward scattered electrons were those with $\pi/2 < \theta \leq \pi$. Backscattered electrons must be distinguished from backward scattered electrons. Backscattered electrons are backward scattered electrons that actually escape from the top surface of a target system into

vacuum. In all calculations, the number of simulated electron trajectories was typically 10,000. The parameters β_f and β_b were obtained from linear least square Gaussian fits to the MC results of the forward and backward scattered electron contributions. The results presented here are those at the resist-substrate interface ($z=T_{RS}$).

III. Results and Discussion

A. Theoretical Results

We shall be concerned here with the results of the parameters (β_b and η_B) that describe the impact of electron backscattering on EBL. With the thinness of the PMMA film used in our calculations, the spatial extent of forward scattered electrons is negligible.

Figure 1 illustrates the dependence of β_b on incident electron energy E_0 for two substrate thicknesses. A monotonic increase in β_b with increasing energy is noted for a thick silicon substrate ($T_{SB} = \infty$), while it is approximately invariant for $T_{SB} = 600$ Å in the energy range used in this study. The increase in β_b with E_0 for $T_{SB} = \infty$ is due to the increase in the electron range with energy. The relationship between β_b and the electron range in silicon is shown in Table 1. Bethe's range R_B was calculated following Everhart and Hoff (14), and the values obtained agree very well with the Monte Carlo range R_{MC} of Parikh and Kyser (11). For $T_{SB} = \infty$, the ratio of β_b/R_B depends weakly on electron energy. This agrees with the results of Parikh and Kyser (11) and Greeneich (15). Their estimation of β_b in relation to R_B is given as $\beta_b \sim 0.4R_B$, while a fair approximation for the work reported here is $\beta_b \sim 0.35R_B$. Estimation of β_b for other electron energies can therefore be made. This estimation rule is only true for silicon and not for other elements such as copper and gold (11). Murata et al. (16) have also done MC calculations for 1000 Å-thick PMMA film on Si. They defined a backscattered electron emission radius r_b as the radius where the integrated backscattered electron radial distribution F(r) is 0.9. Using this definition, they obtained $r_b = 0.75$ μm, 2.5 μm, 5.4 μm at incident electron energies of 10 keV, 20 keV and 30 keV, respectively. These values in terms of r_b/R_B yield 0.49, 0.49 and 0.53 for the respective electron energies. These are somewhat higher than the values of β_b/R_B reported above. The discrepancy should be expected due to the different definitions used in obtaining β_b and r_b.

For $T_{SB} = 600$ Å, β_b/R_B decreases with increasing energy. This is mainly due to the progressive reduction of the scattering volume of incident electrons in thinner substrates with the result that the progressively fewer backscattered electrons transverse limited distances before their exit. This is particularly emphasized in Figure 2 which shows the dependence of β_b on substrate thickness. A linear increase in β_b with T_{SB} is noted until $T_{SB} \sim 0.7$ μm where

saturation sets in. There is, however, a finite increase in β_b in the saturation region. Experimental observation of this dependence should be possible if dots or lines are exposed with enough dosage such that backward scattered electrons dominate the resulting resist profiles.

The parameter η_E has been shown to depend weakly on polymer film thickness and on incident electron energy for thick substrates (11). Values of η_E obtained in this work as a function of E_0 are shown in Table 2 for $T_{SB} = \infty$ and $T_{SB} = 600$ Å. The electron backscatter coefficients η_B are also listed. The values of η_B are for the combined system of PMMA on silicon; however, with the thinness of the resist layer, they should be very close to those of bare silicon. We observe that η_E and η_B are independent of E_0 for a thick substrate for the energy range shown. The fact that η_B is approximately invariant in this energy range has been shown experimentally (17).

For $T_{SB} = 600$ Å, η_E decreases with an increasing E_0 due to a decreasing η_B. Notice in Table 2 that for a specific E_0, there is at least an order of magnitude decrease in η_E for $T_{SB} = 600$ Å as compared with $T_{SB} = \infty$. This justifies the approach of Jones and Hatzakis (18) in their experimental determination of η_E. They derived a value of η_E from the solubility rate data of exposed PMMA on a thin and thick substrate.

The Gaussian parameter η_E as a function of T_{SB} is shown in Figure 3. A monotonic increase of η_E with T_{SB} is observed before saturation. The same trend is observed for η_B. The relationship between η_E and η_B has been defined by Parikh and Kyser (11) and for this work it can be approximated as

$$\eta_E = k_E \cdot \eta_B \qquad (2)$$

where k_E is the ratio of the average energy deposited by backward scattered electrons to that deposited by forward scattered electrons. The factor k_E is estimated to be ~ 3.1 for a thick substrate using the values listed in Table 2. For thin substrates, the values of k_E increases from 2.5 to 3.1 for a substrate thickness range of $600 \text{ Å} \leq T_{SB} \leq 1.5$ μm and for 20 keV incident electrons.

The results presented in this section indicate a systematic decrease in the Gaussian backscattering parameters (β_b and η_E) as substrate thickness is progressively reduced. A reduction in the parameters is also noted at higher incident energies. Since backward scattered electrons are mainly responsible for proximity effects, the results show why ultra high resolution in EBL is possible using thin substrates with higher incident electron energies.

It must be noted here that the results of η_E versus E_0 for a 5000 Å PMMA on a thick substrate obtained using MC calculations (11) differ from that obtained using the analytic model of Greeneich and

Van Duzer (2). Whereas, η_E is somewhat invariant with incident energy for MC calculations, Greeneich (15) obtained a variation of η_E with incident energy given by

$$\eta_E = 0.78 + 0.0073\ (E_0 - 10) \qquad (3)$$

where E_0 is in keV.

B. Comparison with Experimental Results

To date, very few experiments have been done to measure the Gaussian parameters, β_f, η_E and β_b. The experimental values obtained for these parameters are not well established especially in the case of β_f. Table 3 shows a comparison of η_E and β_b calculated in this work with experimental data of various authors (10,18-20) for thick silicon substrates. We can compare theory with experiment inspite of the differing resist thicknesses (T_{RS}) because to a large extent, these parameters do not depend on resist thickness (11).

The theoretical and experimental results of η_E as a function of E_0 listed in Table 3 are plotted in Figure 4. Calculations by Greeneich (15) using an analytic model (2) gave η_E values that are dependent on electron energy. This dependence is given by Equation (3), and the equation yields the dashed line plotted in Figure 4. Also plotted is an experimental point ($\eta_E = 0.6$ at E_0 for 25 keV) which was derived from proximity correction experiment by Parikh (5), and is reportedly not a unique value.

An examination of Figure 4 shows that the theoretical results of Greeneich (15) are higher than MC results which are nearly invariant with energy. Also, experimental data compare fairly well with the results of Greeneich (15). A quick check of the experimental data can be conducted by noting that the factor k_E discussed earlier is similar to the ratio δ_{BE}/δ_{PE} encountered in the theory of secondary electron emission (21). This is the ratio of secondary electrons produced by backscattered electrons compared with that due to primary electrons. This ratio has been determined experimentally (21) and for most materials it is ~ 5. If we assume that $k_E \sim 5.0$ and with $\eta_B \sim 0.16$, we obtain $\eta_E \sim 0.8$. This value falls within the range of the experimental data shown in Figure 4. Efforts are presently being made to understand why MC values of η_E differ from experimentally obtained values.

The dependence of β_b on substrate thickness obtained using MC calculations is shown in Figure 2. It was earlier postulated that it should be possible to obtain this trend experimentally if high dosages are used for exposure. A high dosage insures that backscattering predominates over forward scattering in the resist. The details of such an experiment are reported elsewhere (7). Theoretical results

of β_b are plotted in Figure 5 along with experimental results of dot diameters that were exposed at dosages of 1.0×10^{-9} C and 1.0×10^{-10}C. We find a close agreement between theory and experiment. For both theory and experiment, the linear to saturation region transition occurs at $T_{SB} \sim 0.7$ μm.

The results of β_b for thick substrates are shown in Table 3. The experimental value at 10 keV is much higher than that predicted by theory. A value of $\beta_b = 1.28$ μm is very high considering that Bethe's range in silicon at 10 keV is 1.52 μm. There is however a good agreement between theory and experiment at incident electron energies of 20 keV and 25 keV.

IV. Summary

We have presented a study of the reduction of electron scattering, and in particular electron backscattering, in thin substrates for electron beam lithography. A Monte Carlo method was first used to calculate electron energy distribution in a very thin resist film on various thicknesses of silicon substrates. The distributions were then fitted with Gaussian functions, and the resulting proximity functions were characterized by the parameters β_f, β_b and η_E. Since the primary concern in this paper was the impact of backward scattered electrons on EBL, only β_b and η_E were discussed and compared with experiment. Good agreement was found between calculated and experimental values of β_b. The MC values of η_E were considerably smaller than experimental data. Efforts are presently being made to understand the basis of these discrepancies. We noted also that the values of η_E obtained using Greeneich and Van Duzer model (2,15) agree fairly well with experiment. The Gaussian parameters obtained here are useful in understanding and minimizing the basic limitations due to electron scattering in EBL. These parameters should also be useful in understanding resolution limitations in the area of electron prob microanalysis.

REFERENCES

1. A. V. Crewe, J. Vac. Sci Technol. 16, 255 (1979).
2. J. S. Greeneich and T. Van Duzer, IEEE Trans. Electron Devices ED-19, 286 (1974).
3. R. J. Hawryluk, A. M. Hawryluk, and H. I. Smith, J. Appl. Phys. 45, 2551 (1974).
4. T. H. P. Chang, J. Vac. Sci. Technol. 12, 1271 (1975).
5. M. Parikh, J. Vac. Sci. Technol. 15, 931 (1978).
6. A. N. Broers, J. M. E. Harper, and W. W. Molzen, Appl. Phys. Lett. 33, 392 (1978).
7. I. Adesida, T. E. Everhart, and R. Shimizu, J. Vac. Sci. Technol. (Nov./Dec. 1979).

8. M. Parikh, J. Appl. Phys. 51, 705 (1980).
9. R. L. Laibowitz, A. N. Broers, J. T. C. Yeh, and J. M. Viggiano, Appl. Phys. Lett. 35, 891 (1979).
10. W. Grobman and A. Speth, Proc. 8th Int. Conf. on Electron and Ion Beam Sci and Technol. (Electrochemical Society, Princeton, NJ, 1978) p. 276.
11. M. Parikh and D. Kyser, J. Appl. Phys. 50, 1104 (1979).
12. M. Parikh, J. Appl. Phys. 50, 4371 (1979).
13. D. F. Kyser and K. Murata, Proc. 6th Int. Conf. on Electron and Ion Beam Sci. and Technol. (Electrochemical Society, Princeton NJ, 1974) p. 205.
14. T. E. Everhart and P. Hoff, J. Appl. Phys. 42, 5837 (1971).
15. J. S. Greeneich, J. Vac. Sci. Technol. (Nov./Dec. 1979).
16. K. Murata, M. Kotera, and K. Nagami, Proc. 8th Int. Conf. on X-Ray Optics and Microanalysis (Boston, MA, 1977) p. 14A.
17. E. H. Darlington, J. Appl. Phys. D. 8, 85 (1975).
18. F. Jones and M. Hatzakis, Proc. 8th Int. Conf. on Electron and Ion Bean Sci. and Technol. (Electrochemical Society, Princeton, NJ, 1978) p. 256.
19. N. Sugiyama, N. Aizaki, A. Kawaji and Y. Tarui, ibid., p. 184.
20. D. Stephani and E. Kratshmer, Proc. Microcircuit Eng. 1979, p. 228.
21. H. Seiler, Z. Angew, Phys. 22, 249 (1967).

FIGURE CAPTIONS

Figure 1 The dependence of β_b on incident electron energy for two thicknesses of silicon substrates.

Figure 2 The dependence of β_b on substrate thickness for 20 keV incident electrons.

Figure 3 Variations of η_E and electron backscatter coefficient η_B with substrate thickness for 20 keV incident electrons.

Figure 4 The dependence of η_E on incident electron energy for thick silicon substrates. The analytic theory of Greeneich and Van Duzer (2) is compared with Monte Carlo calculations and experimental data (see Table 3).

Figure 5 Comparison of Monte Carlo calculations of β_b with experimental results of dot diameter dependence on substrate thickness.

Table 1. The dependence of electron range and normalized β_b on incident electron energy.

E_0* (keV)	R_B (μm)	R_{MC} (μm)	β_b/R_B	
			$T_{SB} = \infty$	T_{SB} = 600 Å
15	3.06	3.12	0.33	0.21
20	5.06	5.0†	0.35	0.15
25	7.47	7.36	0.38	0.08
30	10.30	10.0†	0.36	0.07

*At E_0 = 10 keV, R_B = 1.52 μm and R_{MC} = 1.58 μm.

†Interpolated values from Parikh and Kyser (11) data.

Table 2. Variation of Gaussian scattering parameter η_E and backscatter coefficient η_B with incident electron voltage E_0 for two silicon substrate thicknesses.

E_0 (keV)	$T_{SB} = \infty$		T_{SB} = 600 Å	
	η_E	η_B	η_E	η_B
15	0.51	0.162	0.0178	0.0073
20	0.54	0.165	0.0093	0.0034
25	0.52	0.163	0.0043	0.0021
30	0.49	0.160	0.0040	0.0016

Table 3. Comparison of theory with experiment for thick silicon substrates.

E_0 (keV)	T_{RS} (μm)	η_E	β_b (μm)	Reference
10	0.10	0.50	0.56	This work
	0.45	0.72	1.28	(20)
20	0.10	0.54	1.77	This work
	0.45	0.82	1.65	(20)
	0.50	--	1.60	(19)
	1.20	0.91	--	(18)
25	0.10	0.52	2.62	This work
	0.60	0.86	2.35	(10)

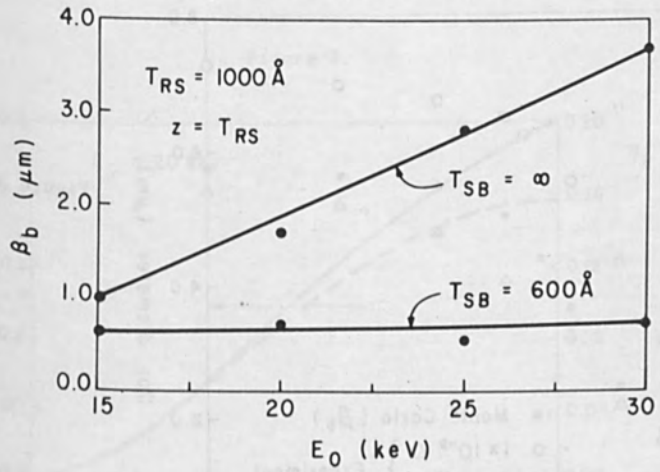

Figure 1.

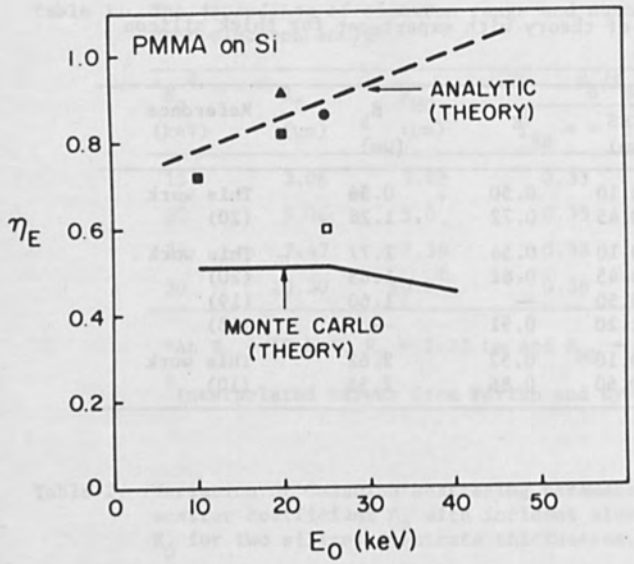

Figure 4.

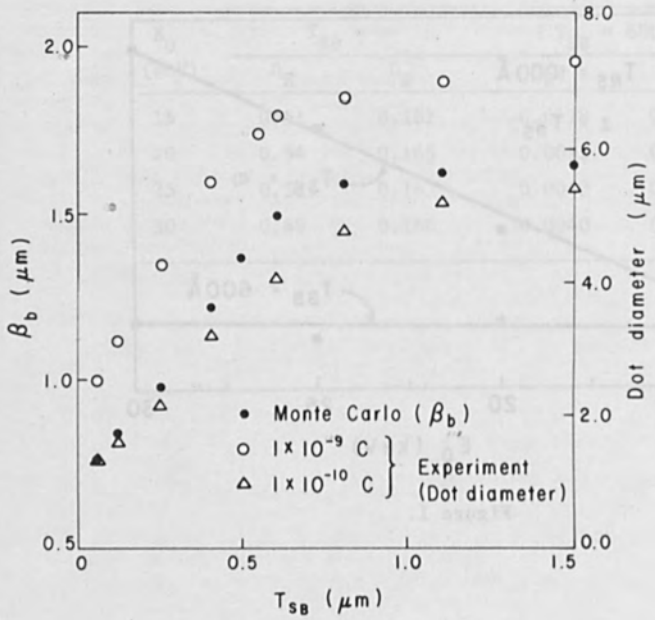

Figure 5.

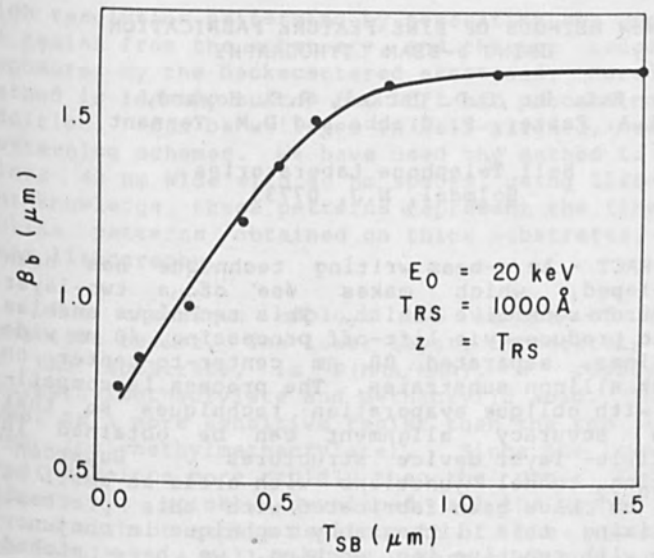

Figure 2.

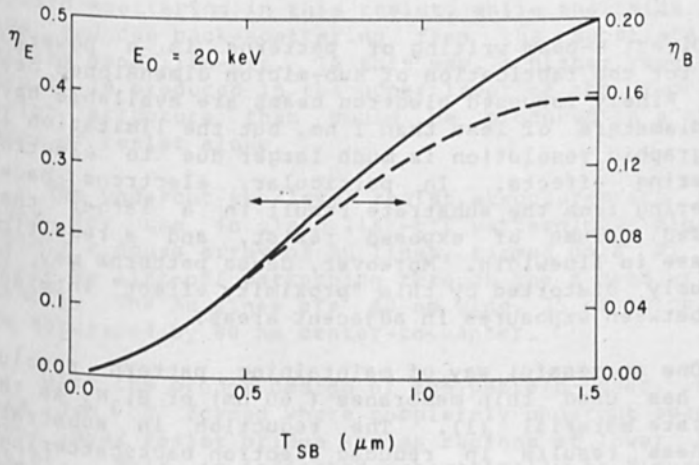

Figure 3.

NEW METHODS OF FINE FEATURE FABRICATION USING e-BEAM LITHOGRAPHY

E.L. Hu ,L.D. Jackel, R.E. Howard,
L.A. Fetter, P. Grabbe and D.M. Tennant

Bell Telephone Laboratories
Holmdel, N.J. 07733

ABSTRACT - An e-beam writing technique has been developed, which makes use of a two-layer electron-sensitive resist. This technique enables us to produce, via lift-off processing, 40 nm wide Au lines, separated 80 nm center-to-center on thick silicon substrates. The process is compatible with oblique evaporation techniques so that high accuracy alignment can be obtained in multiple- layer device structures . Superconducting tunnel junctions with areas as small as 10^{-10} cm^2 have been fabricated with this process. Utilizing this lithography technique in conjunction with reactive ion etching, we have etched pedestals 100 nm wide by 300 nm deep into silicon substrates.

Direct e-beam writing of patterns is a powerful tool for the fabrication of sub-micron dimensioned devices. Finely focussed electron beams are available having diameters of less than 1 nm, but the limitation in lithographic resolution is much larger due to electron scattering effects. In particular, electrons backscattering from the substrate result in a larger than intended volume of exposed resist, and a resulting increase in linewidth. Moreover, dense patterns may be seriously distorted by this "proximity effect" interaction between exposures in adjacent areas.

One successful way of maintaining pattern resolution has used thin membranes (60 nm) of Si_3N_4 as the substrate material (1). The reduction in substrate thickness results in reduced electron backscattering. We have developed an alternative method, utilizing two layers of e-beam resist (2), and which can be used on conventional, thick substrates. This method achieves

high resolution patterning by separating the upper layer of resist from the substrate, and thereby reducing its exposure by the backscattered electrons. Moreover, the method is ideally suited for lift-off processing and, in addition, can be utilized in self-aligned, multi-level patterning schemes. We have used the method to produce lines 40 nm wide with 40 nm spaces, using lift-off. To our knowledge, these patterns represent the finest resolution patterns obtained on thick substrates, using e-beam lithography.

The technique employs two levels of electron-sensitive resist. The lower layer, immediately adjacent to the substrate, is P(MMA/MAA), a copolymer of polymethylmethacrylate and methacrylic acid. This copolymer is a more sensitive resist than the top layer of PMMA (polymethylmethacrylate). Since the lower resist layer develops more rapidly than the upper layer, the pattern is quickly developed all the way to the substrate without excess development of the upper layer. The result is a well-defined undercut of the upper layer by the lower layer. Typically, the thicknesses of the upper and lower layers are, respectively, 100-150nm and 300-400 nm . The use of a thin upper layer minimizes forward scattering in this resist, while the thick lower layer reduces back-scattering from the substrate and permits good lift-off. In this way, a higher resolution stencil is produced in the upper layer of the two-layer resist structure than could be produced in a single layer of resist alone.

The undercut two-level resist structures are ideal masks for use in clean lift-off patterning. Figure 1 depicts a dense array of Au lines, formed on a Si substrate by lift-off patterning through the e-beam written stencil. The Au lines are 40 nm wide, 35 nm thick, and are separated by 80 nm center-to-center.

With the proper design of the pattern used, stencils can be formed where completely undercut spans of upper layer resist bridge across regions of lower level resist. This is indicated schematically in Figure 2A, and photomicrographically in Figure 2B. By successive multiple evaporations made at different oblique angles

under these spans, self-aligned multilayer structures can be formed using a single stencil. These techniques were developed by Dolan (3) for use with optical resists. The extension of the method for use with e-beam -written stencils implies the possiblity of fabricating devices all of whose dimensions are sub-micron. At these dimensions, it is important that the resolution of the process not be compromised by alignment errors. We have used the two layer e-beam resist and oblique evaporation techniques to produce superconducting Pb(In)-oxide-Pb Josephson tunnel junctions having areas of 10^{-10} cm^2. An SEM photograph of such a junction is shown in Figure 3.

Another important consideration in the fabrication of fine-featured patterns is that the methods of pattern transfer must be of at least as high resolution as the methods of pattern writing. Reactive ion etching is one such pattern transfer technique (4). Figure 4 is a micrograph of a 100 nm wide by 300 nm high Si structure formed by (i) lift-off processing of Ni (20% Cr) onto Si by our e-beam writing technique and (ii) use of the Ni (20% Cr) as a mask for the reactive ion etching of Si in $CF_4/10\%O_2$.

Summary

A high-resolution, two-layer e-beam technique has been described, which can be used to write patterns onto thick substrates. The method is ideally suited for use in clean lift-off patterning and can be used in self-aligned, oblique evaporation schemes to produce sub-micron devices in complex arrays. We have used the e-beam writing technique to produce dense arrays on silicon of 40 nm Au lines separated by 40 nm spaces. Using the e-beam technique in conjunction with oblique evaporation techniques, we have fabricated superconducting Josephson tunnel junctions having areas 10^{-10} cm^2. In addition, the writing technique has been employed, with reactive ion etching, to transfer 100 nm structures into silicon substrates.

REFERENCES

[1] A. Broers, J.M.E. Harper, W.W. Molzen, Appl. Phys. Letts 33 , 392 (1978).

[2] I. Haller, R. Feder, M. Hatzakis, E. Spiller, J. Electrochem. Soc. 126 ,154 (1979).

[3] G.J. Dolan, Appl. Phys. Lett. 31 , 331 (1977).

[4] H.W. Lehmann, R. Widmer, D.C. Shaver, Appl. Phys. Lett. 32 , 112 (1978).

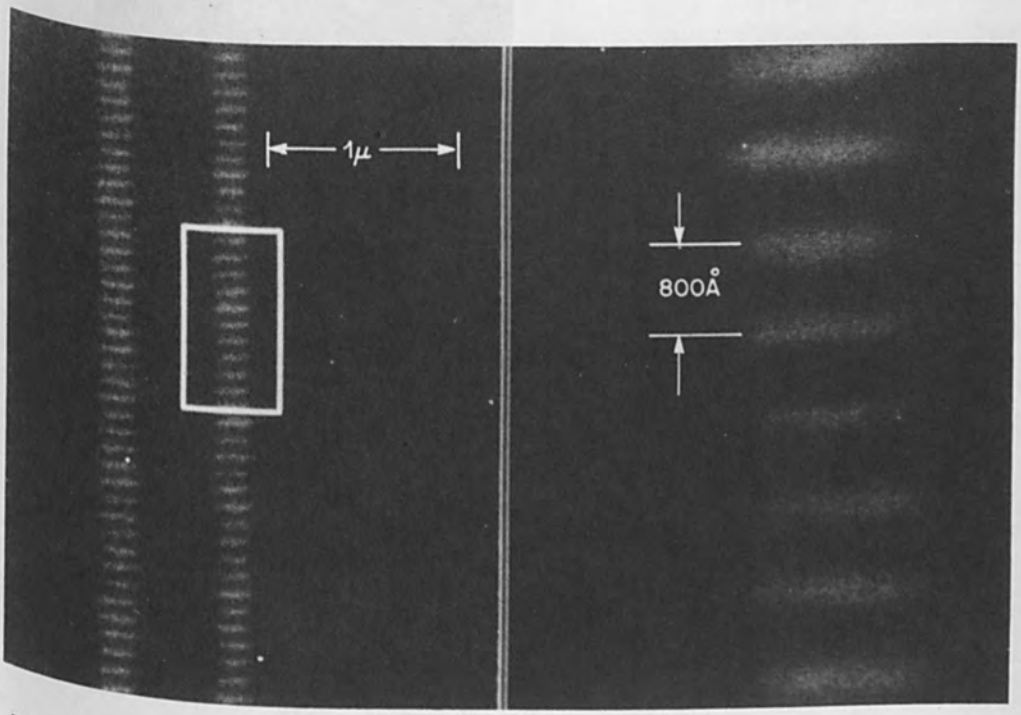

Fig. 1. 40 nm gold lines on 80 nm centers, formed by lift-off on thick silicon substrates.

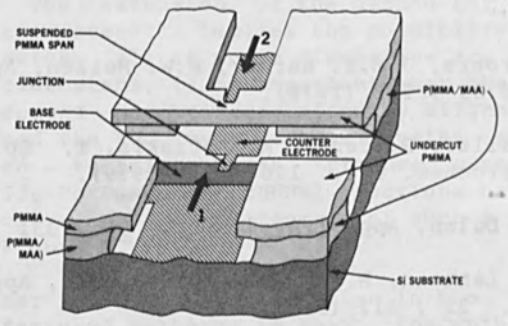

Fig. 2A. Schematic of oblique evaporations made through an undercut span of resist. Arrows 1 and 2 indicate the directions of evaporation of the base and counter electrodes, respectively, as projected in the plane of the substrate.

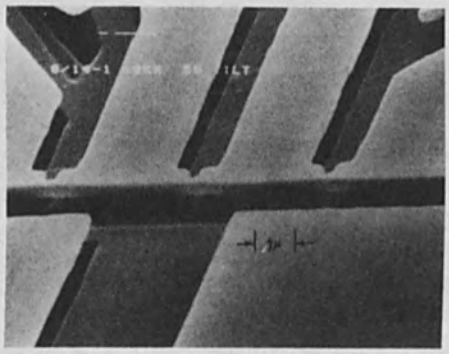

Fig. 2B. An SEM micrograph of the structure described in Figure 2A.

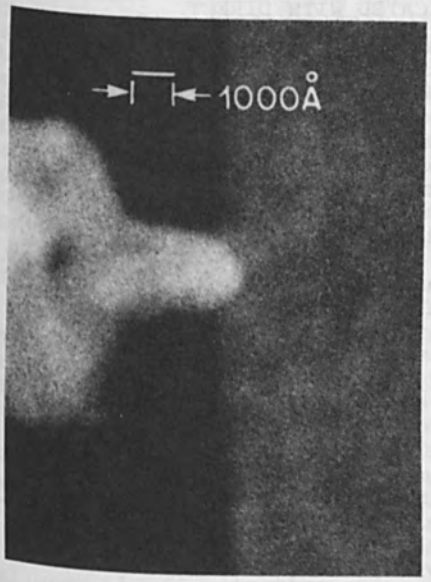

Fig. 3. An SEM photograph of a Pb(In)-oxide-Pb Josephson tunnel junction after lift-off.

Fig. 4. An SEM photograph of a pedestal 100 nm wide by 300 nm high, formed by e-beam patterning and reactive ion etching into silicon.

FAST STATIC RAMS FABRICATED WITH DIRECT ELECTRON BEAM LITHOGRAPHY

P.L. Shah, K.S. Rao, G. Pollack, J. Bartelt, G. Varnell
Semiconductor Research and Development Laboratories
Texas Instruments Incorporated
P.O. Box 225012, M/S 82
Dallas, Texas 75265

and

C. Rhodes, D. Kang, W. Bruncke
Texas Instruments Incorporated
Stafford, Texas

Abstract

A high density, high performance 4K bit static memory is fabricated using electron beam direct slice writing lithography. 1 micron feature definition and 0.25 micron level-to-level registration capability was demonstrated with a vector scanned e-beam exposure system that utilized high speed positive and negative electron beam resists, chip-by-chip alignment scheme. All implanted scaled MOS process with dry etching techniques for Si, SiO_2, Si_3N_4 was used to realize gate delays of 0.18 nsec at 0.09 pj. A full size memory with 2.5 micron features and 49 nsec access times have been fabricated. Scaled static memory with 1.5 micron features now fabricated are projected to yield sub 30 nsec access times.

Introduction

Electron beam lithography is rapidly undergoing transition from a laboratory lithographic technique[1,2,3] to a viable VLSI or VHSIC technology especially for the fabrication of high density devices requiring fine resolution and tight alignment tolerances. Recently, e-beam direct slice writing has been used to fabricate 1μ LSI bipolar circuits[4] and 1μ MOS test devices[5]. This paper details demonstrations of state-of-the-art scaled MOS process compatible with all direct electron beam lithography using state-of-the art fast static memory. A 4K static random access memory (SRAM) with larger component count* compared to dynamic memory (DRAM) is used as a vehicle for eventual scaling of the device to demonstrate density and speed

*4K bit SRAM has almost 5 to 6 times as many components as 4K DRAM

improvement utilizing resolution and registration offered by the present electron beam lithographic technology. The scaled memory now under fabrication utilizing full capability of e-beam resist resolution and individual chip alignment is projected to yield <30 nsec access time 4K SRAM on 12K mil^2 chip. The paper, in addition describes for the first time techniques such as individual chip alignment scheme that is compatible with the conventional projection mask lithography allowing an option that these two can be intermixed for optimum performance and throughput.

Lithography

All the patterns necessary to fabricate devices were defined using Texas Instruments EBMIII a vector scanned, laser controlled electron beam exposure machine with an auto chip-by-chip alignment feature.[1] The present configuration has nominal beam size of 0.7 μm with scan line spacing of 0.25 micron. Minimum 1 μm feature definition was possible using smaller beam at the expense of the writing speed. A system schematic and characteristics of EBMIII used are shown in Fig. 1 and Table 1, respectively.

The significant departure from most previously described alignment schemes[1,2,3,6] is the fact that in the patterning of all levels, except initial marker definition, two sets of markers were used. One set placed on slice is used to accomplish gross alignment followed by an individual chip alignment using markers in the form of crosses etched in the scribe lines. Such a dual marker system allows automatic slice and individual chip pattern alignment. This marker system for the first time allowed placement of the individual memories on the slice without loss of any additional area for markers as well as in a configuration that was identical to that on a mask for intermixing of these two lithographic techniques. (A typical chip layout is shown in Fig. 2.) An average registration accuracy of <0.25μ was achieved using this alignment scheme.

Patterns are defined in high resolution, high speed positive and negative electron beam resists - TI 323A and TI 309, respectively. In the present MOS process three dense levels - active area, gate and metal interconnect - were defined in a negative resist, the contact and implant masks were defined in a positive resist, minimizing total exposure area. The circuit layout, resist thickness, exposure and development was optimized for each step in relation to the subsequent processing and the device geometry constraints shown in Table II.

Process

A scaled polysilicon gate n-mos process with 600A gate oxides, implanted arsenic self-aligned source drains and submerged substrate contact was used. The process uses nine patterning steps, including the initial marker definitions and final protective overcoat. The process forms low, high threshold voltage enhancement and depletion transistors for power down capability. The major process steps are shown in Fig. 3. One important difference from the standard process is that the majority of the etching of Si, Si_3N_4, SiO_2 films was done in a flat plate reactor with fluorocarbon mixtures. The oxide etch processes compatible with the electron beam resists were developed with adequate selectivity in preference to Si and the resists. Thick positive electron resist layers were used as an implant mask for various enhancement and depletion type transistors. The final level interconnect used was 1% Si doped aqueous etchant. Adequate pattern definition and undercut were achieved with a negative electron beam resist. Final overcoat was a plasma deposited Si_3N_4. The vias in the overcoat were patterned using positive photoresist, projection lithography, and plasma etched in a parallel plate reactor.

Device/Process Characterization

A test vehicle that included a wide range of process, device and circuit test sites was used for patterning, alignment, and scaled MOS process optimization. A 19 stage ring oscillator with 1.5 micron gates demonstrated .18 nsec/gate delay at .09 pj/gate speed power product (shown in Fig. 4). The TMS2147 4K x 1 static memory with six transistor cell was designed with fully static peripheral circuitry without any bootstrapping and with a power-down feature using chip select signal. Electrical performance features for initial full size memories and the scaled memory is compared in Table III.

References

1. G.L. Varnell, SPE Conf. on Photopolymers, Principles, Processes, Materials, Ellenville, NY, October 1976.
2. H.N. Yu, R.H. Dennard, T.H.P. Chang, C.M. Osborn, U. Dilonardo & H.E. Luhn, J. Vac. Sci. Tech. 12, 1297, 1975.
3. E. Goto, T. Soma, M. Idesawa, J. Vac. Sci. Tech, 15, 883, 1978.
4. S.A. Evans, S.A. Morris, J. Englade, C. Fuller, L.A. Arledge, IEDM Digest, 196, 1979.
5. W.A. Hunter, L. Ephrath, N. Grobman, C.M. Osborn, B. Crowder, A. Cramer and H.E. Luhn, IEEE Trans. Elect. Device, ED26, 353, 1979.
6. L.D. Yau, L.R. Thibault, J. Vac. Sci. Tech. 15, 960, 1978.

EBMIII CHARACTERISTICS

• Pattern writing time (2.5 μcoul/cm^2 resist) (30% area)	24 sec/cm^2 +10-20% overhead
• X-Y table stepping speed	1.3 cm/s over 12.5 cm x 12.5 cm
• Direct writing pattern registration accuracy (fiducial markers) (every chip alignment)	± 0.25 μm
• Combination laser and fiducial marker alignment (three chip)	± 0.5 μm
• Alignment time	~0.1 second for each chip
• Data Input Complex IC patterns Simple devices and test patterns	 Magnetic tape after decomposition on IBM 370 Card or teletype
• Pattern intermix	Capable of intermix of 50 patterns on a single wafer with equal alignment accuracies
• Pattern generation capability	All normal photomask geometries
• Scan area (field size)	Up to 6.35 x 6.35 mm
• Line resolution	6250 Lines at 3 mrads beam semiconvergence angle (1.0 μm over 6.35 mm x 6.35 mm area)
• Point resolution (Least significant bit size)	0.125 μm (6.35 x 6.35 mm field)
• Pattern nonlinearity	<0.05% of field size
• Figure drafting	Steered beam (vector scan)
• Beam diameter	Variable from 0.25 μm to 5.2 μm (Computer controlled option of preset "large" or "small" beam)
• Accelerating voltage	15 kV
• Objective lens focal length	7.5 cm
• Scanning speed	Programmable from 40 μm/ms to 5 μm/μs

TABLE I

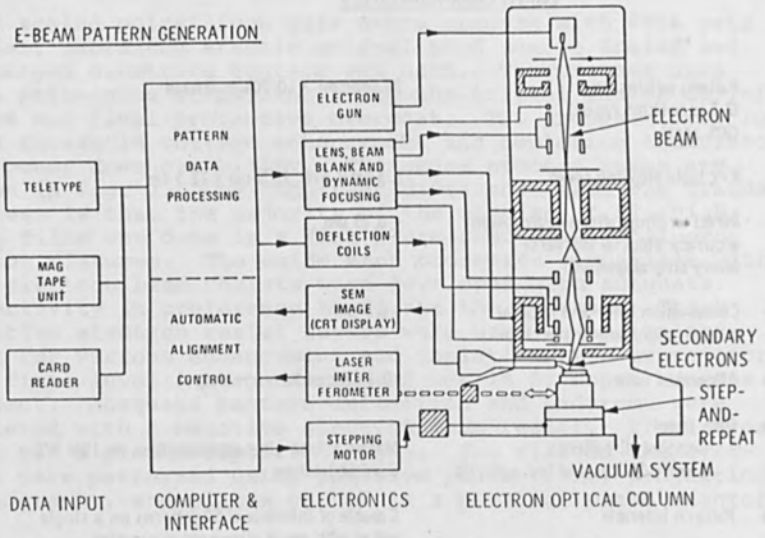

Fig. 1 EBMIII Schematic

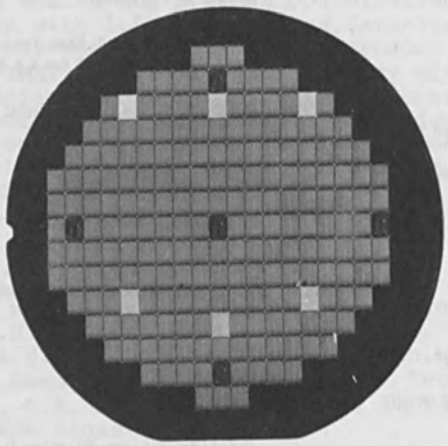

Fig. 2 A Typical Chip and Alignment Marker Layout

STATIC RAM PROCESS FLOW WITH ELECTRON BEAM LITHOGRAPHY

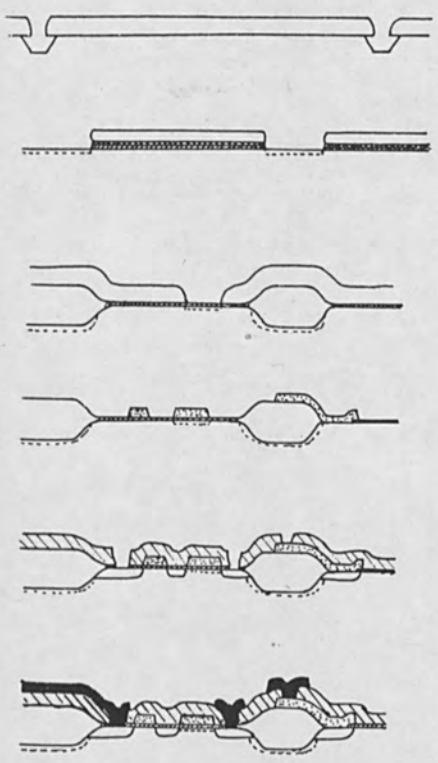

- Starting Slices, 30-40 -cm, 100
- Etch Markers
- Define Active Areas
- Self aligned Field Oxide
- Grow Gate Oxide, 600A°
- V_T Implants
- Depletion Device Implants
- Pattern, Etch Submerged Contacts
- Deposit, Dope Polysilicon
- Pattern, Etch Polysilicon
- Selfaligned Source Drains Arsenic Implant
- Deposit and Densify Interlevel Dielectric
- Pattern, Etch Contacts
- Sputter Deposit Al-Si
- Pattern Etch Al-Si
- Low Temperature Anneal
- Deposit Overcoat
- Pattern, Etch Overcoat
- Multiprobe

Figure 3

S2147 ALL E-BEAM PROCESS

STEP	RESIST	ETCH/IMPLANT	CRITICAL GEOMETRY† SPACE/FEATURE
ALIGNMENT MARKERS	TI-323**	SILICON ETCH	>5 MICRON
INVERSE MOAT	TI-309*	NITRIDE/OXIDE PLASMA ETCH CHANNEL STOP IMPLANT MASK	2 MICRON **
ENHANCEMENT	TI-309	IMPLANT MASK	>3 MICRON
DEPLETION	TI-323	IMPLANT MASK	>3 MICRON
FIRST CONTACT	TI-323	PLASMA ETCH OXIDE	3 MICRON
GATE	TI-309	PLASMA ETCH POLYSILICON, $MoSi_2$, Mo, W	2 MICRON
SECOND CONTACT	TI-323	PLASMA ETCH 10 KA PSG	3 MICRON
METAL	TI-309	WET ETCH ALUMINUM-Si	3 MICRON
PO	TI-323	PLASMA ETCH NITRIDE	>3 MICRON

* TI-309 -- NEGATIVE RESIST

** TI-323 -- POSITIVE RESIST

† FULL SIZE MEMORY

TABLE II

	Full Size Memory	Scaled Memory
Organization	4K x 1	4K x 1
Cell Size	3 mil^2	1.75 mil^2
Chip Size	20K mil^2	12K mil^2
Address Access Time	49 nsec	30 nsec*
Chip Select Access Time	55 nsec	30 nsec*
Power	400 mw	400 mw
Minimum Feature	2.5 µm	1.5 µm
Alignment	1.5 µm	.5 µm
Gate Oxide	600 Å	400 Å

* Estimated at 5V.

TABLE III

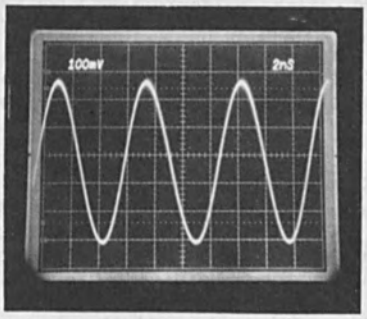

Fig. 4 Output of 19 stage ring oscillator @ 2V bias channel length ~1.5 microns

EXPOSURE TEST PATTERNS FOR EVALUATING ELECTRON BEAM MICROFABRICATOR PERFORMANCE

Joseph L. Kenty

General Motors Research Laboratories
Warren, Michigan 48090

ABSTRACT

Exposure test patterns have been used to test overall exposure performance of an electron beam microfabricator by examination of exposed and developed resist patterns. The patterns test resolution, long and short term beam placement stability, astigmatism, aberrations, distortion, subfield registration, layer to layer alignment, and other microfabricator system features. Most aspects are tested in a single multipurpose pattern, but certain aspects require small separate test patterns. Calibration patterns are concurrently exposed within the multipurpose pattern to allow comparison and rapid determination of the magnitude of test pattern effects. The tests are designed so that optical microscope examination provides maximum information. The exposure test patterns have been used for parametric characterization and diagnostic checking of a vector scan electron beam microfabrication system. The test patterns are easy to use, self-calibrated for rapid evaluation, and show the performance of specific microfabricator sub-systems as well as the overall pattern quality.

INTRODUCTION

The most important aspect of an electron beam microfabricator system is the exposure image quality it transfers to a wafer or mask. There are a variety of specific hardware tests, and computer controlled diagnostic aids which measure specialized sub-system aspects. In the final analysis, however, it is the overall quality of the pattern transferred to the sample which is important. Exposure of the patterns in conjunction with system adjustments and measurements allows correlation of specific system parameters with exposed pattern quality. They thus supplement, but do not replace, the many hardware functional checks.

The test patterns described here test the limits of an electron beam microfabricator (EBMF) system to repeatably expose high resolution, defect free patterns. The test patterns have several applications:

1) to correlate exposed pattern quality with EBMF electronic, mechanical, or electron optical parameters.
2) to evaluate and document EBMF system performance as a reference standard for future comparison.
3) to serve as a continuing diagnostic tool for evaluating the current state of machine performance in relation to previously accepted standards.
4) to aid in correct set-up after electron optical column or stage re-assembly.
5) to judge the effect of modifications on system performance.
6) to establish processing and design rule criteria for device patterns fabricated on the EBMF system.

The EBMF adjustments required to correctly adjust focus and astigmatism, and to minimize spot size while maximizing beam current, are subjective in nature, dependent upon operator experience and judgement. Although they cannot assist an operator during exposure, the test patterns do provide an objective record of the results of his actions. Pattern features are provided for measurement and comparison to correlate the operator controllable parameters with the magnitude of their effect on the pattern. The test patterns thus serve as a vital link in the chain of actions required to train man and machine to expose high quality integrated circuit patterns.

When used on a continuing basis, the test patterns can indicate the need for preventive or corrective maintenance. Catastrophic failure of an EBMF module is readily detectable. In many situations, however, "failure" is only a gradual deterioration in system performance due to long term contamination, drift, or component aging. In this case the first indication of operational difficulty appears in the multipurpose test pattern. When it is exposed routinely at regular intervals, the need for corrective action is seen by comparison with previously photographed examples of not acceptable, acceptable and optimal performance.

Though designed primarily to test EBMF system performance, the tests have an additional merit for testing resist formulations and processing, and other wafer or mask processing. Technicians and process engineers unfamiliar with electron beam microfabrication can rapidly learn to evaluate the impact a given level of EBMF performance will have on subsequent processing.

System and Data Structure Description

These test patterns have been developed for the specific microfabricator at General Motors Research Laboratories, a Cambridge Instruments EBMF 2-150. They apply to other systems to the extent which these systems resemble ours.

The GM system is a commercially available vector scan electron beam microfabrication system in which the beam is directed only to the areas to be exposed. Position of the beam within the scan field is determined by the output of a primary digital to analog converter, appropriately scaled and rotationally corrected, fed into a high speed deflection amplifier and a single post lens deflection coil.

The exposure of the trapezoidal primitives within the scan field is loosely termed raster scan, but more precisely is boustrophedonic motion, i.e., left to right, then right to left. Electrostatic beam blanking plates turn the beam off and on at the sample. Stepping motors drive the stage, whose position is continuously monitored (to 0.026 μm) by a laser interferometer. Continuous feedback to an error correction system brings the deflection system origin into conjunction with that of the instantaneous stage position.

Pattern data is defined in a 13 bit field of 8192 x 8192 exposure elements (exels), where 1 exel = field size/8192. The field size is continuously variable between 0.5 and 5 mm, in increments of 0.001 mm. The exel spacing is thus variable between 0.061 and 0.61 μm. The smallest feature size is coded to be N exels wide in the pattern data, where N = 1 to 16 and typically 4 to 8. The value of N selected by the designer depends on the resolution desired, the nature of the resist, and subsequent processing of the sample. If the chip size/minimum feature size is greater than 8192/N, the chip area is divided into several fields, each exposed separately and joined to its neighbor by precise stage motion. Chip sizes can be, in principle, as large as the 100 mm x 100 mm stage motion.

MULTIPURPOSE TEST PATTERN

Most microfabricator exposure tests can be performed with a single multipurpose test pattern. It is comprehensive enough to test resolution as a function of field size, field location, and data structure, as well as to test short term beam placement stability, astigmatism, deflection aberration, beam blanking characteristics, and others.

The multipurpose pattern is exposed in a 2x2 array joined at the boundaries, or alternatively, in a single field as in Fig. 1. When used in conjunction with complementary second and third layers, it can measure alignment accuracy, and long term beam placement stability. Several other unrelated separate patterns are available for specialized measurements such as distortion.

Resolution Test Pattern

The most important functional elements within the multipurpose test pattern are the series of resolution sub-patterns. They test feature size resolution as a function of 1) position within the field, 2) overall field size, 3) number of passes of the beam, and 4) final aperture size.

The basic resolution sub-pattern, shown repeatedly in Fig. 2, is composed of equal width bars, spaces, squares, and a checkerboard. The small features are four exposure elements (exels) wide, having been exposed by four passes of the electron beam, each pass spaced one exel distance apart. The large features are eight exels wide. The dimensions of the resolution pattern thus depend on field size; at 1.024 mm field size the four exel bar width is 0.5 μm.

The overall pattern is organized such that within the field of the complete test, Fig. 1, the resolution test is exposed in a 5 x 5 matrix. The 25 locations are identified by two exposed numerals, row and column, allowing comparison at the center of the field, location (33), with that at the four corners, location (11, 15, 51, 55), or intermediate field locations. The numbers identify for the inspector the field location quickly and unambiguously.

The resolution sub-patterns are used to evaluate system resolution based on six criteria:

1) Dimensional consistency is maintained between post development feature sizes and the input design data, e.g., adjacent uniformly sized and spaced exposed and nonexposed areas in the data remain uniformly sized and spaced after exposure and development.
2) Uniformity of resolution is maintained across the field, i.e., there is no degradation at the corners relative to the center.
3) Corner sharpness is maintained suitable for the intended use, generally better than 1/8 of the minimum feature size.
4) Edge waviness of long lines is minimal.
5) Edge acuity is retained, i.e., there is no ambiguity in observing the boundary between developed and non-developed areas with an optical microscope.
6) The resist cross-sectional profile is suitable for transferring the pattern to the substrate using the processing specified. Generally a vertical or slightly undercut profile is advisable.

The first five criteria can be applied to pattern evaluation regardless of resist type, and no extensive resist processing expertise is required for use. Patterns judged with these five criteria

are, however, sensitive to machine design and set-up. Pattern quality based on criterion (1) can be influenced by proximity effects at small sizes, so it is useful to expose at several dosages around the optimum. This increases the insensitivity of the resolution pattern to over- or under-development. Criterion (6), although dominant in actual fabrication, is determined more by processing details and not recommended for machine evaluation. It is also the only criterion which cannot be evaluated by a high quality optical microscope.

When compared at differing field locations using these criteria, the figures are very much a function of EBMF operator setup of focus, beam size, and astigmatism. If required for an untrained operator, a "through focus" or "through stigmation" sequence of exposures can be examined. The resolution figures across the field are also sensitive to manufacturing and installation set-up of the mechanical and electron optical alignment. Figure 2 illustrates acceptable resolution across the width of a single exposure field.

The resolution patterns may be used to study resolution as a function of final aperture size. As the area of the final aperture increases, the beam current increases and the exposure time decreases proportionally, but depending on field size and location there is a decrease in resolution. These patterns permit evaluation of this trade-off with only optical microscope examination.

Resolution as a function of field size and data structure (number of beam passes) can be studied using the patterns of Fig. 3 placed at two locations within the field. Their proportions are similar, but they differ in exel width. When the multipurpose pattern is exposed at different field sizes, the same data is used, but the deflection system address structure is changed. Independently, but usually proportionally, the beam diameter is changed. Thus an 8 exel feature of 1 μm width at 1 mm field size may be compared with a supposedly identical 1 μm wide feature exposed with 4 exels at 2 mm. These standardized patterns allow maximization of the field size/feature size ratio and minimization of exposure time by comparing resolution of identically shaped features. They are also useful in geometrical sizing and design rule determinations for device fabrication.

Beam Placement Stability - Short Term

A variation of the basic resolution test can be used to measure beam placement drift. Short term time constants from milliseconds to minutes can be detected, corresponding to the time intervals of the beam placement stability test sub-pattern and the multipurpose test pattern exposure times, respectively. The test records changes

in actual beam position at the sample from whatever the cause: deflection electronics drift, thermal drift, contamination induced charging drift, or others.

The short term beam placement stability test consists, in principle, of exposing the first half of the resolution test, deflecting the beam to another location within the field for a controlled time, then returning to the original position to expose the second half. The time interval between halves is controlled by the microfabricator clock frequency and the number of intervening sub-patterns exposed at the other location. The complete sequence is somewhat involved, as this process is repeated for 4 different time intervals at each of the 25 locations within the field, all interspersed with the other sub-patterns of the multipurpose test pattern.

Four completed test elements A, B, C, D, are shown in Fig. 4, along with three other tests. The time interval between the first and second half exposures is 1, 19, 30 and 100% of the full multipurpose pattern exposure time (seconds in this case) for the locations labelled A, B, C and D. Beam placement positional drifts of 0, 1/2, 1 and 1 exel are shown. Note that these drifts of 0, 0.061, and 0.122 μm are readily apparent with optical microscope examination. The checkerboard pattern is particularly sensitive to relative shifts between the halves.

To relate the magnitude of the beam placement drift with the visual appearance of the pattern, a calibration pattern was created, Fig. 5. The four exel wide pattern data was coded with intentional shifts of 0, 1, 2 and 3 exels and labelled with identifying numbers. Any shift greater than 1 exel is clearly noticeable. Shifts of ~1/2 exel in actual exposures may be estimated. The tests provide a placement accuracy test of 1/2 to 1 part in 8192, or 0.061 to 0.122 μm in a 1 mm field.

Beam Placement Stability - Long Term

Long term beam placement stability can be measured with a technique similar to the short term drift. The first half of a resolution pattern is exposed, then, after a suitable time delay, the second half. For the long term tests the first half is included within the multipurpose test pattern, the second half on layer two, a separate computer file. They are exposed with an operator controllable delay of seconds to hours. During the specified waiting period, other patterns may or may not be exposed elsewhere to keep the digital pattern generator and beam blanking systems in a known state. Likewise the stage may or may not be moved, or other actions taken to isolate the cause of any drift.

Figure 4 shows, for a final aperture known to be dirty, two long term drift tests at locations E and F, and the first half of one more at G. The time interval between the first and second half exposures of E and F was 30 and 60 minutes. If, immediately prior to the exposures of the second halves, a beam to stage position calibration had been performed, then the shift would be zero. Figure 2 shows the long and short term drift effects present in a typical clean system.

Most EBMF systems, including ours, have a beam calibration procedure which corrects for and eliminates long term beam placement drift. This involves moving the stage to a predetermined location, scanning a datum aperture or reference point, calculating its position in deflection system coordinates relative to the laser interferometer coordinates, and applying a static shift to the deflection system. In principle this beam error feedback or calibration may be applied after every single field exposure, but in practice it is required only infrequently, typically hourly. The long term stability test may be used to judge the time interval required between such recalibrations.

The exposure type drift test proposed here has a distinct advantage over reference datum location tests. The latter turn the beam off, move to a reference datum, turn the beam on, scan the feature, calculate its position, readjust the stage or deflection system coordinates as required, then return to the current exposure location. The stage motion time to the datum aperture is longer than the average step motion between exposures, hence a repeatable environment is established. Unfortunately, real exposures have variable environments. Our test allows operator control over the beam conditions immediately prior to test, thus permitting conditions identical to those of an actual exposure.

Stage Repeatability Pattern

The stage repeatability test measures the reproducibility of the system in repositioning the electron beam to a specified point on the sample surface after a stage motion. The test consists, in principle, of exposing one half of a vernier pattern, moving the stage, returning to the original stage position, then exposing the second half. The first half of several verniers are included among the many subpatterns of the multipurpose test pattern. The corresponding second halves are included in the second and third layers.

A completed vernier is shown in Fig. 6, together with another one scaled twice the size. The verniers are exposed in sets, one set parallel to the x-axis, the other to the y-axis, so that displacements in either direction are measurable. The vernier tic marks are single pass lines 1 exel wide, coded with an 8:7 exel spacing ratio (between

tic marks) in first half:second half. A unit shift between halves of the small vernier corresponds to 1 exel, or 0.122 μm when exposed at a 1 mm field size. An estimation of vernier alignment, and therefore stage repeatability, can be made to half the vernier resolution, or 0.061 μm.

For extended testing of stage repeatability, a statistical analysis is required. More patterns need to be exposed than can be accommodated on the multipurpose test pattern, so a nine level pattern set containing only stage repeatability verniers is available (1). Level 0 exposes a group of sixteen vernier first halves with the group repeated at the corners, center, and mid-sides of the field. Each of the remaining levels 1-8 contains a second half at the same locations. Typically ten fields of verniers are exposed across the sample surface. Levels 1 through 4 are exposed after identical stage motions prior to exposure. Levels 5 through 8 are exposed after a random series of stage motions for each level. The direction of stage approach to field 10, for example, is different in level 5 from level 6. Figure 7 shows one group after level 8 has been exposed.

The test data is analyzed by systematically recording each vernier reading, then examining the results for trends. Analysis is speeded by plotting histograms for each chip location or each level. If there are systematic differences between the x and y axes, between the first four and the last four levels, or between one level and the others, a fault exists. Stage wear after prolonged usage, for example, may show up a repeatable pattern of error in this test.

Although this test is considered primarily a measurement of stage reproducibility, it is more precise to consider it a measure of the combined effect of the stage motion and the electron beam positioning system. In our system, as in others, a laser interferometer continually tracks stage position and a difference signal shifts the electric optical axis deflection system, thus compensating for the discrete step motion of the stage itself or other unintentional displacements. If errors in this beam positioning feedback system are suspected, the repeatability pattern may be exposed without intervening stage motions. Since the second half verniers are on separate pattern files, the time delay between exposures is controllable. Hardware adjustments or measurements made in these time intervals may be correlated with the resulting pattern shifts.

The repeatability test verniers may also be exposed, again without stage motion, to look for undesired beam deflection due to contamination induced charging. When used in a diagnostic mode without intervening stage motions, the repeatability verniers are somewhat interchangeable in function with the resolution test figures as used in the long term beam positional stability test. Both demonstrate pattern shifts of less than 1 exel. Both have their first and second

halves on separate levels, hence separate pattern files, so the time interval between exposures is operator variable. Each has advantages. The verniers require a shorter exposure time, and if used to detect beam drift will be sensitive to a different time constant. The vernier patterns also retain their relative shift information even when focus has been poor or gross astigmatism is present. The resolution type patterns have the advantage that their relative shift can be determined quickly, even by untrained personnel. It is also more representative of actual device patterns, hence a process engineer can more clearly evaluate the trouble a shift problem might cause him in subsequent processing. The resolution type pattern retains shift information better than the vernier type if the sample is over- or under-exposed or developed.

Field Joining Accuracy Test Pattern

Field joining accuracy is an important consideration when large area patterns are composed by precise stage motion and connected small (1/2 to 2 mm) field size exposures. Patterns as large as 100 mm x 100 mm may be created with field connection errors much less than the minimum feature size.

The field joining test pattern enables quantitative analysis of field connection errors to an accuracy better than 1 exel. The test, in principle, places one half of a vernier at the edge of an exposure field, moves the stage exactly the field width, then exposes the second half. In actuality there are three x-axis and three y-axis vernier "first halves" along the top edge of the multipurpose pattern, and a similar number along the right edge. The corresponding "second halves" are at the bottom and left edges and produce a completed vernier when the pattern is stepped and repeated.

A field joining test pattern of identical vernier spacing ratio (8:7), accuracy (1 unit shift = 1 exel) and information content was obtained from Wallman (1). In this test, unlike the multipurpose test pattern, the stage motion between exposure fields is made slightly smaller than the field size so the patterns overlap. The patterns are coded such that a perfect match is indicated when the stage motion:field size ratio is 1:1.024. As with previous verniers, they measure a unit shift of 1 exel, or 0.125 μm at 1.024 mm field size. An estimate of field joining accuracy can be made to 1/2 unit, or 0.063 μm.

The appearance of a corner where two fields are overlap-joined vertically is shown in Fig. 8. The uncompleted verniers are used for horizontal joining tests. The verniers are different in appearance from those of Fig. 6 only in tic mark length and alignment of first and second halves. With the "center aligned" verniers of

Fig. 8 it is easier to tell rapidly if the shift is positive or negative, but making a correct numerical reading requires more care.

The true measure of field joining accuracy is not the best accuracy attainable, but the average accuracy and deviation attainable over a large number of stage motions. The field joining test normally exposes a P x P joined array at M locations within the stage travel area. There are thus (M)(6P)(6P) x-axis verniers and an equal number of y-axis verniers. Statistical analysis of the data is similar to that described previously. Histograms for each location within the field enable a rapid decision as to whether a problem exists.

Accuracy in the field joining tests depends not only on beam/stage positioning accuracy, but also on the field size calibration procedure and on the field distortion. In our machine field size calibration errors are not normally a problem as the laser interferometer stage is used as a reference standard, both in the calibration process and in the field joining test.

Deflection distortion has an impact upon field joining accuracy at field sizes around 2 mm and an increasingly significant impact at sizes up to 5 mm. Because of the manner in which the deflection system is calibrated, however, it is only the relative distortion between corners and mid-sides which contributes error. The field size calibration procedure adjusts the deflection field width at the meridians (mid-sides) to an absolute distance as determined by the laser interferometer. Consequently field joining error at the meridians is negligible. Only the distortion at the corners relative to the mid-sides will now appear as an error in field joining. Errors due to anisotropic distortion will also be picked up by the field joining test.

Astigmatism & Aberrations Test Pattern

Both astigmatism and deflection induced aberrations can give a spot shape change and concomitant size increase across a field. These beam profile changes can be measured directly by scanning the beam over a sharp edge (2), but this procedure is time consuming. An alternative technique more related to the exposure end product is to examine developed resist patterns of single spot exposures.

This portion of the multipurpose test pattern consists of exposing single points at each of 25 locations across the field. There are actually three sets of six separate points exposed for each of the 25 field locations. The six points are each exposed with a different clock frequency, the differing dosages allowing comparison of the beam size and shape for different intensity contours. The beam

is turned on and off only once at each point location. Triangular markers, placed to point to the single spots, assist in visually locating them after development.

To separate out the effects of astigmatism, aberrations and other instrumental effects, the size, shape and uniformity of the exposed points are examined as a function of 1) location within the field, and 2) EBMF system parameters. If there is residual uncorrected astigmatism, it will show more clearly in the dots subpattern than in the resolution and most other test patterns. Excess astigmatism will generally yield unidirectional elliptical spots, with all spots throughout the field elongated in the same direction. If desired, it is possible to make a series of exposures at under- and over-compensation to correlate with the amount of astigmatism correction and the visual image observable.

At large field sizes, deflection induced aberrations may be present in the microfabricator, leading to a spot whose size and shape is nonuniform over the exposure field. The magnitude of these aberrations can be determined by comparing the single spot exposures at the 25 various field positions. The aberrations may be permanent and unique to the particular deflection system, or temporary and alterable by electron optical column adjustments. In any event, use of the single exposure point pattern in conjunction with a series of experiments can deduce their origins. It may be useful to replace the final aperture with a suitable annular aperture (3) which emphasizes the size and shape differences.

Beam Blanking Test Pattern

One portion of the multipurpose test pattern can be used to evaluate the performance of the beam blanking system. The test consists of repetitive exposures of a single point at the same location, with the beam turned on and off between each exposure. Within the multipurpose pattern a set of four locations are exposed 80, 160, 320, and 640 times. There are 25 such sets, located at the same 25 numbered locations as the resolution test sub-patterns.

The dwell time for each single exposure spot is the same as that for the majority of the multipurpose test pattern. The hundreds of exposures result in a significantly over exposed region forming a symmetrical halo around the spot. If the beam turn on or turn off time is excessive relative to the exposure dwell time, a streak will also be exposed in the resist. The slower the rise or fall time, or the farther the blanking system is from a conjugate lens plane, the more pronounced the streak.

Figure 9 shows four examples. Figure 9(a) is the normal, desired condition. The central dot is symmetrical, over-exposed resist which has re-polymerized. The surrounding region is more moderately exposed (by back scattering) and is developed away. Figure 9(b) shows the pattern appearance when the rise or fall time has been lengthened by charging on a contaminated beam blanking aperture. Figure 9(c) shows a severe streak, the result of one of the electrostatic beam blanking plates not functioning. Figure 9(d) illustrates that the pattern can also be used to evaluate astigmatism and/or deflection aberrations, as the central region reflects the shape of the beam.

Alignment Test Patterns

There are two test patterns which measure the alignment of one layer with respect to a second layer. The first is the vernier pattern, also used to measure stage repeatability. The second is a more conventional sub-pattern incorporated within the multipurpose test pattern. The second provides a rapid visual indication of misalignment while the first provides measurement capability.

The vernier alignment test first writes layer 0 of the stage repeatability test on a wafer having recognizable alignment features. The sample is removed, but not developed, then reinserted. Layer 1 of the stage repeatability test is then exposed. The process repeats for successive layers and concludes with resist development. The measurement interpretation is as previously discussed. With 1 mm field exposures a unit shift in the vernier reading equals 1 exel, or 0.122 μm. Misalignment between layers can be estimated to 1/2 exel, or 0.061 μm.

The second alignment test pattern, Fig. 10, is incorporated within the multipurpose test pattern at four locations near the field corners. Both the cross and the quad marks are exposed on every layer. This pattern gives a readily visible indication of misalignment and is much quicker to examine that the vernier pattern. The eye is quite sensitive to asymmetries in the gap between marks and can easily detect a 1 exel shift (0.122 μm in a 1 mm field) in one pattern relative to the other.

To demonstrate the sensitivity of the alignment test, a calibration pattern has been exposed. The two halves are exposed on the same layer, with pre-coded shifts of 0, 1, 2 and 3 exels in the x and y axes. The alignment calibration pattern, like Fig. 5, has shifts which are readily visible with only a high power optical microscope.

Stability Test Patterns

There is a class of pattern tests, termed system stability tests, which consist of regular arrays of small features repeated across the field. The human eye is quite sensitive to irregularities in an otherwise large regular field, thus certain microfabricator defects will stand out. Several patterns have been used to detect faults in the main digital to analog (D/A) converter circuit, beam positional drift, ripple, and oscillation in the deflection amplifier.

A stability pattern included in the multipurpose test pattern and widely used in our laboratory is the checkerboard pattern, Fig. 11. The pattern is created by exposing a 4 or 8 exel square diagonally next to an adjacent square. This figure is repeated for an entire row, and each row repeated to form the checkerboard. This pattern shows clearly the effects of drift due to charging. Typically the gap between rows is present only at the start of the row and until the beam blanking/deflection system achieves steady state.

A second type of stability pattern consists of drawing a series of horizontal (or vertical) single pass lines. These patterns, separate and unrelated to the multipurpose pattern, usually cover an entire field. When appropriately spaced (8-32) exels, a large array of such lines will easily reveal irregularities. As an example, Fig. 12 shows the effect of ripple in the deflection system on such a pattern. The nature of a relatively small ripple is readily apparent even with a low power microscope.

Perhaps the most elementary of the stability pattern test is a separate full field, exposed as one large square. If the sample is under-exposed, resist will remain on the sample. Irregularities due to, say, glitches in the main D/A converter will appear readily. An example of such a full field pattern is shown in Fig. 13.

To better illustrate the effect of scan irregularities on the pattern, a calibration test pattern was created, Fig. 14. It shows the effect of a single line not exposed [-1], shifted in position one exel [S1], double exposed [+1], and two rectangles coded to just exactly match [00]. The horizontal and vertical calibration patterns are located within the field such that the anticipated position due to a D/A major state change falls at [?x]. The calibration pattern shows the effect of a D/A glitch is similar to, but less severe than, dropping out a line. Some D/A caused lines are similar to the shift in position of a line.

Distortion Test

A distortion test is presented which graphically demonstrates the deflection distortion present in large fields. The test is separate from the multipurpose test pattern. It consists of firstly exposing a large field, say 4 mm, with equally spaced horizontal (or vertical) lines. Secondly, the stage is moved precisely, and similar smaller fields, say 1 mm, are exposed in the corners of the larger field. The spacing of the line in the two fields may either be identical or vary by a factor of, say 4:1. In either case the resultant pattern reveals a series of Moire fringes, as in Fig. 15. Figure 12 is an enlarged view of the superposed patterns.

Interpretation of the Moire patterns qualitatively gives an indication of the symmetry of the distortion in the four corners. Either a difference in line spacing, or a difference in angular rotation, or both, is sufficient to form Moire fringes. If the spacing or rotation is uniform in both fields, the Moire fringes are straight and parallel. If, however, the line spacing changes within a field, or the lines within a field become slightly nonparallel, the resultant Moire fringes become curved and themselves have a variable spacing. As discussed by Smith, et al (4) for a related example, quantitative calculation is possible in principle, but is complex.

This exposure pattern test of distortion is intended to supplement more conventional methods of distortion measurement (5). The pattern test does have the advantage of providing visually an indication of the symmetry of the distortion.

DISCUSSION

Most of the test patterns are designed for examination with a high quality, or even moderate quality, optical microscope. A large fraction of the information content can be obtained with a rapid visual examination. Use of an optical microscope rather than an SEM maximizes both the efficiency and the ease of examination, hence the tester is much more inclined to routinely expose and examine the test pattern. There is, however, additional information available from these patterns, such as correlation of single spot exposures with resist profiles, which can be obtained only from SEM examination. With the multipurpose test pattern it is cost effective to use SEM examination only occasionally, and to use optical microscope examination for the bulk of the samples.

An important requirement for continued usage of any test is that it be easy to administer and interpret. Although it contains many individual sub-tests, the multipurpose test pattern is a single pattern file, so the operator overhead time in calling it is minimal. Interpretation is straightforward because of the pre-established calibration standards exposed concurrently on the sample.

ACKNOWLEDGMENTS

The assistance of D. E. Keyes in pattern exposure and EBMF system testing is appreciated, as is the assistance of L. C. Ewing in resist preparation and development. The helpful discussions and long time support of J. W. Hile, M. C. Steele, and E. F. Weller are also appreciated.

REFERENCES

1. B. A. Wallman, Cambridge Instruments, private communication.

2. D. C. Joy, Proc. 7th Scanning Electron Microscopy Symposium, IIT Research Institute, 1974, p. 327.

3. K. Amboss and E. D. Wolf, Proc. 11th Symposium on Electron, Ion and Laser Beam Technology, San Francisco Press, 1973, p. 195.

4. H. I. Smith, S. R. Chinn, and P. D. DeGroff, J. Vac. Sci. Technol. Vol. 12, p. 1262, (1975).

5. J. Reeds, K. Amboss, R. Fralick, E. D. Wolf, and B. A. Wallman, Proc. Electrochemical Society Extended Abstracts #410, p. 1018 (1978). (8th International Conference on Electron and Ion Beam Science and Technology).

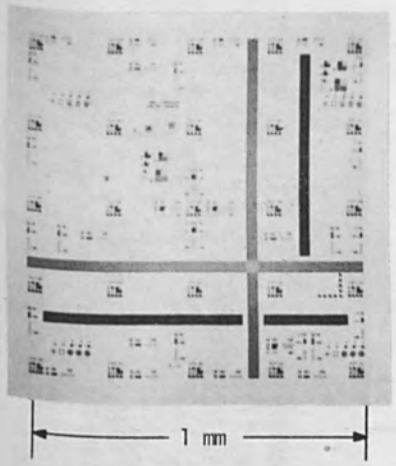

Fig. 1 - Overall View of Multi-purpose Test Pattern.

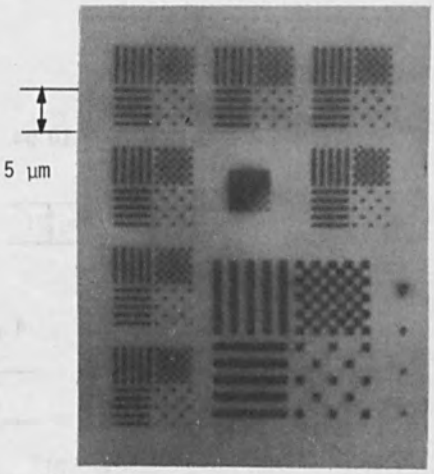

Fig. 2 - Basic Resolution Test with 4 and 8 Exel Wide Bars and Spaces.

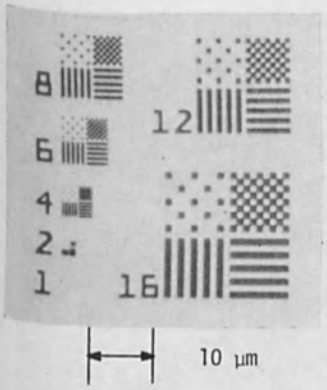

Fig. 3 - Variable Resolution Test (Numbers Indicate Pattern Width in Exels).

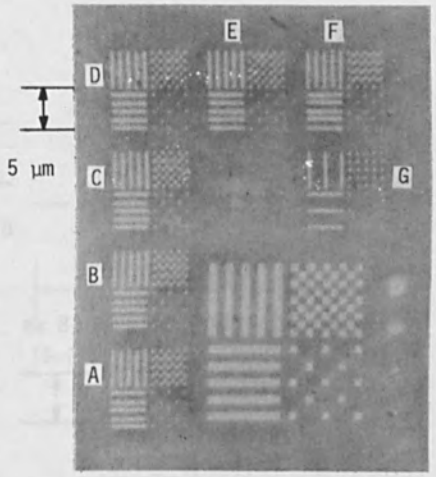

Fig. 4 - Beam Positional Drift Test Pattern.

Fig. 5 - Calibration Pattern for Beam Positional Drift.

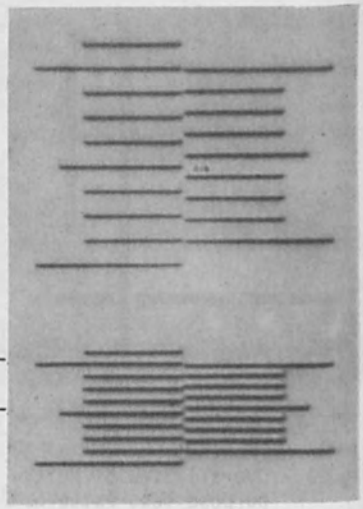

Fig. 6 - Stage Repeatability Test Vernier.

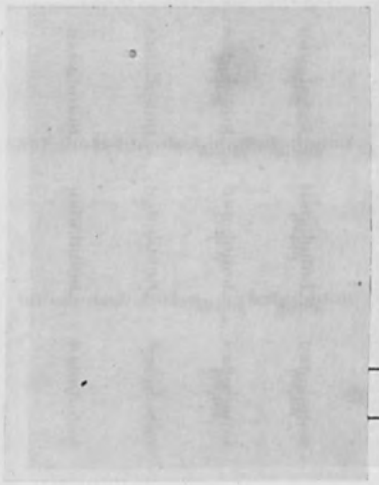

Fig. 7 - Multiple Motion Stage Repeatability Test Verniers.

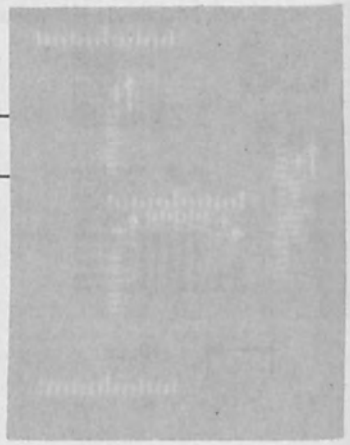

Fig. 8 - Field Joining Test at the Corner where Two Fields are Overlap Joined Vertically.

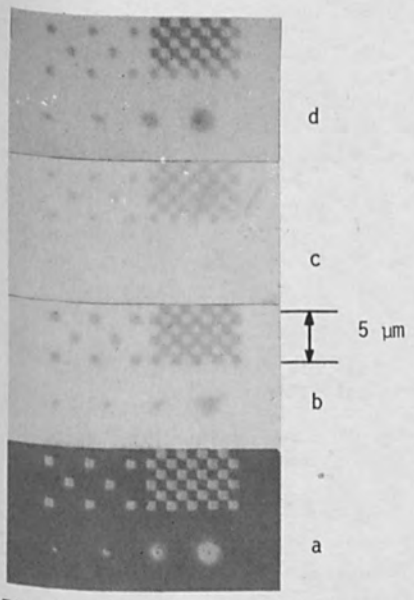

Fig. 9 - Beam Blanking Test Pattern.

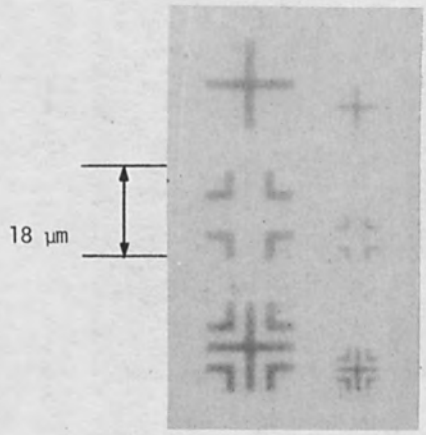

Fig. 10 - Alignment Test Pattern.

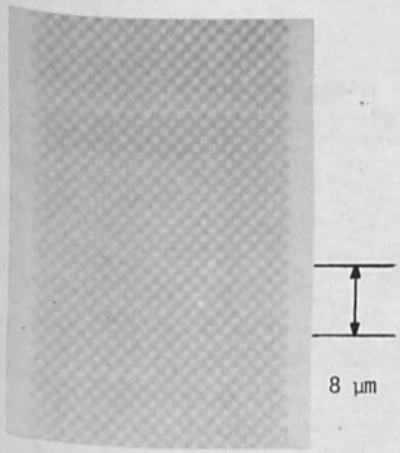

Fig. 11 - Checkerboard Type Stability Test Pattern.

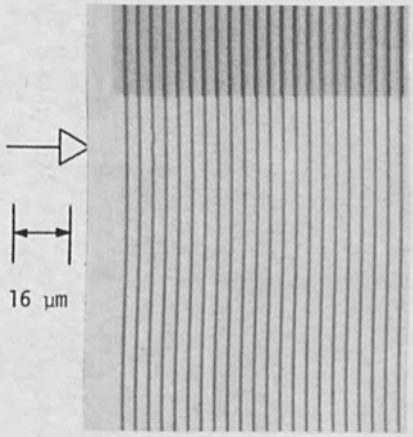

Fig. 12 - Stability Test Pattern of Vertical Lines.

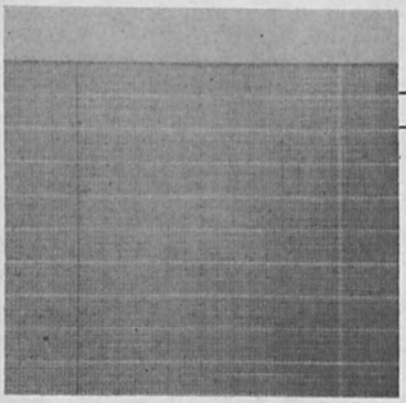

Fig. 13 - Full Field Stability Test Pattern.

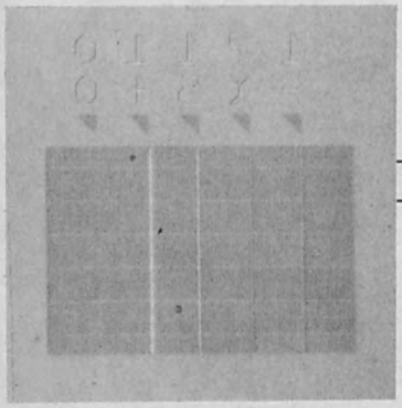

Fig. 14 - Calibration Pattern for Full Field Stability Test.

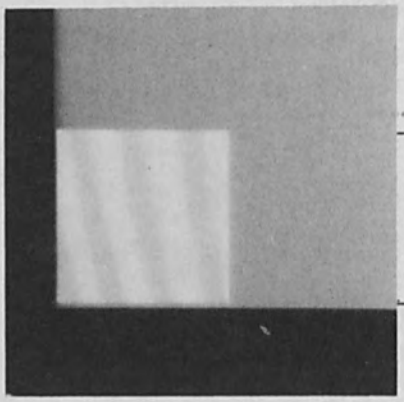

Fig. 15 - Moire Fringe Type Distortion Test.

A STUDY OF ALIGNMENT SIGNALS FOR ELECTRON LITHOGRAPHY

Yi-Ching Lin, Ilesanmi Adesida* and Andrew R. Neureuther

Department of Electrical Engineering and Computer Sciences
and the Electronics Research Laboratory
University of California, Berkeley, California 94720

*National Research and Resource Facility for Submicron Structures
Cornell University, Ithaca, New York 14853

ABSTRACT

High quality alignment signals are required in electron lithography. In this paper, the Monte Carlo method is used to study the alignment signals formed by electrons that are backscattered from tapered etched silicon marks. Effects of the mark geometry and the incident beam voltage are explored. Universal curves of both the contrast and the average signal slope are obtained. The results indicate that although a step of depth greater than 40% of the Bethe range of the primary beam yields a better contrast, too large a step will result in the decrease of the average slope. The quality of the alignment signal can be improved if the detector is positioned to collect the backscattered electrons with small takoff angles. The sum and difference signals from detectors in different azimuthal angles are also examined. The results show that in detecting a topographical discontinuity, the difference signal is preferred rather than the sum signal. Experimental confirmation of the theoretical predictions shows good agreement with the universal curve of contrast versus the normalized step depth. The alignment marks were fabricated by using anisotropic etching techniques in silicon, and the measurements were conducted in an ETEC Autoscan SEM.

I. Introduction

For direct wafer writing in electron lithography, the alignment signal is preferably obtained by detecting backscattered electrons, because they are capable of penetrating the resist coating. Several kinds of alignment marks have been used (1-6), and among them are steps, grooves, pedestals of silicon or silicon dioxide, and heavy metal lines. The alignment signal is generated from the topographical discontinuity or from a change in the electron backscatter coefficient if the mark material differs from the substrate. Automatic alignment with fast throughput has been made possible by using a computer-controlled scanning electron microscope (SEM) (7-9). Rapid and accurate electron beam alignment requires alignment marks that have

high signal contrast detectability, high edge acuity for precise location, and high signal-to-noise ratio (SNR) for rapid data acquisition.

The Monte Carlo method has been applied to study the signal formation by backscattered electrons from alignment marks by several authors (10-12). Shimizu et al. (10) reported the total backscattered signals from an infinite vertical edge, Aizaki (11) studied the total backscattered signal from steps, V- and W-shaped grooves, and Stephani (12) investigated signals from rectangular steps, pedestals and grooves by using a 20 kV beam, where the signals were separated into different takeoff angles and azimuthal angles. In this paper, the alignment signal formed by electrons that are backscattered from a tapered etched silicon alignment mark is investigated by using the Monte Carlo method as well as experimental measurements. Effects of the mark geometry and the incident beam voltage on the signal contrast and the signal sharpness are explored. Other factors which influence the quality of the alignment signal, such as the position of the detector to collect electrons backscattered in different takeoff angles or in different azimuthal angles are also examined. The Bethe range is used to interpret many features of the signals. Universal curves of both the contrast and the average signal slope are presented.

The alignment marks were fabricated by using anisotropic etching of silicon (13). The experiment was conducted in an ETEC Autoscan SEM, and the backscattered electrons were detected with a scintillator-photomultiplier combination system. The beam voltage employed ranges from 10 to 30 kV, and the beam current is approximately 1 to 10 nA. Backscattered signal from different azimuthal angles is reported in section IV. The contrast measured experimentally is also compared with the universal curve predicted theoretically from the simulations.

II. Monte Carlo Simulations

The Monte Carlo simulation program employs the conventional continuous-slowing-down-approximation (CSDA) model used in a previous study (14), with some modifications appropriate for the geometrical conditions of the alignment marks. For example, it is necessary to generalize the program to allow electrons to exist and restrike the non-planar Si surface in several ways. For each electron which eventually leaves the surface and "clears" all the topographical features, the exit location, direction and energy are recorded. This exit information can be reprocessed later for any particular detector configuration.

The CSDA model used will only be outlined here, since detailed discussions can be found in the literature (15-17). Single scattering events are assumed. The screened Rutherford scattering expression is used for a differential cross section of scattering. The

mean free path of an electron is then calculated and can be used as a step length. The directional cosine of an electron after a scattering event is obtained by relating the accumulated function of $P(\theta)$ to a uniform pseudo random number generated by the computer, where $P(\theta)d\Omega$ is the probability of scattering into the solid angle $d\Omega = \sin\theta d\theta d\phi$. The energy loss between scattering events is then found from Bethe's continuous energy loss formula. An electron trajectory is pursued until its energy slows down to 500 eV.

The marks investigated are 54.7° tapered silicon steps. This is close to the angle with which the maximum backscattered electron signal can be achieved for a tapered step, as discussed by Aizaki (11). An incident beam of zero diameter is assumed to scan across the alignment mark. Several values of beam voltages and step depths of the mark were used in the simulations. Individual electron trajectories of 3000 electrons were simulated at each location of impingement of the beam. An example of 30 electron trajectories is shown in Fig. 1 for a beam of 20 kV and a step of 2 μm.

III. Simulated Results

The alignment signal can be recorded by measuring either the number or the energy of backscattered electrons when the beam scans across the mark. From an earlier study (18), we found that the alignment signal obtained from collecting the total backscattered energy is of better quality than that from the total number. In practice, energy sensitive detectors are used and only the energy of electrons backscattered within a certain portion of the solid angle are detected. The takeoff angle (12, 19) θ of backscattered electrons is divided into three equal parts of 30° each. In this manner, we can separate the backscattered electrons into intervals with low, medium and high takeoff angles. Typical simulated backscattered energy signals for the different ranges of takeoff angles are shown in Fig. 2. The actual alignment signal would be similar and would involve convolving these results with the beam shape. The figure shows the contrast is improved when the detector is positioned to collect the electrons with low takeoff angle.

We define the contrast C as the ratio of the maximum signal difference available in the alignment signal to the background signal. Effects of both the step depth and the beam voltage can be expressed in terms of a normalized step depth z, which is the ratio of the step depth to the Bethe range (20) R_B of the primary beam. A universal curve of contrast versus the quantity z is shown in Fig. 3 for the takeoff angle $0 < \theta < 30°$. The contrast increases as z increases from zero and tends to a saturated value of 5.0 when z is greater than 0.4, that is, when the step depth of the mark is greater than 40% of the Bethe range of the primary beam. In comparison with our

earlier results (18) for the total energy signal in which the maximum contrast is 1.4, an improvement of a factor of 3.5 can be achieved. An inherent trade-off is that the collected signal level of backscattered electrons is reduced. The simulated results indicate that about 60% of the maximum signal difference available in the total energy signal will be retained in the angular portion $0 < \theta < 30°$.

Another abscissa x, which is the ratio of the horizontal width of the mark to the Bethe range, is also shown in Fig. 3. For anisotropically etched silicon alignment marks, x equals 0.71 z.

A steeper signal slope is desired, particularly when the collected signal is differentiated (5,21). As a criterion for measuring the signal sharpness, we define an average slope S_{av} as the ratio of the maximum signal difference to the total horizontal distance of the mark transition. Fig. 4(a) depicts S_{av} of the total backscattered energy signal as a function of x (and hence z) for different beam voltages. Note that for the same mark transition, a greater average slope will be obtained if a smaller beam voltage is employed. Furthermore, a normalized quantity S_N can be obtained by using:

$$S_N = S_{av} R_B$$

where S_N can be regarded as the average change in signal magnitude per unit horizontal distance (normalized to R_B) along the transition region. This results in a universal curve of the normalized average slope S_N as shown in Fig. 4(b). From Figs. 3 and 4, one concludes that although a value of z greater than 0.4 is preferred to get better contrast, too large a value of z will result in the decrease of the average slope.

A stereo monitoring system using multiple detectors (5,9,22) will collect electrons backscattered in different azimuthal angles. In our simulation, the azimuthal angle ϕ was divided into four parts of 90° each. These four parts are arranged so that two of them lying opposite to each other are halved by the direction in which the mark is assumed to be of infinite extension (12). The part which faces directly toward the inclined mark edge is called ϕ_1, while the other part which faces just opposite to the edge is ϕ_3. Fig. 5(a) illustrates typical simulated backscattered energy signals collected by detectors in ϕ_1 and ϕ_3. Their sum and difference are shown in Fig. 5(b). The contrast enhancement occurs in the difference signal rather than in the sum signal. This agrees with the experimental results reported by Stickel (5). According to our definition of the contrast, for the case shown in Fig. 5 with a 20 KV beam voltage and a 1 μm step depth, the contrast is improved by a factor of 10 for the difference signal compared with that of the signal ϕ_1. In fact, it has been demonstrated by Kimoto et al. (22) that the difference signal shows the surface topography, while the sum signal enhances the material contrast due to different chemical components.

IV. Experiments and Discussions

The alignment mark was realized by etching anisotropically through an oxide mask into a (100) -silicon substrate (13). This gave a tapered silicon step with an inclination angle of 54.7°. Fig. 6(a) shows a side view of a Si step of 10 μm so fabricated. The edge wall of this well-defined structure is uniform and smooth, as observed in Fig. 6(b), which shows a corner of two edge walls.

The backscattered electrons were detected by using a scintillator-photomultiplier combination system. The scintillator detector was positioned so as to receive electrons that have been backscattered with takeoff angle between about 0 and 15°. The total solid angle of the detected backscattered electrons was about 0.009sr. Fig. 7 shows the recorded signals from a 2.5 μm Si step mark for a 30, 15 and 10 kV beam voltage, respectively. The signals in the top row were collected with the edge facing toward the collector, while the signals in the bottom row were with the edge facing away from the collector. They correspond to the signals ϕ_1 and ϕ_3 illustrated in Fig. 5(a). It is evident that the difference signal gives better contrast than the sum signal. The horizontal line in each case is the beam-off level.

There is a nearly flat plateau of the signal in the region of the mark transition in Fig. 7(iii). This has been predicted from the Monte Carlo simulation in our earlier study (18), and can be explained that once the step depth is greater than the Bethe range (Note that in Fig. 7(iii), z = 1.55), the incident electrons tend to see an identical geometry within a certain portion of the mark transition. Experimental results on the contrast of the signals are compared with the theoretical predictions in Fig. 3. Although the actual solid angle substended by the scintillator is smaller than the assumed solid angle in the simulations which give results in Fig. 3, satisfactory agreement is still obtained. We also notice from Fig. 7 that an electron beam with a smaller voltage will give a signal of narrower spread and greater average slope than a beam with a larger voltage. However, the magnitude of the energy signal is less for a small voltage beam, and hence the SNR will be degraded if the same incident beam current is used (4, 12). In order to obtain a reasonable signal level when a small beam voltage is used, the beam current must be increased. This results in an inherent increase in beam size which will likely degrade the contrast and the average slope attainable in the signal.

Fig. 8 compares the backscattered-electron image with the secondary-electron image of the step. Since the secondary yield is enhanced at all edges, all edges appear brighter in the secondary-electron micrograph. However, in the backscattered-electron image, only the edge which faces toward the detector becomes brighter, while the edge which faces away from the detector becomes darker. This is further evidence that the difference rather than the sum signal provides the greatest contrast.

V. Conclusion

In this paper, Monte Carlo calculations based on a CSDA model were used along with experiments to study the alignment signals formed by electrons that are backscattered from tapered etched Si marks. Effects of the step depth and the beam voltage on the contrast and the average slope were expressed in terms of a normalized step depth z of the mark. A universal curve of the contrast of the energy signal versus z was obtained. For low takeoff angles $0 < \theta < 30°$, the contrast reaches a saturated value of 5.0 when the step depth of the mark is equal to or greater than 40% of the Bethe range of the primary beam. In comparison with our earlier results for the total energy signal in which the maximum contrast is 1.4, an improvement of a factor of 3.5 can be achieved. However, a trade-off is the reduction in the collected signal level. Simulated results indicate that about 60% of the maximum signal difference available in the total energy signal will be retained in the low takeoff angles. A universal curve of the average signal slope was also presented. In general, a beam of smaller voltage will give a signal of narrower spread and greater average slope. Sum and difference in signals from detectors in different azimuthal angles were also considered. It was found that in detecting a topographical discontinuity, the difference signal is preferred. The contrast is typically improved by a factor around 10 in the difference signal. This is mainly due to the fact that the background by using the difference signal is eliminated to a very small value. Again, the trade-off is that the signal level will be reduced. Measurements on tapered etched Si steps were made, which empirically confirm both the universal curve of contrast versus the normalized step depth and that the difference signal gives better contrast than the sum signal.

VI. Acknowledgment

Research sponsored by the Joint Services Electronics Program Contract F49620-79-C-0178.

REFERENCES

(1) G. L. Varnell, D. F. Spicer, and A. C. Rodger, J. Vac. Sci. Technol. 10, 1048 (1973).

(2) A. D. Wilson, T. H. P. Chang, and A. Kern, J. Vac. Sci. Technol. 12, 1240 (1975).

(3) E. D. Wolf, P. J. Coane, and F. S. Ozdemir, J. Vac. Sci. Technol. 12, 1266 (1975).

(4) H. Friedrich, H.U. Zeitler, and H. Biernenke, J. Electrochem. Soc. 124, 627 (1977).

(5) W. Stickel, J. Vac. Sci. Technol. 15, 901 (1978).

(6) Y. Iida and T. E. Everhart, J. Vac. Sci. Technol. 15, 917 (1978).

(7) N. Saitou, C. Munakata, Y. Miura, and Y. Honda, J. Phys. E. 7, 441 (1974).

(8) D. S. Alles, F. R. Ashley, A. M. Johnson, and Townsend, J. Vac. Sci. Technol. 12, 1252 (1975).

(9) D. E. Davis, R. D. Moore, M. C. Williams, and O. C. Woodard, IBM J. Res. Dev. 21, 498 (1977).

(10) R. Shimizu and K. Murata, J. Appl. Phys. 42, 387 (1971).

(11) N. Aizaki, Japan. J. Appl. Phys. 18, supplement 18-1, 319 (1979).

(12) D. Stephani, J. Vac. Sci. Technol. 16, 1739 (1979).

(13) R. M. Finne and D. L. Klein, J. Electrochem. Soc. 114, 965 (1967).

(14) I. Adesida, T.E. Everhart, and R. Shimizu, J. Vac. Sci. Technol. 16, 1743 (1979).

(15) K. Murata, T. Matsukawa, and R. Shimizu, Japan. J. Appl. Phys. 10, 678 (1971).

(16) D. F. Kyser and K. Murata, IBM J. Res. Dev. 18, 350 (1974).

(17) R. J. Hawryluk, A. M. Hawryluk, and H. I. Smith, J. Appl. Phys. 45, 2551 (1974).

(18) Y. C. Lin, I. Adesida, and A. R. Neureuther, Appl. Phys. Lett. 36, 672 (1980).

(19) O. C. Wells, Appl. Phys. Lett. 16, 151 (1970), Appl. Phys. Lett. 19, 232 (1971).

(20) T. E. Everhart and P. H. Hoff, J. Appl. Phys. 42, 5837 (1971).

(21) J. L. Mauer and L. B. Zielinski, IBM Tech. Discl. Bull. 21, 1464 (1978).

(22) S. Kimoto and H. Hashimoto, in The Electron Microprobe (ed. T.D. McKinley, K. F. J. Heinrick, and D. B. Wittry) 480, Wiley, New York (1966).

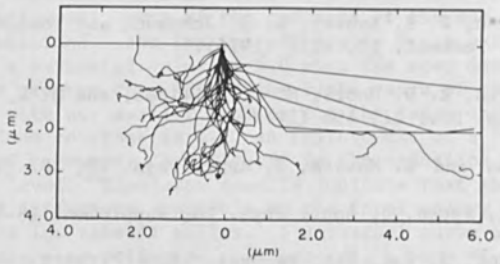

Fig.1 Simulated electron trajectories for 30 electrons of 20 kV beam voltage near a tapered etched Si mark of 2 μm step depth.

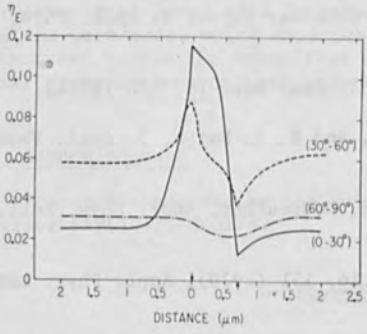

Fig.2 Simulated backscattered energy signals for a beam voltage of 10 kV and a step depth of 1μm. The takeoff angle θ is divided into three equal parts of 30° each.

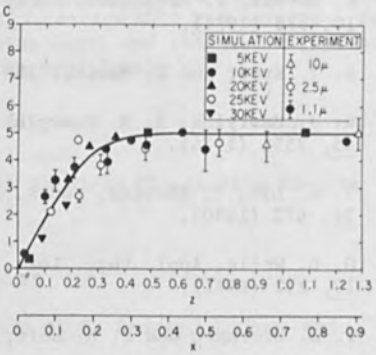

Fig.3 A universal curve of contrast C vs normalized step depth z for low takeoff angles. Different beam voltages are used in the simulation, and experimental results are obtained with various step depths, as shown in the legend. The second abscissa x = .71z can be regarded as the horizontal mark transition normalized with respect to R_B.

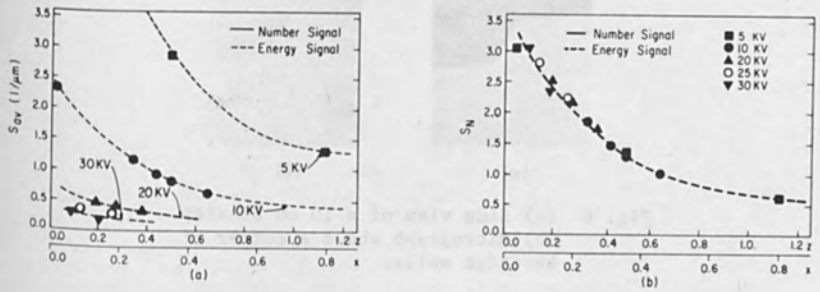

Fig. 4 (a) Average signal slope S_{av} of the total energy signal as a function of x (and z). (b) Universal curve for the normalized average slope S_N.

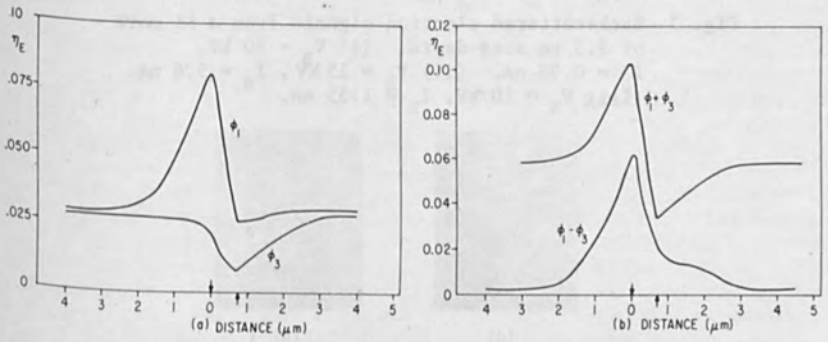

Fig. 5 Simulated energy signals for 20 kV beam incidencing at 1 μm Si step. (a) Signals collected by detectors in $-\pi/4 \leq \phi_1 \leq \pi/4$ and $3\pi/4 \leq \phi_3 \leq 5\pi/4$, respectively.

(b) Sum and difference signals of ϕ_1 and ϕ_3 in (a).

(a) (b)

Fig. 6 (a) Side view of a 10 μm Si step. (b) Micrograph shows a corner of two edge walls.

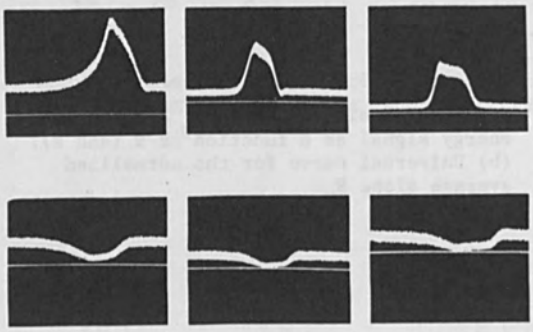

(I) (II) (III)

Fig. 7 Backscattered electron signals from a Si mark of 2.5 μm step depth. (i) V_B = 30 kV, I_B = 0.98 nA. (ii) V_B = 15 kV, I_B = 5.6 nA. (iii) V_B = 10 kV, I_B = 1.55 nA.

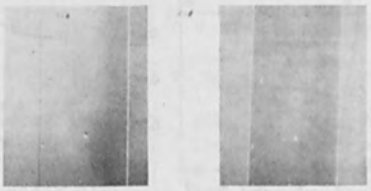

(a) (b)

Fig. 8 Images of steps. (a) Backscattered-electron image. (b) Secondary-electron image.

Section 3.

Proximity Effects and Related Topics.

AN ELECTRON BEAM PROXIMITY PRINTER FOR HIGH SPEED PATTERN REPLICATION

H. Bohlen, J. Greschner, J. Keyser,
W. Kulcke, P. Nehmiz
IBM Deutschland
German Manufacturing Technology Center
D 7032 Sindelfingen, Germany

ABSTRACT

The basic design features of an Electron Beam Proximity Printer are described. A prototype machine has been built which is being used to investigate and verify fundamental properties of this lithographic method for high speed replication of repetitive patterns. Submicron structures in the range of 0.5 µm have been printed. Printing experiments are reported in which pattern imaging has been made at 48 µA beam currents. This result corresponds to an exposure speed of 4 cm^2/s in a 10 $\mu C/cm^2$ resist.

INTRODUCTION

Shadow imaging of a mask is the simplest method to reproduce a pattern. Up to now optical proximity printers are frequently used in the semiconductor industry to print the integrated circuit patterns on wafers. However, with shrinking linewidths new methods must be developed since at the long wavelengths of visible light optical proximity printing is diffraction limited to lines wider than about 1.5 µm.
In several laboratories investigations have been started to extend this simple imaging technique by using radiation of shorter wavelength. Deep UV, soft X-rays or particle beams with electrons or ions are typical examples. A review of the different approaches has been given in (1).
In this paper an Electron Beam Proximity Printer is described. It was designed and built to investigate and verify fundamental properties of this lithographic method for high speed replication of patterns with micron and submicron dimensions. The electron beam was chosen as radiation since it exhibits several properties favourable to this method. Also its control is well understood from existing scanning electron beam pattern generators.
Progress in the fabrication technique of transmission

masks (2) and first results on printing through these masks (3)(4) were encouraging enough to build a prototype machine.
This is being used to demonstrate the capabilities of Electron Beam Proximity Printing with respect to writing speed, positioning accuracy, and overlay.

SYSTEM DESIGN ASPECTS

In the system a collimated electron beam shadow projects the mask pattern to the underlying wafer. For letting the electrons pass through the transparent parts of the mask these must be physical holes. Associated with such hole masks is the mask stencil problem, where ring shaped structures can not support their center. A solution of this problem is the use of a set of two complementary (half) masks (3). These two masks are arranged side by side on one mask substrate. This avoids a mask exchange during the printing cycle. The distance between the two masks is equal to the distance of the chips on a wafer. In this manner the complementary masks are simultaneously exposed to adjacent chips without that additional positioning steps are required.

- Illumination Concept
  For uniform illumination of the two adjacent masks a concept was chosen which differs considerably from that conventionally used in electron beam transmission lithography (5)(6). At conventional illumination an expanded beam irradiates the whole mask area at once. Assuming a gaussian current distribution in the beam the diameter of the beam has to be chosen such that towards the edge of field the beam current density does not decrease to, say, less than 95% of the center value. Best use of the available beam current is made when the shape of the mask is a square. The used portion of the beam, however, decreases when the mask area differs from a square shape as in our case of two complementary masks (Fig. 1a). Even less of the beam is utilized when the chip sizes vary and some mask sizes would not fit the designed beam diameter.
  Best utilization of the beam current and optimum chip size flexibility is achieved by scanning the mask area with a small diameter beam. The beam is collimated by a lens and shaped by a hexagonal aperture (Fig. 1b). A homogeneous illumination of the complementary masks is achieved when the beam is scanned as shown in Fig. 2. It is also indicated in this figure why a hexagonal shape of the beam avoids double and/or unexposed areas when the scan direction differs from its nominal value. Scan

errors result in only slight variations of the desired exposure dose.
Is q the dose per unit area to expose the resist then each scan deposits the dose Q_s.

$$Q_s = (r+h)(c+d)q$$

using the dimensions shown in Fig. 2 and where r is the radius of the circle containing the regular hexagon. The number n of the scans for an illumination of the mask area c x c is given by the following relation

$$\frac{r}{2}(3n-1) \geq c > \frac{r}{2}(3n-4)$$

The total dose Q_t to expose the mask pattern is

$$Q_t = \frac{3}{2}nr(c+\sqrt{3}r)q$$

In the case of a mask area of 5 x 5 mm^2 this dose is only 23% higher at a beam radius r = 0.5 mm than required to expose the scan area by an infinitely small beam.
In practice the beam current available in this concept depends on the gun characteristics, the distance between crossover and lens and the dimensions of the shaping aperture. In the arrangement we have chosen the beam current density drops towards the corners of the hexagon by about 7%. In cases where this decrease is not tolerable, however, a homogeneous illumination can be reestablished using a modified hexagon aperture where the central portion is narrowed by concave boundaries. In the range between 10 and 25 kV a maximum beam current of about 50 µA is available in our column nearly independent of the accelerating voltage. The crossover diameter is smaller than 100 µm at these gun settings so that penumbral shadowing effects are less than 0.1 µm. The small beam concept is also superior for chip registration (which will be described in a later paper) where a high beam current density is desired. Furthermore, as will be described next, this scanning illumination concept provides a means for positional correction of the wafer.

- Image Positioning
A decreasing linewidth in lithography naturally necessitates an increased accuracy for the pattern positioning. In our prototype machine the table position is measured by means of a laser interferometer with a resolution of $\lambda/8$ = 0.08 µm. Five axes of the interferometer are used to monitor the x and y position of the table and its yaw error and the x and y drifts of the mask. When the table is within 1.6 µm of its nominal position the exposure

cycle can be initiated. The shadow image can then be placed into its exact position by inclining the beam with a pivot point in the mask plane (Fig. 3a).
Beam tilting is also used to compensate for rotational positioning errors. This correction procedure is illustrated in Fig. 3b. Since only a small area is shadow imaged at a time the image shift can be changed while the beam scans across the mask. Correction signals

$$\Delta x(t) = \alpha \cdot y(t)$$
$$\Delta y(t) = -\alpha \cdot x(t)$$

are fed to the beam inclination device and provide an image rotation by an angle α. x(t) and y(t) are the positions of the beam during scanning.
The rotational compensation is restricted to small angles ($\alpha \leq 20$ arcsec) since otherwise the pattern would be blurred due to the finite beam diameter.
The rotational correction will be used to compensate table yaw errors and rotational errors occuring when the wafer is not perfectly aligned with respect to the mask orientation.
It is assumed that both types of errors can be maintained within the small correction capability.

EB PROXIMITY PRINTING PROTOTYPE MACHINE

A schematic arrangement of the prototype machine is given in Fig. 4. The upper part of the column - the gun, the gun alignment section, and the lens - are standard parts taken from IBM's scanning exposure system EL1. The beam shaping aperture is inside the lens. For blanking the beam the blanking plates deflect the beam into a Faraday cup located closely to the mask. The blanking section also contains a movable aperture which is used to reduce the beam diameter and beam current for adjustment purposes and special experiments. The lower column section contains the two double deflection yokes: The upper one shifts the beam in the raster scan mode across the mask without changing its inclination. The lower yokes incline the beam for positional error compensation.
The working chamber contains a rigid structure which carries the mask, the x-y table and the associated laser interferometer.
The vacuum system consists of three ion getter pumps - two small pumps to evacuate the gun and one for the working chamber. Roughing of the chamber is achieved by means of a turbomolecular pump which is switched off during the exposure.
Column and working chamber are mounted on an air-cushioned mass plate to diminish vibrations from the floor.

The basic parts of electronic control system are: Gun power supply for the tungsten hair pin gun, gun and brightness servo with similar functions as described in (7). The laser interferometer and its electronic circuits determine the position of the table and drifts of the mask. From these measurements error signals are derived which are fed in a closed loop system to the fine correction unit for beam inclination. The raster scan unit scans the beam across the mask. An IBM S/1 computer controls the whole system. The prototype machine is shown in Fig. 5.

EXPERIMENTAL RESULTS

The system described above is being used to investigate the fundamental properties of this exposure method and the associated problems for high speed pattern replication. In a first phase experiments are directed to verify the high exposure speed. Investigations related o pattern positioning accuracy and overlay will be addressed in a later phase.

- High Resolution
  With the availability of transmission masks containing submicron structures, the high resolution capability could be demonstrated. Fig. 6 shows 0.3 µm wide and 50 µm long bars shadow imaged over a mask-wafer distance of 0.5 mm. The image is obtained in 0.9 µm thick PMMA at an accelerating voltage of 10 kV.
  These submicron structures have been replicated although proximity effects must be taken into account in this submicron range.
  Experiments in this tool indicate, however, that proximity effects can be considerably reduced when a low beam accelerating voltages of about 10 kV is chosen. These results are in agreement with results of D. Kyser and C. Ting (8). Fig. 7 shows the imaging quality at 1.0 µm lines. No difference between the mask detail and its shadow image can be seen. In this case the pattern on the mask was written in the IBM Vector Scan System VSO at the IBM Thomas J. Watson Research Center in Yorktown Heights.
  From these preliminary results it is believed that structures down to 0.9 µm can be replicated without a need for proximity correction.

- Exposure Speed
  In electron beam proximity printing the time required to replicate a chip pattern is independent of the pattern density and the smallest structures in the pattern. The main factor determining the exposure time is the maximum

tolerable heating of the mask. This depends on the energy dissipated in the mask by the beam.
From earlier experiments (3) we knew that the mask foils are under mechanical stress. It was expected, therefore, that a considerable increase of the temperature would only release this stress but not bend the masks. Our experiments were directed to verify these earlier indirectly derived results.
For this reason one chip exposure was made in two steps using the illumination technique described above.
In the first exposure step, it was made sure that the mask remains cold. To that end a movable aperture (Fig. 4) with a hole of 100 µm diameter was put into the beam path. This reduced the beam current by a factor of approximately 100.
This exposure resulted in stripes of about 100 µm width in a raster of 750 µm. We used this exposure as a reference of the pattern image obtained from a cold mask.
In a second step the aperture was removed and the full beam used to expose the chip again.
These experiments have been made up to a beam current of 48 µA at 10 kV. The developed pattern showed no differences between both exposures.
This result corresponds to a writing speed of about 4 cm^2/s assuming a resist sensitivity of 10 $\mu C/cm^2$.

CONCLUSIONS

A prototype machine has been designed and built to investigate electron beam proximity printing for high throughput pattern replication. First results show that 4 cm^2/sec can be exposed independent of the linewidth of the pattern in 10 $\mu C/cm^2$ resist. This exposure speed is high enough to make this method very attractive even if two exposures are required to overcome the mask stencil problem. The beam acceleration voltage is 10 kV which seems to be favourable with regard to the proximity effect and avoidance of mask heating problems.
The resolution achieved in the mask fabrication technique and the replication method can be extended below 0.5 µm. Further investigations are in progress to evaluate the yet unproven requirements: registration techniques, pattern positioning accuracy, and overlay.

ACKNOWLEDGEMENTS

The authors wish to acknowledge the contributions of M. Kallmeyer and K. Elsaesser in designing and building the electronic control system, H. Dinkel for advice in programming, and K. Asch for assistance in mechanical debug.

REFERENCES

(1) A.N. Broers,
Physikalische Blätter,
Vol. 34, No. 12, p. 704 (1978)

(2) J. Greschner et al,
this issue

(3) H. Bohlen et al,
Proc. 8th Int. Conf. on Electron and Ion Beam Science and Technology
(Electrochem. Soc., Princeton N.J., 1978) p. 406

(4) H. Bohlen et al,
to be published in J. Vac. Sci. Technol.
Nov./Dec. issue, 1979

(5) M.B. Heritage,
J. Vac. Sci. Technol.,
Vol. 12, No. 6, p. 1135 (1975)

(6) B. Lischke et al,
Optik (Stuttgart),
Vol. 54, No. 4, p. 325 (1979)

(7) S. Doran et al,
J. Vac. Sci. Technol.,
Vol. 12, No. 6, p. 1174 (1975)

(8) D.F. Kyser, and C.H. Ting,
to be published in J. Vac. Sci. Technol.
Nov./Dec. issue, 1979

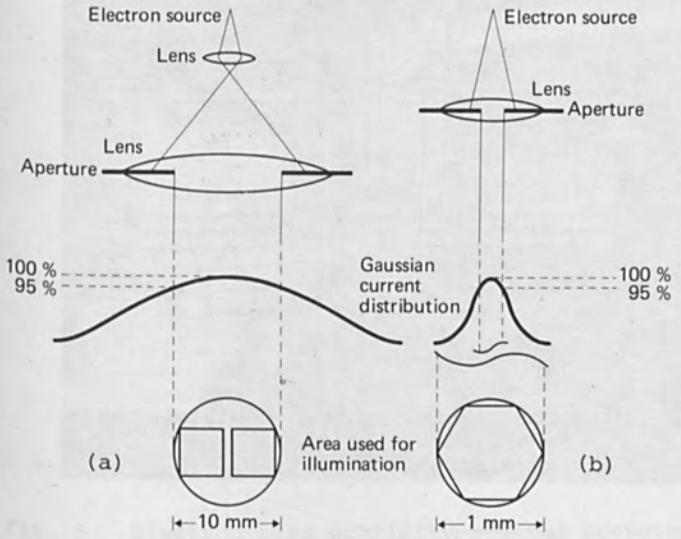

Fig. 1 Mask illumination:
(a) expanded beam
(b) hexagonal shaped small beam

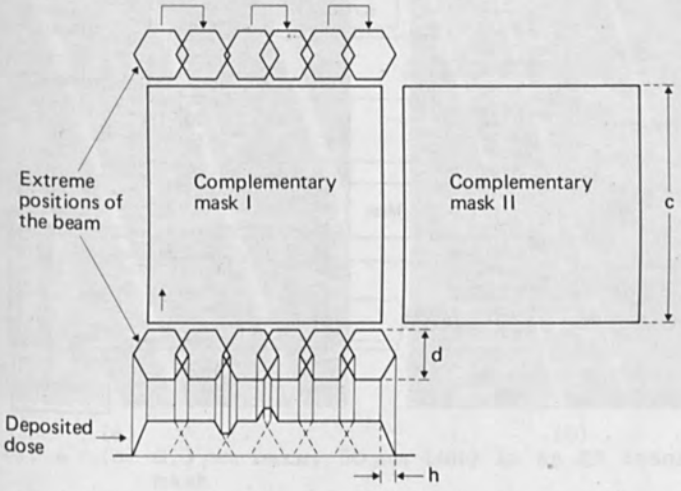

Fig. 2 Raster scanning using a hexagonal shaped beam

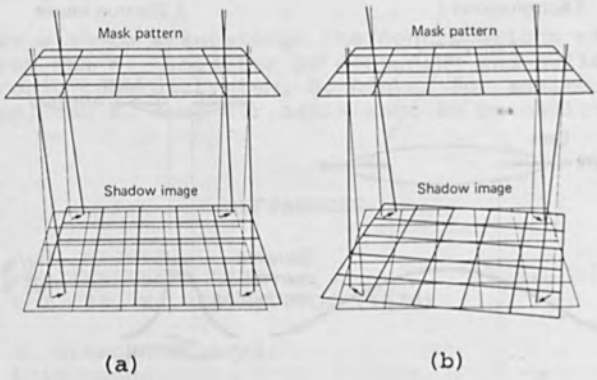

Fig. 3 Fine positioning by beam inclination:
(a) lateral image shift
(b) image rotation

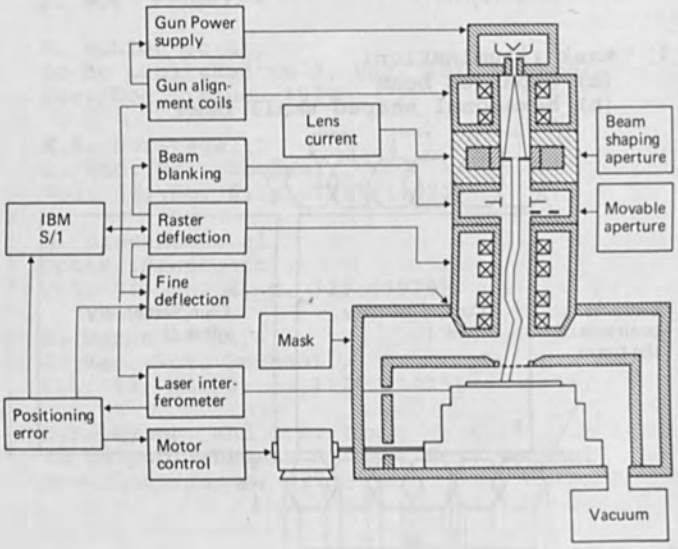

Fig. 4 Block diagram of the EB proximity printer prototype

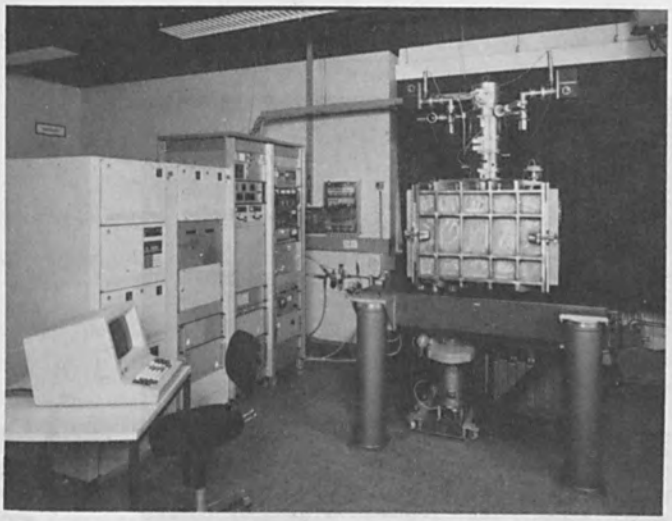

Fig. 5 Electron beam proximity printer prototype

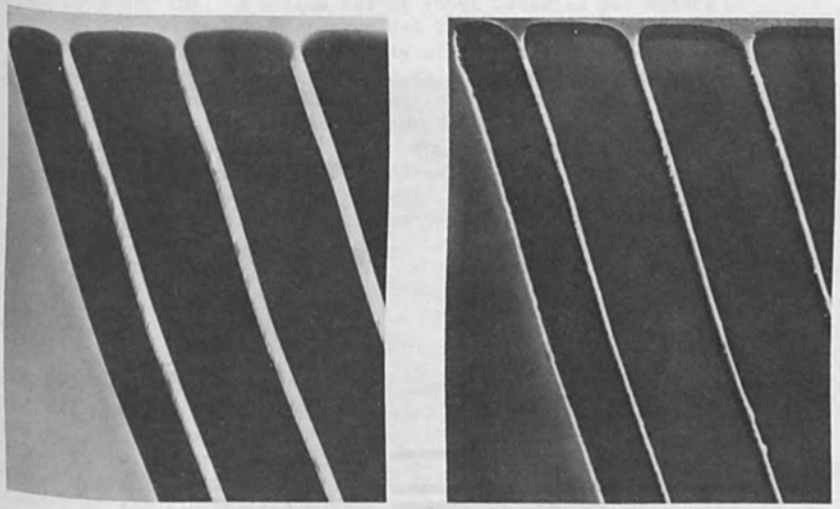

(a) (b)

Fig. 6 (a) 0.3 μm bars, 50 μm long in an EB transmission mask
(b) Shadow image of the detail in 0.9 μm thick PMMA replicated at 10 kV accelerating voltage

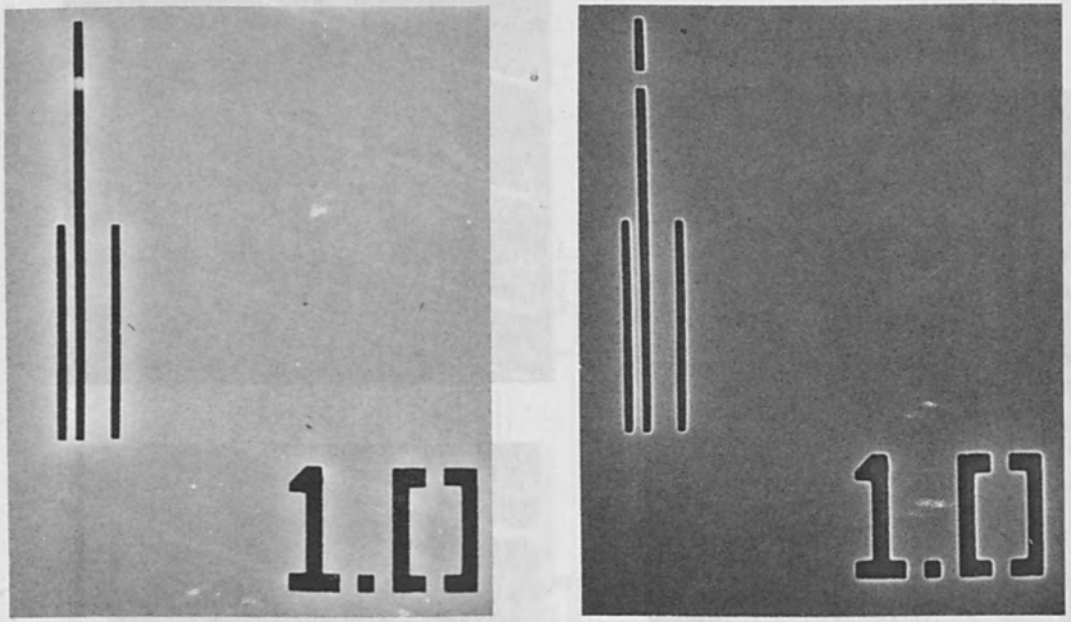

(a) (b)

Fig. 7 (a) 1.0 μm lines in a transmission mask and (b) its shadow image in 0.9 μm PMMA. Accelerating voltage 10 kV, dose 40 $\mu C/cm^2$

PROXIMITY FUNCTION APPROXIMATIONS FOR ELECTRON BEAM LITHOGRAPHY FROM RESIST PROFILE SIMULATION

D. F. Kyser, D. E. Schreiber and C. H. Ting
IBM Research Laboratory
San Jose, California 95193

and

R. Pyle
IBM Data Systems Division
Hopewell Junction, New York 12533

ABSTRACT: The computer program LMS (Lithography Modeling System) for simulation of developed resist profiles has been utilized to predict the electron dose compensation factors (DCF) necessary to correct a simple line pattern for "proximity effects" in electron beam lithography. The proximity correction algorithm SPECTRE (Self-Consistent Proximity Effect Correction Technique for Resist Exposure) was then iterated to provide the same DCF set as that obtained with LMS. A unique set of input Gaussian parameters for SPECTRE was found which provided the best agreement for the same pattern and with a variety of linewidths. The parameters (β_f-η_E-β_b) describe the relative intensity and widths of two coaxial Gaussian distributions as an approximation to the "proximity function" or radial distribution of energy absorbed by the resist film. The parameter set found in this manner includes the significant developer effects on the latent image, and is in good agreement with the limited experimental data available. The dependence of the Gaussian parameters on beam voltage and film thickness is also presented.

I. INTRODUCTION

Electron beam lithography is plagued by "proximity effects" due to electron scattering within both the resist film and substrate material. The spatial contours or profiles developed in the resist film are determined by two separate processes: (1) electron scattering and subsequent energy deposition within the film and (2) chemical development of the electron-irradiated volume with a solvent. Hence the spatial distribution of absorbed energy within the resist film depends on the feature size (intraproximity) and feature spacing (interproximity). Features which differ in absorbed energy will not develop to designed size at the same time.

To correct for such proximity effects, a variety of computer programs have been utilized to process device patterns. One of these techniques is the self-consistent method (SPECTRE) whereby the average electron exposure within each feature is forced to be identical [1]. This technique depends upon the use of an analytic description for the spatial distribution (or proximity function) f(r) of energy absorbed from a point source elecron beam. One approximation currently used for the "proximity function" involves two coaxial Gaussian distributions with standard deviations, β_f and β_b, and with relative areas η_E [2]. The numerical values for these three parameters can be found either from theoretical calculations of electron scattering [3] or by a systematic matrix of measurements on proximity-corrected and developed patterns [4]. However, the parameters found theoretically from energy deposition alone do not account for developer effects in proximity correction, and those found experimentally by different investigators do not always agree with each other. Hence there is a need to deduce the parameters theoretically with a method which includes developer effects in order to compare with any results derived experimentally.

Proximity effects in electron beam lithography have been explored via computer simulation of the developed resist profiles [5,6,7]. Profile simulation is a powerful technique to rapidly investigate the consequences of changes in experimental variables such as electron beam voltage, electron dose, resist film thickness, and development time. In addition, the dose modulation or feature size (design) modulation necessary to correct for proximity effects can be deduced via profile simulation.

This paper presents a method for deducing the three paramaters β_f, η_E, and β_b in the coaxial approximation for f(r). The method begins with the calculation of dose compensation factors (DCF) for a variety of feature sizes with the aid of a profile simulation program, LMS (Lithography Modeling System). Then the program SPECTRE (Self-Consistent Proximity Effect Correction Technique for Resist Exposure) is iterated with various combinations of β_f, η_E, and β_b until the set of DCF obtained are closest to the set obtained via profile simulation. It will be shown that the Gaussian parameters depend on variables such as beam voltage, film thickness, and substrate material.

II. DOSE COMPENSATION FACTORS FROM PROFILE SIMULATION

A comprehensive, highly interactive computer program "LMS" was utilized for simulation of the developed resist profiles [8]. The simulation begins with the three-dimensional distribution of energy deposition in resist films for an ideal line source exposure as obtained from Monte Carlo calculations of electron trajectories [9]. This distribution is then convolved with an envelope function which describes the incident electron beam shape in order to arrive at the latent image within the resist film before development. The time-evolution of the resist profiles are obtained with a

transformation of the latent image (i.e., the spatial distribution of energy density, eV/cm^3) to a solubility rate image (i.e., the spatial distribution of etch rate, Å/sec). This transformation is accomplished by characterizing the solubility rate curve of the particular resist-solvent system with an analytic approximation [5,6]. Then the profiles are calculated by connecting together those regions of resist which have the same total time for dissolution [10].

The intraproximity effect causes smaller features to absorb less energy, and hence develop slower, compared to larger features in the case of a positive resist. The reference point for electron dose and development time is chosen to be that for a very large feature or pad such that the intraproximity effect is saturated. For 20 keV exposure and 1 μm thick resist films on a Si substrate, the intraproximity effect saturates above about 10 μm in feature size. For the PMMA resist films used in the present study, the reference dose Q_o associated with a large pad is 100 $\mu C/cm^2$. The development time is then set by the resist cleanout time for a large feature with the reference dose exposure. The cleanout time is defined as the etch time required to just reach the film-substrate interface. While the edges of the pad feature will not yet have developed to size, the cleanout time is consistent with the concept of an infinite area exposure utilized in SPECTRE [1,2] for a reference point. The development time required to attain the designed pad dimension in LMS will be longer than the cleanout time, of course. However, the use of this definition for cleanout time removes any dependence on the incident beamshape parameters for a reference time.

An example of the output from LMS for a 20 μm wide line is shown in Fig. 1. The simulation corresponds to a 1 μm PMMA film on a Si substrate exposed at Q_o=100 $\mu C/cm^2$. The solubility rate of this "linear" resist is described by [8]

$$R = (R_o + BE^n)\ \text{Å/sec} \qquad (1)$$

where $R_o = 1.0$
$B = 8.0 \times 10^{-37} (cm^3/keV)^2$
E = absorbed energy density (keV/cm^3)
$n = 2.0$.

Note that $E \propto Q$, and that R is spatially varying because E is spatially varying within the resist film. The cleanout time for this particular case is 0.63 minutes.

The dose compensation factors (DCF) for any other feature sizes are simply calculated by designing, with LMS, particular features and incrementing the dose Q until the development time matches that of the 20 μm feature. An example of the results obtained with LMS is shown in Fig. 2 and Fig. 3. In this case the developed dimension at the resist-substrate interface is made equal to the linewidth exposed. A

variety of isolated linewidths are utilized rather than a single value in order to approximate the conditions found in a real device pattern.

A summary of the DCF found in this manner for PMMA on Si substrates is given in Tables 1 and 2. There are several important points to be made about this data. Firstly, the DCF are not dependent upon the base dose Q_o used as a reference point for the pad development time, as long as Q_o is relatively large. The actual development time does change with Q_o, but the DCF do not. Secondly the voltage-dependence of the DCF is complex, and tends to saturate (for low values of E_o) at a smaller linewidth than it does for high values of E_o. In addition, the DCF variation with E_o at small linewidth (e.g., 0.5 μm) in Table 1 goes through a maximum and then decreases. These conclusions are consistent with those found earlier utilizing only the latent image [7]. However, the present work also includes the consequences of the developer action on the latent image.

The last entry in Table 2 shows the DCF for a 2-layer resist system such that the top layer (0.5 μm PMMA) is just developed to size at the interface between the 2 layers. The bottom layer is 1.5 μm thick PMMA. Note that in this case the DCF for the top layer only is approximately the same as that for a single 0.5 μm layer on Si. If the top layer pattern could be transferred through the 1.5 μm bottom layer, then the proximity effects are greatly reduced compared to a single 2.0 μm layer. A reduction of proximity effects for a separated 2-layer resist system has been reported [16].

The simulation program LMS was also utilized to calculate the DCF for a 5-line array with a variety of linewidths and gapwidths. An example of the results obtained for a line array with 1 μm line and gaps is shown in Fig. 4. With a base dose of Q_o=100 μC/cm^2 for each line, the pattern is undeveloped for t=0.63 min. With prolonged development, the central lines can achieve proper size at the interface, but then the outer lines are undersize (Fig. 4b). If the incident dose is different for each line, and also larger than the base dose Q_o, then each of the lines in the array will reach size simultaneously at t=0.63 min (Fig. 5a and 5b). The dose Q for each line, normalized to Q_o, is then the dose compensation factor. A summary of the DCF found in this manner for PMMA on Si substrates at 20 kV is given in Table 3. The comparison of the LMS results with results obtained from SPECTRE will be discussed later.

III. DOSE COMPENSATION FACTORS FROM PROXIMITY CORRECTION ALGORITHM

The proximity correction program SPECTRE [1,2] was utilized to deduce the DCF for the same patterns and feature sizes discussed in Section II. This correction program is based upon the "proximity function" f(r) which is approximated as two coaxial Gaussian distributions (in radius) with standard deviations β_f, β_b and with relative areas η_E:

$$f(r) = k\left[\exp(-r^2/\beta_f^2) + \eta_E \cdot (\beta_f/\beta_b)^2 \exp(-r^2/\beta_b)^2\right] . \qquad (2)$$

Conceptually, SPECTRE solves a set of simultaneous equations which makes the average incident electron exposure within each feature equal, taking account of the intraproximity and interproximity effects via integration of f(r) over the feature field of interest. For a particular set of input parameters β_f, η_E, and β_b, there is a corresponding output set of DCF.

Since SPECTRE has no explicit capability to incorporate the effects of (1) developer effects in the transformation of the latent image to a solubility image or (2) three-dimensional electron scattering effects, i.e., in the z-direction normal to the resist film plane, we can utilize LMS to provide this information via a matching of the DCF from the two techniques. If a satisfactory match is achieved, then new lithography configurations can be simulated a priori any experimental work is planned. Hence SPECTRE and LMS can be utilized in a complementary fashion. In practice of course, only SPECTRE or similar programs are utilized to proximity correct real device patterns.

Since the three Gaussian parameters are completely independent, it is necessary to iterate them and tabulate the DCF output for each particular combination. An example of the output DCF from SPECTRE is shown in Table 4. By comparing the data in Table 4 with that in Table 1, it can be seen that the best match of (β_f-η_E-β_b) for 20 kV is with the Gaussian parameter set (0.075-0.90-2.75). Another set (0.050-1.00-2.50) is only slightly worse, and indicates that there is a small tradeoff in the parameters β_f and η, i.e., a small increase in β_f can be compensated for by a small decrease in η. The parameter β_b is a very weak parameter, in comparison to the other parameters.

For 15 kV, the best match is found with the set (0.075-0.80-2.50) and the second best match is for (0.075-0.90-2.00) with 1 μm resist films.

For 20 kV and 0.5 μm thick resist films, the best match is found with the set (0.050-0.70-2.50) and the second best match is for (0.100-0.60-2.50).

As described previously [3], the value for β_f is appropriate for a specific value of the incident beam shape, either an ideal δ-function line source or a Gaussian line source described by σ. For the results

reported here, a value of σ=0.10 μm was used in LMS for all the simulated profiles. However LMS utilizes a Gaussian distribution in the form $\exp(-r^2/2\sigma^2)$, whereas SPECTRE utilizes the form $\exp(-r^2/\beta_f^2)$. In addition, there is no restriction that $\beta_f \geq \sigma$ due to the poor approximation of the forward-scattered component by a Gaussian. The main criteria is that the two sets of DCF agree, and hence provide a useful Gaussian parameter set. Table 5 shows the best sets found for various conditions. For application to incident beams with $\sigma \neq 0.10$ μm, the values of β_f in Table 5 should be combined in quadrative with β^* to provide an effective value for β_f and β_b, as suggested in reference [3].

In addition to a comparison of the DCF for isolated lines, the DCF for line arrays can also be compared and evaluated. Table 3 also shows the DCF for line arrays calculated by SPECTRE for the same Gaussian parameter set (0.075-0.90-2.75) that was deduced from analysis of the isolated lines. While the quantitative agreement between the two DCF sets (LMS, SPECTRE) is not the same for all combinations of linewidths and gapwidths, a statistical analysis and optimization of the RMS difference for the line arrays showed the best Gaussian parameter set was the same as that when only isolated lines were considered. This is encouraging because a proximity correction algorithm must be able to correct accurately over a wide range of feature sizes with only one set of input parameters. With latitude in development time, it may be possible to correct a small range of feature sizes with a relatively simple algorithm, but the device patterns encountered in practice usually contain a large range of feature sizes which must be developed simultaneously and accurately.

IV. DISCUSSION

As shown in Section III, there is a fairly unique set of input parameters (β_f-η_E-β_b) to SPECTRE which provides the best agreement with the DCF set from LMS. The uniqueness of the set is expected, since it would be fortuitous to find a variety of input parameter sets which produced the same output set of DCF over a wide range of feature sizes. The sensitivity of the output DCF set from SPECTRE to the input Gaussian parameter set has also been presented elsewhere [11].

As reported in reference [3], the values for (β_f-η_E-β_b) were deduced by a least-squares approximation of two coaxial Gaussian distributions to the Monte Carlo-generated distribution of absorbed energy density (eV/cm^3). However, that work required an arbitrary separation of the Monte Carlo distribution into backward and forward-scattered components, as well as forcing the forward-scattered component to be approximated by a Gaussian even though the curve-fit was not as good as that for the backward-scattered component. In that work, the value for η_E did not vary much from 0.50 for a wide variety of conditions. In the present work, it is found that η_E does change systematically with parameters such as beam voltage, film thickness, and even substrate material. The former work [3] utilized only the latent image or "proximity function" for evaluation of the Gaussian parameters while the present work includes the effects of the developer as well. For example, values of η_E=0.9 are found in the present work for 20 kV and 1 μm PMMA films on Si substrates. Hence it seems that there is a significant "developer effect" in proximity corrections, which further enhances the value of a simulation tool such as LMS for resist profile calculations. In addition, a summary and evaluation [12] of the available experimental data for (β_f-η_E-β_b) shows that the results presented in Section III, obtained by matching the SPECTRE and LMS sets of DCF, are in good agreement with an "operationally useful" set (at least for 20 kV exposure on Si substrates). With the present approach, useful sets of Gaussian parameters (or parameters for a different analytic proximity function [13]) can easily be generated theoretically for those cases where no experimental data is yet available.

The independent parameter η_E, which describes the ratio of the energy dissipation (in the z-direction) due to the backward-scattered electrons to that due to the forward-scattered electrons, seems to vary systematically with beam voltage and film thickness. For example, at 20 kV and 1 μm thick resist, $\eta_E \cong 0.90$, whereas at 20 kV and 0.5 μm resist, $\eta_E \cong 0.70$. At 15 kV and 1 μm resist, $\eta_E \cong 0.80$ with Si substrates. Such a systematic variation of η_E is expected, based on the simple approach to estimate η_E from energy loss alone [9,3]. In this simple approach, $\eta_E \cong \eta_s/f$ where η_s is the backscattered electron yield from the bulk substrate material (with an infinitely thin resist film on top) and f is the normalized average energy E_a of a backscattered electron (E_a/E_o). Since $\eta_s \propto Z_s$ (atomic number) for low Z_s, then we would expect $\eta_E \propto Z_s$ also. For finite thickness resist films (with low Z_f) on higher

Z_s substrates, then the "effective" value of η_E is a mixture of electron backscattering from both the film and substrate. The Monte Carlo calculations also show that the electrons enter the substrate at oblique (i.e., non-normal) incidence angles, and hence the use of η_s values for normal beam incidence will underestimate the contribution of electrons backscattered from the substrate. For fixed film thickness and increasing beam voltage E_o, the backscattered electrons will become more representative of the substrate atomic number Z_s. Conversely with decreasing beam voltage, the backscattered electrons (and hence η_E) will become more representative of the film atomic number Z_f. The results given in Section III show that η_E increases for a low Z_f film (PMMA) on a higher Z_s substrate (Si). This may be a simple consequence of the non-normal electron incidence of the film-substrate interface which results in a higher effective value of η_s. The energy distribution of the backward-scattered electrons is also changing with beam voltage and film thickness, and the Monte Carlo simulation of electron scattering and subsequent profile simulation accounts for such effects automatically. The fractional amount of incident electron energy which gets absorbed by the resist has been presented elsewhere [9], and is typically about 10% for a 20 kV beam incident on a 0.5 μm PMMA/Si substrate target.

Recently, another evaluation of η_E with Monte Carlo calculations has been reported [14]. The results are identical to those reported earlier [3], even though the details of the Monte Carlo simulation are different. While the Monte Carlo results show little variation of η_E with beam voltage E_o, an analytic model for electron scattering does show a systematic voltage-dependence of η_E [15]. Once the developer effects are included, then the Monte Carlo results also show a voltage and thickness dependence for η_E.

V. SUMMARY

The resist profile simulation program LMS (Lithography Modeling System) was utilized to deduce the numerical values of the Gaussian parameters (β_f-η_E-β_b) in the proximity correction program SPECTRE. Dose compensation factors (DCF) for a variety of feature sizes were found with LMS, including the significant effects of the developing solvent on the latent image. A unique set of Gaussian parameters for SPECTRE were found which provides the same set of DCF as that from LMS. The Gaussian parameters found theoretically in this manner agree well with the limited experimental data available. Hence the use of a general simulation program for resist profiles has been demonstrated quantitively, and now allows the prediction of DCF for new resist materials and target configurations such as multilayer resists.

VI. ACKNOWLEDGMENTS

The authors thank R. Kobliska, L. Rosier, L. Bushnell, and J. Lounsbury for continuous support of this work. We also thank M. Parikh for technical discussions and advice.

TABLE 1

LMS Dose Compensation Factors for 1 μm Thickness PMMA on Si Substrates Versus Beam Voltage

	Linewidth (μm)			
E_o (kV)	0.5	1.0	2.0	5.0
10	1.64	1.34	1.24	1.24
15	1.80	1.55	1.36	1.30
20	1.85	1.65	1.45	1.35
30	1.80	1.70	1.55	1.40
40	1.75	1.70	1.60	1.45
50	1.70	1.70	1.65	1.50

TABLE 2

LMS Dose Compensation Factors for PMMA, 20 kV, on Si Substrates Versus Film Thickness

	Linewidth (μm)			
Thickness (μm)	0.5	1.0	2.0	5.0
0.5**	1.65	1.50	1.35	1.32
1.0*	1.85	1.65	1.45	1.35
2.0*	2.35	1.75	1.47	1.30
0.5/1.5*	1.60	1.50	1.40	1.30

** 800Å Cr/SiO_2 substrate

* Si substrate

TABLE 3

Dose Compensation Factors for 1 μm PMMA
on Si Substrates, 5-Line Array

Linewidth - Gapwidth (μm)	LMS (20 kV)					SPECTRE (0.075-0.90-2.75)*				
0.5 - 2.0	1.84	1.77	1.75	1.77	1.84	1.81	1.74	1.73	1.74	1.81
0.5 - 1.0	1.71	1.58	1.55	1.58	1.71	1.72	1.61**	1.57	1.61	1.72
0.5 - 0.5	1.61	1.47	1.40	1.47	1.61	1.63	1.51	1.47	1.51	1.63
1.0 - 2.0	1.63	1.55	1.55	1.55	1.63	1.59	1.51	1.51	1.51	1.59
1.0 - 1.0	1.51	1.37	1.37	1.37	1.51	1.51	1.37	1.35	1.37	1.51
1.0 - 0.5	1.44	1.27	1.23	1.27	1.44	1.44	1.27	1.22	1.27	1.44
2.0 - 2.0	1.41	1.37	1.37	1.37	1.41	1.38	1.32	1.32	1.32	1.38
2.0 - 1.0	1.36	1.25	1.25	1.25	1.36	1.32	1.20	1.20	1.20	1.32
2.0 - 0.5	1.32	1.15	1.15	1.15	1.32	1.28	1.12	1.12	1.12	1.28

*$(\beta_f - \eta_E - \beta_b)$

TABLE 4

Dose Compensation Factors - SPECTRE

β_f (μm)	η_E	β_b (μm)	Linewidth (μm) 0.5	1.0	2.0
0.050	0.70	2.50	1.66	1.51	1.33
0.050	0.80	2.50	1.74	1.56	1.37
0.050	0.90	2.50	1.81	1.62	1.40
0.050	1.00	2.50	1.89	1.67	1.43
0.075	0.70	2.50	1.71	1.53	1.34
0.075	0.80	2.50	1.79	1.58	1.37
0.075	0.90	2.50	1.86	1.64	1.40
0.075	1.00	2.50	1.94	1.69	1.43
0.100	0.70	2.50	1.76	1.54	1.35
0.100	0.80	2.50	1.84	1.60	1.38
0.100	0.90	2.50	1.92	1.66	1.41
0.100	1.00	2.50	1.99	1.71	1.44
0.075	0.90	2.25	1.85	1.61	1.38
0.075	0.90	2.50	1.86	1.64	1.40
0.075	0.90	2.75	1.88	1.66	1.43
0.075	0.90	3.00	1.88	1.67	1.45

TABLE 5

Gaussian Parameters for Proximity Function

E_o (kV)	β_f (μm)	η_E	β_b (μm)
10 (0.5 μm)**	0.050	0.50	2.50
10 (1.0 μm)*	0.075	0.75	1.50
15 (1.0 μm)**	0.075	0.80	2.50
20 (0.5 μm)*	0.050	0.70	2.50
20 (1.0 μm)*	0.075	0.90	2.75
30 (1.0 μm)	0.050	1.00	3.00

*Film thickness on Si substrate

**Film thickness on 800Å Cr/SiO_2 substrate

REFERENCES

1. M. Parikh, J. Vac. Sci. Tehnol. 15, 931 (1978).

2. M. Parikh, J. Appl. Phys. 50, 4371, 4378, 4383 (1979).

3. M. Parikh and D. F. Kyser, J. Appl Phys. 50, 1104 (1979).

4. W. Grobman and A. Speth, Proc. Eighth Int. Conf. Electron and Ion Beam Science and Technol. (Electrochem. Soc., 1978), p. 276.

5. D. F. Kyser and N. S. Viswanathan, J. Vac. Sci. Technol. 12, 1305 (1975).

6. A. R. Neureuther, D. F. Kyser, and C. H. Ting, IEEE Trans. Electron Devices ED-26, 686 (1979).

7. D. F. Kyser and C. H. Ting, J. Vac. Sci. Technol. 16, 1759 (1979).

8. D. F. Kyser and R. Pyle, IBM J. Res. Develop. (July 1980), to be published.

9. D. F. Kyser and K. Murata, Proc. Sixth Int. Conf. Electron and Ion Beam Science and Technol. (Electrochem. Soc., 1974), p. 205.

10. F. H. Dill, A. R. Neureuther, J. A. Tuttle, and E. J. Walker, IEEE Trans. Electron Devices ED-22, 456 (1975).

11. M. Parikh, J. Appl. Phys. 51, 700 (1980).

12. M. Parikh, IBM J. Res. Develop. (July 1980), to be published.

13. N. Aizaki, J. Vac. Sci. Technol. 16, 1726 (1979).

14. I. Adesida, Ph.D. Dissertation, Univ. of California, Berkeley (1979), to be published.

15. J. S. Greeneich, J. Vac. Sci. Technol. 16, 1749 (1979).

16. D. Stephani and E. Kratchsmer, Proc. Microcircuit Engineering 1979 (Aachen Univ., 1979), p. 228.

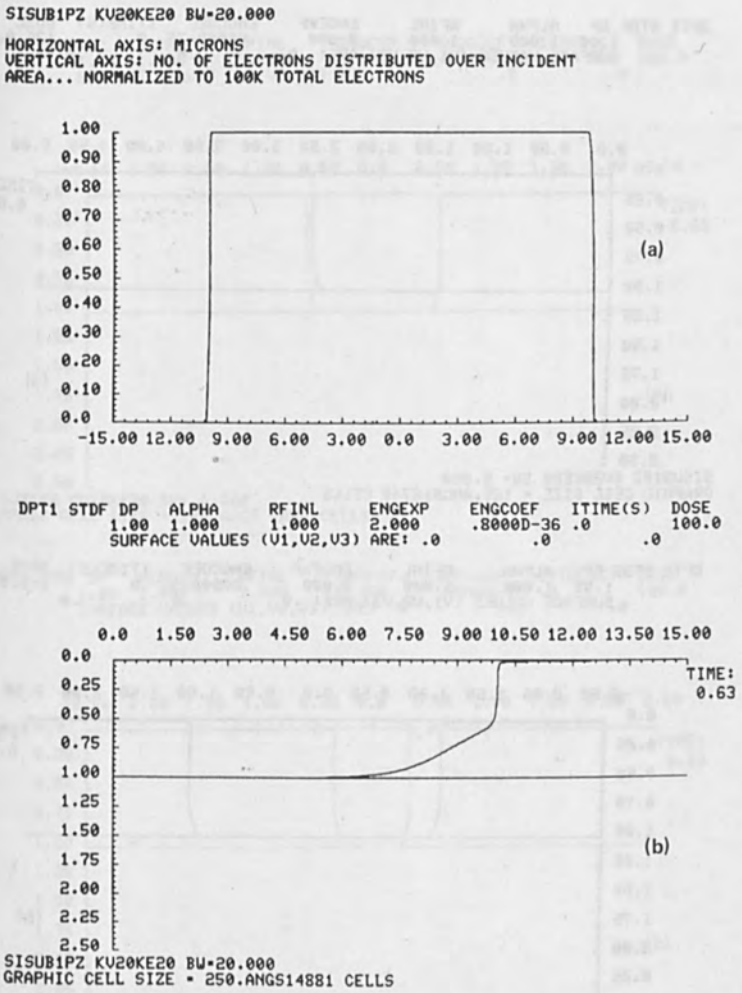

Figure 1. Simulation of a large feature: (a) incident electron exposure for a 20 μm wide line, and (b) developed profile in 1 μm thick resist. The cleanout time t=0.63 minutes for dose Q=100 $\mu C/cm^2$. Note that vertical scale is expanded by 3× in (b).

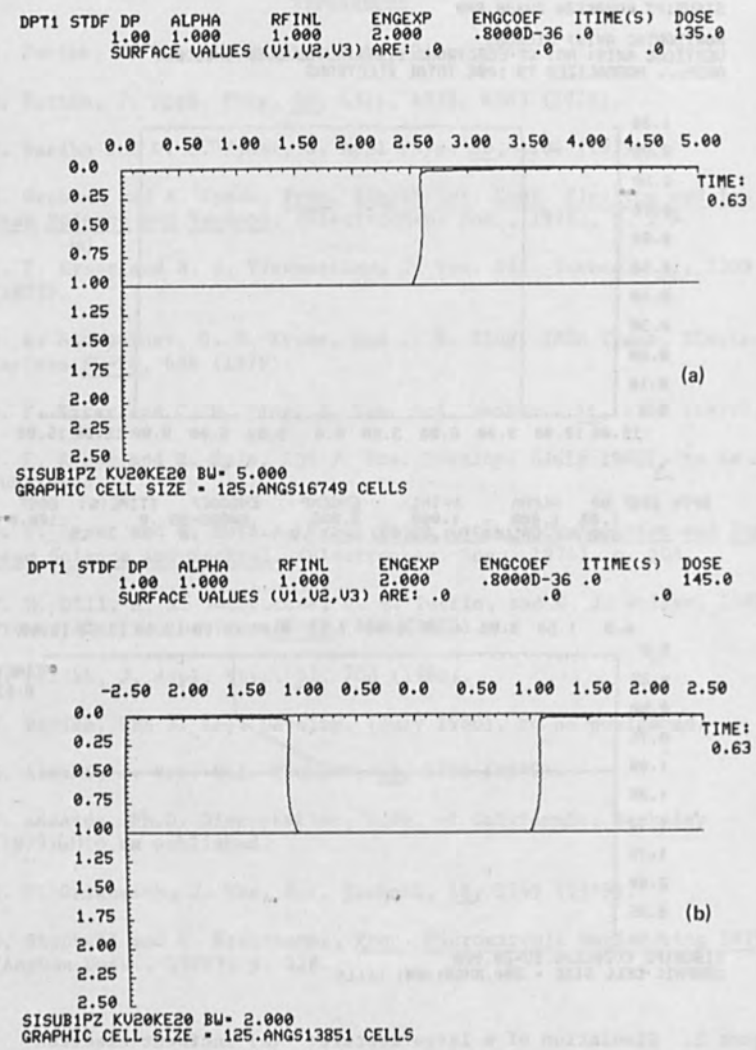

Figure 2. Simulation of developed profiles in 1 μm thick resist with electron dose Q ($\mu C/cm^2$) necessary to produce exposed linewidth at substrate interface for t=0.63 minutes development: (a) 5 μm linewidth and (b) 2 μm linewidth.

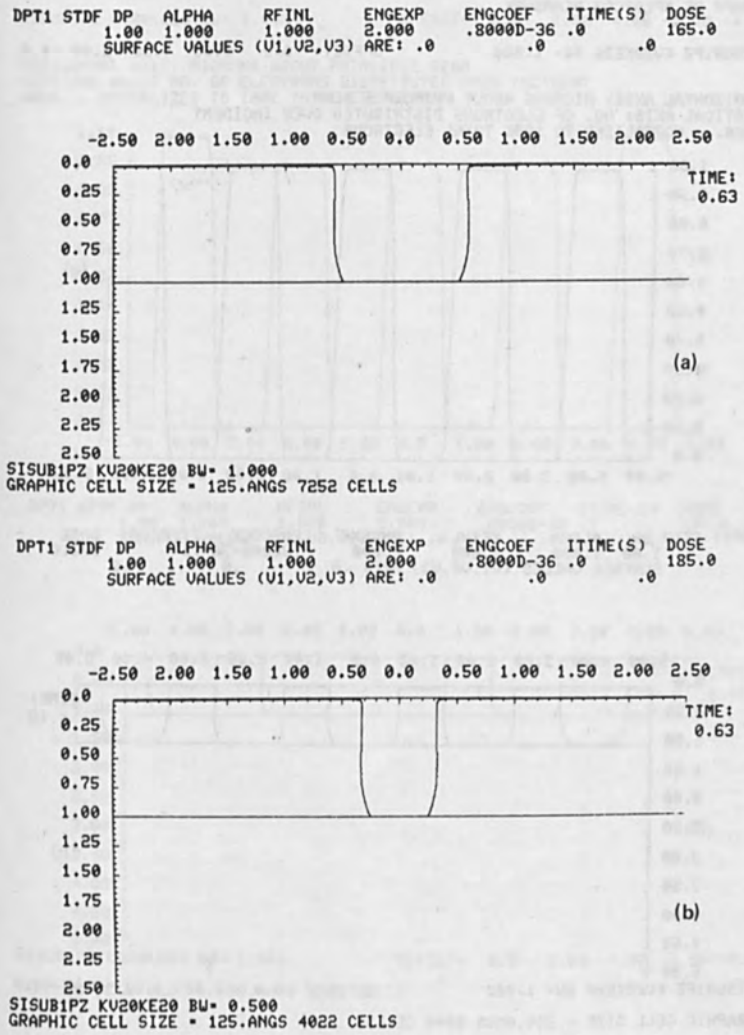

Figure 3. Simulation of developed profiles in 1 μm thick resist with electron dose Q ($\mu C/cm^2$) necessary to produce exposed linewidth at substrate interface for t=0.63 minutes development: (a) 1 μm linewidth and (b) 0.5 μm linewidth.

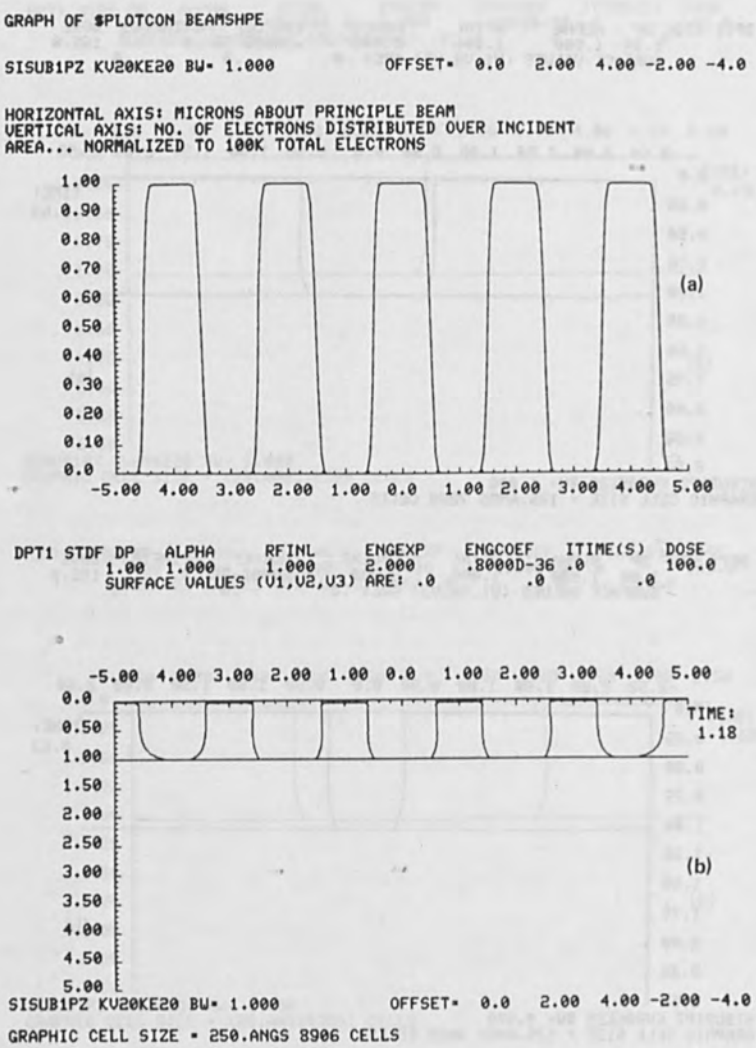

Figure 4. Simulation of a 5-line array with 1 μm lines and gaps in 1 μm thick resist: (a) incident electron exposure equal on each line, and (b) developed profiles at t=1.18 minutes with dose Q=100 μC/cm^2.

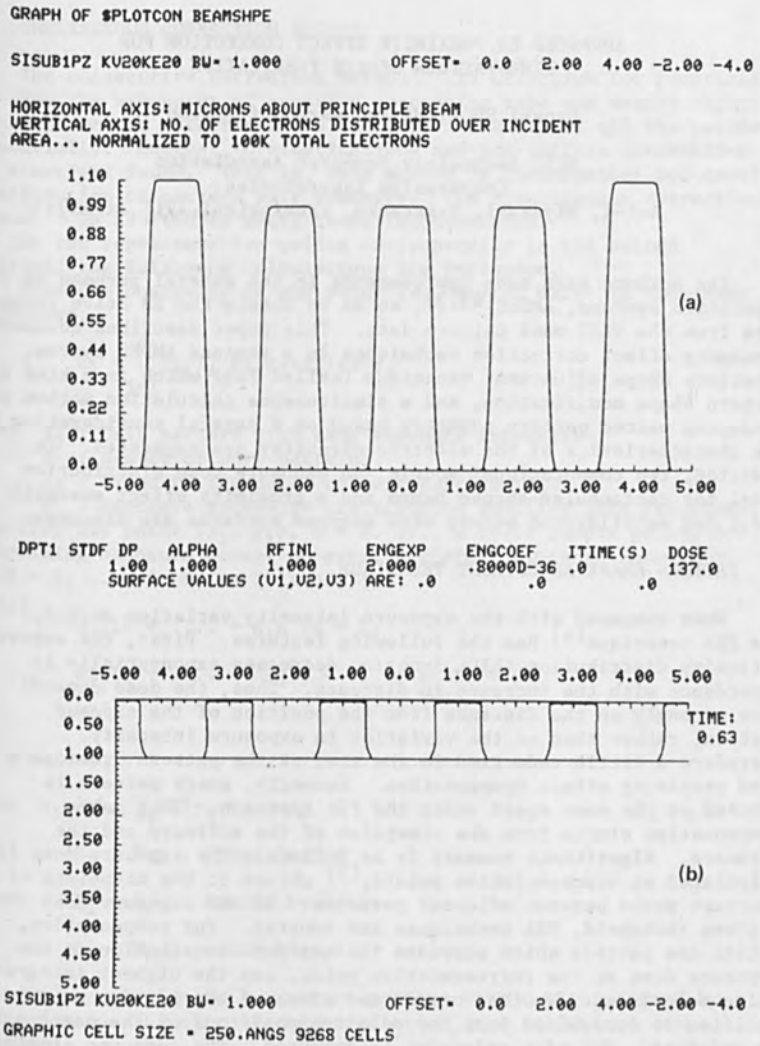

Figure 5. Simulation of a 5-line array with 1 μm lines and gaps in 1 μm thick resist: (a) incident electron exposure with relative values of 1.1-1.0-1.0-1.0-1.1 on each line, respectively, and (b) developed profiles at t=0.63 minutes with dose Q=137 μC/cm^2.

ADVANCED EB PROXIMITY EFFECT CORRECTION FOR FINE-PATTERN DEVICE FABRICATION

Naoshi SUGIYAMA and Kazunori SAITOH

VLSI Technology Research Association
Cooperative Laboratories
4-1-1, Miyazaki, Takatsuku, Kawasakishi, 213 Japan

The authors have made improvements in the general purpose EB data generation systems, AMDES[1][2], so as to obtain the EB drive input data from the VLSI mask pattern data. This paper describes advanced proximity effect correction techniques in a revised AMDES system. A pattern shape adjustment technique (called PSA) which is a kind of pattern shape modification, and a simultaneous calculation method of producing paired pattern symmetry based on a careful consideration of the characteristics of the electric circuitry are suggested. In addition, two computational models, an exposure dose distribution model for rectangular-shaped beams and a proximity effect analysis model for multilayered wafers with stepped surfaces are discusses.

1. PATTERN SHAPE ADJUSTMENT TECHNIQUE

When compared with the exposure intensity variation method,[3] the PSA technique[4] has the following features. First, the exposure intensity distribution (EID) function decreases exponentially in accordance with the increase in distance. Thus, the dose depends more strongly on the distance from the position of the exposed pattern, rather than on the variation in exposure intensity. Therefore a little reduction in the area of the pattern provides a good proximity effect compensation. Secondly, every pattern is exposed at the same speed under the PSA approach. This makes compensation simple from the viewpoint of the software and the hardware. Algorithmic summary is as follows. The exposure dose is calculated at representative points,[5] chosen to the midpoints of the shortest paths between adjacent patterns. If the exposure dose exceeds a given threshold, PSA techniques are adopted. For compensation, select the pattern which provides the maximum contribution to the exposure dose at the representative point, say the highest integration value calculated. Whether one or two sides of the pattern must be modified is determined from the relative positions of the pattern to be modified. The edge reduction is executed. The computer simulation results of PSA techniques for proximity effect correction are shown in Fig. 1 and Table 1. Figure 1 shows proximity effect correction result, where slash area is necessary to be reduced. Table 1 shows the total exposure dose amount at the representative points in corrected and uncorrected patterns. Threshold values in test patterns are given to a relative value of 32.0.

2. SIMULTANEOUS CORRECTION METHOD

The consecutive correction method[6] is effective for practical use from the viewpoint of computer processing time and memory capacity, since the method determines the exposure intensity of all the patterns sequentially. However, overestimations and non-uniform corrections are sometimes found. That is, this method is inconvenient for careful consideration of pattern pair symmetry. The simultaneous correction method[7] is adopted to avoid these inconvenience.
For the two representative points corresponding to the paired patterns, the following calculations are performed.

Exposure dosage E_i at any point (x_i, y_i) on wafer is expressed as follows,

$$E_i = \sum_{j=1}^{n} I_j \iint_{A_j} F(|r_i - f|)\,dxdy,$$

where A_j : Unit pattern with same exposure intensity.
n : Number of unit patterns.
I_j : Exposure intensity on unit patterns A_j.
F : Exposure intensity distribution function (EID function).

Supposing any point (x_i, y_i), $i = 1, \ldots, n$ to be sample points for determining exposure dosage on every patterns, exposure intensity I_i, $j = 1, \ldots, n$ is as follows,

$$a_{11}I_1 + \ldots + a_{1n}I_n = E_1$$

$$a_{i1}I_1 + \ldots + a_{ij}I_j + \ldots + a_{in}I_n = E_i$$

$$\vdots$$

$$a_{m1}I_1 + \ldots + a_{mn}I_n = E_m,$$

where $a_{ij} = \iint_{A_j} F(|r_i - r|)\,dxdy$

$E_i > E_{th}$: inner figure

$E_i = E_{th}$: figure boundary

$E_i \ll E_{th}$: outer figure

In order to coincide well exposure pattern with design pattern by strong demands for circuit characteristics, the followings are proceeded.

At sample points corresponding to symmetrical patterns,

$$\sum_j a_{i_1 j} I_j = E_{i_1}$$

$$\sum_j a_{i_2 j} I_j = E_{i_2} = E_{i_1}$$

is replaced by

$$\sum_j (a_{i1j} + a_{i2j})\ I_j = 2E_{i1}$$

$$\omega \sum (a_{i1j} - a_{i2j})\ I_j = 0 \quad (\omega >> 1)$$

and is solved by least-square method.

3. EXPOSURE DOSE CALCULATION MODEL AND MATHEMATICAL TECHNIQUES

3.1 EXPOSURE DOSE DISTRIBUTION MODEL FOR RECTANGULAR-SHAPED BEAMS

The exposure dose calculation method for Gaussian beams has already been presented. However, it is well-known that the exposure intensity is not uniform throughout a rectangular area due to electron-electron interaction, and that this is different from the Gaussian beam exposure model. Therefore the mathematical formulation of exposure intensity distribution with rectangular shape is necessary for proximity effect analysis.

The exposure intensity distribution of a rectangular-shaped beam can be approximated with the trapezoid shown in Fig. 2. Assuming the same exposure intensity distribution in both the X and Y directions, the total distribution in a rectangular-shaped area is obtained as shown in Fig. 3. In addition, the four corner area (right triangles; type 2 in Fig. 3) have an intensity distribution which is uniform on the lines parallel to the hypotenuse of the triangle. As a result, the exposure dose at the representative point is the integration of the EID function in the nine regions which are expressed as the three different integration types (type 0-2) shown in Fig. 3.

3.2 PROXIMITY ANALYSIS FOR MULTI-LAYERED WAFERS WITH STEPPED SURFACES

As can be seen in Photo. 1 when an electron beam is exposed on a stepped-surface wafer, an extremely conspicuous proximity effect phenomenon appears, which is different from that on flat surface wafers. This phenomenon is considered to be caused by reflection from the stepped surface and by the difference in backscattering effect from several materials. There is the possibility that, when the electron beam collides with the convex section on the wafer, the greater part of the electrons are reflected instead of passing through. From a macro-viewpoint, this electron reflection phenomenon may be considered the same phenomenon as the reflection of rays from a mirror. The mirror reflection model is illustrated in Fig. 4. When a beam of intensity Q is exposed at position $x \in R^2$ is assumed to be E(x; y). For calculation of the exposure dose, the following cases can be distinguished based on the relation of the x and y positions.

i) Both x and y are located in a concave area.

In Fig. 4, the exposure dose at position x is the sum of the dose received through route I and the mirror reflection dose received through route II. The exposure dose received via route I[$E_1(x; y)$] is expressed by $E_1(x; y) = Q \cdot F(|x - y|)$. The exposure dose received via

route II[$E_2(x; y)$] is obtained by multiplying the exposure dose at x' by the coefficient of reflectance.
Therefore, $E_2(x; y) = \gamma \cdot Q \cdot F(|x'-y|)$, where γ is the coefficient of reflectance. The exposure dose $E(x; y)$ at position x is expressed by $E(x; y) = Q[E(|x - y|) + \gamma \cdot F(|x' - y|)]$. When the electron beam is exposed in area A of Fig. 4, the exposure dose $E(x; y)$ at x is given by the following expression.

$$E(x; A) = \iint_{y \in A} Q(y) \, [F(|x - y|) + \gamma \cdot F(|x' - y|)] d^2y$$

ii) Position x is in a convex area; position y is in a convace area.

$$E(x; y) = (1 - \gamma) Q \cdot F \, (|x - y|)$$

$$E(x; A) = \iint_{y \in A} (1 - \gamma) \, Q \, (y) \, F \, (|x - y|) d^2y$$

iii) Both positions x and y are in convex areas.

$$E(x; y) = Q \cdot F(|x - y|)$$

$$E(x; A) = \iint_{y \in A} Q \, (y) \, F \, (|\gamma - y|) d^2y$$

For example of Fig. 5, the exposure dose in regions A', B', C', D', E' is calculated separately as follows.

1. $x \in A'$

$$E(x) = E(x; A) + \gamma \cdot E(x'; A) + E(x; B) + (1 - \gamma)E(x; C) + (1 - \gamma)E(x; D) + (1 - \gamma)^2 E(x; E)$$

2. $x \in B'$

$$E(x) = (1 - \gamma)E(x; A) + E(x; B) + (1 - \gamma)E(x; C) + (1 - \gamma)E(x; D) + (1 - \gamma)^2 E(x; E)$$

3. $x \in C'$

$$E(x) = (1 - \gamma)E(x; A) + E(x; B) + E(x; C) + E(x'; C) + E(x''; C) + E(x; D) + (1 - \gamma)E(x; E)$$

4. $x \in D'$

$$E(x) = (1 - \gamma)^2 E(x; A) + (1 - \gamma)E(x; B) + (1 - \gamma)E(x; C) + E(x; D) + (1 - \gamma)E(x; E)$$

5. $x \in E'$

$$E(x) = (1 - \gamma)^2 E(x; A) + (1 - \gamma)E(x; B) + (1 - \gamma)E(x; C) + E(x; D) + E(x; E) + \gamma E(x'; E)$$

Where x', x" represent positions symmetrical to x.
Computer simulation results are given in Fig. 6, where $C_1 = 26.4$, $C_2 = 0.305$, $\sigma_1 = 0.319$, $\sigma_2 = 1.6$.

ACKNOWLEDGEMENTS

The authors would like to express appreciation to Dr. Y. Tarui, Director and K. Shimizu, Manager of cooperative labs for their helpful discussion and guidance.

REFERENCES

[1] N.Sugiyama, A, Kawaji and Y. Tarui, "Data processing system of electron-beam lithography for VLSI microfabrication", IEEE Trans. Electron Devices. Vol. ED-26, pp. 675, April 1979.

[2] N. Sugiyama and K. Saitoh, "Electron beam exposure system AMDES", Computer Aided Design, vol. 11, pp. 59, March 1979.

[3] N. Sugiyama, K. Saitoh and K. Shimizu, "Proximity effect correction in EB lithography for VLSI microfabrication", ISSCC Dig. Tech. Papers, pp. 88, 1979.

[4] N. Sugiyama and K. Saitoh, "Proximity effect correction in EB lithography using pattern shape adjustment techniques", Trans. IECE, Section (E), March 1980.

[5] N. Sugiyama, K. Saitoh, K. Shimizu and Y. Tariu, "Proximity effect correction in EB lithography", Trans. IECE, Section (C), vol, J62-C, No. 10, pp. 668, 1979 (Japanese)

[6] N. Sugiyama, N. Aizaki, A. Kawaji and Y. Tarui, "A data processing system for electron-beam lithography", Proc. of 8th Int. Conf. on Electron and Ion Beam Sci. and Technol. pp. 184, 1978.

[7] N. Sugiyama, "Computer simulation for self-consistent EB proximity effect correction", Trans. IECE, Section (C), April 1980 (Japanese)

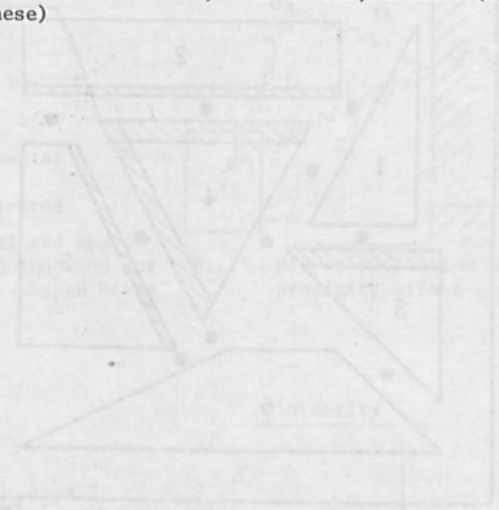

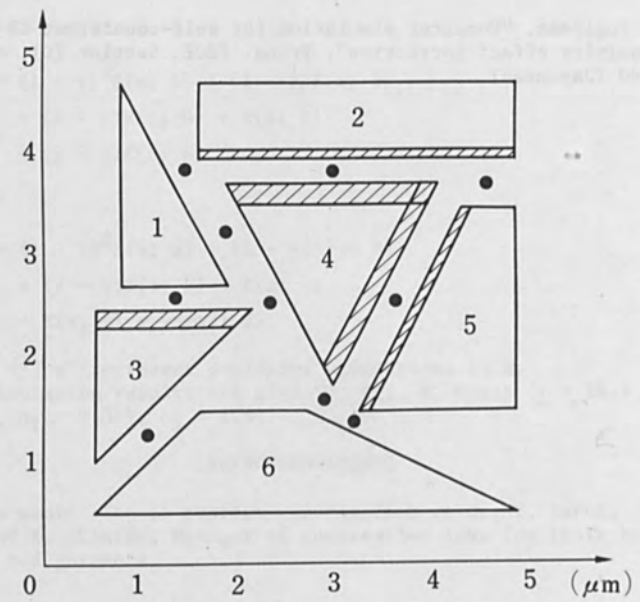

Fig. 1 Computer simulation result by PSA techniques. Dot(•) and slash(/) show representative point and the reduction area, respectively.

Representative point		Exposure dose	
Center pattern	Adjacent pattern	Uncorrected	Corrected
1	2	26.3	——
1	3	42.6	31.0
1	4	27.1	——
2	4	44.9	23.8
2	5	16.0	——
3	4	23.4	——
3	6	31.7	——
4	5	37.1	23.1
4	6	22.0	——
5	6	31.3	——

Table 1 Exposure dose comparison at the representative points in corrected and uncorrected.

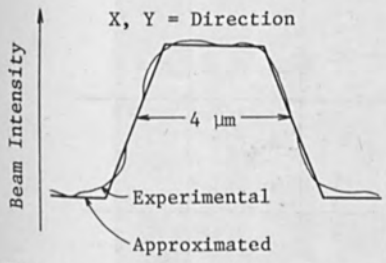

Fig.2 Experimental and approximated EID function for rectangular-shaped beams

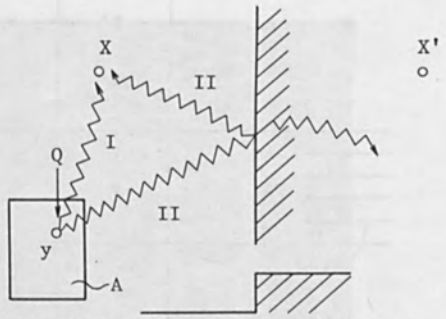

Fig.4 Mirror reflection model for proximity effect analysis

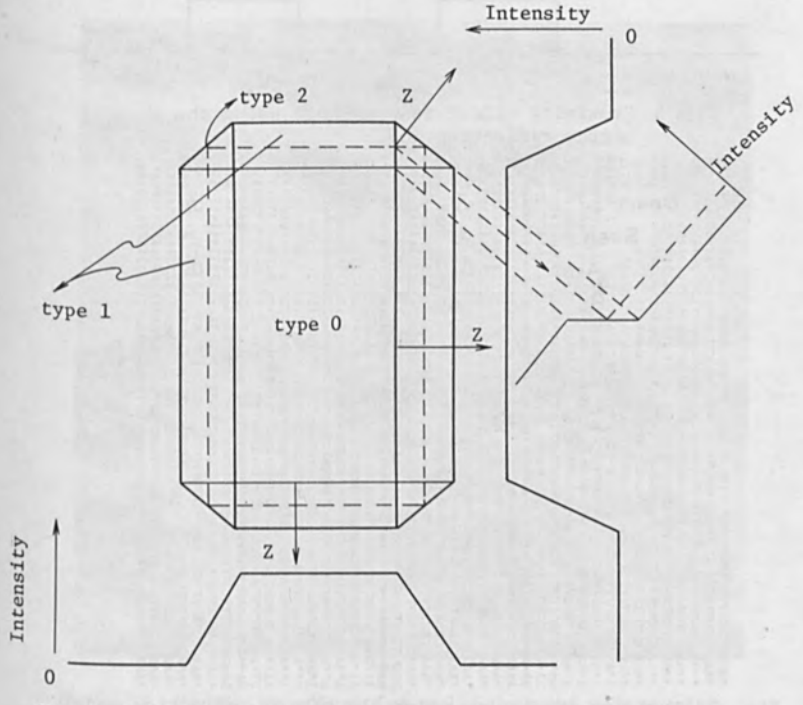

Fig.3 EID calculation method for rectangular-shaped beams

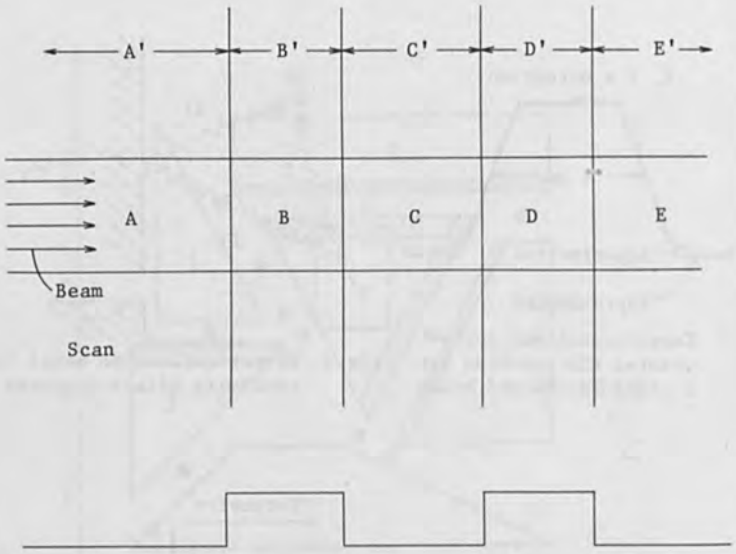

Fig. 5 Proximity effect test example using the mirror reflection model.

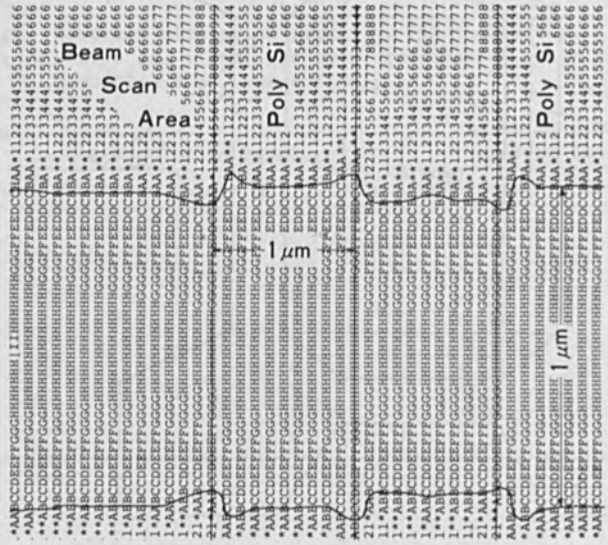

Fig. 6 Computer simulation using the mirror reflection model

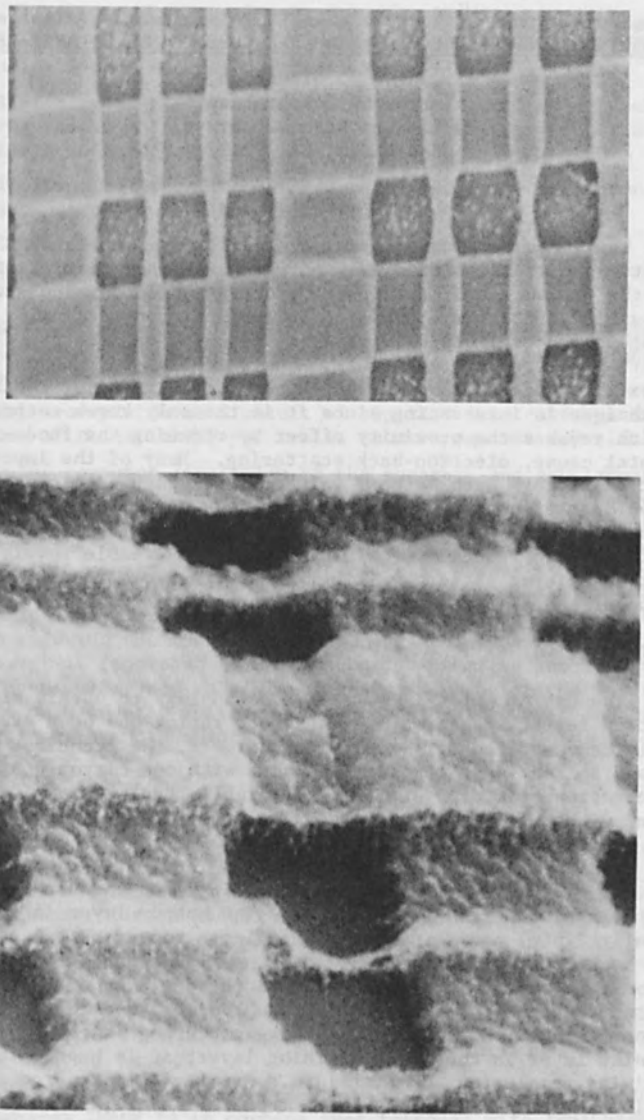

Photo. 1 Proximity effect for multi-layered wafers with stepped surfaces.

PROXIMITY EFFECTS IN ELECTRON-BEAM EXPOSURE OF MULTI-LAYER RESISTS

James S. Greeneich
Burroughs Corporation
16701 West Bernardo Drive
San Diego, CA 92127

ABSTRACT

The image forming properties of electron-beam exposed multi-layer resists are analyzed using computer simulation of the exposure and development processes. In particular, proximity effects are compared between the conventional processing technique of resist on substrate and the use of multi-layer resist techniques. The potential to reduce proximity effects through the use of the multi-layer resist technique is interesting since it is the only known method which reduces the proximity effect by reducing the fundamental cause, electron-back scattering. Many of the important parameters such as beam voltage, substrate atomic number, developer effects and pattern dimensions have been analyzed. Results indicate that multi-layer resist techniques are effective in reducing proximity effects to useable levels for sub-micron pattern writing, and furthermore resist exposures are insensitive to substrate atomic number.

I. INTRODUCTION

The use of multi-layer resist technology to obtain high resolution resist images with high aspect ratios has been experimentally demonstrated (1) - (8). Furthermore, the technique has been used to fabricate complex MOS chips with one-micron design rules using electron-beam exposure (1). Favorable results are also obtained with multi-layer resists using traditional optical exposure of the image defining layer (3).

The multi-layer resist technique involves the use of at least two resist layers (see Fig. 1). The bottom layer is thick (typically 2.0μm) and is used to cover large topographical changes in the substrate, and thereby create a nearly planar surface. In electron-beam exposure, it also becomes the dominant source of back-scattered electrons, and because such a resist is of low density and atomic number, a low level of back-scattering is obtained. The top resist layer is the image defining layer; it is kept thin (<0.5μm) to maximize resolution and linewidth control. In some processing situations, a thin (<0.1μm) pattern transfer layer is sandwiched between the two resist layers (3). Images generated in the top layer are transferred into the bottom layer by patterning the transfer layer , if needed, and then patterning the bottom layer by O_2 etching, chemical etching or by deep UV exposure followed by chemical etching,

as schematically illustrated in Fig. 1 (2) - (6). The advantages of using the multi-layer resist technique for sub-micron direct wafer writing using E-beam exposure of the image defining layer are:

1) Better image resolution and linewidth control as a result of reduced substrate back-scatter and the ability to use a thin image defining layer.

2) Improved tolerance to over-exposure and over-development because of reduced back-scatter.

3) Image defining resist can be optimized for speed since interlayer resist is designed for a high tolerance to a dry etching environment.

4) Reduced proximity effects since the amount of back-scatter is reduced for a thick interlayer resist compared to normal substrate materials (Si, GaAs, etc.).

5) Improved yields as a result of superior step coverage and use of thick interlayer resist to mask against dry etch.

Using computer simulation of the exposure and development of multi-layer resist structures, the image forming properties have been analyzed for a variety of exposure conditions. In particular, the proximity effect is compared for conventional image formation and the use of multi-layer resist techniques. The potential to reduce proximity effects through the use of multi-layer resists is interesting since it is the only known method which reduces the proximity effect by reducing the fundamental cause, electron back-scattering. Therefore, it is important to understand the benefits and limitations in electron-beam exposed multi-layer resists. Many of the important parameters such as beam voltage, type of substrate, developer effects and size of pattern dimensions are reported.

II. SIMULATION PROCEDURE

Computer modeling of the exposure and development of the resist is utilized to study proximity effects under a variety of writing conditions, including the use of multi-layer resists. Program IMAGE models the exposure and development in three steps. First is the calculation of the absorbed energy density $E(x,y,z)$ throughout the volume of resist assuming an incident delta function beam. Two options are available; one uses the two gaussian approximation (9) while the other uses the more accurate analytical model of Greeneich and Van Duzer (10) - (11). In order to analyze multi-layer resists, the analytical model was extended to include up to 10 different material layers.

Once the delta function response is determined, the second step in program IMAGE is to combine that response with real beam shapes by convolution. This convolved response can then be combined with a topographical description of the pattern of interest to generate the latent image in the resist. Points, lines,

rectangles or trapezoids may be inputed into IMAGE. Since proximity effects depend on the particular pattern shapes analyzed, a fixed set of patterns should be treated. In this analysis, we treat a complementary pair of patterns of nominal width W - that is, an isolated line of nominal width W_L and a gap between large area exposures of nominal width W_G.

The final step in the modeling involves developer simulation. After specifying the dose and developer conditions, the local solubility rate (12) of the resist in that developer is calculated throughout the volume of the resist and a "string" model is used to simulate the actual time evolution of the developed image. To evaluate proximity effects, the choice of dose and development times must be specified in a consistent manner. The conditions and methods used in this work are:

1) Evaluate complementary patterns of nominal width W.

2) Use a fixed nominal development time.

3) Adjust the incident dose, D_o such that the nominal linewidth is obtained for the isolated line. Under identical dose and development conditions, the resulting resist gap between two exposed areas is then analyzed for proximity effects.

III. RESULTS

Since it is the use of a thick interlayer resist which reduces the average amount of back-scattering and is fundamentally responsible for reducing the proximity effect in multi-layer resist technology, it is instructive to plot the absorbed energy density in the image defining resist as a function of radial distance. Results at the midpoint of a 0.5μm image layer are shown in Fig. 2 for several different thicknesses of interlayer resist and a 20keV incident beam. Figure 2 is a log-log plot showing the normalized absorbed energy density due to both forward and back-scattered electrons. It is evident from Fig. 2 that a substantial reduction in back-scattering occurs when a thick resist interlayer is used. For example, a 2.0μm resist interlayer reduces the back-scatter by approximately a factor of 3 compared to a Si substrate; this is a result of the smaller back-scattering coefficient, lower density and atomic number of the resist interlayer compared to typical substrate materials of Si, GaAs or gold. Notice in Fig. 2 that the use of 500A^o of Al as a pattern transfer layer somewhat increases the average back-scatter contribution, but the net effect is still considerably below the level for a Si substrate.

The ratio of total energy deposited by back-scattered electrons to that deposited by forward scattered electrons is the parameter, η_e, which appears in the two-gaussian scattering model (9). The larger the magnitude of η_e, the worse proximity effects

are. Therefore η_e provides a useful comparison between single layer and multi-layer resist structures. Such a comparison is shown in Fig. 3; the single layer results are taken from (14) and single layer experimental data is from (15) - (16). Data for a multi-layer resist structure is also shown by the triangles (7). It is clear that the multi-layer resist provides a substantial reduction in η_e and thereby proximity effects. Notice in Fig. 3, that the presence of a 500A° Al interlayer substantially increases η_e at low beam energies (10keV). This is expected because at low energies a larger proportion of back-scattered electrons arise from the Al layer compared to high energies. Quantitative data on developed contours as a function of beam energy is presented below.

It is clear from the results of Figs. 2 and 3 that proximity effects will be reduced when multi-layer resist structures are used; to better quantify the anticipated benefits a comparison of simulated developed images was carried out for a variety of exposure/developer conditions. The data presented here compares the results obtained for simulations with and without the use of a multi-layer resist structure. Specifically, two cases are considered:

Case (1): No resist interlayer; 0.5μm of PMMA resist (image defining layer) on a given substrate.

Case (2): Multi-layer resist; 0.5μm of PMMA resist (image defining layer) on 500A° Al on 2.0μm resist (PMMA) on a given substrate.

Results for both cases pictorially show only the 0.5μm image defining layer. Results for bottom layer patterning will be presented elsewhere. A typical set of results is shown in Fig. 4 which shows the developed contours in the resist at 30 intervals. In each simulation, nominal development time is 120 secs in 1:1 MIBK:IPA developer. Cases (1) and (2) are compared top to bottom respectively. For each case the incident dose was adjusted for the isolated line (left hand side of Fig. 4) such that the nominal linewidth was obtained at the bottom of the image defining resist layer. Because of reduced back-scatter, ≈5% more dose is required to properly develop the isolated line in the multi-layer resist structure. The advantage of the multi-layer resist structure in reducing proximity effects is clearly seen by comparing the developed contours for the 0.5μm gap for the two cases. Notice in case (1), upper right in Fig. 4, that after 120 secs. of development only a thin resist wall remains near the bottom of the image. Furthermore, after another 30 secs. of development the entire resist pattern is gone. This is not the case with the multi-layer resist structure (bottom right in Fig. 4). After 120 secs. of development the resist conforms closely to the designed linewidth and even after an additional 30 or 60 secs. of development, useable resist images remain. Thus the use of multi-layer resist structure reduces the sensitivity of the image to over-development.

The contours at different development times also represent the effects of various incident doses. For a fixed developer concentration with a small background etch rate, the volume of resist removed is proportional both to the incident dose and to the development time. Consequently, contours for times longer than nominal represent the effect of larger incident doses while contours at times less than nominal represent smaller incident doses. As a consequence, we can also conclude from Fig. 4 that the resulting patterns in the multi-layer resist structure are less sensitive to variations in dose than for resist coated on bare Si.

EFFECT OF DEVELOPER STRENGTH

The effect of developer strength on nominal 0.5μm gaps is shown in Fig. 5 for several different conditions. From top to bottom the development conditions are: (a) 1:3 MIBK:IPA (b) 1:1 MIBK:IPA (c) 100% MIBK (d) same as (c) except longer development time. In plots (a) - (c) the contours are at 30 second intervals and nominal development is 120 secs., while in plot (d) the contours are at 150 sec. intervals and nominal development is 600 secs. In each simulation the incident dose was adjusted for the complementary pattern (isolated line) to yield the proper width of line. Results for resist on bare Si are shown on the left in Fig. 5, while results for the multi-layer structure are shown at the right; for each developer the results for the multi-layer structure are considerably better. The influence of developer strength on required incident dose and on resulting resist image characteristics are tabulated in Table 1. Dose is normalized to unity for the 1:1 developer for the case with no resist interlayer. Increasing the developer strength by increasing the proportion of MIBK has the following effects: (1) reduces the required incident dose (more sensitive resist) (2) gap width remains nearly constant (3) remaining resist thickness decreases, and (4) increases the susceptibility to over-exposure or over-development.

EFFECT OF INCIDENT BEAM ENERGY

The effect of incident beam energy on pattern fidelity was examined for 0.5μm lines and gaps following the procedure outlined previously, that is, the optimum dose was established for the isolated line and then the 0.5μm gap was examined at the same dose and developer conditions. Results for a 10-40keV variation in beam energy are shown in Fig. 6 for no resist interlayer (left hand side) and for the multi-layer structure (right hand side). In all simulations, contours at 30 sec. intervals are shown and nominal development was 120 secs. in 1:1 MIBK:IPA. Once again the proximity effect is reduced with the multi-layer resist structure. Notice also in both cases that as beam energy increases, the proximity effect is reduced; this is graphically shown in Fig. 7 where the gap width is plotted as a function of incident beam energy. At larger linewidths (>1 micron) and thin resist layers, beam energies near 10keV may show

less severe proximity effects because the range of 10keV electrons is close to the minimum pattern dimension (13). However, for sub-micron pattern writing, higher beam energies are more effective in obtaining small linewidths and proximity effects are reduced. As the beam energy is increased, the relative contribution of the forward-scattered electrons and back-scattered electrons change. At high energies the forward directed electrons are scattered less and the penetrating beam closely resembles the incident beam. In the case of the back-scattered electrons, the range over which they are distributed increases, but their amplitude is reduced. The net effect is to reduce the detrimental impact of the back-scattered electrons for high incident beam energies.

EFFECT OF SUBSTRATE ATOMIC NUMBER

It is well known that increasing the atomic number of the substrate detrimentally influences pattern fidelity - that is, proximity effects are more severe. The use of multi-layer resist structures is particularly effective in reducing proximity effects for high atomic number substrates. In fact the use of a thick inter-layer resist eliminates variations between different substrate materials. Simulations for 20keV exposures are shown in Fig. 8 for: (a) silicon substrate (b) permalloy substrate (c) gallium arsenide substrate and (d) gold substrate. Results for 0.5μm resist on the indicated substrate are shown at the left, while results using the multi-layer resist structure are shown at the right. It is clearly evident that the proximity effect increases rapidly with increasing substrate atomic number, e.g., when the image defining resist resides on the substrate. Conversely, the multi-layer resist gives a nearly constant developed profile requiring the same incident dose regard-less of the underlying substrate. A more quantitative evaluation of substrate effects is given in Table II. Here the measured gap width normalized to the nominal 0.5 micron gap is tabulated for various substrate and resist interlayer combinations. Also tabulated is the required incident dose (normalized) for the 0.5 micron isolated line pattern. Note that with no substrate the normalized gap width approaches one and that with an infinite resist substrate it approaches three-fourths. Increasing substrate atomic number causes the normal-ized gap width to rapidly decline to zero; however, with the multi-layer resist technique the normalized gap width remains nearly constant and close to the value for an infinite resist layer substrate. Thus optimum exposure conditions including residual proximity effect correction rules can be established for one given substrate and the results will apply to all substrates.

EFFECT OF PATTERN DIMENSION

It is interesting to examine the relative benefit of using the multi-layer resist structure as a function of the absolute pattern size. Figure 9 compares the results for no resist interlayer (left side) and 2.0μm resist interlayer (right side) for nominal

dimensions of 0.25μm to 1.0μm. The incident energy is 20keV and nominal development is 120 secs. in 1:1 MIBK:IPA for all simulations. In all cases the closer the patterns are spaced, the greater the proximity effect. This is more graphically illustrated in Fig. 10 where the fractional remaining gap width is plotted as a function of nominal gap width for both cases. Consistently better pattern fidelity is obtained with the multi-layer structure, but dimensions of ≈0.5μm will still require residual proximity correction to obtain the best quality patterns which electron-beam lithography is capable.

IV. SUMMARY

By using a multi-layer resist technology, the average electron back-scatter from the substrate is substantially reduced. Although proximity effects are not eliminated for half-micron dimensions, the severity is very much reduced. Useable 0.5μm gaps between large area exposures can be exposed without recourse to dose or pattern compensation techniques. Furthermore, patterns exposed using the multi-layer resist technique are insensitive to differing substrates and show only a slight sensitivity to differing developer strength, variations in incident dose or development times. The effect of such variations is minimized because the thick resist interlayer represents a nearly constant and low level back-scattering source to the image defining layer regardless of the underlying substrate or topography or changes in exposure/developer conditions. Consequently, the residual proximity effects may be eliminated by dose control or pattern biasing; and once the design rules are established they will not change for a wide range of exposure conditions.

TABLE 1

TABLE 1

INFLUENCE OF DEVELOPER STRENGTH ON 0.5μm RESIST IMAGES

DEVELOPER	*INTERLAYER*	*RELATIVE INCIDENT DOSE - 0.5μm LINE*	*MEASURED GAP WIDTH/NOMINAL WIDTH*	*REMAINING RESIST THICKNESS*
1:3 MIBK:IPA	NONE	1.63	0.28	4900
1:3 MIBK:IPA	2.0μm Resist + 500A° Al	1.74	0.72	5000
1:1 MIBK:IPA	NONE	1	0.25	4225
1:1 MIBK:IPA	2.0μm Resist + 500A° Al	1.06	0.68	4750
100% MIBK	NONE	0.65	0.29	3550
100% MIBK	2.0μm Resist + 500A° Al	0.69	0.70	4325
100% MIBK (LONG)	NONE	0.20	0.30	2950
100% MIBK (LONG)	2.0μm Resist + 500A° Al	0.21	0.65	3650

TABLE II

THE EFFECT OF SUBSTRATE ON NORMALIZED GAP WIDTH FOR 20keV EXPOSURE

SUBSTRATE	RESIST INTERLAYER	MEASURED GAP WIDTH/NOMINAL WIDTH	REQ'D INCIDENT DOSE (NORMALIZED) 0.5μm LINE
NONE	NONE	0.93	1.11
PMMA	NONE	0.72	1.07
Si	NONE	0.25	1
PERMALLOY	NONE	0.09	0.85
GaAs	NONE	0.00	0.87
Si	2.0μm + 500A° Al	0.68	1.06
PERMALLOY	2.0μm + 500A° Al	0.77	1.07
GaAs	2.0μm + 500A° Al	0.70	1.06
PALLADIUM	2.0μm + 500A° Al	0.78	1.06
GOLD	2.0μm + 500A° Al	0.78	1.06

REFERENCES

1. W.D. Grobman, H.E. Luhn, T.P. Donohue, A.J. Speth, A.D. Wilson, M. Hatzakis, T.H.P. Chang, IEDM Proceedings, 1978, P. 58.

2. M. Hatzakis, D. Hofer, T.H.P. Chang, 15th Symposium Electron, Ion and Photon Beam Tech., 1979. Paper B-5.

3. J.M. Moran, D. Mayden, 15th Symposium Electron, Ion and Photon Beam Tech., 1979, paper B-2.

4. M. Hatzakis, 15th Symposium Electron, Ion and Photon Beam Tech., 1979, paper J-4.

5. B.J. Lin, T.H.P. Chang, 15th Symposium, Electron, Ion and Photon Beam Tech., 1979 paper M-10A.

6. J. Kitcher, 15th Symposium Electron, Ion and Photon Beam Tech., 1979, paper P-4.

7. D. Stephani and E. Kratschmer, Proc. Microcircuit Engineering 1979, Sept. 1979, p. 228.

8. M. Hatzakis; Proc. Microcircuit Engineering 1979, Sept. 1979, p. 135.

9. T.H.P. Chang, J. Vac. Sci. and Technol., Vol. 6, p. 1271, Nov/Dec 1975.

10. J.S. Greeneich and T. Van Duzer, J. Vac. Sci, and Technol., Vol. 10, No. 6, p. 1056, Nov/Dec 1973.

11. J.S. Greeneich and T. Van Duzer, IEEE Trans. Electron Devices, Vol. ED-21, No. 5, p. 286, May 1974.

12. J.S. Greeneich, J. Electrochem. Soc., Vol. 122, No. 7, p. 970, July 1975.

13. D.F. Kyser and C. Ting, 15th Symposium Electron, Ion and Photon Beam Technol., 1979.

14. J.S. Greeneich, 15th Symposium Electron, Ion and Photon Beam Tech., 1979.

15. W.D. Grobman and A.J. Speth, Proc. Eighth Int'l. Conf. Electron and Ion Beams Sci. Technol., R. Bakish, ed. (Electrochemical Society) p. 276, 1978.

16. F. Jones and M. Hatzakis, Proc. Eighth Int'l. Conf. Electron and Ion Beams Sci. Technol., R. Bakish, ed. (Electrochemical Society) p. 256.

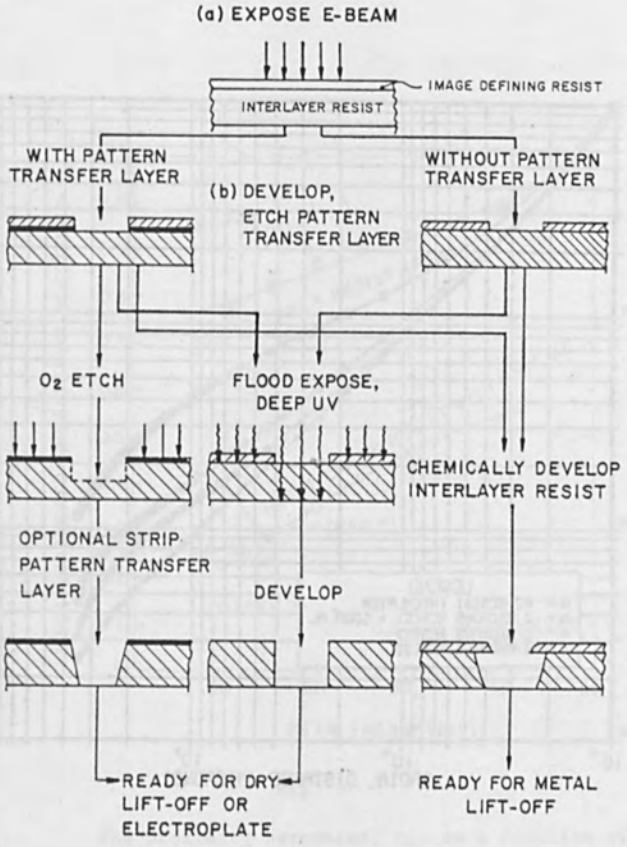

Fig. 1

A schematic illustration of several processing techniques in the multi-layer resist technology.

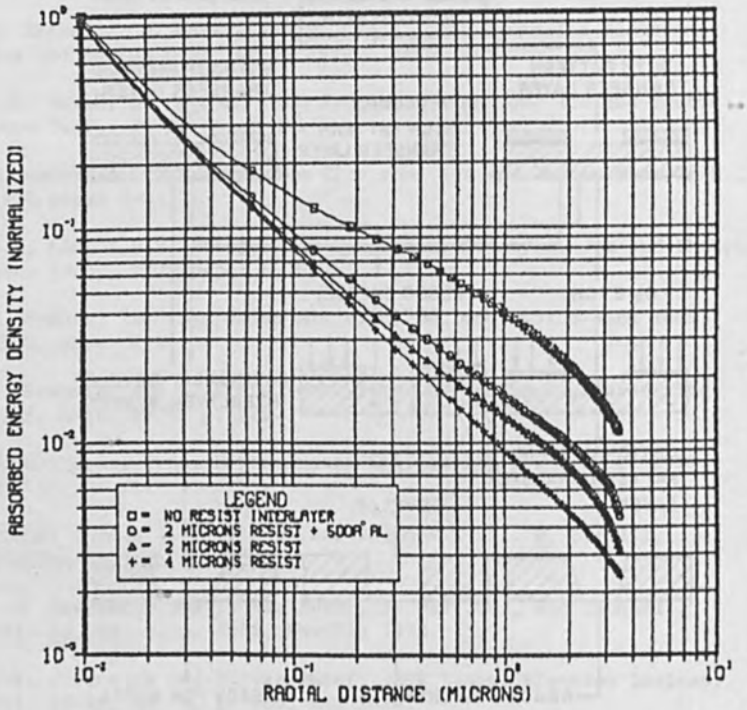

Fig. 2

Radial distribution of absorbed energy density at the mid-point in a 0.5μm top layer resist for various thicknesses of bottom layer materials.

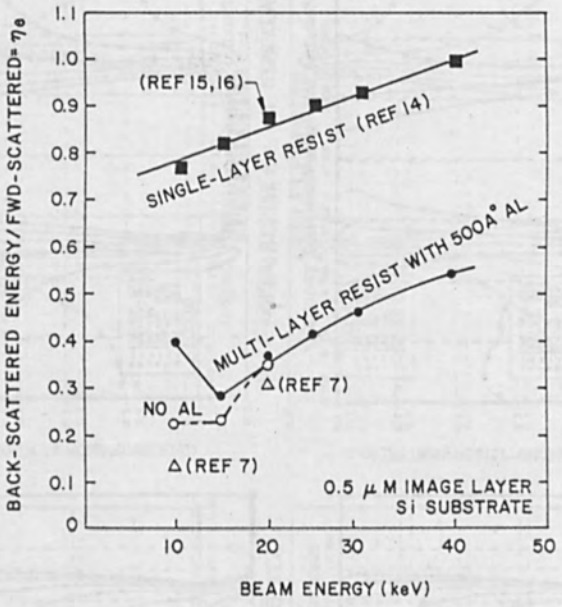

Fig. 3

The proximity parameter, η_e, as a function of beam energy comparing single and multi-layer resist techniques.

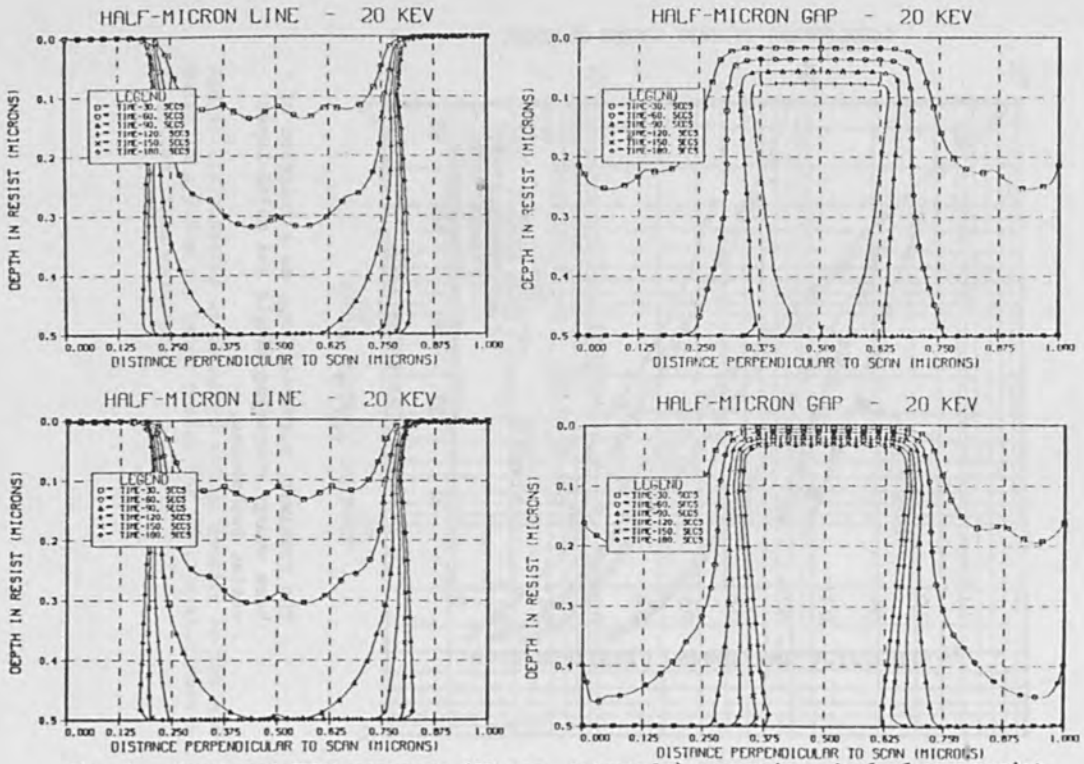

Fig. 4. Developed PMMA contours (30 sec. intervals) comparing single layer resist (top curves) with multi-layer resist (bottom curves). All exposures at 20keV with Si substrate and 1:1 MIBK:IPA developer (120 sec. nominal develop time).

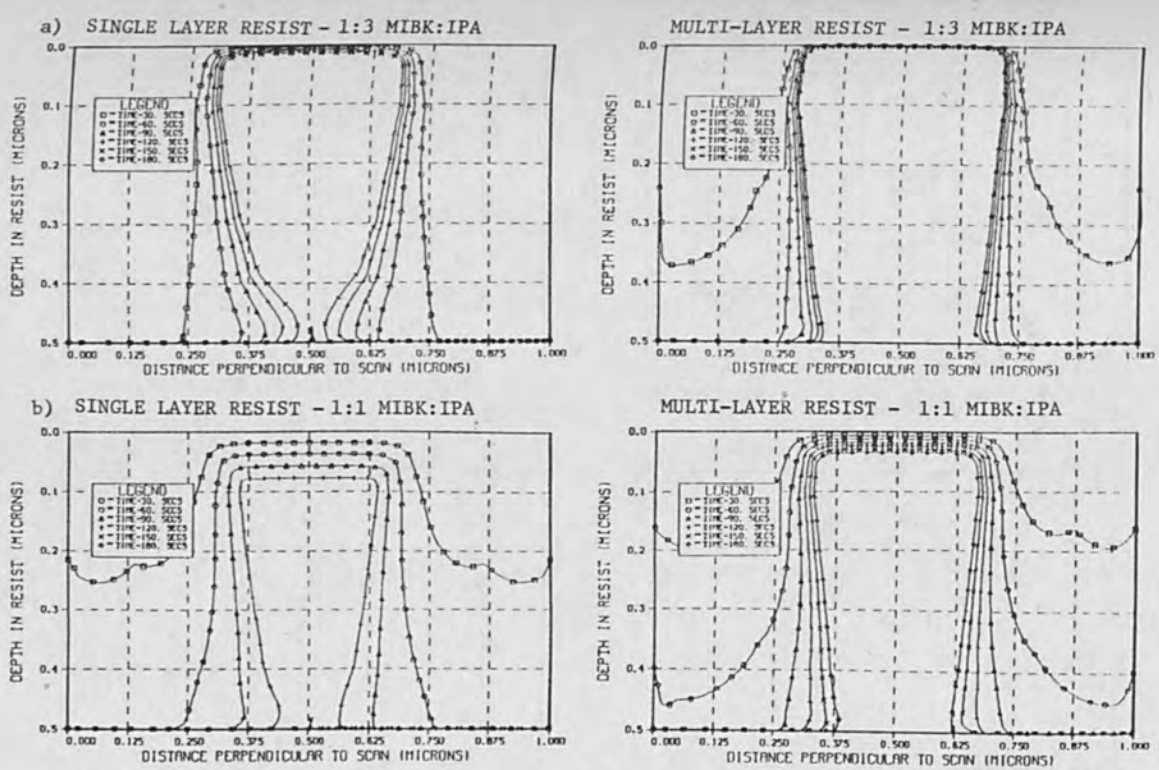

Fig. 5. (a & b) Comparison of gap exposures between single and multi-layer resists for various developer solutions. All exposures are 20keV with Si substrate.

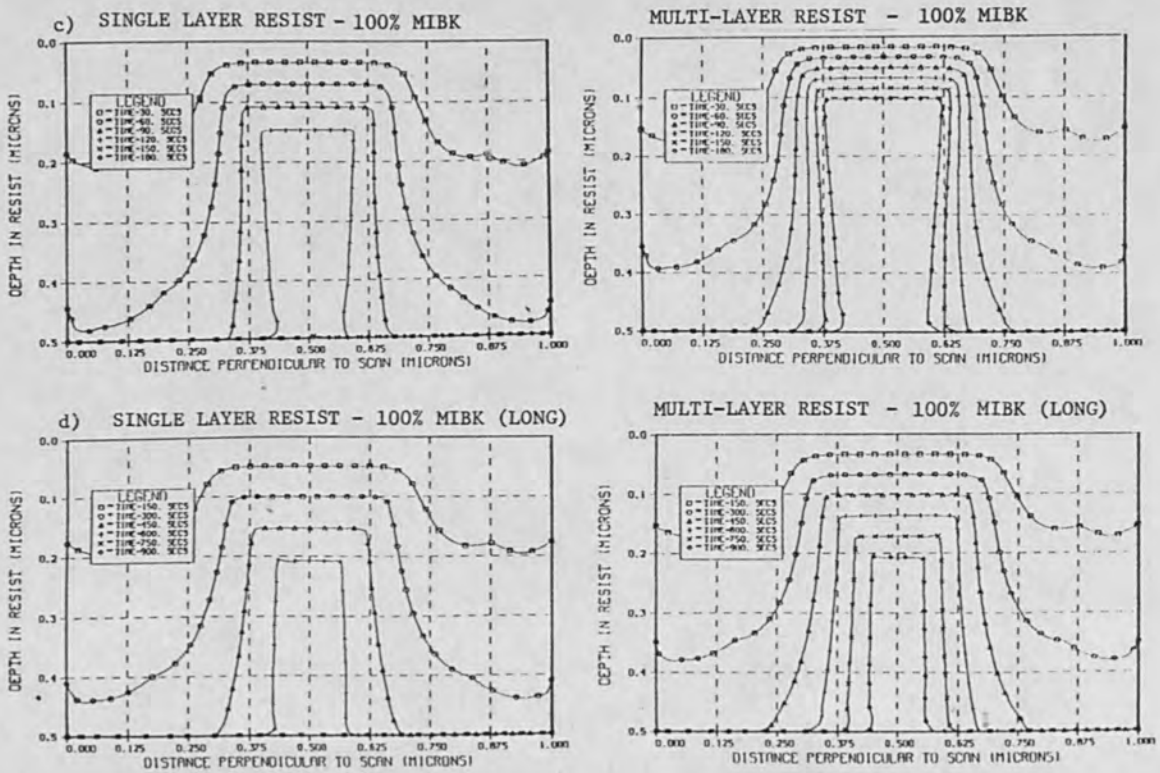

Fig. 5. (c & d) Comparison of gap exposures between single and multi-layer resists for various developer solutions. All exposures are 20keV with Si substrate.

...exposures are 20keV with Si substrate.

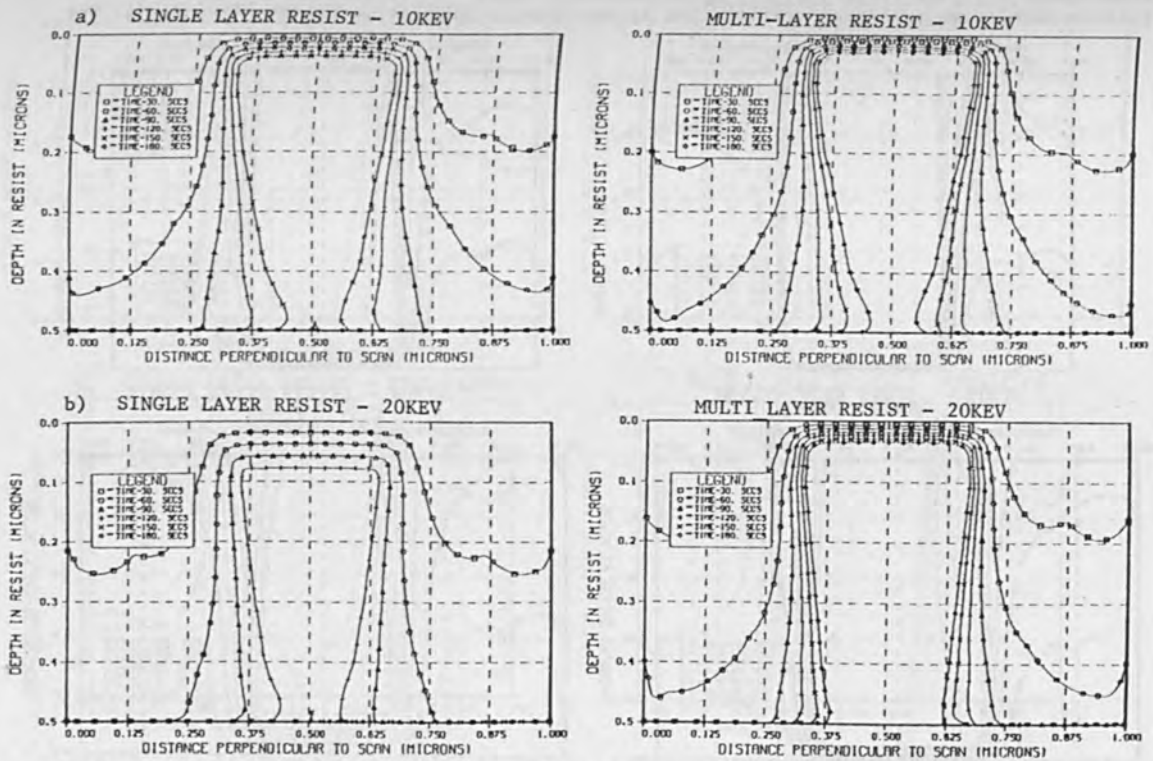

Fig. 6. (a & b) Comparison of single layer resist and multi-layer resist structures at various incident beam energies. Contours at 30 sec. intervals in 0.5μm image defining layer, Si substrate and a nominal 120 sec. development in 1:1 MIBK:IPA.

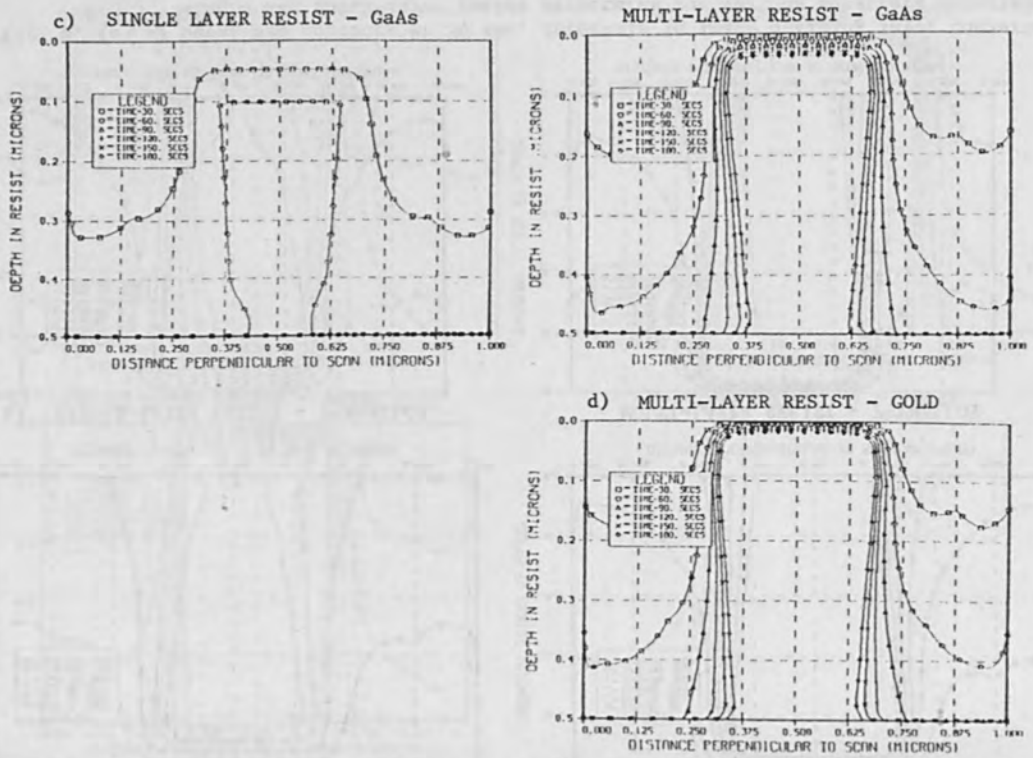

Fig. 8. (c & d) Developed contours at 30 sec. intervals in image defining layer comparing single and multi-layer resist structures for various substrate materials. All exposures at 20keV and 120 sec. nominal development in 1:1 MIBK:IPA.

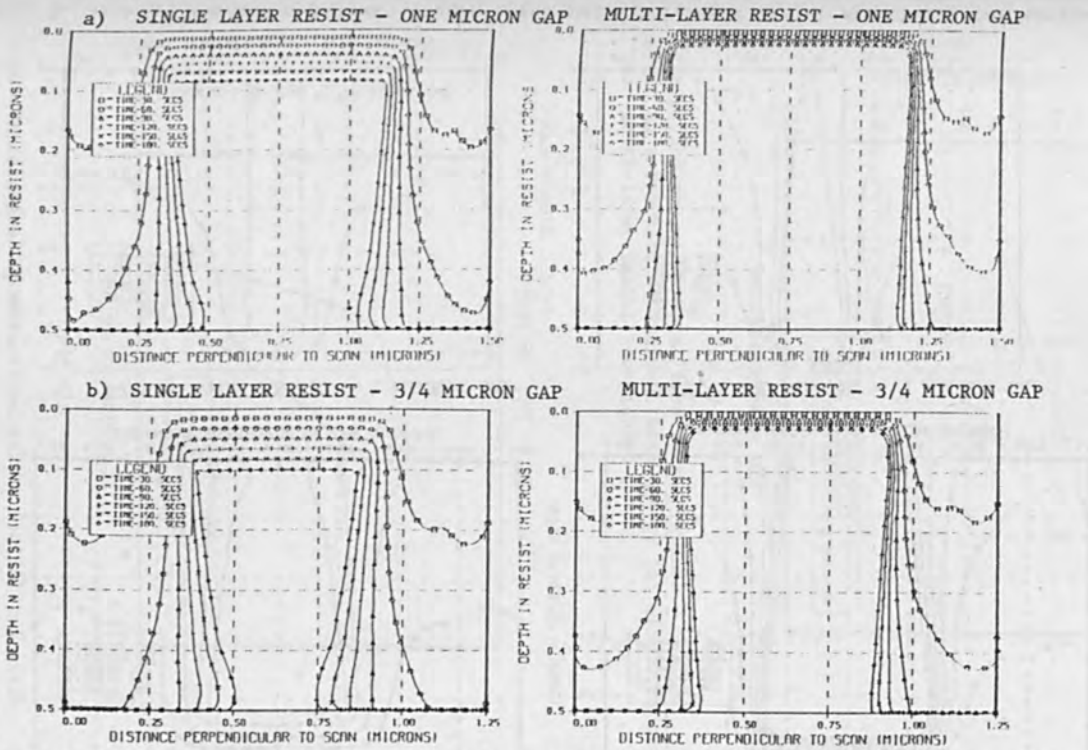

Fig. 9. (a & b) Comparison between single layer and multi-layer resist structures for various nominal gap widths. All exposures at 20keV on Si substrate, 120 sec. nominal development in 1:1 MIBK:IPA.

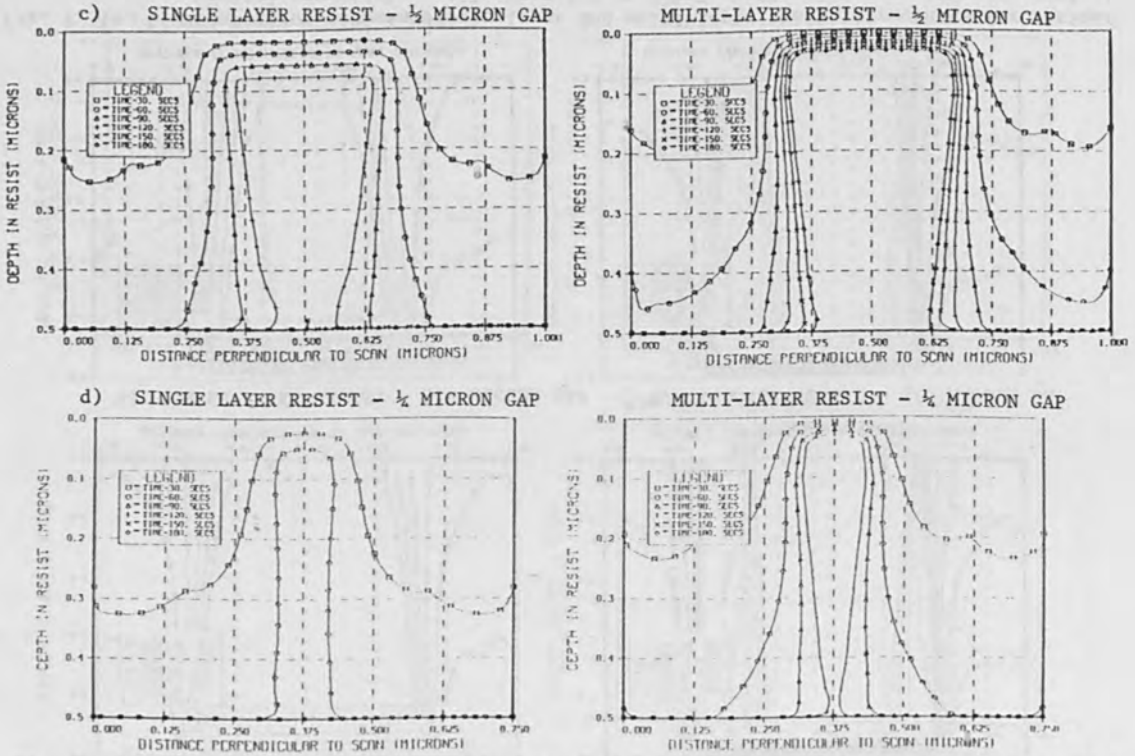

Fig. 9. (c & d) Comparison between single layer and multi-layer resist structures for various nominal gap widths. All exposures at 20keV on Si substrate, 120 sec. nominal development in 1:1 MIBK:IPA.

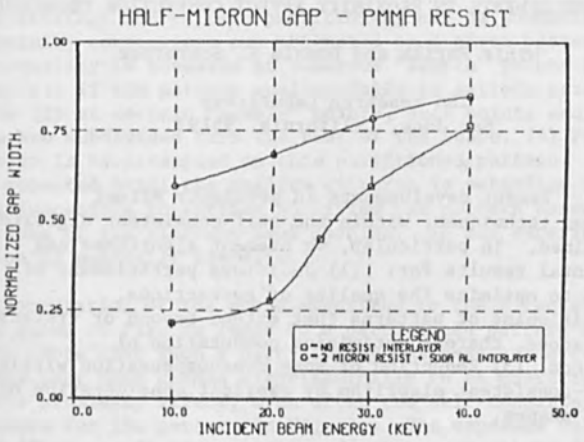

Fig. 7

Developed gap width normalized to the nominal 0.5μm gap as a function of incident beam energy for single layer and multi-layer resist techniques.

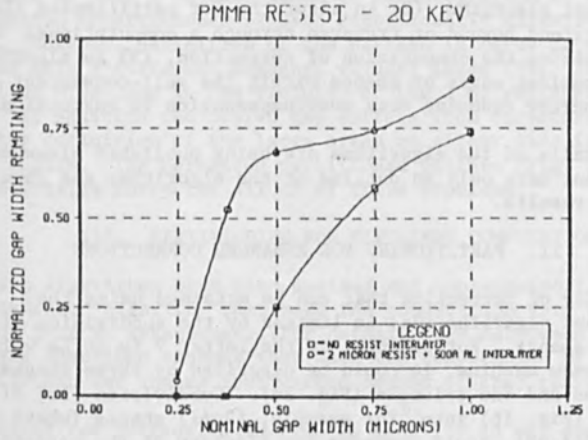

Fig. 10

Developed gap width normalized to the nominal gap width as a function of that normal gap width; this illustrates the effect of pattern size on proximity effects for single and multi-layer resist techniques.

RECENT DEVELOPMENTS IN PROXIMITY EFFECT CORRECTION TECHNIQUES

Mihir Parikh and Donald E. Schreiber

IBM Research Laboratory
San Jose, California 95193

ABSTRACT: Recent developments in proximity effect correction techniques, within the self-consistent algorithm, are outlined. In particular, we present algorithms and experimental results for: (1) Judicious partitioning of patterns to optimize the quality of corrections, (2) Partitioning of patterns that extend beyond or traverse through zones, thereby optimizing computation of corrections, (3) Reduction of some overcompensation within the self-consistent algorithm by explicit consideration of edges of shapes.

I. INTRODUCTION

This paper will briefly outline three new developments that have been incorporated within the framework of SPECTRE (for Self-consistent Proximity Effect Correction Technique for Resist Exposure). These are: (1) An algorithm for judicious automatic partitioning (or subdivision) of patterns in order to optimize the corrections possible with the self-consistent algorithm, (2) An algorithm for partitioning those shapes that extend beyond or traverse through a computational "zone"; thereby optimizing the computation of correction, (3) An algorithm to explicitly consider edges of shapes within the self-consistent algorithm, thereby reducing some overcompensation to correction.

Since details of the algorithms are being published elsewhere [1,2], we will present here only an outline of the algorithms and some experimental results.

II. PARTITIONING FOR ENHANCED CORRECTIONS

The quality of correction that can be attained using the self-consistent algorithm [3a] is limited by the subdivision of a pattern into shapes. For example, if the letter V is to be written by an electron-beam machine, it could be described by three shapes: Two parallelograms and one triangle (Fig. 1a). Subdivision [3c] of each of these shapes (Fig. 1b) into, for example, (2n+1) shapes (where n is the number of vertices), could increase the fidelity of the pattern. However, the increase in the number of shapes (and thus the data volume and computation time) necessitates an intelligent algorithm for the partitioning of a pattern only at those locations that are significantly influenced by proximity effects. Such an algorithm has been presented elsewhere [2]. We present here a brief overview.

The strategy for pattern partitioning can be summarized as follows: (1) Proximity corrections are attempted on a given pattern, (2) The pattern quality is assessed at numerous "sample" points throughout the pattern, (3) If the pattern quality fails to satisfy certain "goodness" criteria (2) at certain "sample" points, such points and the associated regions are subdivided from the rest of the shape, (4) Proximity correction is re-attempted on this partitioned pattern. This procedure can be repeated until the quality criteria is satisfied everywhere or it becomes impossible to further subdivide the pattern based on physical limitations of the electron-beam machine. In our experience, a single iteration is generally adequate.

Implementation of the above algorithm to the 8 rectangles in the pattern shown in Fig. 2a leads to a partitioned pattern shown in Fig. 2b. Note that such a partitioning has been achieved only at those locations that were deemed algorithmically to be suffering from excessive proximity effect, even after the self-consistent calculation of exposure for the pattern in Fig. 2a. The exposure values calculated for the 21 shapes in the partitioned pattern are shown in Fig. 2b.

Experimental results (Fig. 3) show four regions in the pattern in the case of (a) no correction, (b) self-consistent correction, without partitioning and (c) partitioned pattern, self-consistent correction. Note that while the 1 μm wide resist line [region (iii)] in the uncorrected pattern is significantly underdeveloped, the resist gap [region (iv)] is already narrower than the 1 μm design. Further development of such a pattern leads to disintegration of the resist gap. The corrected unpartitioned pattern significantly alleviates the problem. However, definition of the pattern in terms of 8 rectangles (and thus only 8 different exposure values) leads (Fig. 3b) to widening of the 1 μm wide line in the vicinity of the 2 μm rectangles [region (iii)]. In addition the resist gap suffers from curvature [region (iv)] due to the definition of the large areas on either side in terms of only two rectangles. The corrected partitioned pattern (Fig. 3c) seems to have essentially corrected all of of these problems.

III. PARTITIONING FOR EFFICIENT COMPUTATION

Zoning algorithms have been devised and implemented [3b] within the self-consistent algorithm that make the computation very efficient. We will show here an enhancement (for details, see Reference 2) to previously described schemes that make the computation of corrections more efficient for shapes that extend beyond or that traverse a zone.

Consider ten rectangles in Fig. 4a that lie in and around a hypothetical zone (more correctly these are "S zones" of Reference 3b) with indices (I,J). Note that shapes A and J are of such an extent that they are assigned to some zones that are beyond the limits of Fig. 4a. Consider next the seven shapes that would be used in the self-consistent solution of the shapes in the zone (I,J). Since the shapes B, I, and J are not included in the computation, the mutual interactions between

them and the long shape A are incorrectly ignored. In addition, the interaction between shapes G and J is also ignored; this can lead to serious errors in the computed exposure values for shape G.

A solution [2] to these problems can be obtained by cutting up some shapes into smaller ones so that more accurate exposure values can be computed for component pieces. The algorithm for such a shape cutting involves: (1) The definition of a "shape-cutting" frame (Fig. 4b) that circumscribes a zone, (2) The stipulation of cutting up into two pieces those shapes that belong to a zone but extend beyond such a frame, (3) The cutting of the shape, if it is found to be necessary at the zone boundary, (4) The prevention of "sliver" shape formation (for example in the case of shape G) by reassigning the entire shape to a neighboring zone. The application of these rules results in the 13 shapes shown in Fig. 4b.

Examination of Fig. 4b reveals the following. Computation of shapes belonging to the zone to the left of zone (I,J), takes into proper account the interactions between A1 and B. Similarly the computation of shapes in the zone to the right of zone (I,J) takes into proper account the interactions between A3, J, and G. Finally note that shape G was reassigned to the zone to the right of the zone (I,J) in order to prevent the formation of "sliver" shapes as well as to properly consider the interaction with shape J.

IV. EDGE COMPENSATION ALGORITHM

The self-consistent technique considers [3a] the magnitude of the proximity effect within each point in a shape democratically. This leads to an area average consideration (see, for example, Eq. (5) in Reference 3a). If certain points within a shape (e.g., along the periphery or at a corner) are more critical than other points (e.g., within an interior of a large shape), an unequal weighting of parts of a pattern may have to be considered.

An algorithm (for details see Reference 1) that accomplishes this within the "self-consistent" framework considers values of ε (see Eq. (4), Reference 3a), a measure of the magnitude of the proximity effect, at a certain point in each shape. This is arbitrarily chosen to be the midpoint along one edge of the narrower side of a rectangle. It can be shown (1), that ε_A at such a point A decreases with decreasing dimension of an isolated uncorrected shape. This leads to the well known underdevelopement of smaller shapes as compared to large shapes. The self-consistent algorithm (involving area-averaging) leads to an "overcompensation". That is, while perfect compensation should yield ε_A to be <u>independent</u> of the dimension of the shape, the self-consistent correction leads to ε_A that increase with shape dimensions. This overcompensation can be exactly corrected by the multiplication of relative incident exposure n_I by an analytical function F. Results for isolated squares and lines, Fig. 5a, shown in terms of dimensional deviation ℓ_a / ℓ_d indicate that perfect compensation is achieved.

Corresponding values of relative incident exposure n_I is shown in Fig. 5b. Note that the self-consistent technique seems to significantly overcompensate only for dimensions ≤ 0.5 μm.

V. SPECTRE

A new version of SPECTRE (for Self-consistent Proximity Effect Correction Technique for Resist Exposure), with an architecture similar to the earlier version [3c], has been created which includes the above described algorithms. Figure 6 shows the flowchart of the programs that comprise SPECTRE. As before the program is initiated via an interactive program (SPECREAD) that prepares and checks input parameters regarding electron lithographic and pattern conditions to be used for proximity correction. An arbitrary pattern is divided into various zones [3b] (via the program ZONMAP) based on whether the proximity corrections are to be performed on all shapes (if the pattern is nonrepeating) or whether only some shapes are to be corrected (if the pattern is repeating) and the results replicated to the rest of the repeating pattern. A program (WINDOW) separates the pattern data into two parts. One part with the pattern data (COMP.SHAPES-"C.S.") that are to be explicitly used for proximity computations and the other part with the pattern data (ASSOC.SHAPES) that are part of the repeating pattern, which are to be associated with the computed corrections. The "C.S." pattern data is next processed by three programs. The program ZONTAG, tags the pattern according to zones, as described previously [3b]. Using the algorithm described in Section III, shapes that traverse zone boundaries are subdivided by the program SHAPCUT. The program FRMTAG, replicates and tags shapes if they belong in the frames of zones as reported previously [3b]. After a SORT, to arrange pattern data sequentially by zones, the computation of corrections is performed by the program COMPC using the self-consistent algorithm and the algorithm of Section II to automatically subdivide (and recompute corrections) of shapes via the program AUTOCUT.

REFERENCES AND NOTE

1. M. Parikh, "Proximity Effect Correction in Electron Lithography: Magnitude and Correction Techniques," IBM J. Res. Develop. (July 1980), to be published.

2. M. Parikh and D. E. Schreiber, "Pattern Partitioning for Enhanced Proximity Effect Corrections in Electron Lithography," IBM J. Res. Develop. (September 1980), to be published.

3. M. Parikh, "Corrections to Proximity Effects in Electron Beam Lithography. (a) I. Theory, (b) Implementation, (c) Experiments," J. Appl. Phys. 50, 4371, 4378 and 4383 (1979).

Note: Please refer to Reference 1 for a comprehensive review and citation of publications by other workers in this field.

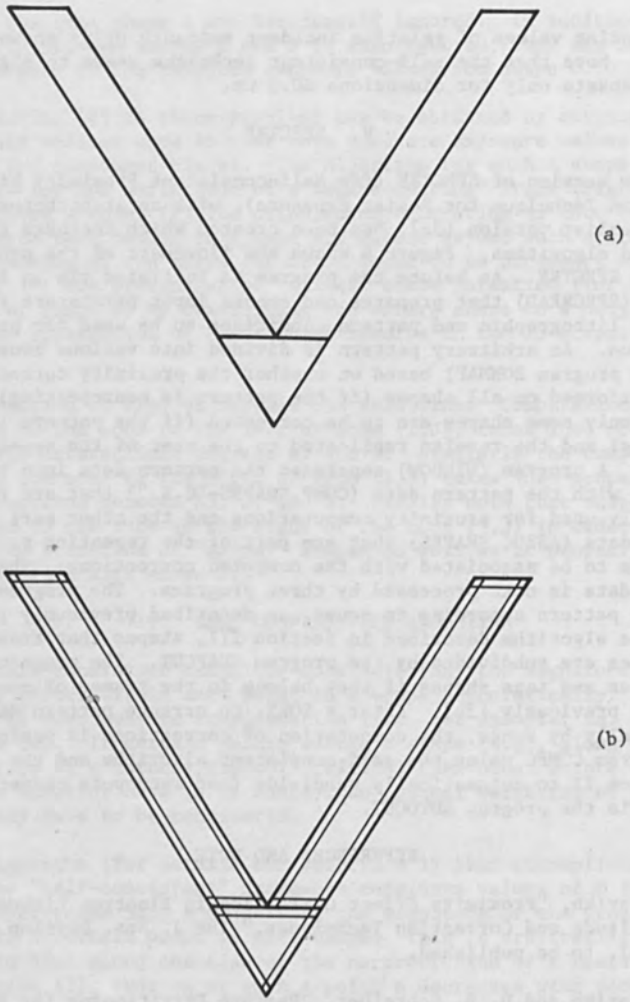

Figure 1. Subdivision of a complex shape into (a) two parallelograms and one triangle (b) 25 shapes. In the latter case, increased pattern delineation can be obtained by exposing the edge and corner shapes with different incident electron exposures as determined using the self-consistent algorithm (from Reference 3c, by permission).

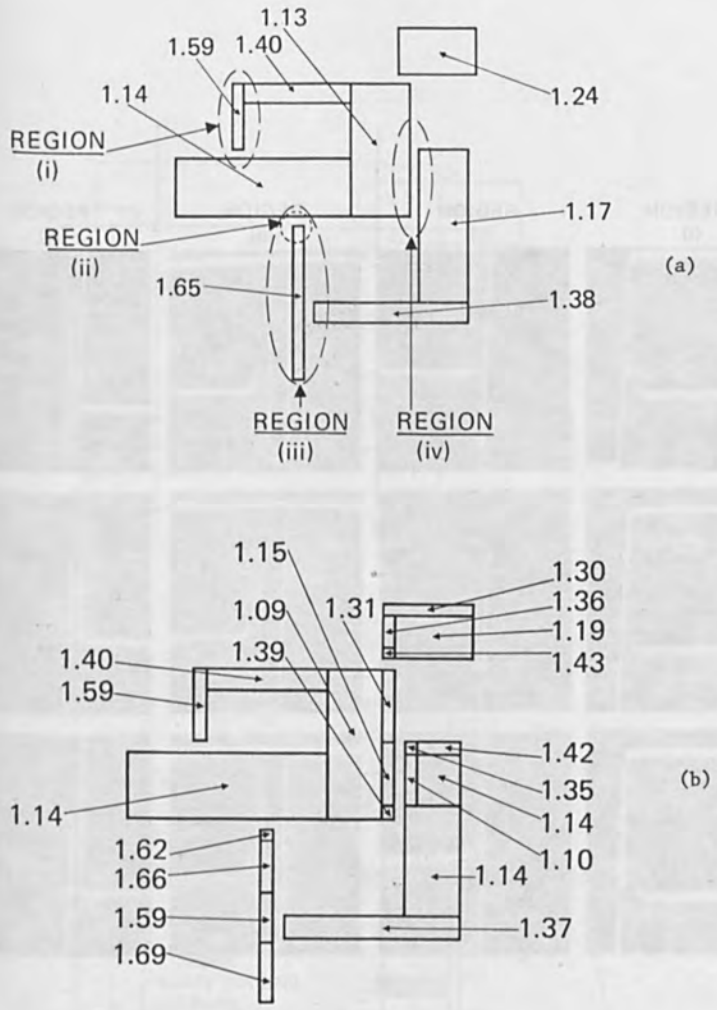

Figure 2. (a) A pattern consisting of 8 rectangles. Note regions (i)-(iv) where proximity corrections are necessary for complete dissolution of the resist as well as pattern fidelity. If this pattern is not proximity corrected, a relative exposure value of unity is given to each rectangle. If this pattern is corrected via the self-consistent algorithm, a relative exposure value as noted in parenthesis in the figure is given to each rectangle. (b) Partitioned pattern with 21 rectangles that are obtained using the algorithm described in Section II, Note the relative incident electron exposures for each of the rectangles computed using the self-consistent algorithm.

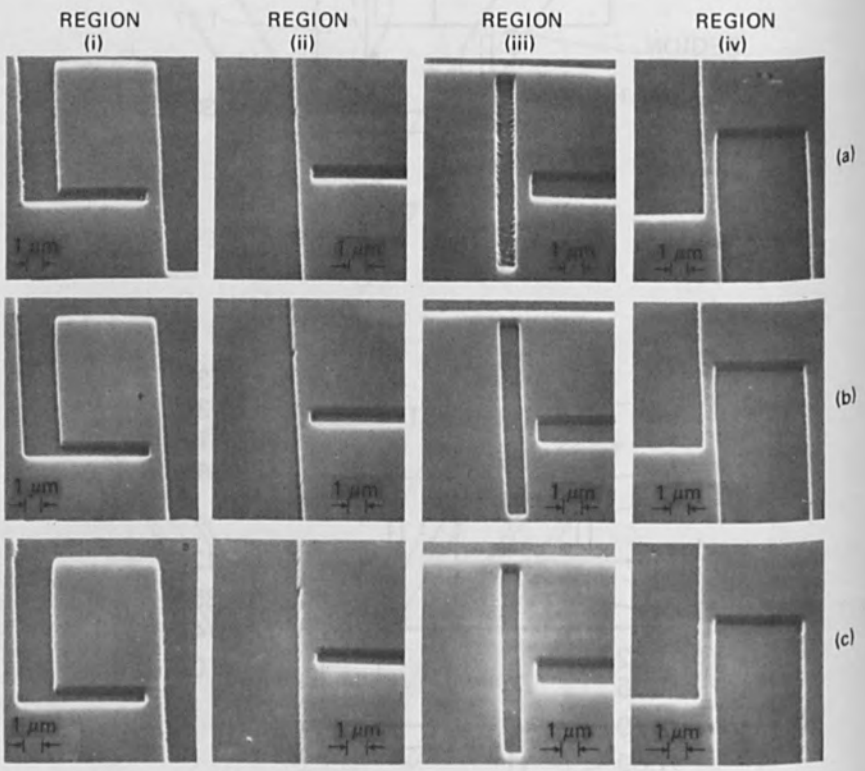

Figure 3. Scanning electron micrographs of the four regions noted in Fig. 2 under three different conditions: (a) Uncorrected pattern, (b) Corrected pattern with the 8 rectangles, each exposed with the relative exposures as noted in Fig. 2, (c) Corrected partitioned pattern with 21 rectangles, each exposed with relative exposures as noted in Fig. 2b. See text for discussions on the micrographs.

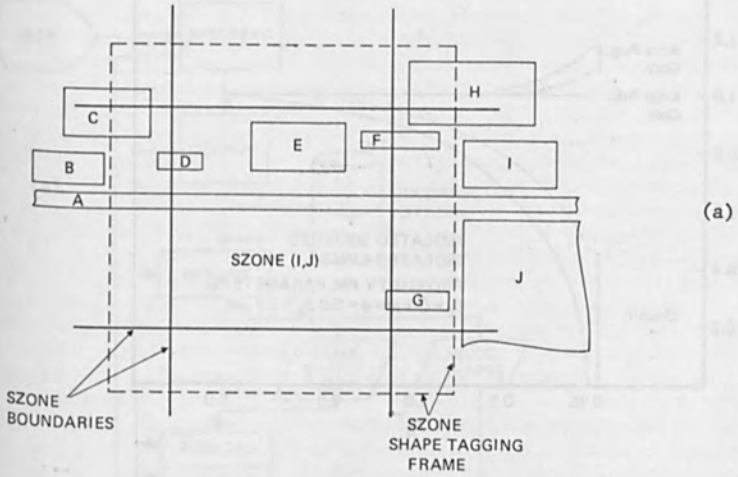

(a)

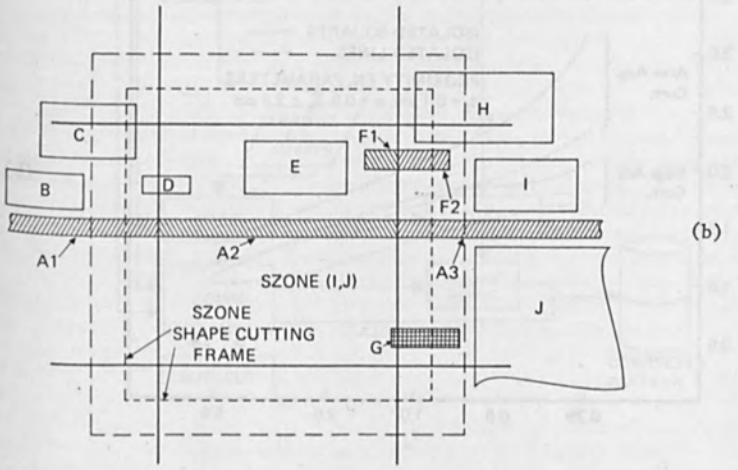

(b)

Figure 4. (a) Ten shapes that lie in and around the Zone (I,J). (b) Corresponding thirteen shapes obtained after partitioning according to the algorithm in Section III.

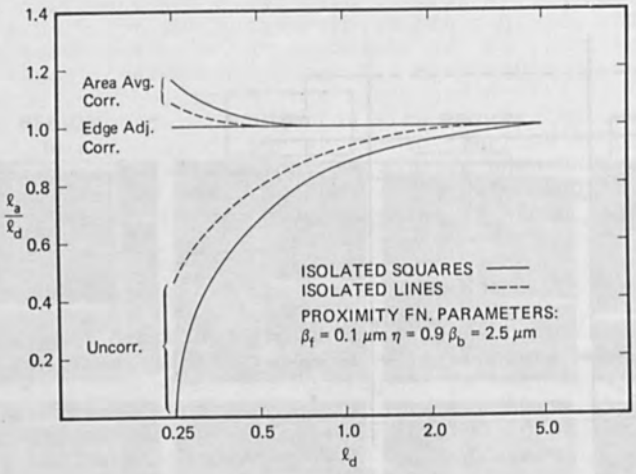

(a)

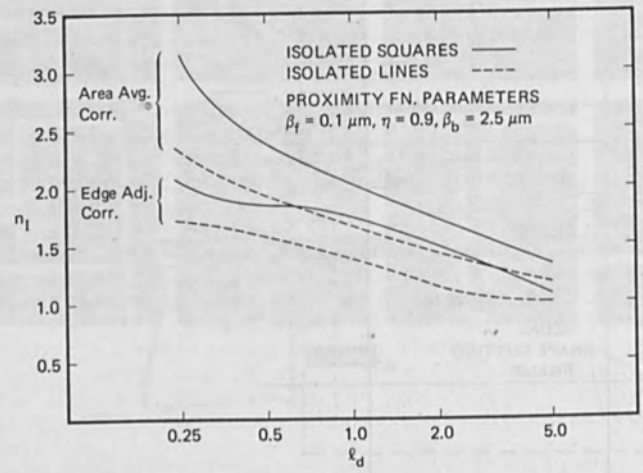

(b)

Figure 5. (a) Dimensional deviation (ℓ_a/ℓ_d) for isolated squares and lines of widths ℓ_d in the case of the uncorrected patterns and of corrected patterns via (i) the self-consistent (area avg. corr.) and (ii) the edge compensation algorithm of Section IV (edge adj. corr.). (b) Corresponding relative incident electron exposures n_I.

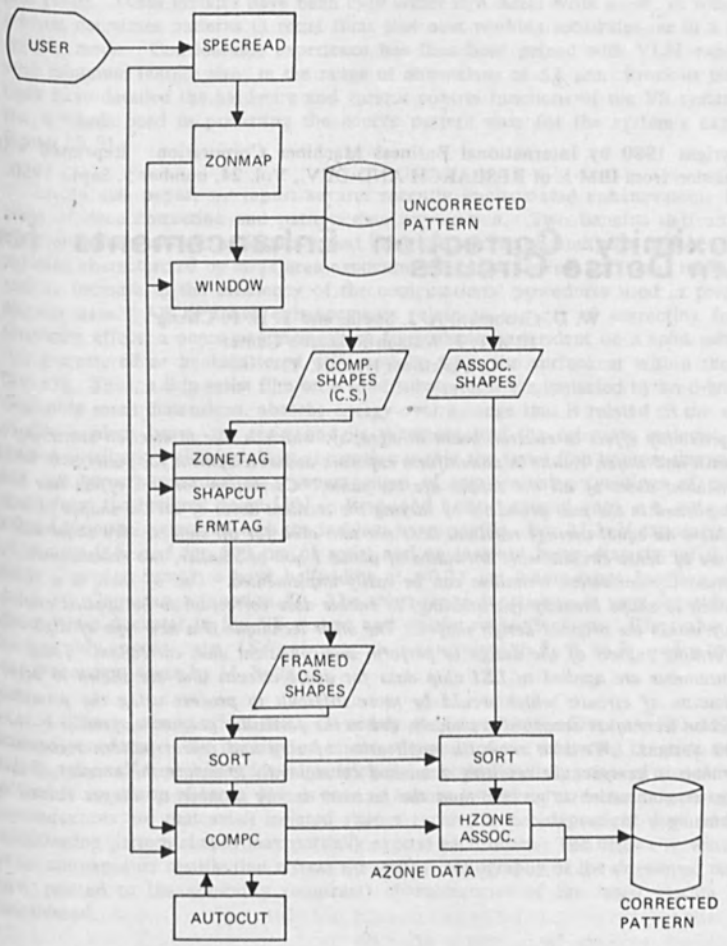

Figure 6. Flowchart to SPECTRE. See text for explanation of individual programs.

Proximity Correction Enhancements for 1-μm Dense Circuits

W. D. Grobman, A. J. Speth, and T. H. P. Chang
IBM T. J. Watson Research Center
Yorktown Hts., N. Y.

The proximity effect in electron beam lithography, which is due to electron scattering in the resist and wafer, results in nonuniform exposure and development for patterns in which the incident doses of all the shapes are the same. Correction for this effect has been accomplished in the past primarily by varying the incident doses of all the shapes in order to achieve an equal average resultant dose per unit area for all shapes. We show that in the case of dense circuits with linewidths of about 1 μm or smaller, two enhancements to the proximity correction technique can be easily implemented. One of these is a simple approach to shape breakup (partitioning) to enable dose correction to be applied nonuniformly within the original design shapes. The other technique is a new type of algorithm for forming subsets of the design to perform self-consistent dose correction. These two enhancements are applied to LSI chip data for dense circuits and are shown to permit fabrication of circuits which would be more difficult to process using the proximity correction techniques described previously, due to the particular geometries present in these circuit designs. We also show the application of step and repeat pattern recognition algorithms to compact the resulting data, and consequently to reduce the amount of data by an amount which is greater than the increase in the number of shapes caused by partitioning.

Introduction

IBM Vector Scan (VS) electron beam (e-beam) systems have been used as the lithographic tools in several research programs involving silicon and bubble technologies [1–6]. These systems have been used either in a direct-write mode, in which the e-beam delineates patterns in resist films that coat working substrates, or in a mask-making mode. Considerable experience has thus been gained with VLSI exposures with minimum feature sizes in the range of dimensions of $\lesssim 1$ μm. Previous publications have detailed the hardware and various control functions of the VS system and the methods used in preparing the source pattern data for the system's exposure format [7–9].

In this paper, we report several recently implemented enhancements in the areas of dose correction and pattern data preparation. Two benefits derived from these enhancements are an improvement in development uniformity for high-resolution patterns characterized by large area exposures separated by fine ($\lesssim 1$ μm) resist gaps, and an increase in the efficiency of the computational procedures used in preparing pattern data. All of these enhancements relate to aspects of correcting for the proximity effect, a phenomenon resulting from electrons incident on a solid substrate being scattered or backscattered differentially from the surface or within the bulk [10–17]. Thus, a thin resist film on a solid substrate, when impacted by an e-beam of negligibly small dimensions, absorbs energy over a range that is related to the energy of the incident beam, the resist and its thickness, and the substrate material. The spatial distribution of this energy absorption within the resist film is three-dimensional but can be approximated as a superposition of two Gaussian functions of position away from the incident beam [13] (a long- and a short-ranged one), *e.g.*, as a point-spread function convolved with the incident beam profile. For 25-keV exposures on Si substrates [16] and for 600 nm of resist and an incident beam diameter of 0.1 μm, these Gaussian functions have halfwidths of ≈ 0.25 μm (short-range function α) and ≈ 2.5 μm (long-range function β). The short-range function α is very dependent on the e-beam diameter in the VS system and on the resist thickness. The value given here is only approximate. [*Editor's note*: α is equivalent to β_f, β, to β_b, and η to η_E in the preceeding paper by M. Parikh.]

The proximity effect has been widely considered in the literature [10–17] from two points of view: the description or measurement of the scattering function and the development of approaches for minimizing the practical consequences of the proximity effect. If a uniform electron dose is used to expose patterns, two commonly recognized consequences are that small isolated shapes receive a size-dependent dose and that neighboring pattern shapes may partially expose each other. The degree to which the resultant exposure distribution affects the surface topography of the developed resist is also related to the solubility (contrast) characteristics of the resist system being considered.

A widely recognized method for the compensation of proximity effects is to correct the incident dose of each shape in a pattern. A computer algorithm (Refs. 14a, 14b) has been developed to compute these corrections in a self-consistent manner for vector-scan (VS) systems. This procedure adjusts the incident dose for each shape so that the resultant average exposure within the boundary of each shape is the same. In order to calculate the doses, shapes are first collected into groups (see left-hand side of Fig. 1). The individual shape doses are translated by the system's pattern generator into a clock frequency, which determines the scanning "fill-in" period for each shape. This procedure has had wide success in the correction of patterns comprised of small exposed regions in the resist (*e.g.*, bubble memory [6], FET circuits [4]). However, in the case of patterns requiring large exposed regions separated by

small resist gaps, the enhancements described in this paper, modifications to the SPECTRE program, are quite important; they are summarized on the right side of Fig. 1. Both approaches operate on identical files of primitive shapes, each compatible in size and geometric type to VS system requirements. The left-hand path provides only for the adjustment of the exposure level of each input shape. The right-hand path performs some similar functions, but first breaks up ("partitions") many of the input shapes. In addition, the right-hand path contains a number of enhancements that allow the computation time to be significantly reduced compared to earlier software, as well as provide for compaction of the output data file and additional dose modification at the center of large shapes.

Enhancements for dense 1-μm circuits

• *Shape partitioning with increased dose at shape centers*

To date, most emphasis on the proximity effect problem has been directed toward correcting exposure levels of small shapes, *i.e.*, those whose smallest dimension is less than the size of the long-range (backscatter) Gaussian function. Shapes whose dimensions are in the range 0.5–2 μm would normally fit into this class. This approach has been reasonable since the experimental exposure and resist development process is normally tailored toward establishing dimensional fidelity of the smallest, and thus most critically sized, detail. However, the exposure distribution within large shapes varies strongly as a function of position, which compromises proper dose correction if the only degrees of freedom are the individual doses for the original shapes. This deficiency becomes critical in cases where narrow gaps ($\lesssim$1 μm) between large shapes are to be accurately delineated.

It has been found that improvements in resist development characteristics can be achieved by partitioning large shapes to better control the effective incident exposure profiles. Such an approach is sketched in Fig. 2, which shows a simple device consisting of two large shapes separated by a 1-μm gap. Figure 2(a) shows the original design version of this device, while Fig. 2(c) shows the device after partitioning. If proximity correction is applied to the two shapes in Fig. 2(a), the resultant dose near the gap is very different from that of the outer edges, as is shown for this shape printed in partially-developed resist in Fig. 2(b). The partitioned design in Fig 2(c) permits proximity correction to adjust the doses in these areas properly, leading to more uniform resist development [see Fig. 2(d)]. Without this simple change in the design, the device is very difficult (or impossible) to process properly. A similar partitioning approach has been developed separately and independently [15].

Figures 3(a)–(d) illustrate the somewhat more general case of a 6-μm-wide line separated by 1 μm from a 1-μm line. Using the same scattering parameters as for Figs. 2(b) and (d) but with α = 0.33 μm, absorbed energy distributions are shown for four distinct situations. Each case also shows a resist solubility distribution. The latter assumes a positive resist and an exposure level for which the solubility-exposure relationship is a square law. This condition is often close to the practical case [16, 17].

Figure 3(a) shows these distributions for the case in which the lines receive the same incident dose per unit area (no dose correction). Here, it is apparent that the 6-μm line will "develop out" well before the 1-μm line. Figure 3(b) shows the result of applying proximity correction without pattern partitioning. The correction increases the incident dose of the narrow line relative to that of the wide line. The facility for tight dimensional control of the narrow line's width is lost because of the continued development required to fully develop the edges of the 6-μm line. In Fig. 3(c), the wide line is partitioned with 1-μm borders, and then the usual dose correction

program is applied. The dose in the edge region of the wide line is now uniform and nominally equal to that of the narrow line. Thus, all edges develop at approximately the same rate. However, although the most critical part of the pattern (the edges) are successfully treated; the development of the edges of the center of the wide line (dips in dose *vs.* x at about 1.3 and 4.6 μm) governs the development time, since only the *average* of this shape is correct. This problem substantially narrows the development process window because additional development of the pattern required to remove all resist in this region results in over development of the edges of the shape.

Finally, in Fig. 3(d) we artificially "override" by 15% the calculated dose-corrected value for the exposure of the central region. Both the edge region and the central area of the large stripe are now seen to have a relatively uniform exposure and thus, "develop out" uniformly. Control of the development time can thus be determined by the most critical features, the fine detail.

This approach is now used in processing all patterns. Any rectangular shape whose x and y dimensions both exceed some threshold width (presently 2-μm) is broken into four perimeter shapes of 1-μm width and one central shape. Shapes with x or y dimensions <2 μm are not altered. After dose correction, shapes which are >2 μm in both dimensions are recognized to be "center" shapes, and their doses are replaced by 1.15 times the nominal dose (see Fig. 1).

For dense circuits, this partitioning approach is quite successful in producing uniform development, which is the key to successful processing. Figure 4 demonstrates this point. Resist patterns that are almost totally developed are shown both for the case of non-partitioned and partitioned patterns. In these circuits, dose correction has been applied in the same manner to both patterns. These patterns demonstrate the utility of partitioning in achieving uniform resist development at the edges of shapes, which are the most critical areas. They also show the importance of breaking up shapes before dose correction for significant classes of circuit patterns.

• *New proximity correction shape-grouping algorithm*

Another enhancement we have made is in the portion of the dose correction technique that groups patterns into subfields to improve the efficiency of the computation of doses. Figures 5(a)–(c) illustrate aspects of the scheme used in Ref. [14c], while Fig. 5(d) illustrates our technique. Figure 5(a) is a schematic representation of a small portion of a chip in which there are areas densely populated with small shapes (*e.g.*, memory arrays) as well as areas in which long shapes predominate (*e.g.*, support circuits). In order to calculate the self-consistent proximity effect of all the shapes on one another, shapes belonging to "subzones" of the chip are grouped together and then the interactions between all the shapes in each subzone are calculated. As is indicated in Fig. 5(a), subzones are defined by an arbitrary coarse grid on top of the design, and shapes are defined to belong to a subzone if the lower left corner of the shape is within the subzone. Two typical subzones (labeled I, J and I′, J′) are shown with shapes belonging to them shaded. Before calculating the effects of all the shapes in a subzone on one another, it is important to consider the effects of shapes not belonging to the subzone of current interest but having an effect on its shapes.

Figure 5(b) shows the implementation of Ref. [14c] for including such neighboring shapes. A frame is drawn around a subzone of interest and shapes not in the subzone but having a vertex within the frame are included in the calculation. The frame size is the same for every subzone in the chip, and is an input parameter to the computer program. For the frame size shown, the dense pattern of small shapes in subzone (I, J) has neighboring shapes properly accounted for in calculating the doses;

however, the (I′, J′) subzone has one long shape that extends far outside of the frame associated with it. The interaction of this shape with others thus cannot be properly calculated.

Figures 5(c) shows solutions to this problem achieved by simply changing the frame dimensions to very large ones. Then, long shapes extending far from their subzone can have their dose properly calculated. However, this approach suffers the serious disadvantage that its central processing unit (CPU) time efficiency is low. The enlargement of the frame dimension incorporates many shapes that often have no effect on the shapes of interest into the calculation of the (I′, J′) subzone shape doses. In dense memory areas this approach has brought a great many more shapes into the calculation and many of these are not required at all [see A in Fig. 5(c)]. In attempting to properly calculate the doses for subzone (I′, J′) in this example, one has unnecessarily increased the size of the (I, J) subzone calculation by a large factor.

We have developed a new algorithm for incorporating shapes associated with those in a particular subzone. In the shape-grouping step of the calculation, we first find all the shapes in a particular subzone, and then generate for each subzone a frame that is tailored to the requirements of the shapes it contains; see Fig. 5(d). The frame has been constructed so that it is the smallest rectangle that includes all of the shapes of the subzone of interest. This rectangle is expanded slightly beyond the range of the proximity effect (typically ≈ 5 μm). This technique properly calculates the effect of neighboring shapes belonging to a particular subzone in a manner independent of other subzones. In this way, CPU time is decreased while the effects of all shapes on one another are properly calculated. The implementation of this new algorithm has been instrumental in reducing CPU time for large-chip postprocessing. It also prevents errors which the original scheme makes if improper subzone and frame sizes are chosen when running the dose correction program.

• *Dose "blurring" and data compaction*

One additional data manipulation has been used to compact the data (see Fig. 1) and thereby reduce the size of the data set produced by the partitioning software. A great deal of the data for dense circuits can be represented as regular rectangular repeats of a given shape ("step and repeats" of the shape). In the VS systems, the pattern generator [18, 19] contains hard-wired circuits that can accept a step-and-repeat command and execute a subsequent e-beam write of a step-and-repeat pattern. By using software that recognizes step-and-repeated shapes in the pattern data flow, the final circuit data, formatted for the VS e-beam machine, can be greatly compacted. This procedure is discussed in detail in Ref. [19].

This approach has been applied to partitioned circuits written on the VS system and has resulted in a factor of two to four data-volume improvement. However, to ensure significant compaction, the doses resulting from proximity correction (which calculates doses to 1 part in 1000 precision) must be made more coarse-ranged. This step is required so that large blocks of shapes that differ only slightly in dose can be treated as having the same final written dose, thus permitting the step-and-repeat pattern recognition technique [19] to be used to obtain significant compaction. This "blurring" of shape doses is done in such a way that dose steps are of the order of a few percent. This is still fine enough so that proximity correction is properly implemented but is coarse enough to permit significant data compaction to be achieved.

Summary

We have described here two changes for improving proximity correction calculations. One of these is a simple technique for breaking up individual shapes before dose correction, in order to permit dose correction to more flexibly tailor dose *vs.* position. Such an approach is especially needed in the case in which fine resist features are to remain, separating larger exposed areas. Such an approach has not been needed for devices produced from exposing small individual devices (Refs. [4, 6]), but it is needed in other types of patterns such as those in which subtractive etching is used rather than lift-off or plating. This approach may, however, lead to a significant increase in the size of the pattern data set. There are potentially more sophisticated algorithms which "look for" areas requiring partitioning, based on a calculation of geometrical areas that would benefit from shape breakup [20]. However, such shape-shape interaction calculations are lengthy. The simple scheme presented here is thus an attractive alternate approach to this problem.

We have also presented here for the first time a new approach to grouping shapes prior to dose corrections. This approach is potentially much more efficient in CPU time than previously reported schemes and is not subject to errors caused by a choice of parameters which do not fit properly with a particular design.

Finally, we have made these changes along with others which further improve dose distribution and compact the resulting data. These new approaches to proximity effect correction not only increase the ease with which resist is processed, but also improve the linewidth control.

Acknowledgments

The technical assistance of K. Murphy, T. Donohue, H. Luhn, J. Powers, and H. Voelker, is gratefully acknowledged. We have had useful discussions with many people including B. Crowder, C. Osburn, and T. W. Studwell.

References

1. H. N. Yu, R. H. Dennard, T. H. P. Chang, C. M. Osburn, V. DiLonardo, and H. E. Luhn, "Fabrication of a Miniature 8K-bit Memory Chip using Electron Beam Exposure," *J. Vac. Sci. Technol.* **12**, 1297 (1975).
2. H. N. Yu, A. Reisman, C. M. Osburn, and D. L. Critchlow, "1 Micron MOSFET VLSI Technology: Part I – An Overview," *IEEE J. Solid-State Circuits* **SC-14**, 240 (1979).
3. W. R. Hunter, L. Ephrath, W. D. Grobman, C. M. Osburn, B. L. Crowder, A. Cramer, and H. E. Luhn, "1 Micron MOSFET VLSI Technology: Part V – A Single-Level Polysilicon Technology Using Electron Beam Lithography," *IEEE J. Solid-State Circuits* **SC-14**, 240 (1979).
4. W. D. Grobman, H. E. Luhn, T. P. Donohue, A. J. Speth, A. Wilson, M. Hatzakis, and T. H. P. Chang, "1 μm MOSFET VLSI Technology: Part VI–Electron Beam Lithography," *IEEE J. Solid-State Circuits* **SC-14**, 282 (1979), and *IEEE Trans. Electr. Dev.* **ED-26**, 360 (1979).
5. T. H. P. Chang, M. Hatzakis, A. D. Wilson, A. J. Speth, A. Kern, and H. Luhn, "Scanning Electron Beam Lithography for Fabrication of Magnetic Bubble Circuits," *IBM J. Res. Develop.* **20**, 376 (1976).
6. D. C. Hofer, J. V. Powers, and W. D. Grobman, "X-Ray Lithographic Patterning of Magnetic Bubble Devices with Submicron Dimensions," *Proceedings of the Fifteenth Symposium on Electron, Ion , and Laser Beam Technology*, Boston, MA, May 29–June 1, 1979, T. H. P. Chang, Ed., American Vacuum Society, American Institute of Physics, New York, to be published.

7. A. J. Speth, A. D. Wilson, A. Kern, and T. H. P. Chang, "Electron Beam Lithography using Vector Scan Techniques," *J. Vac. Sci. Technol.* **12**, 1235 (1975).
8. T. H. P. Chang, A. D. Wilson, A. J. Speth, and C. H. Ting, "Vector Scan I: An Automated Electron Beam System for High Resolution Lithography," *Proceedings of the Seventh International Conference on Electron and Ion Beam Science and Technology*, Washington, DC, May 1976, R. Bakish, Ed., The Electrochemical Society, Princeton, NJ, 1976, p. 392.
9. T. H. P. Chang, A. J. Speth, C. H. Ting, R. Viswanathan, M. Parikh, and E. Munro, "The Probe Forming and Deflection System for the Vector Scan I E/B Lithography System," *loc. cit.*, Ref. [8], p. 377.
10. T. O. Sedgwick, A. N. Broers, and B. J. Agule, "A Novel Method for Fabrication of Ultra-Fine Metal Lines by Electron Beams," *J. Electrochem. Soc.* **119**, 1769 (1972).
11. J. S. Greeneich and T. Van Duzer, "An Exposure Model for Electron Sensitive Resists," *IEEE Trans. Electron Devices* **ED-21**, 286 (1974).
12. D. F. Kyser and K. Murata, "Monte Carlo Simulation of Electron Beam Scattering and Energy Loss in Thin Films on Thick Substrates," *Proccedings of the Sixth International Conference on Electron and Ion Beam Science and Technology*, R. Bakish, Ed., The Electrochemical Society, Princeton, NJ, 1974.
13. T. H. P. Chang, "Proximity Effect in Electron Beam Lithography," *J. Vac. Sci. Technol.* **12**, 1271 (1975).
14. M. Parikh, (a) "Self Consistent Proximity Effect Correction Technique for Resist Exposure (SPECTRE)," *J. Vac. Sci. Technol.* **15**, 931 (1978); (b) "Corrections to Proximity Effects in Electron Beam Lithography. I. Theory, (c) II. Implementation, (d) III. Experiment," (e) "Proximity Effects in Electron Lithography: Magnitude and Correction Techniques," *IBM J. Res. Develop.* **24**, XXX (1980, this issue) and *J. App. Phys.* **50**, 4371, 4378, 4383 (1979).
15. J. H. C. Phang and H. Ahmed, "A New Proximity Effect Correction Method for Accurate Pattern Fidelity," *Proceedings of Microcircuit Engineering '79*, September 1979, Institute of Semiconductor Electronics, Aachen, Germany, to be published.
16. W. D. Grobman and A. J. Speth, "An Exposure Wedge for Electron Beam Lithography Development Control and for the Determination of Resist Development and Proximity Parameters," *Proceedings of the Eighth International Conference on Electron and Ion Beam Science and Technology*, Seattle, WA, May 1978, R. Bakish, Ed., The Electrochemical Society, Princeton, NJ, p. 276. *Proceedings Volume* **78-5**, 276 (1978).
17. A. R. Neureuther, D. F. Kyser, K. Murata, and C. H. Ting, "Electron Beam Resist Line Edge Profile Modeling," *loc. cit.*, Ref. [16], p. 265.
18. A. M. Patlach, P. R. Jaskar and T. W. Studwell, "Electron Beam Lithographic Pattern Generation System," *Proceedings of the Fourteenth Symposium on Electron, Ion, and Laser Beam Technology*, Palo Alto, CA, May 1977, G. L. Varnell and J. L. Bartelt, Eds., American Vacuum Society, American Institute of Physics, New York. See also *J. Vac. Sci. Technol.* **15**, 874 (1978).
19. W. D. Grobman and T. W. Studwell, "Data Compaction and Vector Scan Electron Beam System Performance Improvements using a Novel Algorithm for Recognition of Pattern Step and Repeats," *Proceedings of the Fifteenth Symposium on Electron, Ion, and Laser Beam Technology*, T. H. P. Chang, Ed., Boston, MA, May 29–June 1, 1979, American Vacuum Society, American Institute of Physics, New York, to be published.
20. T. P. Chang, W. D. Grobman, and A. J. Speth, "Partitioning E-Beam Data for Proximity Corrections," *IBM Tech. Disclosure Bull.* **20**, 3809 (1978).

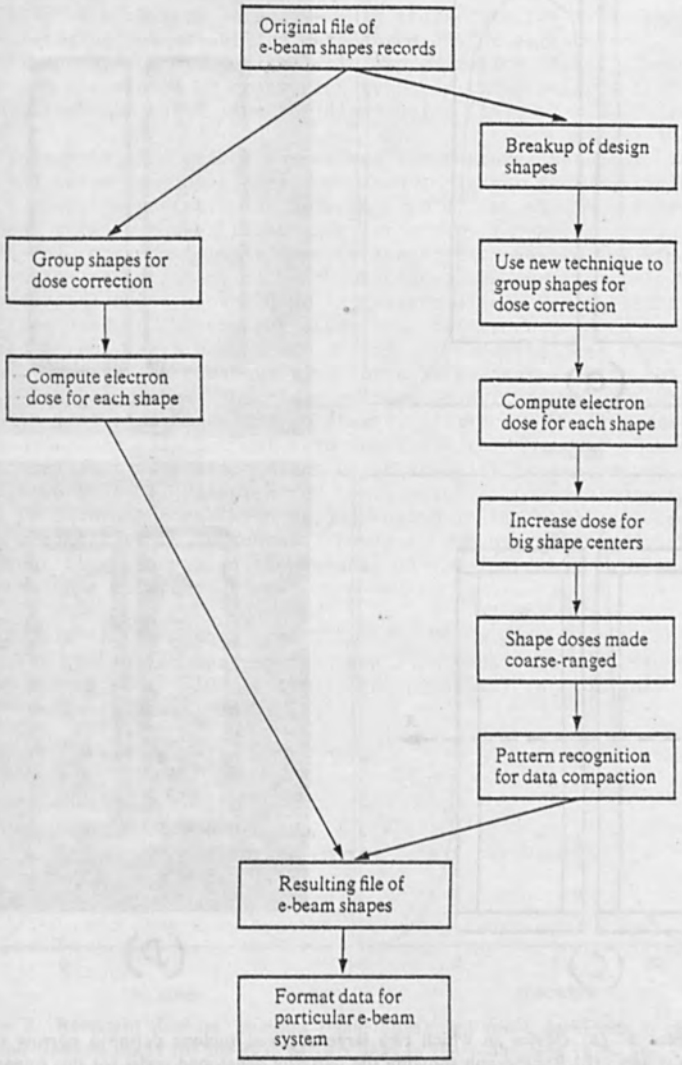

Figure 1 Data processing streams for dose correction scheme without partitioning [14] (left-hand side) and with partitioning (current scheme) (right-hand side).

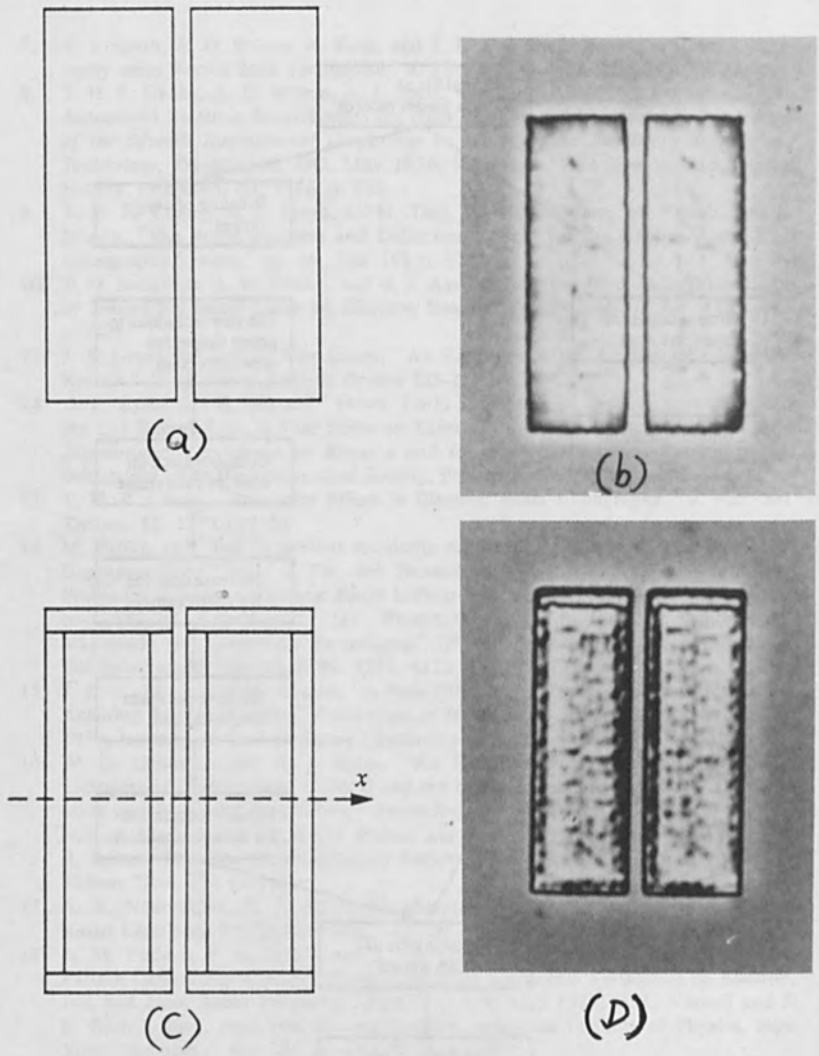

Figure 2 (a) Device in which two large exposed regions define a narrow ($\lesssim$1-μm) resist gap. (b) Photograph showing the partially developed resist for this unpartitioned case. (c) Same device design, but partitioned according to the scheme of the present paper. This permits the dose correction scheme of Ref. [14] to more uniformly tailor the dose received by the resist. (d) Photograph showing the partially developed resist for this partitioned case.

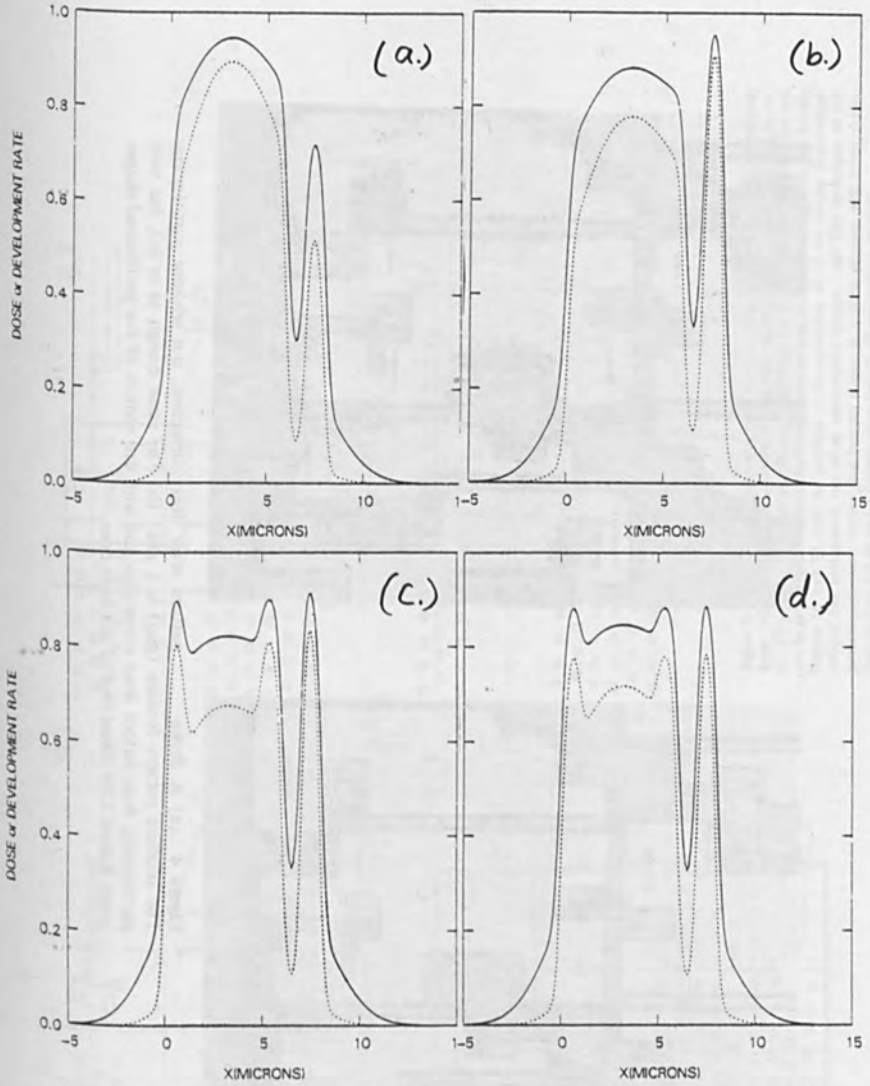

Figure 3 Resultant dose *vs.* position (solid lines) and resist development rate *vs.* position (dashed lines) for the case of two lines in the y direction (a 6- and a 1-μm line), separated by 1 μm. The electron scattering parameters used were $\alpha = 0.33$ μm, $\beta = 2.35$ μm, $\eta = 0.86$ μm. (η is the ratio of the deposited energies from the short-range and long-range components.) (a) Case where dose is uncorrected; (b) dose correction of the original design; (c) dose correction after partitioning; and (d) dose correction after partitioning, but with the center shape given 1.15 times the nominal dose.

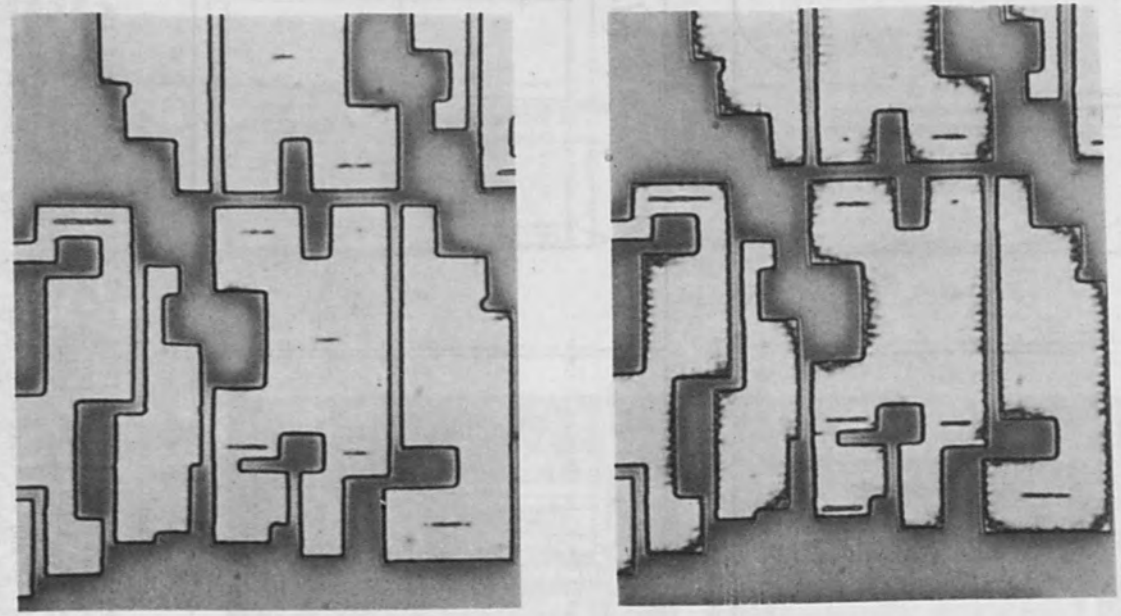

Figure 4 (a) A dense pattern after dose correction, but without partitioning. The smallest pattern feature (gap) is 1 μm. (b) The same design as in (a), but with partitioning done before dose correction and with the centers of the partitioned shapes given a dose 1.15 times that of the base dose.

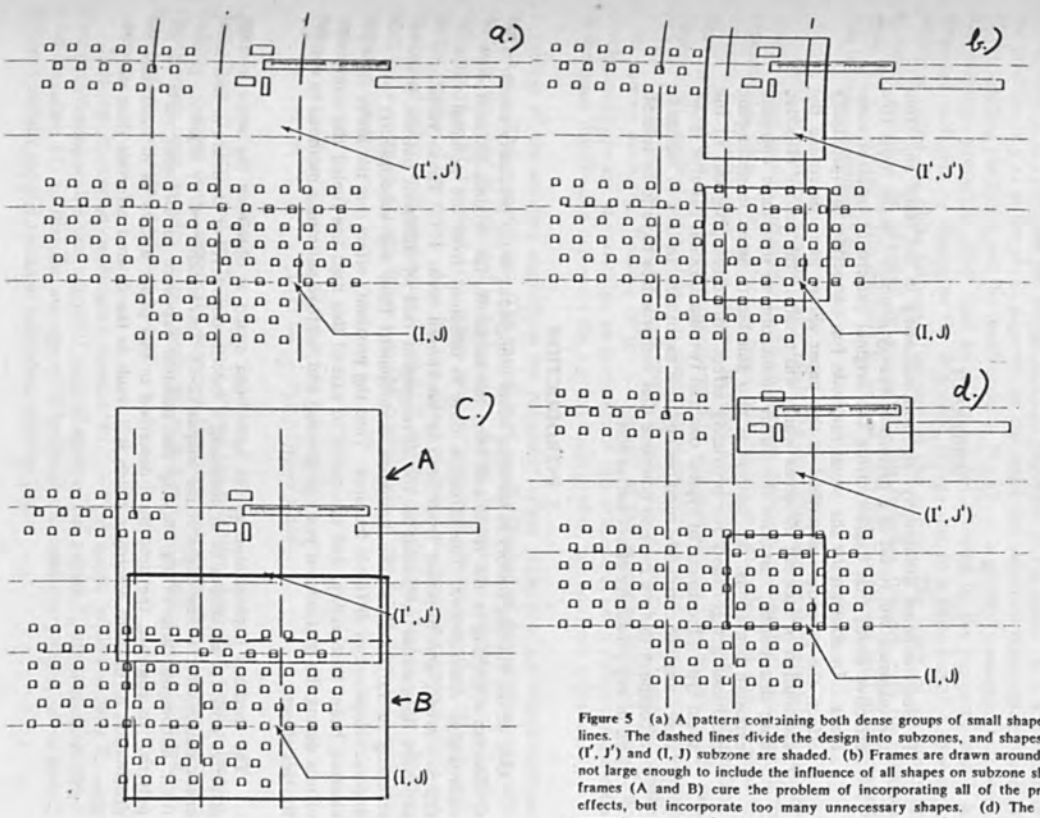

Figure 5 (a) A pattern containing both dense groups of small shapes and sparse long lines. The dashed lines divide the design into subzones, and shapes belonging to the (I', J') and (I, J) subzone are shaded. (b) Frames are drawn around subzones but are not large enough to include the influence of all shapes on subzone shapes. (c) Larger frames (A and B) cure the problem of incorporating all of the proper shape-shape effects, but incorporate too many unnecessary shapes. (d) The technique of the present paper uses frames that interact shapes in a given subzone with fewer shapes than in 5(c), but in such a manner as to include all interactions properly.

A NOVEL APPROACH TO PROXIMITY EFFECT CORRECTION

Dieter P. Kern

IBM Thomas J. Watson Research Center
Yorktown Heights, New York 10598

ABSTRACT

In electron-beam lithography, electron scattering in the resist and from the substrate will result in a pattern of energy deposited in the resist (the effective dose) that deviates from the original pattern of incident electrons. In contrast to the usual methods for correcting this proximity effect, the procedure described in this paper allows us to determine the distribution of incident electrons which will result in the desired effective dose distribution. Besides the direct application to determine optimum exposure conditions, the method is also suitable to assist in developing partitioning algorithms for proximity effect correction programs of the usual type. Treatment of typical one and two dimensional patterns shows that complete correction requires negative exposures. In lack of means to accomplish this we have to conclude that compromises have to be tolerated in any proximity effect correction.

I. INTRODUCTION

One of the limiting factors in electron beam lithography is the proximity effect. Due to electron scattering in the resist and from the substrate, the original incident dose of electrons is redistributed. The effective dose is different from the nominal value in exposed areas, and different from zero in unexposed areas (1). These variations in exposure dose cause variations in the development rate of different pattern features, resulting in variations of the optimum development time and subsequently over- or underdevelopment of different features. Thus the proximity effect sets the lower limit for electron beam lithography, and the desire to extend this limit has fueled the continuing efforts during the past several years to develop and improve patterning methods to correct for this effect.

The methods implemented so far have been aimed at obtaining the same average effective dose for all shapes or at obtaining a specific dose level at contours or individual check points close to the edges of the shapes (2-4). This is achieved by adjusting geometrical dimensions and/or by varying the nominal exposure in different parts of the pattern. In contrast, the procedure described in this paper allows us to determine the distribution of incident electrons which will result in the desired effective dose distribution.

II. THEORETICAL MODELS

In electron beam lithography, a layer of resist on a substrate is irradiated with electrons of a given energy. The pattern is defined by the lateral distribution P(x,y) of the incident electrons. These electrons are scattered in the resist and in the substrate from which backscattered electrons can also affect the resist. The solubility of the resist varies according to the amount of energy deposited. So the first step in modeling electron beam lithography is to determine the energy E(x,y,z) deposited in the resist. It is a function of the position (x,y,z) in the resist, depends on the resist and substrate materials, the energy of the incident electrons, and the incident dose, P(x,y). It is generally assumed that resist and substrate properties other than solubility are not affected by the exposure, and it is therefore sufficient to determine the deposited energy due to a delta-function exposure, which is called the point-response function of the system. The result of an arbitrary exposure can then be obtained by convolving this response function with the incident dose P(x,y). Monte Carlo methods as well as analytical models are used in calculating this response function (5,6).

There are several models which relate the deposited energy to the solubility of the resist. These models are mostly based on phenomenological relationships which are fit to experimental data (7-9). Once a given relationship is determined, it can be used to simulate the development of a pattern in resist and provide the resultant resist profiles. Simulations of this type have been performed by different authors for line patterns (a two dimensional problem) as well as two dimensional patterns (a three dimensional problem) (9,10). Using these models, the final result of a specific exposure under specific conditions can be predicted. Because of the complexity of the processes involved and of the development process in particular, an inversion of this procedure, i.e. a direct computation of the input distribution necessary for a given resist profile, has not been achieved.

Most of the existing algorithms for proximity effect correction are established on certain simplified assumptions. The variation of the distribution of deposited energy with depth in the resist is neglected in most cases. A two dimensional distribution of effective dose $E(x,y) = E(\vec{r})$ is used (13), which includes scattering effects as well as development characteristics of the resist. Also for this effective dose a δ–function response, $G(\vec{r})$ can be derived either from experimental data (13) or from simulations (10,14). The effective dose for a complex pattern follows as the convolution of the input dose $P(\vec{r})$ with this response function

$$E(\vec{r}) = \int P(\vec{r}') \, G(\vec{r}-\vec{r}') \, d^2r' \qquad (1)$$

The effect is illustrated in Figure 1. It shows the effective dose that results from a δ–function input dose, namely the response function, and, using this response function, the effective dose resulting from a constant input dose over a square area. The redistribution effect discussed earlier is evident.

Existing correction techinques assume $P(\vec{r}) = P_n = \text{const.}$ within a shape S_n, or after partitioning within the individual parts of shapes. The values P_n are then determined from Equation (1) so that the average of E becomes the same everywhere, or so that E assumes certain specific values at inidvidual check points.

III. CORRECTION ALGORITHM

A new correction algorithm is proposed here based on this effective dose concept. Starting with a desired effective dose derived from the pattern to be produced, the necessary input dose is calculated by deconvolution. The principal situation is the following: the exposure process is described by the dose of incident electrons $P(\vec{r})$ and the response function $G(\vec{r})$, the effective dose is given by the convolution expression of Equation (1). The task then consists of determining the input dose $P(\vec{r})$ which will result in the desired pattern $E(\vec{r}) = E_0$ in exposed areas, $E(\vec{r}) = 0$ in areas not addressed by the beam. Mathematically this means a deconvolution. This can be performed by means of Fourier transformation. The convolution theorem for Fourier transforms states the equivalency between the convolution of two functions and the product of their Fourier transforms. If we define the following set of functions and corresponding transforms:

	functions	transforms
incident dose	$P(\vec{r})$	$p(\vec{q})$
point response	$G(\vec{r})$	$g(\vec{q})$
effective dose	$E(\vec{r})$	$e(\vec{q})$

then the convolution

$$E(\vec{r}) = P(\vec{r}) \otimes G(\vec{r}) \tag{2}$$

is equivalent with the product

$$e(\vec{q}) = p(\vec{q}) \cdot g(\vec{q}) \tag{3}$$

So we have

$$p(\vec{q}) = e(\vec{q}) \,/\, g(\vec{q}) \tag{4}$$

and finally

$$P(\vec{r}) = \int [e(\vec{q}) \,/\, g(\vec{q})] \cdot \exp[-2\pi i\, \vec{q} \cdot \vec{r}]\, d^2q \tag{5}$$

In Equations (4) and (5) problems might arise with the division if $g(\vec{q})$ has zeroes. Also for small values of g, noise (in form of truncation errors) will be amplified. For numerical calculations the Fourier integrals have to be replaced by finite Fourier series, which can result in additional problems. For the type of response function (double Gaussian) which will be used here, these problems do not really occur.

The determination of the ideal input dose is closely analogous to the problem of interpreting images in electron microscopy, e.g. in the case of weak phase objects (12). The phase distribution of the electron wave after passing the object is described by a function $P(\vec{r})$ and its Fourier transform $p(\vec{q})$. In terms of image transfer theory, the

effect of the microscope can be described by a contrast transfer function $k(\vec{q})$ so that the Fourier transform of the image contrast is given by

$$c(\vec{q}) = k(\vec{q}) \cdot p(\vec{q}) \quad , \tag{6}$$

analog to the expression for the transform of the effective dose in Equation (3). Here the contrast transfer function is an oscillating function which complicates the reconstruction of the object phase distribution from electron micrographs. It is actually common practice to associate the resolution limit of a specific microscope with the first zero of the contrast transfer function.

A response function which has been found very useful by a number of authors (e.g. (1,13,14)), and which we shall adopt here is given by

$$G(\vec{r}) = \frac{1}{\pi(1+\eta)} \{\frac{1}{\alpha^2} \exp[-\frac{r^2}{\alpha^2}] + \frac{\eta}{\beta^2} \exp[-\frac{r^2}{\beta^2}]\} \quad . \tag{7}$$

It is a superposition of two Gaussians. The first one, with width-parameter α , describes the small angle scattering events, the second one, with width-parameter β , describes the large angle and backscattering events. η is the ratio of the contributions of these two parts to the total effective dose. This response function has the Fourier transform

$$g(\vec{q}) = \frac{1}{1+\eta} \{ \exp[-\pi^2\alpha^2q^2] + \eta \exp[-\pi^2\beta^2q^2]\} \quad . \tag{8}$$

Thus $g(\vec{q}) \to 0$ only for $|\vec{q}| \to \infty$. Since for numerical calculations we have to use finite Fourier series, i.e. we can perform the calculations only with finite resolution, $g(\vec{q})$ remains nonzero for all practical purposes.

A block diagram of the procedure used to determine the corrected input dose is shown in Figure 2. Starting with a desired effective dose distribution we calculate its Fourier transform. The transformation of the response function (Equation (7)) can be performed analytically (Equation (8)). By division we obtain the transform of the necessary input dose and by performing an inverse Fourier transformation, we finally obtain the input dose distribution which will result in the desired effective dose.

IV. APPLICATION TO TYPICAL PATTERNS

First the algorithm was applied to a few typical examples of line patterns, as shown in Figures 3 - 5 . The upper left picture shows the desired effective dose, namely the dose distribution we would like to obtain after exposure. In order to avoid problems with the use of finite Fourier series this desired dose has been modified by filtering out the highest spatial frequencies. The upper right picture shows the calculated necessary input

dose which will result in the desired effective dose. So the two distributions in the upper graphs are equivalent. The lower left graph shows the effective dose obtained from a uniform dose as distribution of incident electrons. It represents the result of an exposure without any correction. The lower right graph shows the effective dose corresponding to exposure with the corrected input dose with the exception that the negative values have been replaced by zero. In all of the examples these response function parameters have been used: $\alpha = .1\mu m$, $\beta = 1.8\mu m$, and $\eta = 0.8$. These are typical numbers, but their specific values are irrelevant for the type of general conclusions which are to be drawn from this work.

Figure 3 shows the example of a narrow gap between large exposed areas. Uncorrected exposure results in a distribution with a loss of dose close to the gap and an appreciable dose inside the gap. The corrected input dose shows how these effects have to be compensated: by continuously increasing dose towards the edges of the exposed areas and negative exposure inside the gap. Since there are no means for generating negative exposure we can utilize only the positive parts, assuming zero in the gap. This results in a much improved distribution which is slightly overcorrected outside the gap, and the nonzero values in the gap remained.

Figure 4 shows the example of a narrow gap and line close to a large exposed area. Again the corrected input distribution shows increasing dose at the edges of the exposed area and even higher dose for the isolated line and also the negative doses in the gap and at the edges of the unexposed area. Utilizing the positive part of this distribution for exposure at least allows to maintain the desired exposure level in the exposed areas.

A similar situation is found for the example of a narrow line separated by narrow gaps from large exposed areas as shown in Figure 5. This example was used to demonstrate that the continuously varying corrected dose distribution can be successfully approximated by piece-wise constant distributions, e.g. as reported in (15). The left graph in Figure 6 shows in the dashed line the input dose derived from the upper right graph in Figure 5 and the corresponding result after exposure. The width of the edge-area with increased exposure was chosen to $.6\ \beta$. In the right graph the result from exposure with the positive part of the continuously varying distribution is reproduced.

The algorithm was also applied to two dimensional pattern features like a square (Figure 7) and two bars in close vicinity (Figure 8). Again the upper left plots show the desired dose distributions and below them the result of uncorrected exposure is plotted. In both cases there is a considerable loss of dose in the exposed areas which is scattered into the areas not addressed by the beam. The upper right plots show the calculated corrected input distributions. They clearly display the need to increase the dose around the edges and in particular in the corners. Again negative values are required in order to compensate for the dose scattered into the unexposed areas. The lower right plots show the result of exposure with the corrected input neglecting negative values. They indicate the feasibility of correcting for the dose loss in the exposed areas.

V. SUMMARY

For a point response function of the double Gaussian type a computational inversion of the proximity effect problem has been presented. Using Fourier transform techniques,

the input distribution necessary for achieving a desired effective dose is determined by deconvolution. Uniform effective dose inside exposed areas can be obtained by continuous variation of the lateral dose distribution of incident electrons, especially increasing exposure towards the edges and corners of exposed areas. Piece-wise constant approximation of the continuously varying input dose distribution with edge zones of width $.6\,\beta$ yields acceptable results. Negative input dose would be necessary to avoid nonzero dose in areas not directly addressed by the beam. Since there are no means of generating this negative dose, any proximity effect correction method has to accept this compromise.

ACKNOWLEDGEMENTS

Many useful discussions with T.H.P. Chang and W.D. Grobman are gratefully acknowledged.

REFERENCES

(1) T.H.P. Chang, J. Vac. Sci. Technol. 12, 1271 (1975)
(2) M. Parikh, J. Appl. Phys. 50, 4371-4387 (1979)
(3) H.I. Ralph and H. Sewell, Proc. of the 8th International Conference on Electron and Ion Beam Science and Technology 1978, p. 354, ed. R. Bakish
(4) J.C.H. Phang and H. Ahmed, Proc. Microcicuit Engineering '79, p. 219, ed. H. Beneking, Aachen
(5) R. Hawryluk, A. Hawryluk, and H. Smith, J. Appl. Phys. 45, 2552 (1974)
(6) D.F. Kyser, and K. Murata, Proc. of the 6th International Conference on Electron and Ion Beam Science and Technology 1974, p. 205, ed. R. Bakish
(7) M. Hatzakis, C. Ting, and N. Viswanathan, same as (6), p. 542
(8) F. Jones and M. Hatzakis, same as (3), p. 256
(9) J.S. Greeneich, J. Appl. Phys. 45, 5264 (1974)
(10) D. Kyser, D. Schreiber, C. Ting, and R. Pyle, Proc. 9th International Conference on Electron and Ion Beam Science and Technology 1980, ed. R. Bakish
(11) F. Jones, J.R. Paraszczak, and M. Hatzakis, same as (10)
(12) F. Lenz, Electron Microscopy in Material Science, New York (1971)
(13) W.D. Grobman and A.J. Speth, same as (3), p. 276
(14) M. Parikh and D. Kyser, same as (3), p. 371
(15) W.D. Grobman, A.J. Speth, and T.H.P. Chang, same as (10)

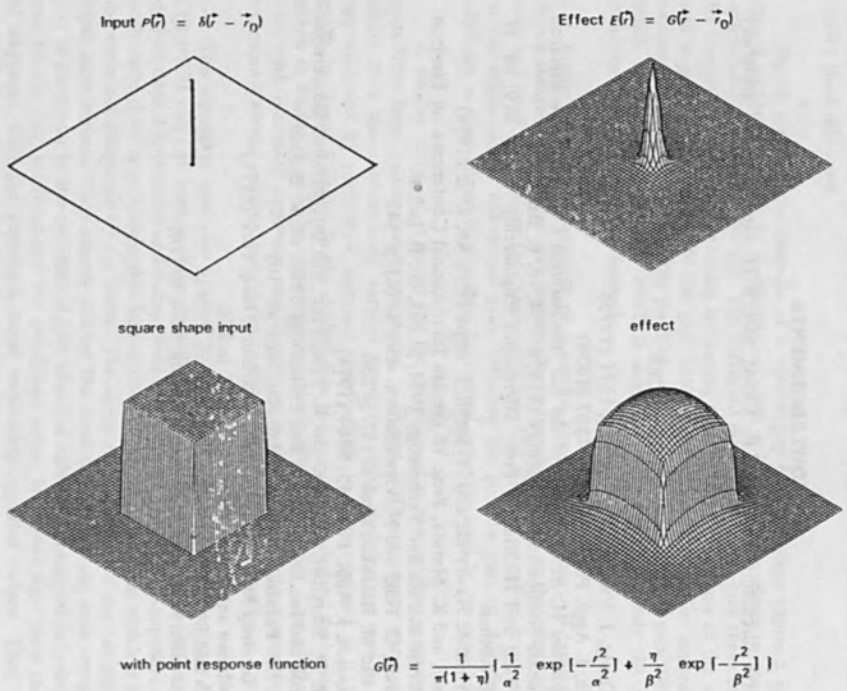

Figure 1: Illustration of scattering events causing proximity effect

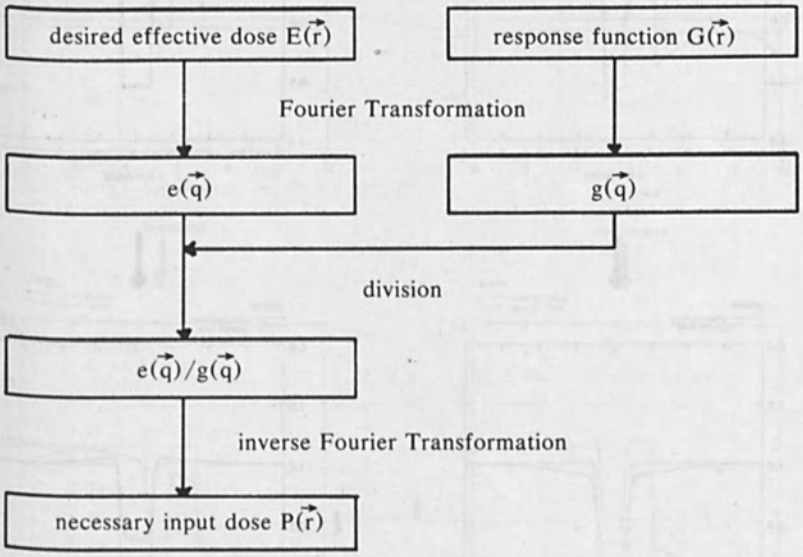

Figure 2: Block diagram of procedure to reconstruct the dose of incident electrons $P(\vec{r})$ resulting in an effective dose $E(\vec{r})$

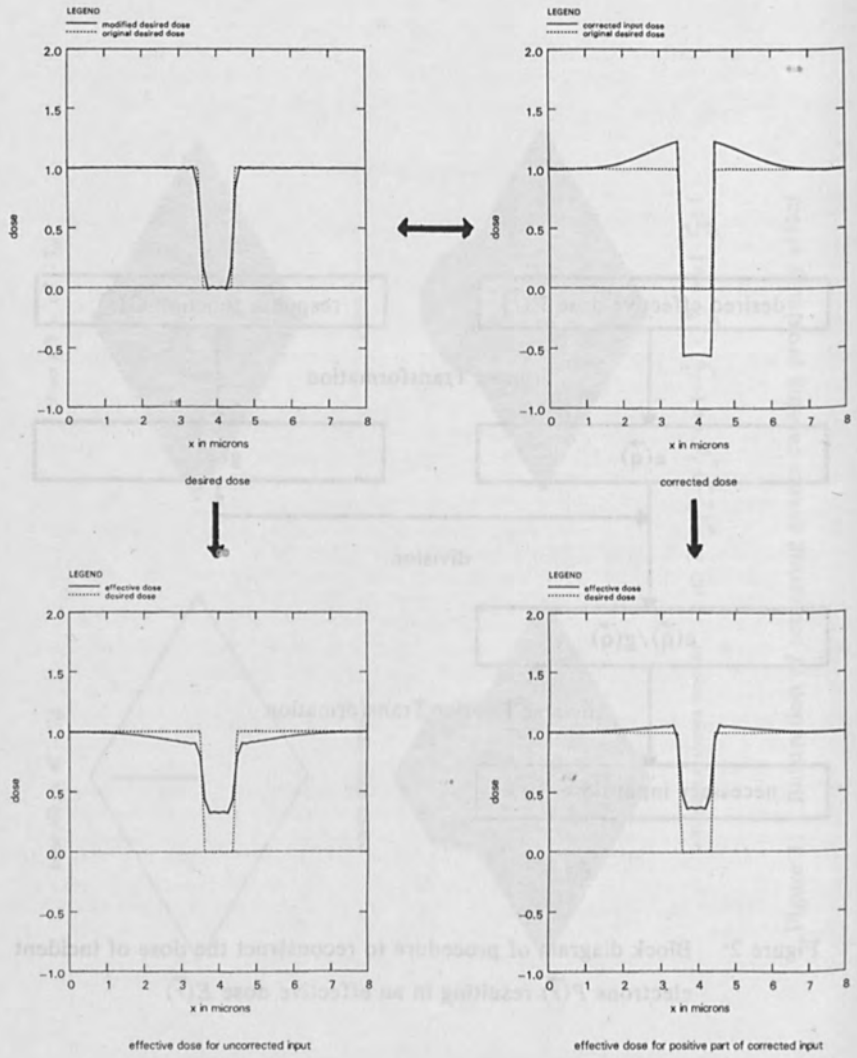

Figure 3: Application of the correction algorithm to a line pattern: gap between large exposed areas

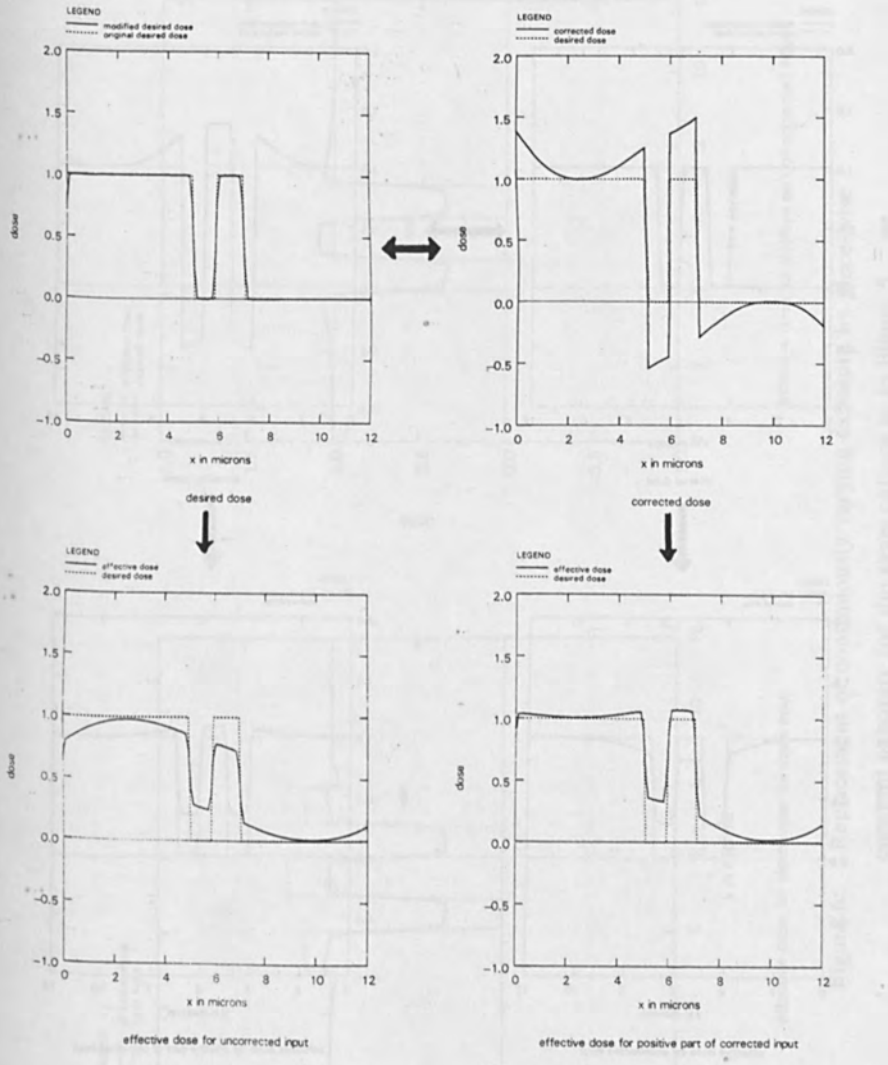

Figure 4: Application of the correction algorithm to a line pattern: narrow line and gap close to large exposed area

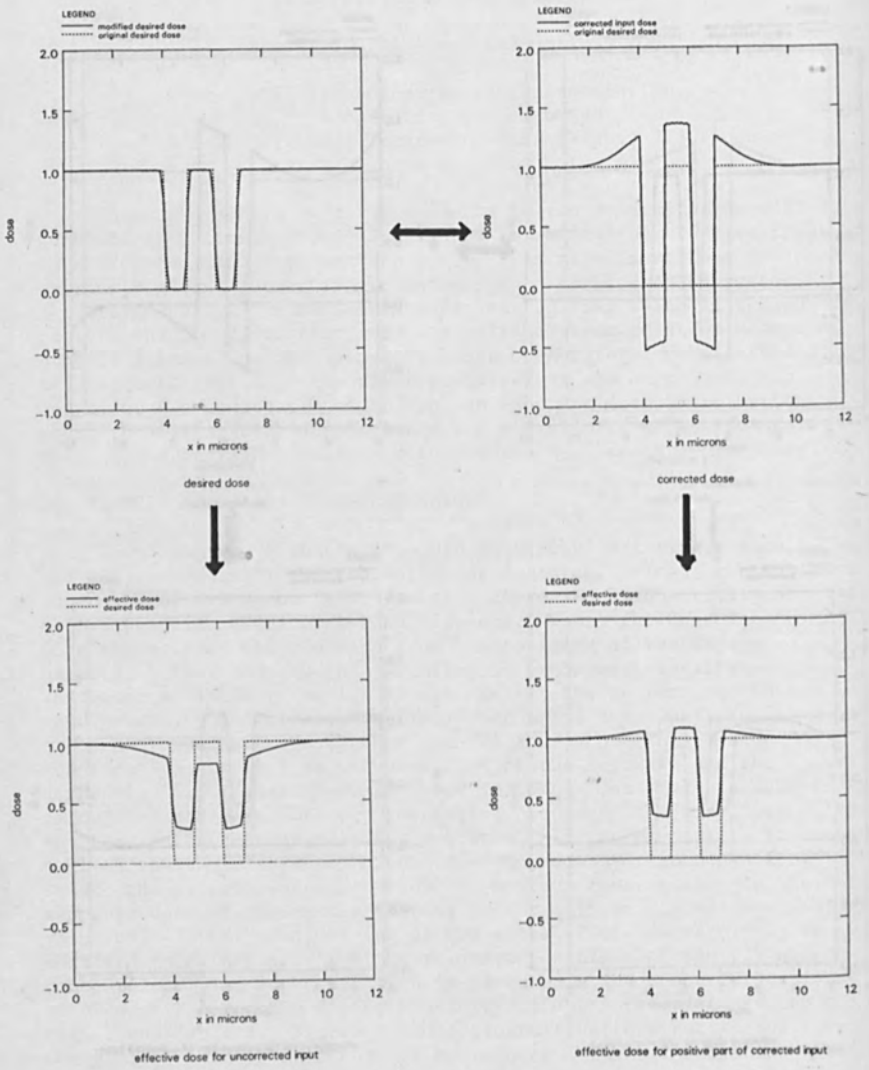

Figure 5: Application of the correction algorithm to a line pattern: narrow line separated by narrow gaps from large exposed areas

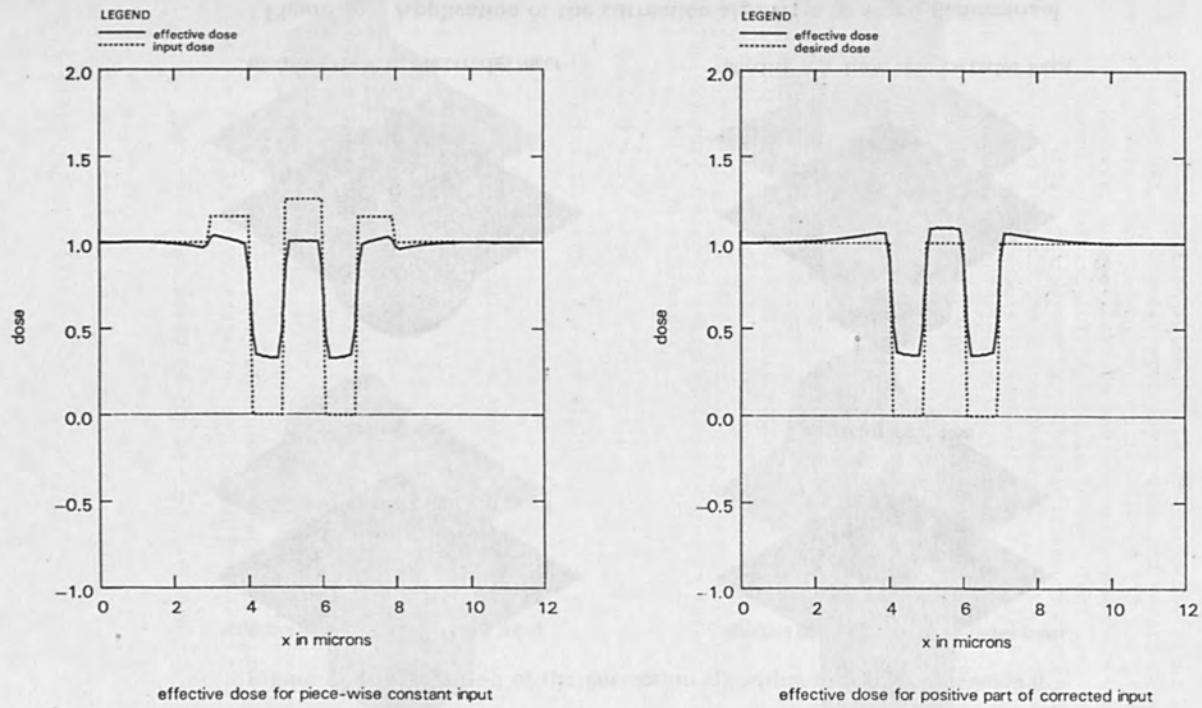

Figure 6: Replacement of continuously varying exposure by piece-wise constant exposure for the same pattern as in Figure 5.

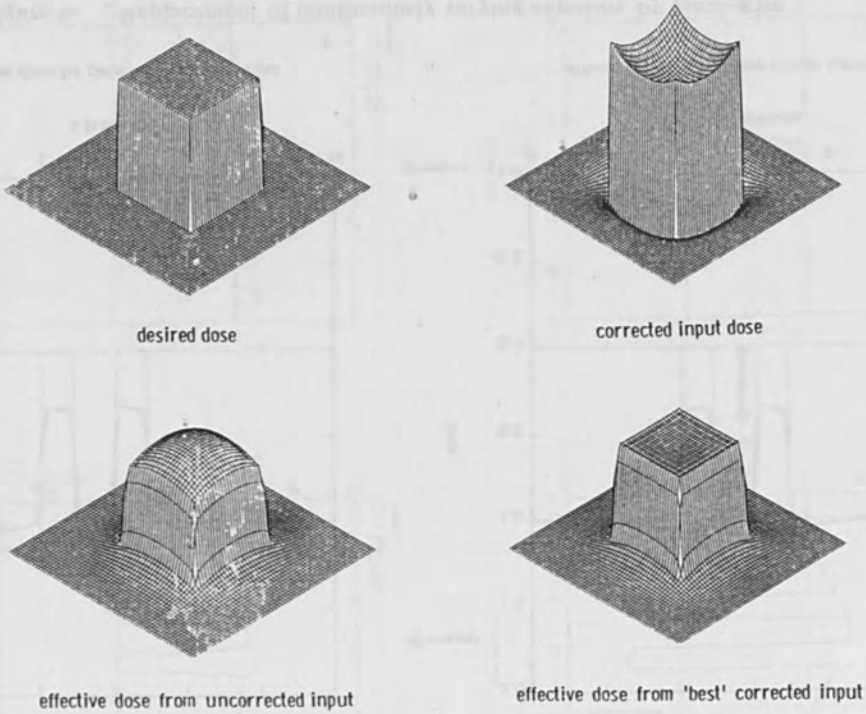

Figure 7: Application of the correction algorithm to a two-dimensional pattern: isolated square

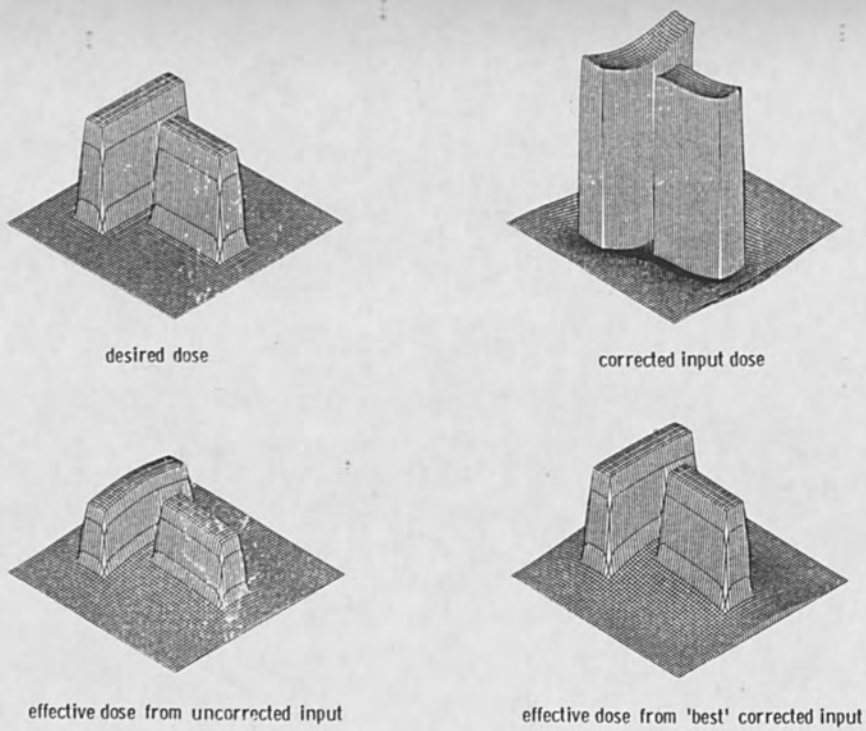

Figure 8: Application of the correction algorithm to a two-dimensional pattern: two bars in close vicinity

Section 4.

Resists and Related Topics.

A METHOD FOR RAPIDLY SCREENING POLYMERS AS ELECTRON-BEAM RESISTS

Robert G. Brault and Leroy J. Miller

Hughes Research Laboratories
3011 Malibu Canyon Road
Malibu, California 90265

ABSTRACT

A rapid, simple screening test to evaluate potential electron-beam resists is described. A matrix of 100 squares was generated by systematically changing dwell time and point spacing at a given beam current. The thickness of the partially developed squares was measured with a Nanospec AFT microarea film thickness gauge. Sensitivity and contrast were determined from plots of normalized thickness versus log E. The sensitivity and contrast of 10 polymethacrylate positive resists and 14 negative resists were determined by this method and are presented.

INTRODUCTION

The search for new, improved electron resists could be greatly facilitated by having methods available for rapidly determining sensitivity (Q) and contrast (γ). Improved sensitivity is necessary to obtain desirable throughput, and good contrast is a necessary (although not a sufficient) condition for achieving high resolution (1). Such a rapid test would be useful not only for screening candidate resists, but also for accelerating subsequent process development, such as the optimization of developer composition, development time, and bake conditions. To evaluate Q and γ accurately, it would be desirable to have a large number of areas exposed at different doses, as many as 50 per decade, in the dose range of interest. The exposed areas should be as small as practical to minimize exposure time. Finally, a rapid, accurate method for measuring the thickness of each area on the developed wafer is needed. This paper describes a test method in which writing the test pattern takes about 30 min and making the required thickness measurements takes about another 30 min.

TEST METHOD

The test pattern consists of a 10 x 10 matrix of squares each 25 μm on a side (see Figure 1). The dosage received by each square is varied systematically by increasing the dwell time linearly along one axis of the matrix and increasing the point spacing linearly along the other. The squares are large enough to eliminate the proximity effect as a variable if the thickness measurement is made at the center, where

the losses due to electron scattering are compensated for by scattering contributions from the surrounding area. Each matrix covers a range of dosages extending over more than two orders of magnitude. By writing two, three, or four such matrices at different beam currents, an extremely wide range of exposures can be obtained with very small dose increments. When different processing procedures are to be tested, several such sets of matrices can be exposed on a single wafer with a single pump-down to achieve further time savings.

After the exposed image has been developed, the sensitivity can be estimated by examining the matrix under a microscope. With positive resists, the squares that are developed out cleanly can easily be identified, and the sensitivity is estimated as the minimum dose required to produce a cleaned-out square. In the case of negative resists, a distinct value for the sensitivity cannot be determined by simple visual examination, since the sensitivity is generally taken as the dose required to produce an image with a thickness that is some specific fraction of the thickness of the undeveloped resist.

A plot of the normalized thickness (t_N) versus the log of the exposure (log E) is a more convenient and accurate method for determining both sensitivity and contrast of both positive and negative resists. This plot requires knowing the thickness of the residual resist in underexposed squares. But since the squares are too small to allow the thickness to be measured easily by a mechanical stylus technique, we investigated using a Nanospec AFT microarea film thickness gauge for this purpose (2). This instrument measures thickness by recording the spectrum of visible light reflected from the coated silicon wafer and comparing it with standard data previously recorded for similar films and stored in memory. Its unique advantage is that it can measure the thickness of extremely small areas, the minimum spot size being 3.5 μm in diameter. For our purposes, a spot diameter of 9 μm was most suitable.

Among the programs currently available with the Nanospec are some for measuring the thickness of resist on both oxidized and unoxidized silicon surfaces. Since these programs had been prepared for positive photoresists, the validity of applying them to the measurement of other polymeric coatings was open to question. Therefore, 17 silicon wafers coated with poly(methyl methacrylate) (PMMA) in thicknesses ranging from 150 to 19,500 Å were prepared and measured using the mechanical stylus technique with a Sloan Dektak surface profile measuring system as well as with the Nanospec photoresist-on-silicon program. As shown in Figure 2, the Nanospec values are linear with the Dektak thicknesses. The linear-regression plot has a slope of 1.078 and a y intercept of 83.4 Å. We are interested primarily in the normalized thickness t_N, which can be determined accurately from the formula $t_N = (t - b)/(t_o - b)$, where t and t_o are the thicknesses obtained with the Nanospec program for the exposed and unexposed resist, respectively, and b is the reading obtained on an area of the same wafer with no resist.

To obtain the data reported in this paper for positive resists, we routinely determined t_o as the average value for the unexposed areas at the four corners of the developed image of the matrix. Consequently, whenever there was any thinning of the unexposed resist during development, t_N was based on the thinned resist. Values for b were the averages of about four individual measurements on squares that received substantially different, but obviously excessive, doses and that clearly were developed completely and cleanly. For negative resists, we used a t_o value obtained before the image was developed, and the values for b were the average of several readings on cleaned areas of the developed wafer.

The surface of underexposed and partially developed resist coatings is often quite non-uniform, being uneven in thickness or having a bubbly appearance. In spite of this, the Nanospec generally yields internally consistent data that can be plotted to form smooth curves. There are some exceptions, however, where the Nanospec measurement is obviously faulty. The overall quality is illustrated by the plot of t_N as a function of log E for poly(tert-butyl methacrylate) (PtBMA) shown in Figure 3. In most cases, it is a simple matter to ignore the results that are clearly erroneous. Frequently, other areas that received approximately the same exposure to radiation are satisfactory for Nanospec measurement.

SCREENING RESULTS

These methods were used to determine the electron-beam sensitivity and contrast for 10 polymethacrylate positive resists and 14 negative resists, half of which were polystyrene derivatives. Many of the development conditions used in this study were previously reported in the literature. In the case of positive resists, conditions were chosen to produce a limited amount of thinning of the unexposed resist (about 5%, but up to about 20% in one case). No attempt was made to optimize the development procedure. Tables I and II provide pertinent data on the polymethacrylates, the methods of development, and the results. Usually, the sigmoidal curves that were obtained from the t_N versus log E plots were similar to those of PMMA and PtBMA shown in Figure 4. No effort was made to eliminate the "toe" at the higher doses just short of those resulting in clean development. Additional rinses with weak solvents, particularly spray rinses, are sometimes useful in minimizing the size of the toe. The sensitivity (Q) determined by simple inspection of the matrix corresponded to the end of the toe. A second value for the sensitivity (Q_{ext}) could be obtained by extrapolating the approximately linear, descending portion of the sigmoidal curve to the baseline. Q_{ext} may be assumed to be the limiting value for the sensitivity if one is completely successful in removing the toe with appropriate rinses or a light plasma etch. The size of the toe varied with the resist and the development method. This is also illustrated in Figure 4 with the curves for poly(iso-propyl methacrylate) and poly(sec-butyl methacrylate). The particularly prominent

toe in the curve for the latter resist was due to a discontinuous coating of polymer droplets that remained on the incompletely developed surface. The tendency to leave this type of residue was responsible for the large but poorly defined value for the contrast γ.

Values for γ were generally obtained as the absolute value of the slope of a least-squares plot of "acceptable" data points. The subjective selection of the points that were acceptable was made from an examination of the graph, and it excluded the obviously erroneous readings previously discussed as well as those points clearly belonging to the regions in which the plot curves away from the straight-line, descending portion of the plot. Usually, the acceptable points were for t_N values ranging from 0.1 at the lower end to 0.4 to 0.8 at the upper end, depending on how quickly the curve deviated from a straight line at decreasing exposures.

Data for four of the resists included in Table II were derived from coatings on oxidized silicon wafers. The Nanospec measurements on these wafers were made using a program designed for photoresist on SiO_2-coated silicon, where the thickness of the SiO_2 was determined separately on a clean wafer and entered as a constant into the memory. The procedure used and the results obtained were otherwise normal in all respects.

One resist, poly(n-butyl methacrylate), was so uneven after development that we could not obtain enough acceptable points to prepare a plot of t_N versus log E. This was true for tests on both oxidized and unoxidized silicon wafers.

The results from screening a series of negative resists are presented in Tables III and IV. Some of the data in these tables were previously reported for comparative purposes (3). In the case of negative resists, we report Q_{50}, the dose required to give a film thickness of 50% of t_o, as the sensitivity. Although other values have also been used to represent sensitivity, this value seems reasonable to us for comparing experimental resists since the contrast curve of some resists starts to turn over soon after that value. The contrast is the slope of the ascending portion of the curve and is usually the same as the tangent to the curve at $t_{0.5}$. It is sometimes impossible to obtain as many closely spaced points at the low dose end of negative resist plots as one would desire, because these squares do not adhere and frequently are removed during development.

The test method described is a quick and convenient method for screening polymers as resist materials. It can also be used in the preliminary stages of process development to help establish reproducible conditions for such processing variables as baking time and temperature, developer composition, and development time. We have found that the reproducibility in measuring the thicknesses of individual squares with the Nanospec AFT is about 5 to 20 Å. The measurements of four different matrix sets of PMMA made over a period of a week gave

sensitivity measurements that range from 1.84 to 1.91 10^{-4} C/cm^2, and Y values from 7.01 to 7.59.

ACKNOWLEDGMENTS

We thank Mr. Vincent Coates and Mr. Russell Lewis of Nanometrics, Inc. for their assistance and hospitality in permitting us to use the Nanospec AFT microarea film thickness gauge in their facility. We also wish to acknowledge the help of Mr. Philip Coane and Ms. Judi Thompson for making the electron-beam exposures, the consultation of Dr. Edward Wolf and Dr. Faik Ozdemir, and the technical assistance of Mrs. Camille Van Ast and Mr. Willis Smith.

REFERENCES

1. K. Murase, M. Kakuchi, and S. Sugawara, "Newly Developed Electron and X-Ray Resist Materials," International Conference on Microlithography, Paris, France, 21-24 June 1977, pp. 261-269.

2. Available from Nanometrics, Inc., Sunnyvale, CA.

3. R.G. Brault and L.J. Miller, Regional Technical Conference, Society of Plastics Engineering, Ellenville, N.Y., Oct. 10-12, 1970; Polym. Eng. Sci., in press.

Table I. Source and Molecular Weights of Polymethacrylates Evaluated as Positive Electron Resists, $CH_2C(CH_3)(COOR)_n$

R	Source[a]	$\overline{M}_W \times 10^{-5}$[b]	$\overline{M}_W/\overline{M}_N$[b]
CH_3	DuP	4.00	2.86
C_2H_5	SPP	3.42	2.05
n-C_3H_7	Pos	13.0	3.27
i-C_3H_7	Pos	6.58	3.12
n-C_4H_9	HRL	2.52	1.19
s-C_4H_9	Pos	0.89	2.47
t-C_4H_9			
High $\overline{M}_W$	HRL	30.7	1.48
Low $\overline{M}_W$	Pos	1.17	2.05
c-C_6H_{11}	HRL	6.81	3.23
$C_6H_5CH_2$	HRL	15.0	3.04
C_6H_5	HRL	13.9	3.28
CF_3CH_2	HRL	0.44	1.68

[a]Ald = Aldrich Chemical Co., Milwaukee, WI
DuP = Dupont Co., Plastics Dept., Wilmington, DE
HRL = Synthesized at Hughes Research Laboratories
Pos = Polysciences, Inc., Warrington, PA
SPP = Scientific Polymer Products, Inc., Webster, NY.

[b]Determined by gel permeation chromatography on Microstyragel columns using tetrahydrofuran solutions.

TABLE II. Processing Parameters, Sensitivity and Contrast of Polymethacrylate Electron Resists

R	Prebake		Development			Sensitivity,[e] $\mu C/cm^2$		Y
	Time, Hr.	Temp, °C	Developer Solvent[b]	Time, sec	Percentage Thinning (or Thickening)	Q	Q_{ext}	
CH_3	1/3 (air)	145	3:1 IPA: MIBK	30	0	198	184	7.59
C_2H_5	4 (vac)	160	2:1 IPA: MA	15	5	55.1	47.3	2.98
n-C_3H_7	4 (vac)	160	2:1 IPA: MA	30	2	49.5	24.2	11.6
i-C_3H_7	4 (vac)	160	2:1 IPA: MA	15	(6)	46.1	39.1	3.30
n-C_4H_9 (on SiO_2)	0.5 (air)	110	30:1 IPA: MIBK	60	21	2.99		
n-C_4H_9	4 (vac)	160	MA	15	6	197	~34	~15
t-C_4H_9								
High $\bar{M}_w$	15 (vac)	160	Carb	180	(3)	31.6	22.0	11.3
Low $\bar{M}_w$ (on SiO_2)	4 (vac)	160	Carb	180	(3)	14.2	13.5	5.76
c-C_6H_{11} (on SiO_2)	4 (air)	115	1:1 IPA: MIBK	60	4	45.8	40.5	1.68
$C_6H_5CH_2$	4 (vac)	155	2:1 MEK: IPA	30	0	299	147	1.68
C_6H_5	4 (vac)	155	Dioxane	30	2	38.0	36.0	3.91
CF_3CH_2 (on SiO_2)	1 (air)	115	3:1 IPA: MIBK	15	6	30.7	24.0	1.34

[a] Tested on silicon or, where indicated, on SiO_2-coated silicon wafers.

[b] Carb = carbitol or 2-(2-ethoxyethoxy)ethanol
IPA = isopropyl alcohol
MA = methyl alcohol
MEK = methyl ethyl ketone
MIBK = methyl isobutyl ketone

[c] Sensitivity Q was obtained by inspection of the matrix with the optical microscope; Q_{ext} was obtained by extrapolation of the linear portion of the t_N versus log E curve to the baseline where $t_N = 0$.

Table III. Source and Molecular Weights of Polymers Evaluated as Negative Electron Resists

Resist	Material Source[a]	$\bar{M}_W \times 10^{-5}$[b]	$\bar{M}_W/\bar{M}_N$[b]
Poly(diallyl phthalate)	Pos	0.99	3.5
Poly(methyl vinyl ketone)	SPP	2.05	2.50
Poly(vinyl acetate)	Pos	2.83	3.07
Poly(vinyl cinnamate)	Pos	1.42	2.77
Poly(vinyl chloride)	UCC	0.60	1.66
Polyvinylpyrrolidone	Pos	($\bar{M}_N = 4 \times 10^4$)	
Poly(glycidyl methacrylate — co-ethyl acrylate)	Mead	——	——
Polystyrene	Ald	3.21	3.80
Poly(4-chlorostyrene)	Pos	2.90	2.97
Polyvinyltoluene (mixed isomers)	Pos	2.77	4.76
Poly(vinylbenzyl chloride) (60/40 mixture of ortho/para)	Ald	1.24	3.74
Poly(4-bromostyrene)	Ald	5.34	2.01
Poly(4-iso-propylstyrene)	Ald	——	——
Poly(4-tert-butylstyrene)	Pos	0.6	2.03

[a] Ald = Aldrich Chemical Co., Milwaukee, WI
HRL = Synthesized at Hughes Research Laboratories
Mead = Mead Chemical Co., Rolla, MO
Pos = Polysciences, Inc., Warrington, PA
SPP = Scientific Polymer Products, Inc., Webster, NY
UCC = Union Carbide Corp., New York, NY

[b] Molecular weights were determined by gel permeation chromatography at Hughes, except for the value in parenthesis, which was the vendor's characterization.

TABLE IV. Processing Parameters, Sensitivity, and Contrast of Negative Electron Resists

Resist	Bake		Development		Sensitivity, C/cm^2 ($Q_{0.5}$)	γ
	Temperature, °C	Time, hr	Solvent[a]	Time, sec		
Poly(diallyl phthalate)	50 (Vac)	16	1:1 CB:AA	30	3.0×10^{-6}	0.83
Poly(methyl vinyl ketone)	50 (Vac)	16	MIBK	30	1.7×10^{-4}	1.29
Poly(vinyl acetate)	150	0.5	Tol	30	4.4×10^{-5}	0.94
Poly(vinyl cinnamate)	50 (Vac)	60	MEK	30	3.0×10^{-6}	1.15
Poly(vinyl chloride)	50 (Vac)	60	CB	30	7.4×10^{-5}	0.86
Polyvinylpyrrolidone	150	0.5	Water	30	4.1×10^{-5}	0.66
Poly(glycidyl methacrylate-co-ethyl acrylate)	90	0.25	COP dev	15	4.2×10^{-7}	0.72
Polystyrene	60 (Vac)	16	CB	30	4.6×10^{-5}	1.43
Poly(4-chlorostyrene)	50 (Vac)	16	CB	30	4.6×10^{-6}	1.82
Polyvinyltoluene	50 (Vac)	1	CB	30	4.6×10^{-5}	1.43
Poly(vinylbenzyl chloride)	50 (Vac)	1	CB	30	2.0×10^{-6}	2.1
Poly(4-bromostyrene)	60 (Vac)	1	CB	15	1.7×10^{-6}	1.89
Poly(4-iso-propylstyrene)	90 (Vac)	1	Tol	5	8.1×10^{-5}	1.20
Poly(4-tert-butylstyrene)	90 (Vac)	1	Tol	5	2.9×10^{-4}	2.88

[a] AA = Amyl acetate
CB = Chlorobenzene
COP dev = COP developer, including 2 rinses
MEK = Methyl ethyl ketone
MIBK = Methyl isobutyl ketone
Tol = Toluene

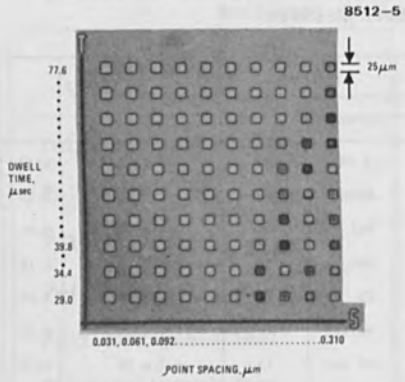

Figure 1. Image of the test matrix in resist. At 3 x 10^{-11} A, the exposures range from 2.42 x 10^{-4} C/cm^2; at upper left to 9.05 x 10^{-7} C/cm^2 at lower right.

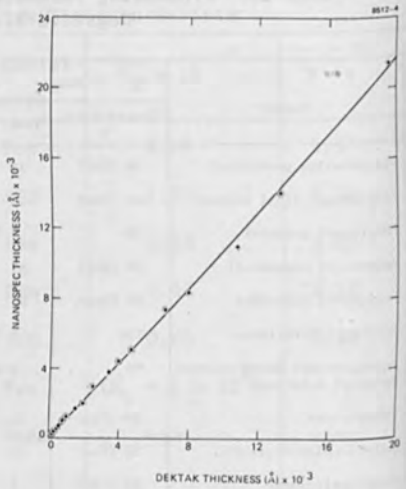

Figure 2. Correlation of PMMA thickness measurements using the Sloan Dektak and the Nanospec AFT with the program for photoresist on silicon. The anticipated error in Dektak measurements is about ±2.5%.

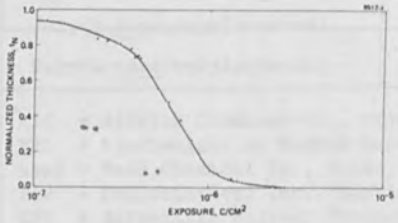

Figure 3. Typical plot of normalized thickness as a function of the log of the exposure to 20 keV electrons. Resist is poly(tert-butyl methacrylate), 0.5 μm thick on silicon, baked 4 hr at 147°C in vacuo, and developed with 33% methyl ethyl ketone: 67% acetonitrile for 30 sec.

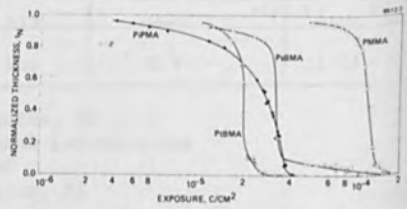

Figure 4. Illustrative plots of t_N versus log E for poly(alkyl methacrylates). The alkyl groups are: PtBMA, tert-C_4H_9; PiPMA, iso-C_3H_7; PsBMA, sec-C_4H_9; and PMMA, CH_3.

A THREE DIMENSIONAL MODEL FOR RESIST DEVELOPMENT SIMULATION

Fletcher Jones, Jurij Paraszczak, Michael Hatzakis
IBM Thomas J. Watson Research Center
Yorktown Heights, New York 10598

Abstract: For several years, the simulation of the development process for resist patterned using optical or electron beam radiation has been confined to patterns consisting of long parallel lines. The simulation takes place in a section perpendicular to the direction of the resist lines, and therefore, such models are usually called two dimensional. Using a computer program recently created for the simulation of resist development in three dimensions, we have simulated the development of electron beam exposed resist patterns for three patterns that cannot be properly investigated by a two dimensional model. The test resist used is polymethylmethacrylate, and the developer is 1:1 methylisobutylketone/isopropanol. We find that the results of our simulations are in very good agreement with our experiments.

Introduction

Dill, Neureuther, Walker and Tuttle[1] have constructed a two dimensional cellular developer model for the purpose of simulating the development of long, parallel line images exposed in resist materials using optical, electron beam, or X-ray illumination. This model has been applied to a variety of situations and has yielded useful information about the time evolution of the two dimensional profiles of these images. A number of questions such as sensitivity of image profile to relative changes in illumination levels, development time, and bias variations are readily answered for line images. However, LSI circuit patterns are not only composed of line patterns; in most cases they contain pattern elements which are very small and do not possess a high degree of symmetry. The low symmetry pattern elements cannot be investigated using the two dimensional model developed by Dill, et al[1]. A computer program which can simulate resist development in three dimensions (RD3D) was recently constructed. In particular, the RD3D program has been used to simulate the development of electron beam exposed resist patterns. The results of the RD3D program for resist patterns that cannot be analyzed by a two dimensional resist simulation routine are presented in this paper, and in some cases a comparison is made between the RD3D results and our experimental results. We find that the agreement between the simulated and the experimental results are excellent.

Electron Beam Exposure of Resist Materials

High energy electrons passing through a thin film (1.3 microns) of polymethylmethacrylate (PMMA) on a silicon substrate will undergo many collisions with the atomic nuclei in the resist film and in the silicon substrate. A fraction of the kinetic energy of the electrons will be dissipated in the resist due to collisions. This dissipated energy brings

about the destruction of bonds in the polymer. The energy dissipated per unit volume, Ev, in the resist arises from three sources: (i) electrons scattered in the forward direction in the resist, (ii) electrons backscattered in the resist by the PMMA nuclei, and (iii) electrons backscattered from the silicon substrate into the resist. Ev can be calculated by using an analytical function or by using a Monte-Carlo[2] model which simulates the scattering of electrons passing through the resist. Hawryluk, Hawryluk, and Smith[3] have performed an in depth comparison of the two methods. It is found that the analytic and Monte-Carlo models are in very good agreement for substrates having low atomic numbers (e.g. Al, Si, SiO_2), while strong disagreement is found between the two models when the substrates have a high atomic number(e.g. copper). The fabrication of LSI circuits for all practical cases involves low atomic number materials. On the other hand, using an IBM 370 computer the computing time (19 seconds) required to evaluate Ev from an analytic model is much shorter than the computer time (30 minutes) required to evaluate Ev using the Monte-Carlo model. Therefore, the analytic model described by Hawryluk, Hawryluk, and Smith[3] is used to evaluate Ev.

Calculations of the Energy Dissipated Per Unit Volume By an Electron Beam

It is not our intent to reconstruct the theory of electron scattering in resist materials and therefore most of the details associated with the construction of the theory will be omitted. In this section, we simply give the equations used to produce the energy distributions used by RD3D in calculating the developed resist patterns shown below. For more details, see Ref. (3).

Energy Dissipated Per Unit Volume by Forward Scattered Electrons

In Fig. 1, let z be the vertical distance measured along the direction of electron penetration (assumed to be perpendicular to the resist surface). Let r be the radial distance measured from the axis of incidence. The spatial probability density of a forward scattered electron is given by

$$H(r,z) = \left(\Lambda/4\pi z^3\right) \exp\left(-3\Lambda r^2/4z^3\right) \tag{1}$$

where[4]

$$\Lambda(\text{Å}) = \frac{5.12\times10^{-3}\ E_o^2 A}{\rho_{PMMA}\ Z_{carbon}^2\ \ln\left(0.725\ E_o^{1/2}/Z_{carbon}^{1/3}\right)}. \tag{2}$$

In equation (2), E_o is the incident energy of the primary electron, A is the atomic mass number of carbon, Z_{carbon} is the atomic number of carbon, and ρ_{PMMA} is the density of the PMMA film; the value of the parameters used in this paper are 25 x 10^3 ev, 12, 6, and 1.22 g/cm^3 respectively. The energy dissipated per unit volume by a single electron scattered in the forward direction is given by

$$I_1(r,z) = \frac{2\pi q^4 n_e}{E_o}\ \ln\left[\frac{E_o}{I}\left(\frac{e}{2}\right)^{1/2}\right] H(r,z) \tag{3}$$

I, the mean excitation energy for electrons in the PMMA film, has a value of 65.6ev. n_e is the density of atomic electrons in the PMMA film. q is the electronic charge.

Energy Dissipated Per Unit Volume By Backscattered Electrons

When an incident electron passes close enough to an atomic nucleus in the resist or the silicon substrate, it can be scattered through angles greater than 90 degrees relative to the incident direction. The number of primary electrons backscattered by the resist is small compared to the number backscattered by the silicon substrate. Therefore, the contribution of electrons backscattered by the resist is neglected in all that follows. The energy dissipated per unit volume in the PMMA film by electrons backscattered from the substrate is given by

$$I_2(r,z) = \beta/\pi(R^s_{TW})^2 \times \int_o^{\xi_{max}} \frac{(1-\xi)^{\beta-1}}{\left\{(\xi+\delta)+\left[\kappa^2+(\xi+\delta)^2\right]^{1/2}\right\}^2}\left(-\frac{dE}{dS}\right)d\xi \qquad (4)$$

where

$$-\frac{dE}{dS} = 2\pi q^4 n_e \ln\left[\frac{E_o}{I}\left(\frac{e}{2}\right)^{1/2} g(\xi,\kappa,\delta)\right]/g(\xi,\kappa,\delta) \qquad (5)$$

and

$$g(\xi,\kappa,\delta) = \left(1-\xi-\frac{\xi}{\xi+\delta}\left[\kappa^2+(\xi+\delta)^2\right]^{1/2}-\frac{\rho_{PMMA}}{\rho_s}\frac{\delta}{\xi+\delta}\left[\kappa^2+(\xi+\delta)^2\right]^{1/2}\right)^{1/2} \qquad (6)$$

ξ, κ, and δ are defined by Fig. 1. ρ_s, the density of silicon, is 2.33 g/cm^3. β is $\sim 0.045 Z_{carbon}$. R^s_{TW}, the range of the electron in the silicon substrate, is equal to $V_o^4/C_T\rho_s$ where V_o is the speed of the incident electron, and $C_T = 5.65\times10^{42}\ cm^6/g\ \text{sec}^4$. For a given κ and δ, ξ_{max} is found by solving the equation

$$\frac{E_o}{I}\left(\frac{e}{2}\right)^{1/2} g(\xi_{max},\kappa,\delta) = 1. \qquad (7)$$

Total Energy Dissipated Per Unit Volume by A Single Electron

The total energy dissipated per unit volume by a single electron in passing through a resist of thickness T is given by

$$\delta_s(r,z) = I_1(r,z) + I_2(r,z) \quad \left(Kev/cm^3\text{electron}\right) \qquad (8)$$

Energy Dissipated Per Unit Volume In Exposing a LSI Pattern

Let Q(x,y) represent the dose in coulombs/cm^2 given to a point (x,y) on the resist surface by the incident electron beam in exposing the resist to an LSI circuit pattern. The energy dissipated per unit volume Ev(x,y,z) at the point (x,y,z) in the PMMA film is obtained by convoluting Q(x,y) with $\delta_s(r,z)$. Therefore,

$$Ev(x,y,z) = \int_A Q(x',y')\ \delta_s(x'-x,y'-y,z)dx'dy' \quad \left(Kev/cm^3\right) \qquad (9)$$

where the A on the integral sign denotes integration over the surface area of the resist. The energy dissipated per unit volume, Ev, for all the resist patterns given below was calculated using equation (9) with the parameters as given above.

Dependence of Solubilty Rate on Resist Exposure Dose

The solubility rate as a function of dose was obtained by uniformly exposing squares 10 microns on a side in 13280Å of resist and recording the time required to develop out the center of the square. The squares were exposed at doses of 0.0, 20.0, 40.0, 60.0, 100.0, and 120.0 microcoulombs/cm^2. The thickness of the resist film before development was measured using an IBM Film Thickness Analyzer. The results of the experiments are given in columns 1 and 2 of Table I.

In the center of the square the value of Ev at the resist surface Ev^S and at the resist-substrate interface Ev^I is given in columns 3 and 4 of Table I respectively. In a thin film of resist, Ev increases linearly with respect to position below the surface of the resist. Hence the average value, E, of Ev^S and Ev^I represents the energy dissipated per unit volume at one half the distance below the surface of the resist. E as a function of Q_o is given in column 5 of Table I.

A cubic polynomial of the form

$$\log_e R(\text{Å}/\text{ sec}) = A + BE + CE^2 + DE^3 \qquad (10)$$

was least square fitted to the R vs E data in columns 1 and 5 of Table I. A, B, C, and D were found to be 2.122, 0.00255, -6.233 x 10^{-7}, and 7.382 x 10^{-11}, respectively; E is in joules/cm^3. The error of the least square fit is less than 1.6%.

Resist Development In Three Dimensions (RD3D)

In order to simulate the development of resist patterns, we first divide the resist into cells. Ev is calculated for each cell. The value of Ev assigned to a given cell will depend on Q(x,y) as described earlier. Next a solubility rate is assigned to each cell based on the dose it received during the exposure of the resist pattern. It is important to emphasize that the assigned rate represents the rate at which the cell will develop once it is in contact with the developer.

It is beyond the scope of this paper to give a detail description of the computer program, RD3D, which simulates the development of exposed resist patterns in three dimensions. A description of the outline of the program will be published elewhere. In this paper only a cursory description of the method used will be given.

When a cell which is in contact with developer dissolves, new facets on adjacent cells are exposed to developer. These new facets may belong to the cells which are already in contact with developer, or they may belong to the cell which has just been uncovered. The number of facets on a cell which is being removed determines (a) the dissolution rate of the cell, (b) the number of newly exposed facets on adjacent cells, and (c) the rate at which these newly exposed cells dissolve. By keeping track of the cells in contact with developer and their associated facets, RD3D is able to simulate the development process. The result of the simulation is a matrix, TR, which contains the time at which each cell in the resist is removed. Graphical contouring programs can then be used to plot the shape of the developed resist pattern as a function of time from the information in TR.

Applications

3 x 3 Array of 1.0 Micron Contact Holes

The first case considered was that of a 3 x 3 array of 1.0 micron contact holes (see Fig. 2a) exposed at a dose of 100μ coul/cm^2. The separation between the contact holes was also 1.0 micron. Ev was calculated for the array using equation (9). The central contact hole was chosen for examination.

Figure 2b is an orthogonal projection of a three dimensional plot of the contact hole at a development time of 110 seconds. The lines parallel to arrow A represent the surface of the resist. The separation between these lines is 0.1μm. The somewhat square contours show how the diameter of the contact hole varies in going from the top to the bottom of the contact hole. The plot in Fig. 2b is put together in sections. The sections can be spread out as shown in Fig. 2c. The latter method of display is equivalent to the sectioning of real samples in order to observe the profiles of contact holes using a scanning electron microscope. In frame a of Fig. 2c, the horizontal line represents the surface of the resist. The distance from the top of the frame to the horizontal line is a measure of the amount of resist removed during the development process. Frames e through o show that the contact hole is open at the substrate. By symmetry, the maximum width of the contact hole is found by counting the number of frames from e to o. Since the separation between sections is 0.1 microns, the width of the opening is 1.0 microns. Although the linear extent of the contact hole is 1.0 microns, it can be seen from Fig. 2b as well as from Fig. 2c that the width of the contact hole is not uniform across the open region. In particular, the contact hole is rounded at the corners. By counting the number of sections participating in the rounding effect in Fig. 2b, we see that the corner rounding is confined to ~ 0.2 microns of resist. The amount of corner rounding is not easily determined from a two dimensional resist development scheme.

Staggered Array of 1μm Contact Holes

The next example considered for simulation was the exposure and development of a staggered array of 1μm contact holes as shown in Fig. 3a. The separation between the contact holes along the vertical direction is 1μm. The separation between columns is also 1.0μm. This pattern is useful when profiles of contact holes have to be studied using a scanning electron microscope. Taking sections of chips for scanning electron microscopy can often be laborious when dealing with small geometries. More often than not, the chip will split along a direction which does not pass through the pattern element under investigation. This is not the case with the pattern shown in Fig. 3a since it is impossible to section this chip without passing through a lot of contact holes. Fig. 4 shows PMMA samples that were exposed in the vector scan system[5] and developed for times ranging from 50 to 130 seconds in 1:1 methylisobutylketone/isopropanol. The rounding at the corners of the contact holes is evident, and the characteristic curvature of the e-beam exposed and developed resist is also apparent.

In the simulation, the nine contact holes in Fig. 3a were exposed at a dose of 100μ coul/cm^2. However, only the region enclosed by the dashed line was examined by the RD3D program. Fig. 3b shows a view of the resist pattern after 70 seconds of development. Contour A runs from the top to the bottom of the figure. In doing so, it passes through the contact holes labeled Y and Z. The fact that contour A passes across the

bottom of the contact holes indicates that the overall resist pattern is underdeveloped. The depth of the contact hole relative to the resist surface is determined by counting the number of rings within the contact hole. The number of rings in contact hole Y is 17. The thickness of the resist is 1.3 microns, and the resist is divided into 23 layers for simulation purposes. Hence, the depth of the contact hole is 0.9 microns. The width of the developed contour at the top of the contact hole can be found by counting the number of contours of type A which pass through it. The number of sections which pass through contact hole Y is 12; and therefore, the width of the contact hole at the top of the resist is 1.1 microns. These results can be compared with the experimental results shown in column b of Fig. 4 at a development time of 70 seconds. The depth of the contact hole is found to be approximately 1.0 microns, and the width of the contact hole at the top of the resist is found to be 1.1 microns. At a development time of 110 seconds, Fig. 3c shows that the contact holes have developed down to the substrate. The depth of contact hole Y is 1.1 microns. The width of contact hole Y at the top and bottom of the resist is 1.2 and 1.0 microns respectively. The experimental results for a development time of 110 seconds are shown in column b of Fig. 4. Measurements from this figure show that the depth of the contact hole is 1.1 microns and that the width of the contact hole at the top and bottom surfaces is 1.2 and 1.0 microns respectively. Hence, the agreement between the results of the RD3D program and the experiment is quite good.

Array of Connected and Separated Rectangles

The last example investigated was the pattern shown in Fig. 5a. The pattern to be exposed consists of a 2 x 2 micron square surrounded by rectangles 0.6 microns in width. The region of interest in this example is surrounded by the dashed line. This pattern was chosen for study because it clearly demonstrates the way in which backscattered electrons contribute to the dissolution of electron beam sensitive resists. Although the developed resist patterns shown below have many aspects worthy of discussion, only the most salient ones are considered.

The results of the RD3D program are shown in Figs. 5b-e. Fig. 5b is a top view of the developed resist pattern after a development time of ten seconds. Short development times such as this are found to be useful in practice because the actual pattern exposed in the resist can be examined before much of the resist has developed away. In Fig. 5b, the separation between lines along the direction of arrow A is 0.1μm. Using this fact, the length and width of all the rectangles as well as the distance between them can easily be deduced. Fig. 5c shows the developed resist pattern at a development time of 70 seconds. The gap shown between the 0.6 micron rectangle of Fig. 5b shows up as a kink in the developed resist pattern. The pattern is clearly underdeveloped. At a development time of 200 seconds (see Fig. 5d), the region of the resist which was directly exposed by the electron beam has developed out. However, a bridge of resist remains in the central portion of the pattern. The reason for the occurrance of the resist bridge is as follows. First of all, Fig. 5b shows that there is more resist at the inside corners than at any other place within the roughly annular region of unexposed resist. Secondly, the square is closer to the rectangle on the right than it is to the rectangles on the left and below. The backscatter of electrons into the annular region will increase its dissolution rate. The energy dissipated per unit volume by the backscattered electrons will be greater on the right hand side and, therefore, that portion of the annular strip will dissolve away first. The energy dissipated by the backscattered electrons and thus the dissolution rate of the

resist is greatest at the substrate. Hence, the solvent inside the rectangles on the left and below and inside the square dissolves the resist under the annular region faster than it dissolves the resist near the surface of the annular region. In time, the resist at the substrate will be completely dissolved. Since the width of the resist in the corners is greater than the width of the resist anywhere else in the annular region, the resist in the corners will dissolve last. Fig. 5d shows that the resist in the corners eventually serve as pedestals for the resist bridge.

Finally, after 260 seconds, the resist bridge has completely developed out as shown in Fig. 5e.

Summary and Conclusions

A resist developer model called RD3D has been constructed and used to calculate the time evolution of resist profiles in three dimensions. Using polymethymathacrlylate as a test resist and 1:1 methylisobutylketone/isopropanol as the developer, it was found that the predictions of the model are in excellent agreement with the experimental observations. Three cases were studied in this paper: (i) a 3 x 3 array of 1.0 micron contact holes, (ii) a staggered array of contact holes, and (iii) an array of connected and separated rectangles. The above patterns contain elements whose electron beam exposure profiles vary quite rapidly and possess low symmetry over the region of interest. Prior to the construction of RD3D, resist modeling was essentially two dimensional because only very long line patterns could be considered. Using RD3D, it is now possible to model the development of very complicated LSI resist pattern elements. This model can and will be used to obtain quantitative information about the development of sensitive resist structures at the micron and submicron size.

References

1. F. Dill, A. Neureuther, T. Tuttle, and E. Walker, IEEE Trans. Electron Devices, vol. ED-22, no. 7, pp. 456 (1975)

2. D. Kyser and K. Murata, Proc. Sixth Int'l Conf. on Electron and Ion Beam Sci. and Tech. (Electrochemical Society 1974) pp. 205

3. R. Hawryluk, A. Hawryluk, and H. Smith, J. Appl. Phys. vol. 45, no. 6 pp. 2551 (1974)

4. R. Nosker, J. Appl. Phys., vol. 40, no. 4, pp. 1872 (1969)

5. T. H. P. Chang, A.D. Wilson, A. J. Speth, and C. H. Ting, Proc. Seventh Int'l Conf..on Electron and Ion Beam Sci. and Tech. (Electrochemical Society 1976), pp 392

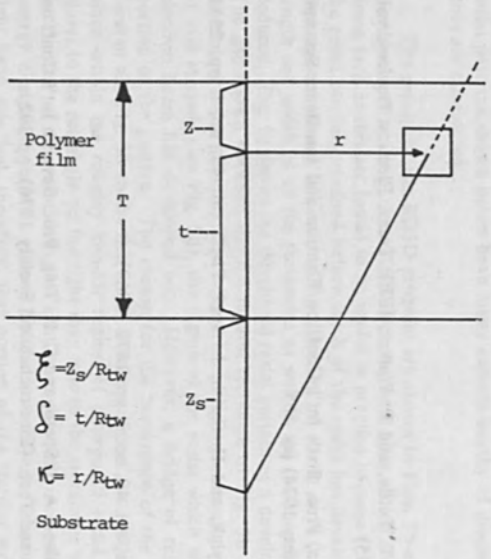

Figure 1.

Co-ordinate system used to calculate the energy dissipated in a polymer film by forward and backscattered electrons.

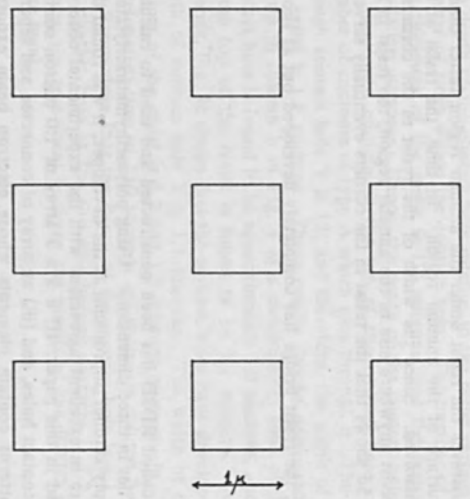

Figure 2(a).

Pattern layout for a 3 by 3 array of contact holes

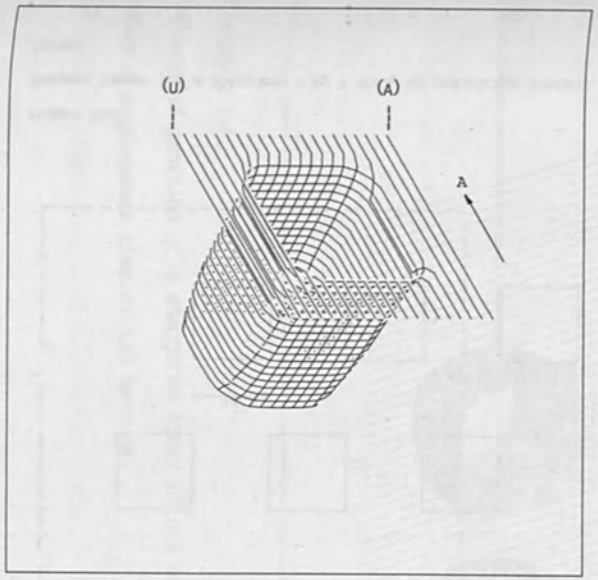

Figure 2(b).

Result of simulating the development of a one micron contact hole in PMMA,developed in a mixture of 1:1 MIBK:IPA,after a dose of 100 microcoulomb/cm^2. The vertical(open) contours are spaced 0.1 microns apart; the horizontal (closed) contours are spaced 0.06 microns apart.

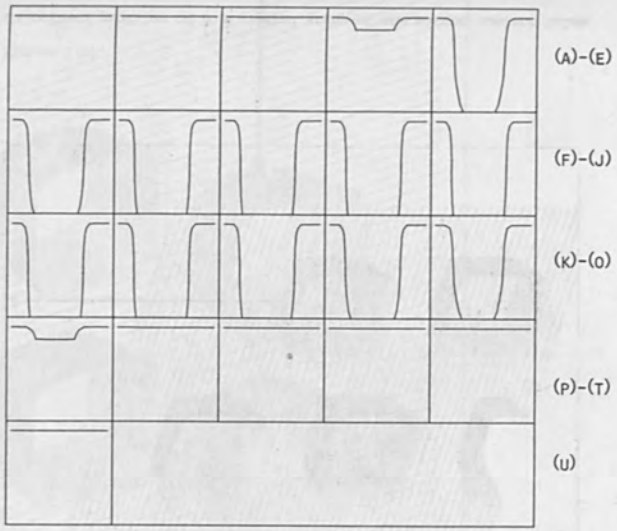

Figure 2(c).

Same as figure 2(b) ,contours laid out in sequence.Note that the vertical magnification is 2.3 times the horizontal

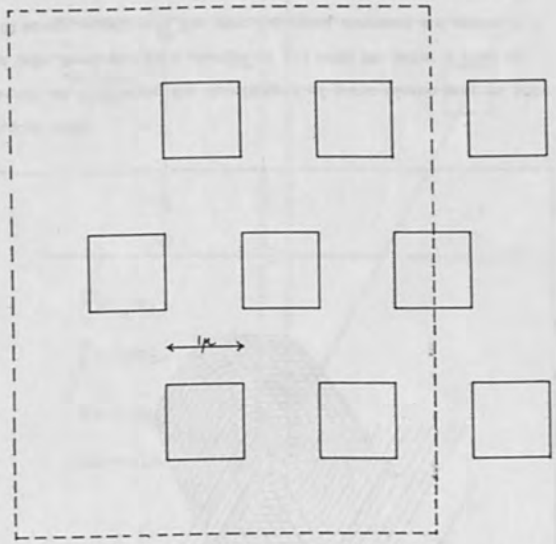

Figure 3(a).
Pattern layout for a staggered 3 by 3 array of one micron contact holes.

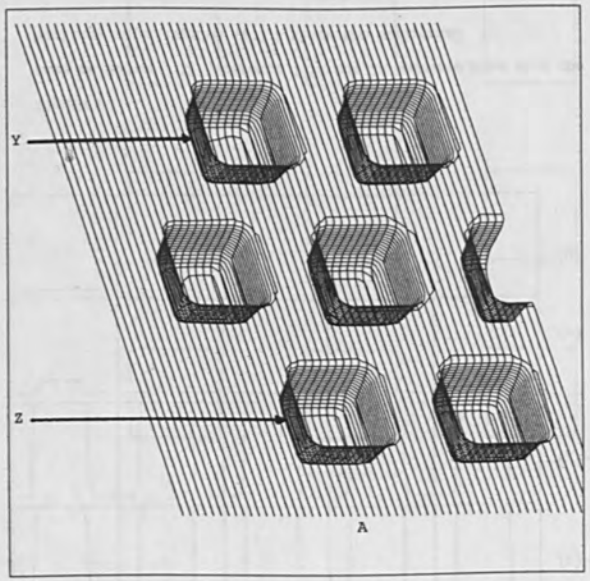

Figure 3(b).
Calculated profiles of a staggered array of one micron contact holes after a development time of 70 seconds

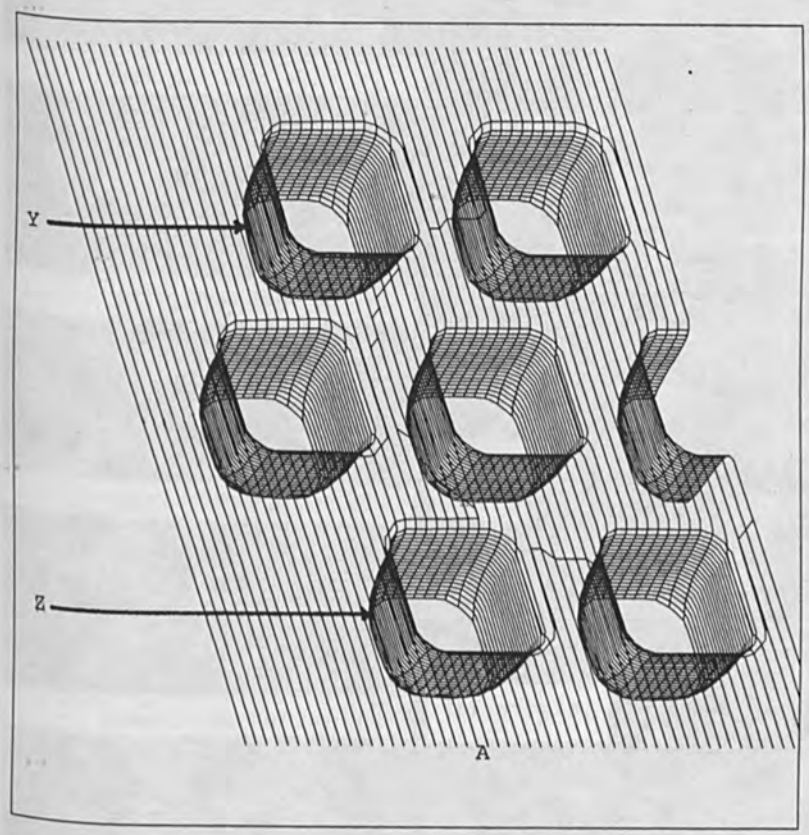

Figure 3 (c).

Calculated profiles of a staggered array of one micron contact holes after a development time of 110 seconds.

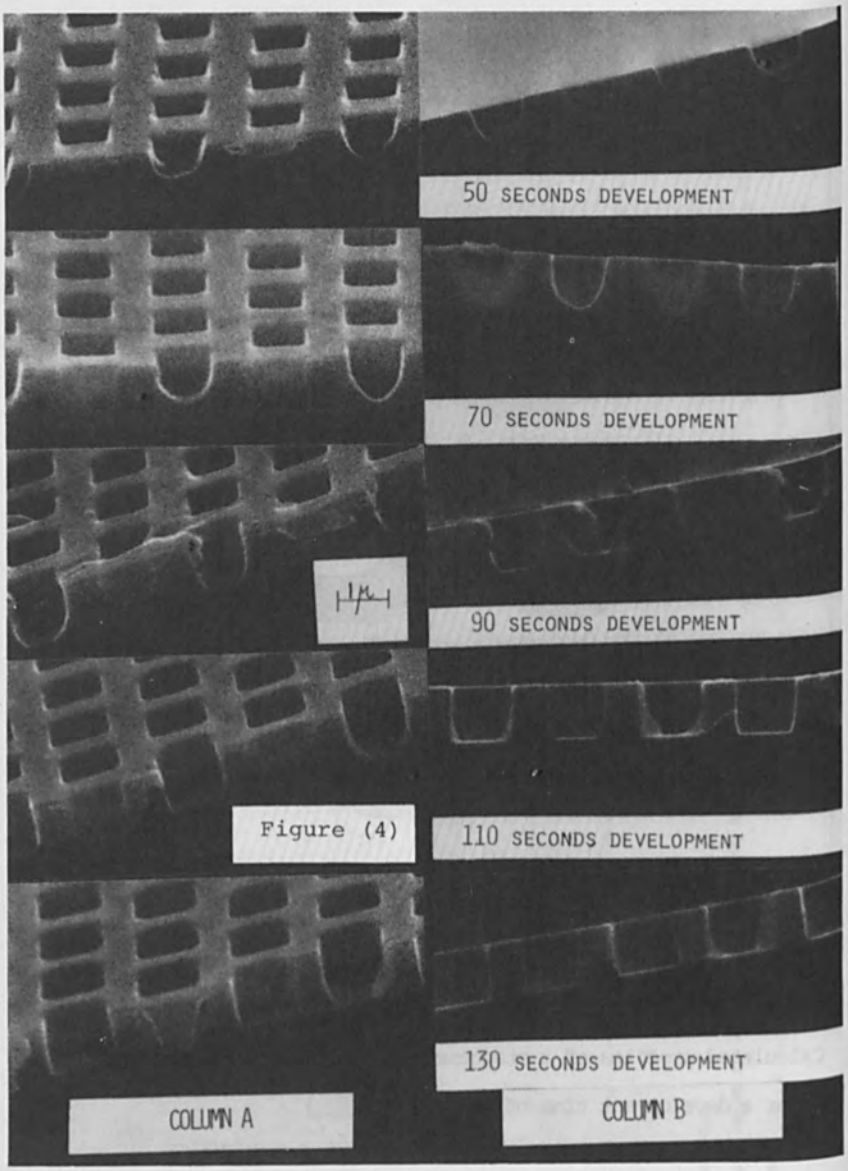
50 SECONDS DEVELOPMENT
70 SECONDS DEVELOPMENT
1μ
90 SECONDS DEVELOPMENT
110 SECONDS DEVELOPMENT
130 SECONDS DEVELOPMENT
COLUMN A
COLUMN B

Figure (4)

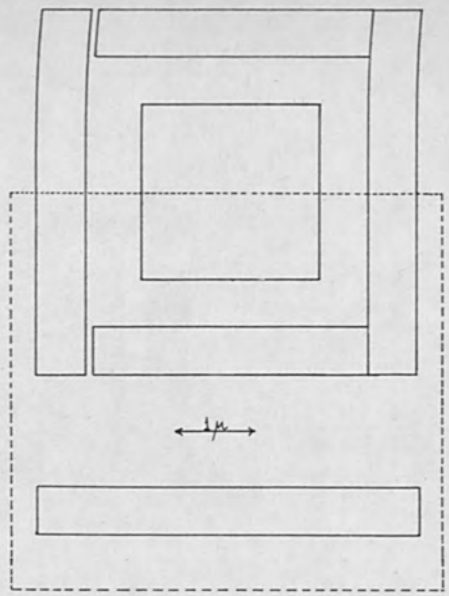

Figure 5(a).

Pattern layout of connected and separated rectangles.

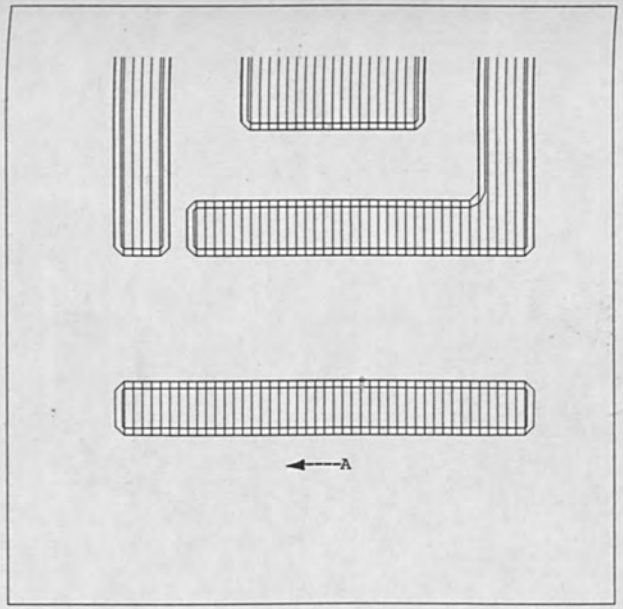

Figure 5(b).

Calculated profiles of exposed pattern in figure 5(a) after 10 seconds of development in 1:1 MIBK:IPA. Exposure dose is 100 microcoulombs/cm^2

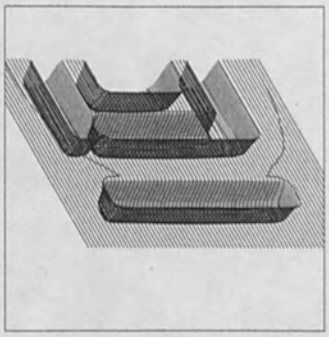

Figure 5(c).
Same as figure 5(b), but development time is 70 seconds

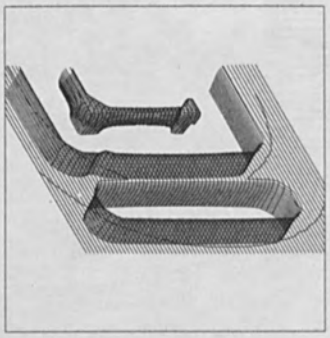

Figure 5(d).
Same as figure 5(b), but development time is 200 seconds.

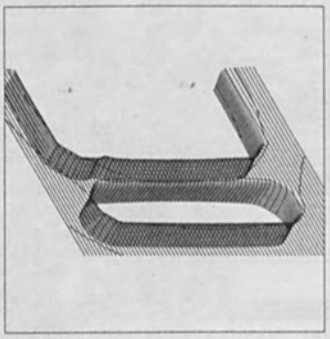

Figure 5(e).
Same as figure 5(e), but development time is 260 seconds

INTERFACE AND MONOMOLECULAR FILM SOLID STATE REACTIONS APPLICATION TO MICROLITHOGRAPHY

by

André BARRAUD
Services d'Electronique de Saclay
Centre d'Etudes Nucléaires de Saclay
B.P. N° 2 - 91190 Gif-sur-Yvette - France

ABSTRACT

The organized structure of monomolecular layers is shown to be a powerful tool to study adhesion and interface reactions. Examples of such reactions are given, together with the means of observation used to study them : X-ray and electron diffraction, ESR, Auger analysis and infrared linear dichroism. The peculiarities of the solid state, two dimensional polymerization which can be induced in monolayers are described. They are applied to give rise to a new class of ultrathin, high performance resists specially intended for submicron electron beam lithography : monomolecular resists, the main characteristics of which are given.

INTRODUCTION

The challenge to achieve finer and finer structures in microelectronics is presently leading microlithographists to use thinner and thinner resist films. This results in adhesion problems, and interface effects then play a significant role. A useful tool for studying interface effects lies in organized planar structures such as monomolecular layers.

These layers are made from amphiphilic molecules, i-e molecules possessing a hydrophilic group (acid function for instance) linked to a long hydrophobic hydrocarbon chain. They are prepared at the surface of a water trough by the classical Langmuir-Blodgett (1) technique (by spreading and compression) and transferred onto a solid substrate by dipping it up and down through the water surface (fig.1). This technique is very well adjusted now, since Langmuir films have been used for years in many laboratories for basic research (2,3,4). These two-dimensional, solid, crystal-like films are a valuable tool for studying interface and solid state reactions : all the molecules are oriented the same way, have the same environment, and all of them are active.

In the first paragraphs examples of adhesion reactions, condensations and solid state polymerizations are given to emphasize the versatility of monolayers as a tool for chemists and physico-chemists.

In the last section the properties of solid state polymerization combined with specific properties of monolayers are shown to give rise to a new class of high contrast resists especially designed for sub-micronic electron beam lithography.

MEANS OF ANALYSIS

The main problem which arises in monolayer studies is the sensitivity of the means of observation : NMR, elemental chemical analysis, and the classical ways of measuring molecular weights suffer from a tremendous lack of sensitivity. The only techniques that can be operated are X-ray and electron diffraction, Auger analysis, ESR, and infrared (or U.V.) absorption.

1. X-ray and electron diffraction

X-ray diffraction has been widely used to obtain monolayer crystal parameters (5). It needs a large number of superimposed layers, unlike grazing angle electron diffraction, which gives structural information on the last monolayer near the surface.

2. Auger analysis

Auger analysis is typically a surface method of analysis, since Auger electrons do not escape from more than a few tens of Å below the surface (6). It is well suited for studying adhesion reactions, provided the overlying layer is homogeneous and thin enough to allow electron escape, which is the case with monolayers.

Auger microanalysis under the beam of a scanning electron microscope provides a simple way of detecting local defects in layers 30 Å thick (7). Advantage can be taken from elements emitting several Auger electrons (such as Aluminium), to find out the nature of the defects. Fig.2 shows microphotographs of the same area of an aluminium sample partly coated with one monolayer of stearic acid. The three pictures were taken at different Auger energies. The monolayer appears black on the low energy Aluminium peak, white on the carbon peak, and transparent on the high energy Aluminium peak. The two point defects on the right of the picture appear black in the three pictures. That means they are thick opaque sediments on top of the layer, and not holes as it might be believed from the middle picture alone, or from other ESM micrographs.

The sensitivity of the method is high enough to work on a single layer of molecules, and give information on the elemental content of that layer (6).

3. E.S.R.

E.S.R. apparatus are sensitive enough now to be operated on a few layers. Although they can be used to sort out radicals and active species, they are most useful to detect paramagnetic ions in the hydrophilic plane (8). Rates and mechanisms of ion diffusion through a set of monolayers is orders of magnitude slower than through bulk organic material ; this is due to the forbiddance for ions to jump through the hydrophobic layer. As a consequence, the ion diffusion rate is highly dependant on the defect density in the layers, and diffusion rate measurements are a sensitive way of checking film quality.

E.S.R. also gives information on the orientation of the polar group : tilt angle average value and distribution can be obtained by introduction of markers such as Cu or Mn ions (8).

4. Infrared absorption

Infrared absorption is the most powerful means of investigation for monolayers. Absorbance sensitivities down to 10^{-4} are now available (10), so that functions giving rise to weak bands can be observed even in a fraction of a layer. This affords an easy way to follow the kinetics of chemical reactions involving a few or even one monolayer.

But the most powerful infrared technique is I.R. linear dichroism, which allows the determination of the orientation of every I.R. active bond in the molecule (11). This gives access to molecular conformation and film structure. It can be used before, during and after the reaction and it completes X-ray diffraction helpfully.

ADHESION REACTIONS

1. Adhesion to substrates

It has been known for long that, in some instances, organic acids deposited onto aluminium, give rise to an adherent residue upon removal by a solvent which should dissolve the whole film. The mechanism of this adhesion reaction can be easily studied by putting down one monolayer of calcium stearate onto aluminium. Owing to the extreme thinness of the film (25 A), Auger analysis can be performed through the layer to check for calcium. When the substrate is clean, surprisingly no calcium is found in the first layer (fig.3), although it is present in the upper ones (fig.4). But in case the substrate is submitted to pollution prior to deposition, calcium is found even in the first layer (fig.4). In this latter case, adherence is poor, while it is quite good in the former.

The absence of calcium shows that an ion exchange actually takes place upon film deposition, giving rise to an ionic bond between the ionized molecule and the aluminium ions of alumina. Such an ion exchange cannot take place on polluted substrates, since organic layers a few A thick are enough to screen the surface. The reaction is similar in the case of organic acids, and the first layer of molecules is converted into a salt, which no longer dissolves in the organic solvents of the acid.

Advantage can be taken from these specific reactions between monolayers and substrates to promote adherence by a proper choice of the first layer. For instance, molecules prone to coordination bonds give rise to good adherence on noble metal substrates where salt formation is impracticable, and the oxygen doublets of ethers and epoxides promote adherence onto silica (12).

2. Reactions between layers

The interface between two adjacent layers is a powerful tool for studying reactions between facing molecules in the solid state. The long aliphatic chains needed for monolayer formation play an important role because they determine the crystal lattice of the monolayer. This lattice will help or hinder the reaction between chemical functions at the interface since the compact structure of the chains dictates a distance of about 4.5 A between two corresponding atoms of neighbouring molecules, implying strong lateral stresses when a 1.5 A bond is established (as the chemical reaction joining two carbons for instance occurs). However at the interface the chemical groups

have some freedom of movement which allows chemical reactions to take place in the solid state.

These reactions can take place either with small molecules which can diffuse, or between amphiphilic molecules belonging to adjacent layers.

i) Diffusion

H. Kuhn (13) was the first to demonstrate the diffusion of small molecules in monolayers. It can be used to induce reactions at the hydrophilic interfaces, such as the conversion of acid into the highly reactive acid chloride species by diffusing thionyl chloride vapors through the layers, or the polycondensation of octadecyl urea with formol by dipping the sample into an aqueous solution of formaldehyde (14). These reactions can be helpful to link neighbouring molecules together in order to harden or cross-link the film.

ii) Reaction between amphiphilic molecules

Interlayer linking can be obtained through esterification between two different layers. For instance, alternate layers of behenic acid and docosanol undergo partial esterification upon a moderate temperature increase (15), as shown by the development of a shoulder characteristic of a saturated ester in the infrared spectrum at 1745 cm^{-1} (fig.5). Similarly a self-esterification takes place between two adjacent molecules of α-hydroxy-stearic acid in the same layer (fig.5).

POLYMERIZATION REACTIONS

1. Choice of the molecules

Langmuir layers have been used for years as models for basic research on solid state polymerization, since reactions are topochemical most of the times because of the strong lattice forces, and since the pre-ordered array of the molecules orient the reaction (2,3,16,17). If crystal parameters are properly chosen, the ordered array of the chemical functions in the hydrophilic or in the hydrophobic plane may be fruitful to induce long range two dimensional, matrix controlled polymerizations. Amphiphilic molecules with an unsaturated group at the hydrophobic end (position ω) or at the hydrophilic end, or at both, can be designed for polymerization. The ends of the molecule are the best locations for the polymerizable group, because of the freedom needed for the reaction to carry on. The simplest molecules of that kind possess one double bond in ω , and give rise to a linear polymer upon polymerization (18). Thus upon electron beam irradiation ω -tricosenoic acid yields a linear high molecular weight ($\sim$ 20,000) polymer insoluble in cold alcohol but soluble in chloroform.

A second polymerizable function can be added to the molecule in the hydrophilic plane so as to cross-link (19). This increases the mechanical resistance and the protecting capabilities of the film. This offers the additional possibility of selective irradiations by the choice of polymerizable functions sensitive either to ultraviolet radiations or to electrons or X-rays. An example of that versatility is provided by 2-4 docosyl pentadienoate

$$CH_3 - (CH_2)_{21} - O - CO - \underset{(1)}{CH} = \underset{(2)}{CH} - \underset{(3)}{CH} = \underset{(4)}{CH_2}$$

which polymerizes in three steps, each of them being triggered by a selective irradiation (17) : a first exposure to near U.V. produces dimers, a second to far U.V. then yields a linear polymer, which is finally reticulated by electron beam irradiation. Such step-by-step systems are useful tools to study the mechanisms of the solid state polymerization, and orientation phenomena.

2. Structural effects

A typical feature of these solid state polymerizations is that they are topochemical, i.e. controlled by the crystal lattice. The linear polymer is obtained in a nearly monodispersed form, stresses induced by the solid matrix of the aliphatic chain being assumed to stop propagation at the same distance from the initiation site everywhere in the plane (20).

The physical properties of these low dispersity polymers are well-defined and threshold effects arising from that feature can profitably give rise to high contrast. Similarly upon cross-linking the gel point is reached at a well-defined dose. Then the solubility of the polymer suddenly drops, giving rise to high contrast accordingly (19).

APPLICATION TO RESISTS

Advantage was taken from the specific characteristics of monolayers to design a new class of resists with original properties :

i - monolayer films are solid, compact and nearly hole free.

ii - films are very thin (thickness is a multiple of 30 Å) and their thickness is highly uniform.

iii - amphiphilic molecules are inert towards most chemical reagents.

iv - their pre-ordered structure is suitable to set up highly efficient solid state polymerization.

Molecules designed to afford both high quality films and highly efficient polymerization were synthesized and used as negative electron-resists (20). The most simple of them is ω-tricosenoic acid, films of which can be transferred onto solids at a pressure as high as 35 mN/m. The exposure curves of 900 A thick films of that molecule are given in fig.6. Sensitivity is typically 0.5 $\mu C/cm^2$ at 5 kV and as expected contrast is high : 2,5 to 3.5 according to development conditions. The resolution obtained after development is quite high since 600 A wide lines separated by 600 A wide blanks were obtained by electron beam microlithography on a 900 A thick film deposited onto aluminium (fig.7).

Polymerized films of ω -tricosenoic acid seem to whithstand plasmas well : the rate of wear is 5 to 6 times lower for the resist than for aluminium in CCl_4 plasmas (21).

Adherence problems are easily solved with monomolecular resists since the first layer may be chosen different from the upper ones to specifically match the surface chemistry of the substrate.

CONCLUSION

The pre-organized structure of Langmuir monolayers makes them an exceptional tool for basic research and the possibility of piling up layers of different nature offers versatility to study the mechanisms of adhesion and interface reactions. Furthermore, the long range propagation of the lattice-controlled polymerization, added to the specific qualities of monolayers, give rise to a new class of high sensitivity, high contrast, high resolution resists which are definitely different from classical spinned resin films. Although these resists are not fully characterized yet, they might be of some help for electron beam microlithography in the largely submicronic range. In this range, film thickness, compactness and contrast are of prime importance ; all these parameters are favoured in monomolecular layers.

REFERENCES

(1) - K. BLODGETT, Jour. Am. Chem. Soc., 57, 1007 (1935)

(2) - A. CEMEL, T. FORT, J-B. LANDO, Jour. Polym. Sci., Part A1, 10, 2061 (1972)

(3) - M. HATADA, M. NISHII, K. HIROTA, Jour. Colloid Interface Sci., 45, 502 (1973)

(4) - D. WHITTEN, F. HOPF, F. QUINA, G. and H. SPRINTSCHNIK Pure and Appl. Chem, 49, 379 (1977).

(5) - W. LESSLAUER, Acta Cryst, B, 30, 1932 (1974)

(6) - C. LE GRESSUS, Le Vide, 189, Supplément, 101 (1978)

(7) - A. BARRAUD, A. ROSILIO, C.LE GRESSUS, H. OKUSUMI, A. MOGAMI, Electron Microscopy 1974, Vol. 1, 682 (1974) The Australian Academy of Science publ., Canberra, Australia.

(8) - J. MESSIER, G. MARC, Jour. Phys., 32, 799 (1971)

(9) - M. HOCLET, private communication (1979)

(10) - P-A. CHOLLET, private communication (1979)

(11) - P-A. CHOLLET, Thin Solid Films, 52, 343 (1978)
P-A. CHOLLET, Thin Solid Films, 68, 17 (1980)

(12) - A. BARRAUD, Final report DGRST n° 77-7-0975 (1978)

(13) - H. KUHN, D. MOBIUS, Angew. Chem. Int. Ed., 10, 620 (1971)

(14) - C. ROSILIO, A. RUAUDEL-TEIXIER, Jour. Polym. Sci (Chem. ed.) 13, 2459 (1975)

(15) - A. BARRAUD, A. RUAUDEL-TEIXIER, C. ROSILIO, Ann. Chimie, 10, 195 (1975)

(16) - M. PUTERMAN, T. FORT, J-B. LANDO, Jour. Colloid Interface Sci, 47, 705 (1974)

(17) - A. BARRAUD, C. ROSILIO, A. RUAUDEL-TEIXIER, Polymer Preprints, 19, 179 (1978)

(18) - A. BARRAUD, C. ROSILIO, A. RUAUDEL-TEIXIER, Jour. Colloid. Interface Sci. 62, 509 (1977)

(19) - A. BARRAUD, C. ROSILIO, A. RUAUDEL-TEIXIER, Thin Solid Films, 68, 95 (1980)

(20) - A. BARRAUD, C. ROSILIO, A. RUAUDEL-TEIXIER, Solid State Technology, 22, 120 (1979)

(21) - A. BARRAUD, C. ROSILIO, A. RUAUDEL-TEIXIER Microcircuit Engeneering 79 (IEEE), Aachen (Sept.1979), 127 (1979).

FIGURE CAPTIONS

Fig.1 - Successive steps of the Langmuir-Blodgett technique. Bottom : structure of the built up film.

Fig.2 - Auger micrographs of an aluminium substrate partly coated with one monolayer of stearic acid. The top picture is taken with the analyzer tuned on the Al low energy peak, the bottom one on the high energy one, and the middle one on the Carbon peak.

Fig.3 - Auger spectrum of one monolayer of Ca stearate on a clean aluminium substrate.

Fig.4 - Auger spectrum of one monolayer of Ca stearate on an aluminium substrate subjected to pollution prior to deposition. The spectrum of three layers is also given to calibrate the Ca peak (in this case the Ca peak is due to the Ca content of the two upper layers, regardless of the nature of the first layer).

Fig.5 - Top : Infrared absorption spectrum of alternate layers of behenic acid and docosanol, before and after moderate heating.
Bottom : Infrared absorption spectrum of α -hydroxy-octadecanoic acid before (dotted line) and after (full line) heating.

Fig.6 - Exposure curve of ω -tricosenoic monomolecular resist (900 Å thick) exposed to 5 kV electrons and developed in ethanol.

Fig.7 - Resolution test on a 900 Å thick film of ω-tricosenoic acid. The grating with a 1200 A period (600 A linewidth + 600 A blank) is still resolved.

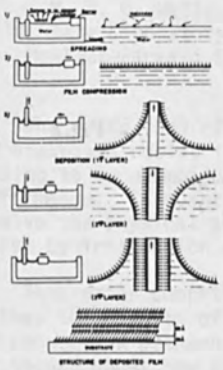

fig.1

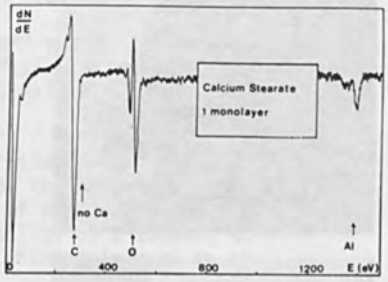

fig.3

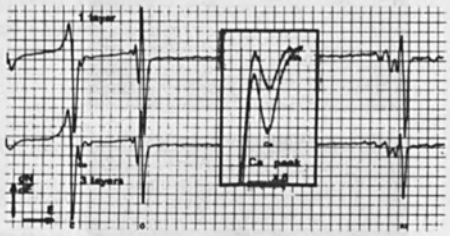

fig.4

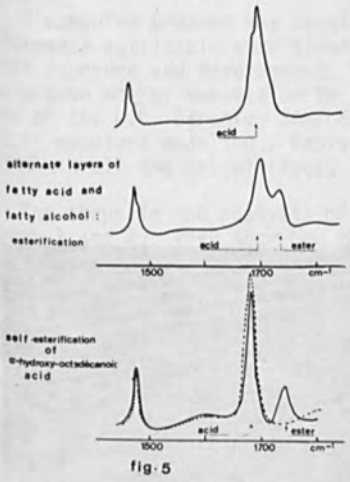

fig.5

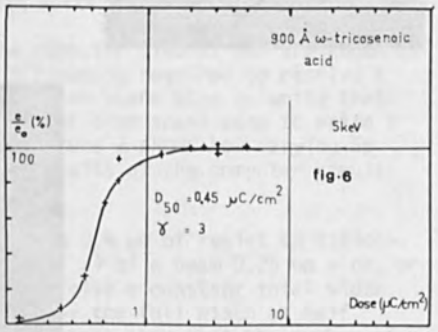

fig.6

Al 58 eV

C 272 eV

Al 1370 eV

Fig.2

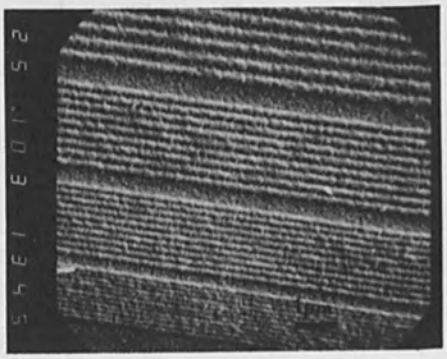

Fig.7

SOLUBILITY RATIO, SENSITIVITY AND LINE PROFILE CONTROL IN POSITIVE E-BEAM RESISTS

M. P. C. Watts,* P. Rissman** and F. J. Kahn*
*Solid State Laboratory and **Physical Electronics Laboratory
Hewlett-Packard Laboratories, Palo Alto, CA 94304

The ratio (S_R) of solubility rates between the exposed and unexposed resist is shown to be the critical parameter leading to an unambiguous measure of positive resist performance. S_R quantifies the ability of a solvent to resolve the physical and chemical changes induced in the resist by irradiation.

This paper comprises two sections; the first describes the results of computer simulations that establish the connection between S_R and lithographic performance. The second shows how this solubility analysis can be applied to experimentally define resist sensitivity and to illuminate the mechanisms determining resist performance.

SIMULATION OF LITHOGRAPHIC PERFORMANCE

A computer program was developed to calculate the lithographic performance attainable at a given S_R in order to simulate positive resist exposure and development. It combines a Monte Carlo simulation of electron energy deposition in the resist with the development routines of the U.C. Berkeley SAMPLE program originally developed for optical exposure modeling. Resist contrast was kept constant and equal to PMMA in all the calculations. Beam voltage was 20 keV.

The steps in the analysis of the computer simulations are shown in Figures 1 and 2. They show how the minimum S_R required to resolve a given feature depends on the number of beam scans used to write that feature. Figure 1 shows how the number of beam scans used to write a feature affects the resist profiles. Figure 2 shows how varying S_R also affects the resist profile. The results of the computer simulations are summarized in Figure 3.

Consider an isolated line written in 0.4 μm of resist on silicon. This line can be written with one scan (1 x) of a beam 0.25 μm wide, or with multiple scans of a smaller beam to give a constant total width (Figure 1a). The beam width is defined by the full width at half height for a Gaussian beam. The calculations show that the number of scans causes a change in the energy distribution in the resist (Figure 1b). The multiple scanned line has a higher maximum energy deposited and a squarer profile. Consequently, the developed profiles in the resist are significantly different (Figure 1c). (The development was

stopped when a vertical wall was obtained.) A clearer comparison of the profiles is obtained in Figure 1d. This shows the change in line width at the resist-silicon interface with development time (t) relative to the time (t_0) at which the resist breaks through to the Si substrate. Three points are illustrated by this graph. First, the line width changes slowly at a constant rate when $t/t_0 > 1.5$. This slow change in line width will give good line width control. Because the vertical resist walls are obtained in the region of good line control, the vertical walls represent an appropriate condition for comparing results obtained with different resist parameters. Second, the line written with several scans is smaller and has a smaller rate of change with time than the single scan line. Third, the line width for all three cases is much larger than the original total beam width of 0.25 μm.

The influence of the number of beam scans on the lithographic performance has been established; the effect of changing S_R will now be examined.

The effect of variations of S_R on the vertical wall profile in the resist is shown in Figure 2a for a line written with 2 scans. A rapid change is apparent for $S_R < 40$. The onset of this change is seen more clearly in Figure 2b, where the effects of S_R on line width are shown for the different beam scan combinations. Below a certain S_R the line width changes rapidly, preventing effective resolution of the line. Therefore, a minimum S_R for satisfactory lithographic performance may be measured. To resolve a line with one beam scan, the resist must be exposed sufficiently to generate an $S_R > 50$; for 2 beam scans the S_R must be > 40, and for 4 beam scans the S_R must be > 30. Therefore, a connection has been made between S_R and lithographic performance.

These calculations were extended to include different resist thicknesses, beam widths and wall angles. It was found that the minimum feature size that can be resolved at a given S_R is determined solely by the number of beam scans used to write the feature. This is independent of the resist thickness (0.2 → 1.0 μm) and absolute beam width (0.0625 → 1.0 μm), provided that the resultant line width is greater than the resist thickness. Results are summarized in Figure 3, with the S_R values and corresponding minimum feature sizes shown on the y axis. For instance, a line with vertical walls requires an S_R of 50 when written with a single beam scan (1 x address). The same line with vertical walls, written with 4 scans of a beam one-quarter the size (4 x address), requires an S_R of 30, and the 4 x address line with 70° wall angle requires an S_R of 10.

ANALYSIS OF EXPERIMENTAL S_R DOSE DATA

The advantages of this analysis method are illustrated by the experimental data in Figure 3. The S_R-dose data for PMMA in methyl

isobutyl ketone (MIBK), a common developer, shows that the operational sensitivity can vary from 80 μCoul cm^{-2} to 20 μCoul cm^{-2}, depending on the beam size and desired resist profile. The S_R vs. dose plot shows how the exposure can be tailored to allow maximum writing speed for the particular feature required. Furthermore, an unambiguous comparison between resists can be made by measuring the dose required to generate a given S_R.

A second example of the use of S_R is to understand the origin of performance differences between PMMA and PMMA-acrylonitrile copolymer (PMMA-AN), a commercially available resist (Tokyo Ohka OEBR 1030). PMMA-AN is claimed to be more sensitive than PMMA, but its radiochemical properties are identical (1); this analysis shows that the developer is the source of the improved performance.

Our experimental data for PMMA shows that at the same temperature the S_R is greater for isoamyl acetate (IAA) developer than for MIBK. On irradiation the resist evolves gas and its porosity changes. Isoamyl acetate molecules are smaller than the pores in irradiated resist and larger than the pores in unirradiated resist (2), whereas MIBK molecules are smaller than both sets of pores. IAA resolves both the molecular weight change and the porosity change and hence has a higher S_R. The solubility ratios for PMMA-AN and PMMA are identical for the same developer. However, IAA is the recommended developer for PMMA-AN, so the operational sensitivity is higher (2.5 x) than for PMMA developed in MIBK. IAA is not a recommended developer for PMMA because of development times > 30 mins, a result of PMMA's higher Tg (2). Therefore, the improved operational sensitivity of PMMA-AN is a result of a lower Tg which allows the effective use of a developer that resolves both the molecular weight change and the porosity change.

CONCLUSIONS

1) To resolve a feature in positive resist, sufficient exposure must be used to generate a minimum difference in solubility rate ratio (S_R) between exposed and unexposed resist. This minimum S_R is dependent on the number of beam scans used to write the feature.

2) The dose required to generate a given S_R is an unambiguous measure of resist sensitivity.

3) S_R measurements are an important tool leading to a better understanding of resist mechanisms.

ACKNOWLEDGMENTS

The authors gratefully acknowledge the contribution of Elaine Poon (Solid State Laboratory, Hewlett-Packard Laboratories), who did the S_R measurements, and of A. Neukermans, T. Okada and S. Eaton

(Physical Electronics Laboratory, Hewlett-Packard Laboratories), who wrote the computer simulation program.

REFERENCES

1. H. Hatano, H. Shiraishi, Y. Taniguchi, S. Hoigome and S. Nonogaki, Preprint, 8th Electron and Ion Beam Science and Technology Meeting, Electrochemical Society, 1979.

2. A. C. Ouano, Polym. Eng. & Sci. 18, 306 (1978).

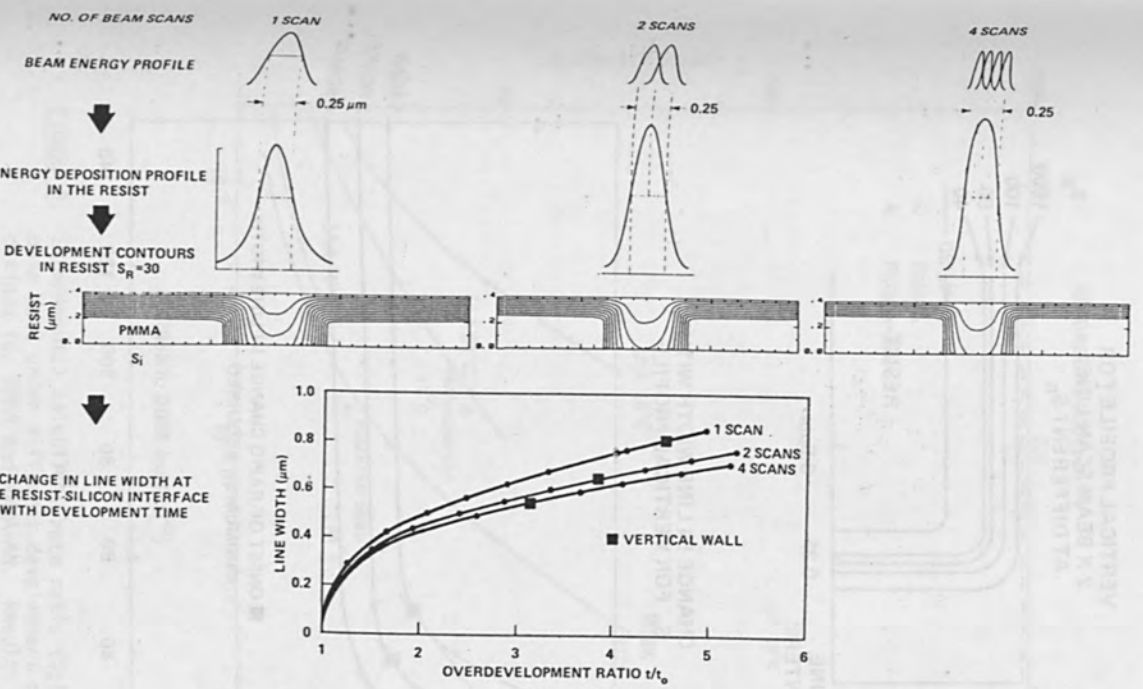

FIGURE 1. The relation between the number of beam scans used to write a feature, the energy deposition profile in the resist, and the developed resist profiles.

2a

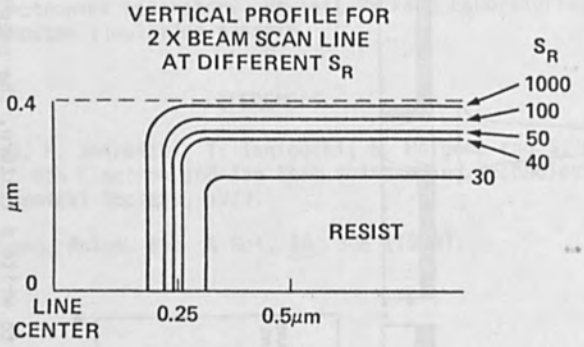

2b

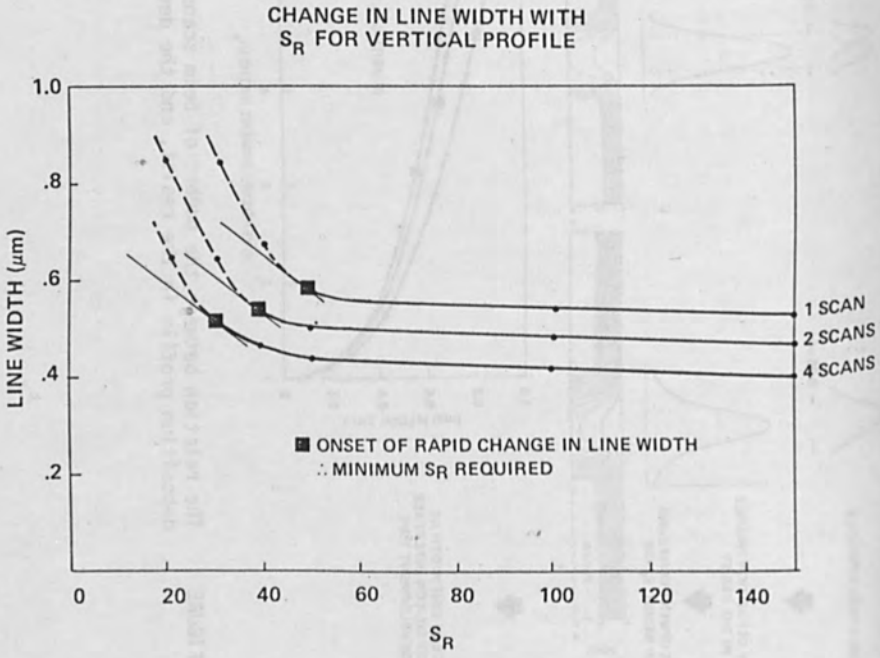

FIGURE 2. The relation between S_R and the generation of vertical walled resist profiles.

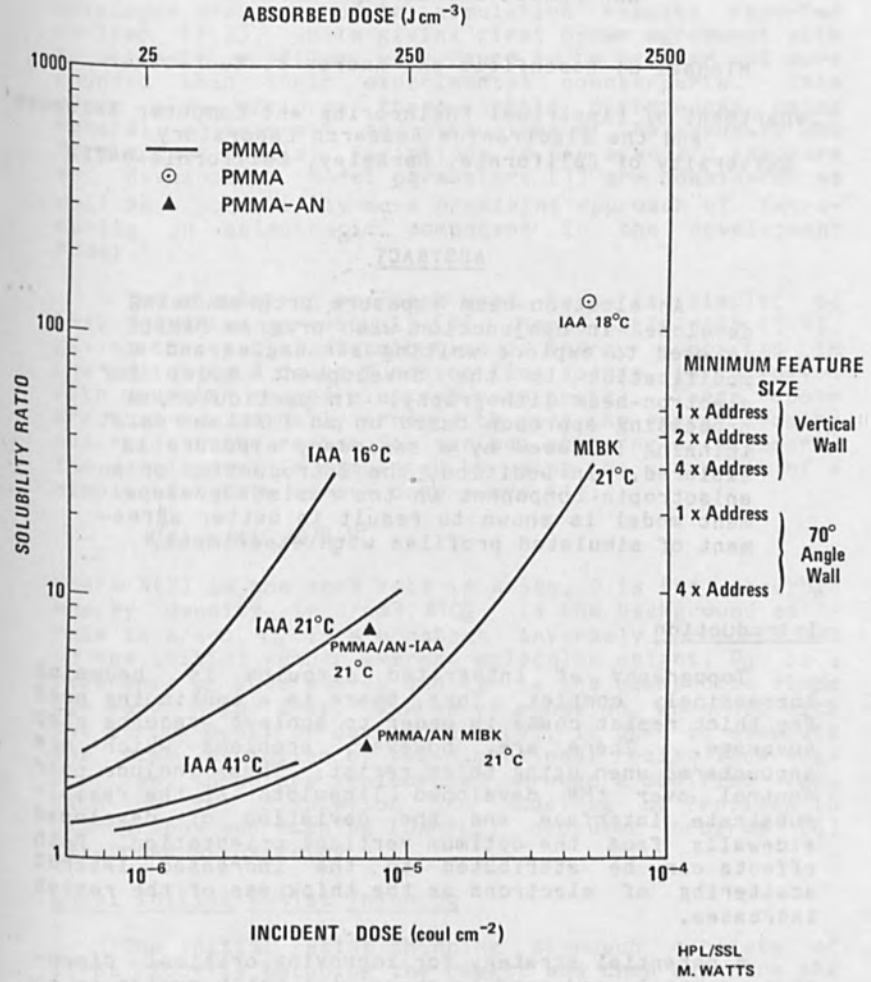

FIGURE 3. Experimental solubility rate ratio (S_R)-dose data under different development conditions for PMMA and PMMA-AN. Results of computer calculations showing the minimum feature size attainable at a given S_R are also shown on the right axis. Beam voltage was 20 keV for both experimental and calculated data.

EXPLORATION OF ELECTRON-BEAM WRITING STRATEGIES AND RESIST DEVELOPMENT EFFECTS

Michael G. Rosenfield and Andrew R. Neureuther

Department of Electrical Engineering and Computer Sciences
and the Electronics Research Laboratory
University of California, Berkeley, California 94720

ABSTRACT

An electron-beam exposure program being developed in conjunction with program SAMPLE is used to explore writing strategies and a modification to the development model for electron-beam lithography. In particular, a processing approach based on an initial resist thinning followed by a secondary exposure is explored. In addition, the introduction of an anisotropic component in the resist development model is shown to result in better agreement of simulated profiles with experiment.

Introduction

Topography of integrated circuits is becoming increasingly complex. Thus, there is a continuing need for thick resist coats in order to achieve adequate step coverage. There are, however, problems which are encountered when using thick resist. These include poor control over the developed linewidth at the resist-substrate interface and the deviation of developed sidewalls from the optimum vertical orientation. Both effects can be attributed to the increased lateral scattering of electrons as the thickness of the resist increases.

A potential strategy for improving critical dimension control and profile shape with thick resist is to locally expose and develop (thin) the initial resist and then make a secondary exposure of the critical features as shown in Figure 1. The desired features are then precisely detailed in the remaining thinner resist layer. In this paper, simulation is used to explore the quantitative advantages of this local initial resist thinning procedure.

Another important issue for simulation is the quality of agreement of predicted profiles with experiment. Developed resist profile simulation results reported earlier [1-2], while giving first order agreement with experimental profiles, were found to be broader and more rounded than their experimental counterparts. This paper also explores these subtle differences using several adjustments and extensions of the exposure and development models. Variations in the standard exposure and development model parameters [1] are considered as well as a potentially more promising approach of introducing an anisotropic component in the development model.

The simulation approach used here is similar to that reported previously [1]. Monte Carlo data [3-4], giving the spatial distribution of energy deposited in the resist by a delta-function line source, is convolved with Gaussian shaped electron-beam spots. These spots are then periodically arrayed to give the energy density absorbed in the resist for various patterns of exposure. The development is simulated by using the curve fit of a simple etch rate versus dose curve [1]:

$$R(S) = R1(C_m + D/D_0)^{\alpha}$$

where R(D) is the etch rate in A/sec, D is the absorbed energy density in J/cm3, $R1C_m^{\alpha}$ is the background etch-rate in A/sec, C_m is a constant inversely proportional to the initial number average molecular weight, D_0 is a reference or knee energy and α is the asymptotic slope at very high dose. The above equation, combined with the string model of development [5], is used to simulate the time evolution of two-dimensional resist line-edge profiles. These are implemented through a modified version of the Simulation And Modeling of Profiles in Lithography and Etching (SAMPLE) computer program [6] developed at Berkeley.

Local Initial Resist Thinning

The initial resist thinning approach consists of first locally thinning the resist and then exposing the critical features. It can be implemented as illustrated in Figure 1. A primary exposure is made in the thick resist in the areas of the desired openings. The resist is then developed so that the resist thickness is significantly reduced only in the desired areas. A second exposure is made in these thinner resist regions and the critical dimensions are then precisely developed out.

This approach is particulary suited to masking applications such as the opening of contact windows. In an attempt to somewhat realistically reflect the electron-beam writing throughput limitations, the combined dose of the primary and secondary exposures was constrained to be the same as the total dose used in the more conventional single exposure method.

An alternative version of the initial resist thinning procedure would be to use a large area, rather than local, exposure, develop, and then expose and develop a pattern in the thinned region. Clearly, this procedure would not work as well as the local thinning method since the initial large area exposure would contribute to the background etchrate and result in less control over the linewidth with development time. Also, it would require a much higher dose than that used conventionally. It is, however, much easier to accomplish experimentally as no realignment is required. An experiment of this type was used to illustrate the basic technique and more importantly to establish the credibility of simulation in predicting profiles for various initial resist thinning strategeies.

The experiment was carried out on the VS-1 electron-beam system at IBM Research Laboratories in San Jose, California, with the assistance of C.H. Ting and A. Kraft. Silicon wafers, coated with approximately 1.4 um of PMMA 2010, were exposed with 20 keV electrons over large areas with a dose of 30 uc/cm2. The resist was developed for 8 minutes in a stationary 1:1 solution of MIBK:IPA. A secondary exposure of different sized lines was then made at a higher dose, 120 uc/cm2 (so that the lines would develop out faster than the background area exposure), and the wafers were developed a second time. Experimental profiles of .3 um and .5 um lines (i.e. lines written with 3 and 5 electron beam spots, respectivaly, at a spot density of 10 spots/um) exposed in the thinned resist are shown in Figure 2.

Simulation of the initial resist thinning strategy was performed by the superposition of the absorbed energy densities due to the primary and secondary exposures. The secondary exposure's energy density was added to the primary exposure's energy density starting at the initial resist thinning depth, d (Figure 3). In the case study used here a further expediant assumption was made in that only one set of Monte Carlo data was used, that for the initial resist thickness. In using 1 um PMMA on silicon for a simulation of initial resist thinning at a depth of .5 um, this amounted to reusing

the top .5 um of the 1 um Monte Carlo data to simulate the secondary exposure. Although these assumptions will slightly affect the quality of the experiment-simulation comparison, they should adequately illustrate the basic concept.

The direct use of the parameter values, for PMMA 2010 developed in 1:1 MIBK:IPA [1], did not accurately simulate the profiles in Figure 2. To account for a slow rate of development of the experimental profiles, the reference rate R1 was reduced from 1.0 to .74. After adjusting only this parameter and using the measured electron-beam spot size (Full width half maximum, FWHM, of .1 um) and a secondary exposure depth of .9-1.0 um, simulated profiles were obtained corresponding to those of Figure 2 (Figure 4). Contours correspond to development times of 480 to 560 seconds in 20 second intervals. As can be seen, first order agreement between simulation and experiment is good. All linewidths, measured at the resist- substrate interface, and resist heights agree to within the uncertainty of the measurements (about .10 um).

The simulated contours have, however, sharper corners and slightly less undercut than the experimental contours. This can be attributed to the fact that beam size is not a precisely measured parameter (i.e. a larger beam diameter would give more rounded simulated profiles for example) and the assumption of the top .5 um of 1.4 um Monte Carlo data (which was the top 1.4 um of 1.5 um Monte Carlo data [4]) being the same as Monte Carlo data for .5 um PMMA on silicon. Other factors also contributing to deviation between simulation and experiment are that the initial resist thickness and secondary exposure depth were not acurately known. Generally, however, the agreement is sufficiently accurate to establish the credibility of using simulation to study tradeoffs in the various initial resist thinning approaches.

The more desirable initial resist thinning technique is to thin the resist only in the areas where an opening is to be made as illustrated in Figure 1. This approach was explored by simulation. As mentioned previously, the comparison between the conventional single exposure method and the initial resist thinning method will be made with the constraint of the same total exposure for both techniques. A nominal .5 um linewidth at the resist-silicon interface in 1 um PMMA developed in 1:1 MIBK:IPA was chosen as the critical dimension for comparison purposes.

A conventional single exposure method used to open a .5 um line is shown in Figure 5a. The four electron-beam spots have a FWHM of .125 um and were thus spaced accordingly at 8 spots/um density. The dose was 45.6 uc/cm2 and each spot was weighted equally (given an equal share of the total dose). The developed contours correspond to development times of 400 to 600 seconds in 20 second intervals. As can be seen, the contours about the .5 um nominal linewidth are overcut and rounded with the linewidth increasing at a rate of .0029 um/sec.

In an effort to improve on the developed profiles of Figure 5a, the relative doses of the four beam spots were adjusted while keeping the total dose the same. In effect, the two middle spots were given approximately four times the dose of the outer two spots. The developed contours, corresponding to development times of 260 to 400 seconds in 20 second intervals, are shown in Figure 5b. In this case, the sidewalls are more vertical and the linewidth is advancing at a lower rate of .0021 um/sec about the .5 um nominal linewidth.

In Figure 6, the reduced spot writing scheme of Greeneich [7] is simulated. This method uses only two spots spaced at a distance equal to twice their FWHM value (.125 um). The total dose was again 45.6 uc/cm2. The developed contours correspond to development times of 280 to 480 seconds in 20 second intervals. The contours are slightly improved over the contours of Figure 5a in that the sidewalls are slightly more vertical and that the linewidth is advancing at .0026 um/sec about the .5 um point.

Several versions of the initial resist thinning approach were explored in attempting to obtain greater linewidth control and improved shape. The first method simulated was simply a normal four spot initial exposure, as in Figure 5a, at half the dose (22.8 uc/cm2) and an identical secondary exposure at a depth in the resist of .5 um as illustrated in Figure 7. The contours correspond to development times of 700 to 900 seconds in 20 second intervals. The sidewalls are more vertical and the linewidth is advancing at .0021 um/sec which is an improvement over both the conventional technique of Figure 5a and the two spot approach of Figure 6.

An effort was then made to improve upon the resist contours of the initial resist thinning process by weighting the exposure spots. The method which appears to give the most significant improvement is shown in

Figure 8. The initial exposure is still four spots; however, the middle spots were given five times more dose than the outer spots. The secondary exposure then utilized only two spots directly below the initial two middle spots at a depth of .5 um. The secondary exposure was given three and one-half times more dose than the initial outer spots. The total dose was still constrained to be 45.6 uc/cm2. The developed contours correspond to development times of 280 to 480 seconds in 20 second intervals. The contours show significant improvement over results of previous techniques. The sidewalls are vertical and the linewidth is developing out at a much slower rate, .0013 um/sec about the .5 um nominal linewidth.

For comparison purposes, the use of two spots similar to those used in the preceeding secondary exposure were simulated using a conventional approach. Contours corresponding to development times of 200 to 400 seconds in 20 second intervals at a dose of 45.6 uc/cm2 are shown in Figure 9. The sidewalls are slightly curved and the linewidth is opening at a rate of .0018 um/sec about the nominal .5 um linewidth.

A plot of linewidth versus development time for the various exposures discussed is shown in Figure 10. As can be seen, the optimized initial resist thinning procedure gives about 28% better linewidth control (defined as the slope of the curve about the .5 um nominal linewidth) over the two spot exposure of Figure 9, a 40% improvement over the weighted conventional exposure technique of Figure 5b, a 50% improvement over the technique of Greeneich in Figure 6, and a 55% improvement over the conventional technique of Figure 5a.

A figure of merit to compare the various exposure techniques is defined as the inverse of the sensitivity to development time normalized with respect to development time and linewidth. That is:

$$F.M. = \left(\frac{td}{LW}\frac{\partial(LW)}{\partial(td)}\right)^{-1}$$

where F.M. is the figure of merit (the higher the better), LW is the linewidth, and td is the development time. Table 1 lists the figures of merit for the various exposure techniques discussed. As expected, the four spot conventional approach of Figure 5a has a low figure of merit. The two spot approach of Greeneich shows improvement in this respect. However, the weighted four spot approach of Figure 5b has a significantly greater figure of merit than either of the

preceeding methods. The two spot exposure of Figure 9 has the highest figure of merit; however, its edge profile is undercut and it is apt to be limited by edge scalloping effects not simulated. The optimized initial resist thinning approach of Figure 8, although having a slightly lower figure of merit than the two spot method of Figure 9, has vertical sidewalls and a a substantially higher figure of merit than any of the other more conventional techniques. Scalloping effects in this case would tend to be reduced by by the four spot initial exposure.

Potential problems with the initial resist thinning procedure are control over the thinning thickness and registration of the secondary exposure. It is also possible that the use of heavily weighted spots will increase scalloping. Some of these effects are being explored. Simulation has shown, for example, that the developed contours are relatively unchanged with an error of vertical placement of .1 um and lateral registration of .05 um.

Second order improvements of the initial resist thinning method are currently being explored. These include reducing the secondary spot size and/or using different beam voltages for the initial and secondary exposures. The latter may have possible implications in correcting for proximity effects. [8]

Investigation of the Resist Model

Several approaches were used to explore improving the agreement of the simulated profiles reported earlier [1] with experiment. Adjusting the beam size and R1 in the etch rate curve did not give any further fundamental improvement. For example, making the beam size smaller in an attempt to eliminate the rounded simulated profile resulted in the top corners becoming too sharp with little improvement of the rounded contours. The shape of the etch rate versus dose curve was also adjusted by changing the D_0, α, and R1 parameters; but, again there was no improvement. Thus, it appears that the resist exposure development model must be generalized to achieve better experimental agreement.

One possible generalization is to allow the development to occur more rapidly approximately along the direction of the primary electron trajectories. This anisotropic effect was implemented approximately by a fractional reduction in the lateral motion of the nodes in the string algorithim as is illustrated in Fig-

ure 11. Figure 12 is a comparison of experimental and simulated profiles from [1] and simulated profiles with a 70% reduction in lateral development. The adapted profiles correspond to development times of 20 to 180 seconds in 20 second intervals. The experimental contours from [1] correspond to a 180 second development time while the simulated profiles from [1] correspond to development times of 20 to 200 seconds in 20 second intervals. All other parameters are the same as in [1].

For the case of isolated lines in Figure 12, the profiles with this simple reduction in lateral development rate more closely track the experimental contours. However, for arrays of lines in Figure 12, the correction was not as necessary. A possible explanation is that development tends to occur more rapidly along the trajectories of the high energy electrons. The physical mechanism causing such an effect might be related to the generation of volatile products and micropores during exposure [9]. This preferential development along trajectories is consistent with there being more of a need to correct the simulated profiles for isolated lines as compared to arrayed lines. For single lines, the electron trajectories would be fairly vertical with spreading increasing with depth in the resist. For arrayed lines, however, proximity effects contribute a significant mix of non vertical backscattered electrons which would tend to average out the preferential effects. Other and possibly more basic physical mechanisms including the scattering model might be involved. However, the simple addition of a preferential development factor appears to be a simple procedure for significantly improving the agreement of simulated profiles with experiment.

Conclusion

One of the advantages of simulation is its flexibility to explore potential processing approaches. Various assumptions have been used to explore writing strategies and an improved resist model for electron-beam lithography. An initial resist thinning and secondary exposure particulary applicable to contact opening has been suggested. It results in more vertical profiles and greater linewidth control than obtainable conventionally. Several possible exposure and resist development effects were explored to improve the detailed fit of simulation to experimental line-edge profiles. Introducing a preferred anisotropic etching approximately in the direction of the primary electron

trajectories was found to give a significant improvement in the comparison, especially for isolated lines.

Acknowledgment

The authors want to thank C.H. Ting and A. Kraft of IBM Research, San Jose for making the VS-1 experimental comparison possible. We would also like to thank D.F. Kyser, S.N. Nandgaonkar, and Y.C. Lin for valuable discussions during the course of this work.

Research sponsored by the National Science Foundation Grant ENG77-14660.

References

[1] A.R. Neureuther, D.F. Kyser, and C.H. Ting, IEEE Trans. Electron Devices, vol. ED-26, no. 4, pp 686-693, 1979.

[2] K. Murata, E. Nomura, K. Nagami, T. Kato, and H. Nakata, J. Vac. Sci. Technol., vol. 16, no. 6, pp. 1734-1738, Nov./Dec. 1979.

[3] D.F. Kyser and K. Murata, Proc. 6th Int. Conf. on Electron and Ion Beam Sci. Tech. (Electrochemical Society, 1974), pp 205-223.

[4] I. Adesida, "Electron Energy Dissipation in Layered Media", Ph.D dissertation, Dept. of EECS, U.C. Berkeley, 1979.

[5] R.E. Jewett, P.I. Hagouel, A.R. Neureuther, and T. Van Duzer, Polymer Eng. Sci., vol. 17, no. 6, pp. 381-384, 1977.

[6] W.G. Oldham, S.N. Nandgaonkar, A.R. Neureuther, and M.M. O'Toole, IEEE Trans. Electron Devices, vol. ED-26, no. 4, pp. 717-722, 1979.

[7] J.S. Greeneich, J. Vac. Sci. Technol., vol. 16, no. 6, pp. 1749-1753, Nov./Dec. 1979.

[8] D.F. Kyser and C.H. Ting, J. Vac. Sci. Technol., vol. 16, no. 6, pp. 1759-1796, Nov./Dec. 1979.

[9] A.C. Ouano, Polymer Eng. Sci., vol 18, no. 4, pp. 306-313, 1978.

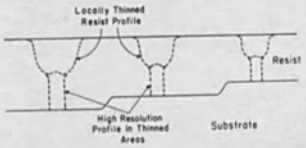

Fig. 1. Local initial resist thinning strategy.

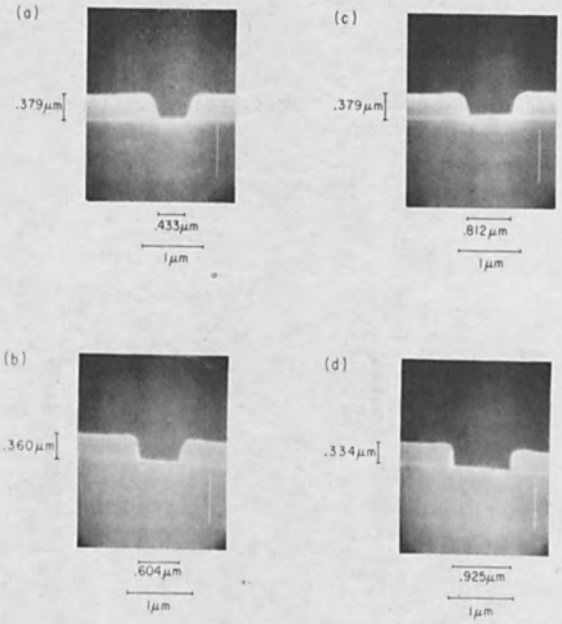

Fig. 2. SEM resist profiles for an initial 30 uc/cm^2 area exposure and 8 min. dev. followed by secondary exposures. a) .3um line, 60 sec. dev.; b) 3 um line, 80 sec. dev.; c) .5 um line, 60 sec. dev.; d) .5 um line, 80 sec. dev. secondary dose: 120 uc/cm^2.

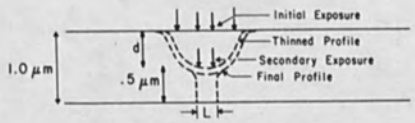

Fig. 3. Local initial resist thinning-simulation approach.

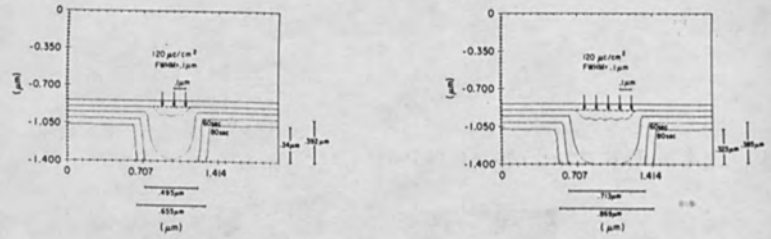

Fig. 4. Simulated profiles corresponding to Figure 2. a) .3 um line, b) .5 um line.

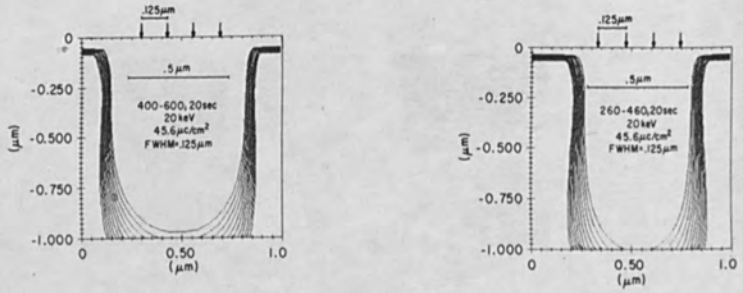

Fig. 5. Simulation of conventional exposure techniques. a) Equally weighted spots, b) weighted spots, -- inner spots have 4x dose of outer spots.

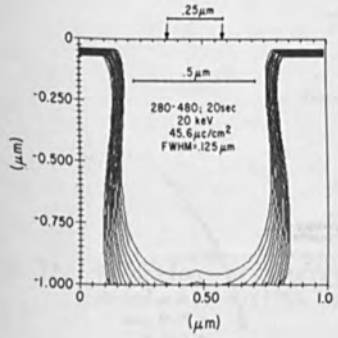

Fig. 6. Simulation of reduced spot technique -- two spots equally weighted.

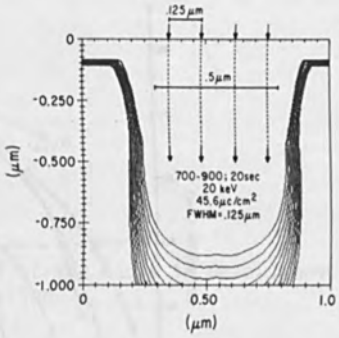

Fig. 7. Simulation of local initial resist thinning technique identical initial and secondary exposures.

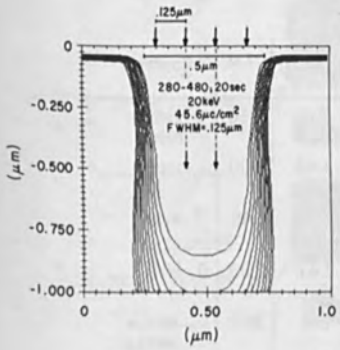

Fig. 8. Simulation of optimized local initial resist thinning weighted initial exposure. (Inner spots have 5x dose of outer.) Secondary exposure spots have 3.5x dose of outer spots.

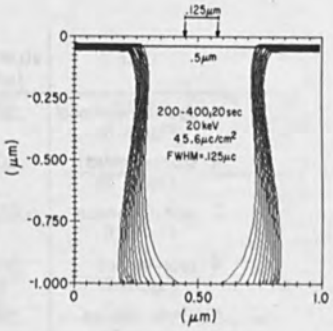

Fig. 9. Simulation of a two spot conventional exposure similar to secondary exposure of Fig. 8.

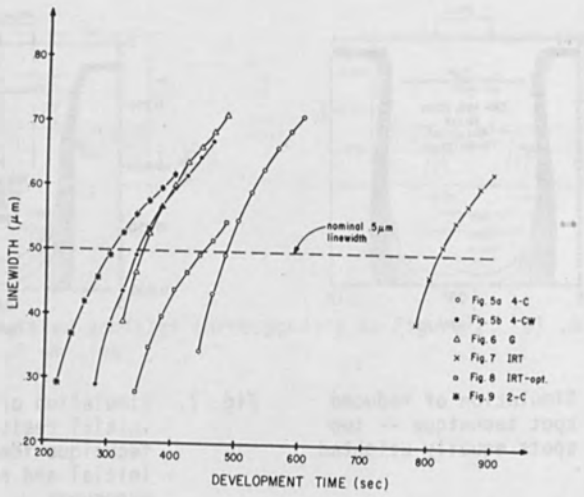

Fig. 10. Linewidth versus development time for the various exposure techniques.

Case	Sensitivity ∂(LW)/∂(td) (μm/sec)	td (sec)	S = td/LW · ∂(LW)/∂(td)	F.M.	Comment
4 spot-conventional Figure 5a	.0029	484	2.81	.356	0-wide overcut
4 spot-weighted Figure 5b	.0021	345	1.45	.690	+-good
2 spot-Greeneich Figure 6	.0026	350	1.82	.549	0^{+}-wide
4 spot-thinned Figure 7	.0021	825	3.47	.289	0-wide
Optimum-thinned Figure 8	.0013	445	1.16	.864	++-narrow vertical
2 spot-conventional Figure 9	.0018	305	1.10	.911	+-scalloping slight undercut

Table 1. Figure of merit comparison of the various exposure techniques.

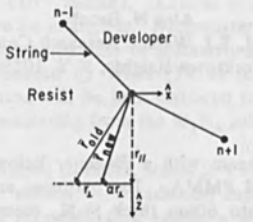

Fig. 11. Reduction of lateral motion of string nodes in development model. (1-α)x100% is the reduction.

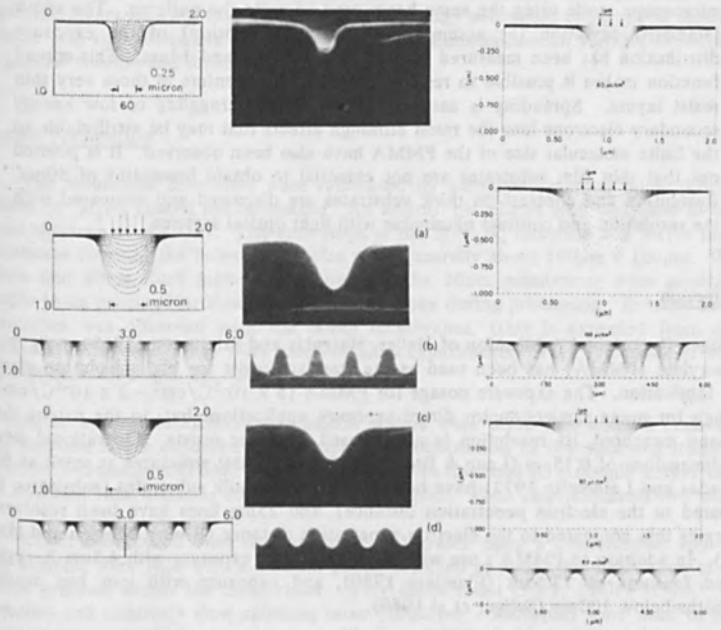

Fig. 12. Comparison of earlier simulated and experimental resist profiles [1] with simulated profiles corresponding to a 70% reduction in lateral string motion. Simulated contours correspond to 20 sec. intervals. Experimental dev. time is 180 sec.

RESOLUTION LIMITS OF PMMA RESIST FOR EXPOSURE WITH 50kV ELECTRONS

Alec N. Broers
IBM, T.J. Watson Research Center
Yorktown Heights, N.Y. 10598

Abstract: An electron beam with a diameter below 1nm has been used to measure the resolution of PMMA. Test patterns are written in 30nm thick PMMA layers coated onto 60nm thick Si_3N_4 membrane substrates. Both lateral scattering of electrons in the resist and backscattering from the substrate are negligible for these samples. Preliminary results obtained with 50kV electrons are presented in this paper. The test patterns contain nominal linewidths down to 4.4nm. The exposure distribution is determined by measuring the exposure dose needed to open up lines with widths smaller than the width of the distribution. Samples are examined in the scanning transmission microscope mode using the same beam used to write the patterns. The width (standard deviation (σ) assuming a normal distribution) of the exposure distribution has been measured to be between 11nm and 14nm. This spread function makes it possible to resolve lines on 35nm centers in these very thin resist layers. Spreading is assumed to be set by straggling of low energy secondary electrons into the resist although effects that may be attributable to the finite molecular size of the PMMA have also been observed. It is pointed out that thin film substrates are not essential to obtain linewidths of 50nm. Resolution and contrast on thick substrates are discussed and compared with the resolution and contrast obtainable with light optical systems.

Introduction

Since the original publication of Haller, Hatzakis and Srinivasen (1968), poly methyl methacrylate (PMMA) has been used as the standard resist for high resolution electron beam fabrication. The exposure dosage for PMMA ($5 \times 10^{-5}C/cm^2$ - $2 \times 10^{-4}C/cm^2$) is too high for many semiconductor direct exposure applications but, to the extent that it has been measured, its resolution is unsurpassed by other resists. Operational devices with dimensions of 0.15μm (Lean & Broers 1970), and metal structures as small as 60nm (Mayadas and Laibowitz 1972) have been fabricated on bulk substrates (substrates thick compared to the electron penetration distance), and 25nm lines have been resolved on substrates thin compared to the electron penetration distance (Broers, Molzen and Harper 1978). In addition to PMMA's use with electron beams, exposure with 4.5nm X-rays has yielded features of 17.5nm (Flanders 1980), and exposure with ions has produced linewidths below 100nm (Seliger et al 1979).

The resolution that can be obtained in an electron resist layer is usually determined by lateral scattering of electrons in the resist layer and by electron back-scattering from the underlying substrate. In order to measure the resolution in the absence of significant electron scattering we have used 50kV electrons to expose very thin (~ 30nm) layers of PMMA supported on thin (~ 60nm) Si_3N_4 membrane substrates. Under these conditions, resolution becomes effectively limited only by the basic physical processes involved in breaking the bonds in the methacrylate polymer. The probability that lateral scattering of electrons will be significant can be estimated from the theoretical and experimental data of Misell (1973), if it is assumed that scattering in PMMA is similar to that in carbon.

Such an estimation shows that in passing through a 50nm thick carbon film, less than 1% of 50kV electrons will be scattered through angles equal to or exceeding the convergence angle of the electron beam (10^{-2} radian). Lateral scattering effects in a 30nm thick PMMA layer should therefore be negligible. Backscattering from the Si_3N_4 substrate can be estimated by calculating the probability of Rutherford scattering events through angles greater than 90°. Data presented by Wells (1974) indicate that there is only a 10^{-3} probability that a 50kV electron will be backscattered from a 60nm thick film of atomic number 12. Therefore, backscattering from the Si_3N_4 substrate should also be negligible.

The minimum energy required to break bonds in PMMA can be estimated to be 5eV from the wavelength of the "softest" UV radiation capable of exposing the resist (Lin 1975). With electrons, it is proposed that exposure is effected predominantly by low energy secondary electrons because the cross-section of these electrons for bond scission will be very much greater than the cross-section of the high energy primaries. The secondaries can be excited at a distance from the path of the high energy primaries and they can travel further into the resist before their energy is fully dissipated. The overall distance the secondaries travel blurs the pattern and determines the ultimate resolution of the resist exposure process. Measurements of the secondary electron yield from thin dielectric layers indicate that the range of low energy secondary electrons in dielectrics is several tens of nanometers (Seiler 1967). The measurements on PMMA presented here in general confirm this deduction.

Sample Preparation

The membrane substrates were fabricated by selectively etching holes through the silicon of Si_3N_4 coated silicon wafers. An anisotropic silicon etch was used to etch the holes (Molzen et al 1978). The etch stops at the Si-Si_3N_4 interface and leaves the Si_3N_4 membrane covering the holes. The holes were generally about 100μm x 100μm. We used 30nm and 60nm thick membranes, however, the 30nm membranes were generally too fragile to be practicable; almost half of them broke during processing. Because no loss in resolution was observed with the 60nm membranes, (this is expected from electron back-scattering data), they were used for most experiments. Very few cases of breakage were encountered with the thicker membranes.

After window fabrication, the silicon wafers were diced into chips 2.6mm x 1mm. For electron beam exposure and subsequent examination in the scanning transmission electron microscopy (STEM) mode, the chips were mounted in a sample holder designed for standard 3mm diameter electron microscope grids. Each chip contained two windows.

Resist was coated onto the membrane substrates using a conventional spin-coater. The samples were held with a vacuum chuck designed to avoid the application of atmospheric pressure across the membranes. Very dilute resist (50:1, 2010 PMMA : chlorobenzine) and relatively slow spinning rates (2000rpm - 3000rpm) were used to produce resist layers with thicknesses between 30nm and 100nm. As discussed below precise measurement of resist thickness was made from STEM images of the developed samples after shadowing the samples with a thin layer of metal. Resist thickness was uniform to better than 10nm over the window areas. Resist layers were baked at 160°C for one hour to remove residual solvent.

In order to provide detail on the sample for focusing, a 5nm thick PdAu layer was vapor deposited onto the underneath of the membrane. Structure in this layer provided high contrast in the bright field STEM image and made it easy to determine that the beam diameter was less than 1nm. The number of primaries back-scattered from this layer is

less than 1 in 500 (Wells 1974), and few low energy secondaries formed at the PdAu/Si_3N_4 interface will penetrate the Si_3N_4 membrane to the resist. The PdAu layer should therefore have little effect on resist exposure.

Image spreading due to the finite angular width of the beam was about 2nm (resist thickness 30nm, substrate thickness 60nm, beam half angle 10^{-2} radian) assuming that the beam was focused accurately on the bottom of the Si_3N_4 membrane. The AuPd layer had sufficient conductivity to avoid sample charging during exposure.

Exposure

Patterns were written in a STEM (Broers 1973 & 1979) with an electron beam diameter of less than 1nm. The patterns were written under the control of a flying spot scanner. The exact nominal exposed linewidths were measured from the video signal produced by the STEM bright field detector. The linewidth is given by the width of the "beam-on" pulses on the video signal. This method eliminated any errors that might have arisen due to the finite resolution of the flying spot scanner. In practice the linewidths scaled very closely with the actual mask dimensions.

Beam current was measured using a Faraday cup located below the sample. Beam current had to be kept at a level of about 2×10^{-12} amp because of the small area of the pattern and the relatively slow scan rate of the STEM system (minimum frame time of 10 sec). The pattern was typically $2.5\mu \times 2.5\mu$ for a minimum nominal linewidth of about 2.5nm.

Before each pattern was exposed, the beam was offset to an area adjacent to the exposed area and the beam focused on the PdAu layer underneath the membrane. The sample was mechanically moved approximately 20μ between exposure sites. The vertical accuracy of the sample stage was such that adjustment of focus after movement was unnecessary in the majority of cases.

Samples were developed for about 50 seconds with the standard PMMA developer; one part methyl isobutyl ketone to three parts of isopyl alcohol. Our measurements indicated that the developer dissolved the unexposed resist at a rate of about 25nm per minute so the initial resist thickness was approximately 20nm thicker than that measured for the developed patterns.

After development, 5nm of AuPd was vapor deposited onto the top of the resist at an incidence angle of 45°. This metal layer clearly outlined the resist pattern, and the shadow length was an accurate measure of the resist thickness.

Determination of Exposure Distribution

The test pattern used in these experiments is shown in fig. 1. The pattern was written at a size that yielded a minimum nominal linewidth of 4.4nm. The broadest line was about 120nm wide. Eleven different exposure times were used for each experimental run. The shortest time gave an exposure dose which was below that needed to open up the largest shapes. The longest time was such that the resist developed through in the site of the narrowest line.

If the exposure distribution is Gaussian, then using the "reciprocity principle" of Chang (1975), the exposure dose (Q_w) received at the center of an infinitely long rectangle of width w can be shown to be given by

$$Q_w = Q_o \, erf(w/2\sigma)$$

where Q_o is the exposure dosage in the center of an infinitely large shape and σ is the standard deviation of the distribution.

Fig. 2 is a bright field STEM micrograph of the test pattern exposed at a dose slightly greater than that needed to open large shapes. The standard deviation (σ) of the exposure distribution was calculated from patterns of this type exposed at progressively greater doses. σ was calculated from the nominal linewidth (w) of the narrowest line that had developed through to the substrate, and the ratio of the exposure dosage for the given test exposure to the exposure dosage needed to develop through to the substrate in the sites of the large shapes (Q_w/Q_o). If the distribution is truly Gaussian, then the same σ will be found for each of the test exposures. In practice, this was not the case. Heavier exposures, in which narrower lines had developed through to the substrate, in general yielded σ values higher than those deduced from lower exposure doses. In a series of five separate experiments, the average values of σ varied from 11nm to 14nm. The resist thickness was about 30nm. The fractional exposures received for different linewidths are plotted in fig. 3. The fractional exposure was determined from the exposure times needed to open up different linewidths. For example, it took about five times longer to open the 5nm nominal linewidth line than it did to open the large shapes. Fig. 3 also shows the fractional exposure that would be obtained with a resist with a Gaussian distribution (σ = 12.5nm). An additional experiment in which identical exposures were made on three different resist thicknesses (50nm, 80nm and 100nm) showed that, as expected from electron scattering data, there was no significant dependence on resist thickness for thicknesses below 100nm.

The narrowest line that opened up at the dose required to open up the large shapes ($\sim 3 \times 10^{-4} C/cm^2$) was between 20nm and 25nm wide (line 5 and line 6). In practice the developed lines were close to their nominal width. As the exposure dose was increased to open the narrower lines, the linewidth of the wider lines increased. The rate of increase can also be used to estimate the σ of the spread function in the resist, however, this will not be discussed here.

If exposure is due to low energy secondary electrons alone, and the excitation of secondaries is isotropic and random, it would appear reasonable for the distribution to be Gaussian. The deviation observed could be the result of a dependence of development rate on linewidth. Development may be slower for narrower lines because the lines become comparable in size to the molecular size of the PMMA. slows the development process.

If the exposure distribution is Gaussian, then the ratio of the exposure dose received at the center of a line (Q_l), to the exposure dose received at the center of a space (Q_s) for an array of infinitely long parallel lines with equal linewidth and spacing is given by

$$\frac{Q_l}{Q_s} = \frac{erf\, S/4 + \sum_{n=1}^{n=m} [erf(4n+1)S/4 - erf(4n-1)S/4]}{\sum_{n=1}^{n=m} [erf(4n-1)S/4 - erf(4n-3)S/4]}$$

where s is the center to center spacing between the lines, and m = the number of lines taken in account on either side of the line under consideration. It is also useful to define

what we shall call the Resist Contrast Function (R.C.F.), K, where

$$K = \frac{Q_l - Q_s}{Q_l + Q_s}$$

This definition is similar to that of the Modulation Transfer Function (M.T.F.) for an optical system except that for the optical case the pattern distribution is generally assumed to be sinusoidal rather than the square wave we have assumed for the electron beam resist case. Fig. 4 shows the R.C.F. for a resist that exhibits a Gaussian exposure distribution. For a thin substrate, 60% contrast (K = 0.6) corresponds to a spatial frequency (ν) of $0.28\sigma^{-1}$. If it is assumed that the distribution for PMMA is Gaussian and that σ = 12.5nm, then 60% contrast is obtained for $\nu = 0.28 \div 12 \times 10^{-7} = 2.24 \times 10^5$ lines/cm (44.6nm center to center spacing). As already discussed, it is assumed that the electron beam diameter is zero and that lateral electron scattering in the resist is negligible. 60% is the order of contrast normally required for adequate definition in a developed resist pattern. Broers, Harper, and Molzen (1978) reported a minimum center to center spacing of 50nm for a 110nm thick PMMA layer on top of a 20nm layer of AuPd on a Si_3N_4 membrane. This is in good agreement with the results reported here. The R.C.F. for a thick substrate shown in fig. 4 is discussed in the next section.

Resolution with Thick Substrates and with Optical Systems

On thick substrates, both backscattered and primary electrons produce secondaries and contribute to resist exposure. It has been found that exposure by the backscattered electrons can be approximated by a Gaussian distribution with a standard deviation of several microns. The total exposure contribution of the backscattered electrons is approximately equal to that of the primary electrons. Several workers have modeled and measured the parameters associated with backscattering from targets of different materials & thicknesses (e.g. Jones & Hatzakis 1978, Parikh & Kyser 1978, Greeneich 1979, Aizaki 1979, and Adesida, Shimizu & Everhart 1979). We shall assume that for silicon, the standard deviation of the distribution is 2.3μ, and the total exposure due to backscattered electrons is 0.86 times that of the primaries (Grobman and Speth 1978). According to these parameters, the backscattered contribution to an isolated line 25nm wide on a silicon substrate is $0.86\ Q_o\ erf\ (0.025/4.6) = .004Q_o$ where Q_o is the incident dosage. The contribution is, therefore, so small that it can be ignored. This is the case for an isolated shape that is very small compared to the area from which backscattered electrons re-emerge from the sample. For an array of such shapes that covers an area that approaches, or is greater than, the area from which the backscattered electrons emerge, then backscattering becomes significant and gives rise to the well known proximity effect (Chang 1975). The dotted curve in fig. 4 shows what happens to the R.C.F. in this case. In the example shown, it is assumed that $\sigma_{backscattered} = 184 \times \sigma_{resist}$ ($\sigma_{backscattered}$ = 2.3μ, σ_{resist} = 12.5nm), and that the total backscattered contribution is η times the contribution of the primary beam, where η = 0.86 (silicon substrate). The maximum contrast is 0.54 under these conditions.

Fig. 5 shows the resist contrast functions for PMMA plotted against linewidth. Again it is assumed that the pattern consists of an infinite array of equal lines and spaces. The contrast for a light optical system with a numerical aperture (N.A.) = 0.41 and operating wavelength (λ) = 405nm is also shown. The dotted version of the optical curve shows the contrast for a square-wave target (Smith 1966) rather than a sinusoidal target. Several observations can be made from fig. 5.

1. For electron beam (50kV) exposure of PMMA on a thin substrate, 60% contrast is obtained for a linewidth of 22.3nm.

2. For the thick silicon substrate, the electron beam R.C.F. for PMMA is essentially flat from 50nm to 2μ, meaning that it should be no more difficult to produce 50nm lines and spaces than it is to produce 2μ lines and spaces. As before, this assumes that resolution is not limited by the electron optical system or by lateral electron scattering in the resist (i.e. the resist must be very thin). Proximity correction will probably have to be used in most cases. The algorithms used for computing proximity corrections will depend on the ratio of the size of the pattern elements to the width of the backscattered distribution. For very small pattern features, proximity correction may be easier because it may be possible to treat the backscattered contribution as a uniform background. For intermediate dimensions, it may be adequate to use the average exposed area in regions surrounding each pattern element, rather than to take individual pattern elements, and even partial elements, into account as is done for one micron dimensions.

3. On the thick silicon substrate, 54% contrast is reached for a linewidth of 50nm, whereas on the thin substrate, 54% contrast is reached at 20nm. In other words, minimum lines 2.5 times smaller should be obtained on the thin substrate.

4. The 0.41 N.A. optical system has higher contrast than the electron beam on a thick substrate for linewidths above about 0.5μ. At 1.25μ linewidth, the contrast of the optical system is 85% compared to 54% for the electron beam. It is important to realize, however, that the exposure transition at the boundary between a line and a space can be sharper for the electron beam case than it is for an optical system even when the nominal contrast is lower. This is illustrated in fig. 6 which simply compares the exposure profiles of four lines and three spaces for an optical system with 85% contrast, and for an ideal electron beam system with 54% contrast.

All of the preceding discussion relates to the contrast obtained for an infinite array of lines and spaces. When the total pattern area is small compared to the area from which the backscattered electrons emerge, resolution on bulk substrates should be as good as that on thin membranes. This is the case for several of the experimental structures and devices built to date, for example, nanobridges (Laibowitz, Broers, Yeh and Viggiano 1979) and SQUIDS (Voss, Laibowitz, and Broers 1980). These devices were fabricated using contamination resist and thin substrates, however it would seem quite possible to make them using PMMA on thick substrates. In support of this, lines of 40nm have recently been produced on a thick substrate using a high contrast double layer resist process (Howard et al 1980).

A significant practical disadvantage of samples on bulk substrates is that they have to be examined in the conventional surface SEM with relatively low contrast and resolution. When the samples are on thin membranes, they can be examined by transmission electron microscopy with much higher contrast and resolution. This is particularly important for structures smaller than about 20nm in size where we have had difficulty with the SEM in examining resist patterns, in knowing whether samples were completely etched, or even in knowing whether the films from which the structures were fabricated were continuous.

Acknowledgement

The author would like to acknowledge and thank W. Molzen and J. Speidell for preparation of the Si_3N_4 membrane substrates, and M. Hatzakis, W. Grobman, C.D. Cullum, and F. Hohn for fruitful discussions.

REFERENCES

I. Adesida, R. Shimizu and T.E. Everhart, J. Vac. Sci. Technol. 16, 1979, p. 1743.

N. Aizaki, J. Vac. Sci. Technol. 16, 1979, p. 1726.

A.N. Broers, J.M.E. Harper and W. Molzen, Appl. Phys. Lett. 33, 1978, p. 392.

A.N. Broers, Appl. Phys. Lett. 22, 1973, p. 610, and To be published J. Vac. Sci. Tech., Nov./Dec. 1979.

T.H.P. Chang, J. Vac. Sci. Tech. 12, 1975, p. 1271.

D.C. Flanders, Appl. Phys. Lett. 36, 1980, p. 93.

J.S. Greeneich, J. Vac. Sci. Technol. 16, 1979, p. 1749.

W.D. Grobman and A.J. Speth, Proc. 8th Int. Conf. on Electron and Ion Beam Technology, Seattle, Washington, R. Bakish, Ed., 1978, p. 276.

I. Haller, M. Hatzakis and R. Srinivasen, IBM J. Res. Develop. 12, 1968, p. 251.

R.E. Howard, E.L. Hu, L.D. Jackel, P. Grabbe and D.M. Tennant, Appl. Phys. Lett. 36, 1980, p. 592.

F. Jones & M. Hatzakis, Proc. 7th Int. Conf. on Electron and Ion Beam Technology, Seattle, Washington, R. Bakish, Ed., 1978, p. 256.

R.B. Laibowitz, A.N. Broers, J.T.C. Yeh and J.M. Viggiano, Appl. Phys. Lett. 35, 1979, p. 891.

E.G. Lean and A.N. Broers, Microwave Journal 13, 1970, p. 97.

B.J. Lin, J. Vac. Sci. Technol. 12, 1975, p. 1317.

A.F. Mayadas and R.B. Laibowitz, Phys. Rev. Lett. 28, 1972, p.156.

D.L. Misell, Advan. Electron. Electron Phys. 32, 1973, p. 63.

W.W. Molzen, A.N. Broers, J.J. Cuomo, J.M.E. Harper and R.B. Laibowitz, J. Vac. Sci. Tech. 16, 1974, p. 269.

M. Parikh and D.F. Kyser, Proc. 8th Int. Conf. on Electron and Ion Beam Technology, Seattle, Washington, R. Bakish, Ed., 1978, p. 371.

H. Seiler and Z. Angew, Phys. 22, 1967, p. 249.

R. Seliger, J.W. Ward, V. Wang and R.L. Kubena, Appl. Phys. Lett. to be published.

W.J. Smith, quoted in: Handbook of Optics, W.G. Driscoll, Ed., McGraw-Hill, New York, 1978, p. 2-35.

R. Voss, R.B. Laibowitz and A.N. Broers, Submitted to Phys. Rev. Lett., 1980.

O.C. Wells, Scanning Electron Microscopy, McGraw Hill, N.Y., Chapter 3, 1974.

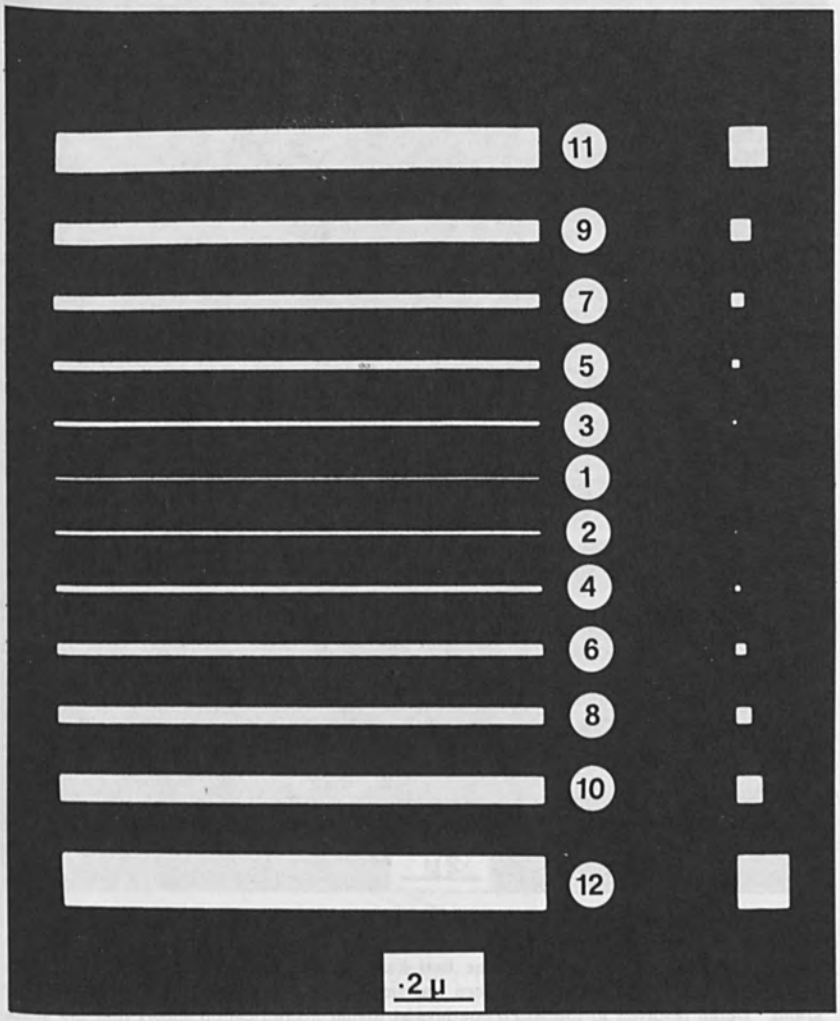

Figure 1 Pattern used to evaluate exposure distribution in PMMA. Nominal linewidths in the exposed patterns were as follows: (1) 4.4nm, (2) 7.5nm, (3) 11nm, (4) 14nm, (5) 20nm, (6) 26nm, (7) 33nm, (8) 38nm, (9) 53nm, (10) 62nm, (11) 96nm, (12) 120nm.

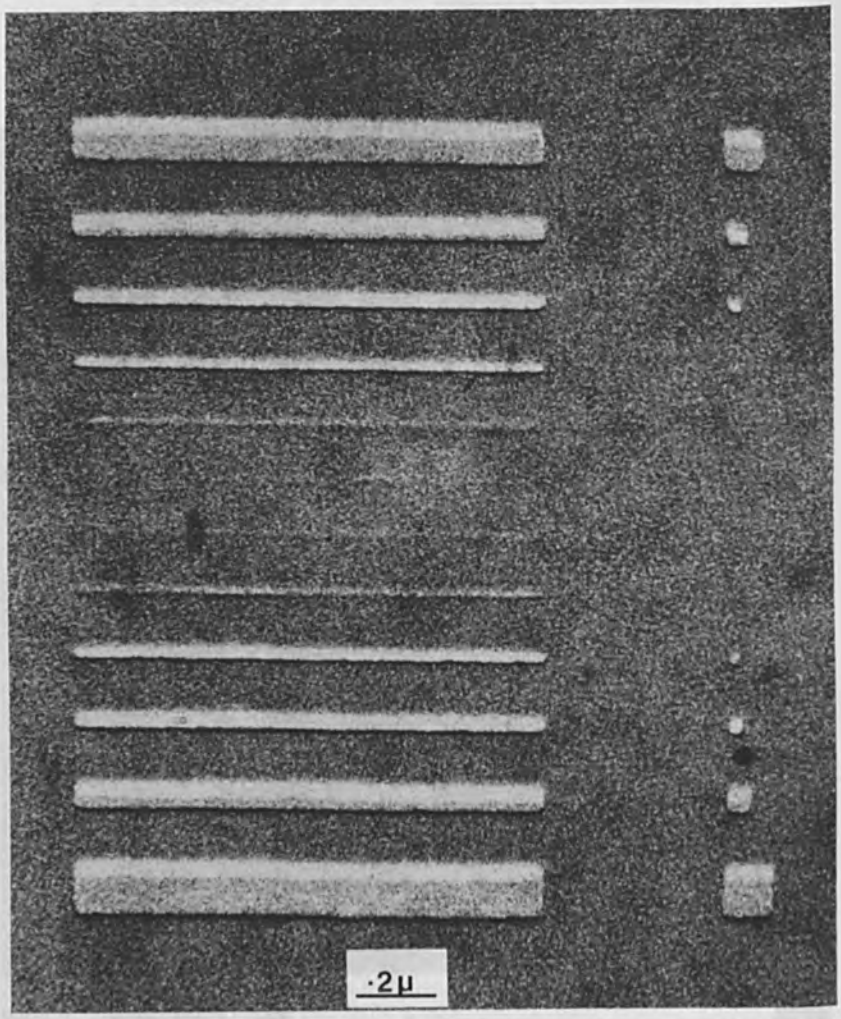

Figure 2 Bright field STEM micrograph of test pattern exposed at a level slightly greater than that necessary to open up shapes that are as large, compared to the width of the exposure distribution. Narrowest line that has opened up in this case is 20nm wide. Electron beam used to write the pattern was smaller than that used to obtain this micrograph. Detail resolved in the AuPd coatings at higher magnification shows that the beam diameter is less than 1nm. Sample is shadowed at 45° with AuPd to reveal resist thickness.

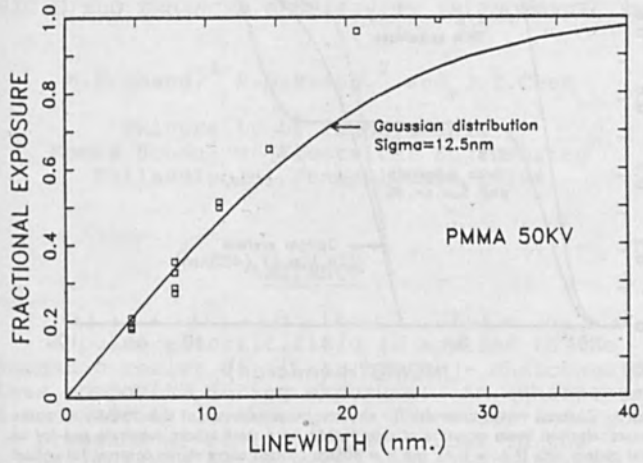

Figure 3 Fractional exposure received at the center of isolated lines of various widths for PMMA exposed on a thin substrate with 50kV electrons. Curve shows case for a Gaussian exposure distribution with σ = 12.5nm.

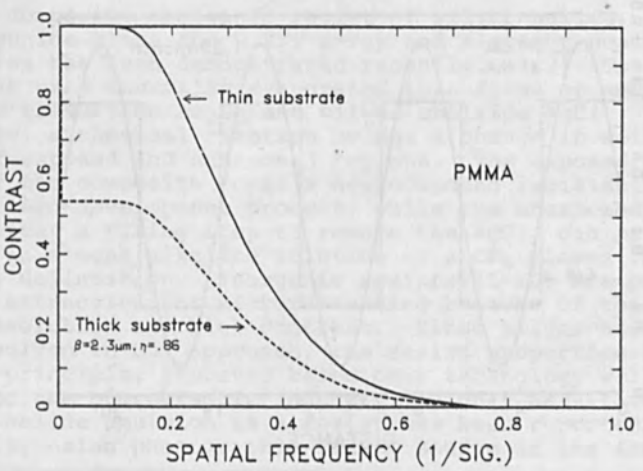

Figure 4 Resist Contrast Function (R.C.F.) for a resist with a Gaussian exposure distribution. Thick substrate curve assumes that the width of the backscattered distribution >> that of the resist exposure distribution, and that the total backscattered exposure contribution is 0.86 times that of the incoming beam.

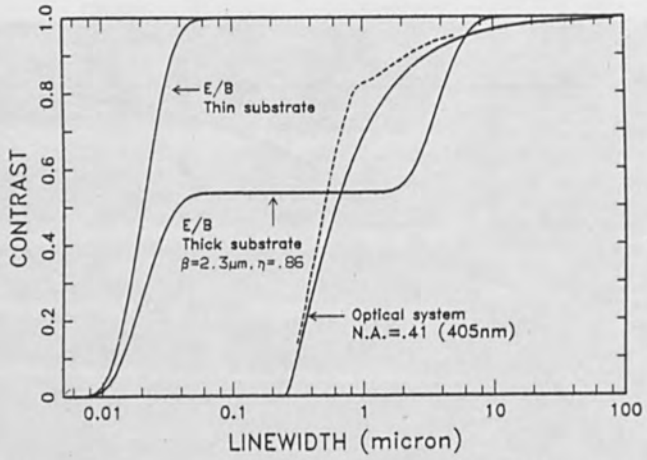

Figure 5 Contrast versus linewidth for electron beam exposure of thin PMMA on a thin substrate, electron beam exposure of thin PMMA on a thick silicon substrate and for an optical system with N.A. = 0.41 and λ = 405nm (dotted curve shows contrast for optical system when target has a square-wave distribution). Contrast is calculated for an infinite array of equal lines and spaces.

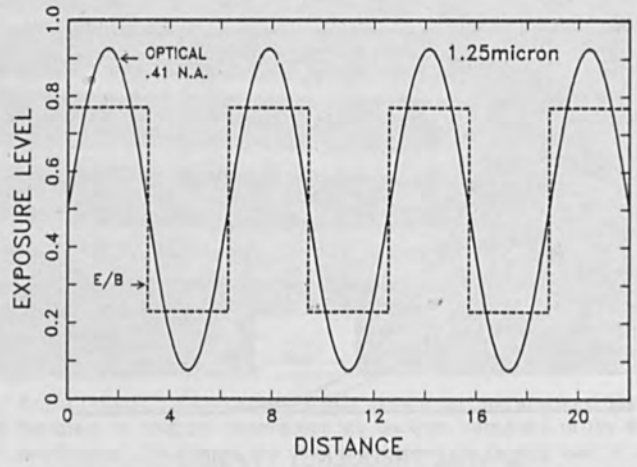

Figure 6 Exposure distribution for an ideal electron beam system exposing thin resist on a thick substrate (contrast 54%), compared to exposure distribution for an optical system with 85% contrast. In the electron beam case, the transition between line and space is sharp, but there is an overall background exposure due to the backscattered electrons.

ELECTRIC FIELD ENHANCED SENSITIVITY IN INORGANIC RESISTS

M.S.Chang,[1] H.D.Hwang,[2] and J.T.Chen

University of Pennsylvania
Moore School of Electrical Engineering
Philadelphia, Pennsylvania 19104

ABSTRACT

A pulse electric field is applied to the inorganic resist of silver halide - chalcogenide glass composite during exposure. An enhancement in sensitivity is observed. The study indicates the presence of positive silver ions in the photostimulated solid state reaction process.

INTRODUCTION

A composite inorganic resist of silver halide - chalcogenide glass for U.V., x-ray and electron-beam exposures has been demonstrated recently. (1,2) The approach uses thermally evaporated thin films of amorphous arsenic trisulfide As_2S_3 and silver cholride $AgC\ell$. Upon exposure, a chemical reaction brings a change in solubility of exposed and unexposed regions. The exposed portion of the composite forms a new compound resistant to the pattern development process, while the unexposed portion, after a fixing step to remove the $AgC\ell$, can be etched in a weak alkaline solution or a CF_4 plasma for pattern delineation. Inorganic resists (1-10) are potentially attractive for micropatterning because of their high resolution and high contrast. Since silver halides are involved in our approach, the resist properties can be, in principle, improved based on a technology well known to the photographic industry. Highly sensitive silver halide emulsion as a resist has been reported.(11) Recently, using photographic silver source in the inor-

---

1. Present address: Hewlett-Packard Laboratories, Palo Alto, California 94304.
2. Present address: Signetics Corporation, Sunnyvale, California 84086.

ganic resist to improve the sensitivity down to 0.1 mJ/cm^2 in U.V. exposure has been demonstrated.(12) In this paper, an experimental study on the effect of an electric field across the resist layer during exposure is described. An enhancement in the resist sensitivity is observed.

EXPERIMENT

The schematics of the composite inorganic resist processing is depicted in Fig. 1. Heavily doped silicon wafers with resistivity of 0.007 Ω-cm and thickness of 250 μ were employed as substrates. The composite consisted of typically 300 nm As_2S_3 and 20 nm AgCℓ deposited thermally in two separate vacuum systems. After exposure, the sample was dipped in a conventional fixing solution to remove the unexposed AgCℓ. The pattern was finally delineated by etching in a weak alkaline solution. A CF_4 plasma development process is possible but is not employed in this study. Fig. 2 shows the experimental arrangement with an electric field across the resist layer during exposure. The sample was placed on an aluminum plate, which, together with the low resistive Si wafer, acted as the bottom electrode. The top electrode was a U.V. transparent, electrically conductive SnO_2-coated borosilicate glass plate. No attempt was made to make good contact between the sample and the electrode. Finite air gap was believed present. Hence, the electric field in the following discussion is given by the voltage across the two electrodes rather than the usual unit.

RESULT

An arbitrary pulse electric field was applied to the resist during U.V. exposure. The results are shown in Fig. 3. The pulse amplitude was 15 V with the top electrode biased positive. The pulse period was 1 μsec with a 0.5 μsec pulse width. An improvement in the inorganic resist sensitivity is observed. The electric field alone, e.g. without the U.V. exposure, did not give rise to the resist action. A d.c. electric field applied during the U.V. exposure also has no effect on the resist action.

The effect of polarity of the pulse electric field on sensitivity is shown in Fig. 4. The U.V. exposure energy was 1.9 J/cm^2. The pulse period was fixed at 1 μsec with 0.5 μsec pulse width. The pulse amplitude was varied from negative to positive. It is noted from Fig. 4 that a negative pulsed field retards while a positive

pulse field enhances the resist sensitivity. Fig. 5 shows the effect of positive pulse field at various exposure energies. A linear electric field dependence is observed.

The effect of the pulse period and pulse width on the resist sensitivity are shown in Fig. 6 and 7, respectively. In both cases, the U.V. exposure energy was 1.4 J/cm^2 and the pulse amplitude was set at 15 V. It is observed that the pulse width is the predominant factor in enhancing the resist sensitivity. The best result was achieved at 0.1 μsec pulse width, and was limited by the shortest pulse width obtainable from the available pulse generator. The data points in Fig. 6 can be fitted by an exponential expression $R(\%)=A(E)\exp(-B(t))$, where the parameter A(E) is dependent on the pulse amplitude, and the parameter B(t) is relatively constant for pulse period ranging from 1 to 4 μsec. For the result shown in Fig. 6, A = 65 and B = 43. Fig. 7 shows that the resist sensitivity is inert to the variation of the pulse period. By keeping the pulse width constant, i.e. 0.5 μsec in this experiment, the length of the discharging cylcle does not influence the resist sensitivity.

With the optimum parameters of the pulse field, a composite of 20 nm AgCℓ and 100 nm As_2S_3 is evaluated for its resist sensitivity under an electric field. The result is shown in Fig. 8. Using the available pulse generator, the pulse amplitude was 18 V, which was the maximum without output distortion. The pulse period was 1 μsec and the pulse width was 0.1 μsec. Defining the 50% remaining film thickness as the sensitivity, an enhancement factor of 20 due to the applied pulse electric field is obtained, from 2 J/cm^2 without field down to 100 mJ/cm^2 with the applied field.

DISCUSSION

There is no clear understanding yet on the mechanism of the resist action in the silver halide - chalcogenide glass composite. Upon exposure, a three-step process is believed to take place: a photostructural change (13) in the chalcogenide glass, a photodissociation(14) of the silver halide, and a photostimulated solid state chemical reaction(15,16) between the photodissociated silver halide and the photosensitive chalcogenide glass. This process can be expressed as

$$As_2S_3 \xrightarrow{h\nu} As_2S_3^{*}$$ photostructural change

$AgC\ell \xrightarrow{h\nu} Ag^{+} + C\ell^{-}$ photodissociation

$Ag^{+} + As_2S_3^{*} \xrightarrow{h\nu} Ag\text{-}As_2S_3$ photostimulated solid state reaction

The exposed area thus forms a new compound resistant to the etchant for the chalcogenide glass.

The present study indicates that a pulse electric field during exposure can influence the resist sensitivity of the composite. The result in Fig. 4 shows that the silver atoms, derived from the photodissociation process, are positively ionized. Since the resist sensitivity depends on how fast and how deep the silver ions react chemically with the chalcogenide glass to alter its chemical solubility, a positive electric field enhances, while a negative electric field retards, the transport of the silver ions. Furthermore, the linear electric field dependence on the resist sensitivity (Fig. 4 and 5) also supports the presence of the silver ions. It should also be pointed out that the pulse electric field alone without any radiation gives no resist action to the composite.

The pulse electric field provides a driving force during the charging cycle to the silver ions when they are still photoactive. (Fig. 6) The discharging cycle has no effect on the sensitivity. (Fig. 7) The results indicate that the photoexcited species responsible for the resist action are short-lived. The lifetime is apparently shorter than 0.1 μsec as limited in this experiment by the available pulse generator. A d.c. electric field has no effect on the resist sensitivity whether the composite is positively or negatively biased.

CONCLUSION

The sensitivity enhancement in a composite inorganic resist of silver halide - chalcogenide glass with a pulse electric field is demonstrated. The resist action is the photostimulated solid state reaction of silver ions and the chalcogenide glass. The transport of the positive silver ions is enhanced by a pulse electric field. An enhancement factor of 20 in resist sensitivity is obtained in photolithography. Similar work in x-ray lithography is in progress. Preliminary result indicates only a factor of 2 improvement in sensitivity with the same pulse field.

ACKNOWLEDGEMENT

This work was supported by the Air Force Office of Scientific Research under Grant Number 77-3432.

REFERENCES

1. K.D.Kolwicz and M.S.Chang, J.Electrochem. Soc., 127, 135(1980).
2. M.S.Chang, IEEE Conference Record, Third Biennial University/Industry/Government Microelectronics Symposium, p.124, 1979. IEEE Cat. #79CH1385-4REG5.
3. A.Yoshikawa, O.Ochi, H.Nagai and Y.Mizushima, Appl. Phys. Lett., 29, 667(1976).
4. A.Yoshikawa, O.Ochi, H.Nagai and Y.Mizushima, Appl. Phys. Lett., 31, 161(1977).
5. M.S.Chang and J.T.Chen, Appl. Phys. Lett., 33, 892 (1978).
6. T.W.Hou and M.S.Chang, Appl. Opt., 18, 1753(1979).
7. K.Tai, L.F.Johnson, D.W.Murphy and M.S.C.Chung, Abstract No. 94, Extended Abstracts,Vol.79-1, Electrochem. Soc., Princeton, New Jersey, 1979, p.244.
8. M.S.Chang, T.W.Hou, J.T.Chen, K.D.Kolwicz and J.N. Zemel, J.Vac. Sci. Technol., 16, 1973(1979).
9. K.L.Tai, W.R.Sinclair, R.G.Vadimsky, J.M.Moran and M.J.Rand, J.Vac. Sci. Technol., 16, 1977(1979).
10. A.Yoshikawa, O.Ochi, H.Nagai and Y.Mizushima, Appl. Phys. Lett., 36, 107(1980).
11. R.B.Marcus, T.Shankoff, D.Smith, C.D.Capio, T.F. Retajczyk and A.Timko, in International Electron Device Meeting Technical Digest, 1978, p.591, IEEE Cat.#79Ch1324-3ED.
12. J.I.Masters, G.M.Goldberg and J.M.Lavine, IEEE Elect. Dev. Lett., EDl, 61(1980).
13. J.P.deNeufville, in Optical Properties of Solid - New Developments, edited by B.O.Seraphin, North-Holland, Amsterdam, 1976, p.439.
14. J.P.Ballantyne and W.C.Nixon, J.Vac.Sci.Technol., 10, 1094(1973).
15. J.Malinowski and A.Buroff, Contemp. Phys., 19, 99(1978).
16. I.Shimizu, H.Sakuma, H.Kokado and E.Inoue, Photogr. Sci. Eng., 16, 291(1972).

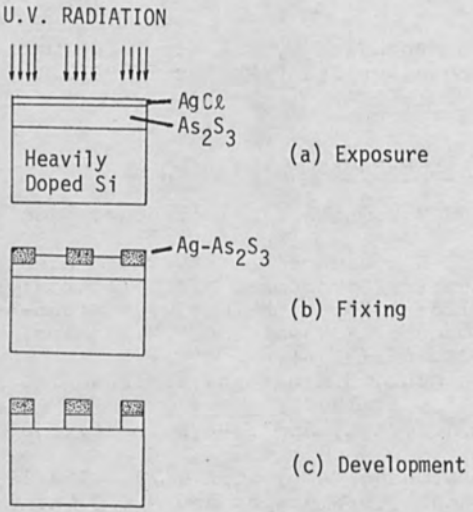

Fig. 1 Schematics of inorganic resist processing.

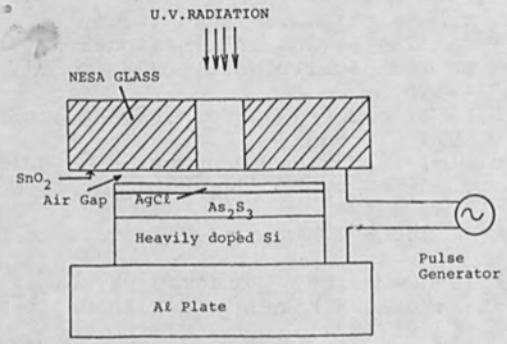

Fig. 2 Schematic of electric field enhanced sensitivity experiment.

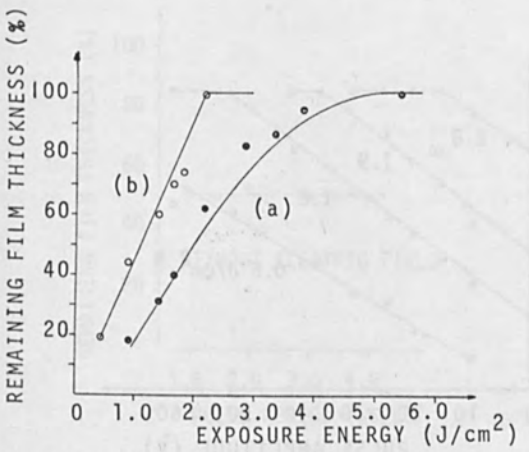

Fig. 3 Sensitivity curves of AgCℓ (20 nm) - As_2S_3 (300 nm) inorganic resist without (a) and with (b) a pulse electric field. The pulse amplitude is 15 V with a pulse period of 1 μsec and a pulse width of 0.5 μsec.

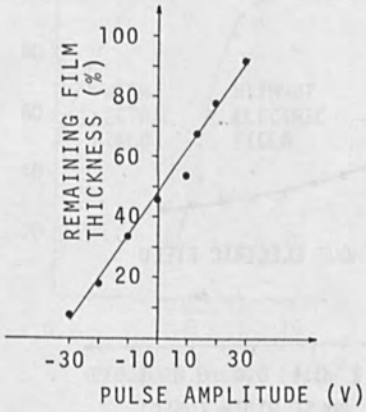

Fig. 4 Effect of polarity of pulse electric field on sensitivity. The exposure energy is 1.9 J/cm². The pulse period is 1 μsec and the pulse width is 0.5 μsec.

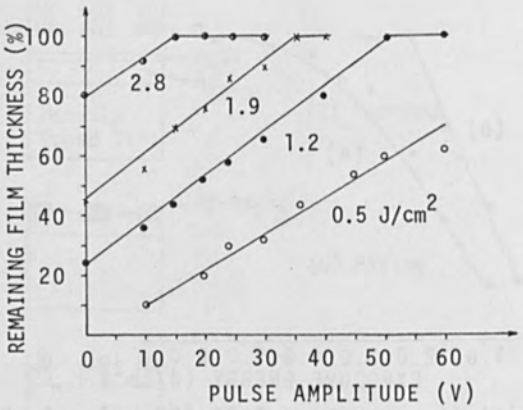

Fig. 5 Effect of electric field on sensitivity with exposure energy as a parameter. The pulse period is 1 μsec and the pulse width is 0.5 μsec.

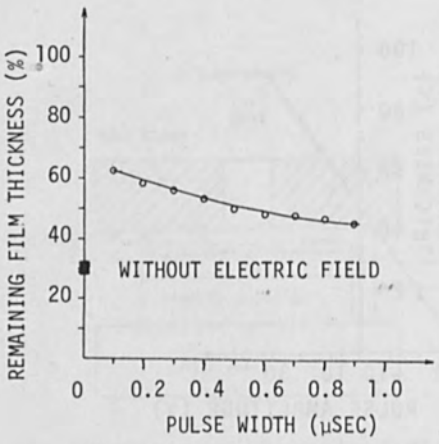

Fig. 6 Effect of pulse width on sensitivity. The exposure energy is 1.4 J/cm^2. The pulse amplitude is 15 V and the pulse period is 1 μsec.

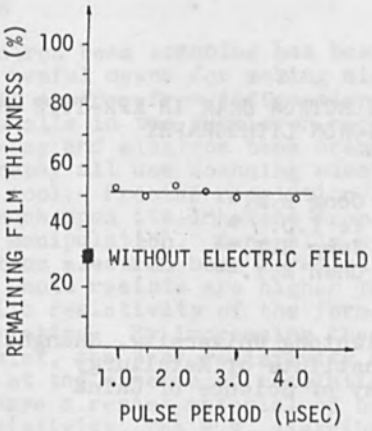

Fig. 7 Effect of pulse period on sensitivity. The exposure energy is 1.4 J/cm^2. The pulse amplitude is 15 V and the pulse width is 0.5 μsec.

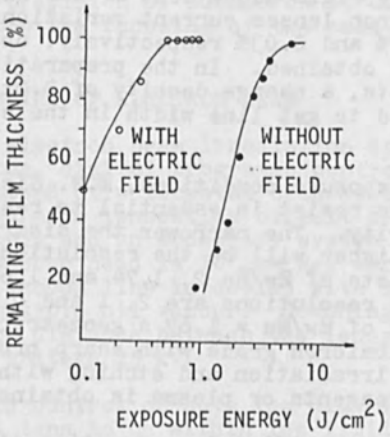

Fig. 8 Electric field enhanced sensitivity in AgCℓ (20 nm) - As_2S_3 (100 nm) inorganic photoresist. The pulse has 18 V, 1 μsec period and 0.1 μsec width.

PRECISE FOCUSING OF ELECTRON BEAM IN KPR-TYPE RESIST SUBMICRON LITHOGRAPHY

Gong B.M.*
Ye Y.D. *
Jang H.Z.**
Chen E.Y.**

* Shanghai Jiaotong University, Shanghai
** Shanghai Institute of Metallurgy
Academy of Science of China

ABSTRACT

In order to get a resist of submicron grade, precise focusing of electron beam is of paramount importance. By rigid adjustment of the high voltage and electron lenses current variations to less than 0.02% and 0.03% respectively, optimal results are obtained. In the preparation of KPR-type resists, a charge density of 3.0×10^{-5} coulomb/cm^2 is used to get line width in the submicron regio.

Under fixed exposure conditions, M.W. distribution of negative resist is essential to resolution and resistivity. The narfower the distribution range, the higher will be the resolution. For KPR-type resists of $\bar{M}w/\bar{M}n$ 2, 1.74 and 1.67, the corresponding resolutions are 2, 1 and 0.6 μ. From a resist of $\bar{M}w/\bar{M}n = 1.67$ a geometric pattern of the submicron grade with sharp profile by electron beam irradiation and etching with either chemical reagents or plasma is obtained.

PVA samples are purified by a fractionation process before esterification.

INTRODUCTION

Electron beam scanning has been considered as a practically useful means for making micro lithographic patterns, as it is free from diffraction defects and gives geometric details in the submicron region. Deep ultraviolet, soft X-ray and electron beam scanning-surface irradition lithography all use scanning electron beam as an indispensible tool. Precise resolution of a photo resist depends very much upon its inherent properties as well as the mode of manipulation. Generally speaking, under ultra violet light or electron beam irradiation, the resolution of positive photo resists are higher than that of negative resists, while resistivity of the former being lower than that of the latter. By increasing the layer thickness of positive resist, the poor resistivity may be counterbalanced somewhat at the expense of resolution. It is, therefore, desired to have a resist material of both high resolution and good resistivity. The M.W. distribution of a negative resist has been found to be a fundamental factor effecting resolution, therewith, the problem of making polymers of narrow M.W. distribution range should be solved.

In making KPR-type resists of improved properties, commercial PVAs are fractionated to an acceptable M.W. distribution range which are then esterified to the cinnamates. The precision of submicron structure depends, furthermore, upon the focusing of the beam on the object.

PRECISE FOCUSING OF ELECTRON BEAM

The electron beam irradiation apparatus is an experimental one, digital programme controlled. The lens-tube is composed of a tungsten cathode triode electron gun, a 2-stage magnetic lensset, a circuit switch, a magnetic deflection coil and an accessory system for manual operation. The vaccum head is 10^{-5} mm Hg, working vaccum at 10^{-4} mm Hg. The vaccum line is cooled with dry ice in order to catch any possible oil vapour. Scanning area is 2 x 2mm^2, and operation distance between the lense and the object 65 mm, working voltage 25 kv.

Rigid control of both the high voltage and current of the first lens to be within the limit of 0.02 - 0.04% has been observed. In order to get good focusing, the current of the secondlens must not vary more than 0.03%. After the focusing is fixed, current variation should be less than 0.03%.

Line width varies with the focus current in the following manner:

Relative variation of focusing cur't	0.	0.03%	0.06%
Line width (μ)	0.5	0.7	1.0

Line width varies as well with the focusing voltage, expressed in terms of charge density, in the following way:

Charge density (coul./cm²)	1.5×10^{-5}	2.0×10^{-5}	3.0×10^{-5}
Line width (μ)	0.5	0.7	1.0

It can be seen from these data the importance of carecontrol of the two parameters in order to get submicron structure.

MOLECULAR WEIGHT DISTRIBUTION

Besides precise focusing, the mode of M.W. distribution of the photo-resist plays an important role in the fabrication of micro structure. Other relevant factors to be observed are mean M.W.($\bar{M}w$), distribution of the photosensitive functional groups within the polymer (i.e. degree of esterification in the case of polyvinyl cinnamate) and the thickness of resist layer.

Using resists of different M.W. distribution to get a definite line width of, say 1 μ, on a 4000 Å thick layer, the charge density required are as follows:

$\bar{M}w$	341562	345306	369924
C.D. (coul./cm²)	4.0×10^{-5}	3.0×10^{-5}	1.5×10^{-5}

It is shown that the photo-sensitivity increases as the mean M.W. That is to say, wider range of M.W. distribution causes greater difference in sensitivity, therewith resolution drops accordingly.

On 2000 Å thick resist layers of different M.W. distribution, irradiated under preferential focusing conditions the corresponding resolutions obtained are as follows:

Heterogenity ($\bar{M}_w/\bar{M}_n$)	2.2	1.74	1.65
Resolution (μ)	2	1	o.6

On photoresists of differennt M.W.distribution and different layer thickness irradiated under the same focusing conditions as the above experiments, the resolution obtained are as follows: Fig. 1. The influence of M.W. distribution and layer thickness on resolution of the resist is clearly shown by the curves.

The inherent property such as pinhole density of a resist should be mentioned. From resists of same thickness but different M.W. distribution, their pinhole densities varies as follows:

$\bar{M}_w/\bar{M}_n$	2.2	1.74	1.64
Pinhole / cm^2	7	0.5	0.02

It seems that pinhole density decreases sharply as $\bar{M}_w/\bar{M}_n$ ratio decreases.

Since contraction of M.W. distribution range enhances resolution as seen above, it is wondered if polyvinyl cinnamate could be made from the possibly best range of M.W. distribution. fractionations are carried out as follows.

Start from commercial polyvinyl alcohol, a 9 % aqueous solution was blown together with compressed air into 7 times its volume of 85 % ethyl alcohol solution (ethyl alcohol content must be kept not less than 75%). The fibrous precipitate formed is collected but not dried, and used as once-purified PVA denoted by PVA-1 in the table. This is further treated in exactly the same manner as the original material to give twice-fractionated PVA(PVA-2) Purification process is repeated to get the denoted PVA. The so treated PVAs are acetylated to form their respective polyesters. The results of Gel Permeate Chromatography (GPC) analyse of the polymeric esters are shown in table 1.

It seems that the first purification treatment always offers the best efficiency and further treatments does not give too much help. Repeated purifications induce dropping of heterogenity indice down to 1.65-1.67, thus purification of more than 4 time is excessive. Samples of sets 1, 11 and 111 show the fact that on repeated fractionation, average M.W. duly increase. This phenomena may be explained by the assumption that, during

treatment, low M.W. polymers are partly removed by dissolution. The wet PVAs of set 1, 11 and 111 dissolve almost completely to form 9% aqueous solution. The insoluble matter is filtered off, and the filtrate used as usual. Average M.W. showed a gradual decreasing tendency. Since lowering of $\bar{M}_w$ of a resist will be detrimental to its sensitivity, the method used in samples set 1V is not recommended.

CONCLUSION

In the fabrication of a negative resist by means of scanning electron beam for making submicron geometric structure, it is necessary to keep precise controls of not only the electron-photo parameters but also the M.W.distribution. As to KPR type resist, fractionated PVA should be used to give product of improved property. Polyvinyl cinnamate of heterogenity index below 1.7 are prepared from fractionated PVA of different origin. By exposure under precisely focused scanning electron beam 0.6μ lithographic patters with submicron lines of sharp profile can be obtained by chemical as well as plasma etching.

ACKNOWLEDGMENTS

The authors would like to thank Yang Min Je and Chen Pay Run Shanghai Institute of Metallurgy Academy of Science of China for their supporting in plasma etching and the scanning electron micrographs and Wang Yong Rui Shanghai Jiaotong University for his electron micrographs. Prof.Chen Bing have been most helpful in the preparation of this paper.

REFERENCES

1. P.K.Agnihotri, F.P.Hood, L.G.Lesoine, J.A.Offenbach, Photo Sci. Eng., 15, 141 1971

2. L.M.Minsk, J.G.Smith, W.P.Van Dausen, J.Appl. Poly.Sci. 11 (6),302 1959

3. M.Tsuda, J.Polym. Sci., A2, 2907 1964

4. L.F.Thompson, J.P.Ballantyne, E.D.Feit, J.Vac.Sci. Technol., Vol. 12 No. 6 11/12 1975

5. E.D.Feit, Photoresists: Photoformation of Relief Image in Polymeric Films-9 NJ 1978

6. M.Hatzakis, J.Vac.Sci. Technol. Vol. 12 No. 6 11/12 1975

7. M.Hatzakis, Applied Polymer Symposium No. 23, 73-56 1974

8. Gong B.M., Ye Y.D. and Gu M.Q., Journal of Shanghai Jiaotong University No.2, 1979

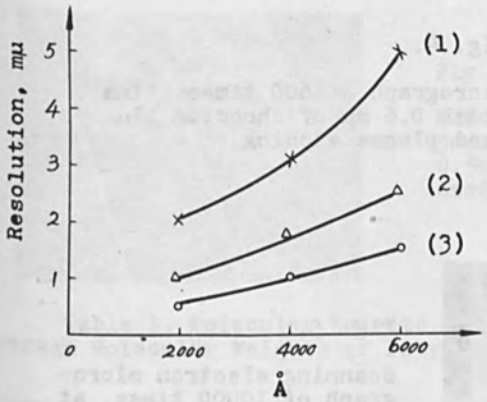

(1) $\bar{M}w/\bar{M}n$ 2.2

(2) $\bar{M}w/\bar{M}n$ 1.74

(3) $\bar{M}w/\bar{M}n$ 1.65

Fig. 1.

The relation of thickness and resolution.

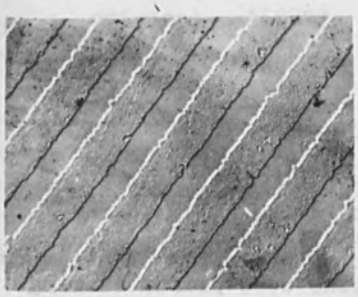

Fig. 2.

Electron micrograph of 5000 times, line width 1mμ of chromium line used chemical etching.

Fig. 3.

Micrograph of 600 times,line width 1mμ of chromium line used plasma etching.

Fig. 4.

Micrograph of 600 times, line width 0.6 mμ of chromium line used plasma etching.

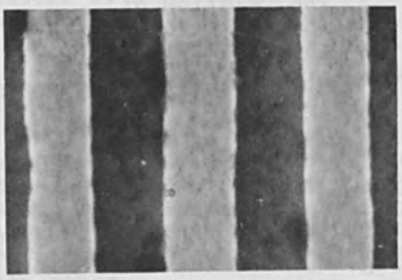

Fig. 5.

Scanning electron micrograph of 10000 times, at right angles of incidence, line width 1mμ of chromium line used plasma etching.

Fig. 6.

This SEM micrograph were taken at 45° angles of incidence, 10000 time, line width 1mμ of chromium line used plasma etching.

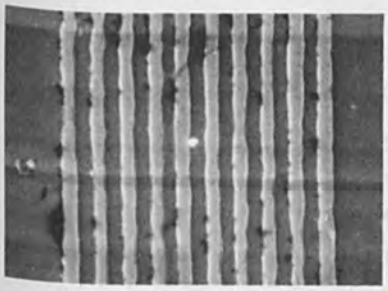

Fig. 7.

Scanning electron micrograph of 10000 times, at right angles of incidence, line width 0.6mμ of chromium line used chemical etching.

Fig. 8.

Electron micrograph of 5ooo times, line width 0.5mμ of chromium line used chemical etching.

Table 1. Molecular Weights Distribution and the Average Molecular Weights of Polyvinyl Acetate (GPC Data)

Polyvinyl Acetate		$\bar{M}w$	$\bar{M}n$	$\bar{P}w$	$\bar{P}n$	$\bar{M}w/\bar{M}n$
Sample 1.	original	168877	84423	1964	982	2.0
	PVA-1	164697	87390	1915	1016	1.88
	PVA-2	170888	97937	1997	1139	1.74
	PVA-3	182875	109785	2126	1216	1.65
Sample 2.	original	198423	96880	2307	1126	2.05
	PVA-5	228805	136360	2661	1586	1.67
Sample 3.	PVA-4	163734	98039	1904	1141	1.67
Sample 4.	original	160249	70280	1863	817	2.28
	PVA-1	168723	93773	1692	1090	1.80
	PVA-2	168971	98574	1965	1146	1.71
	PVA-3	176101	103041	2048	1198	1.71
	PVA-4	172324	103438	2004	1203	1.67
	PVA-5	158319	94600	1841	1100	1.67
	PVA-9	164819	94800	1917	1102	1.73

Section 5

X-Ray Lithography

"EQUIVALENT DATA RATE OF X-RAY LITHOGRAPHY SYSTEMS"

Henry I. Smith*

Lincoln Laboratory, Massachusetts Institute of Technology

Lexington, Massachusetts 02173

ABSTRACT

An expression for the equivalent data rate of an x-ray lithography system is derived and plotted as a function of ΔS, the local control of gap. Equations for maximum permissible source diameter and maximum gap are also given. For a minimum linewidth of 1 μm, a maximum data rate of 54 MHz is predicted using a conventional 10 kW Al_K source. Plasma sources offer a promising approach to very high data rates (in excess of 100 MHz) by virtue of their small source diameters and potential for x-ray output equivalent to, or exceeding, conventional sources.

Both serial and parallel microlithographic techniques are being developed for exposing large-area, complex patterns with submicrometer linewidths. An important figure-of-merit for comparing the economics of various microlithographic techniques is the "equivalent data rate" or number of pattern elements ("pixels") exposed per unit time. In an earlier paper (1) the equivalent data rate of an x-ray lithography system was calculated for a variety of sources and for the case where the minimum linewidth replicated was 0.2 μm. In this article additional details on this "data rate" analysis are given and it is expanded to cover a broader range of linewidths.

The efficiency of x-ray emission from conventional sources, in which electrons bombard a solid target, or from hot plasma sources, in which plasmas are created by high power lasers or electrical discharges, can be characterized by a power efficiency parameter, B, which gives the x-ray power radiated per unit solid angle per unit power input. For the case of a solid aluminum target bombarded with 20 keV electrons, B is approximately 58 X 10^{-6}W/Sr/W (Ref. 2). For the case of a hot plasma source, B is somewhat more difficult to estimate. We will assume a hypothetical plasma source having an overall efficiency of conversion of electrical or optical power to x-rays of 10%, and that 10% of this radiation is in a band useful for lithography (3-5). For isotropic emission, B is approximately equal to 8 X 10^{-4} W/Sr/W. Thus, the hypothetical plasma source would be about 14 times more efficient than a conventional aluminum source operated at 20 kV and the same average input power. Expressed another way, a 10 kW, 20 kV conventional aluminum source would be equivalent to the hypothetical plasma source with a time averaged input power of 725 W. Although

*Also, Department of Electrical Engineering and Computer Science, Massachusetts Institute of Technology, Cambridge, Massachusetts 02139.

such plasma sources are not readily available at present, they appear feasible using either high repetition rate lasers or direct electrical discharges (3-5).

The x-ray power incident on a substrate surface is given by $BPT\Omega$, where P is the input power to the source, Ω is the solid angle subtended by the pattern area, and T is the fractional transmission of the vacuum window and mask membrane. The data rate, R, or number of pixels exposed per unit time is given by

$$R = \frac{BPT\Omega}{J\rho^2} \tag{1}$$

where J is the sensitivity of the resist in energy per unit area required to fully expose, and ρ^2 is the area of a pixel. Obviously, the data rate increases rapidly as ρ is reduced. In most analyses of lithographic data rates, ρ is chosen to be 1/4 or 1/5 of the minimum linewidth. Here we choose ρ equal to the minimum linewidth to avoid any artificial inflation of data rate. The reader can easily multiply our results by 16 or 25 if one of the smaller choices of ρ is desired.

Figure 1 illustrates the replication of a grating pattern of linewidth ρ located at the outer perimeter of a mask. At this outer perimeter the angle between the substrate normal and the direction of the locally incident x-rays is γ. Obviously, pattern elements on the mask are shifted laterally by an amount ℓ given by

$$\ell = S\gamma. \tag{2}$$

As pointed out in Ref. 1, this corresponds to a uniform magnification of the mask pattern onto the substrate that can be varied by varying S. This ability to vary magnification is considered a distinct advantage of x-ray lithography since it permits one to compensate for homogeneous expansion or contraction of a substrate which can arise from temperature changes or from processing. The right half of Fig. 1 illustrates the superposition error, ε, that occurs if the mask-sample gap, S, at a given location changes by ΔS in between two successive exposures. ε given by

$$\varepsilon = \gamma\Delta S. \tag{3}$$

This expression, which is plotted in Fig. 2, connects Ω and ΔS:

$$\Omega \tilde{=} \pi\gamma^2 = \pi\left(\frac{\varepsilon}{\Delta S}\right)^2 . \tag{4}$$

The curves of Fig. 2 are cut off, somewhat arbitrarily, at $\gamma = 0.15$ under the assumption that slant angles greater than this value are undesirable. Substituting Equation (4) into Equation (1) yields

$$R = \frac{BPT}{J}\left(\frac{\varepsilon^2}{\rho^2}\right)\left(\frac{\pi}{\Delta S}\right)^2 . \qquad (5)$$

Equation (5) is plotted as a function of ΔS in Fig. 3 for the case where the superposition precision, ε, is 1/5 of the minimum linewidth, ρ. J and T are given the values 20 X 10^{-3}J/cm^2 and 0.3 respectively. The vertical lines in Fig. 3 correspond to $\gamma = 0.15$ for ρ = 1 μm (ε = 0.2 μm), ρ = 0.5 μm (ε = 0.1 μm), ρ = 0.25 μm (ε = 0.05 μm) ρ = 0.125 μm (ε = 0.025 μm). Clearly, control of ΔS is important in order to maximize data rate. Optical or capacitive sensing techniques may enable ΔS to be controlled to a tolerance below 1 μm. Conformable contact schemes can probably provide control of ΔS to about 0.1 μm (6).

If the area of a mask over which the distortion is less than ε is smaller than the area of a full substrate or wafer, then multiple exposures would be required. The number of pixels replicated in any given exposure is related simply to the mask stability. If this stability can be characterized by a single number, N, (i.e., N^{-1} is the fractional distortion) then the maximum permissable mask diameter is $N\varepsilon$, and the number of pixels replicated in an exposure is N^2. Although only a limited amount of information is available on mask distortion, it appears that values of N in the range 1 X 10^5 to 5 X 10^6 are feasible (7,8).

Up to now we have not considered the fact that any real source has a finite size, which gives rise to penumbra. The penumbra, δ, is given by

$$\delta = S(d/D). \qquad (6)$$

D is simply related to γ and the mask diameter, $N\varepsilon$,

$$\gamma = \frac{N\varepsilon}{2D} . \qquad (7)$$

From Equation (3), $\gamma = \varepsilon/\Delta S$. Thus,

$$d = \frac{\delta N \Delta S}{2S} . \qquad (8)$$

Letting $\delta = 2\varepsilon$

$$d = \frac{N\varepsilon\Delta S}{S} . \qquad (9)$$

This equation relates the source diameter to the mask diameter, $N\epsilon$, the gap, S, and the control of the gap, ΔS. For various practical reasons one would like S to be relatively large, in the range 20 to 30 μm. Table I gives source diameters consistent with maximum data rates (i.e., $\gamma = 0.15$) for a set of values of minimum linewidths and for $N = 5 \times 10^5$ and $N = 1 \times 10^5$. A gap of 30 μm is chosen except when $\rho = 0.25$ μm and $\rho = 0.125$ μm. In these cases, diffraction dictates gaps of 20 μm and 5 μm respectively (see Appendix A).

TABLE I

N	ρ_{min}(μm)	S(μm)	ΔS(μm)	d(mm)
5×10^5	1.0	30	1.33	4.4
5×10^5	0.5	30	0.67	1.1
5×10^5	0.25	20	0.33	0.4
5×10^5	0.125	5	0.17	0.4
1×10^5	1.0	30	1.33	0.9
1×10^5	0.5	30	0.67	0.2
1×10^5	0.25	20	0.33	0.08
1×10^5	0.125	5	0.17	0.09

The source diameter of a conventional 10 kW rotating anode x-ray system can be about 4 mm. Thus, Table I together with Fig. 3 predicts that for minimum linewidths of 1 μm the maximum data rate obtainable is 54 MHz if $N \geq 5 \times 10^5$. For linewidths of 0.5 μm, the maximum data rate predicted by curve (2) of Fig. 3 is 220 MHz, but for $S = 30$ μm this requires a source diameter of about 1 mm at $N = 5 \times 10^5$ or 0.2 mm at $N = 1 \times 10^5$. Plasma sources offer the possibility of obtaining such small diameters at x-ray outputs equivalent to or exceeding conventional 10 kW sources, and thus may be a better approach to obtaining high data rates. With conventional sources one would have to reduce S to less than 10 μm to achieve the maximum data rate predicted for $\rho = 0.5$ μm. Figure 3 together with Equation (9) provide a general basis for calculating the equivalent data rate of x-ray lithography systems given source and mask characteristics, gap control specification and minimum linewidth.

Electron storage rings and synchrotrons are capable of providing much higher data rates than either conventional or hot plasma sources. Grobman (9) has analysed the advantages and special features of synchrotron radiation for x-ray lithography and compared throughput with conventional sources.

Appendix A

It is frequently assumed that diffraction is negligible in x-ray lithography. This is not the case for linewidths in the 0.1 μm range at gaps of several micrometers. We will use the following criterion for the maximum allowable gap for a given minimum linewidth

$$S = \frac{\rho^2}{4\lambda} . \qquad \text{A-1}$$

At a linewidth of $\rho = 0.125$ μm, the maximum allowable gap is $S_{max} = 5$ μm.

ACKNOWLEDGMENTS

The author is grateful to N. P. Economou, D. C. Flanders and D. C. Shaver for valuable suggestions and helpful discussions. This work was sponsored by the Department of the Air Force and the Defense Advanced Research Projects Agency.

REFERENCES

1. H. I. Smith and D. C. Flanders. J. Vac. Sci. Technol., 17, 533 (1980).

2. S. E. Bernacki and H. I. Smith, IEEE Trans. Electron Devices, ED22, 421 (1975).

3. D. J. Nagel, J. M. McMahon, R. R. Whitlock, J. R. Greig, R. E. Pechacek and M. C. Peckerar, Jpn. J. Appl. Phys., 17, 472 (1978); D. J. Nagel, "X-ray Emission from High-Temperature Laboratory Plasmas", Advances in X-ray Analysis, Vol. 18, Ed. W. L. Pickles, C. S. Barrett, J. B. Newkirk, and C. O. Ruud, Plenum Publishing Corporation, New York, (1975).

4. R. A. McCorkle and H. J. Vollmer, Rev. Sci. Instrum., 48, 1055 (1977).

5. N. P. Economou, "Plasma X-ray Sources for Lithography" MIT Lincoln Laboratory Technical Note, TN 1980-17.

6. C. Cohen, Electronics International, p. 73, February 28, 1980.

7. D. Maydan, G. A. Coquin, H. J. Levinstein, A. K. Sinha, D. N. K. Wang, J. Vac. Sci. Technol., 16, 1959 (1979).

8. R. K. Watts, K. E. Bean, and T. L. Brewer, p. 453, Proc. Symp. on Electron and Ion Beam Science and Technology, Ed. R. Bakish, The Electrochemical Society, 1978.

9. W. D. Grobman, "Synchrotron Radiation X-ray Lithography", Handbook of Synchrotron Radiation, Vol. I, Ed. E. E. Koch, D. E. Eastman, and Y. Farge, North Holland, Amsterdam, In Press.

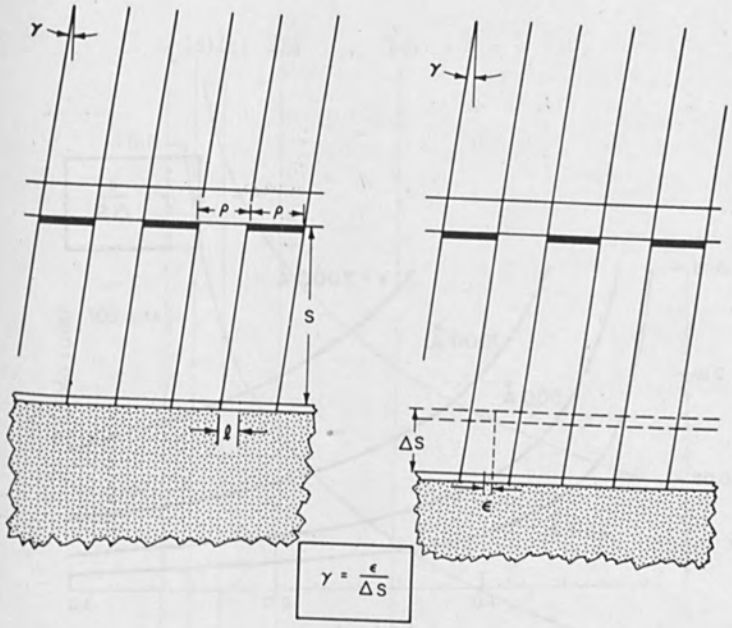

FIGURE 1 Illustration of the superposition error, ε, that occurs if the mask-sample gap, S, changes locally by ΔS from one exposure to another.

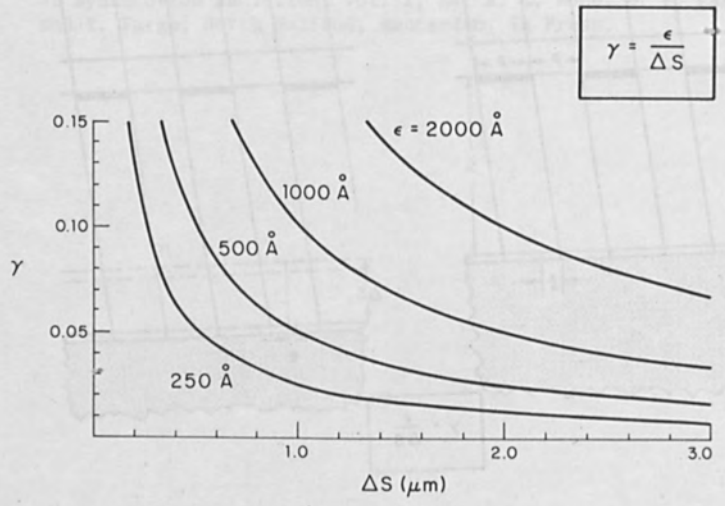

FIGURE 2 Plots of γ versus ΔS for several values of ε. The maximum allowable value of γ is chosen to be 0.15.

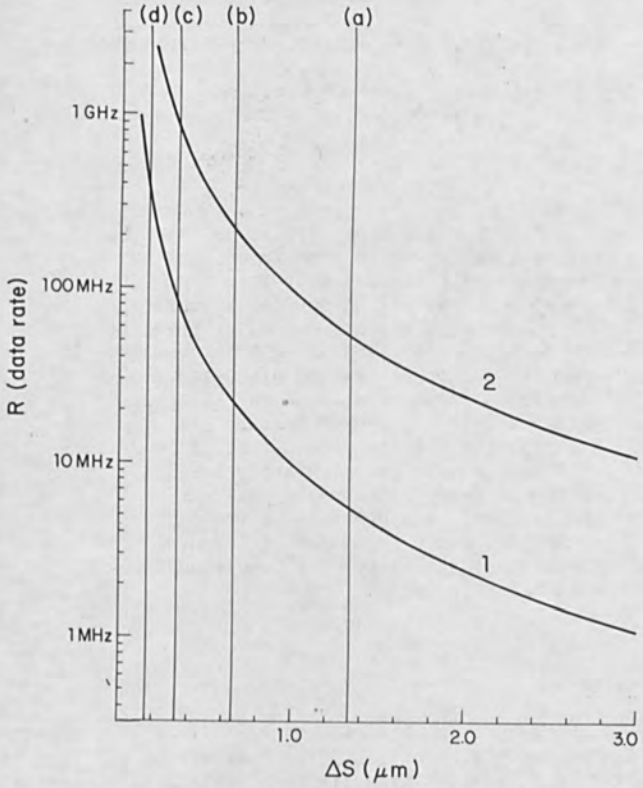

FIGURE 3 Plot of the data rate of an x-ray lithography system, as given by Equation (5), for $\varepsilon/\rho = 1/5$ as a function of ΔS, the repeatability of mask-sample gap at a given location. J and T were given the values 20 X 10^{-3}J/cm^2 and 0.3 respectively. Curve (1) is for a conventional Al_K source operating at 1 kW input power or a hypothetical hot plasma source operating at about 73 W input power. Curve (2) is for a conventional Al_K source operating at 10 kW or the hypothetical hot plasma source operating at 725 W input power. The vertical lines marked, (a), (b), (c), (d), correspond to $\varepsilon = 0.2$ μm, $\varepsilon = 0.1$ μm, $\varepsilon = 0.05$ μm and $\varepsilon = 0.025$ μm at $\gamma = 0.15$, respectively. Thus, the intersections of these lines with the data rate curves correspond to the maximum data rates obtainable at $\rho = 1$ μm, $\rho = 0.5$ μm, $\rho = 0.25$ μm and $\rho = 0.125$ μm (recall $\rho = 5\varepsilon$).

X-RAY LITHOGRAPHY MASK TECHNOLOGY

W.D. Buckley, J.F. Nester, H. Windischmann

The Perkin-Elmer Corporation
Norwalk, Connecticut 06856

A high yield process will be described for fabricating large area free standing membranes of thickness down to 0.5 μm for use as an X-ray lithography mask substrate. The choice of material, method of preparation and technique for separating the membrane from its substrate will be discussed Techniques for generating X-ray absorber patterns with sub-micron feature size are reported. These methods result in absorber geometries which are uniquely suited to X-ray lithography mask applications. Measurements of the mask patterning distortion and the temporal dimensional stability of a completed X-ray mask are reported.

1. INTRODUCTION

X-ray lithography is a proximity mask replication technique that permits the definition of submicron features on silicon wafers or other substrates. Like its counterpart, U.V. proximity printing, it utilizes a patterned photomask. However, because soft X-rays are the exposing radiation there are significant differences in the photomask technology (1, 2). The ideal X-ray mask should meet many difficult, seemingly contradictory, criteria. It should be relatively thin, yet rugged, flat and dimensionally stable, have a low atomic number and a favorably located absorption edge relative to the source wavelength; be fabricable in large area with low defect density and uniformly thin; have isotropic mechanical properties, be optically transparent, relatively inexpensive and impervious to process chemicals commonly encountered in the semi-conductor industry. In addition the absorber must be deposited with low intrinsic stress so not to induce pattern distortions.

Since X-ray lithography permits the choice of a range of exposing wavelengths the mask technology must be selected in the context of the overall system selection. In this paper a mask technology is described which is compatible with the X-ray exposure system described in reference 3 and the alignment approach described in reference 4. The X-ray lithography mask chosen consists of a thin (~ 1 μm) titanium membrane stretched on a support ring. The desired pattern is defined on the membrane by a gold absorber.

In order to be useful for submicron lithography the membrane must be dimensionally stable in order to permit overlay of sequential mask patterns. In addition the membrane must have a smooth surface morphology to permit submicron absorber definition and to avoid defects. These requirements constrain the choice of fabrication process and pattern definition technology. In the following discussion, membrane fabrication, tensioning, patterning and dimensional stability are described.

2. Membrane Fabrication

Titanium membranes are produced by electron beam evaporation onto a glass substrate. In order to ensure membrane dimensional stability the deposition conditions are chosen to produce bulk strength films (5) of uniform thickness with isotropic physical characteristics, zero intrinsic stress and smooth surface morphology.

Films are deposited onto 12.5 cm diameter photomask quality soda lime glass. This glass is chosen because of the close match of its thermal expansion coefficient with titanium and because the high quality surface minimizes defects. The combination of high rate, high deposition temperature (400°C) and matched expansion coefficent produces large area bulk strength films with low intrinsic stress. The evaporation system geometry is chosen to ensure membrane thickness variations of less than 2% across a 8.6 cm active diameter.

A gold parting agent is used to facilitate separation of the titanium membrane from the glass substrate. The choice of parting agent, its thickness and deposition temperature are critical to the membrane fabrication process and to the membrane surface morphology. Because gold has a relatively low recrystallization temperature (150°C) it must be deposited at low temperature to minimize grain growth which has a deleterious effect on the titanium surface morphology. Similarly a thin gold film (< 500 A°) is used to minimize the effect of grain growth during titanium deposition. A titanium surface with features smaller than 0.2 μm is obtained by minimizing the heating cycle. The lower limit of gold parting layer thickness is determined by the interdiffusion kinetics of the Au-Ti system. It has been observed (6 and 7) that the Au-Ti system is susceptible to significant intergranular

diffusion at temperatures above 300°C. Furthermore, the diffusion rate is ambient dependent. Faster diffusion occurs in vacuum than in air possibly due to oxide formation at the titanium grain boundaries which act as interdiffusion barriers (8). Therefore, to assist peeling, it is necessary to minimize the elapsed time in vacuum after the completion of titanium deposition. The use of a gold parting layer results in a peeling yield of greater than 90% for 1 μm thick titanium films 12.5 cm in diameter. We have demonstrated that films as thin as 0.4 μm can be peeled successfully by this technique.

The titanium film is removed from the glass by mechanical peeling as illustrated in figure 1. A thin flexible ring is attached to the titanium by means of double sided adhesive tape. Peeling proceeds under water until the membrane is free standing on the flexible ring. The water acts as a surfactant to reduce peeling forces at the film-glass interface. Separation occurs at the weakly bonded gold glass interface and a titanium-gold film is obtained. The gold surface replicates the original glass substrate and is featureless at 10 KX magnification in an SEM. This surface is used for subsequent lithography and patterning. After separation the mebrane is slack on its mounting ring indicative of the absence of intrinsic stress.

The peeled membrane is tensioned and attached to a support ring. Figure 2 is a photograph of a 1 μm thick tensioned membrane and support ring with an 8.6 cm unsupported diameter suitable for exposing 7.5 cm diameter silicon wafers. Figure 3 illustrates schematically the tensioning procedure. The membrane (M) mounted on its peeling ring (P) is placed symmetrically over the smoothly machined rim (A). Weights (W) are added at the periphery to apply a known tension to the membrane and the permanent support ring (T) is expoxied in place. Membranes are typically tensioned to approximately 10^4 psi.

3. Mask Patterning

The tensioned membranes described above serve as substrates for the subsequent generation of a completed masks with the desired absorber pattern. Unlike optical photomasks the absorber in an X-ray mask may have significant transmission. The X-ray transmission may be minimized by increasing the absorber thickness. However, the patterning process becomes progressively more difficult as the absorber thickness increases. Therefore, a practical compromise is necessary between the conflicting requirements of thick absorbers to produce high contrast and thin absorbers to facilitate high resolution patterning.

The choice of absorber thickness is influenced by the overall system configuration. For a W_m lithography system a contrast of 4:1 (analogous to that achieved by an optical system operating at 60% MTF mandates a gold absorber thickness of at least 0.5 μm as shown in figure 4. In practice, gold thickness of about 8000A is used corresponding to 8:1 contrast.

Submicron patterning of the absorber has been achieved by both additive and subtractive processing. Both of these processes require a photoresist thickness comparable to the absorber thickness. Submicron resist pattern generation was achieved by electron beam lithography using a MEBES instrument.

Since it is difficult to achieve submicron pattern features in thick electron resist we have used tri-level or stencil processes The additive stencil process is shown in Figure 5. The tri-levels consist of 1 μm of PMMA on the membrane which is coated by 0.1 μm of evaporated Cr (or Al) on top of which is a 0.4 μm layer of electron resist (PBS). The PBS is electron beam patterned and the developed resist serves as an etch mask for patterning the metal layer. The PBS is then stripped in an oxygen plasma and the metal stencil is transferred to the PMMA by deep U.V. exposure. After developing the PMMA in MIBK, and removing metal by etching, the gold absorber is electroplated onto the thin parting layer which is used as a plating base. The final process process step is removal of the PMMA in acetone. This process is attractive when Cr is used as the metal stencil since the electron beam resist patterning and metal etching use established photomask fabrication technology.

The electroplating process takes advantage of the conductivity of the titanium membrane. The plating apparatus is shown schematically in figure 6. In this scheme the entire mask is surrounded by an insulated housing with both surfaces of the membrane exposed to a conducting liquid solution. An internal electrode is placed in close proximity to the back surface of the membrane. In this configuration gold plating occurs onto the front surface of the membrane through openings in the PMMA resist pattern. Since the current flow is perpendicular to the membrane plane current distribution problems are avoided and uniform absorber thickness is obtained independent of position on the membrane surface. Figure 7 is a scanning electron micrograph of 1 μm lines and spaces produced by this process.

For an X-ray exposure system using a relatively short source to mask distance and a thick absorber, geometrical shadowing effects may result in linewidth variations as illustrated in figure 8. However, in the process described above, if a point deep U.V. source is located at the same source to mask distance as in the X-ray exposure system, then a leaning pattern is produced in the PMMA. Electroplating faithfully reproduces this profile in the absorber and eliminates the shadowing effects as illustrated in figure 8.

During exposure, X-rays absorbed in the titanium membrane produce photoelectrons which can cause spurious exposure of the X-ray resist. In order to minimize this effect a 1 μm thick coating of low atomic number material, such as PMMA, is applied to the unpatterned surface of the membrane. Figure 9 is a photomicrograph of a finished patterned X-ray mask.

The subtractive version of the mask patterning process is similar to that described above except that a thick layer of absorber is deposited before stenciling layers are applied. Absorber patterning proceeds by sputtering or ion etching.

In its present state of development a finished mask has an optically-visible defect density of less than 20 cm^{-2}. Straightforward improvements in cleanliness and process techniques are expected to lead to a notable improvement.

4. Mask Dimensional Stability

A practical X-ray lithography system mask must permit accurate overlay of successive mask layers. The dimensional stability of the overall mask structure is thus critical. Dimensional instabilities include distortions introduced by the mask patterning process as well as those associated with the membrane itself.

In order to measure these distortions we have fabricated X-ray masks with vernier test patterns. These masks were patterned by means of a Micralign™ projection printer using a quartz master photoplate. The X-ray mask was subsequently compared with the original photoplate by using the optomechanical alignment system of the projection printer to read the vernier patterns. A patterned silicon wafer was also measured periodically to insure against changes in the measurement system. Using these methods the precision of our measurement technique was estimated to be ± 0.25 μm.

The X-ray alignment system (4) permits the detection and compensation of small linear scale changes in the X-ray mask by adjustment of the mask to wafer distance. Therefore, our major concern is with random or nonlinear dimensional changes remaining after a single linear magnification correction. We have analyzed our dimensional stability data in terms of linear and non-linear distortions.

Figure 10 illustrates the average linear scale change of a 7.5 cm diameter mask with time. The data indicates a small continuous shrinkage of the mask pattern with time. However, most of the shrinkage occurs in the first 1000 hours. This suggests that patterning of the stretched membrane after an initial aging could result in no further scale change. (Although the small scale change illustrated in Figure 10 is, in fact, well within the compensating capability of the system.)

Figure 11 illustrates the temporal variation of the residual non linear distortion term. It can be seen that this random term is small and within our measuring uncertainty at all times. It is important to note that this data includes pattern distortions introduced by the fabrication process.

An X-ray multiple exposure technique was also used to measure the temporal stability of the X-ray mask. The X-ray lithography system was used to expose a silicon wafer and the pattern was etched in silicon dioxide. A second exposure using the same mask created an image in a new resist coating. The second exposure was offset from the first so that a vernier mask pattern could be used to measure misregistration. The vernier measurement uncertainty was approximately 0.1 μm. Misregistration was measured at seventeen locations in the wafer. The linear alignment errors were removed mathematically and the residual non linear errors are shown in figure 12. This figure summarizes the data for 8 wafers with an elapsed time of three weeks between exposures. The data shows that to within 1 standard deviation there is no non linear error within the measuring precision.

5. Conclusion

Using a unique combination of materials and novel processing techniques we have developed a fullfield X-ray mask fabrication process. The masks are; rugged, have a relatively high X-ray transmittance, stable and sufficiently blemish-free to be suitable for device fabrication.

REFERENCES

1. H.I. Smith, D.L. Spears and S.E. Bernacki, J. Vac. Sci. Tech. 913, 10, 1973.

2. D. Maydan, G.A. Coquin, J.R. Maldonado, S. Somelch, D.Y. Lou and G.N. Taylor, IEEE Trans. Electron Devices, 429, 22, 1975.

3. W.D. Buckley, G.P. Hughes, "An X-ray Lithography System", 157th Meeting of ECS, St. Louis, Mo. 1980.

4. W.D. Buckley, G.P. Hughes, D.H. Kittell, J.L. Kreuzer, and M.P. Eisenberg,"An X-ray Lithography Alignment System, 157th Meeting of ECS, St. Louis, Mo., 1980.

5. B.A. Movchan and A.V. Demshishin, Fizik. Metal, 83, 28, 1969.

6. J.M. Poate, and P.A. Turner, W.J. BeBonte, J. Appl. Phys. 4275, 46, 1975.

7. W.D. Sylwestrowicz, H.A. Elkholy and G.W. Kammlott, J. of Matl. Sci., 873, 14, 1979.

8. R.S. Nowicki and I. Wang, J. Vac. Sci, Tech., 253, 15, 1978.

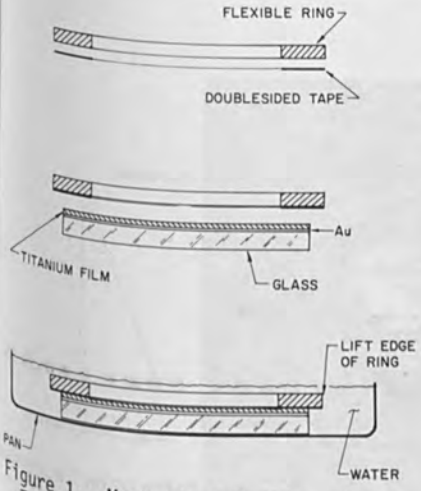

Figure 1. Mechanical Peeling of a Titanium Membrane From a Glass Substrate

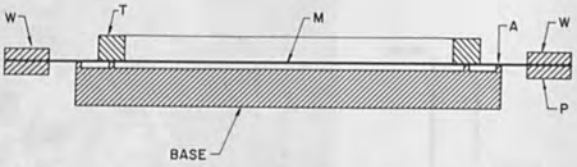

Figure 3. Titanium Membrane Tensioning Procedure. The Support Ring (T) is Epoxied to the Membrane (M) which is Tensioned by Applying a Load (W)

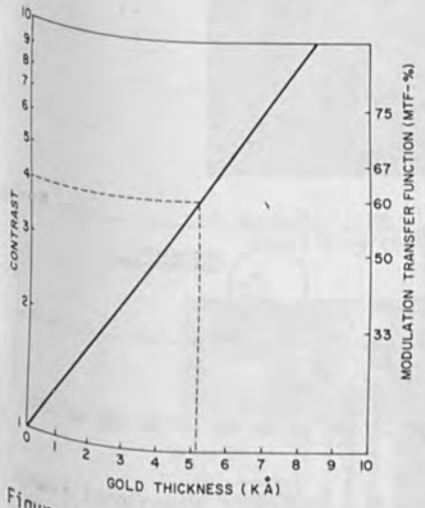

Figure 4. Contrast and MTF Dependence on Gold Absorber Thickness. The dashed line indicates an M.T.F. of 60% a value generally used to define the minimum feature size for practical lithography using optical systems.

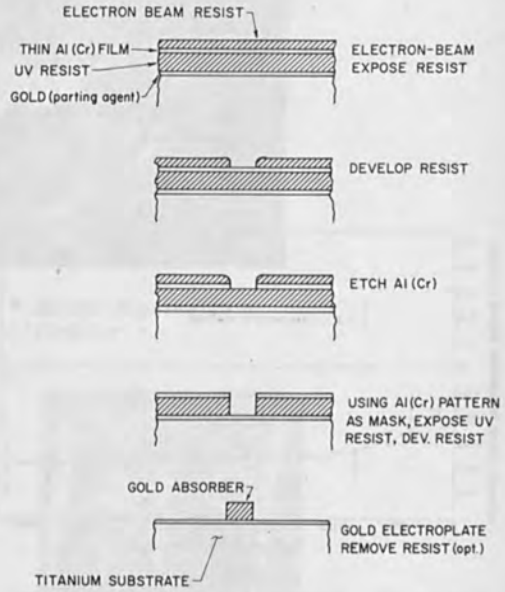

Figure 5. Additive Absorber Definition Process. The Pattern is defined in the Upper Resist by Electron Beam Lithography. This pattern is transferred to the Thick Lower Resist by U.V. Exposure. Subsequent Absorber Definition is by Low Stress Gold Plating.

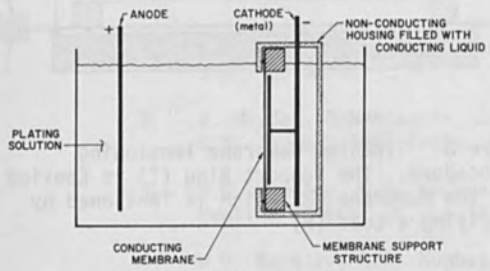

Figure 6. Apparatus for Electroplating a Titanium Mask Membrane

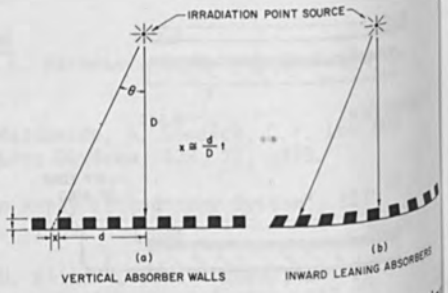

Figure 8. Absorber Definition Technique which Eliminates Shadowing Effects

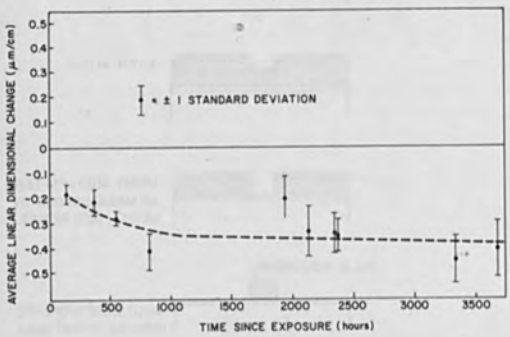

Figure 10. Average Linear Magnification Change as a Function of Time for a 1μm Thick Titanium Mask Membrane.

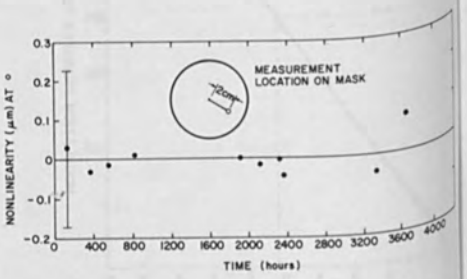

Figure 11. Nonlinear Dimensional Change as a Function of Time at a Fixed Location on a Titanium Mask Membrane.

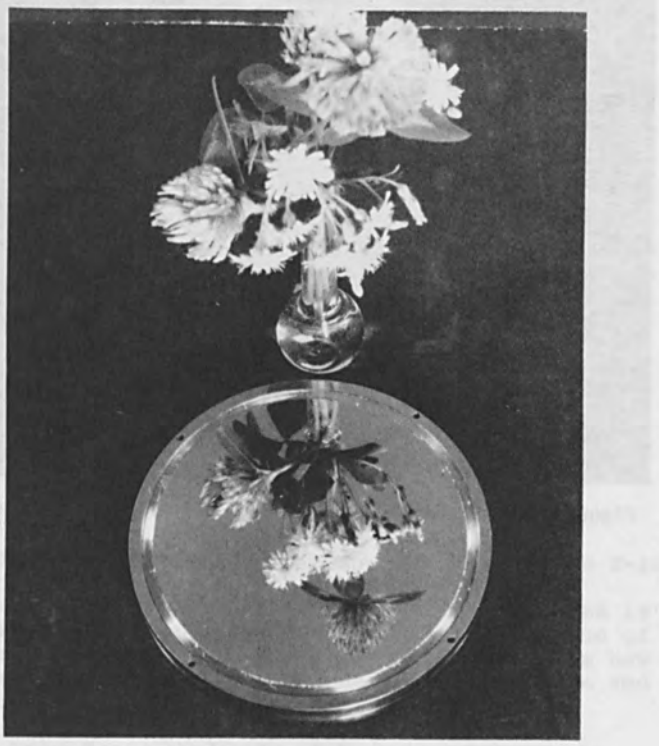

Figure 2. 1 μm Titanium Membrane Mounted on a Rigid Ring ready for patterning.

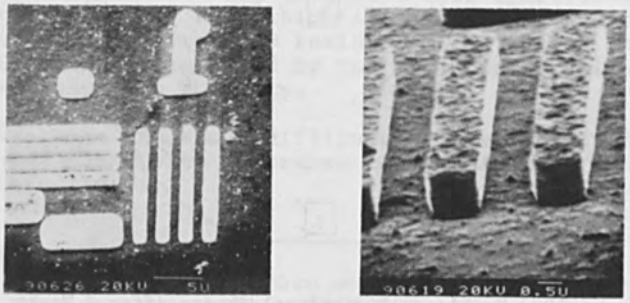

Figure 7. 1 μm Features x 1 μm Thick Electroplated Gold Test Patterns on Titanium X-Ray Mask.

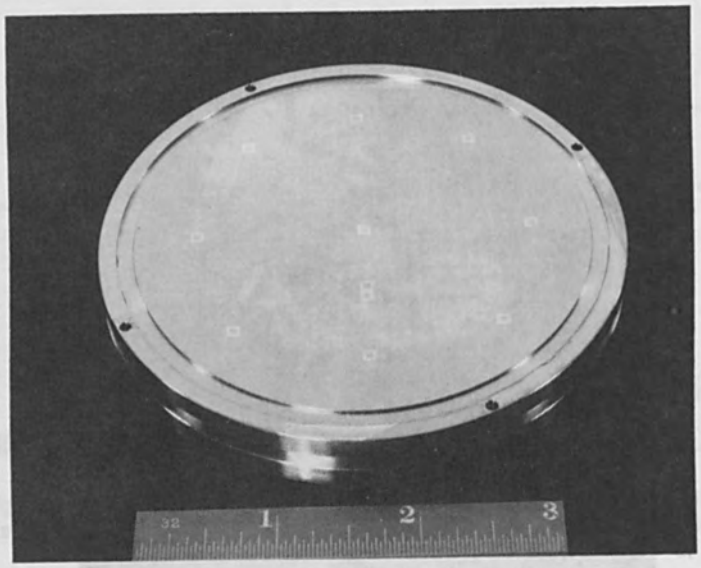

Figure 9. Titanium X-Ray Mask with Gold Absorber Pattern.

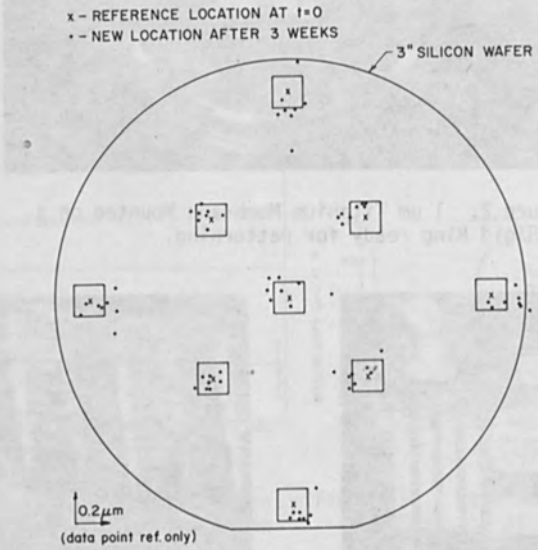

Figure 12. Nonlinear Dimensional Change after 3 Weeks for 8 Wafers and a Single Mask. The Data Scatter is of the same magnitude as the Measuring Uncertanity.

NEW SILICON-POLYIMIDE COMPLEX X-RAY MASKS

F. Yamagishi, M. Okabe, Y. Furukawa and T. Inagaki
FUJITSU LABORATORIES LTD.
1015 Kamikodanaka, Nakaharaku, Kawasaki, 211, Japan

ABSTRACT

Newly-developed X-ray masks of silicon-polyimide feature high strength and low distortion.

The polyimide layer gives these complex masks the needed membrane strength, but the surface strain is much smaller than in polyimide single masks due to the rigid silicon layer. Those features were fully demonstrated experimentally. The complex X-ray masks have been used in an auto-alignment X-ray system, with sufficient overlay accuracy.

I. INTRODUCTION

To fabricate precisely overlapping patterns in X-ray lithgraphy, X-ray masks with flat surfaces and small distortion are required. One way to get flat surfaces is to make membranes with a large area, since the tension of the membrane produces a flat surface. The problem is how to get a large area membrane with sufficient strength and low distortion.

There have been two kinds of X-ray masks. One is inorganic, made of Si (1), $Si_3N_4/SiO_2/Si_3N_4$ (2), or SiC (3), but they are fragile and are often broken by shock. Polymer masks such as polyimide (4),Mylar (5), or Parylene are tough and flexible, but they have much more distortion than inorganic masks. Distortion is caused by the stress of gold absorber patterns and resist applied during the mask fabrication process, and by the X-ray irradiation (6) and by the changes in humidity.

To overcome the above difficulties, we developed complex X-ray masks with membranes consisting of organic and inorganic layers.

II. COMPLEX X-RAY MASK

Fig.1 is a schematic cross section of the silicon-polyimide complex X-ray mask. This structure is as strong as polyimide, with the small distortion of silicon membranes As the Young's moduli of silicon ($1.3 \times 10^{11} N/m^2$)

is more than an order higher than polyimide ($3 \times 10^9 N/m^2$), apparent Young's moduli of the complex mask is expected to be as high as that of silicon.

Another feature of this mask is the layer of gold plated onto the back of the silicon support frame, which cancels the tensile stress of the polyimide on the front, thus helping to keep the surface of the support frame flat. Fig.2 shows the flatness of the complex X-ray mask surface observed by optical interferometer. The tensile stress of the gold pattern on the back surface usually keeps the surface flat within 5 μm.

Fig.3 illustrates the fabrication process of a complex X-ray mask. A silicon wafer is doped with a boron concentration 2×10^{20} cm^{-3}. Then 2 μm thick etching mask patterns of gold are plated on the back of the wafer, through which silicon is etched with a well-known anisotropic etchant, leaving 2 μm of silicon membrane. Onto this polyamic acid is spun very carefully and baked 30 min. at 150°C and 15 min. at 400°C. The order of the above step is important, since if the polyimide coating is in place before anisotropic etching,the polyimide is damaged by etchant. An X-ray blank mask is obtained by evaporation of the plating base of Cr and Au. X-ray absorber patterns of the device are electroplated after resist pattern delineation by electron beam lithography. Finally, the electroplating base around the marks for optical alignment is etched away.

The above process usually obtains a yield of more than 80 %.

III. BURST STRENGTH

Fig.4 shows the burst strength of silicon,polyimide and complex masks with membranes 33 mm in diameter. Silicon masks are so weak (0.05Kg/cm²) that they are often broken by shock, which indicates that they can hardly be used practically. Our requirement for burst strength is more than 0.15 Kg/cm², so that ultrasonic cleaning can be used safely. Considering the burst strength of polyimide membrane 1 to 3 μm thick, a polyimide coating 2 μm thick satisfies our requirement. So we coated polyimide 2 μm thick onto silicon 2 μm thick, making a complex membrane with enough burst strength.

IV. DISTORTION

We examined three types of distortion for both complex and polyimide masks as follows.

(1) distortion caused by the stress of gold absorber patterns
(2) distortion caused by the decreased stress when the resist is removed
(3) distortion caused by X-ray irradiation

We evaluated the above distortion by measuring the displacement between the replicated patterns by an X-ray mask before and after the stress exertion. Fig.5 shows the auto-alignment X-ray exposure system we used. This tool has positioning resolution less than 0.03 μm and the alignment accuracy better than 0.1 μm (7).

Fig.6 shows the distortion caused by evaporated gold. For simplicity, we placed a circular pattern of evaporated gold at the center of both complex and polyimide mask. It can be seen that the tensile stress of the gold causes compressive distortion. In the polyimide mask,shown by dotted line, the distortion is as large as 3 to 4 μm. On the other hand, distortion of a complex mask is much less, and of the same order as measuring error.

Fig.7 shows the distortion caused by resist coating. As in Fig.6, a circular pattern of PMMA resist, 1 μm thick was placed at the center of the mask. A curve similar to that in Fig.6, but quantitatively different was obtained. Though the amount of distortion was 1/4 less than that caused by the gold pattern, distortion more than 1 μm was measured for the polyimide mask, but the distortion of the complex mask was on the order of the measuring error.

Fig.8 shows the distortion as a function of Al(K_α) X-ray irradiation. Here, for the sake of non-uniform irradiation, a non-irradiated X-shaped pattern was intentionally made. In the figure, the vertical axis shows the distortion at a point 10 mm from the center of the mask. The horizontal axis shows the number of exposures for positive resist FBM-110, whose sensitivity is 30 times as high as that of PMMA. The radial distortion due to the increased tensile stress by X-ray irradiation increases as the irradiation time increases. Here the distortion in the complex mask is 1/3 less than that of polyimide.

V. OVERLAY REPLICATION WITH COMPLEX MASKS

Pairs of complex masks with major/minor bubble patterns were fabricated. Fig.9 shows a complex mask with 16 chips of 1 Kbit memory. Fig.10 shows the SEM photographs of the overlapping bubble patterns with overlay accuracy less than 0.1 μm. For pattern ruling of 1 μm

this accuracy is sufficient.

VI. CONCLUSION

New silicon polyimide complex X-ray masks have been developed. By a double layer of silicon and polyimide membrane, strength enough to retain window size 33 mm in diameter was easily realized. By the distortion measurements, the complex mask was shown to have much less distortion than the polyimide mask.

With the complex X-ray masks a bubble memory pattern was replicated with the good accuracy.

ACKNOWLEDGMENT

The authors wish their appreciation to Mr. A. Ihaya for his helpful guidance, and Y. Kitamura and Y. Kimura for their experimental help. They wish to thank members of semiconductor laboratory for performing electron beam delineation, and members of components laboratory for designing bubble memory patterns.

REFERENCES

(1) R.L.Sears and H.I.Smith,"X-ray Lithography -A High Resolution Replication Process",Solid State Technology, July,p.21 (1972)
(2) T.Hayashi,"Electron beam and X-ray lithography for very large scale integration devices", Proceedings of the Symposium on Electron and Ion Beam Science and Technology,(8th International Conference)p.85 (1978)
(3) R.K.Watts, K.E.Bean,and T.Brewer,"X-ray lithography with aluminum radiation and SiC mask",ibid,p.453 (1978)
(4) D.C.Flanders and H.I.Smith,"Polyimide membrane X-ray lithography mask fabrication and distortion measurements", Proc. 14th Symposium on Electron,Ion and Photon Beam Sci. and Tech. (1977)
(5) D.Maydan, G.A.Coquin, J.R.Maldonado, S.Somekh, D.Y.Lou and G.N.Talor,"High Speed Replication of Submicron Features on Large Areas by X-ray Lithography", IEEE Trans. El.Dev. ED-22 p.429 (1975)
(6) D.Tisher, B.Schneider-Gmelch and H.G.Wolff,"Stability of Polyimide X-ray Masks", Proceedings Microcircuit Engineering '79 p.90 (1979)
(7) T.Uchiyama, M.Oda and K.Nakamura, "Precision Auto Mask Aligner",FUJITSU Scientific and Technical Journal vol. 15, No.4, p.77 (1979)

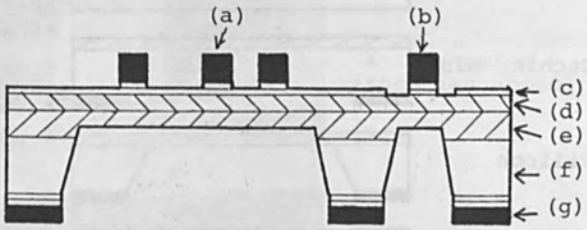

(a) device pattern (b) alignment pattern
(c) plating base (d) polyimide layer
(e) boron diffused silicon layer
(f) support frame (g) Au plating

Fig.1 Cross section of silicon-polyimide complex mask

Fig.2 Photographs of flatness of a complex X-ray mask observed by an optical interferometer. Fringe interval corresponds to 0.27μm variation of flatness. Surface flatness is 3.3 μm in the area of 2 inches in diameter.

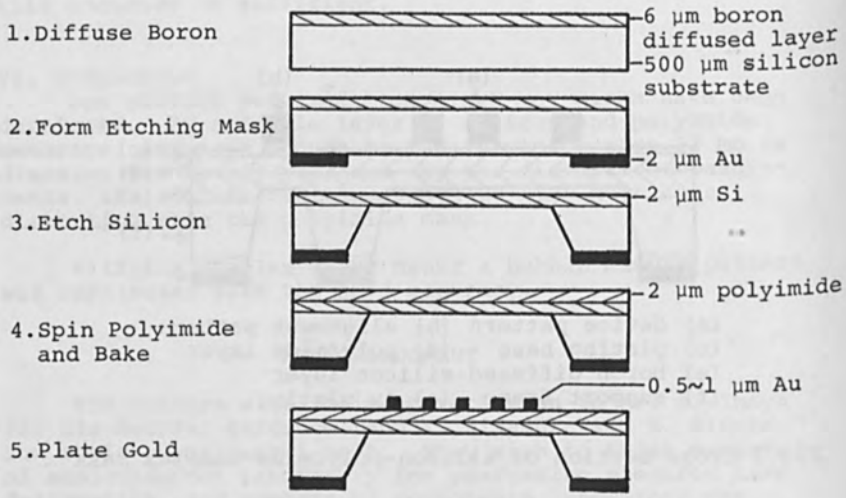

Fig.3 Fabrication process of the complex mask.

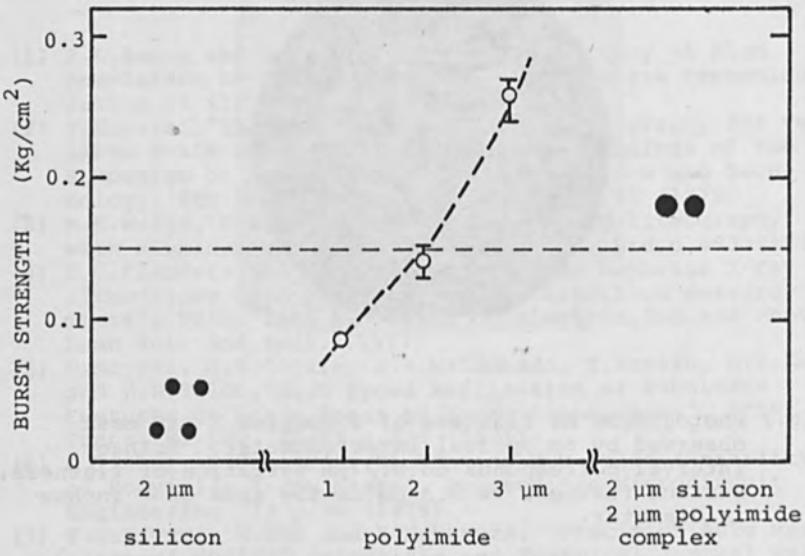

Fig.4 Burst strength of silicon, polyimide and complex mask with 33 mm window diameter.

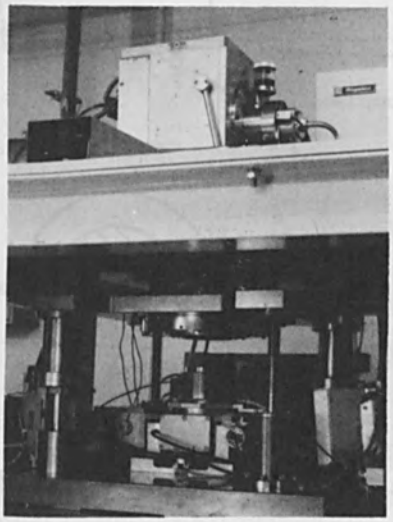

Fig.5 Auto-alignment X-ray exposure system.

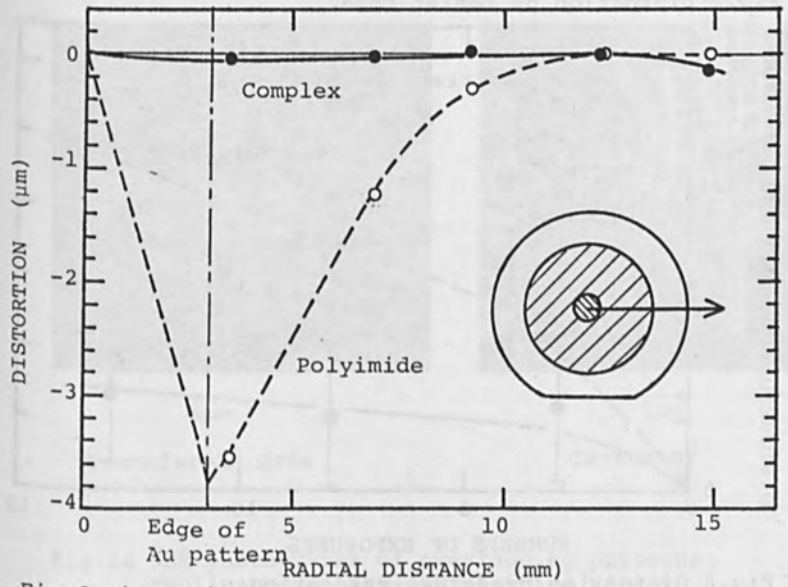

Fig.6 Distortion by evaporated gold. Thickness of gold is 3000 Å.

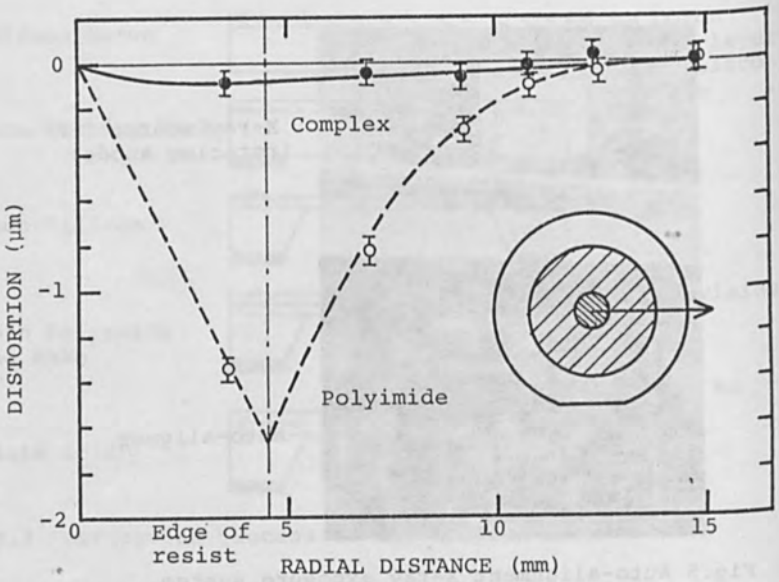

Fig.7 Distortion by resist PMMA.

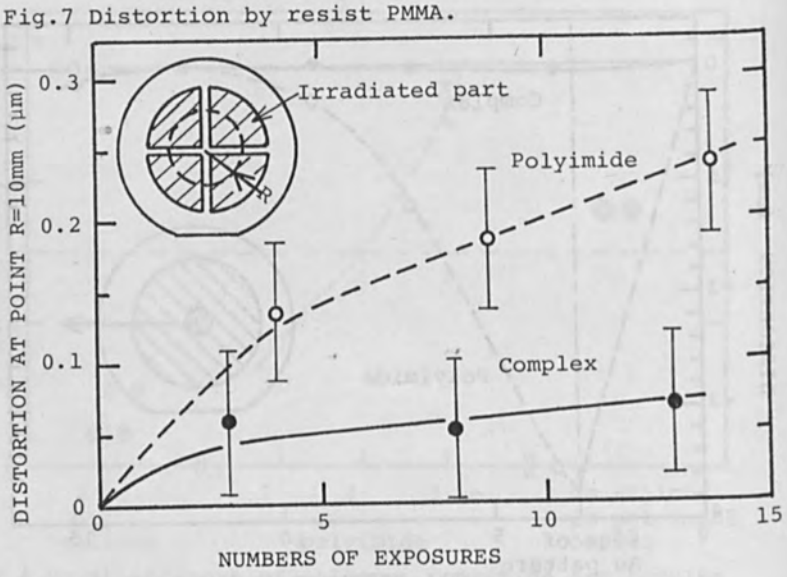

Fig.8 Distortion by X-ray irradiation.

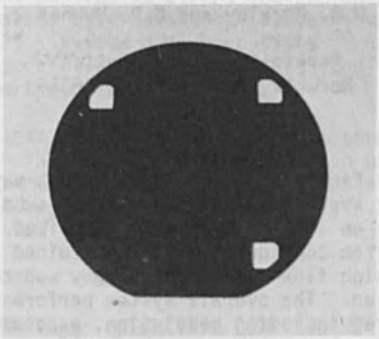

Fig.9 Complex mask with bubble memory.

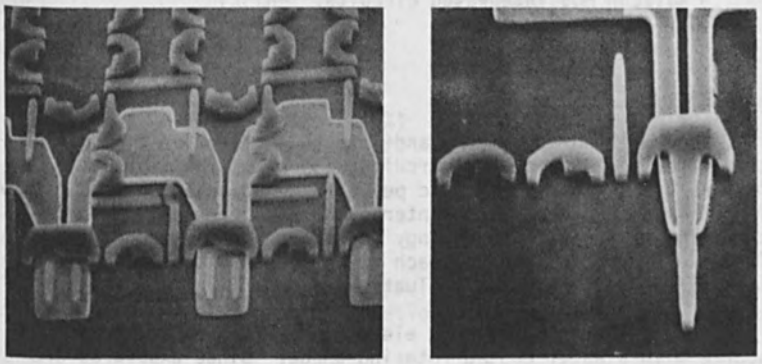

Transfer-In Gate Generator

Fig.10 SEM photographs of overlapping patterns replicated on FBM-110 positive resist. Minimum feature size is 1 μm.

AN X-RAY LITHOGRAPHY SYSTEM

W.D. Buckley and G.P. Hughes

Perkin-Elmer Corporation
Norwalk, Connecticut 06856

A full field, short exposure time X-ray lithography system which is capable of submicron lithography on silicon wafers is described. The optimum system configuration is determined and and a new high flux X-ray lithography source is identified. The overall system performance is summarized including resolution, exposure time, overlay capability, mask stability and technology, experimental X-ray resist evaluation and evaluation of source radiation effects on silicon MOS integrated circuits.

1. INTRODUCTION

X-ray lithography is a candidate technology for the fabrication of silicon integrated circuits with submicron minimum feature size. The lithographic performance of an X-ray lithography system is determined by the interaction of the exposure source, the aligner, the mask technology and the photoresist. (Figure 1) This paper discusses an approach to one such system and reports its performance including evaluation of radiation damage.

The system is based on a electron beam generated X-ray source with a water cooled rotating anode. Since exposures are performed in helium at atmospheric pressure, a thin Be window separates the source vacuum chamber from the exposure chamber. A compatible mask technology has been developed based on titanium mask membranes and gold absorbers. The fabrication, patterning and stability of these masks is described in reference 1. Similarly an optical aligner has been developed compatible with optically opaque or transparent masks. The principle and performance of this aligner is described in (2).

2. System Considerations

In any lithography system, the parameters of practical interest are the resolution, linewidth control, exposure time and overlay capability. In an X-ray lithography system these dependent parameters are controlled by the independent parameters, source diameter(s), mask to wafer distance (d), exposure distance (D) and source power (P). System design consists of optimizing the geometric factors to satisfy the conflicting requirements of high resolution and short exposure time.

Table 1 lists typical system parameters for a three inch wafer exposure system. The mask-to-wafer separation of 50 μm is chosen so as to minimize the possiblity of mask damage during exposure and is large enough to ensure an effectively infinite mask life.

TABLE 1

SYSTEM PARAMETERS: GEOMETRIC LIMITATIONS

Selected Parameters	Control Factor	Control Parameters	Limiting Value
d = Mask to Wafer Gap	Mask Life		50 μm
D = Wafer to Source Distance	Exposure Uniformity (±5%)	D ≥ 3x Wafer radius	D ≥ 12 cm
	Minimum Exposure Time	D, Window Thickness, Resolution	D = 15 cm
S = X-ray Source Diameter	Resolution (0.5 μm)	Penumbral $\frac{S}{D}$ d	S ≤ 0.15
	Linewidth Variation (> 5%)		S ≤ 0.15 cm
	Variatiion in d (1 μm)	$\frac{S}{D}$ Δ d	
	Temperature Corrections (± 1°C)	$\frac{S}{D}$ Δ d	
	Wafer Noflatness 5 μm)	$\frac{S}{D}$ Δ d	

The optimum exposure distance (D = 15 cm) is determined by the consideration of exposure flux uniformity and the exposure time. Since the wafer is illuminated by a quasi-point source of X-rays, the exposure flux at the wafer decreases radially. In order to ensure an exposure uniformity within ± 5% across the wafer it is necessary that the exposure distance be greater than three times the wafer radius. For the 15 cm exposure distance used here, the flux uniformity is ± 3%.

The exposure time is determined by absorption in the vacuum window, mask membrane, helium atmosphere and photoresist and by the photoresist sensitivity. In addition two other factors are important.

First, for a fixed wafer diameter, as the exposure distance increases the diameter of the vacuum window can be reduced. In principle a thinner window can be used and, because of reduced absorption, the exposure time is decreased.

Second, it is usual to consider the effects of exposure distance variations at constant source power. However, it is more useful to examine these effects at constant resolution. This perspective has a major effect on the permissible power since the electron beam diameter can vary with exposure distance.

The situation is summarized in Figure 2. In calculating these curves a 5 μm thick mylar mask, a helium atmosphere and the resist sensitivity of COP were assumed. A source power of 10 KW was assumed for constant power calculations and a constant Be window thickness of 25 μm where appropriate. Similarly 1 μm penumbral blurring was assumed for the constant resolution curve.

The Constant power, constant window thickness curve is dominated by the inverse square law term and the exposure time is proportional to D^2. This is the basis of the conventional exposure time curve. When the window thickness variation is included, the square law term is significantly modified and, over most of the range illustrated, the exposure time is approximately proportional to D. Finally, for the constant resolution curve, an entirely different conclusion is apparent. An optimum exposure distance exists for which the exposure time is at a minimum. For greater distances the exposure time is approximately proportional to $D^{1/2}$. In addition, the exposure time is only a weak function of exposure distance and, over the distance range illustrated, the increase is less than 50% above the minimum. The minimum exposure time is obtained at the optimum exposure distance which for an aluminum source and a three inch wafer is 15 cm. Because the exposure time is relatively insensitive to exposure distance, other system requirements may, in fact determine the distance. However, in general a shorter distance is preferred in order to minimize power requirements.

The optimum source spot diameter is determined by the desired resolution and by the maximum permissible linewidth variation. In order to provide process latitude for 1 μm lithography, and to have the capability of extending to the sub-micron regime, a penumbral resolution limit of 0.5 μm was selected. This requires a 1.5 mm spot diameter, a 15 cm exposure distance and 50 μm mask to wafer separation.

Linewidth variations can arise from variation in the wafer surface and from uncontrolled or controlled variations in mask to wafer separation. For a 1.5 mm spot linewidth variations are 80 A° per μm variation in gap.

Deliberate variations in the gap are part of the alignment procedure. These variations cause linear magnification changes at the image plane due to the inherent nature of point source imaging. The magnitude of the change is given by the relation $\Delta R/R = \Delta d/D$. For the system geomtry chosen this results in a magnification change of about 0.25 μm per μm of gap variation at the periphery of a 3 inch wafer. This effect can be used to compensate for linear magnification changes in the mask or wafer which can occcur due to thermal or wafer processing effects (3). It can also compensate for linear magnification changes in the mask and, in so doing, considerably relax mask stability requirements.

Uncontrolled variations in the gap between exposures can result in image distortions which will limit the overlay precision. The magnitude of these distortions is given by the relation above and amounts to about 0.25 μm per μm of uncontrolled gap variation at the periphery of a 3 inch wafer. In order to minimize this effect a 'bed of nails' wafer chuck was used. This reduces the chance of particle entrapment by simultaneously reducing the total contact area between the chuck and wafer and distributing this area over an array of small studs. The chuck surface was polished flat and served as a reference surface for the back of the of the wafer. In this manner the front surface profile of the wafer was controlled.

As a result of the discussion above one defines the geometrical parameters of the system as d = 50 μm, D = 15 cm and s = 0.15 cm. The source power is the only unspecified independent parameter. Its value is determined by the maximum permissible power input to the specified source size for the anode material chosen.

The maximum power dissipation P of a rotating anode can be expressed as a function of the maximum allowable temperature rise, ΔT, (4,5) by:

$$P = \pi^2 (\rho C_v K s^3 v)^{1/2} \frac{\Delta T}{16}$$

where v is the surface velocity of the anode, K is the thermal conductivity, C_v is the specific heat, ρ is the density and s is the spot diameter. The quantity (ΔT) is limited by melting or by the fatigue failure limit.

The equation predicts that the maximum power is proportional to the 3/2 power of the spot diameter. This relationship has been confirmed in the literature and by commercially available Al_K rotating anode sources. In Figure 3, the data points are for X-Ray sources available from Rigaku. The line labelled Rigaku-Al obeys the theoretical power law. The highest power commercial source uses a 250 mm diameter Al target rotating at 8000 rpm. A projection for this source is also shown in Figure 3. Also shown in figure 3 is the calculated power dissipation for a Pd anode (6).

It is apparent (Figure 3) that the maximum power dissipation for an Al source and a 0.15-cm spot diameter is about 3.5 kW. Reference to Figure 2 indicates an exposure time of approximately 100 seconds. This consideration led us to evaluate alternate anode materials with the objective of increasing the power and reducing the exposure time. It was confirmed experimentally that a tungsten source is as efficient as aluminum in exposing both COP and PMMA resist. However, as shown in figure 3, the tungsten source can dissipate about six times more power than either the aluminum or palladium source (for a constant spot size) and results in a projected exposure time of less than 20 seconds.

The lithographic capability of a tungsten M line (7A°) source is illustrated by Figure 4, a scanning electron micrograph of resolution patterns with 1 μm thick lines and spaces imaged in a 1 μm thick PMMA film. One micron resolution in COP was also demonstrated and reported previously (7).

Table 2 summarizes the projected characteristics of an X-ray lithography system based on a tungsten source and a resist with the sensitivity of COP. For this system exposure time is not a limiting parameter. The table specifies a 3 inch wafer although the performance parameters are relatively insensitive to wafer size.

TABLE 2

THEORETICAL PERFORMANCE CHARACTERISTICS OF AN OPTIMIZED X-RAY SYSTEM

Wafer Diameter	3 inches
Exposure Distance	15 cm
Exposure Time	17 seconds
Power	20 kw
Spot Size	1.5 mm
Resolution (Penumbral)	0.5 μm
Printing Capability	< 1.0 μm
Linewidth Variations	
Nonflatness (±5 μm)	0.04 μm
d Variation (± 1 μm)	0.008 μm
Temperature Correction (±1°C)	0.006 μm

It is informative at this point to compare this system with conventional lithographic tools. It is customary to describe the performance of lithographic tools by the vague term resolution. However, King and Goldrick (8) have shown that the modulation transfer function (MTF) is a useful concept in describing the performance of photolithographic tools. MTF is a plot of the image modulation as a function of the spatial frequency of the mask pattern. Current practice is to associate an MTF value of 60% with the minimum feature size acheivable in production.

Gopala U.V. Rao has shown how to calculate the MTF of an X-ray lithography system.(9) Figure 5 compares the MTF of a an F3 projection aligner and the X-ray lithography system described above. The large improvement in MTF obtained with the X-ray system is apparent. However, it is important to remember that the overall system MTF is determined by the product of the MTF of the imaging system and the MTF of the mask. For an optical system, with a high contrast mask, the mask MTF is essentially 100% and the system MTF dominates. For the X-ray system the mask contrast is less and dominates for features larger than about 0.5 μm.

Figure 6 illustrates the mask contrast and MTF for a gold absorber and a tungsten source. As can be seen the contrast depends on the accelerating voltage of the electron beam X-ray source due to continuum radiation. For an 8 Kv source a gold thickness of 0.5 μm results in an MTF of 60% and at 20 Kv 0.7 μm of gold is necessary. For these masks a resolution of 0.5 μm is achievable. Thicker gold increases the mask contrast and reduces the minimum feature size towards 0.3 μm. Clearly, the higher MTF possible with an X-ray system should result in better linewidth control in the presence of exposure non-uniformities In addition the absence the multiple reflection endemic to optical system (ref 10) should also aid in linewidth control.

3. System Performance

An experimental system has been constructed. (Figure 7) consisting of a tungsten anode X-ray source with a ring cathode electron gun. For this system the source power is limited to 10 Kw by a low anode rotational speed(2000 rmp). This system has operated reliably at Perkin-Elmer for more than a year. A similar system at a customer facility has experienced less than 2% down time. The exposure time is longer than predicted since a nonoptimum exposure distance (D = 17 cm) was used at 10Kw beam power. For COP resist an exposure time of about 1 minute is typical

The use of a tungsten anode simplifies the electron gun design. Since tungsten deposition on the anode from the gun filament is not an issue, direct line of sight from the filament to the anode is acceptable. Consequently we have constructed a ring cathode electron gun by adapting the design of a linear cathode gun from a conventional X-ray tube. This configuration is not optimized for X-ray lithography and is presently limited to a minimum spot size of about 2.5 to 3mm. Although larger than our ultimate goal of 1.5 mm this spot size results in a system MTF that is quite adequate for submicron lithography.

The PBS resist is somewhat slower than COP but appears capable of developing finer features. Patterns consisting of 0.75 μm lines and spaces and isolated 0.5 μm geometries of either polarity can be replicated.(figure 8) A statistical comparison of 1 μm features on a mask and wafer indicates a 100% yield as measured at 50 locations Extensive determination of critical dimension control has not yet been undertaken. Preliminary measurements on COP resist indicate a linewidth standard deviation of about 0.1 μm for a 2 μm feature.

We have evaluated the exposure characteristics (figure 9) of several conventional U.V. and experimental photoresists. Experimental resist EK88 prepared by Eastman Kodak is attractive. This negative resist is almost twice as sensitive as COP with better resolution in thicker layers. The resist γ is about 1.25, compared to $\gamma = 1$ for COP. Figure 10 is a scanning electron micrograph of 1 μm lines and spaces in EK88. The initial resist thickness of 1 μm was exposed and developed to a final thickness of about 0.5 μm.

Radiation damage evaluation has been performed by a major semiconductor manufacturer using both discrete MOS devices and MOS integrated circuits. X-ray lithography was simulated by exposing completed MOS devices to 1, 3 and 10 times the PBS exposure dose. All devices exhibited parametric changes but the differences for the different doses were small. Discrete device results indicate that radiation effects are removed by a conventional aluminum alloy process for all exposure doses. Similar experiments were performed on an integrated circuit chosen for its expected sensitivity to radiation damage. Radiation effects were removed by an additional aluminum anneal of the finished circuits. No significant behavior difference was observed between the irradiated devices and a control group.

The mask technology utilizes a titanium membrane (1) Experiments so far indicate that this material is stable to better the 0.2 μm, the measurement precision over at least 5 months. An optical aligner has been evaluated (2) using these masks. In its present form this experimental system has achieved an overlay error standard deviation of less than 0.5 μm. Data analysis indicates that 1/8 μm overlays are achievable in a reconfigured system.

4. Conclusion:

An X-ray proximity lithography system with a well developed source, mask, and alignment system has been described. The fundamental problems of X-ray lithography have been addressed and shown to be tractable. The use of a high brightness X-ray source with conventional E-Beam resist has reduced exposure times to less than a minute. Experimental resists result in exposure times comparable to optical lithography systems. The use of ductile titanium masks with gold absorber layers has yielded high contrast, low distortion, overlays. The mask and bright exposure source in conjunction with an optical alignment system have been used to demonstrate the feasibility of X-ray lithography as a high resolution tool.

REFERENCES

1. W.D. Buckley, J.F. Nester, H. Windischmann, "X-ray Lithography Mask Technology" 157th Meeting of ECS, St. Louis, Mo. 1980.

2. W.D. Buckley, M.P. Eisenberg, G.P. Hughes, D.H. Kittell, and J.L. Kreuzer, "An X-ray Lithography Alignment System" 157th Meeting of ECS, St. Louis, Mo. 1980.

3. Nan-Hsinng Tsai, Carl N. Alquist, "Characterization of In-Plane Wafer Distortion in NMOS Process". Semiconductor Microlithography V, San Jose, California (1980).

4. W.J. Osterkamp, Phillips Res. Rep. 3; 303 (1948)

5. G.A. Wardly, E. Munro, R.W. Scott, "High Brightness Ring Cathode Rotating Anode Source for X-ray Lithography" International Conference on Microlightography, Paris, France (1977).

6. J.R. Maldonado, M.E. Roulsen, T.E. Saunders, F. Vratny and A. Zacharias, "X-Ray Lithography Source Using a Stationary Solid Pd Target." J. Vac. Sci. Technol. 16 (1979).

7. W.D. Buckley, and J.A. DalleAve, "X-ray Exposure and Development Characteristics of Polyglycidal Methacrylate - Ethyl Acrylate", Electron and Ion Beam Science and Technology Meeting, Seattle, Washington (1978).

8. M.C. King and M.R. Goldrick, "Optical MTF Evaluation Techniques for Microelectronic Printers", Solid State Technology (February 1977).

9. Gopala U.V. Rao and Au-Liang Soong, "An Intercomparison of the Modulation Transfer Function of Square and Circular Focal Spots", Medical Physics, 1, 204 (1974).

10. C.N. Alquist, W.G. Oldham, P. Schoen "A Study of a High Performance Profection Stepper Lens" Microcircuit Engineering 1979, Achen, 339-349.

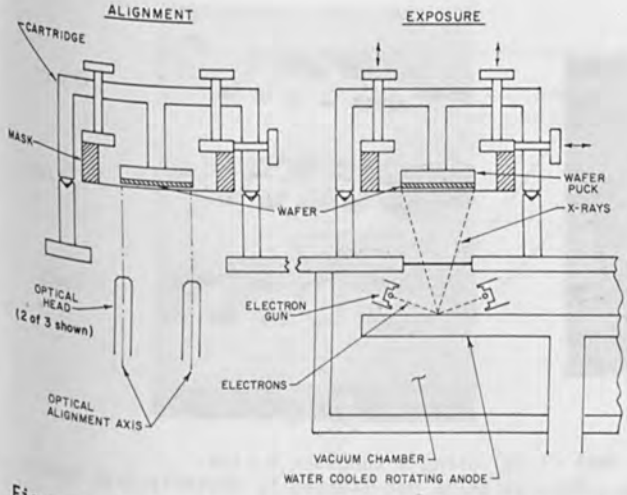

Figure 1. X-Ray Lithography System (Schematic). The mask and wafer are carried in a cartridge which fits in turn over the alignment and exposure system.

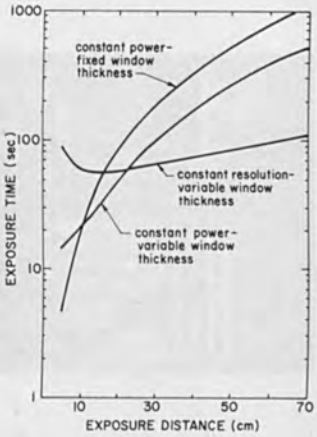

Figure 2. Various relationships between exposure time and source-to-wafer distance. The conventional model assumes a constant window thickness and derives the exposure time for constant power.

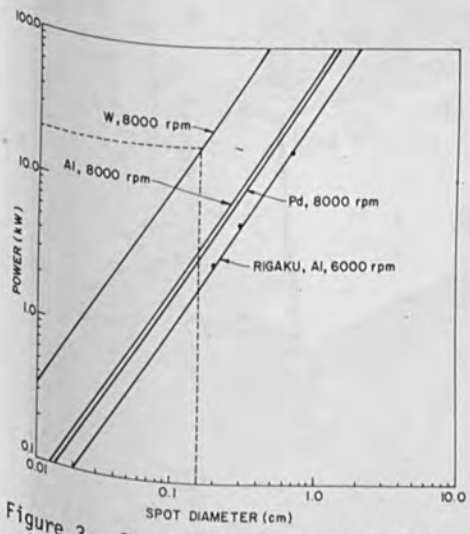

Figure 3. Input Power V Spot Diameter for water cooled, rotating anode X-ray anodes.

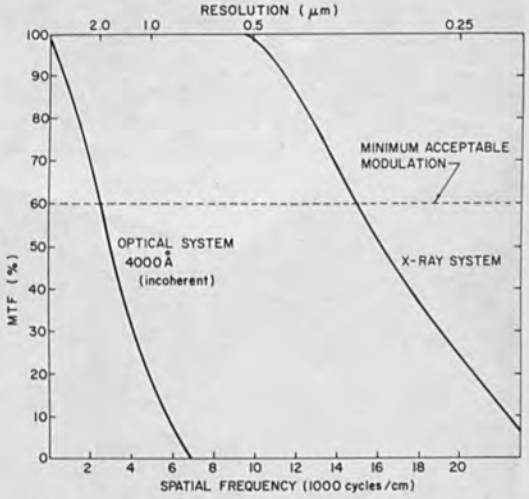

Figure 5. A comparison of the MTF of an optical Lithography System (F3 Projection Aligner) with the MTF of the Proposed X-Ray Lithography System.

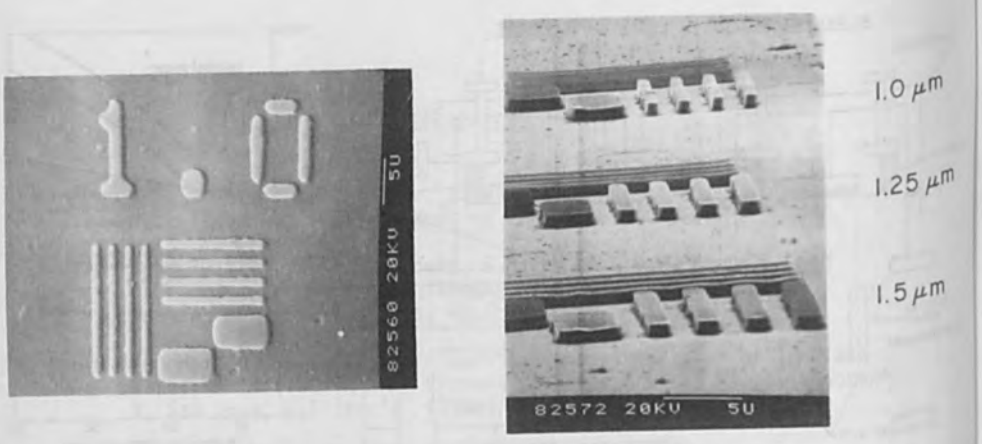

Figure 4. X-Ray Lithography in PMMA (1 μm) using a tungsten M-Line (W_m = 7A^{O}) Irradiation source. Resolution is not limited by photoelectron range.

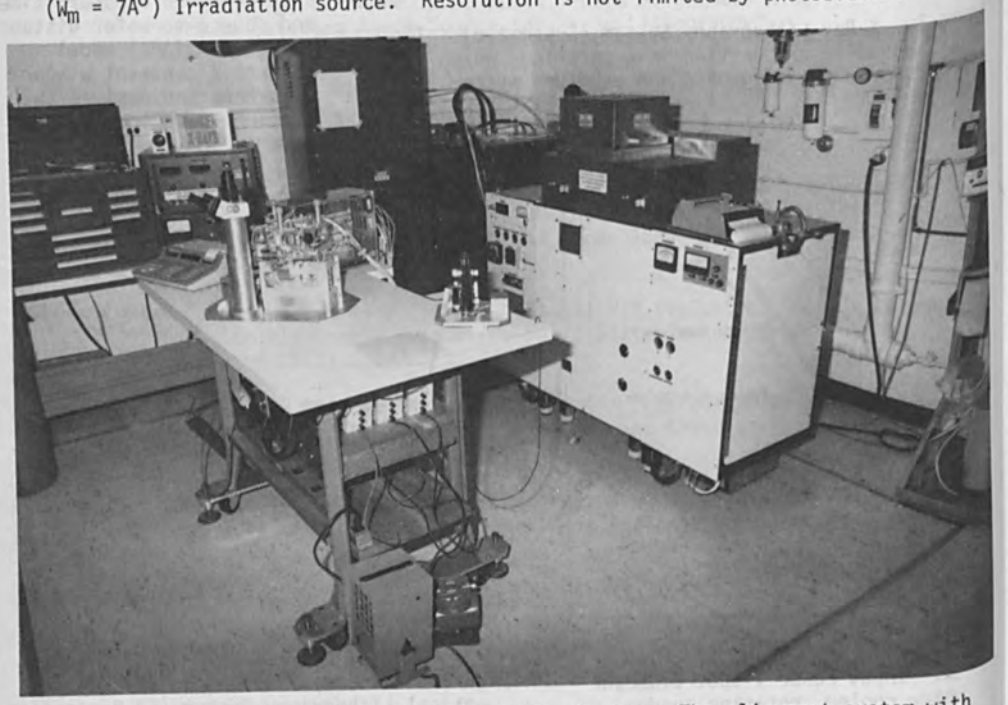

Figure 7. An Experimental X-Ray Lithography System. The alignment system with the Removable Cartridge is on the left and the exposure system of the right.

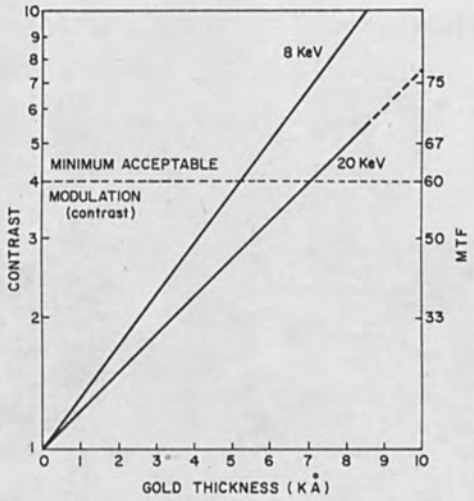

Figure 6. The contrast of an X-Ray mask using a gold absorber and a tungsten M line source. The lower energy excitation reduces bremstrahlung radiation and produces approximately theoretical contrast.

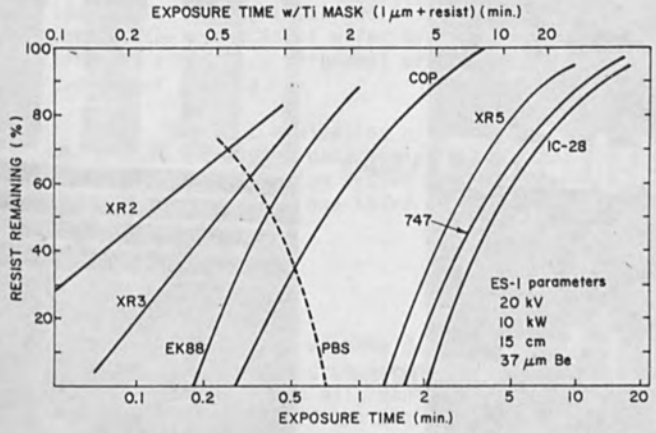

Figure 9. Exposure characteristics of a selection of commercial and experimental resists. The high gama and sensitivity of Eastman Kodak experimental resist EK88 is notable.

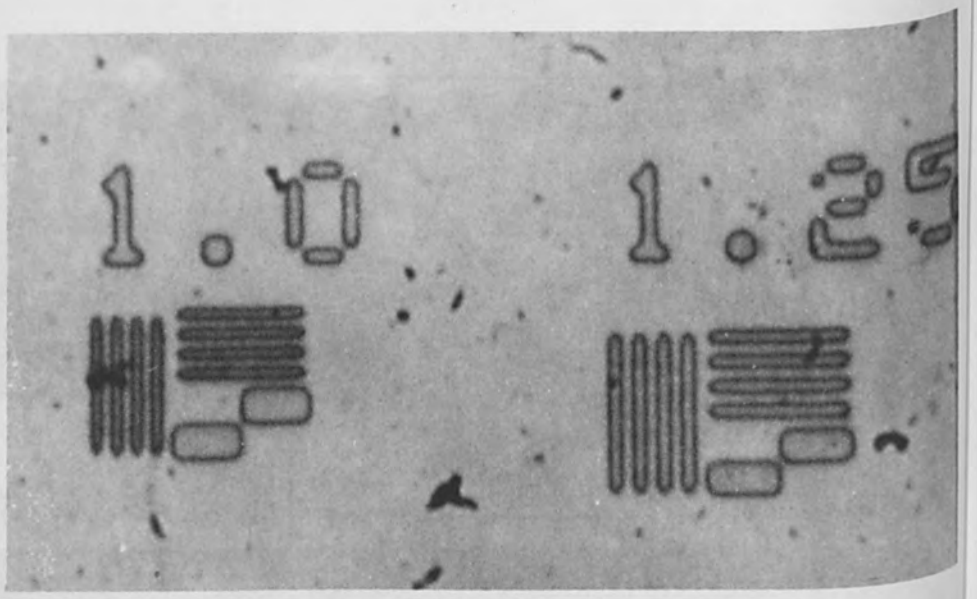

Figure 8. X-Ray Lithography in PBS Resist Using a Tungsten Source.

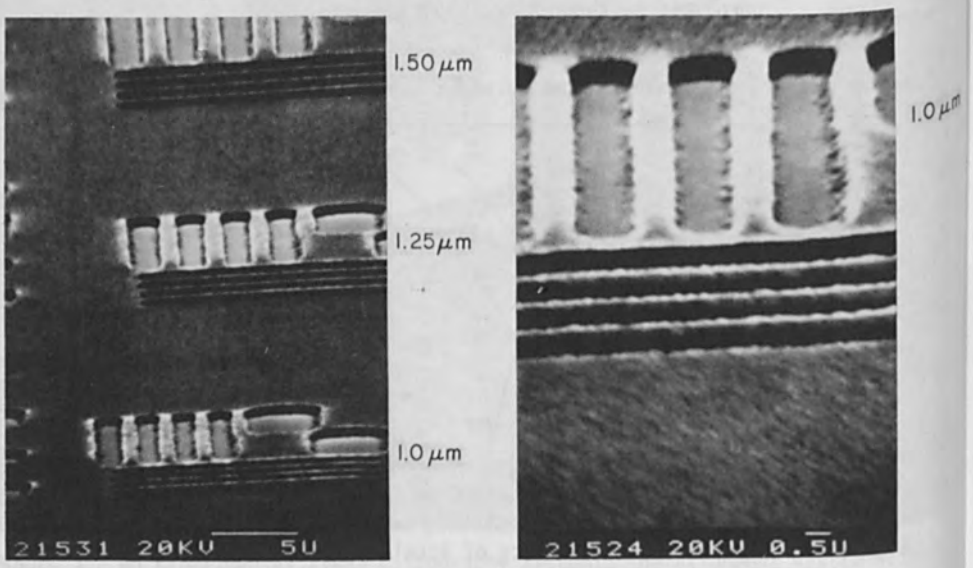

Figure 10. X-Ray Lithography in Eastman Kodak Experimental Resist EK88. The smallest features are 1 μm lines and spaces.

AN X-RAY LITHOGRAPHY ALIGNMENT SYSTEM

W.D. Buckley, M.P. Eisenberg, G.P. Hughes

D.H. Kittell and J.L. Kreuzer

The Perkin-Elmer Corporation
Norwalk, CT 06856

The design, operation and performance of an experimental alignment system which is suitable for use with an X-ray lithography exposure system will be described.

The system consists of optical, mechanical and electronic subsystems and permits alignment of either opaque or transparent masks by means of an optical alignment detection and transfer system. A computer assisted procedure permits mask to wafer overlay with a mean plus standard deviation of less than 0.5 μm. The alignment algorithm automatically compensates for linear magnification changes in the mask or wafer by varying the mask to wafer separation.

A data reduction scheme is described which identifies the major sources of misalignment and permits the analysis of wafer overlay data in terms of rigid body alignment errors in six degrees of freedom.

The component evaluation of the system along with the system data analysis indicate that a second generation system should have overlays of less than one third that of the prototype.

1. INTRODUCTION

In another publication (1) we have described an X-ray lithography exposure system capable of submicron lithography. In order to fully exploit this capability an alignment system with an overlay accuracy of one half to one third the minimum feature size is required. In addition the alignment system must be compatible with the overall lithography system and mask technology. A mask technology based on titanium membranes has been described (2). The use of this mask technology mandates that the aligner be capable of aligning optically opaque masks.

Since X-ray lithography is based on point source projection imaging, the gap between the mask and wafer results in a magnification of the mask pattern. The image on the wafer is enlarged by an amount $\Delta = Rd/D$ where d is the mask to wafer gap, R is the radial distance from the wafer center and D is the exposure distance. Consequently, in order to minimize magnification changes between consecutive exposures the mask to wafer separation must be controlled.

The cumulative overlay error of one level to another will be influenced by in plane wafer distortions. However, recent studies have shown that these changes manifest themselves principally as a linear change in wafer dimensions. Similar changes will result from thermal differences between exposures. Consequently, the magnification of an X-ray system can be used to advantage if the proximity gap can be fine-tuned to compensate these effects.

2. Alignment System

An alignment system based on optical detection and an optical alignment transfer standard can satisfy all of the requirements defined above.

The basis of the approach is illustrated in figure 1. The center of the wafer alignment target is located in space on the axis of an optical alignment channel by means of precise lateral and vertical alignment positioners. The wafer is then displaced a known distance, typically 50 μm, in order to provide the mask to wafer separation. Next the mask is inserted and the alignment procedure is repeated. Since the location of the wafer alignment target is retained in the transfer standard at the optical axis location, it is not necessary to view the wafer during mask alignment. Therefore either transparent or opaque masks can be aligned. In order to locate the mask parallel to the wafer, three alignment channels are used.

The overall alignment system consists of an optical detection system, a mechanical positioning system, a mensuration system and a computer assisted alignment algorithm.

The optical system detects both lateral and vertical position of the alignment target simultaneously by means of a combined interferometer objective. A point in space is thus defined along the optic axis which serves as an alignment transfer standard and permits the alignment of opaque masks.

Lateral alignment is accomplished by means of a microscope (NA = 0.60) and prism assembly. The prism assembly includes a beamspitter and the overall effect is to generate two images rotated 180° relative to each other. When the center of the

alignment target is not coincident with the axis of the optical system, a double image is seen. If the alignment target center is brought into coincidence with the optic axis, the two images coincide and a single image is seen as illustrated in figure 3. The subsequent insertion of an opaque mask prevents viewing of the wafer alignment target directly, however, mask-to-wafer alignment is then accomplished by aligning the mask to the viewing optics.

A white light interferometer is used to define the position of the alignment mark in the z direction, i.e., along the optic axis. The interferometer is operated in a null fringe mode in which a single interference fringe fills the entire viewing field. This interferometer yields a unique signature, characteristic of the surface being viewed when the two path lengths are nearly equal, and a minimum signal at the point of precise equality. The axial location of the alignment target can be determined to a small fraction of a micron.

In the experimental alignment system a Leitz 'Mirau' interference objective is used to implement the white light interferometer. In this device the beamsplitter and reference mirror are combined in an assembly that mounts directly on the objective. Consequently, the same optical channel can be used for both lateral and vertical alignment.

In order to evaluate the alignment scheme, a single-channel optical alignment system was established using conventional microscope components and interference objectives. Experimental repeatability tests were run for both alignment axes. The test involved performing the appropriate alignment, then displacing the stage an unknown amount and repeating the alignment without viewing the position sensor readout. The position of the stage after each alignment was recorded and the alignment procedure was repeated ten or more times. The mean and standard deviations were computed for each data set. This repeatability experiment was performed both on an X-ray mask and on ten substrates which were supplied by a commercial silicon device manufacturer and represented different stages of circuit fabrication. Each of the silicon devices was coated with 1.0 μm of photoresist in order to simulate a realistic alignment situation. The results are shown in Table 1. In all cases the precision of the system was 0.25 μm or better.

TABLE 1

SINGLE CHANNEL VISUAL ALIGNMENT REPEATABILITY

	Standard Deviation (μm)	
	z	x
A - X-Ray Mask	0.10	0.06
B - Resist-Coated Wafers		
1. Thick/Oxide/Metal*/Protective Overcoat	0.12	0.26
2. Thick Oxide/Multilevel*/Metal	0.18	0.24
3. Thick Oxide/Poly Si*/Metal	0.17	0.16
4. Gate Oxide*/Metal	0.14	0.18
5. Resist Oxide*/Multilevel	0.08	0.15
6. Gate Oxide/Poly Si*/Multilevel	0.12	0.12
7. Thick Oxide*/Multilevel	0.12	0.16
8. Thick Oxide*/Poly Si	0.18	0.08
9. Thick Oxide*/Gate Oxide	0.20	0.11
10. Thick Oxide/Poly Si*/Poly Si	0.13	0.10

* z target level

The mechanical positioning mechanism is capable of positioning the mask and wafer at the required point in space defined by the optical channel. It is necessary to control both mask and wafer in six degrees of freedom. The basic building block of the mechanical positioning system is the lever reduction machine. It consists of a differential screw mechanism in conjunction with a lever. The differential screw is loaded against the long

side of the lever, which is mounted to a base by two rotary flexures. Fine adjustment is obtained by directly turning the differential screw, whereas coarse adjustment is obtained by turning a knob threaded about the screw. The threads are selected so that one complete turn of the fine adjustment results in a 25 μm displacement at the short end of the lever. The total range is about 600 μm. The lever pivot flexure bearing was selected for its ability to pivot with minimal lost motion or stickslip effects. (The average backlash is less than 0.03 μm) At the short end of the lever is a push rod. This assembly is axially stiff but flexible in all other directions. It is designed to provide axial motion with minimal cross coupling to other directions.

A mensuration system is included in order to permit full characterization and control of the mask or wafer position. Each control axis has a corresponding position sensor. This is an eddy current, noncontacting proximity-position-detecting device, which exhibits good linearity over the design range of ± 300 μm. The combination of a lever reduction LR machine and gauge permits deliberate movements as small as 0.01 μm for each control axis.

The temporal stability of a single control axis was measured at a fixed knob setting by recording the gauge reading as a function of time. The results obtained are illustrated in Figure 4. The experiment was performed in a laboratory environment over a period of about 30 minutes. The results obtained represent cumulative drift due to mechanical and thermal effects as well as the stability of the gauge and gauge control and readout circuits. Approximately 26 minutes elapsed before the accumulated drift read 0.1 μm.

As a general conclusion, the mechanical positioning mechanism gauge combination exhibited excellent linearity, backlash, and temporal stability characteristics and has been used for all the mechanical motions required for alignment.

The alignment system was divided into an optical subsystem and a mechanical subsystem as shown schematically in Figure 5. The mechanical subsystem or cartridge mounts on top of the optical subsystem and is located by means of a ball bearing and groove arrangement.

The optical assembly contains the three optical channels required to provide the overall alignment capability. This assembly, referred to as the optical head, contains a total of six mechanical positioning mechanisms. Three are used to move the optical channels in order to locate the individual channels over their respective alignment targets. The other three change the position of the cartridge relative to the optical head by moving the mounting grooves in which the bearings rest.

The cartridge contains a fixed wafer stage and a mask stage. The mask stage is mounted on three vertical and three horizontal mechanical positioning mechanisms and is kinematically constrained. Auxiliary clamps are not required to maintain the position of the mask after alignment.

The alignment procedure requires that the optical head be first aligned to the wafer. Next, the cartridge is removed to permit installation of the mask, and the mask is then aligned to the optical channels. Since the alignment transfer standard is the axis of the optical channels, they are not disturbed after the first alignment. Subsequent alignments are by means of the mask stage position controls. Successful alignment requires accurate replacement of the cartridge after loading the mask. This can be done within an RMS error of less than 0.05 μm. Exposures are performed by placing the cartridge containing the mask and wafer over the exposure source.

Alignments are performed with computer assistance. The computer interrogates the gauges and aids the operator through the alignment procedure. The alignment algorithm compensates for mask to wafer scale differences and determines the appropriate mask to wafer separation. The system is designed so that all alignment steps consist of nulling a digital voltmeter readout. Figure 6 is a photograph of the complete alignment sytem.

3. Aligner Evaluation

The aligner evaluation was performed using oxidized silicon wafers and a titanium Xray mask. A double exposure technique was used. The wafer was first coated with COP resist and the aligner was used to set the masktowafer spacing and center the mask over the wafer. After exposure by means of the Xray source, the resist image was developed and the underlying oxide was etched. The resist was then stripped and the wafer was recoated. In subsequent experiments, the mask was aligned to the image defined in the oxide and then exposed. After development, the position of the resist image relative to oxide image was used to determine the overlay performance of the aligner.

Since the same mask was used for the overlay, the evaluation was independent of mask-to-mask distortions. In addition, since the wafer was not subject to high-temperature processing after the oxide etch, wafer distortions did not affect the results. In order to read the overlay errors a vernier mask pattern was used. Overlay was achieved by shifting the mask laterally 300 μm to produce an overlay image. The central vernier pattern had a resolution of 0.2 μm.

Figure 7 is an example of a double exposure overlay on a three inch wafer. The dots on the wafer represent the location on the wafer where the vernier patterns were read and the vectors represent (to the scale drawn) the magnitude and direction of the measured misalignment. In this example, the mask was misaligned toward the lower left, however, the displacement vectors lie on diameters with a common center to within the measuring accuracy. This is an indication that the mask is undistorted and stable. Figure 8 summarizes the results for 8 wafers. The data point represent the heads of all of the displacement vectors. The boxes are ± 1.0 μm misalignment limits.

The alignment precision can be estimated from figure 9 which is a histogram of the overlay errors at 17 data points on each of nine wafers. The curve illustrates the percentage of data points within a particular overlay error.

Both the histogram and the curve indicate that the alignment accuracy has a standard deviation of about 0.5 μm. In these experiments no attempt was made to control the temperature or to vary the mask to wafer gap to compensate for scale changes.

4. Alignment Error Analysis

X-ray lithography alignment consist of aligning a mask to a wafer each of which has six degrees of freedom. Assuming the mask and wafer are rigid bodies, errors in alignment can be represented by a set of rigid body alignment error terms as shown in figure 10. These errors include translational errors (εX, εY), mask to wafer spacing error (εZ), in plane rotational errors ($\varepsilon\theta_z$), and mask to wafer tilt ($\varepsilon\theta_x$, $\varepsilon\theta_y$). The rigid body errors act in combination to produce overlay errors (ΔX, ΔY) on the wafer. In order to relate the rigid body errors to the displacement errors the coordinate system of figure 11 has been adopted. At any coordinate (X,Y) the total displacement error on the wafer due to the rigid body error terms is given by:

$$\Delta X = \varepsilon X + \left(\frac{X}{D}\right)\varepsilon Z + \left(\frac{X\,Y}{D}\right)\varepsilon\theta_x + \left(\frac{X^2}{D}\right)\varepsilon\theta_y - \left(Y\right)\varepsilon\theta_z \qquad (1)$$

and

$$\Delta Y = \varepsilon Y + \left(\frac{Y}{D}\right)\varepsilon Z + \left(\frac{X\,Y}{D}\right)\varepsilon\theta_y + \left(\frac{Y^2}{D}\right)\varepsilon\theta_x + \left(X\right)\varepsilon\theta_z \qquad (2)$$

Using these equations and the overlay displacement errors a best fit set of rigid body terms can be computed for each overlay wafer. Figure 12 represents the result of subtracting the

vectors determined by the best fit overlay data from the measured overlay error vectors. The standard deviation of the X and Y components of these residuals is ± 0.1 μm which is the reading error of the vernier targets. Thus the alignment errors as shown in figure 7 can be represented, within our measuring accuracy, by the rigid body error terms implying that there is no measurable wafer or mask distortion.

Another measure of the alignment performance can represented by Table 2 which details the mean and standard deviation of the rigid body error for the wafer overlays in figure 8.

TABLE 2

ALIGNMENT PERFORMANCE OF NINE WAFERS

	Rigid Body Error Terms		Calculated Error on Wafer at 1.5" Radius	
	Mean	S.D.	Mean	S.D.
Translation				
εX (μm)	-0.17	0.37	-0.17	0.37
εY (μm)	0.03	0.53	0.03	0.53[a]
εZ (μm)	-1.08	4.8	-0.12	
Rotational				
θx (arc-sec)	0.74	8.6	0.01	0.15
θy (arc-sec)	3.45	12.0	0.06	0.21
θz (arc-sec)	0.55	1.6	0.08	0.26

[a] Includes temperature variation contribution

The effect of these rigid body terms on the edge of a 3" wafer is also included. Note that the mean values are all small and thus represent no systematic alignment error. The standard deviation is consistent with the histogram of figure 9. The standard deviation of the axial alignment term (εz) is a major contributor to the overall alignment error. This result is not surprising since this data was obtained without correcting for magnification changes which result from the poorly controlled thermal environment. The use of the linear scale change capability should significantly reduce this term.

5. Conclusion

The basic concept, approach and elements of an optical alignment system suitable for Xray lithography have been described. An experimental alignment system has demonstrated overlay performance with a standard deviation of less than 0.5 μm, using optically opaque Xray masks and 3 inch silicon wafers. This performance is limited by the aligner and not by mask or wafer stability. Readily implemented improvements including a temperature controlled environment, high resolution viewing optics and linear magnfication change compensation should result in an overlay standard deviation of better than 1/8 μm.

REFERENCES

1. W.D. Buckley, G.P. Hughes, "An X-Ray Lithography System", 157th Meeting of ICS, St. Louis, Mo. 1980.

2. W.D. Buckley, J.F. Nester, H. Windischmann, "X-Ray Lithography Mask Technology" 157th Meeting of ECS, St. Louis, Mo. 1980.

3. Nan-Hsinng Tsai, Carl N. Alquist, "Characterization of In-Plane Wafer Distortion in NMOS Process". Semiconductor Microlithography, V, San Jose, California (1980)

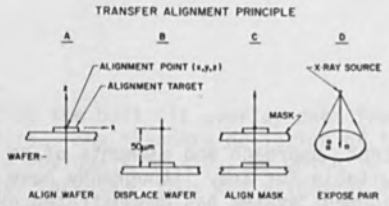

Figure 1. Simplified single-channel alignment procedure. Three channels are needed to set the mask and wafer parallel as shown on the right.

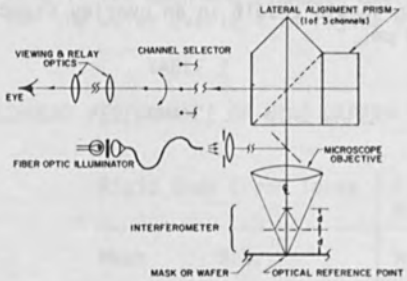

Figure 2. Mask-on-wafer aligner optical schematic. It uses an image shearing prism to define the optical axis for both mask and wafer levels along with an interferometer to define the vertical plane of the alignment.

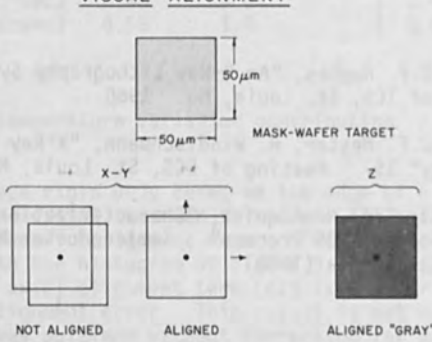

Figure 3. An Alignment Target as seen through an optical channel. The left hand side illlustrates lateral alignment relative to the optic axis indicated by the dot. The right hand target illustrates the axial alignment signal. Correct positioning along the optic axis is achieved when a minimum brightness fringe is observed.

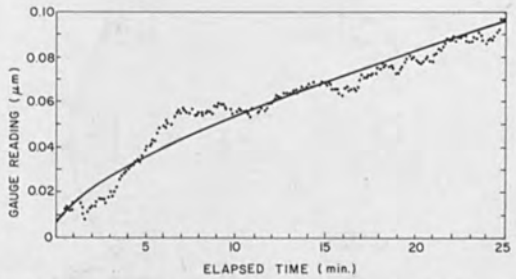

Figure 4. Temporal stability of the positioning mechanism as measured by an eddy current sensor. The drift is representative of the entire system including the gauges and thermal effects.

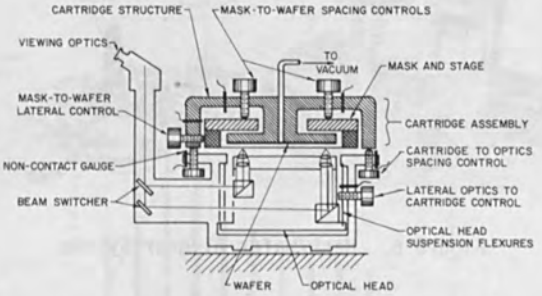

Figure 5. Schematic diagram of the alignment cartridge. Mask and wafer are aligned separately to three optical channels (two of which are shown). In order to expose, the cartridge is removed together with the mask and wafer, and placed over the exposure source.

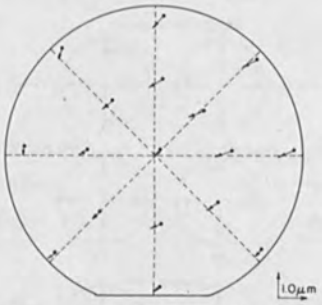

Figure 7. Overlay Performance using Titanium Mask. The arrows represent (to scale) the displacement vector at each location. The dashed lines are diameters with a commong center. All the vectors lie in the lines indicating that the mask is stable. i.e. behaving as a rigid body.

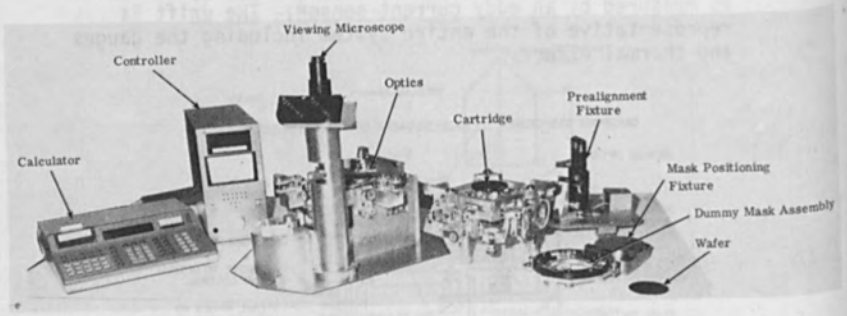

Figure 6. Mask/Wafer Aligner System

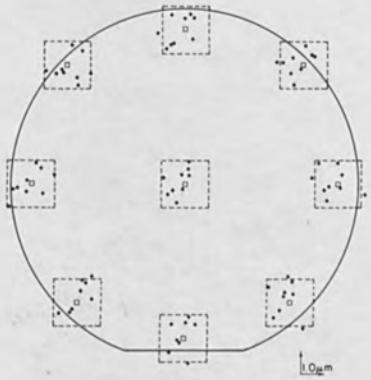

Figure 8. Composite of Double Exposure Overlays for 9 wafers. The dots represent a single wafer. The boxes are consistent with an alignment error with a standard deviation of less than 0.5 μm.

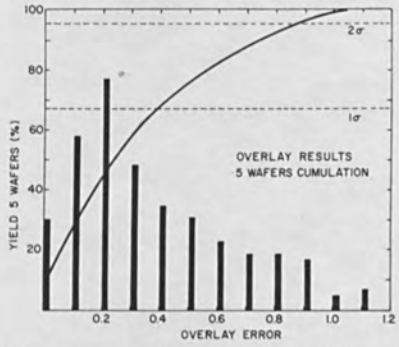

Figure 9. Histogram of the alignment data. Alignment has been achieved with a 0.5 μm standard deviation in a non-temperature-controlled environment.

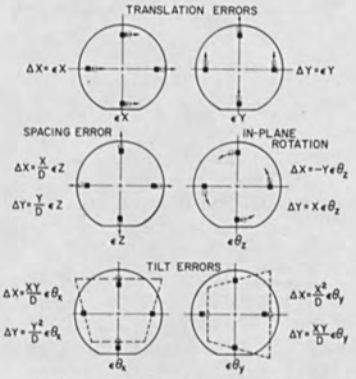

Figure 10. Rigid body misalignment errors. These terms are used to evaluate aligner performance.

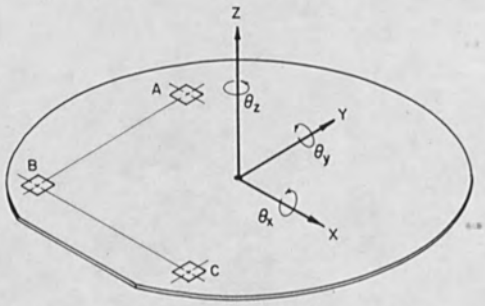

Figure 11. The co-ordinate system used for overlay data reduction. Alignments are made by an optical channel located at each of point A, B and C.

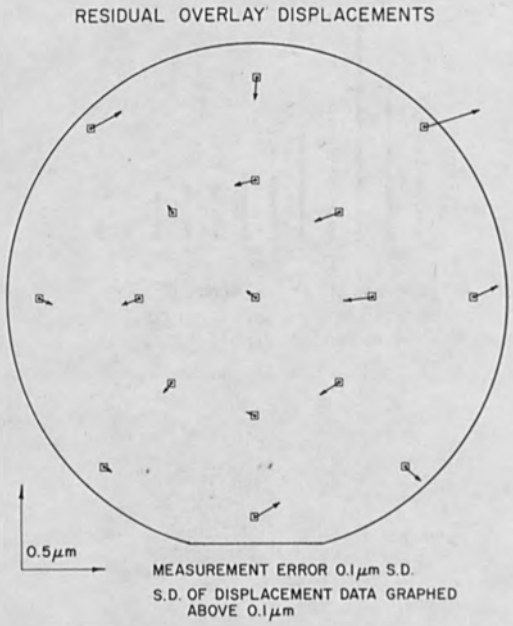

Figure 12. Residual misalignment vectors for one wafer after rigid body error compensation. These residuals have the same standard deviation as the measuring error indicating that their is no measurable mask instability.

PERFORMANCE OF Si-Kα X-RAY LITHOGRAPHY

Hideo Yoshihara, Seitaro Matsuo, and Toshiro Ono
Musashino Electrical Communication Laboratory
Nippon Telegraph and Telephone Public Corporation
Musashino-shi, Tokyo, 180, Japan

ABSTRACT

In x-ray lithography, shortening of exposure time is an important problem. In order to solve this problem, development of high power x-ray source and high contrast x-ray mask, utilization of high sensitivity resists, and new dry etching for the resists were investigated. X-ray Si target as high power x-ray source was prepared by plasma deposition process, and high contrast x-ray mask suitable to Si-Kα x-ray was developed by double lift-off method. For utilizing high sensitivity and resolution resists, new plasma reactive sputter etching with wafer cooling method was developed. Consequently, the exposure time with Si-Kα x-ray could be reduced by about one-third of that with Al-Kα x-ray. Submicron pattern can be replicated on thicker than 8000 Å. Particularly, new dry etching was applied to form poly-Si gates and PSG contact holes. Furthermore, all these technologies were examined by the fabrication of MOS devices synthetically. In MOS device characteristics, sufficient results were obtained.

INTRODUCTION

X-ray lithography, proposed by Smith (1), can be replicated submicron patterns, because it uses shorter wavelength than that of ultraviolet light. X-ray lithography has been investigated by many workers (2-5), and has been applied to device production in the laboratory. From the results of these investigations, it is confirmed that x-ray lithography is a very promising method for fine pattern replication because of its high resolution, applicability to thick resist layer and so on.

However, in order to put x-ray lithography into practical use, many problems must be solved. For example, development of high accuracy alignment of mask and wafer, shortening of exposure time, and establishment of an efficient x-ray mask fabrication process are necessary. The development of exposure system with high accuracy alignment apparatus has been reported by Yamazaki (6). Furthermore, in device fabrication process, many problems must be solved. For example,wafer distortion must be reduced to the required accuracy of alignment of mask and wafer. Heat durability of high sensitivity resists must be improved. Etching process which enables the use of heat feeble high sensitivity resists must be developed.

Particularly, in x-ray lithography, shortening of exposure time is an important problem. In this paper, development of high power x-ray source, utilization of high sensitivity resists, and development of dry etching suitable to the resists were investigated in order to solve this problem. Concretely, the following factors were investigated : 1) Preparation of x-ray Si target for realization of high power x-ray source. 2) Preparation of high contrast x-ray mask suitable for Si-Kα x-ray. 3) Development of new plasma reactive sputter etching process for utilizing high sensitivity and resolution resists.

X-RAY SILICON TARGET

Si target has the following advantages shortening exposure time. Si-Kα x-ray has high transparency to Si compound mask substrates. The electron beam input power for generating Si-Kα x-ray can be kept high, because Si has a high melting point. However, conventional Si deposition method makes it difficult to use Si target in practice, because of low evaporation rate.

Figure 1 shows the external appearence of the rotary x-ray Si target alone and mounted on a rotator. As shown in Fig.1, the target is cylindrical, 95 mm in diameter and 35 mm in length. Cu substrate is used because of its good heat conductivity. The alloying reaction between Cu and Si occurs at temperatures lower than 802 °C due to the inter-diffusion of Cu-Si. To prevent this reaction, a Mo layer was provided between the Cu substrate and the Si layer. Mo layer adhesion to Cu substrate and Si layer adhesion to Mo layer must be excellent, compared with adhesion in conventional methods (e.g. vacuum evaporation, sputtering). Furthermore, high throwing power in deposition is required, because Mo and Si must be deposited on the outside of the cylindrical substrate. Figure 2 shows the deposition apparatus used. The vacuum chamber is divided into a low-pressure region and a high-pressure region by a pressure control valve. The low-pressure region is connected to an evacuation system. In the high-pressure region, the substrate holder is connected to a DC power supply, and the coil for generating plasma is connected to an RF power supply (13.56 MHz). Two variable leak valves for supplying Ar and SiH_4 are attached. Mo layer was deposited by conventional RF ion plating. Sequentially, Si film was deposited by plasma deposition process (7), in which Si was supplied by SiH_4. These processes ensure good adhesion and high throwing power. It was found that Mo film thicker than 2000 Å was necessary to prevent Cu-Si inter-diffusion.

The x-ray Si target as a high power x-ray source was mounted on an x-ray lithographic system. The target was water-cooled and operated at 6000 rpm. Figure 3 shows the x-ray characteristics of Si target, in which the thickness of Si layer is about 2 μm. When electron beam input power is about 20 kW (i.e. 20 kV, 1A),

strong Si-K line and weak Mo-L line can be observed. Therefore, Si layer than 3 μm must be deposited to prevent Mo-L line generation from the Si/Mo/Cu target. Figure 4 shows the superiority of Si/Mo/Cu target, compared with Si/Cu and Al/Cu targets. In the three-layer target, x-ray intensity increases linearly with electron beam input power, and can be kept stable for a long time. In the two-layer targets, alloying reactions bigin to occur at 10-15 kW, and x-ray intensities decrease above 10-15 kW with increasing electron beam input power.

X-RAY MASK

An x-ray mask suitable to Si-Kα x-ray was developed. X-ray mask substrate requires the following conditions : 1) High transparency to Si-Kα x-ray. 2) Sufficient strength for practical use. 3) High transparency to visible light for mask alignment convenience. X-ray mask substrate consists of a three layer $Si_3N_4/SiO_2/Si_3N_4$ membrane(8). $Si_3N_4$and SiO_2 films were prepared by CVD and sputtering respectively. The stress in Si_3N_4 film is tensile, and the stress in SiO_2 is compressive. In the three-layer x-ray mask substrate, a large size window, 6-8 mm square, can be fabricated by the control of thickness ratio of each film, so as to balance tensile and compressive stresses.

Au was chosen as an absorption material. The Au thickness of 1 μm is necessary to gain 15 dB in mask contrast. The minimum line width of Au pattern is less than 1 μm, and therefore the aspect ratio is larger than 1.

The preparation of such Au pattern was realized by double lift-off method. Figure 5 shows the procedure of double lift-off method. The procedure is as follows : 1) Ti and Au thin films were deposited on a three-layer $Si_3N_4/SiO_2/Si_3N_4$ membrane by vacuum evaporation in sequence. 2) Polyimide and resist were coated by spinner in sequence. 3) Fine resist pattern on polyimde was formed by EB lithography. 4) Ti thin film was deposited on fine resist pattern, and then Ti lift-off process followed. 5) After Ti lift-off process, polyimide was etched by reactive sputter etching with O_2 without undercutting. 6) Au pattern was formed by electroplating, and polyimide was removed. 7) Finally, Au and Ti films on the membrane were removed by plasma etching. Double lift-off method has an advantage in fine pattern formation with EB lithography. Figure 6 shows electron backscattering effect of underlying substances, when fine resist patterns are formed by EB lithography. The minimum line width of resist pattern on 2 μm thick polyimide film is about 0.5 μm, and that on 8000 Å thick Au/Ti film is about 1 μm. Furthermore, resist patterns finer than 1 μm can be easily written on 2 μm thick polyimide film by EB lithography, because pattern width is relatively insensitive to electron dose due to a small quantity of electrons backscattered. On the other hand, on 8000 Å thick Au/Ti films, resist

patterns finer than 1 μm can not be easily written, due to a large quantity of electrons backscattered from Au/Ti films. These effects are caused by the difference of electron backscattering from underlying substances such as Au/Ti and polyimide. Therefore, fine Au pattern can be easily obtained by double lift-off method. Figure 7 shows an SEM photograph of a cross-section of Au pattern on x-ray mask. The line width of the pattern is 1 μm, and the thickness is 1.2 μm. The sidewalls of Au pattern are almost perpendicular.

PLASMA REACTIVE SPUTTER ETCHING

In plasma reactive sputter etching, selective etching of SiO_2 and Si_3N_4 on Si, and poly-Si on SiO_2 can be realized with C_2F_6 and $CBrF_3$ gases, respectively (9,10). Figure 8 shows the relation between C_2F_6 gas pressure and etching rate of various materials. The SiO_2 etching rate is about 5 times larger than that of Si, and the Si_3N_4 etching rate is about 10 times larger than that of Si. Furthermore, the selectivity of SiO_2 relative to Si can be improved to be larger than 10 by mixing ethylene into C_2F_6 gas. Several kinds of SiO_2 show almost no difference in etching rate, regardless of their growth condition or phosphorous doping. Similarly, single crystal Si and poly-Si have almost the same etching rates. Figure 9 shows the relation between $CBrF_3$ gas pressure and etching rate of various materials. The Si and Mo etching rates are about 6 times larger than that of SiO_2. That is, the opposite condition mentioned in Fig.8 is realized. Moreover, photoresist AZ1350J and Si_3N_4 have intermediate etching rate. In selective etching of Si on SiO_2 by conventional plasma etching with CF_4 gas, undercutting phenomena always appear, but in plasma reactive sputter etching with $CBrF_3$ gas, undercutting phenomena do not appear at all. Pattern transfers from mask to underlying substance can be performed uniformly without undercutting for selective etchings, with higher accuracy than in conventional plasma and sputter etching. Etching reactions in these processes are caused by energetic ions (CF_n^+ etc.), and that in conventional plasma etching is caused by free radical (fluorine atom), respectively. In principle, the etching mechanism of plasma reactive sputter etching differs from that of conventional plasma etching.

In dry etching, generally, high sensitivity and resolution resists easily suffer thermal deterioration, because they have low softening temperature. In order to keep the surface temperature of Si wafer low, a new plasma reactive sputter etching method was developed. Figure 10 shows schematic diagram of new plasma reactive sputter etching with wafer cooling method. The wafer was thermal-contacted to a water-cooled electrode by electrostatic force between wafer and electrode DC potentials. Figure 11 shows surface temperature rise of specimens during etching, when the wafer cooling method was adopted, in comparison with conventional method. In conventional method, the temperature of specimens rises for instance to 100-180 °C

after several minutes. On the other hand, in new plasma reactive sputter etching, the Si wafer temperature is lower than 60 °C. Furthermore, etching characteristics are independent of wafer temperature and electrode DC potential supply.

FABRICATION PROCESS

The exposure time of Si target could be reduced by about one-third, in comparison with that of Al target. Figure 12 shows an SEM photograph of FBM resist (11) pattern replicated by Si-Kα x-ray exposure. Resist pattern ranging from 1.5 μm to 1 μm can be easily obtained, even though the thickness of positive and negative resist patterns is above 0.8 μm. Figure 13 shows the SEM photograph of resist pattern after the replication of poly-Si gate pattern on SiO_2. As shown in Fig.13, the quality of replication resist patterns hardly deteriorates on steps in devices. After the replication, PSG thicker than 6000 Å and poly-Si thicker than 3000 Å were etched by new plasma reactive sputter etching with high sensitivity and resolution resists as the etching mask. For example, in etching PSG film thicker than 6000 Å, FBM resist does not suffer any thermal deterioration. Figure 14 a and b shows the SEM photographs of PSG contact hole pattern and poly-Si gate pattern on SiO_2 made by new plasma reactive sputter etching respectively. Resist patterns are transferred to PSG and poly-Si with high accuracy.

The advantages of these technologies were examined by the fabrication of MOS devices (12). That is, MOS transistor matrix and MOS ring oscillator were fabricated. These were operated stably. The dispersion of the threshold voltages in MOS transistors were very small.

CONCLUSION

The exposure time with Si-Kα x-ray could be reduced by about one-third of that with Al-Kα x-ray. Using high contrast x-ray mask, submicron pattern can be replicated on resists than 8000 Å. These technologies were adopted in MOS device fabrication process. Particularly, new dry etching was applied to form poly-Si gates and PSG contact holes. In MOS device characteristics, sufficient results were obtained.

ACKNOWLEDGMENT

The authors wish to thank J.Matsui and K.Suzuki of NEC Ltd. for device fabrication and S.Yamazaki, S.Nakayama and R.Kaneoya for useful discussions and encouragements.

REFERENCES

1. D.L.Spears and H.I.Smith, Electro. Lett., vol. 8, 102 (1972)
2. S.E.Bernacki and H.I.Smith, IEEE Trans. E. D., vol. ED-22, 421 (1975)
3. P.A.Sullivan and J.H.McCoy, ibid, vol. ED-23, 412 (1976)
4. D.Maydan, G.A.Coquin, J.R.Maldonado, S.Somekh, D.Y.Lou and G.N.Taylor, ibid, vol. ED-22, 429 (1975)
5. R.Feder, E.Spiller and J.Topalian, J. Vac. Sci. Technol., vol. 12, 1332 (1975)
6. S.Yamazaki, S.Nakayama, T.Hayasaka and S.Ishihara, ibid, vol.15, 987 (1978)
7. H.Yoshihara, H.Mori and M.Kiuchi, Jpn. J. Appl. Phys., vol. 16, 2047 (1977)
8. K.Suzuki, J.Matsui, T.Kadota and T.Ono, ibid, vol. 17, 1447 (1978)
9. S.Matsuo,ibid, vol. 17, 235 (1978)
10. S.Matsuo, Appl. Lett., vol. 35, No. 5 (1980) (To be published)
11. K.Murase, M.Kakuchi and S.Sugawara, Internl. Conf. on microlithography, Paris, 1977, p. 261.
12. K.Suzuki, J.Matsui, Y.Saito and S.Matsuo : Abstract of the 27th Spring Meeting of the Japan Society of Applied Physics, 1980, p. 4p-N-10

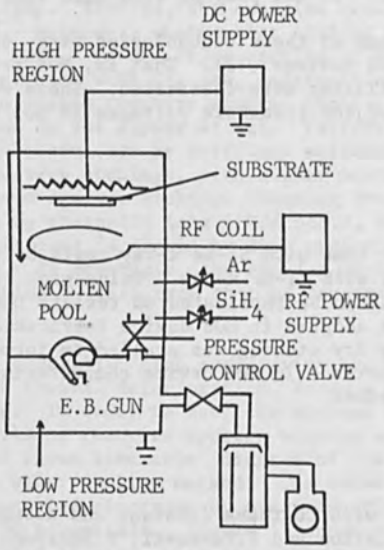

Fig.2. Deposition apparatus

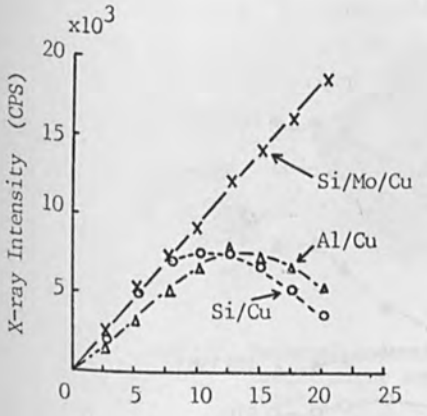

Fig.4. X-ray output characteristics for respective targets.

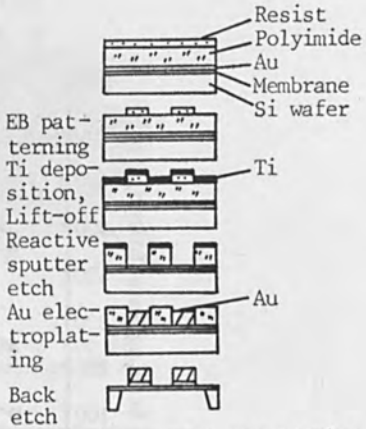

Fig.5. X-ray mask preparation process.

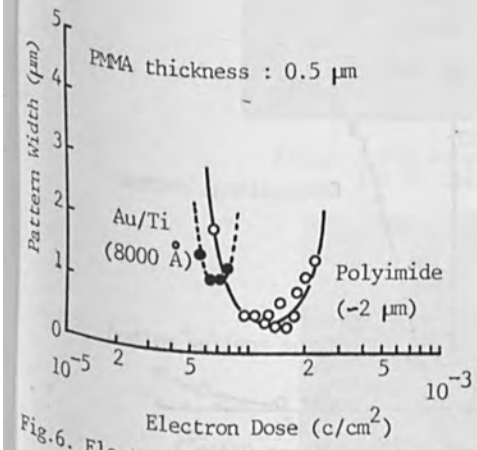

Fig.6. Electron backscattering effect of underlying substances in fine pattern formation with EB lithography

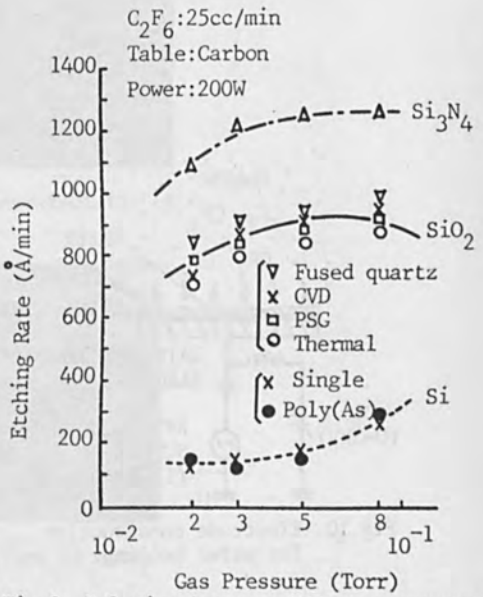

Fig.8. Relation between C_2F_6 gas pressure and etching rate of varios materials.

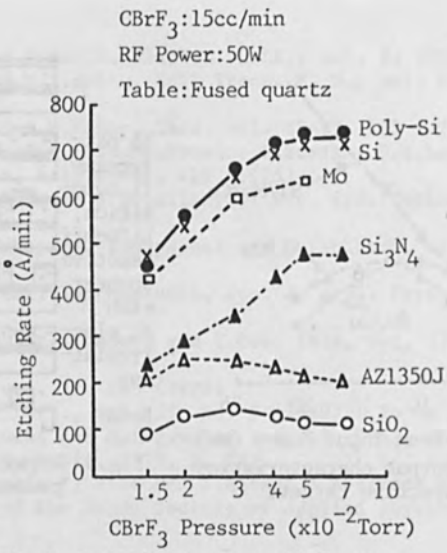

Fig.9. Relation between $CBrF_3$ gas pressure and etching rate of various materials.

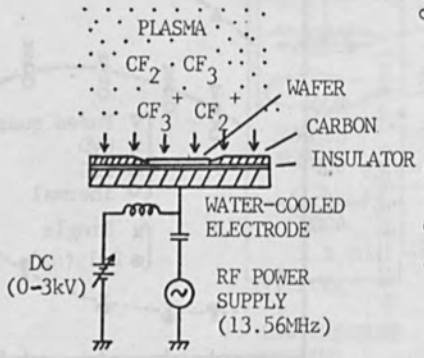

Fig.10. Electrode construction for wafer cooling.

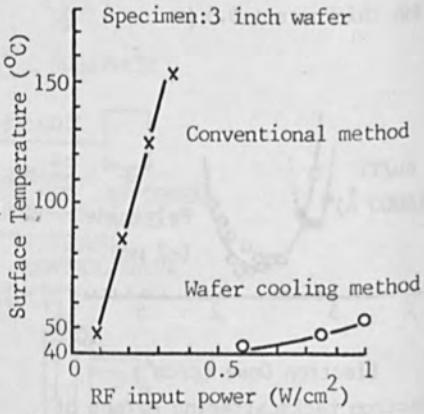

Fig.11. Effectiveness of wafer cooling method.

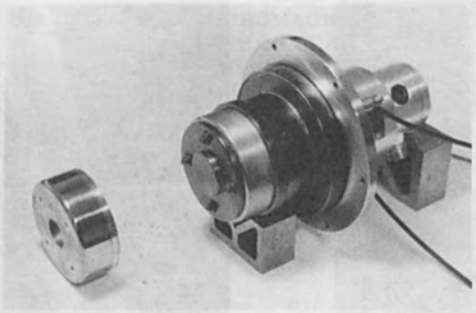

Fig.1. External appearence of the Si target alone and mounted on a rotator.

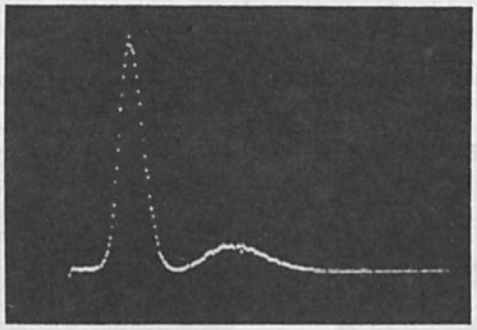

Fig.3. X-ray output characteristic of the Si target.

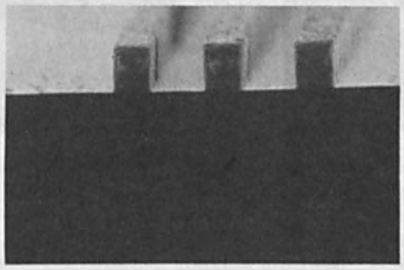

Fig.7. Cross-section view of x-ray mask.

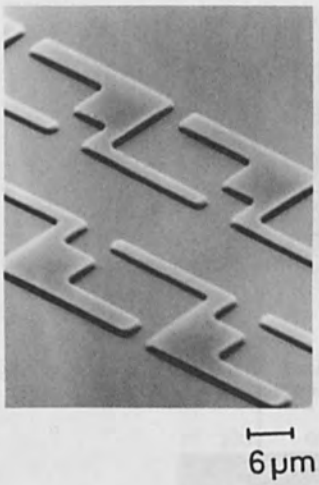

Fig.12. FBM resist pattern.

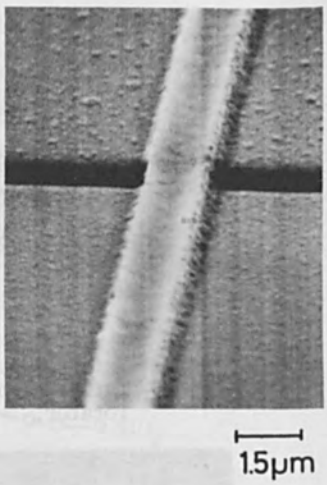

Fig.13. Resist pattern after the replication of poly-Si gate.

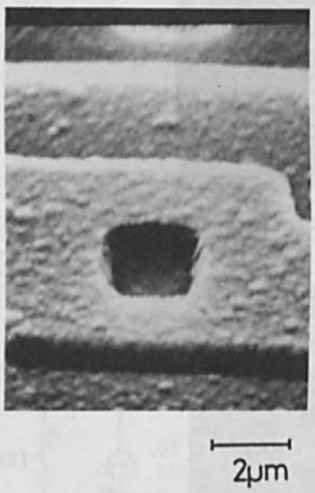

(a) PSG contact hole

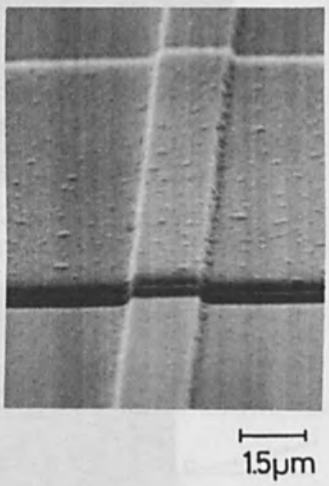

(b) Poly-Si gate

Fig.14. Etching patterns of PSG contact hole and poly-Si gate.

A RIGOROUS ELECTROMAGNETIC THEORY FOR THE USE OF GRATINGS FOR OVERLAY AND SPATIAL PERIOD DIVISION IN X-RAY LITHOGRAPHY

Dieter P. Kern and David A. Nelson, Jr.

IBM Thomas J. Watson Research Center
Yorktown Heights, New York 10598

ABSTRACT

There has been a continuing interest in the possible use of a pair of gratings in series as alignment marks for x-ray lithography. A semi-analytical theory for diffraction of electromagnetic radiation from infinitely conductive gratings with rectangular grooves, presented by Maystre and Petit, has been applied here to the x-ray alignment configuration in which a transmission grating and a reflection grating are in series. It is found that although strong alignment signals can be obtained with properly designed gratings, their construction and application is not as simple as often assumed. This theory has also been applied to the near field diffraction of carbon K_α x-rays by transmission gratings to simulate the effect called spatial period division by Flanders, Hawryluk, and Smith.

I. INTRODUCTION

In 1978, Austin, Smith, and Flanders demonstrated that gratings could be used as alignment marks for x-ray lithography (1). Figure 1 illustrates this technique in which a laser beam is diffracted from a grating on the mask, then from a grating on the wafer underneath the mask, and once again from the grating on the mask. When the gratings on the mask and on the wafer are in phase with each other (zero relative displacement), the intensity diffracted in a plus order will be equal to that diffracted into the corresponding minus order. When the two gratings are out of phase (non-zero relative displacement), the intensity diffracted into one order is greater than that in the other. Thus, the difference of the signals from two photo diodes collecting these opposite orders can be used to align the pattern on a mask to the pattern on a wafer.

Theoretical investigations of such alignment schemes using either a Fresnel or a Fourier approximation are inadequate, since the grating structures and the distance between the gratings are typically of the same order of magnitude as the wavelength of the laser radiation used. In addition, the finite depth of the grooves further complicates the application of Kirchhoff's formula. A semi-analytical theory for diffraction of electromagnetic radiation from infinitely conductive gratings with rectangular grooves has been presented by Maystre and Petit (2). This theory has been extensively used by Loewen, Neviere and Maystre (3) to investigate the efficiency of various reflection

gratings. In this paper, it will be applied to the grating alignment technique in order to determine the optimum grating architecture as well as the constraints on the technique. Here optimum means that the difference signal from the grating system is maximized and its sensitivity to changes in parameters characterizing the system is minimized.

This theory can also be applied to the near field diffraction of carbon K_α x-rays by transmission gratings. At well defined locations close to the grating periodic intensity modulations in the wave field occur. The periodicity is an integer multiple of that of the original grating. If a resist sensitive to these x-rays is placed at the proper location, a grating with a period which is some integral fraction of the original can be produced. This is the phenomenon called spatial period division by Flanders, Hawryluk, and Smith (4).

II. GRATING ALIGNMENT THEORY

The basis of the theory is to divide the area in which the wave equation must be solved into distinct regions and to solve the boundary value problem for each region separately. Figure 2 illustrates the four regions of interest for the grating alignment scheme, using gratings with period d, gaps of width c_1 and depth h_1 at the mask, grooves of width c_2 and depth h_2 on the wafer, and a mask to wafer separation of S. For an incident plane wave (*wavelength* = λ) with the electric field parallel to the direction of the grating grooves and assuming infinitely conductive grating lines, the wave field in each region can be represented by the following expansions:

$$E_I(x,y) = e^{ik_x x - ik_y y} + \sum_{n=-\infty}^{\infty} A_n e^{i\gamma_n x + i\chi_n y} \tag{1}$$

$$E_{II} = \begin{cases} \sum_{n=1}^{\infty} [a_n \cos(\mu_n y) + b_n \sin(\mu_n y)] \sin(npx) & ; 0 \le x \le c_1 \\ 0 & ; c_1 \le x \le d \end{cases} \tag{2}$$

$$E_{III} = \sum_{n=-\infty}^{\infty} \left[B_n e^{i\chi_n (y-y_2)} + C_n e^{-i\chi_n (y-y_1)}\right] e^{i\gamma_n x} \tag{3}$$

$$E_{IV} = \begin{cases} \sum_{n=1}^{\infty} c_n \sin[\nu_n (y-y_3)] \sin[nq(x-\delta)] & ; 0 \le x-\delta \le c_2 \\ 0 & ; c_2 \le x-\delta \le d \end{cases} \tag{4}$$

where:

$$k = \frac{2\pi}{\lambda};\ k_x = k \sin\theta;\ k_y = k \cos\theta;$$
$$K = \frac{2\pi}{d};\ \gamma_n = k_x + nK;\ \chi_n = \sqrt{k^2 - \gamma_n^2};$$
$$p = \frac{\pi}{c_1};\ \mu_n = \sqrt{k^2 - n^2p^2};\ q = \frac{\pi}{c_2};\ \nu_n = \sqrt{k^2 - n^2q^2}; \qquad (5)$$
$$y_1 = -\frac{h_1}{2};\ y_2 = y_1 - S;\ y_3 = y_2 - h_2$$

It should be mentioned here, that for $\gamma_n^2 > k^2$, $np > k$, $nq > k$; χ_n , μ_n , and ν_n become imaginary so that solutions with exponential behavior in y are included.

The coefficients for these four expansions, which represent the wave field in the four regions, are determined from the sets of linear equations which are obtained when the transition conditions at interfaces between adjacent regions are applied. Here the following transition conditions were used:

1) $E_I = E_{II}$ at the interface of region I and region II with similar conditions on the other region interfaces (continuity of the field)
2) $\partial E_I / \partial n = \partial E_{II} / \partial n$ at the interface of region I and region II with similar conditions on the other region interfaces. (continuity of the normal derivative)

The full derivation of the solution for the grating alignment scheme will not be discussed here as it is quite complex, rather lengthy, and will be presented elsewhere. Basically the infinite expansions are converted into finite sums with a sufficient number of terms to satisfy the boundary conditions, including solutions with exponential behaviour. The computational problem is then reduced to the solution of a set of linear matrix equations which has a unique solution for a given set of grating parameters. Efficient computer programs, based on complex matrix manipulation, have been developed for this particular solution as well as for the solutions for individual transmission and reflection gratings.

III. GRATING ALIGNMENT SIMULATION

The number of parameters that can be varied in the grating alignment system (*ie.* d, c_1, c_2, h_1, h_2, and S) and the complex dependence of the alignment signal on these parameters complicate the intended optimization process, even with computers at one's disposal. However, if some of the parameters are constrained by other considerations, such as a desired working distance (S) and a desired mask thickness (h_1), conditions can be found which yield a significantly enhanced alignment signal compared to the set of parameters with which we started and which initially appeared reasonable. This will be illustrated for the case of a grating alignment system with $d = 1\ \mu m$, $.4\ \mu m < h_1 < .6\ \mu m$, and $S \sim 10\ \mu m$ and using a He-Ne laser ($\lambda = 0.6328 \mu m$).

During the optimization cycle, the variation in the intensity difference signal (see Figure 1) as a function of each grating parameter is calculated, holding all other parameters constant. The results of these calculations for an initial design ($d = 1\ \mu m$, $S = 10\ \mu m$, $c_1 = c_2 = .5\ \mu m$, and $h_1 = h_2 = .5\ \mu m$) are shown in Figure 3. Figure 4 has a similar set of plots for the final design ($d = 1\ \mu m$, $S = 10\ \mu m$, $c_1 = c_2 = .66\ \mu m$, $h_1 = .44\ \mu m$, and $h_2 = .5\ \mu m$). This result was obtained after several design cycles because the effects of all the parameters defining the grating architecture are interdependent. It also included an attempt to maintain reasonable process windows and to comply with realistic limits for resultant architecture (e.g. $c_1 = .9\ \mu m$ would be unrealizable). At this juncture, the difference signal for this grating system was calculated as a function of mask-wafer separation. It is apparent from the plot in Figure 5 that for this design an operating distance of $S = 9.85 \pm .12\ \mu m$ would be the most advantageous in the vicinity of $S = 10.0\ \mu m$, the bounds being chosen to prevent a phase flip in the difference signal. As a final test, the intensity difference vs. grating displacement was calculated for the initial and final design (Figure 6). This particular grating system design shows a signal improvement of $\sim 10^3$ over the initial design. The results also clearly reveal the high sensitivity of the signal strength with respect to small changes in the architecture. For a reasonable signal, the parameters c_1, h_1, and h_2 have to be defined within about $.1\mu m$. In order to avoid a phase flip in the alignment signal mask-wafer separation has to be maintained within $\pm .1\ \mu m$. These constraints indicate that it would be very difficult to use the grating technique for alignment.

IV. SPATIAL PERIOD DIVISION THEORY

The wave transmitted through a grating like that on the mask in Figure 2 can be represented by

$$E(x,y) = \sum_{n=-N}^{N} C_n e^{-i\chi_n y} e^{i\gamma_n x} , \tag{6}$$

as in Equation (3) of Section II and with the definitions of Equation (5) in effect. N is a number large enough to describe the diffraction problem with sufficient accuracy. The intensity is then given by

$$\begin{aligned} I(x,y) &= E(x,y)\ E^*(x,y) \\ &= \sum_{m=-N}^{N} \sum_{n=-N}^{N} C_n\ C_m^*\ e^{i(\chi_m-\chi_n)y}\ e^{i(\gamma_n-\gamma_m)x} \end{aligned} \tag{7}$$

Now, recognizing that $\gamma_n - \gamma_m = (n-m)K$, we can rearrange the summations in Equation (7) with $l = n-m$ and obtain:

$$I(x,y) = \sum_{l=-2N}^{2N} F_l(y)\ e^{ilKx} \tag{8}$$

where:

$$F_l(y) = \sum_{n=l-N}^{N} C_n \, C^*_{n-l} \, e^{i(\chi_{n-l} - \chi_n)y} \; ; \; l = 0,1,\ldots,2N \tag{9}$$

and

$$F_l(y) = F^*_{-l}(y) \; ; -2N \leq l \leq -1 \; . \tag{10}$$

Further rearrangements, with $F_l = |F_l| \, e^{i\alpha_l}$, results in

$$I(x,y) = F_0 + \sum_{l=1}^{2N} 2\,|F_l(y)| \cos(lKx + \alpha_l) \; . \tag{11}$$

Thus, it is apparant that $2\,|F_l(y)|$ is the contribution for the $(l-1)^{th}$ harmonic of the original spatial frequency K to the intensity in the plane y. It is at the planes where these contributions of different harmonics have their maximum that one would expect to find a local intensity modulation with a period that is some integral fraction of the original period. Although the conductivity assumptions made above will certainly not be true for x-rays, this failure has negligible affect for $\lambda << c_1 < d$.

The above expressions can be reduced to the expressions used by Flanders et. al. (4) and defined by Winthrop and Worthington (5) and Konitz (6), if additional assumptions are made. With $\lambda << d$ and assuming that the magnitude of higher Fourier-coefficients drop sufficiently fast, so that $n\lambda << d$ for all significant terms, we obtain

$$\chi_n = \sqrt{k^2 - \gamma_n^2} = k - \frac{1}{2}\frac{n^2K^2}{k} \tag{12}$$

for a normal incident plane wave. Therefore,

$$\chi_{n-l} - \chi_n = \frac{1}{2}\left[(2nl - l^2)\frac{K^2}{k}\right] \tag{13}$$

and we obtain from Equation (9)

$$F_l(y) = e^{-i\pi\frac{\lambda}{d^2}l^2 y} \sum_{n=l-N}^{N} C_n \, C^*_{n-l} \, e^{-i(2\pi\frac{\lambda}{d^2}yl)n} \tag{14}$$

For $y = 0$, i. e. in the center plane of the grating, all the exponentials are equal to 1. This condition occurs whenever

$$y = y_m = m\frac{2d^2}{\lambda} \; ; \; m = 1,\ldots,\infty \tag{15}$$

The intensity distributions in the planes at distances y_m reproduce the intensity distribution in the plane of the grating and are the "Fourier images" of the grating. The condi-

tion for maximizing $|F_l|$ for each harmonic individually is

$$y = y_{l,j} = j\frac{d^2}{\lambda l} \; ; \; j = 1,...,\infty \tag{16}$$

These are the planes where the "Fresnel images" occur and the $(l-1)^{th}$ harmonic of the original grating reaches a maximum. If the harmonic is the dominant term in this plane, the intensity distribution will have a period which is an integral fraction of the original grating period.

V. SPATIAL PERIOD DIVISION SIMULATION

Using the theory described above, it is possible to simulate the wave field transmitted through a grating such as the one described by Flanders et al. (4), ie. $d = .1968\ \mu m$, $h_1 = .25\ \mu m$, at $\lambda = .0045\ \mu m$. The objective is to optimize the design of a single transmission grating with the goal of obtaining a copy of this grating with a period which is one half or one third of the original. Figure 7 illustrates the intensity distribution close to the grating for the following set of parameters: $c_1 = .06\ \mu m$ and $h_1 = .25\ \mu m$. These parameters seem to offer the maximum depth of field while maintaing good contrast for doubling or tripling the grating frequency. In Figure 8, the Fourier components of Equation (9) are plotted versus distance from the center plane of the grating. The plots indicate that for this grating, "Fresnel" images based on the fourth harmonic or higher ($l \geq 5$) will have a significant contribution from the fundamental frequency. These higher harmonic images can be accentuated if c_1 is reduced. This, however, greatly reduces the depth of field for the lower harmonic images. It is interesting to note that the only significant difference between the "Fourier" image and the zero harmonic "Fresnel" image is a shift in the x direction by one half of the period. The table below lists the planes in which the various Fresnel and Fourier images occur for this particular grating (Equation (9)) and as calculated using Equations (15) and (16).

	y(in μm)	
Harmonic	(9)	(15) & (16)
N=1	16.95	17.23
j=1, l=1	8.40	8.61
2	4.15	4.30
3	2.70	2.87
4	1.90	2.15
5	1.50	1.72

The effect of placing a wafer coated with a resist, such as PMMA, at a given distance from the parent grating can now be simulated. For doubling the frequency of the grating, the optimum distance is $y = 4.15\ \mu m$ and the depth of field is $\sim \pm .15\ \mu m$. Figure 9 shows the intensity distribution plots for several planes starting at the optimum

distance. Now using the x-ray exposure data of Spiller and Feder (7) and the resist development algorithm of Kern and Zarowin (8), we can simulate the exposure and development of the doubled pattern in .30 μm of PMMA, the optimum distance being placed in the center of the resist. The plots in Figure 10 show the line shapes in the resist as it is developed for successively longer periods of time. The affect of the finite depth of the resist can be seen in the fact that the open lines are wider at the bottom and at the top of the resist than at the center.

VI. CONCLUSIONS

From the study above, it is clear that proper grating system design can result in a grating alignment scheme for x-ray lithography with a good signal to noise ratio. Such an alignment scheme, however, is very sensitive to mask-wafer separation (requiring control to within $\pm.1$ μm), and also to the details of the architecture. Process windows on the order of $\pm.1$ μm are available and adequate care must be taken in the grating mark construction. This may be more difficult than originally assumed. One advantage to using gratings for alignment purposes is that localized grating degradation due to processing will have relatively little affect on the alignment signal. This is due to the averaging character of the system. The grating architecture described here is not necessarily the optimum, as countless other designs have not been explored or evaluated.

From the Spatial Period Division simulations, it is possible to determine the conditions under which a grating can be constructed with a period being an integral fraction of that of the parent grating. Care must be taken, however, to copy the parent at the correct distance and to take into account the corresponding depth of field. This depth of field as well as the contributions of different harmonics depent on the architecture of the specific grating.

REFERENCES

1. S. Austin, H.I. Smith , and D.C. Flanders, J. Vac. Sci. Technol., vol. 15, 984 (1978).
2. D. Maystre and R. Petit, Optics Communications, vol. 5, 90 (1972).
3. E.G. Loewen, M. Neviere, and D. Maystre, Applied Optics, vol. 18, 2262 (1979).
4. D.C. Flanders, A.M. Hawryluk, and H.I. Smith, J. Vac. Sci. Technol., vol. 16, 1949 (1979).
5. J.T. Winthrop and C.R. Worthington, J. Opt. Soc. Am., vol. 55, 373 (1965).
6. H. Konitz, Optik, vol. 53, 419 (1979).
7. E. Spiller and R. Feder, Topics in App. Phys., vol. 22, ed. by H.J. Queisser, Springer-Verlag, Berlin, 1977, p. 35.
8. D.P. Kern and C.B. Zarowin, paper presented at the 157^{th} Meeting of the Electrochemical Society, St. Louis, MO, May, 1980.

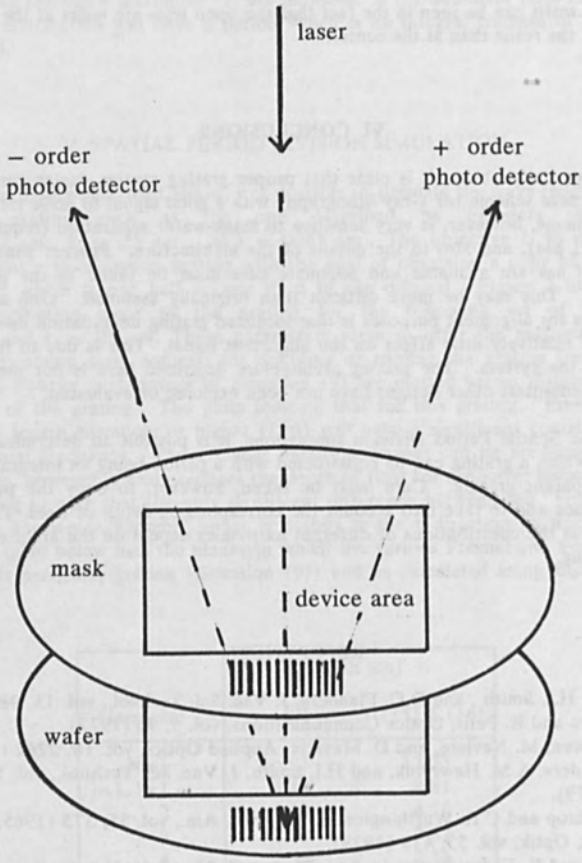

Figure 1 - Grating Alignment Technique

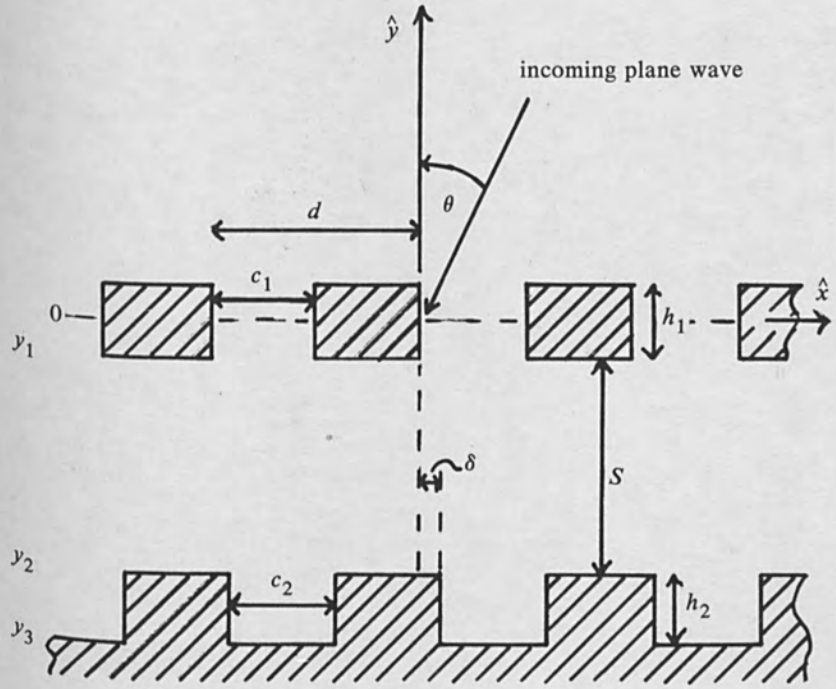

Space is partitioned into 4 Regions:

Region I: $y \geq \frac{h_1}{2}$

Region II: $-\frac{h_1}{2} < y < \frac{h_1}{2}$

Region III: $-S - \frac{h_1}{2} < y < -\frac{h_1}{2}$

Region IV: $-h_2 - S - \frac{h_1}{2} < y < -S - \frac{h_1}{2}$

Figure 2 - Regions and Parameters for Grating Alignment Solution

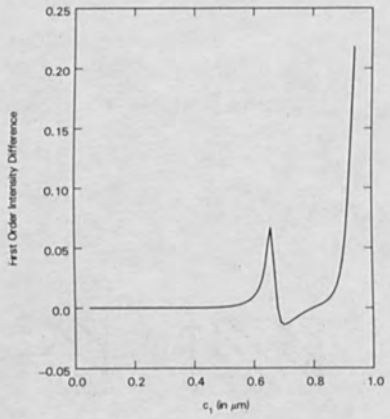

(λ=.6328, d=1., c_2=.5, h_1=h_2=.5, δ=.15 and S=10.0 μm; θ=0.)

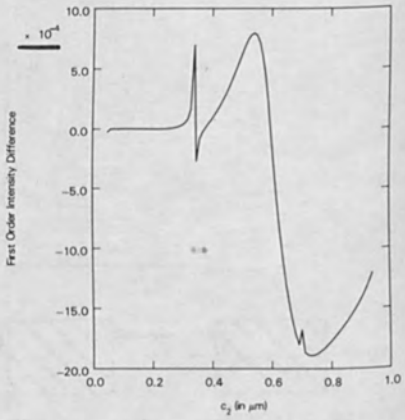

(λ=.6328, d=1., c_1=.5, h_1=h_2=.5, δ=.15 and S=10.0 μm; θ=0.)

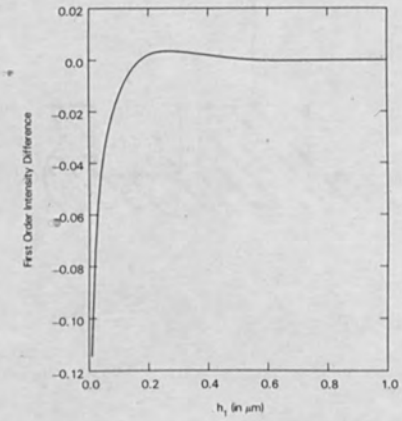

(λ=.6328, d=1., c_1=c_2=.5, h_2=.5, δ=.15 and S=10.0 μm; θ=0.)

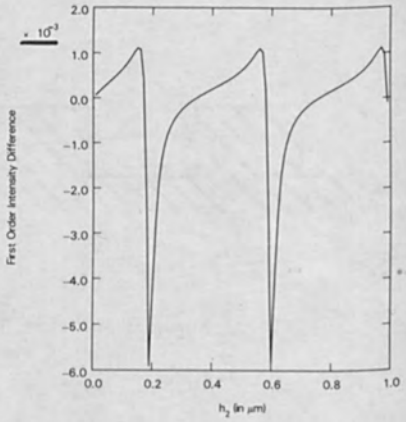

(λ=.6328, d=1., c_1=c_2=.5, h_1=.5, δ=.15 and S=10.0 μm; θ=0.)

Figure 3 - Initial Design Process Windows

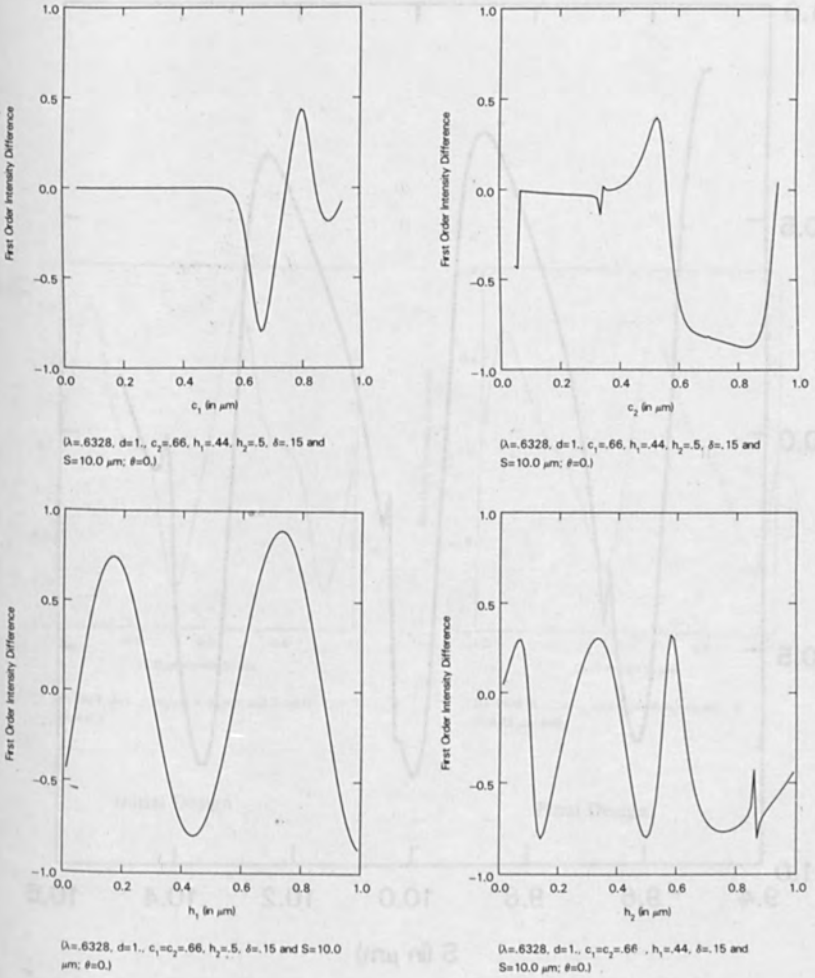

Figure 4 - Final Design Process Windows

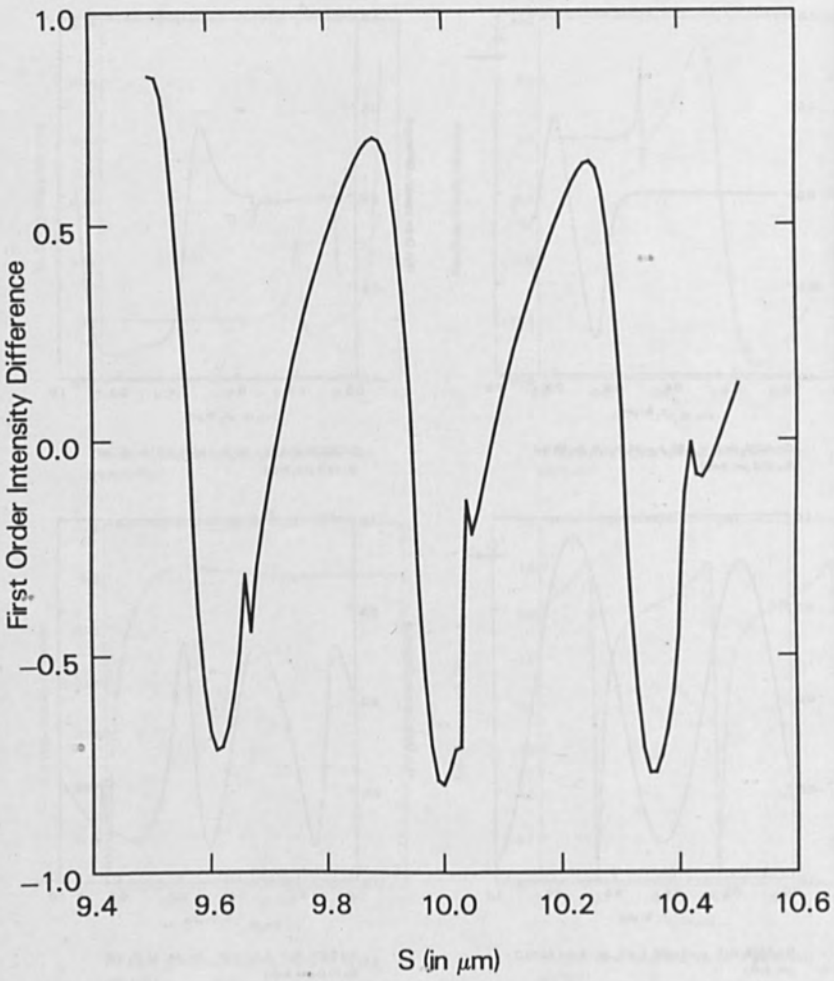

(λ=.6328, d=1., c_1=c_2=.66, h_1=.44, h_2=.5, and δ=.15 μm; θ=0.)

Figure 5 - Difference Signal vs. Mask-Wafer Separation (S)

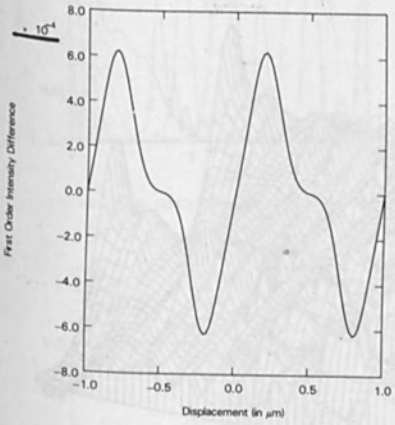

(λ=.6328, d=1., c_1=c_2=.5, h_1=h_2=.5, and S=10.0 μm; θ=0.)

Initial Design

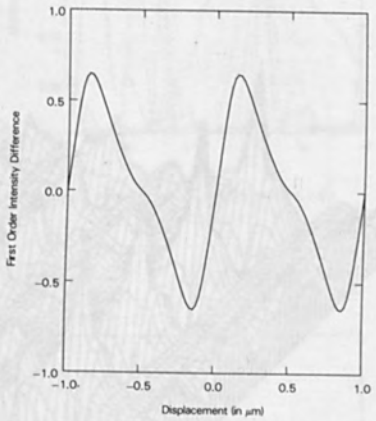

(λ=.6328, d=1., c_1=c_2=.66, h_1=.44, h_2=.5, and S=9.85 μm; θ=0.)

Final Design

Figure 6 - Alignment Signal vs. Displacement for Initial and Final Designs

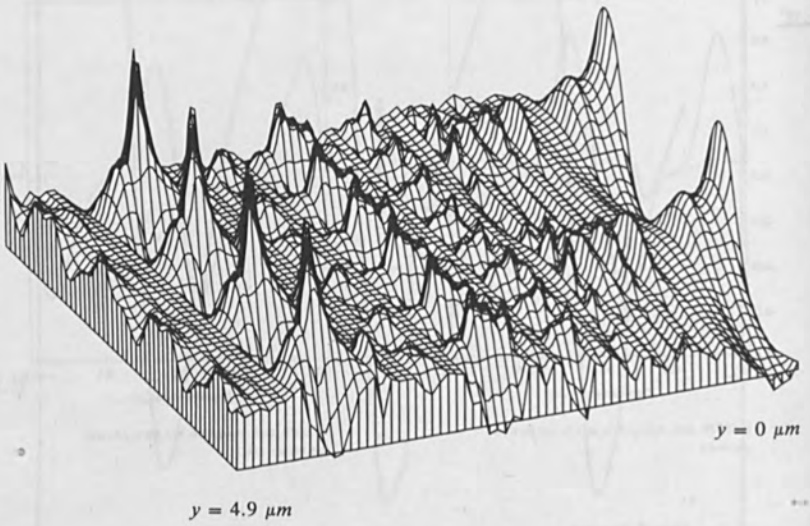

Figure 7 - 3-D Intensity Distribution

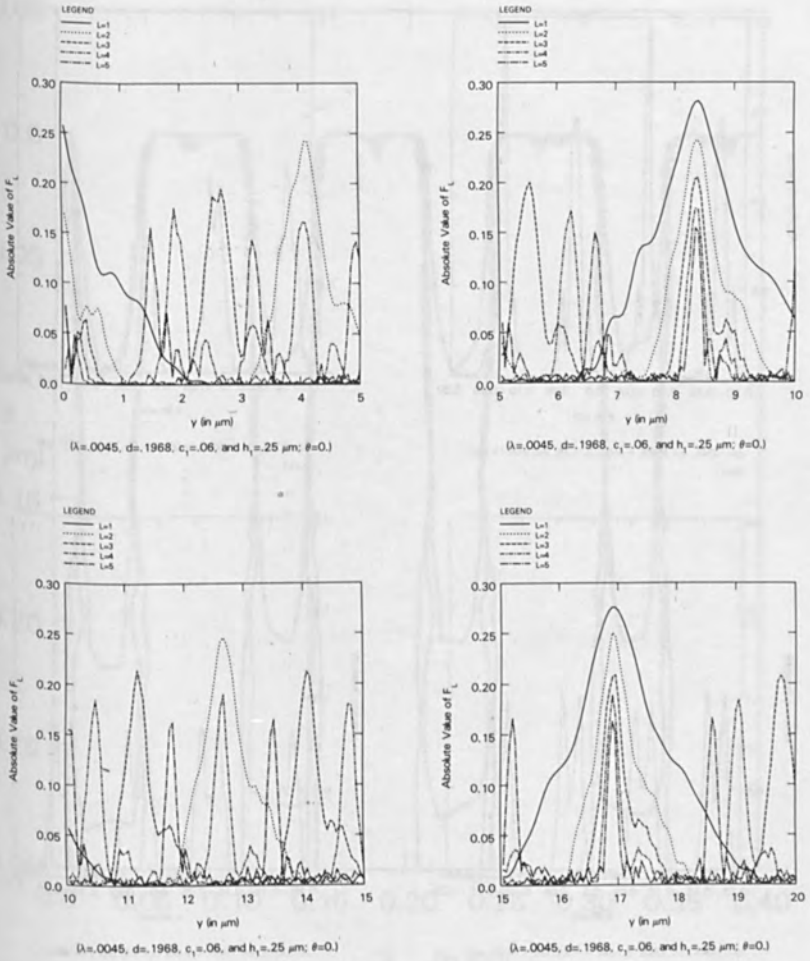

Figure 8 - Fourier Components (F_l) vs. y

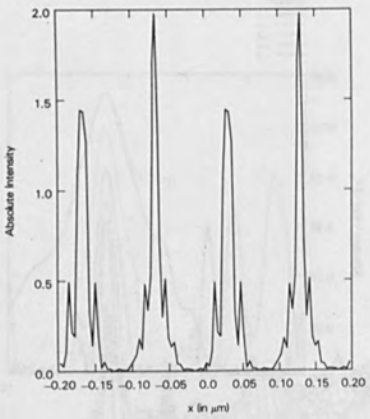

(λ=.0045, d=.1968, c_1=.06, h_1=.25, and y=4.15 μm; θ=0.)

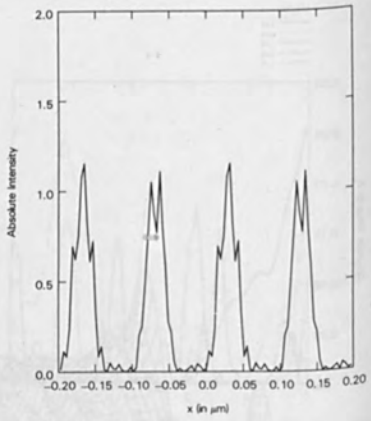

(λ=.0045, d=.1968, c_1=.06, h_1=.25, and y=4.20 μm; θ=0.)

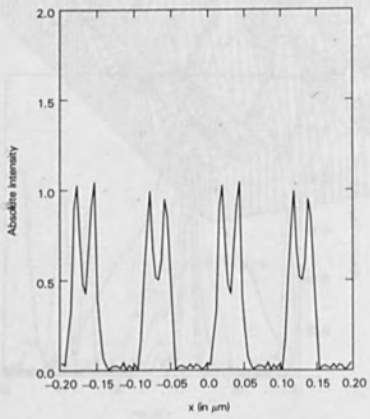

(λ=.0045, d=.1968, c_1=.06, h_1=.25, and y=4.25 μm; θ=0.)

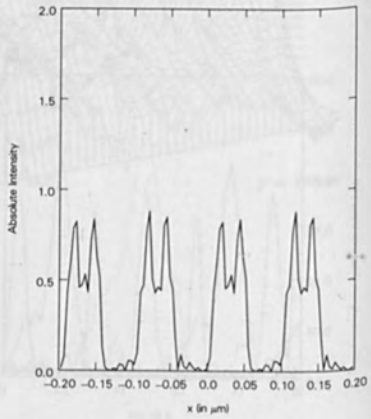

(λ=.0045, d=.1968, c_1=.06, h_1=.25, and y=4.30 μm; θ=0.)

Figure 9 - Variation of Intensity Distribution with *y*

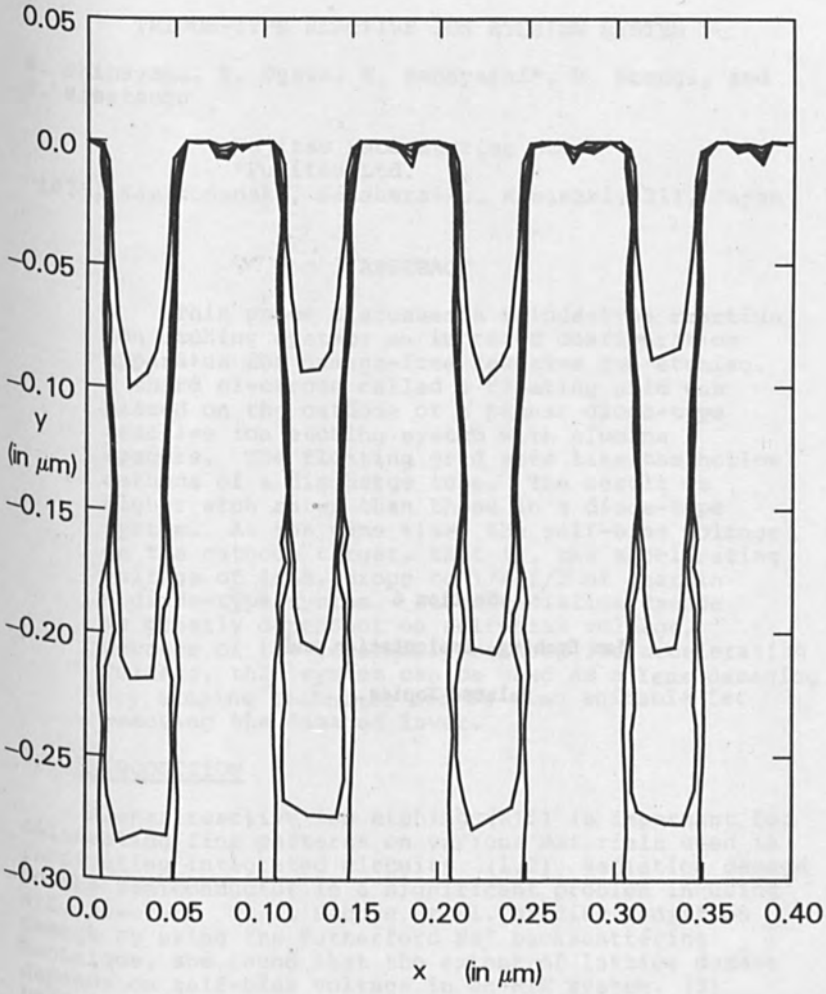

Figure 10 - Resist Development Simulation of Half Period Copy

Section 6

Ion Etching, Implantation and Related Topics.

TRIODE-TYPE REACTIVE ION ETCHING SYSTEM

H. Shibayama, T. Ogawa, K. Kobayashi*, M. Kosugi, and T. Hisatsugu

Fujitsu Laboratories Ltd.
*Fujitsu Ltd.
1015, Kamikodanaka, Nakahara-ku, Kawasaki, 211, Japan

ABSTRACT

This paper discusses a triode-type reactive ion etching system; an improved configuration apparatus for damage-free reactive ion etching. A third electrode called a floating grid was placed on the cathode of a planar diode-type reactive ion etching system with alumina spacers. The floating grid acts like the hollow cathode of a discharge tube. The result is higher etch rates than those in a diode-type system. At the same time, the self-bias voltage on the cathode target, that is, the accelerating voltage of ions, drops to 1/4-1/2 of that in a diode-type system. Since radiation damage is greatly dependent on self-bias voltage, because of the remarkably reduced ion accelerating voltage, this system can be used as a less damaging dry etching technique and is also suitable for removing the damaged layer.

1. INTRODUCTION

Planar reactive ion etching (RIE) is important for delineating fine patterns on various materials used in fabricating integrated circuits. (1,2) Radiation damage to the semiconductor is a significant problem in using RIE, however. G. W. Sachse et al. studied radiation damage by using the Rutherford He^+ backscattering technique, and found that the extent of lattice damage depends on self-bias voltage in an RIE system. (3) Self-bias voltage is defined as the DC potential difference between electrodes of the RIE system during operation. It takes place due to the difference in mobility between ions and electrons in plasma. (4) Ions in plasma are accelerated by the self-bias voltage and the radiation damage is caused by bombardment of these accelerated ions.

This paper presents a triode-type reactive ion etching system (TRIES), an improved configuration apparatus for reactive ion etching to achieve damage-free dry etching. In this system, self-bias voltage corresponding to the accelerating voltage of ions can be remarkably reduced as compared with that in a conventional diode-type system. The effect of self-bias voltage is discussed by comparing the potential distribution in plasma. Lattice damage examined by the backscattering technique and the surface state density of MOS capacitors are presented. Finally, the application to contact hole formation in the MOS-IC fabrication process is also presented.

2. APPARATUS

Figure 1 shows a schematic diagram of the triode-type reactive ion etching system (TRIES). A third electrode called a floating grid (FG) was placed on the cathode target of a conventional planar diode-type RIE system with alumina spacers. The floating grid is made of aluminum with the same diameter (250 mm) as the cathode target and has many perforations with a typical diameter of 8 mm, like the grid electrode in a vacuum triode tube. The typical distance between the cathode and the FG is 16 mm. An RF power of 13.56 MHz was supplied to the cathode target and the anode via a capacitor, with the anode being grounded. Reactive gas was introduced into the chamber through a needle valve and the gas pressure was kept constant by adjusting the conductivity of a main valve in the evacuation system. The specimens to be etched were placed on a water-cooled cathode target. The self-bias voltage between the cathode and ground was measured with a high input impedance voltmeter.

Figure 2 shows photographs of the discharge glow of a diode-type system and of TRIES observed from outside the chamber. Both reactors were operated at the same RF power and the same gas pressure of CF_4 mixed with 5% O_2. The intensity of emitted light between the FG and cathode increased remarkably as compared with that in a diode-type RIE system. This is attributed to the increased plasma density of the TRIES.

3. RESULTS AND DISCUSSION

Figure 3 shows the potential distribution between the anode and cathode in plasma when the RF power of 150 W is supplied for diode-type system, TRIES, and hollow cathode-type system. Potentials were measured

with a probe inserted in the plasma. The FG of the hollow cathode-type system shown in Figure 3(c) was electrically connected to the cathode target. This configuration is similar to the hollow cathode in a glow discharge tube, known as the method for increasing plasma density. (5) In the TRIES and hollow cathode-type system, the potentials of the plasma between the FG and cathode are higher than those around the cathode in a diode-type system. The hollow of the potential is also noted. These phenomena are due to the hollow cathode effect. The plasma density is higher between the FG and cathode because of increasing discharge current. In a hollow cathode-type system, the self-bias voltage can be greatly reduced in all ranges of RF power; however, the ions in the discharge glow are not accelerated because of the lowered electric field around cathode. The etch rate is less than that in the TRIES and the extent of undercutting is greater. This system is not suitable for etching fine patterns. On the other hand, the potential on the cathode target with the TRIES is different from that on the FG as shown in Figure 3(b). This system reduces the self-bias voltage with an electric field around the cathode comparable with that in a diode-type system. Thus, the triode-type reactive ion etching system with an electrically floating grid is a superior etching apparatus for etching fine patterns with low self-bias voltage.

Figure 4 shows the etch rates of (100) oriented silicon substrates and the self-bias voltage (Vsb) as a function of RF power with CF_4 mixed with 5% O_2 at a pressure of 0.01 torr. In the TRIES, the etch rates of Si are higher than those in a diode-type system and the Vsb values are 1/4-1/2 lower at the same RF power. This is due to the higher plasma density between the FG and cathode target. Moreover, a stable glow discharge can be sustained even at a Vsb of 20 V in the TRIES, whereas the glow discharge becomes unstable at a Vsb below 75 V in a diode-type system.

In general, the radiation damage caused by RIE processing is dependent on the Vsb, that is, the accelerating voltage of ions in discharge glow. Such radiation damage can be examined by analyzing the surface state density (Nss) of MOS capacitors. (6) In this experiment, capacitors were fabricated on (100) oriented p-type silicon substrates etched to a depth of 3000 Å at various self-bias voltages using both systems. Gate oxidation was carried out at 1000°C in dry O_2 with an oxide thickness of 300 Å, then the Al electrodes were

formed on the gate oxide. The surface state density was measured by the quasi-static C-V technique. The results are shown in Figure 5. Figure 5(a) shows the surface state density as a function of RF power in both systems. The Nss related to radiation damage can be greatly reduced in the TRIES as compared with that in a diode-type system at the same RF power. Figure 5(b) shows the Nss as a function of the Vsb. The Nss is dependent on self-bias voltage; therefore, the amount of contaminants knocked in the silicon, such as decomposed constituents of reactive gas, increase as the Vsb increases. The contaminants remain near the Si-SiO_2 interface after the gate oxidation process. Further, in etching with the TRIES at a Vsb of 20 V, the Nss is the same as that fabricated on a chemically etched Si surface. The silicon substrate is not damaged under this etching condition. To study the crystallographic defects near the silicon surface, the backscattering spectra in both random and channeling directions with a 1.5 MeV He^+ ion were measured. The results are shown in Figure 6. The surface peak for sample A etched at a Vsb of 550 V is about twice that for a single silicon crystal (sample C). This shows that there is a damaged layer related to lattice disorder near the surface. Sample B was etched with the TRIES at a Vsb of 20 V. The surface peak is the same as that for sample C. The radiation-damaged layer related to lattice disorder is not induced into silicon substrate during etching at a Vsb of 20 V. The result is in good agreement with the result of the Nss as shown in Figure 5. Therefore, the TRIES provides a dry etching technique with minimal damage in fabrication processing of Si devices, especially MOS-IC.

The contact hole formation process was studied as another example of the TRIES application. The etching of a CVD SiO_2 film on a Si wafer is necessary to form the contact hole for metallization. In this case, when CHF_3 gas is used at a high Vsb, a higher etching rate can be obtained for SiO_2 than for Si, because etched Si surface is covered with a carbon layer. Radiation damage and a carbon accumulation layer on the Si surface become problems in the device characteristics. Removal of these layers was carried out with the TRIES at a Vsb of 20 V. This condition provides a damage-free etching as shown in Figures 5 and 6. The effect was evaluated by measuring contact resistance. A CVD SiO_2 film which was deposited on the arsenic ion implanted layer with a dose of 10^{15} ions/cm^2 and an energy of 120 KeV was etched with the RIE process with

CHF_3 gas at a Vsb of 550 V. The aluminum was then evaporated on it. The dimensions of contact area were 2 μm x 30 μm. The results are shown in Figure 7. A high contact resistance in an as-etched sample was caused by the carbon accumulation and the damaged layer existed in the region of the etched surface. If etching with CF_4 gas mixed with O_2 at a Vsb of 20 V is carried out before metallization, good contact can be obtained with normal resistance and a low degree of scatter. This sequential etching is suitable for removing the damaged layer.

4. SUMMARY

A triode-type reactive ion etching system (TRIES) is proposed to achieve a damage-free dry etching process. Compared with a conventional diode-type reactive ion etching system, the system has the following advantages:

(1) Plasma density is increased between the cathode and the floating grid placed on the cathode with alumina spacers, thus the etch rates of various materials are greatly increased at the same RF power.
(2) Self-bias voltage is drastically reduced.

This can be explained by the fact that the floating grid acts like the hollow cathode of a discharge tube. Radiation damage with the RIE process is dependent on the Vsb. Thus, the TRIES can be used as a no-damage etching technique for the coming VLSI.

5. ACKNOWLEDGEMENTS

The authors wish to thank to Dr. T. Sakurai, and Messrs. S. Tatsuta and H. Hashimoto for the Rutherford He^+ ion backscattering analysis; Drs. T. Misugi, Y. Fukukawa, and H. Ishikawa for their useful discussions and encouragement.

REFERENCES

1. H. W. Lehmann and R. Widmer, J. Vac. Sci. Technol., 15, 319 (1978).
2. R. L. Bersin, Solid State Technology, 19, 31 (1976).
3. G. W. Sachse, W. E. Miller, and C. Gross, Solid State Electronics, 18, 431 (1975).
4. H. S. Butler and G. S. Kino, Phys. Fluids, 6, 1346 (1963).

5. A. Güntherschulze, Z. Tech. Phys., 11, 49 (1930).
6. H. Yano, H. Hashimoto, and Y. Tōyama, Proc. of the 8th Inter. Conf. on Electron and Ion Beam Science and Tech., 582 (1978).

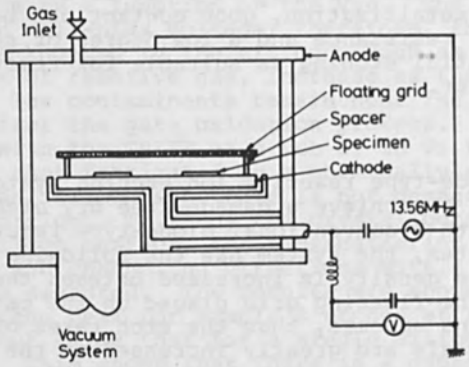

Fig. 1 Schematic diagram of triode-type reactive ion etching system (TRIES)

(a) (b)

Fig. 2 Intensity of emitted light of plasma observed from outside the chamber at the same RF power (a) conventional diode-type reactive ion etching system (b) TRIES

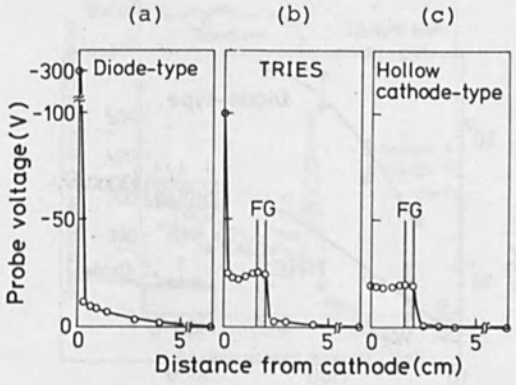

Fig. 3 Potential distribution between anode and cathode using probe method. RF power was constant at 150 W.

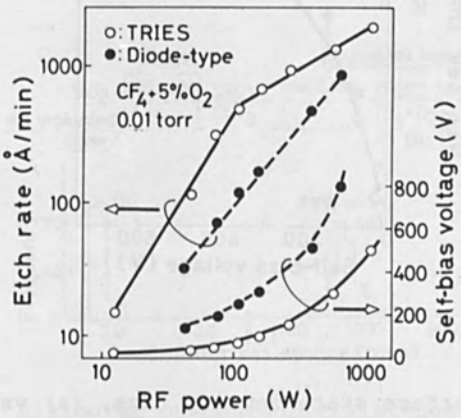

Fig. 4 Etch rates of silicon and self-bias voltage vs. RF power

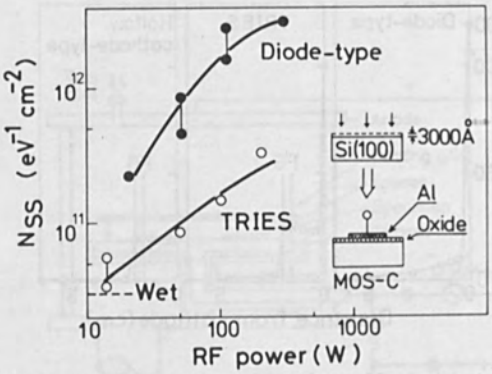

(a)

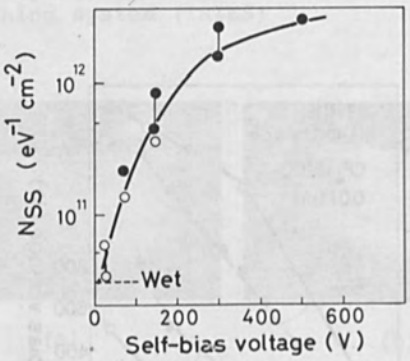

(b)

Fig. 5 Surface state density, Nss, (a) vs. RF power (b) vs. self-bias voltage

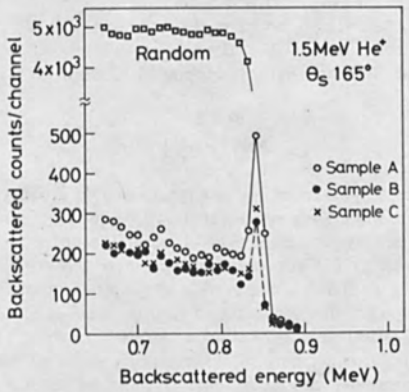

Fig. 6 Backscattering spectra for etched silicon surface. Sample A and B were etched at a Vsb of 550 V and 20 V respectively.

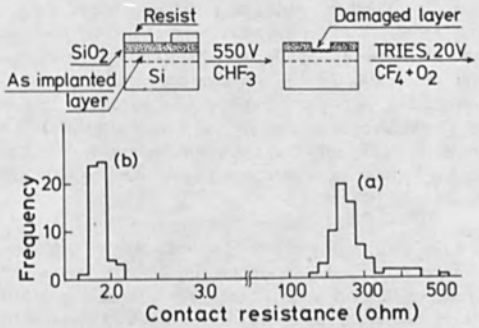

Fig. 7 Histogram of contact resistance (a) as-etched sample (b) sequentially etched sample by the TRIES at a Vsb of 20 V

LOW ENERGY ION BEAM ETCHING

J.M.E. Harper, J.J. Cuomo, P.A. Leary, G.M. Summa
IBM Research Center, Yorktown Heights, NY 10598
H.R. Kaufman
Colorado State University, Fort Collins, CO 80523
F.J. Bresnock
IBM Data Systems Division, Hopewell Junction, NY 12533

ABSTRACT

We present two developments in low energy ion beam etching. First, we have extended the usable ion energy range for broad beam ion etching down to tens of eV by using a single extraction grid of very fine aperture size. High ion current densities (up to 1.0 mA/cm²) are achieved below 100 eV ion energy while maintaining a collimated beam with low energy spread (about 10 eV). Second, we have applied this capability to reactive ion beam etching (RIBE) of Si and SiO_2, and introduce a quantitative parameter which characterizes the effectiveness of ion bombardment in enhancing chemical etching. This parameter is obtained from etch rate measurements using Ar and CF_4 gases over the ion energy range 20 – 1500 eV. Step edge profiles are also examined.

I. INTRODUCTION

In this paper we present two developments in low energy ion beam etching. First, we have extended the usable ion energy range for broad beam ion etching down to tens of eV by replacing the conventional dual grid ion extraction system with a single grid of very fine aperture size. High ion current densities (up to 1.0 mA/cm²) are achieved at low ion energies (down to 20 eV) while maintaining a collimated beam with low energy spread (about 10 eV). Second, we introduce a quantitative parameter which characterizes the effectiveness of ion bombardment in enhancing chemical etching, the basis of reactive ion etching (RIE). The ion enhancement parameter is obtained from the energy dependence of the etch rates of a material using reactive and inert gases. We have measured the etch rates of Si and SiO_2 with Ar and CF_4 gases over the energy range 20 – 1500 eV. We find, for example, that in etching SiO_2 with CF_4 at an ion energy of 200 eV, the ion enhancement parameter is about 3, indicating that for each substrate atom removed by physical sputtering, two additional atoms are removed by enhanced chemical etching. Above an ion energy of 500 eV this enhancement parameter decreases to unity, indicating that ion enhancement of chemical etching has reached its maximum effectiveness. These measurements may be used to optimize etch rate selectivity in reactive ion beam etching (RIBE).

We also compared the step edge profiles obtained using CF_4 etching of SiO_2 with those obtained with Ar ion etching. Inert gas ion etching usually leaves sloping walls, and may cause trenching and redeposition on mask edges. These problems are minimized by using a reactive ion beam etching process at an energy low enough to cause little physical sputtering. Ion beam systems operate at two orders of magnitude lower pressure than a glow discharge RIE system, reducing the effect of neutrals. The mean free path of ions and etch products exceeds the chamber dimensions, minimizing loading effects, contamination by backscattering, and chemical effects of the sample holder. The ion energy spread is low, and the energy and current density may be independently controlled and measured. These advantages provide an incentive to extend the useful energy range to below 100 eV, and to take advantage of the selectivity available with chemically reactive species. These two topics are addressed here, beginning with the limits encountered when the ion energy is decreased.

II. THEORY – LIMIT ON ION CURRENT DENSITY AT LOW ENERGY

Ion beam etching is usually carried out using broad beam electron bombardment ion sources (1). Figure 1 shows the general configuration. This diagram shows a single extraction grid, whereas typically a dual grid system is used. A low voltage magnetically enhanced discharge is maintained between the thermionic cathode and surrounding anode, and ions are extracted through the grid system to form a directed beam. The ion energy is close to the anode potential V_a. The beam is aimed at the material to be etched, and normally a flow of electrons is supplied from a neutralizer filament to avoid surface charging effects (1). The conventional dual grid configuration is shown in Fig. 2a. In this design the screen grid potential differs from the discharge plasma potential by the magnitude of the discharge voltage V_d, and the accelerator grid is held negative to prevent backstreaming of electrons into the discharge chamber. Further details of operation are given in References 1 and 2. These ion sources easily generate ion current densities of 0.5 mA/cm² at 500 eV, but such high ion energies may cause device damage, knock-on penetration of contaminants or intermixing of layers. Lower ion energies are desirable, but below about 100 eV the ion current density is space charge limited to only a few hundredths mA/cm². Since this current density corresponds to less than one tenth monolayer of bombardment per second, practical ion etching cannot be carried out below 100 eV with a dual grid system.

The space charge limit on current flow may be stated as follows. The maximum current density obtainable from an ion source (1) is related to the ion acceleration voltage V and the acceleration distance d by:

$$j_{max} \propto V^{3/2}/d^2 \qquad (1)$$

In a dual grid system (Fig. 2a) V is the potential difference between the discharge plasma and the accelerator grid, and d is approximately the distance between the plasma sheath and the accelerator grid. To generate a low energy ion beam, V must be decreased, and since d is fixed by the grid spacing (typically 1 mm or greater), j_{max} decreases also. This relationship is shown in Fig. 3, in which the maximum current density obtained from a dual grid ion source is plotted as a function of $V_t^{3/2}$, where V_t is the potential difference between the grids and is nearly equivalent to the ion acceleration voltage V. Therefore, while a current density of 3.0 mA/cm² is obtained at an ion energy of 1500 eV ($V_t^{3/2}$ = 67000), only 0.05 mA/çm² is obtained at 100 eV ($V_t^{3/2}$ = 1153). This space charge limitation on ion current density is a ceiling above which a dual grid source cannot operate, even by increasing the ion density in the source.

In order to maintain high current density at low ion energy, we use a single extraction grid (3) (Fig. 2b) which overcomes the space charge limitation of a dual grid system. The single grid is formed from a material with a very fine aperture size a. The aperture size must be comparable to or less than the thickness of the plasma sheath l_s for effective operation. With this condition satisfied, ions leave the discharge plasma in almost parallel trajectories, with a certain fraction passing through the grid as a collimated beam. Although the grid is bombarded by ions, sputtering damage is minimized by operating at low ion energy.

The single grid differs markedly from the dual grid system by maintaining high current density at low ion energy. The acceleration distance d is now equivalent to the sheath thickness l_s, which is on the order of 0.1 mm. As the ion energy is decreased, d is no longer fixed, and the sheath thickness l_s decreases to keep the ion current density equal to the space charge limit. Therefore almost constant current density is maintained down to about 20 eV ion energy.

III. EXPERIMENTAL PROCEDURE

A. Single Grid Ion Source

We have tested the single grid design on two ion sources of 3.5 cm and 7.5 cm beam diameter by simply replacing the grid system with a single grid of electroformed nickel mesh of 0.2 mm aperture size and 82% transparency (100 lines per inch). The 3.5 cm source is shown schematically in Fig. 1. Cathode and neutralizer filaments are tungsten.
Typical operating parameters which generate a 100 eV argon beam are:

sample chamber pressure = 10^{-2} Pa (8×10^{-5} Torr)
discharge voltage = 40 V
discharge current = 0.2 A
anode voltage = 100 V
grid voltage = – 20 V
grid current = 3 mA
beam current = 7 mA
current density at grid = 0.73 mA/cm²
current density 14 cm from grid = 0.32 mA/cm²
ion energy = 95 ± 5 eV

The current density and energy distribution in the ion beam are measured using a retarding grid analyzer. Measurements confirm that current densities up to 1.0 mA/cm² can be obtained at ion energies as low as 20 eV. This result demonstrates that the sheath thickness adjusts itself to maintain the beam current density independent of ion energy. The ion current density is now determined by the ion density in the source, and is not limited by grid geometry. Thus a wide range of operating conditions is available at low ion energy, as shown in Fig. 4. In this figure the operating range of the dual grid source is shown for ion energies up to 200 eV. The solid curve is the upper limit of this range and corresponds to the low energy portion of Fig. 3. Also shown is the operating range of the single grid. With the single grid, ion energies higher than 200 eV may be used, but sputtering of the grid must be taken into account. Current densities above 1.0 mA/cm² can be obtained, but are limited eventually by overheating of the grid. Energy analyzer measurements indicate an energy spread of about 10 eV, similar to that obtained with a dual grid source. We have operated the single grid source as low as 20 eV ion energy, but below this value the ion energy spread becomes comparable to the average ion energy, and the beam can no longer be considered almost monoenergetic. Over the entire operating range shown in Fig.4, however, the energy spread remains far smaller than the broad energy distributions found in r.f. glow discharge systems, and the current density is much higher than a dual grid system can generate. Thus quantitative measurements of etch rates can be carried out with current densities on the order of 1.0 mA/cm² over a wide range of low energies by using the single grid design.

A convenient feature of the single grid design is that it may be easily used on an existing dual grid ion source. The discharge chamber remains unchanged, while the low energy performance of the ion source is greatly improved. Finer mesh grids up to 333 lines per inch were also tested, but these developed holes during operation. With care, a 100 mesh grid can be used for 5 to 10 hours operation including several exposures to air.

B. Etch Rates of Si and SiO_2 with Ar and CF_4.

We have measured the etch rates of Si and SiO_2 using Ar and CF_4 gases in the ion source, over an ion energy range of 20 to 1500 eV. The 3.5 cm diameter single grid source was used for ion energies below about 200 eV, and the 2.5 cm diameter dual grids were used on the same ion source for higher ion energies. Ion source parameters were similar to those listed above, except that with CF_4 a discharge voltage of 70 V was used. The sample chamber was evacuated to an initial pressure of typically 5×10^{-5} Pa (4×10^{-7} Torr), then raised to an Ar or CF_4 pressure of $1 - 5 \times 10^{-2}$ Pa ($0.8 - 4 \times 10^{-4}$ Torr) for etching. Etch rate measurements were made using a coated quartz crystal rate monitor located 14 – 20 cm from

the ion source, and were supplemented by step measurements on masked Si and oxidized Si wafers. Several measurements were also made using a larger diameter (7.5 cm) single grid source. Ion current density and energy were measured above the sample using a retarding grid analyzer. Current densities of typically 0.1 mA/cm² were used, with etch times of 10 – 90 minutes. These measurement times were longer than time constants associated with the rate monitor temperature or the establishment of steady etching conditions (4).

Etch rates were divided by the ion current density to calculate the etching yield in atoms/ion for each ion/sample combination. Argon ion current densities were corrected for the resonant charge exchange process (2,5) which converts a fraction of the energetic beam ions to energetic neutrals. This fraction increases with background pressure and causes the measured ion current density to underestimate the total energetic particle flux striking the sample. Correcting for this process allows measurements at different pressures to be reliably compared. Current density values with CF_4 were not corrected for charge exchange since this process should not be significant for CF_3^+ ions (the dominant species) passing through mostly CF_4 gas.

To examine the step edge profiles generated by low energy RIBE, several wafers of oxidized Si were coated with a 1 μm thick photoresist pattern. After etching with CF_4 at 200 eV ion energy, the photoresist was removed and the steps were examined by scanning electron microscopy. The step profiles were then compared with steps etched using 500 eV argon ions.

IV. RESULTS

Etching yields are given in Fig. 5 as a function of ion energy, for Si and SiO_2 using Ar or CF_4. To convert these yields to etch rates, in the case of Si a yield of 1 atom/ion means that in an ion beam of current density 1.0 mA/cm², the Si etch rate is 12.5 Å/sec. For SiO_2, a yield of 1 atom (either Si or O) per ion means that in an ion beam of current density 1.0 mA/cm², the SiO_2 etch rate is 9.5 Å/sec. For reference, the asterisk in Fig. 5 indicates the maximum chemical etching yield of SiO_2 by a single CF_3^+ ion to yield SiF_4 plus CO and CO_2, according to the equation:

$$4CF_3 + 3SiO_2 \rightarrow 2CO + 2CO_2 + 3SiF_4$$

This maximum yield is 0.75 SiO_2 molecules, or 2.25 atoms (Si or O) per CF_3^+ ion. The significance of this value is discussed in the next section. The data obtained with the single grid ion source are shown as circles, and those taken with the dual grid are shown as triangles. These measurements merge smoothly at 200 eV in the case of Ar/SiO_2, but for CF_4/SiO_2 there is a significant difference in etch rates measured by these two grid systems. This difference appears to be caused by a mild rate of deposition of polymeric material from the CF_4 discharge, which competes with the etching process, especially at low ion energy. The multiple data points shown at the same ion energy in Fig. 5 were obtained from different samples, using various values of gas pressure and ion current density to assess the overall reproducibility of the process.

Step edge profiles are shown in Fig. 6. The initial photoresist mask shape is shown in Fig. 6a. A 1 μm deep step in SiO_2 etched with CF_4 at 200 eV is shown in Fig. 6b, and a 0.5 μm deep step in SiO_2 etched with Ar at 500 eV is shown in Fig. 6c. The step edge profile obtained with CF_4 has almost vertical walls with no evidence of trenching. This indicates directional, anisotropic etching with mostly volatile products. The wall is not quite vertical because of the sloping mask shape (Fig. 6a) and the slight divergence angle of the ion beam (about 10°). Since the mask is etched at about 1/5 the rate of the SiO_2, the lateral movement of the step edge contributes to a slightly sloping wall. The step edge profile obtained with Ar

(Fig. 6c) shows a sloping wall with a shallow trench formed by reflected ions. This shape evolves when etching is by purely physical sputtering, causing partial redeposition on the wall of the step. Although this redeposited material may be simultaneously removed by sputtering, it has the effect of decreasing the etch rate of the sloping wall, contributing to a shallower slope. Also with Ar sputtering, the photoresist mask and the SiO_2 substrate etch at similar rates. The mask edge therefore moves a greater distance laterally than in etching with CF_4 to the same depth, again contributing to a sloping step edge. Trenching can be more severe than shown in Fig. 6c, as shown in Ref. 6. Also redeposition on mask edges can leave unwanted fringes (7,8). These artifacts of inert gas ion etching are minimized by using low energy RIBE.

A fringe is evident in Fig. 6b, but this is not due to redeposited sputtered material. The deposit on the top of the step is the polymer coating obtained when using CF_4 in the ion source. The polymer coated the side of the photoresist, and then fell onto the top surface of the SiO_2 when the photoresist was removed. The formation of this polymeric coating on the sample being etched caused wide variations in the measured etch rate of CF_4/SiO_2 at ion energies below 100 eV, and probably accounts for the roughness of the etched surface in Fig. 6b. Under certain operating conditions the deposition process dominated and showed a positive deposition rate exceeding the etch rate. Competition from this deposition process was minimized by operating at low gas pressure ($< 10^{-2}$ Pa) and large distances from the ion source (> 10 cm). Preliminary etch rate measurements using the larger diameter (7.5 cm) ion source were inconclusive because net deposition always occurred below 100 eV ion energy. The larger diameter source acts as a broad area vapor source for deposition on the sample. When CF_4 was used in either ion source, an insulating coating also formed inside the discharge chamber. This coating gradually increased the resistance of the discharge circuit and after several hours operation the discharge would be extinguished. Cleaning the anode surface quickly restored normal operation. The complications which arise from the deposition of polymeric material on both the sample and the discharge chamber surfaces may possibly be eliminated by using a different gas mixture. However, above ion energies of 200 – 300 eV, etch rates with CF_4 did not seem to be affected by polymer deposition. Also, when using argon the operation of the ion source was straightforward, and reproducible etch rates were obtained at ion energies as low as 20 eV (Fig. 5).

The ratio of etching yields between CF_4/SiO_2 and Ar/SiO_2 is plotted in Fig. 7. Also shown is the ratio of the slope of the CF_4/SiO_2 etch yield curve to the slope of the Ar/SiO_2 curve. This ratio is defined as the ion enhancement parameter p, to be discussed in the following section.

V. DISCUSSION

A. Comparison of Etching Results

The etch rate measurements (Fig. 5) over the range 20 – 1500 eV demonstrate several points. The etch rates of Ar/SiO_2, CF_4/Si and Ar/Si are very similar. Etching of Si or SiO_2 by Ar is a purely physical sputtering process, and etching of Si by CF_3^+ ions has been shown to be almost entirely by physical sputtering (4). These results also indicate that in RIBE there is a low concentration of F radicals involved in etching, in contrast to glow discharge systems (9). We find, therefore, that when CF_4 is used in the ion source, the dominant etching species is CF_3^+ ions, and that etching by neutral species is less important. This assumption is reasonable in a system which exposes the sample to a collimated ion flux extending far from the ion source, whereas neutral etching species are spread over a wide solid angle upon leaving the source. Since mean free paths are long in the ion beam system, gas phase reactions and loading effects should be negligible.

The CF_4/SiO_2 etch rate curve (Fig. 5) represents the etch rate of SiO_2 by CF_3^+ ions, apart from the undesirable effect of polymer deposition. We can estimate the magnitude of this deposition effect by comparing the etch rates obtained with the single grid (circles) and dual grid system (triangles). Due to differences in open area fraction and beam diameter, the single grid exposes more than three times the area of discharge plasma to substrate line of sight than does the dual grid system. Therefore the deposition flux should differ by at least a factor of three for these two measurements. With this in mind, we can estimate that if polymer deposition were completely absent, the CF_4/SiO_2 etch rate should be only slightly higher than the curve obtained with the dual grids.

In the following discussion we will consider the CF_4/SiO_2 etch rate curve obtained with the dual grids to be an accurate measurement of the SiO_2 etch rate by CF_3^+ ions. The CF_4/SiO_2 etch rates measured here are consistent with SiO_2 etch rates obtained in glow discharge RIE (9) when reasonable assumptions are made for ion energy and current density, which are not directly measurable in RIE. Also, recent etch rate measurements of SiO_2 in ion beams of other fluorocarbon gases are in good agreement with the results presented here. Meusemann (8) reports SiO_2 etch rates in CHF_3 and in $CF_4 + 4\%O_2$ giving etching yields of about 3.1 atoms/ion at 1000 eV, in agreement with Fig. 5. Horiike et al. (10) report SiO_2 etch rates in C_2F_6 over a range of ion energies, but give no values of ion current density. Using Eq. (1) we can estimate the values used, and arrive at etching yields consistent with Fig. 5. The general agreement between etching yields of SiO_2 in different fluorocarbon gases supports our interpretation that the main etching species in these cases is the CF_3^+ ion. Step edge profiles shown in references (8) and (10) are also nearly vertical, with no trenching.

B. Model of Ion Enhanced Chemical Etching

The etch rate of SiO_2 using CF_4 is significantly higher than with argon because of the combined effect of ion bombardment and chemical etching. In RIE, much progress has been made in understanding the etching effects of neutral radicals (F, CF_3), reactive ions (CF_3^+) and the role of ion bombardment (4,9). However, experiments with finely focused ion beams (4) are not easily extended to low ion energy and large sample areas, and studies in glow discharge RIE systems (9,11) lack direct measurements of ion energy and current density on which to base a model. Low energy RIBE is a more well-defined process, in which ion energy and flux are easily measured and controlled, allowing us to model the effects of ion bombardment in chemical etching.

In this section we introduce a quantitative parameter which characterizes the effect of ion bombardment in enhancing chemical etching. To describe this parameter, we focus on the CF_4/SiO_2 etching yield curve of Fig. 5. This curve is shown schematically in Fig. 8 as y_n, the net etching yield, which is made up of three components:

1) A physical sputtering yield, y_s

This component is the etching yield due to sputtering by CF_3^+ ions. Since the CF_4/Si, Ar/SiO_2 and Ar/Si yields are close, we expect the sputtering component of the CF_4/SiO_2 etching yield to be similar to these curves.

2) A residual chemical etching yield, y_r

This component requires only low energy ion impact (< 20 eV) and not sputtering. Its magnitude is given by the extrapolated zero-energy intercept of the CF_4/SiO_2 curve and equals approximately 0.4 atoms/ion. Considering the F atom content of CF_3^+, the maximum etching yield of SiO_2 by purely chemical etching is 2.25 atoms per CF_3^+ ion, as described earlier. This value is labeled by an asterisk in Fig. 5 and is indicated by y_c in Fig. 8. Therefore the residual chemical etching yield y_r is well below its potential value of y_c. If the residual chemical etch rate were at its maximum, the sum of this value plus the physical sputtering yield would be the curve ($y_s + y_c$) in Fig. 8. This curve represents the maximum

yield possible due to both sputtering and chemical etching, assuming no other etching species are present.

3) An ion enhanced chemical etching yield, y_i

After subtracting the residual chemical etching component y_r and the sputtering component y_s from the net CF_4/SiO_2 etching yield y_n, there remains a component which is the ion enhanced chemical etching yield y_i. This component increases with energy in a manner similar to the sputtering component y_s, and is approximately a multiple of y_s at low energy. At an energy E_1, y_i reaches a value of $(y_c - y_r)$. Above E_1, y_i remains constant, indicating that ion enhancement of the chemical etching process has saturated. At high energy, therefore, the net etching yield follows the sum of the sputtering yield y_s and the maximum chemical etching yield y_c.

The energy dependence of these etching yields suggests the following interpretation of ion enhanced chemical etching. Ion impact increases the reactivity of the chemical etching process from a low value at low energy (< 20 eV) to its full value at some high energy E_1. Above this ion energy the CF_4/SiO_2 etching yield should follow the curve $(y_s + y_c)$. The data of Fig. 5 show that below 500 eV the CF_4/SiO_2 etching yield rises rapidly with energy, as does y_n in Fig. 8. Above 500 eV the CF_4/SiO_2 etching yield follows a similar slope to the Ar/SiO_2 curve. Although the Ar/SiO_2 curve cannot be equated directly to the sputtering component y_s of CF_4/SiO_2 etching, they are expected to be very similar. Therefore, above 500 eV the CF_4/SiO_2 etching yield follows the sum of a sputtering component and the maximum chemical etching yield (the asterisk in Fig. 5).

The physical picture is that in CF_3^+ etching of SiO_2 the rate of formation of volatile etch products is limited by the number of active sites available on the SiO_2 surface. This point is confirmed by a low value of the residual chemical etching yield y_r. The creation of more active sites adds to the chemical etching yield a contribution proportional to the number of additional sites. Physical sputtering creates active surface sites by removing atoms and creating surface defects. We expect the number of additional sites to be approximately proportional to the sputtering yield, or equivalently to the sputtering component of the CF_4/SiO_2 etch rate, y_s. It is therefore reasonable that the ion enhanced chemical etching component y_i be a multiple of the sputtering component y_s, at least at low ion energy where the enhancement has not saturated. The multiplying factor is the ratio of the slope of the net etching yield curve y_n to the slope of the sputtering component y_s. We define this ratio as the ion enhancement parameter p. The parameter p gives a quantitative measure of the ion enhanced chemical etching process. From the CF_4/SiO_2 and Ar/SiO_2 etching yield curves of Fig. 5 we obtain values of the parameter p as a function of energy. These results are shown in Fig. 7. A value of p=2 (at 300 eV, for example), means that in addition to residual chemical etching, each departing sputtered atom (Si or O) leaves behind enough active sites to cause on the average one additional atom to be removed by chemical etching (formation of volatile products). The enhancement parameter p shows a high value at low energy, decreasing to unity above about 500 eV ion energy. Since the shape of the low energy portion of the CF_4/SiO_2 etching yield curve is not precisely known, the energy dependence of p in Fig. 7 should be regarded as a trend. We find that the enhancement of chemical etching by ion bombardment saturates at an ion energy E_1 of approximately 500 eV.

The energy dependence of the ion enhancement parameter p (Fig. 7) illustrates several phenomena. At ion energies below E_1, ion impact has a multiplicative effect on the etching yield. Ions in the range of 100 – 200 eV are effective at stimulating additional chemical etching, and the ratio of the net etching yield to the sputtering yield is high. Above E_1, at 500 – 1000 eV, chemical etching has been increased to its maximum effectiveness, and individual ions do not have as great a multiplicative effect on the etching yield. The yield becomes the additive sum of sputtering plus maximum chemical etching. The energy E_1 is consistent with CF_3^+ ions penetrating the SiO_2 surface, dissociating and depositing their energy within the top few layers. This process generates maximum chemical reactivity, whereas at lower energies the

molecular ion would dissociate on the surface, but active sites may not be available to complete the reaction with the substrate.

Having measured the enhancement parameter p for a given ion/material combination, we can now choose an energy for ion beam etching which optimizes the ratio between chemical etching and sputtering. For example, in etching a vertical structure as shown in Fig. 6b, it is important to minimize the sputtering component of etching to reduce mask erosion and redeposition of sputtered material. Simultaneously, the chemical etching component should be maximized to gain highly anisotropic etching. From Fig. 7 it looks most attractive to carry out the etching at the lowest ion energy, where the enhancement parameter p is maximized. However, at very low energy the net etching rate may be too low for practical applications (Fig. 5). An optimum etching energy would be closer to E_1, around 300 – 500 eV for CF_4/SiO_2. Here the net etching yield is high, and the etching yield ratio between chemical etching and sputtering is still high. Little would be gained by increasing the ion energy above 1000 eV, because the net etching yield does not increase significantly, while the sputtering yield rises by more than a factor of two. The ratio between the net etching yield and the sputtering yield (Fig. 7) decreases gradually as the ion energy is increased above E_1. High ion energy sacrifices selectivity while generating more substrate damage. Similar considerations apply to applications in which a reactively etched film is to be removed down to an underlying nonreactive substrate. Here again, the sputtering yield should be minimized to avoid overetching, and an energy near E_1 would be optimum for high selectivity combined with short etching time.

We have demonstrated that low energy ion beam etch rate measurements give quantitative information on the process of reactive ion etching. From the energy dependence of etching yields, an ion enhancement parameter p is obtained which characterizes the effectiveness of ion bombardment in stimulating chemical etching. This parameter guides the choice of the optimum ion energy for practical RIBE applications.

For low energy ion beam etching, the single grid modification to a broad beam ion source can be used to obtain high ion current density at low ion energy. This capability extends practical ion beam etching down to tens of eV. In addition to the application to RIBE discussed in this paper, such low energy ion bean etching is appropriate for surface cleaning applications prior to thin film deposition, or in conjunction with analytical techniques where surface damage is to be minimized.

ACKNOWLEDGMENTS

The authors thank D. Irmischer, D.L. Goldman and G.A. Waters for help in carrying out etch rate measuremnts, J.L. Speidell for preparation of step edge test wafers, and C.F. Aliotta for electron microscopy. We also thank J.W. Coburn for helpful discussions.

REFERENCES

1. H.R. Kaufman, J. Vac. Sci. Technol. *15*, 272 (1978).
2. H.R. Kaufman, J.M.E. Harper, J.J. Cuomo, J. Vac. Sci. Technol. *16*, 899 (1979).
3. P. LeVaguerese and D. Pigache, Rev. Phys. Appl. *6*, 325 (1971).
4. J.W. Coburn, H.F. Winters and T.J. Chuang, J. Appl. Phys. *48*, 3532 (1977); J.W. Coburn and H.F. Winters, J. Vac. Sci. Technol. *16*, 391 (1979)
5. R.S. Robinson, J. Vac. Sci. Technol. *16*, 185 (1979).
6. S. Somekh, J. Vac. Sci. Technol. *13*, 1003 (1976).
7. R.E. Lee, J. Vac. Sci. Technol. *16*, 164 (1979).
8. B. Meusemann, J. Vac. Sci. Technol. *16*, 1886 (1979).
9. G.C. Schwartz, L.B. Rothman and T.J. Schopen, J. Electrochem. Soc. *126*, 464 (1979).

10. Y. Horiike, M. Shibagaki and K. Kadono, Jap. J. Appl. Phys. *18*, 2309 (1979).
11. J.L. Mauer, J.S. Logan, L.B. Zielinski and G.C. Schwartz, J. Vac. Sci. Technol. *15*, 1734 (1978).

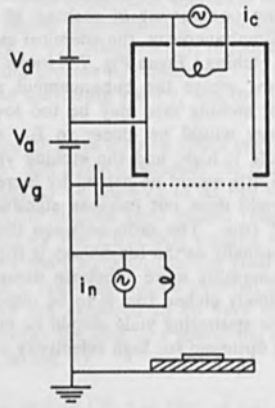

1. Diagram of single grid ion source, showing cathode current i_c, discharge voltage V_d, anode voltage V_a, grid voltage V_g, neutralizer current i_n and sample on a grounded holder.

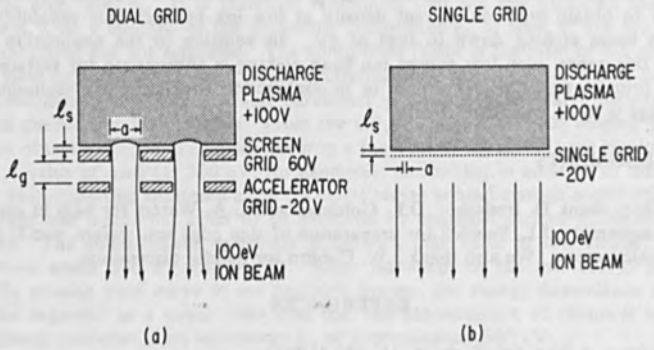

2. Comparison of the extraction grid region of (a) dual grid ion source and (b) single grid ion source, showing the grid aperture diameter a, discharge sheath thickness l_s, grid spacing l_g, and potentials typical for generating a 100 eV ion beam.

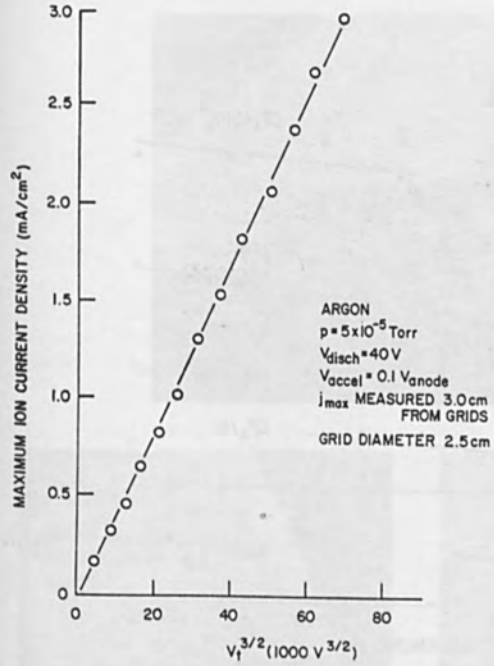

3. Maximum current density obtained from a dual grid ion source as a function of $V_t^{3/2}$, illustrating the space charge limit on current density. V_t is the potential difference between the two grids.

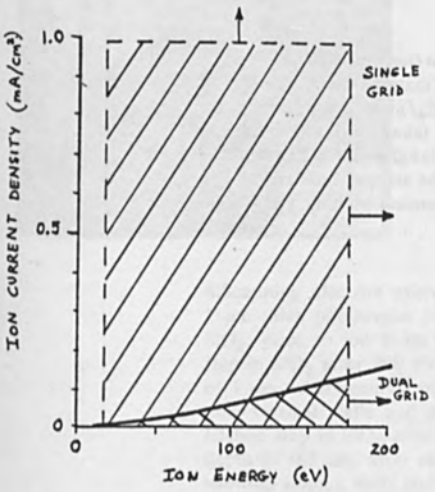

4. Comparison of the low energy operating range of the single grid and the dual grid ion source.

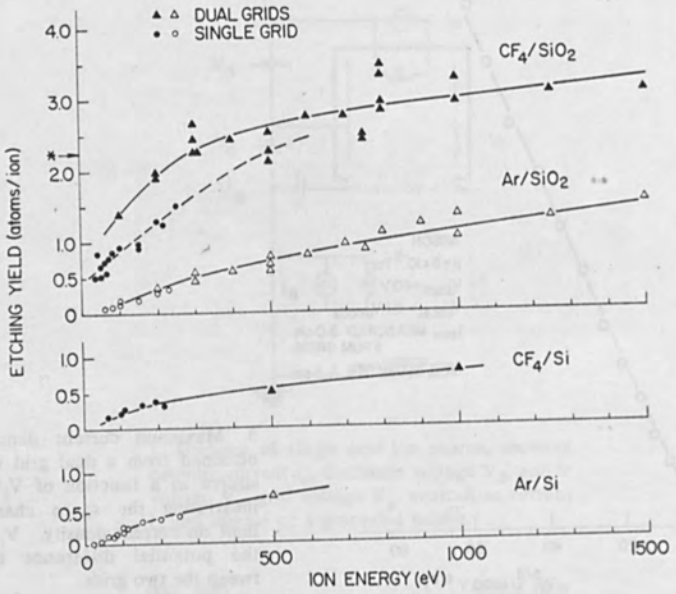

5. Etching yields (atoms/ion) as a function of ion energy for four ion/material combinations: CF_4/SiO_2, Ar/SiO_2, CF_4/Si and Ar/Si. Circles are measurements taken with the single grid ion source, and triangles are taken with the dual grid system. The asterisk indicates the maximum CF_4/SiO_2 chemical etching yield of 2.25 atoms/ion.

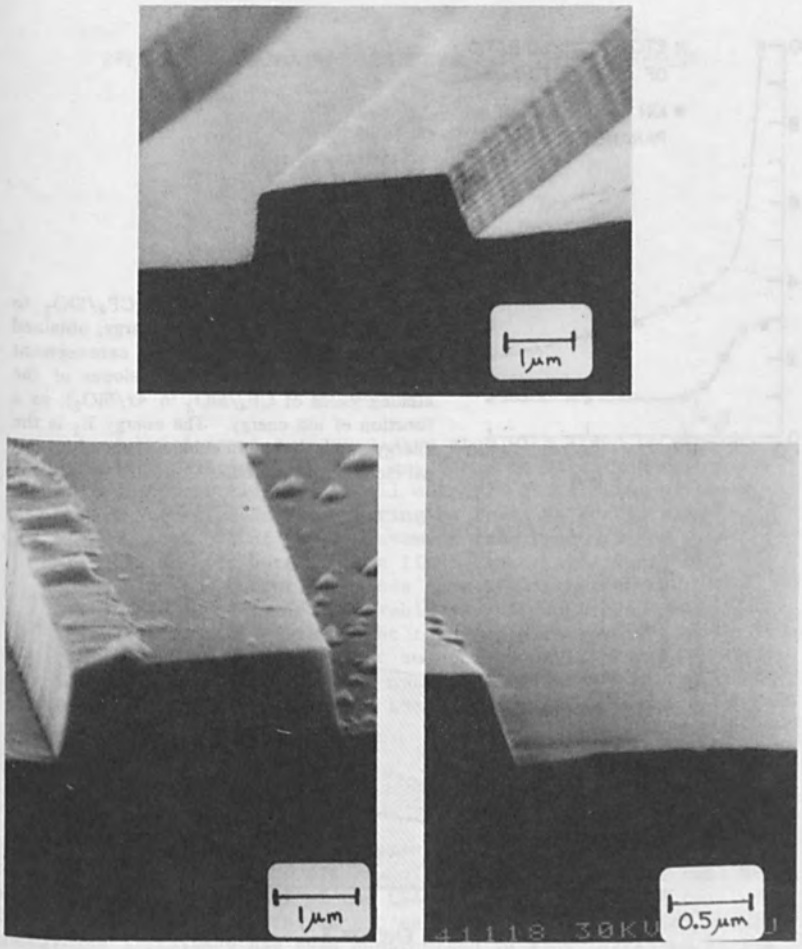

6.Scanning electron micrographs showing: (a) 1 μm thick photoresist pattern on 1 μm thick SiO_2, prior to ion beam etching. (b) Etched step in SiO_2 after 200 eV CF_4 etch to a depth of 1 μm, after removal of photoresist, showing near-vertical walls and polymer residue. (c) Etched step in SiO_2 after 500 eV Ar etch to a depth of 0.5 μm, after removal of photoresist, showing sloping walls and shallow trench.

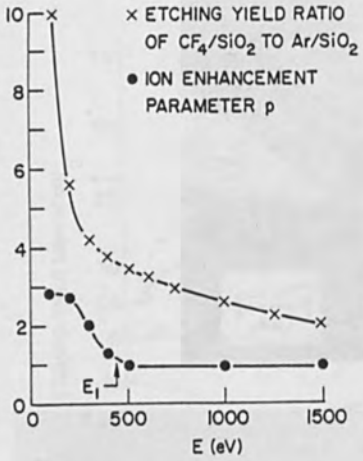

7. Ratio of etching yields of CF_4/SiO_2 to Ar/SiO_2 as a function of ion energy, obtained from data of Fig. 5, and the ion enhancement parameter p (the ratio of the slopes of the etching yields of CF_4/SiO_2 to Ar/SiO_2), as a function of ion energy. The energy E_1 is the energy at which the ion enhancement of chemical etching is saturated.

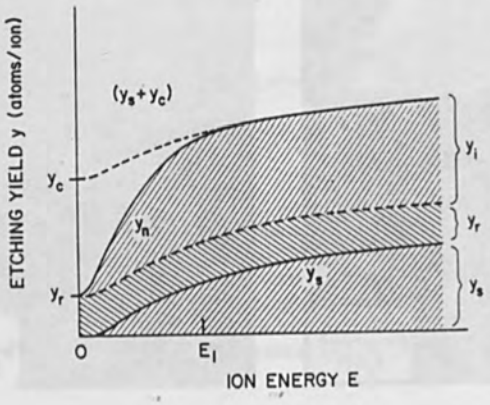

8. Schematic diagram of the components involved in RIBE. y_s is the physical sputtering yield, y_r is the residual chemical etching yield, y_i is the ion enhanced chemical etching component, y_c is the maximum chemical etching yield, and y_n is the net etching yield. The energy E_1 is indicated, at which point the ion enhancement of chemical etching is saturated.

EFFECTS OF PLASMA ETCHING SOLAR CELL FRONT SURFACES

W. E. Taylor
S. M. Bunyan
Spectrolab, Inc.
12500 Gladstone Avenue
Sylmar, CA 91342

C. E. Olson
Jet Propulsion Laboratory
4800 Oak Grove Drive
Pasadena, CA 91103

ABSTRACT

A brief front surface plasma etch with Freon 14 + 8% O_2 or sulfur hexafluoride (SF_6) was found to significantly improve terrestrial solar cell output. SEM studies of these samples revealed surface pitting on Freon 14 etched samples. About 50% of the improvement from Freon etched samples can be attributed to the light capturing effects of surface pits. Output increases from SF_6 plasma etched cells were found to be comparable with freon etched cells after subtraction of the light trapping effects. The excess output improvement might be attributed to reduced junction depth or removal of near surface lattice damage. Investigations attempting to identify the cause will be described.

Introduction

This paper describes development work done at Spectrolab for the JPL-LSA program on the effects of plasma etching solar cell front surfaces. The main thrust of the LSA-JPL program has been to develop a low-cost fabrication process for terrestrial solar modules. Conversion efficiency has been compromised in many instances by the introduction of low-cost processes which decrease cost per peak watt. The replacement of evaporated metal contacts by screen printing technology is one example (1).

With evaporation, a chromium (or titanium)-palladium-silver front contacts system is normally applied. Chromium (or Ti) forms an ohmic contact, and palladium renders the system humidity resistant. If silver sintering is necessary they also form a barrier to silver diffusion into silicon. This allows the use of shallow junctions (.1 μ) which optimize cell spectral response, especially in the

blue-violet region (.45 to .6 μ). With screen printing, however, appreciable current leakage is observed with shallow (.1 μ) junctions. A deeper junction (> .3 μ) is needed to reduce electrical shunting through the junction.

Improved cell performance would result if the junction depth were reduced after the sensitive cell processing steps and before AR coating. Wet chemical etching of contacted wafers to provide a shallower junction is not satisfactory due to non-uniform etching and damage to the metal contacts by the etchant. Dry ion, "plasma", etching can be used to accomplish this goal without incurring the deficiencies of wet chemical etching.

A brief plasma etch was found to significantly improve solar cell output. This improvement might be attributed to one or more of the following: reduced junction depth, reduced impurity scattering absorption, surface pitting, or removal of near surface lattice damage. Investigations attempting to identify the cause will be described.

Freon Etching Experiments

A mixture of Freon 14 + 8% oxygen was used to etch the front surface of a series of finished, non-AR coated solar cells. The etch rate of single crystal (100) silicon with Freon 14 + 8% oxygen at a power level of 100 watts was measured and found to be approximately 1800 Å per minute. Cells were etched from 12 to 240 seconds in a Tegal Plasmaline 100 plasma etcher. The RF power supply was held at 100 watts forward power and 1-2 watts reflected power for all runs. Current-voltage (I-V) curves were taken before and after each run. An increase in output was seen in the first cell etched for 12 seconds. Short circuit current increased 30 mA and open circuit voltage decreased 10 mV. All but the first cell were severely degraded by the etching process. Cells etched for longer times had a gray to bluish film. I-V curves for 12 second and 24 second etching are shown in Figures 1 and 2.

A second experiment was performed in which cells were plasma etched 3 to 24 seconds at 3 second intervals. Cells etched in the range of 12 to 18 seconds showed significant improvement in short circuit current (I_{sc}) and current at load (I_{450}) (Figure 3) with no change in open circuit voltage.

The amount of material removed from the front surface (300-500 Angstroms) suggested that the improvement may come from elimination of minority carrier recombination losses by removal of the "dead layer". However, the replacement of dead layer recombination processes by surface recombination processes makes this interpretation somewhat unlikely.

Spectral response measurements taken before and after plasma etching the cells reported in Figure 3 are shown in Figure 4. In all cases cell response to wavelengths between .4 μ and 1.5 μ increased, with the greatest percent increase seen at .65 μ to .75 μ (Figure 4). The greatest increase was seen in the red rather than in the blue which was not supportive of the dead layer hypothesis.

In the first experiment it had been observed that long etch times produced a blue stain. This observation suggested that long wavelength effects might be due to an antireflective stain or plasma etch induced surface pits acting as light traps. The cells used in the second experiment (Figure 3) were subsequently AR coated with evaporated silicon monoxide (SiO). The normal expectancy is that this treatment will increase short circuit current by 35%. The observed increases are shown in Figure 5. It will be seen that the antireflective coating enhancement of I_{sc} decreased by an increasing amount as the plasma etch time increased. This observation is consistent with the AR hypothesis.

However, the combined enhancement of I_{sc} due to plasma etching and AR coating exceeded 35% over much of the range of etching times which were used (Figure 6). For example at 15 seconds etch time combined enhancement is 44% (28% for AR coating plus 16% for plasma etching). The excess of 9% over the normal 35% enhancement must be attributed to front surface phenomena (other than pitting) influenced by the etching process.

These phenomena could include a pre-etch passivation layer which might arise from high temperature sintering or diffusion processes. Plasma etching would remove the passivation layer increasing surface recombination velocity, decreasing cell output and thus accounting for the initial dip in the curve of Figure 6. Output gains from junction depth shallowing may then overcome this effect as etch time increases (Figure 6; > 10 sec.).

Sulfur Hexafluoride Etching Experiments

The etching experiments were repeated with sulfur hexafluoride as the reactive agent. The SF_6 plasma etch rate of (1-0-0) silicon was found to be 900-1000 Å/min. as determined by step etching and step measurement with a Talysurf profilometer. A series of 12 finished cells were etched 6 to 90 seconds. Short circuit current and load point current (500 mV) were measured before and after each run. The results showed maximum cell performance improvement (approximately 12% after a 60 second etch (Figure 7).

Spectral response measurements performed before and after plasma etching are shown in Figure 8. A significant I_{sc} increase was seen at long wavelengths as well as short wavelengths. If reduced junction depth were the only cause, the greatest spectral response increase would be seen at short wavelengths.

Output increases from SF_6 plasma etched cells were found to be comparable with Freon etched cells after subtraction of the light trapping effects of the surface pitting for the latter. By comparing device output gains at equivalent amounts of material removed for both etchants, an assessment was made of the pitting contribution to observed short circuit current improvement for Freon 12 + 8% O_2 etched samples. After 500 Å were removed ($\sim$ 35 seconds SF_6 etch time) a 6% I_{sc} enhancement was seen as compared to 15% for Freon 14 + 8% O_2 etched samples. About 9% of the improvement with Freon 14 + 8% O_2 can therefore be attributed to surface pits acting as light traps, a result consistent with the previously noted observation on the effectiveness of AR coating these samples.

Comparison of F_{14} and SF_6 Etching

Freon 14 + 8% O_2 plasma etched samples were compared with sulfur hexafluoride etched samples using a scanning electron microscope. Three groups of wafers were fabricated for the experiment. The first group was P type, 1-3 ohm-cm material that had only been given the standard 30% NaOH surface etch. These wafers were kept as the controls. The second group of wafers were also P type, 1-3 ohm-cm material that had been given the standard surface etch, but these wafers were further subdivided and plasma etched for five and ten minutes in Freon 14 + 8% O_2 and SF_6. The third group of wafers were chemically etched P type, 1-3 ohm-cm material that had been diffused with phosphorus. These wafers were also etched for five and ten minutes in Freon 14 + 8% O_2 and SF_6. These samples were examined with a scanning electron microscope, and photos were taken (Figures 9-13). The white spots appearing on these photos were shown by EDAX measurements to contain iron. This residue is a suspected corrosion product of the plasma etch platen. Careful examination of all samples showed the iron compound to be nonuniformally distributed over the sample. This explains the absence of contaminants on some photos.

Comparison of both diffused and non-diffused samples plasma etched with SF_6 or Freon 14 + 8% O_2 revealed dramatic differences. Most notable were the large pits on Freon 14 + 8% O_2 etched samples which do not appear on the relatively smooth SF_6 etched wafer surface.

Phosphorus diffused samples etched with Freon 14 + 8% O_2 appear to have larger pits than non-diffused wafers (Figures 9 and 10). Surface damage and near surface phosphorus precipitates formed during diffusion may enhance the plasma etch induced pitting action. Precipitates removed during etching could leave voids which may broaden and deepen with further etching. Pitting enhancement was not apparent on SF_6 etched wafers.

Pitting may cause current leakage (shunting) in cells plasma etched to shallow the junction region. A series of non-contacted cells were plasma etched 3-48 seconds in CF_4 + 8% O_2 and SF_6. Evaporated contacts were applied and shunt resistance measurements (R_{sh}) were taken. All samples were etched under standard plasma etching conditions at room temperature and at a chamber pressure of less than one torr. Observed shunt resistances are reported in Table 1. Cells etched 3 to 24 seconds in SF_6 showed R_{sh} readings comparable with unetched controls. Low R_{sh} readings were taken from cells etched more than 24 seconds. CF_4 + 8% O_2 etched samples were lower by approximately 7000-8000 ohms. This result is consistent with observed pitting from the Freon 14 + 8% O_2 plasma etch.

Conclusions

Significant improvement in solar cell output may be gained by a brief sulfur hexafluoride plasma etch. Investigations indicate that reduced junction depth partially accounts for output increases. Experiments further suggest that application of a suitable post etch surface passivation would reduce losses due to a high post etch surface recombination velocity. Further experimentation will provide a better understanding of these effects, and may influence future device design and fabrication.

REFERENCES

(1) Mardesich, N., Bunyan, S., Pepe, A., Edwards, B., Olson, C., Proc. 14th IEEE Photovoltaic Specialists Conference 1980, "Low Cost Photovoltaic Cell Process Based on Thick Film Techniques."

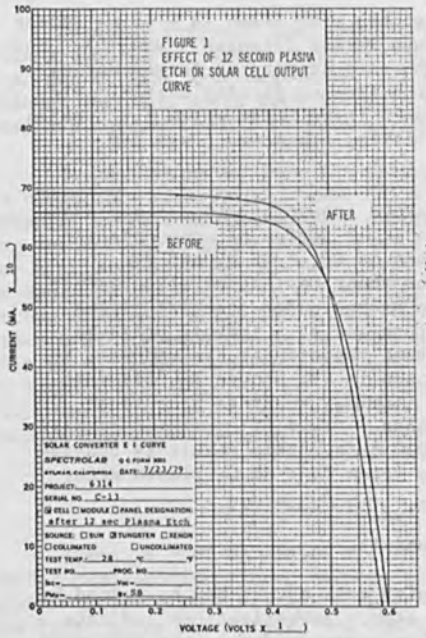
FIGURE 1
EFFECT OF 12 SECOND PLASMA ETCH ON SOLAR CELL OUTPUT CURVE
AFTER
BEFORE
CURRENT (MA. X 10)
VOLTAGE (VOLTS X 1)
SOLAR CONVERTER E I CURVE
SPECTROLAB
DATE: 7/23/79
PROJECT: 6314
SERIAL NO. C-13
CELL MODULE PANEL DESIGNATION:
after 12 sec Plasma Etch
SOURCE: SUN TUNGSTEN XENON
COLLIMATED UNCOLLIMATED
TEST TEMP: 28 °C
TEST NO. PROC. NO.
Isc= Voc=
Pmp= @ Vmp=

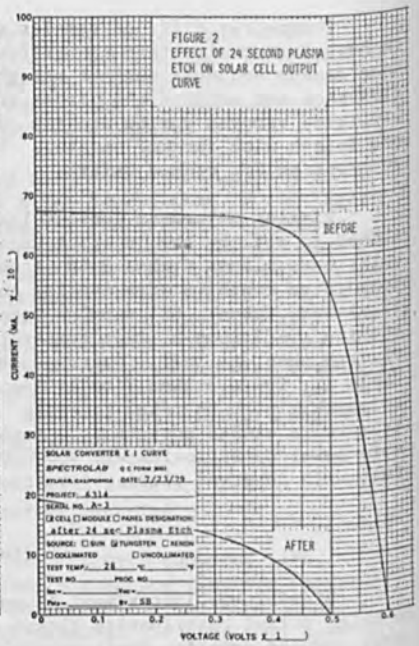
FIGURE 2
EFFECT OF 24 SECOND PLASMA ETCH ON SOLAR CELL OUTPUT CURVE
BEFORE
AFTER
CURRENT (MA. X 10)
VOLTAGE (VOLTS X 1)
SOLAR CONVERTER E I CURVE
SPECTROLAB
DATE: 7/23/79
PROJECT: 6314
SERIAL NO. A-1
CELL MODULE PANEL DESIGNATION:
after 24 sec Plasma Etch
SOURCE: SUN TUNGSTEN XENON
COLLIMATED UNCOLLIMATED
TEST TEMP: 28 °C
TEST NO. PROC. NO.
Isc= Voc=
Pmp= @ Vmp=

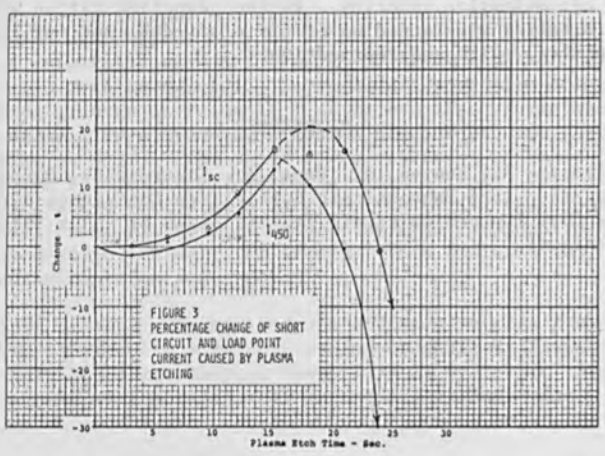
FIGURE 3
PERCENTAGE CHANGE OF SHORT CIRCUIT AND LOAD POINT CURRENT CAUSED BY PLASMA ETCHING
Change - %
Plasma Etch Time - Sec.
Isc
I450

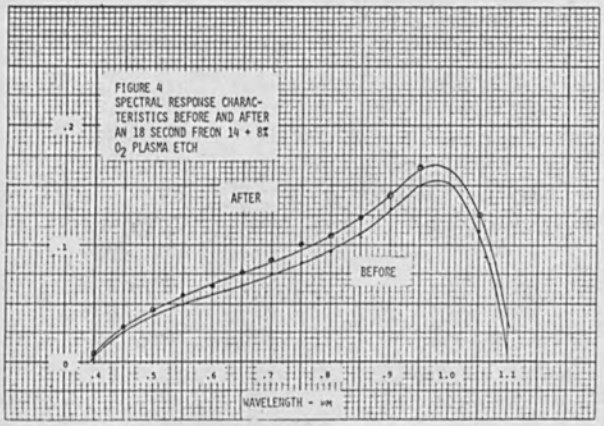

FIGURE 4
SPECTRAL RESPONSE CHARACTERISTICS BEFORE AND AFTER AN 18 SECOND FREON 14 + 8% O_2 PLASMA ETCH

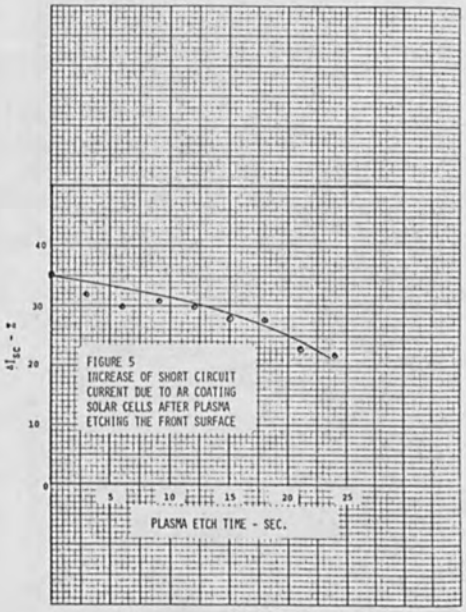

FIGURE 5
INCREASE OF SHORT CIRCUIT CURRENT DUE TO AR COATING SOLAR CELLS AFTER PLASMA ETCHING THE FRONT SURFACE

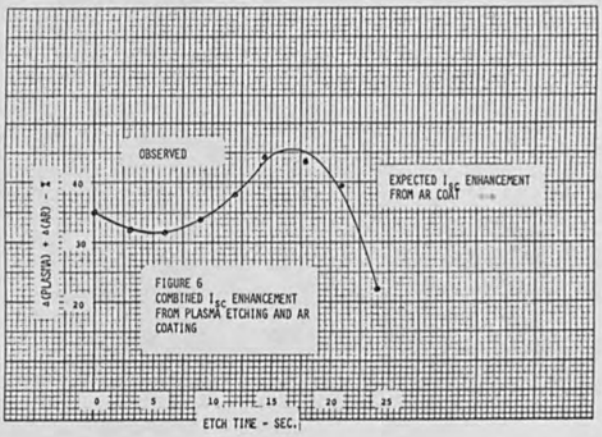

FIGURE 6
COMBINED I_{SC} ENHANCEMENT FROM PLASMA ETCHING AND AR COATING

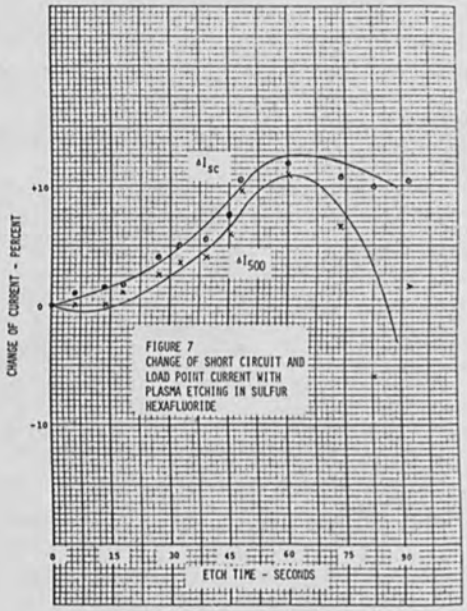

FIGURE 7
CHANGE OF SHORT CIRCUIT AND LOAD POINT CURRENT WITH PLASMA ETCHING IN SULFUR HEXAFLUORIDE

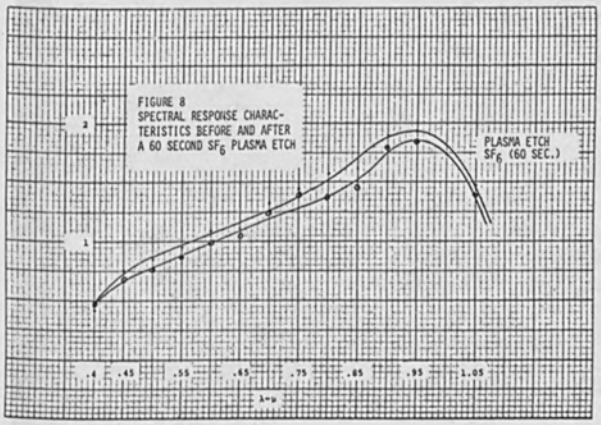

FIGURE 8
SPECTRAL RESPONSE CHARACTERISTICS BEFORE AND AFTER A 60 SECOND SF_6 PLASMA ETCH

TABLE 1

Plasma Etch of Diffusion Oxide

	Etch Time	Sample #	R_{sh} (Ω)
SF_6 (etched)	3 sec.	$1A_1$	16,667
		$1A_2$	10,000
	12 sec.	$1B_1$	8,333
		$1B_2$	12,500
	24 sec.	$1C_1$	12,500
		$1C_2$	1,136
	48 sec.	$1D_1$	3,333
		$1D_2$	225
CF_4+8%O_2 (etched)	3 sec.	$2A_1$	4,545
		$2A_2$	5,000
	12 sec.	$2B_1$	1,087
		$2B_2$	7,143
	24 sec.	$2C_1$	5,000
		$2C_2$	3,125
	48 sec.	$2D_1$	4,545
		$2D_2$	5,555
Control		1	16,000
		2	8,000
		3	10,000
		4	16,667
		Average	12,667

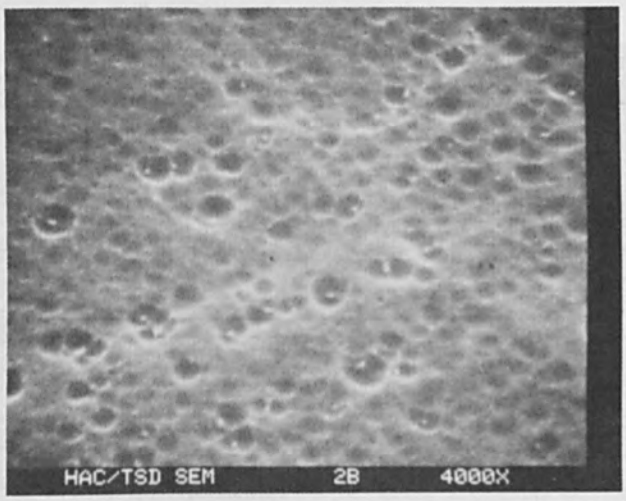

Figure 9. Phosphorus diffusion on boron doped base etched 10 min. with Freon 14 + 8% O_2
Mag. 4000X

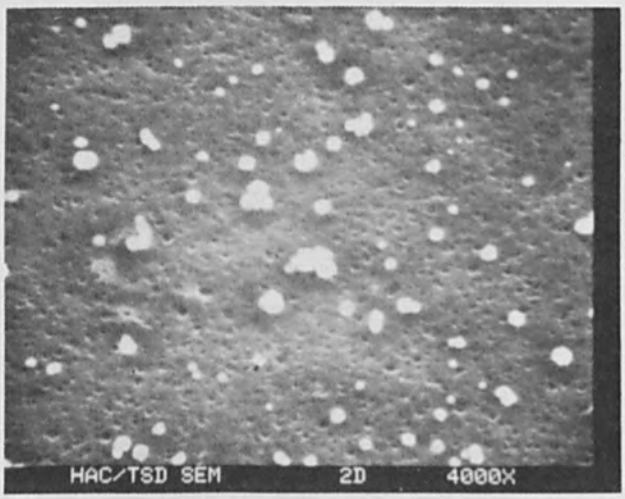

Figure 10. Boron doped base material etched 10 min. with Freon 14 + 8% O_2 at 26°C
Mag. 4000X

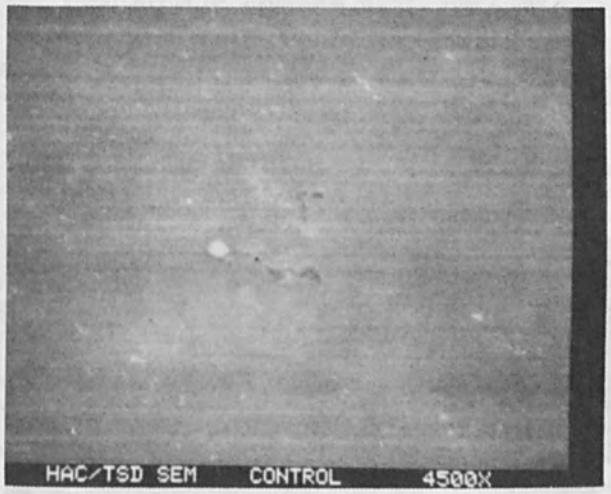

Figure 11. Control sample standard boron doped base given standard 30% NaOH surface etch
Mag. 4500X

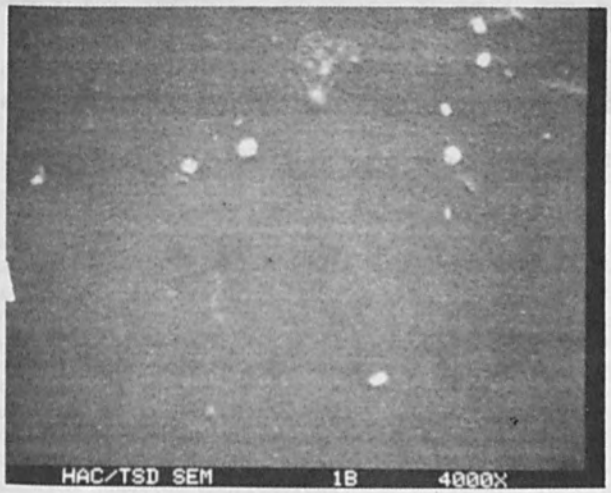

Figure 12. Phosphorus diffusion on boron doped base etched 10 min. with SF_6 at 26°C
Mag. 4000X

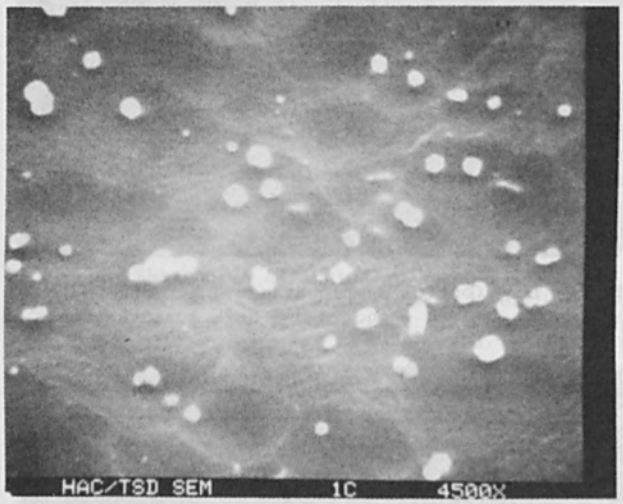

Figure 13. Boron doped base material etched 10 min. with SF_6 at 26°C
Mag. 4500X

FABRICATION OF JOSEPHSON TUNNEL JUNCTIONS BY REACTIVE ION MILLING

Alan W. Kleinsasser and Robert A. Buhrman
School of Applied and Engineering Physics and National Research and Resource Facility for Submicron Structures
Cornell University, Ithaca, New York 14853

A new technique has been developed for growing high quality, ultrathin oxide layers on metal films, suitable for use as tunneling barriers in Josephson junction devices. The oxides are produced with an argon-oxygen ion beam, and the rate of growth is determined by the competition between oxidation and sputtering by the ions. The oxidation technique has been applied to the fabrication of high current density submicron niobium-lead alloy Josephson junctions. High quality junctions have been produced with critical current densities exceeding 10^5 amp/cm^2 and having low leakage currents at voltages below the energy gap. An edge geometry has been developed, allowing in-line junctions to be formed on the ion mill-patterned edge of Nb film. In this way, junction width is controlled by the Nb film thickness.

I. INTRODUCTION

Reactive gases have long been used in sputter deposition and etching (1), and the technique of reactive sputtering has been extended to include reactive ion etching, in which the chemical component of the etching process is emphasized (2). Although these techniques are primarily associated with attempts to enhance etching rates and achieve anisotropic etching for patterning purposes, it is basically a reactive sputtering technique which was introduced by Greiner (3) to fabricate Josephson tunneling barriers on superconducting films.

Ion milling is an extension of the technique of sputter etching and, recently, work has been reported on reactive ion milling (4-9), in which reactive gases are either added to the ion source (4-7) or introduced in the region of the substrate (8,9). Significant enhancement of etching has been reported in organic materials (4) and SiO_2 (5,6,8,9), but results in Si (5,8,9) and metals (7,8) have not been as striking, at least with low accelerator voltages. As with reactive sputtering, reactive ion milling can be used to produce chemical changes on a substrate surface. We have applied this principle to devise a new technique for growing thin oxide films, primarily for Josephson junction applications.

In fabricating Josephson tunnel junctions it is desirable to use a hard material, such as niobium, at least for the base electrode in

order to provide mechanical stability and thermal cyclability. In fact, niobium has become the superconductor of choice for many applications. In most cases, this means that the tunneling barrier will be niobium oxide. Here problems are encountered due to the existence of numerous oxide phases. In addition to Nb_2O_5, which is the desired tunneling barrier, NbO_2, NbO, and various suboxides can form, as can niobium-oxygen mixtures. The presence of these phases can seriously impair junction performance. For example, there is some evidence (10) that the interface between Nb and Nb_2O_5 in thermally grown oxide films consists of NbO and NbO_2, and poor junction quality has been attributed to such layers. Tunnel junctions have been successfully fabricated on Nb using thermal (11) and dc glow discharge oxidation (12,13), however the rf plasma oxidation technique (3) results in the highest current densities (14), an important consideration in high performance junctions.

The rf plasma oxidation method relies upon the competition between oxidation and sputter etching to determine the growth rate of the oxide film. With lead, a steady state thickness is eventually reached, after which the oxide thickness remains constant with time. With niobium, however, good junction quality depends upon oxidizing in a regime in which sputter etching is insignificant (15). Attempts to perform the oxidation with sputter etching present results in the presence of undesirable niobium oxides and poor junction quality (14, 16). In addition, care must be taken as to what materials are present in the vacuum system, since extensive scattering of sputtered material occurs at the gas pressures used.

Ion milling offers a number of advantages over sputter etching. Among them are confinement of the discharge to a region away from the substrates, control of substrate bombardment, and low operating pressures. In an unneutralized argon-oxygen ion beam, only Ar^+, O^+, and O_2^+ are likely to be present, while negative ions are not present in the beam (neutral species are, of course, present in the system). This is in contrast to the rf plasma technique, in which negative ions are thought to be important in the oxidation process (3,15). The mean free path of species in the gas is at least 25 times longer at typical ion milling pressures (2×10^{-4} torr), so that impurity problems resulting from scattering of sputtered material are reduced greatly. No special cleaning or other preparation of surfaces, such as the substrate holder, is necessary, and high quality tunnel junctions can be fabricated in an ordinary vacuum system.

II. FABRICATION

We have used an argon-oxygen beam produced by a commercial Kaufmann type ion beam source (17) as a means of growing niobium oxide films. Fabrication proceeds as follows: A niobium film is deposited on a sapphire or glass substrate by rf bias sputtering. A

typical film has a resistance ratio (R_{300K}/R_{10K}) exceeding 3 and a transition temperature of 9.2K. The niobium film is patterned by chemical etching and ion milling using a photoresist mask. The counterelectrode pattern is then defined by photolithography. The film is placed in the ion beam system (the vacuum system is a diffusion-pumped bell jar system with a liquid nitrogen trap. Typical base pressure is around 10^{-6} torr) and cleaned in a low current density (.15 mA/cm^2) neutralized argon beam (acceleration voltage: 600V, Ar pressure: 2×10^{-4} torr in chamber). Oxygen (1×10^{-5} - 1×10^{-4} torr) is then admitted to the ion source, and oxidation is carried out at a reduced current density (5 - 150 μA/cm^2) in an unneutralized beam for a time of less than 1 minute. The counterelectrode, ε-phase Pb-Bi (18,19) is then immediately deposited. The substrate table is cooled by liquid nitrogen throughout the entire procedure. The counterelectrode is patterned by liftoff. The completed junction is protected by a layer of Kodak photoresist.

Junction areas can easily be reduced by at least a factor of 10 by using an edge geometry, in which the thickness of a thin film defines one of the junction dimensions (20-22). In our technique, edges are defined by coating a portion of the Nb counterelectrode with a film of Al_2O_3, which is ion beam deposited in an argon-oxygen atmosphere. Ion milling is then used to form the edge (Fig. 1). The counterelectrode overlaps the Nb, but can only make contact at the edge, since the Nb top surface is protected by the Al_2O_3 film (Fig. 2). The resulting devices had areas of 1-2μ x .1-.2μ. The characteristics of these junctions were essentially identical to those of the simple overlap junctions described above, although the thickness of oxide formed on an edge was found to be less than that formed on top of a film, for a given set of oxidation parameters.

III. OXIDATION

The ion beam oxidation method, like the rf plasma technique, involves, in principle, simultaneous sputter etching and oxide growth. However, the etching rate for Nb in the ion beam system with a beam current of .15 mA/cm^2 is approximately .12 Å/sec. The etch rate of Nb_2O_5 is significantly lower than that of Nb. For ion beam oxidation, the current density is usually kept between 5 and 30 μA/cm^2 for best results. A typical oxide barrier (thickness approximately 20 Å) is grown in less than a minute. Thus sputter etching of the oxide is thought to be insignificant.

Preliminary experiments have been performed in which lower oxygen pressures were used in an attempt to enlarge the role of sputter etching in the process. The IV characteristics of junction obtained in these runs exhibited large (subgap) leakage currents. This is in general agreement with results obtained with the rf plasma method (15). These conclusions are only tentative, however, and experiments have

been planned to pursue these studies in a better vacuum system, in which background gases can be better controlled.

The system parameters which determine the final oxide thickness include, among others, oxygen pressure, beam current density, and oxidation time. Other possible influential variables, such as accelerator and discharge voltages and argon pressure, were held constant in these experiments. The behavior of oxide thickness (as determined by junction resistance or current density), as a function of changes in these parameters, was observed to be reproducible, but did not show any simple form. Increases in oxygen pressure, beam current density, and oxidation time all brought about significant changes in final oxide thickness, but oxide thickness was not in simple proportion to ion dose.

There are two sources of oxygen which contribute to the growth of the oxide film: positive oxygen ions from the beam and neutral gas which is not ionized in the discharge chamber. The film will adsorb neutral oxygen (the time necessary to adsorb a monolayer is of order 10^{-2} sec at a pressure of 10^{-4} torr), and the ion beam supplies energy which can help react adsorbed oxygen. In addition, the ion beam can cause ionization of neutral gas atoms. In order to grow an oxide film, the oxygen must be transported through the growing film to the metal-oxide interface. The energy supplied by the beam can also affect this process.

Estimates of the contribution of the oxygen ions in the beam to the oxide growth reveal that it is an important factor, but that there are insufficient ions present in the beam to account for the total oxide thickness. Adsorbed neutral oxygen, reacting with the aid of energy supplied by the beam would explain the difference. Experiments are being considered which would use an ion mill system in which a larger ratio of pressure in the ion mill discharge chamber to bell jar pressure could be maintained. This would result in a smaller neutral oxygen concentration in the substrate region, enhancing the effect of the beam, and allowing greater control of the process.

The ion beam contains both argon and oxygen. It is difficult to even guess at the proportions. Negative oxygen ions play a prominent role in argon-oxygen discharges (15), and are believed to be important in rf plasma oxidation (3), but they are not extracted by the grids of the ion mill. Heats of formation of positive oxygen ions (O^+, O_2^+) are similar to that of argon ions, but larger than those of negative oxygen ions (O^-, O_2^-) (15). The use of a mass spectrometer to probe the makeup of the beam would help to clarify the situation. The use of a pure oxygen beam would remove the complicating effects of the argon ions, but would also speed up oxidation. With niobium, the argon is needed at least as a dilutant (3,15) because niobium tends to oxidize rather easily.

In principle, thermal oxidation involving the neutral oxygen

could play a role in the oxide growth. The influence of thermal oxidation, unaided by the ion beam, was investigated by fabricating junctions using oxygen at pressures typical to ion milling, but without the ion beam. The resulting current-voltage characteristics showed critical currents well in excess of 10^6 amp/cm^2 with no features associated with tunneling. Therefore, we conclude that thermal oxidation plays no significant role in the process.

IV. JUNCTION PROPERTIES

The principal aim of this work was the construction of small, high current density niobium Josephson devices. The motivation behind this was the fact that the hysteresis parameter β (23) is inversely proportional to critical current density. For most applications, a low β (non-hysteretic IV) is desirable. We felt it important to investigate the limits of high current density for niobium oxide barrier junctions. We have attained critical current densities as high as 6.5×10^5 amp/cm^2. For such a junction, the calculated value of β is approximately 0.2, while the observed ratio of lower switching current to critical current was .61. Experiments are in progress to investigate still higher critical current densities, the effect of the non-equilibrium state induced by extremely high quasiparticle injection, and the usefulness of external resistive shunting to remove hysteresis completely in these junctions.

Junctions with moderate critical current densities (below about 10^4 amp/cm^2) were characterized by very small currents at voltages below the sum of the energy gaps. A typical current-voltage characteristic is shown in Figure 3. From the structure at the difference of the energy gaps and the steep rise at the gap sum, it was determined that Δ_{Nb} and $\Delta_{Pb\text{-}Bi}$ were 1.5 and 1.7 meV, respectively, in agreement with accepted values. (Note: All reported measurements were taken at 4.2K. Nb and Pb alloy transition temperatures were 9.2 and 8.4 K.) Using these values, the product of critical current (I_C) and normal state resistance (R_N, taken to be the dynamic resistance for voltages well above the gap) is predicted to be 2.5 mV at T=0 (24). Typical observed $I_C R_N$ products were in the range 1.5-1.8 mV. The product $\Delta I\ R_N$, where ΔI is the size of the step at the sum of the energy gaps, was typically 2.5 mV. The quasiparticle current at subgap voltages, when fitted to a straight line, yields a characteristic resistance R_J. Ratios R_J/R_N larger than 20 and products $I_C R_J$ as high as 30 mV were obtained with junctions having critical current densities of 10^3 amp/cm^2.

For junctions with critical current densities approaching or exceeding 10^4 amp/cm^2, the hysteresis in the current-voltage characteristic was reduced as critical current density increased. The current-voltage characteristic for such a junction is shown in Figure 4. The hysteresis parameter (23), from the resistively shunted junction model, provides an indication of the degree of hysteresis expected. Realiz-

ing that $I_C R_N$ is a characteristic of the materials used, we express β as:

$$\beta = \frac{2\pi}{\phi_o} (I_C R)^2 \left(\frac{\varepsilon \varepsilon_o}{J_C w}\right),$$

where J_C is the critical current density, w is the oxide thickness and ε is the relative dielective constant of the oxide. (Since capacitance increases linearly as oxide thickness decreases, while critical current increases exponentially, β is decreased by going to high current densities.) Using values of ε and w extrapolated from work on junctions fabricated using the rf plasma method (25), we obtained values of β, for junctions having critical current densities of 10^4 and 10^5 amp/cm^2, of 9.2 and 1.0. Comparison of experimental data with model calculations which include the nonlinear quasiparticle characteristic (26) yielded satisfactory results.

Results for thermally cycled junctions (room temperature to 4K and back to room temperature) were quite satisfactory. Some of the junctions were cycled up to eight times over a period of weeks with only very small changes in resistance and essentially no qualitative change in quasiparticle characteristic. Extensive cycling and lifetime tests have not been performed, however, good thermal cyclability of Nb/Pb junctions has been noted by other workers (27), and the superior properties of the ε phase of Pb-Bi (as compared to other Pb alloys) have recently been reported (19).

Although our experimental set-up was not conducive to study of the uniformity of the process (i.e., variation from run-to-run in critical current density or other junction properties), some relevant comments can be made: Critical current densities of 8 samples on a single substrate typically varied by a factor of 2-3, and the factor could be made smaller than 1.5 if the sample was well aligned in the ion beam. Variations in critical current density in samples fabricated in different runs were usually larger, but the variation could be kept within a factor of 3 if care was taken. (Note that a monolayer of oxide corresponds to roughly an order of magnitude change in critical current density.) Improvement in uniformity should be possible through use of a large diameter and very uniform ion beam, and a system in which the ion mill position was well fixed relative to the substrate table (our ion mill was removable and its position on the base plate of the vacuum system was not well fixed). Also, substrate rotation would help uniformity. Finally, care must be taken in aligning the ion beam current density probe with respect to the beam and substrate.

Incidentally, the edge junctions tended to be more uniform in properties than the simple overlap junctions. This is due to the fact that the growth of oxide was faster on the top film surface than on the edge of a film. Since the edge can contribute significantly to the properties of a small overlap junction, this can introduce a variability into the overlap junctions which is not well controlled.

SUMMARY

We have successfully applied a new oxidation technique to the fabrication of very small, very high current density niobium-based tunnel junctions. The technique utilizes the advantages of ion beams in growing oxide tunneling barriers, and is quite flexible, putting no special requirements on system vacuum or preparation.

The motivation for this work has been the study of Josephson junctions and, although the contributions of various mechanisms to the growth of the oxide are not well understood at the present time, the technique has yielded Josephson junctions of excellent quality and has led to the reproducible fabrication of submicron devices with unsurpassed critical current densities.

ACKNOWLEDGMENT

Research supported by NSF through the National Research and Resource Facility for Submicron Structures and the Materials Science Center at Cornell University.

REFERENCES

1. See, for example, L. I. Maissel and R. Glang, Handbook of Thin Film Technology, McGraw-Hill, New York (1970).
2. See, for example, J. A. Bondur, J. Vac. Sci. Tech. 13, 1023 (1976).
3. J. H. Greiner, J. Appl. Phys. 42, 5151 (1971).
4. P. D. DeGraff and D. C. Flanders, 15th Symposium on Electron, Ion, and Photon Beam Technology, Boston (1979).
5. Y. Horiike, M. Shibagaki, and K. Kadono, Jpn. J. Appl. Phys. 18, 2309 (1979).
6. M. D. Feuer and D. E. Prober, Appl. Phys. Lett. 36, 226 (1980).
7. D. Cox (private communication).
8. R. Buhrman, A. Callegari, and A. Kleinsasser (unpublished work).
9. P. Reader (private communication).
10. I. Lindau and W. E. Spicer, J. Appl. Phys. 45, 3720 (1974).
11. J. E. Nordman, J. Appl. Phys. 40, 2111 (1969).
12. L. O. Muller and D. B. Sullivan, J. Appl. Phys. 40, 2115 (1969).
13. R. Graeffe and T. Wiik, J. Appl. Phys. 42, 2146 (1971).
14. P. C. Karulkar and J. E. Nordman, American Vacuum Society Symposium, New York (1979).
15. P. C. Karulkar and J. E. Nordman, J. Appl. Phys. 50, 7051 (1979).
16. P. C. Karulkar and J. E. Nordman (to be published).
17. Ion Tech, Inc., Fort Collins, Colorado.
18. J. G. Adler and S. C. Ng, Can. J. Phys. 43, 594 (1965).
19. S. K. Lahiri, S. Basavaiah, and C. J. Kircher, Appl. Phys. Lett. 36, 334 (1980).

20. R. H. Havemann, J. Vac. Sci. Tech. 15, 389 (1978).
21. J. H. Greiner (private communication).
22. R. E. Howard, E. L. Hu, L. D. Jackel, L. A. Fetter, and R. H. Bosworth, Appl. Phys. Lett. 35, 891 (1979).
23. W. C. Stewart, Appl. Phys. Lett. 12, 277 (1968); D. E. McCumber, J. Appl. Phys. 39, 3113 (1968).
24. V. Ambegaokar and A. Baratoff, Phys. Rev. Lett. 10, 486 (1963).
25. S. Basavaiah and J. H. Greiner, J. Appl. Phys. 47, 4201 (1976).
26. W. C. Stewart, J. Appl. Phys. 45, 452 (1974).
27. K. Schwidtal, J. Appl. Phys. 43, 202 (1972).

Figure 1. Formation of edge by ion milling (schematic).

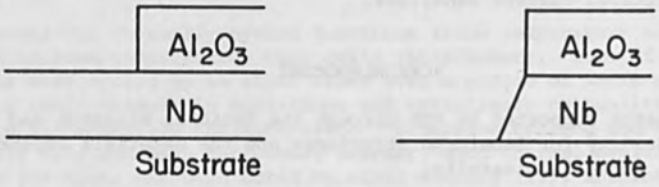

(a) Before milling (Ar beam). (b) After milling.

Figure 2. Josephson junction with edge geometry (schematic).

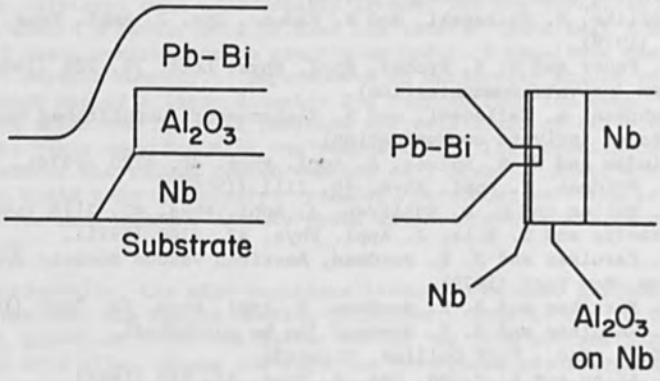

(a) End-on view. (b) Top view.

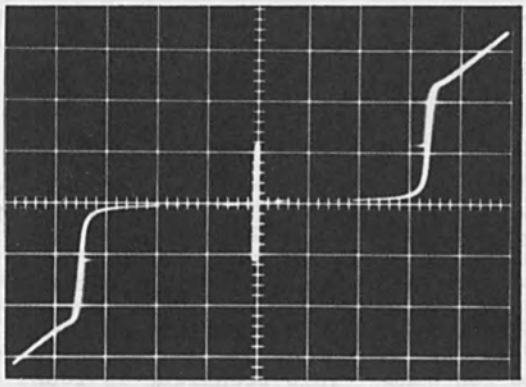

Figure 3. Current-voltage characteristic of a junction having a critical current density of 1.3×10^3 amp/cm^2. Scales are 0.5 mA and 1 mV per division.

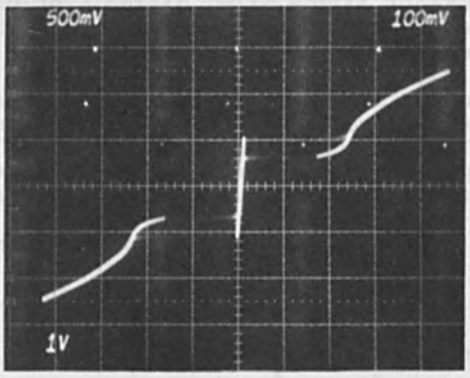

Figure 4. Current-voltage characteristic of a junction having a critical current density of 2.6×10^5 amp/cm^2. Scales are 0.5 mA and 1 mV per division.

FABRICATION OF SiO_2 BLAZED GRATINGS BY REACTIVE ION-BEAM-ETCHING

S. Matsui, T. Yamato, H. Aritome, and S. Namba
Faculty of Engineering Science, Osaka University
Toyonaka, Osaka 560, Japan

ABSTRACT

The Ar ion-beam-etching technique, successfully employed to produce PMMA blazed gratings, is not applied to produce SiO_2 gratings, because the etching rate of SiO_2 is lower than that of AZ1350, the mask material for ion etching. In the present report, a CF_4 reactive ion-beam-etching technique with a high etching rate of SiO_2 is applied to produce original SiO_2 blazed gratings. The blaze angle of gratings can be controlled easily by varying the incident angle of the ion beam. This technique is found very useful for producing blazed gratings made of various materials.

INTRODUCTION

The holographic technique for producing gratings has various advantages over the conventional techniques by using ruling engines because of high accuracy of peiodicity and capability of producing high groove densities. An Ar ion-beam-etching technique was successfully applied to produce Ge (1), PMMA and GaAs(2,3) and Si(4) blazed gratings. Recently, it was reported that the PMMA blazed gratings thus produced can be practically used for monochromators(5,6).

SiO_2 is considered to be more suitable than PMMA for a grating material because of excellent thermal and mechanical stabilities. The Ar ion-beam-etching technique, however, has not been applied to produce SiO_2 blazed gratings, since the etching rate of SiO_2 is lower than that of AZ1350.

In this paper, we report SiO_2 blazed gratings produced by means of a CF_4 reactive ion-beam-etching(7).

FABRICATION OF SiO_2 BLAZED GRATINGS

A schematic diagram of the ion-beam-etching apparatus is shown in Fig. 1. As shown in the figure, the sample stage was water-cooled to prevent the sample from heating. The stage could be tilted to select an appropriate beam angle. The accelerating voltage of ions was 500 V and the ion current

density was 0.4 mA/cm^2.

Figure 2 shows the angular variation of the etching rates for SiO_2 (fused quartz) and AZ1350 at an Ar ion beam of 0.4 mA/cm^2. Figure 3 shows the dependence on the incident angle of the etching rates for SiO_2 (fused quartz and thermally oxidized Si) and AZ1350 at a reactive ion beam by CF_4. The ion current density was 0.4 mA/cm^2. The etching rates of fused quartz and that of thermally grown SiO_2 are the same at reactive ion beam etching by CF_4. The etching rate of SiO_2 by an Ar ion beam is lower than that of AZ1350, however, is higher than that of AZ1350 in the case of CF_4 reactive ion beam. The angular dependence of the etching rates for SiO_2 and AZ1350 in the case of CF_4 reactive ion beam etching is differnt from those in the case of an Ar ion beam. The difference is considered to arise because the etching mechanism in the case of CF_4 gas includes not only sputtering but also chemical reaction (7).

Figure 4 shows a fabrication process of SiO_2 blazed gratings. A thermally grown SiO_2 was used as a sample. Gratings on SiO_2 substrates were made holographically by using a He-Cd laser (3250 Å). The photoresist and the developer used were Shippley AZ1350 and AZ1350 developer, respectively. The thickness of photoresist on the substrates was 0.13 μm.

Figure 5 shows a SEM photograph of a profile of the reactive ion-beam-etched holographic gratings with a period of 4800 Å. Blaze angles between 4 to 27 degrees were obtained when the incident angle of the ion beam varied from 85 to 60 degrees. This result indicates that the reactive ion-etching technique can be applied to produce SiO_2 blazed gratings. Figure 6 shows the dependence of the blaze angle on the incident angle of the ion beam (shown in Fig. 1). From Fig. 6, one may notice that the blaze angle can be controlled by varying the incident angle of the ion beam.

CONCLUSION

SiO_2 blazed gratings was produce by the CF_4 reactive ion-beam-etching. The blaze angles between 4 and 27 degrees were obtained. The blaze angles can be controlled by varying the incident angle of the ion beam. The reactive ion-beam-etching technique seems promising for producing not only SiO_2 blazed gratings but also gratings made of other various materials.

ACKNOWLEDGEMENTS

We would like to thank Dr. Y. Aoyagi for his helpful discussions and Mr. H. Ito, Mr. K. Mino and Mr. M. Nishida for their experimental assistance.

REFERENCES

(1) H.L. Garvin, Solid State Technol. 16, No.11, 31 (1973).
(2) Y. Aoyagi and S. Namba, Jpn. J. Appl. Phys. 15, 721 (1976).
(3) Y. Aoyagi and S. Namba, Opt. Acta 23, 701 (1976).
(4) T. Fujiwara, M. Nunoshita, K. Hamanaka and M. Hirano, Meeting of the Institute of Electronics and Communication Engineers, Japan (March 1980); and K. Hamanaka, T. Fujiwara, K. Kuroda and M. Nunoshita (submitted).
(5) Y. Aoyagi, K. Sano, and S. Namba, Optics Commun. 29, 253 (1979).
(6) K. Sano, Y. Aoyagi and S. Namba, Oyo Butsuri 48, 539 (1979) (in Japanese).
(7) J.W. Coburn and H.F. Winters, J. Vac. Sci. & Technol. 16, 391 (1979).

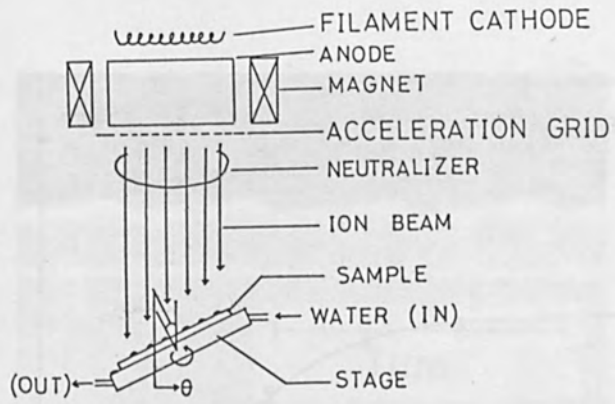

Fig. 1. A schematic diagram of the ion-beam-etching apparatus.

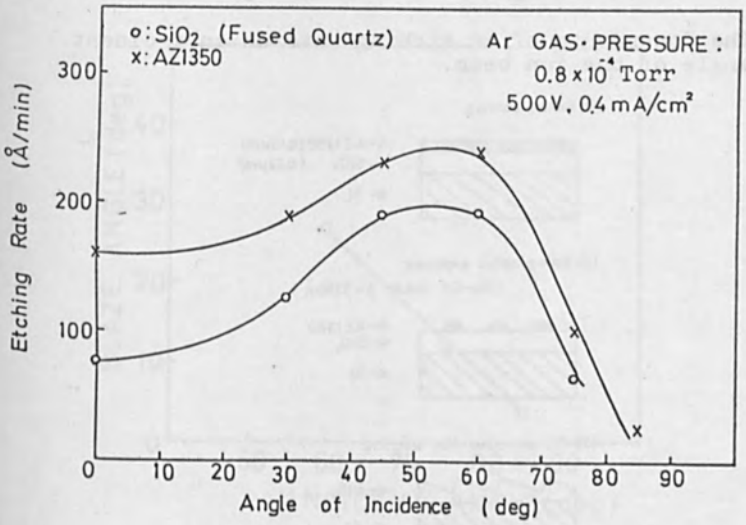

Fig. 2. The dependence of an etching rate on an incident angle of an Ar ion-beam.

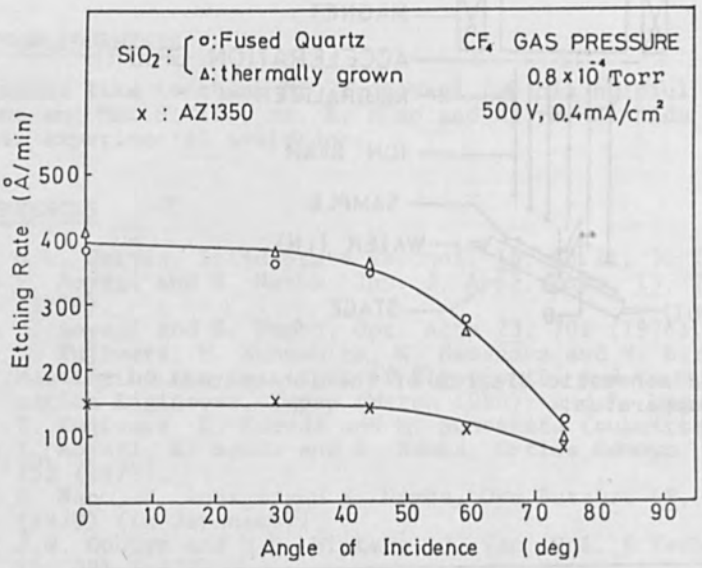

Fig. 3. The dependence of an etching rate on an incident angle of the ion beam.

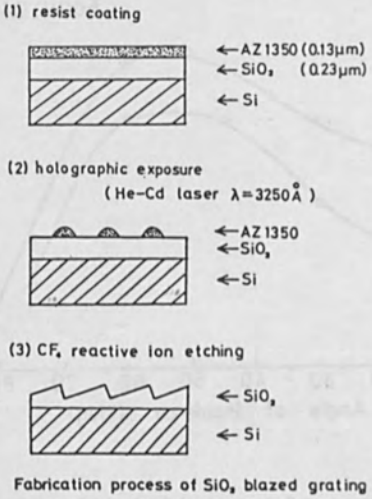

Fig. 4. The fabrication process of SiO_2 blazed grating.

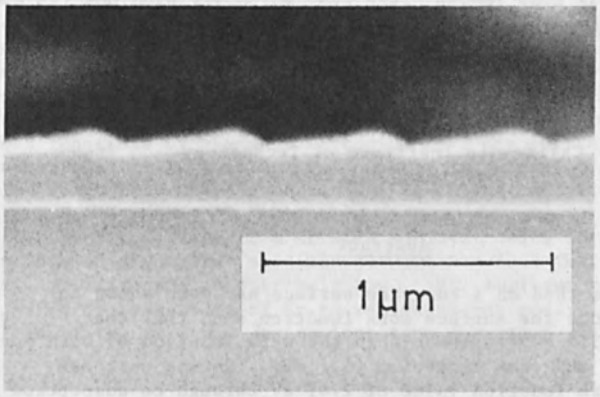

Fig. 5. A SEM photograph of a blazed grating of SiO_2 on Si. The period is 4800 Å.

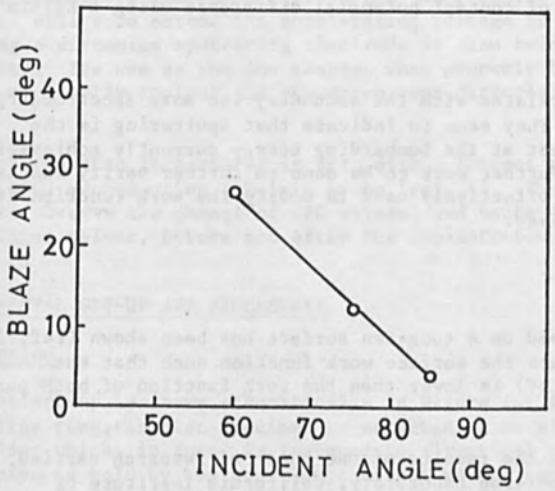

Fig. 6. The dependence of a blaze angle on an incident angle of the ion beam.

WORK FUNCTION MODIFICATION USING ION IMPLANTATION*

Y. S. Kuo**

Jet Propulsion Laboratory
California Institute of Technology
Pasadena, California

Abstract

Zirconium adsorbed on a tungsten surface has been shown to significantly reduce the surface work function such that the resulting value (3.1 eV) is lower than the work function of both pure tungsten (4.6 eV) and pure zirconium (4.1 eV). Recent work has achieved a low work function value of 2.67 eV through co-adsorption of Zr and oxygen followed by inward diffusion into the bulk portion of the tungsten specimen.

This paper presents an alternative method of modifying tungsten electrode work functions by means of zirconium ion implantation. A recoil implantation approach is adopted to make use of the implanter being developed in its current stage. Zr layer coated on tungsten surface is bombarded by Xe ion beam. The work function is studied with the measurement of contact potential difference using a Kelvin probe.

Results are correlated with the secondary ion mass spectrometry (SIMS) measurement. They seem to indicate that sputtering is the major bombarding effect at the bombarding energy currently achievable by this implanter. Further work to be done to further verify whether this approach can be effectively used to modify the work function is identified and discussed.

I. INTRODUCTION

Zirconium adsorbed on a tungsten surface has been shown (ref. 1) to significantly reduce the surface work function such that the resulting value (3.1 eV) is lower than the work function of both pure

*This paper presents the results of one phase of research carried out at the Jet Propulsion Laboratory, California Institute of Technology under contract NAS7-100, sponsored by the National Aeronautics and Space Administration.
**Engineer - Electrical Power and Propulsion Section.

tungsten (4.6 eV) and pure zirconium (4.1 eV). Recent work (ref. 2) has achieved low work function value 2.67 eV through co-adsorption of Zr and oxygen followed by inward diffusion into the bulk portion of the tungsten specimen.

This paper presents an alternative method of modifying tungsten electrode work functions by means of zirconium (Zr) ion implantation. Ion implantation has the capability of 1) doping to a level greater than its solid solubility and, 2) tailoring the dopant concentration profile.
The method is expected to lead to a Zr rich sublayer being formed below the surface of a tungsten specimen despite the fact that the solid solubility of Zr in W is extremely low. This sublayer could serve as an effective reservoir of Zr to replenish any possible desorptive loss of the Zr atoms during long term operation at high temperature.

The ion implanter being developed is still at its early stages. The ion source performs very well when inert gases are employed, but does not possess the capability of forming zirconium ions for the time being. The major difficulty lies in the refractory nature of zirconium metal. Therefore the work reported in this paper uses the method of recoil implantation (ref. 3) which means in this case to vapor-deposit a Zr layer on a W specimen and then bombard the deposited layer with a Xe ion beam. The accelerating voltage in operation is relatively low (6-15 kV). A new power supply is being assembled and will soon extend the accelerating voltage to 45 kV. An ion gun using a zirconium sputtering electrode is also being designed and fabricated. Its use as the ion source, when properly biased, is expected to eventually implant the zirconium ions directly into the specimen.

The work function is measured in situ with a contact potential difference (CPD) method using a Kelvin probe (ref. 4). The major concern is to observe the change of CPD values, and hence the change of work function values, before and after the implantation process.

II. EXPERIMENTAL SET-UP AND PROCEDURES

Description

The test set-up is shown schematically in Figure 1. A small polycrystalline tungsten disc specimen is attached on an aluminum specimen holder which, in turn, is fastened to a vertical copper pipe. The pipe is held by the top flange of the vacuum target chamber and can be rotated along its axis, manually, from outside the chamber (Fig. 2). Also fastened to the pipe is a small double quartz crystal microbalance (DQCM) assembly with its electronic package

(ref. 5). This Cu pipe can be filled with liquid nitrogen to provide cryogenic cooling to both the specimen holder and the DQCM. These two are oriented in the same direction such that the amount of vapor deposition onto the specimen can be monitored with the DQCM. An electrically actuated shutter, made of stainless steel, is attached to the Cu pipe through a teflon base and can block the aperture of the DQCM when the microbalance should not be in operation (during the ion bombardment for instance). The tungsten specimen, in form of 0.5 inch diameter disc, is so positioned that its surface will not be reached by any atomic species which could be sputtered off from the aluminum holder during the ion bombardment. Figure 2 shows also the Kelvin probe (a variable condenser made of essentially a vibrating reed) and the Zr strip evaporator. During the experiment, the evaporator is actually surrounded with a stainless steel shield except for a small hole such that the evaporated Zr species are only deposited on the specimen as well as the collecting surface of the DQCM. Figure 3 gives a close up of the vibrating-reed Kelvin probe placed in a position to measure the CPD. The shutter is open only to show the microbalance window. The whole probe is designed to be translationally mobile in order to allow the rotation of the vertical Cu pipe and also to enable the probe to be placed in an appropriately shaded location from the bombarding or sputtered ions. At the left hand side of the vacuum chamber (shown on Figure 2) is a stainless steel shield plate which has a central hole so aligned that a constant portion of the incoming ion beam would precisely hit the specimen.

The ion source is located approximately 1 m to the left from the target chamber and can successfully extract 5-10 mA Xe ion current from a slit measuring 3.8 cm x 0.08 cm. The vacuum of the stainless steel chamber is obtained and maintained with a mechanical pump and a diffusion pump and is degraded to 3×10^{-4} torr when the ion beam is being operated.

A frequency generator with power supply is used to oscillate the Kelvin probe of which the vibrating reed is driven through a piece of piezoelectric crystal (ref. 4). The vibrating reed is made of 8 mil thick molybdenum, but was vapor coated with a layer of gold from a tantulum evaporator. The resonance frequency of the vibrating reed was found to be around 205 Hz. An optical pyrometer is used to monitor the Zr strip filament temperature through a quartz window from outside the test chamber, when the Zr vapor deposition is done. A milliammeter is electrically connected to the specimen to measure the ion current thereby received during the ion bombardment. However, it is disconnected from the electronic measuring system to avoid any possible damage to the circuit due to the operation of the high voltage power supply coupled with the ion source.

A PAR-5204 lock-in analyzer constitutes the heart of the electronic system in measuring the CPD in form of a voltage drop across a 10 Megaohm load resistance which is transduced from the variable capacitance between the Kelvin probe and the specimen surface. This lock-in analyzer, with its phase sensitive detector coupled with a tuned amplifier, enhances the signal-to-noise ratio effectively and makes it possible to extract the weak CPD signal which is displayed simultaneously on an oscilloscope and a digital voltmeter. This signal is then balanced off by a proper d.c. voltage bias; the bias value thus obtained gives the CPD value; which is simply the difference between the specimen work function and the work function of the vibrating reed of the Kelvin probe.

Procedures

The electrolytically polished tungsten specimen surface was cleaned with acetone before it is placed on the aluminum specimen holder. The high purity (99.8%) Zr strip was acid etched with 5% HF aqueous solution. The chamber was then pumped down to 8×10^{-6} torr and the CPD value was measured.

The specimen was turned toward the Xe ion source, bombarded at 9 kV and 0.12 mA for eleven minutes to sputter clean the surface. The CPD value was measured again.

The specimen (and DQCM) was then turned toward the Zr evaporator. The shutter of the DQCM window was opened and the Zr filament was heated to a temperature of no more than 1580°C as monitored from the pyrometer. The ensuing evaporation-deposition was continued until the DQCM frequency signal dropped by approximately 1160 Hz, equivalent to a mass deposition of 95 monolayers of Zr deposition. The CPD value was measured.

The specimen was turned toward the ion source and bombarded with the Xe ion beam of 0.29 mA at 14 kV for 1 minute. The CPD value was measured again. The specimen was bombarded again with an ion current of 0.37 mA at the same voltage for another 1.5 minutes. Again the CPD value was measured. The specimen was bombarded a third time for 85 sec with 0.3 mA ion current at the same voltage. The CPD value was then measured for the last time.

III. RESULTS AND DISCUSSIONS

The gold coated vibrating reed is assumed to have a work function 4.3 eV as recommended by Samsonov in his "Handbook" (ref. 6). Gold coating was selected as the reference electrode since it was favorably suggested by Riviere (ref. 7) and later by Surplice

and D'Arcy (ref. 8). However, the high work function value of gold obtained in ultra-high vacuum is not adopted here since the vacuum condition does not apply. The film thickness of the zirconium deposition is chosen based on several findings reported on literature. It was reported by Nishi et. al. (ref. 12) that the recoil implantation occurs most effectively when the film thickness is fairly smaller than the projected range of incident ions in the metal film. This means that the deposited Zr film should be thin since the projected range, as estimated from LSS theory (ref. 14), would be in the vicinity of 100A only. However, it was also established through experiment as well as calculation (ref. 15) that the backsputtering Or sputter removel yield could easily be 10 times or greater than the recoil implantation yield. If the deposited film is too thin, the total implantation dose of the recoil implanted species will be too low. In a recoil implantation experiment using two ion guns, one of which was to dynamically supplement the backsputtered atoms during the recoil implantation by sputtering deposition, this large (nearly 10) coefficient of backsputtering was essentially confirmed (ref. 16). The tradeoff is complicated by an uncertain factor which is the possible formation of a very thin carbonaceous film as a result of the diffusion oil vapors. Such a thin film could decrease considerably the backsputtering yield according to Smith et al (ref. 17).

The CPD value measured prior to evaporation was 0.133 volt, giving tungsten work function a value of 4.43 eV; not far from the 4.5 eV recommended by Samsonov. After evaporation-deposition of Zr, CPD obtained was -0.41 volt which yields a zirconium work function of 3.89 eV, again fairly close to the value of 3.7 eV recommended by Samsonov. In fact, it also sits between the two values recommended by Kohl (ref. 1).

After the first ion bombardment, the CPD measured was 0.555 volt giving rise to a value of 4.855 eV for the tungsten work function, being slightly higher than the recommended value for tungsten (4.5 eV) as cited above. It thus appears that the first Xe ion bombardment had sputtered off all the Zr layer deposited on the specimen surface. Further bombardments, the second and third, gave CPD values of 0.835 eV and 0.876 eV respectively. Correspondingly, the specimen surface work function was again increased by roughly 0.3 eV which could be attributed to the lattice damage upon the specimen surfce (ref. 9) as caused by the ion bombardment. This amount of work function change seems to agree very well with previous work reported by Lawson and Carter (ref. 9) when they brought up this lattice damage explanation. However, X-ray diffratiometry graphs obtained before and after the implantation test did not give any evidence of considerable damage of crystal lattice. Another possibility, which is more favored by the author, is that the

ion beam tends to activate the hydrocarbon vapor or deposited organic species and tends to form a polymerized thin film on the specimen and to, consequently, modify the work function (ref. 10, ref. 13). Since Xe is known to have a high tendency of saturating the cold trap panels (ref. 11), the back stream of diffusion oil species does have ample chances to fill into the test chamber. This was in fact evidenced by the fact that, during the bombardment procedures, the vacuum chamber pressure was found to be raised to 2×10^{-4} torr during the bombardments and still above 5×10^{-5} torr even when the ion beams were shut off. These oil species could then contribute to the slight increase of the measured work function.

Since the overall Xe ion bombardment dosage amounted to 1.23×1017 ions/cm^2, considering an areal atomic density of Zr to be approximately 2×10^{15} atoms/cm^2, this total dosage is equivalent to 60 or more monolayers of atoms being recoil implantated. Even if an average removal rate is taken as 20 to include both backscattering and resputtering loss. The recoil implanted Zr atoms could still be equivalent to 3 monolayers and would form a doping composition of considerable fraction, if spreaded, across a thin layer of several monolayers depth. It is therefore surprising that the work function measurement did not provide any alloying effect. The specimen was then sent for the profile sputtering examination using the secondary ion mass spectrometry (SIMS) which used 20 Kv 0^{18} ions as the projectile. The specimen surface was found to have two different types of areas, the majority looked clean and has very low level of Zr whereas the smaller "dark" areas showed much stronger zirconium characteristic X-ray. Fig. 4 is a typical depth profile obtained from a clear area which showed a surface concentration of Zr about 0.1%, decreasing with the depth. The dark area (Fig. 5), on the other hand, showed a Zr concentration of several percent for a depth of approximately 160 A which however correspond to a layer of material constituted almost 100 percent carbon. Since the SIMS is insensitive to both hydrogen and xenon, it suggested that the dark area is covered by an organic, perhaps polymerized, layer which has contained several percent of Zr apparently as a result of the recoil bombardment. The small amount of tungsten observed within this layer, increasing with the depth, indicate atoms back scattered from the surface layers of the tungsten specimen by the recoil implanted species which, however, include both Zr and C. The latter, carbon, has in fact penetrated far deeper obviously because of its far lighter atomic mass. By comparing Fig. 4 and 5, the oxygen level which remains essentially constant across the specimen depth was probably off scale but does appear to come from the original impurity level of the tungsten specimen. An appreciable degree of (110) preferred orientation detected from X-ray diffraction of the original specimen also provides a suggestion that, from the small bumps on the

profile curves of both Zr and C, a slight degree of channeling seemed to have occurred.

The sputtering removal of the deposited Zr layer is therefore confirmed. The results however are not conclusive because of the carbonaceous film contamination which apparently existed during the ion bombardment.

CONCLUSIONS

The 14 kilovolts Xe ion beam does not seem to suffice to recoil implant Zr into tungsten for the purpose of work function modification. The sputtering removal seemed to be the major problem. Further work requires much higher energy beam. An annealing process will also be needed in order to verify whether the implanted sublayer can serve as a Zr reservoir in order to form an effective thin film cathode. However, in order to achieve a better vacuum and to assure less contamination by carbonaceous species, it is preferred and perhaps necessary to replace (1) the Xe with Ar in the ion source and (2) the diffusion pump oil with the perfluorinated polyether fluid as suggested by Tsai (ref. 18)

ACKNOWLEDGEMENT

Thanks are due to Mr. D. Fitzgerald for the use of his ion source and to Mr. Roy Adams for his assistance in the electronics.

REFERENCE

1. Kohl, W.H. "Handbook of Materials and Techniques for Vacuum Devices," 1967, Reinhold Publishing Corporation.

2. Danielson, L.R., and Swanson, L.W., "High Temperature Co-adsorption Study of Zr and Oxygen on the W(100) Crystal Face," Surface Sci. 88 (1979), p. 14.

3. Nelson, R.S., "The Theory of Recoil Implantation," Radiation Effects 2 (1969), p. 47.

4. Besocke, K. and Berger, S. "Piezoelectric Driven Kelvin Probe for Contact Potential Difference Studies," Rev. Sci. Instrum., 47 (1976), p. 840.

5. Termuelen, J. Ph. et al "The Use of Double Oscillating Quartz Crystals in Mass Determination," of "Progress in Vac. Microbalance Techniques," Vol. I. (1972), Hayden & Son Ltd.

6. Samsonov, G.V., "Handbook of Thermionic Properties," Plenum Press Data Division, N.Y., 1966.

7. Riviere, J.C., "The Surface Potential of Oxygen on Uranium," British J. of Appl. Phys., 15 (1964), p. 1341.

8. Surplice, N.A. and D'Arcy, R.J., "A Critique of the Kelvin Method of Measuring Work Functions," J. Phys. E3 (1970), p. 477.

9. Lawson, R.P.W. and Carter, G. "Inert Gas Ion Bombardment Induced Work Function Changes in Polycrystalline Tungsten and Gold Ribbon," Vacuum 18 (1968), p. 205.

10. Petit-Clerc, Y. and Carette, J.D., "Effect of Temperature on Surface Charges Caused by An Incident Electron Beam on a Metallic Surface," Appl. Phys. Letters, 12, (1968), p. 227.

11. Fuller, C.T., "A Sputtered-Ion Source for the Lintott Ion Accelerator," SAND 76-0040 (1076).

12. Nishi, H. et al, "Effect on Ion Bombardment on Metal-Silicon Interface," Proc. of Internal. Conf. on Ion Implantation in Semiconductor and Other Materials, Osaka, Japan, ed. by S. Namba (Plenum Press, 1975).

13. Shimizu, K. et al, "Surface Contamination by Ion Bombardment," Proc. of the 4th Intn'l Symp. on Surface Contamination, Washington, D.C., Sept. 1978 (Plenum Press, 1979), p. 113.

14. Dearnaloy, G.1. et al, Ion Implantation, (American Elsevier, 1973). Tabulated Values on Appendix, p. 773.

15. Moline, R.A. et al "Recoil Implantation of O-18 From SiO_2 by Heavy Projectiles" Proc. of the 5th Int. Conf. on Atomic Collisions in Solids (1973), p. 159.

16. Fischer, G. et al "A Two-Gun Ion Beam System for Dynamic Recoil Implantation" Vacuum 28 (1978), p. 277.

17. Smith, Jr., H.P., et al "Effect of Thin Carbonaceous Films on 500 Kev He Ion Sputtering of Copper, J. Appl. Phys. 36 (1965), p. 1952.

18. Tsai, M.Y. et al "Study of Surface Contamination Produced during High Dose Ion Implantation", J. Electrochemical Soc. 126 (1979), p. 98

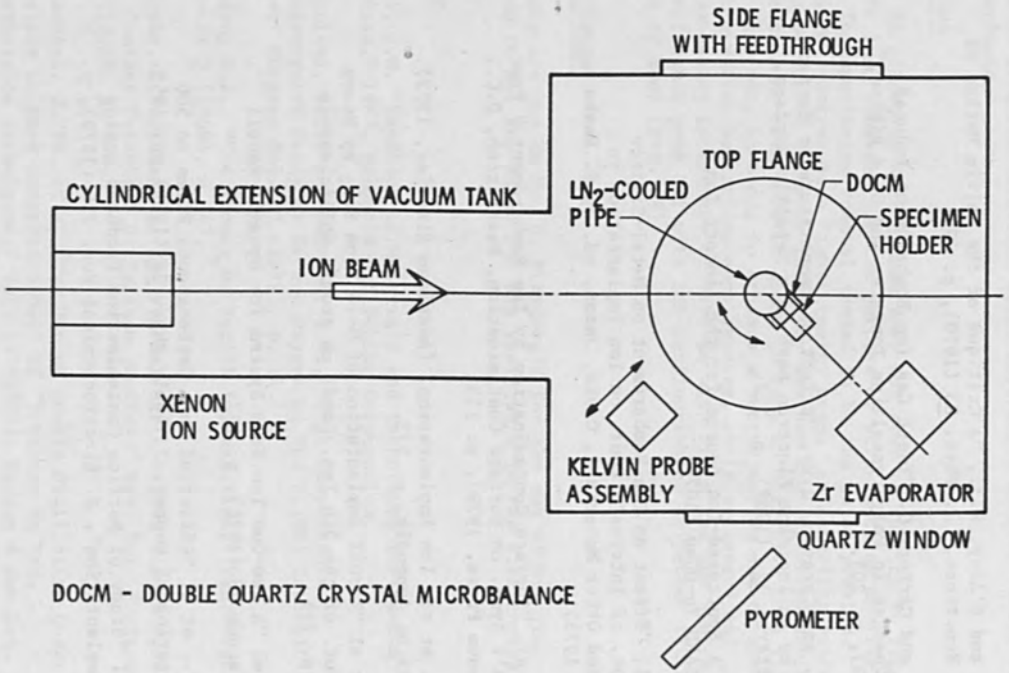

Figure 1. Schematic Setup (Top View) of the Stainless Steel Vacuum Tank for Zr Vapor Deposition and Recoil Implantation.

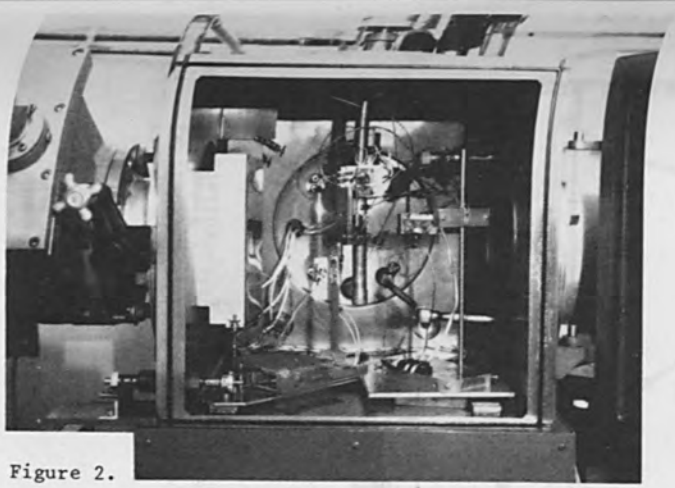

Figure 2.

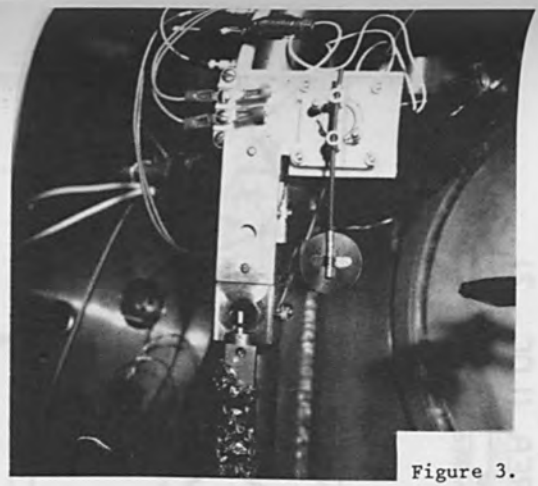

Figure 3.

Figure 2. Target Chamber of Recoil Implantation. The Specimen Holder, The Double Quartz Crystal Microbalance Assembly and an Electrically Actuated Shutter Are Fastened to a Central Copper Pipe. A Stainless Steel Plate Shields Against the Ion Beam From the Left. At the Right is the Zirconium Evaporator Without Its Cylindrical Stainless Steel Shield.

Figure 3. Close-Up Photo of the Central Portion of Figure 2, Showing the Kelvin Probe, the Specimen and the DQCM Window With Its Shutter Open.

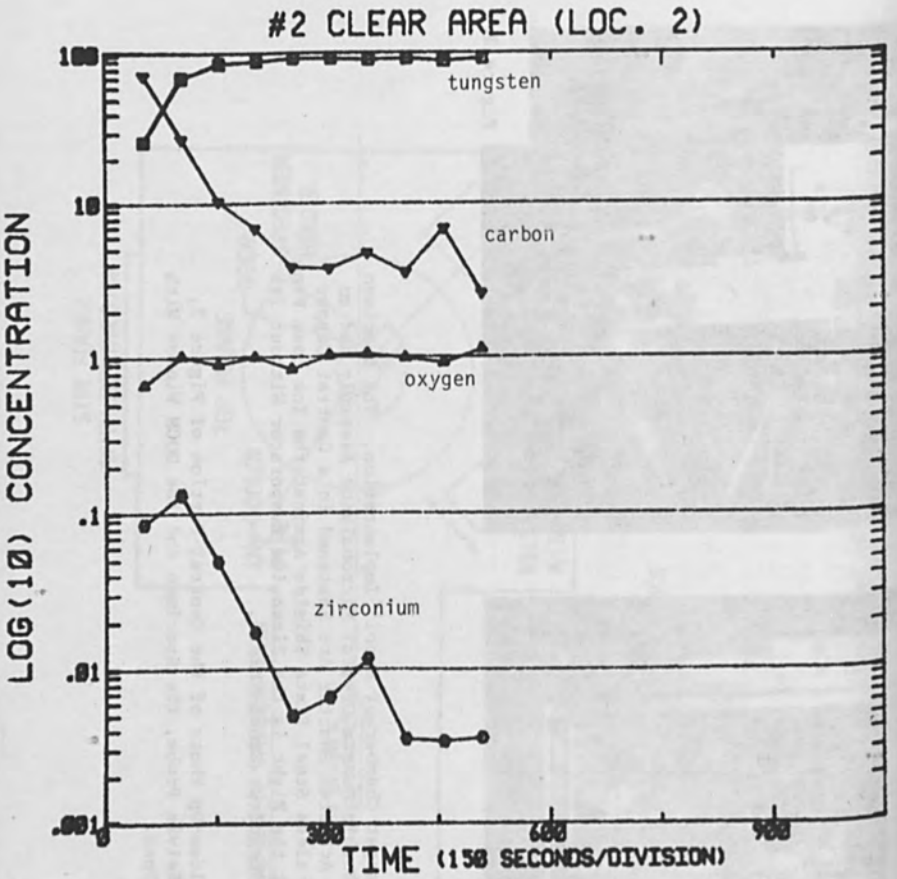

Figure 4. Depth Profile Obtained by SIMS, A Plot of Concentration versus Sputtering Time. (Sputtering Rate Approximately 0.6 angstrum/sec)

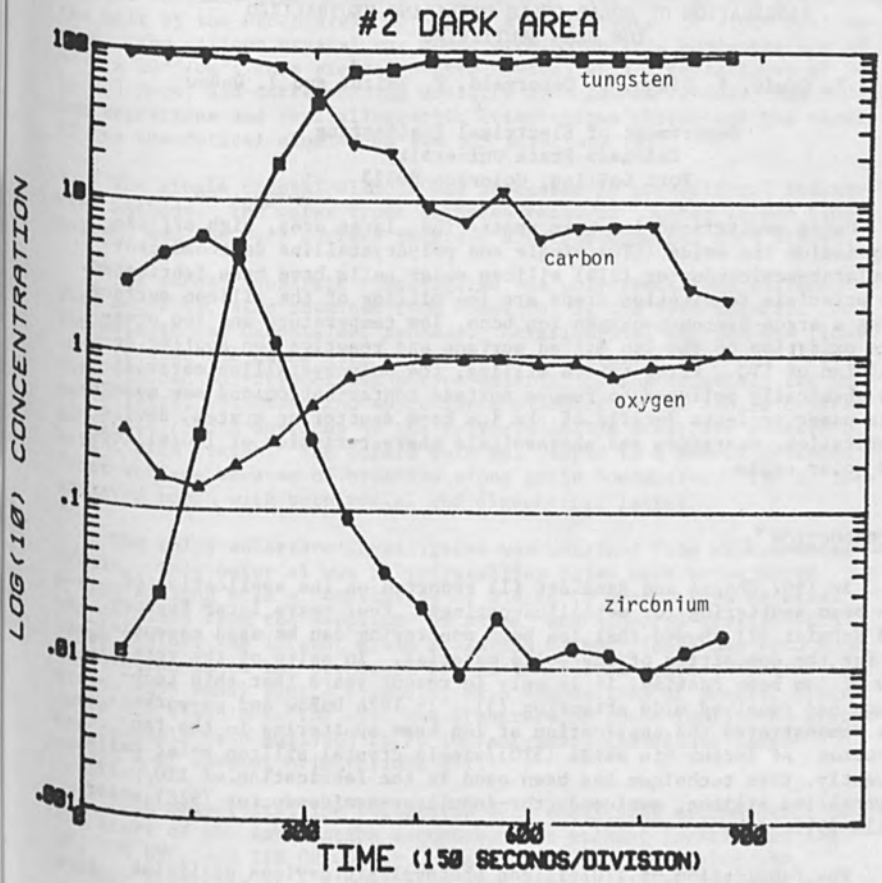

Figure 5. Depth Profile Obtained by SIMS, A Plot of Concentration versus Sputtering Time (Sputtering Rate Approximately 0.6 angstrum/sec)

FABRICATION OF SOLAR CELLS UTILIZING NEUTRALIZED ION BEAM SPUTTERING

A.P. Genis, R. Singh, C. Osterwald, P. Smith, and J. DuBow

Department of Electrical Engineering
Colorado State University
Fort Collins, Colorado 80523

Using neutralized ion beam sputtering, large area, high efficiency indium tin oxide (ITO)/single and polycrystalline semiconductor-insulator-semiconductor (SIS) silicon solar cells have been fabricated. The principle fabrication steps are ion milling of the silicon surface using a argon-hydrogen-oxygen ion beam, low temperature and low pressure oxidation of the ion milled surface and reactive ion sputter deposition of ITO. Prior to ion milling, the polycrystalline material was chemically polished to remove surface contamination and saw damage. This paper presents details of the ion beam sputtering system, device fabrication, operation and photovoltaic characteristics of ITO/silicon SIS solar cells.

INTRODUCTION

In 1967 Chopra and Randlett (1) reported on the application of ion beam sputtering for metallic coatings. Four years later Spencer and Schmidt (2) showed that ion beam sputtering can be used essentially for the deposition of any solid material. In spite of the versatility of ion beam coating, it is only in recent years that this technique has received wide attention (3). In 1976 DuBow and co-workers (4) demonstrated the application of ion beam sputtering in the fabrication of indium tin oxide (ITO)/single crystal silicon solar cells. Recently, this technique has been used in the fabrication of ITO/polycrystalline silicon, semiconductor-insulator-semiconductor (SIS) solar cells (5).

The fabrication of ITO/silicon photovoltaic devices utilizing neutralized ion beam sputter deposition technology has yielded reproducible high efficiency solar cells on both single and polycrystalline silicon substrates. The objective of this paper is to present the details of the ion beam sputtering system, device fabrication procedure, operation and photovoltaic characteristics of ITO/single and polycrystalline silicon (SIS) solar cells.

SUBSTRATE MATERIALS

To date, three types of silicon substrates have been studies in depth, The first type of substrate consisted of 2 inch dia. single

crystal obtained from Monsanto Corporation. The crystal was drawn from the melt by the Czochralski method on a seed crystal of <100> orientation. The silicon crystal was doped with boron at a concentration of $\sim 3 \times 10^{17}/cm^3$; this yielded p-type crystal with a resistivity of 0.1 to 0.3 Ω-cm, and corresponding mobility of ~ 200 $cm^2/v\text{-}sec$. The doping concentrations and crystallographic orientations chosen are the result of the theoretical studies on the SIS structure (6).

The single crystal silicon was processed by conventional industrial methods. The wafer front surfaces received a water lapped fine polish, and the back surface received a bright chemical etch finish.

The second substrate investigated was polycrystalline silicon. This material, also obtained from Monsanto, is the feed material for the melt in the Czochralski process. Metallurgical silicon was float zone refined and doped with boron at a concentration of $3 \times 10^{17}/cm^3$. This yielded polycrystalline p-type material of approximately the same resistivity, thickness and approximate diameter as the single crystal substrate. Both surfaces of the polycrystalline substrate receive a bright etch finish. The wafers were not lapped to a smooth polished front surface because of breakage along grain boundaries. The surface appeared rough with both radial and diametrical lamina.

The third substrate investigated was obtained from Wacker Chemitronic. This material was polycrystalline Silso cast, boron doped, p-type silicon with a resistivity of 0.5 to 10 Ω-cm. This material was obtained from the supplier "as sawed" and appeared grayish with large grains, the largest grain measuring 22 mm. There has been some speculation as to the structure of the individual grains, whether the grains were small single crystals, or a composition of smaller structures not visible to the eye. The structure of these individual grains has recently been analyzed to be in fact small individual single crystals of varying orientations (7).

Both polycrystalline substrates were chemically etched prior to the start of the fabrication sequence. The etchant constituted 13% HF, 75% HNO_3 and 12% CH_3OOH by volume. This mixture etched the silicon substrate at a slower rate than did the 25% HF 75% HNO_3 etch used previously (5). The etch rates for the two etchants were 750 Å / sec. and 5000 Å/sec., respectively. After completion of the etch, the wafer were placed in a resistive evaporation system. Gold was evaporated to a thickness of 500 Å on one side of the wafer to form a back contact. This gold layer is then sintered to the silicon in the fabrication process to form a good ohmic contact to the silicon.

FABRICATION SYSTEM

The vacuum system used in the fabrication process was a modified NRC 3117. The schematic diagram of the system is shown in Figure 1. The vacuum is achieved by means of a six inch diameter, three-stage,

liquid nitrogen trapped oil diffusion pump. The pump has a pumping capacity of 2000 ℓ/s and can achieve a vacuum of 1×10^{-7} Torr in the chamber.

The high purity gases (argon, hydrogen,and oxygen) needed in fabrication processes are introduced directly into the ion source. The gases were controlled by Brooks 5810 leak valves which allow repeatable setting of flow rates. The gas flow rate was monitored by Brooks model 5810--1CZDYA thermal mass flow sensors with their analog outputs fed into Brooks model 5820-1-YA meters calibrated in 0-5 sccm. This system permits reproducible flow rates accurate to within $\pm$ .05 sccm.

The ion source used in the fabrication process was a model 10-1000-200 manufactured by Ion Technology, of Ft. Collins, CO. A schematic diagram of the ion source is shown in Figure 2. The gases are introduced into the ion source behind the anode pole piece assembly. Both the anode and cathode assemblies are electrically isolated from the source body. Electrons thermonically emitted from the tantalum cathode experience increased path length due to the magnetic field produced by the anode assembly. This increased path length increases the probability of the electron striking an atom to produce an ion. The ion source is capable of generating ions with energies from 50 to 1000 eV. Depending on the mode of operation, the beam density can attain values in excess of 2.5 mA/cm^2, with a divergence half angle of less than 7°.

The operation of an ion source can lead to the generation of a space charge region in the path of the beam. The creation of such a region can influence the density, profile and divergence of the ion beam. The field due to the space charge region can become sufficiently intense as to cause the ions to be repelled back toward the source. This could result in termination of the ion beam. To prevent this process, a neutralizing wire is placed across the accelerator grid structure. When a current is passed through the neutralizer, electrons are released by thermonic emission. The current can be controlled to effect a net volume neutralization of the beam, even though electron-ion recombination may not take place.

A major disadvantage of the use of neutralizer wire is that material from the wire is milled off by the ion beam. This material contaminates both sputtering target and substrates. Tantalum from the neutralizer wire has been detected in the solar cells using Auger/ESCA profiling techniques. For this reason, a plasma bridge neutralizer has been constructed. This system of neutralization, injects a beam of electrons into the ion beam by means of argon propellant. Nothing is present in the ion beam to provide a source of contamination, and more complete neutralization may be achieved. Better neutralization results in lower beam divergence and reduced contamination by reducing sputtering of the fixturing.

The substrate heater was comprised of a commercially available heating element bonded to a stainless steel plate which was milled to accomodate the silicon substrate. The heater maintains less than a 2°C gradient across the silicon wafer at 400°C. The stainless steel plate is protected from the milling process by a carbon mask. Carbon was chosen due to its low milling rate and its low coefficient of thermal expansion. The mask also is used to define the cell areas on the substrate.

The sputtering target was composed of 90% indium oxide and 10% tin oxide, this is the optimum ratio of the oxides for solar cell fabrication (4).

The ITO target utilized in the system was pressed commerically by Metals Mart, located in Great Neck, New York. The target material was hot pressed and sintered, yielding a structurally sound, electrically conducting, dense disc. The target material has a nominal thickness of 3/8 inch and a diameter of 8 inches. This ITO disc was indium soldered to a chrome plated, water cooled copper backing plate.

The mechanical stability offered by this target allowed for complete control of the target angle. This permitted placement of the substrate heater in the central lobe of the sputter beam. To this date the sintered target has survived 775 runs with no visible degradation.

FABRICATION SEQUENCE

The fabrication of ITO/silicon solar cells is basically a five step process. First, a substrate is selected and placed on the heater surface, and a carbon mask is selected, depending on the number and size of the cells desired, and is placed over the wafer. The system is evacuated and the substrate heater is activated. During the time required for the substrate heater to reach the desired temperature, argon hydrogen and oxygen flow rates are adjusted and allowed to stablize.

The argon, hydrogen, and oxygen gases were adjusted to a partial pressure of 4×10^{-5}, 2×10^{-5}, and 2×10^{-5} Torr respectively, for a total system pressure of 9×10^{-5} Torr. Secondly, the ion beam source was adjusted to a beam energy of 800 eV, current density of 2 mA/cm^2, and allowed to mill the silicon substrate for approximately five minutes. Studies have shown that ion milled silicon oxidizes much more rapidly than a chemically etched surface, thus facilitating the needed oxide growth. Third, after the required milling time, a shutter was rotated between the ion source and substrate heater to allow the interfacial oxide to form. The substrate heater was rotated into deposition position and, after the oxide growth time, the shutter was removed and the ion beam allowed to impinge on the sputtering target, thus sputtering ITO onto the thermally grown oxide.

It has been shown that the ITO layer forms an antireflection coating on silicon with a thickness of 750 Å (8). At this thickness ITO forms a 1/4 wavelength coating for the peak in the visible spectrum of 6000 Å wavelength.

When the ITO film has reached the desired thickness of 750 Å, the sputtering process is stopped and the ITO/silicon solar cells removed from the system.

To complete the fabrication process, a front grid contact is evaporated through a shadow mask. Due to adherence problems of some metals on ITO, a multilayer thin film structure is evaporated on ITO. A 50 Å thick Cr layer is first evaporated, followed by 400 Å of nickel. The chromium acts as a adherence layer and the nickel allows the front grid contacts to be subsequently solder dipped to reduce series resistance in the grid structure. The structure of the finished device is shown in Figure 3.

OPERATION OF ITO/Si SOLAR CELLS

An examination of the crystal structures, lattice parameters, and thermal expansion coefficients of Si (diamond, a = 5.431 A°, $\alpha = 2.3 \times 10^{-6}/°C$) and ITO (cubic, a = 10.118 Å, $\alpha \simeq 10.2 \times 10^{-6}/°C$) shows that the ITO/Si system would have too many mismatch defects at the interface to form a good heterojunction diode. A large density of interface states will yield a poor photovoltaic performance. An interfacial layer between the oxide-semiconductor (ITO) and the base semiconductor (Si) can ameliorate the matching of the crystal structures, lattice constants, and the coefficients of thermal expansion, effectively grading one side of the junction into the other. The incorporation of this interfacial layer in the oxide semiconductor/base semiconductor system results in a semiconductor-insulator-semiconductor (SIS) configuration. The operation of SIS solar cells can be found in our previously published papers (6,9,10). However, for completeness we reproduce the essential features.

The thickness of the interfacial layer is the most important parameter in the optimization of SIS solar cells. It should be less than d_1, but greater than d_2, where d_1 is the thickness at which efficiency saturation occurs due to semiconductor limited current flow and d_2 determines the thickness for which the interfacial films becomes noncontinuous, and the operation is approximately described as a p-n heterojunction diode. The interfacial layer can be classified as one of the two types: (a) native interfacial layer (generally an oxide) which are grown from the base semiconductor or (b) deposited dielectrics. The interfacial layer should be such that(10)

$$E_{gi} \geq (X_s - X_i + E_{gs})$$

where E_{gi}, E_{gs} and X_i, X_s are the energy band gap and electron affinity of the insulator and the base semiconductor respectively.

To get optimum device performance, the work function of the top oxide-semiconductor should be less than or equal to the electron affinity of p-type base-semiconductor and, for an n-type base-semiconductor, the work function of the top contact should be greater than or equal to the sum of its electron affinity and band gap.

As stated in earlier publications (6,9-10) if a particular oxide semiconductor can ensure inversion at the interface, the SIS diode behaves like a p-n junction diode. A lower substrate resistivity decreases the dark current of the device and the optimum substrate resistivity is the same as in p-n junction devices. However, if the electron affinity of the oxide semiconductor is not correct, then the best efficiency will be obtained by using moderate base semiconductor resistivities.

It is worth mentioning here that the interfacial layer need not be perfect in order to obtain good performance. By selecting the oxide-semiconductor with the proper work function, the surface of the base-semiconductor can be in strong inversion and the device can perform well even for large densities of surface states ($\sim 10^{13}/cm^2$ -eV or so) since these will be filled by minority carriers. If the surface is not inverted, then the device performance can be degraded by the surface states. The performance of surface state controlled devices should still be better than an equivalent heterojunction diode but poorer than an optimized SIS solar cell.

SOLAR CELL CHARACTERISTICS

The light and dark current-voltage (I-V) and capacitance-voltage (C-V) characteristics were measured using an automated measurement and analysis system described elsewhere (11). The ELH light intensity was adjusted to AM1 by monitoring the short circuit of a NASA Lewis standard p-n junction silicon solar cell. The accuracy of the standard cell was verified using an Epply Pyranometer (Model #8-48). All measurements were performed at 28 $\pm$ 0.5°C. The C-V data was obtained with a Boonton 72B 1 MHz capacitance meter. A Bausch and Lomb 1/4 meter grating monochrometer, with appropriate filters to block out harmonics, was used for spectral response measurements. The relative intensity incident on the cell was obtained by monitoring the short circuit current of the NASA Lewis standard cell at wavelengths for which the spectral response of the standard cell was known.

The light and dark I-V characteristics of three ITO/polysilicon SIS solar cells are shown in Figure 4 and 5. Sample 661 is a diode that was fabricated with Wacker polysilicon as it was ob-

tained from the supplier. The surface of sample 664 was prepared by chemical etching as described earlier to reduce the surface damages. In the fabrication of diode 660B, hydrogen was incorporated during the milling and oxidation to passivate the surface defects. As can be seen from Figures 4 and 5, the diode characteristics were improved by chemical treatement of the surface. Since no grids were applied to these diodes, the fill factor is low. The hydrogen passivation further reduces the electrostatic and recombination role of surface states. Since the open circuit voltage, V_{oc}, of hydrogenated cells is better than the other two diodes, it indicates that hydrogen at the interface reduces the electrostatic effect of surface states and enhances the open circuit voltage. This is supported by the barrier height measured by C-V method. These results are shown in Table I and the hydrogenated cell has the highest barrier height. The increase in short circuit density, J_{sc}, with surface etching and slight increase due to hydrogen incorporation indicates that recombination role of surface states is reduced. This can be checked from the spectral response measurements which are shown in Figure 6. For the untreated surface diodes, the spectral response is inferior at all wavelengths. Due to the low barrier height, the presence of large density of surface states decreases the spectral response (12). The reduced barrier leads to lower concentration of carriers at the insulator-semiconductor interface and recombination at surface states is high and causes degradation in the spectral response at all wavelength. With hydrogen treatment, the spectral response at lower wavelength increases slightly presumably due to passivation of defects. The crossover in the spectral response of hydrogenated and nonhydrogenated diodes in the intermediate wavelength could be due to possible differences in the substrate transport properties.

The advantages of surface preparation and hydrogen incorporation on the photovoltaic properties of small area diodes was exploited in making large area cells. During our work on ITO/silicon SIS solar cells we have seen that small diodes amplify problems of surface leakage currents over the large area cells (13). The photovoltaic output of the best large area devices are listed in Table II.

For the first time we have shown that large area (> 10 cm^2), high efficiency (> 10% based on total area), SIS polysilicon solar cells have been fabricated. The slightly lower fill factor in 18.64 cm^2 devices is due to a nonoptimized grid pattern. As can be seen from Table II, the photovoltaic output of Monsanto devices is lower than Wacker polysilicon. This is possibly due to the intragrain recombination problem associated with Monsanto polysilicon.

To date, the largest device we have fabricated is 18.64 cm^2. It would be possible with some system modification to fabricate production size devices (3-4 inch diameter) by increasing the size of the substrate heater.

We also fabricated ITO/Si SIS diodes on low quality substrate like Honeywell silicon-on-ceramic (SOC) material. The sample used was not one of the best available and no attempt has yet been made to optimize these diodes. These photovoltaic parameters were measured for device R719: V_{oc} = 498 mV, J_{sc} = 24.7 mA/cm^2, active area= 1.17 cm^2, fill factor= 0.75, efficiency= 8.9%.

The sheet resistivity of 750 Å ITO films measured on fabricated diodes is about 40 Ω/□. Thus, in addition to fabricating large area high efficiency, SIS solar cells, such low resistivity ITO has many other applications in solar cells. This includes using ITO or any other oxide semiconductor on the top of the thin metal layer in transparant type MIS solar cells (14). Such a combined transparant conducting layer has low resistivity and good transmittance. In addition, for concentrator applications, the conducting oxide-semiconductor may serve as a partial AR coating layer and will provide low series resistance to p-n junction solar cells.

CONCLUSION

The details of ion beam sputtering system, fabrication, operation and photovoltaic characteristics of ITO/polysilicon solar cells have been described. Large area and high efficiency devices have been fabricated for large grain size polysilicon. Initial results with low quality silicon-on-ceramic substrate are very encouraging. The method is applicable to fabricate any oxide-semiconductor/insulator base-semiconductor (SIS) solar cells. Since junction formation and high temperature processing is impossible for many materials (such as compound semiconductors) considered for advanced solar cells, MIS/SIS structures may be the only viable device structure for them. Ion sputtering is a cost effective technique for cell fabrication. Therefore, Ion beam sputtering technology may play a major role in the goal of low cost solar cells.

REFERENCES

1. K. L. Chopra and M. R. Randlett, Rev. Sci. Instrum. 38, 1147 (1967)

2. E.G. Spencer and P.H. Schmidt, J. Vac. Sci. Technol. 8, 568 (1971) and P.H. Schmidt, R.N. Castellano, and E.G. Spencer, Solid State Technol. 15, 27 (1972).

3. G.R. Thompson, Jr. Solid State Technol. 21, 77 (1978).

4. J.B. DuBow, D. Burk and J. R. Sites, Appl. Phys. lett. 29, 496 (1976).

5. A. Genis, P. Smith, K. Emery, R. Singh, and J. DuBow, App. Phys. Lett. (In Press).

6. J. Shewchun, J. DuBow, A. Myszkowski and R. Singh, J. App. Phys. 49, 855 (1978).

7. A.K. Ghosh, T. Feng and H.P. Maruska, "Thin Film Polycrystalline Silicon Solar Cells", Final Report DOE-SAN/23047-4, Dec. 1979.

8. G. Cheek, A. Genis, J. B. DuBow and V.R. Pai Verneker, Appl. Phys. Lett. 35, 495 (1979).

9. R. Singh, J. Shewchun, J. App. Phys. 49, 4588 (1978).

10. R. Singh, K. Rajkanan, D. E. Brodie and J. F. Morgan, IEEE Electron Devices, April 1980 (In Press).

11. K. Emery and J. DuBow, Proc. 14th IEEE Photovoltaic Specialistis Conf. 1980 (In Press).

12. M.A. Green, J. App. Phys. 50, 1111 (1979).

13. P. Smith, R. Singh, and J. B. DuBow, J. App. Phys., April 1980 (In Press).

14. P.Petrou, R. Singh,& D.E. Brodie, App. Phys. Lett. 35, 930 (1979).

Table 1

Effect of Various Surface Treatment on the Characteristics of ITO/Wacker Polysilicon SIS Solar Cells

Device	Surface Treatment	Total Area (cm^2)	Illumination & Temperature	Barrier Height (mV)	V_{oc} (mV)	J_{sc} mA/cm^2	FF	Efficiency %
R661	No Surface Treatment	0.079	100 mW/cm^2 28°C	798	335	18.1	0.273	1.75
R664	Chemical Etched	0.079	100 mW/cm^2 28°C	932	509	30.7	0.388	6.03
R660B	Chemical Etched & Hydrogenerated	0.079	100 mW/cm^2 28°C	956	512	33.2	0.456	7.73

TABLE II

Photovoltaic Output of Best ITO/Si SIS Solar Cells Measured at AM1 (100 mW/cm^2) 28°C

Sub-strate	Total Area (cm^2)	Active Area (cm^2)	V_{oc} (mV)	I_{sc} (mA)	FF	Total Area Efficiency %	Active Area Efficiency %
Single Crystal p-Si <100>	11.46	9.67	526	328.9	0.79	11.9	14.1
Wacker poly Silicon p-type	11.46	9.67	522	322.1	0.79	11.5	13.7
Wacker Poly Silicon p-type	18.64	16.02	522	485.3	0.70	9.5	11.1
Monsanto poly silicon p-type	11.46	9.67	496	267.0	0.77	10.5	8.9

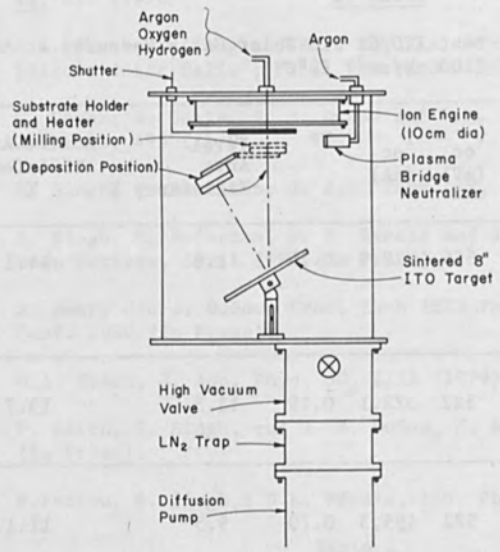

Figure 1: Schematic diagram of ITO sputtering system.

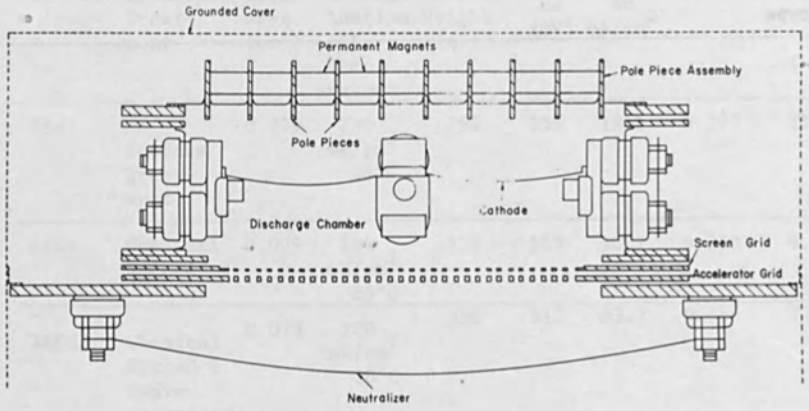

Fig. 2. An Ion Tech. Engine used for Ion-Beam Sputtering.

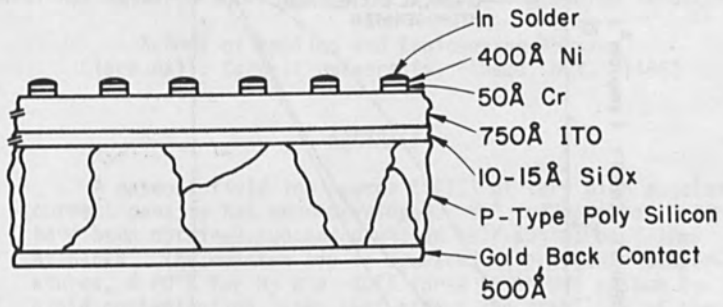

Figure 3: Physical Structure of a ITO-SiO_x-poly Si solar cell.

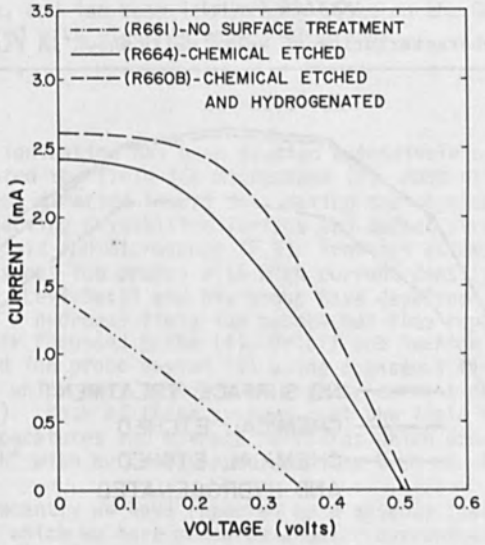

Figure 4: Current-Voltage Illuminated (AM1) characertisics of ITO/ Wacker polysilicon SIS solar cells for various surface treatments.

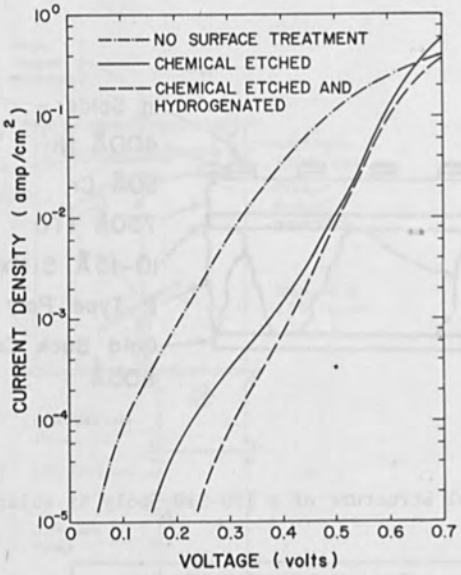

Figure 5: Dark I-V characteristics of solar cells shown in Figure 4.

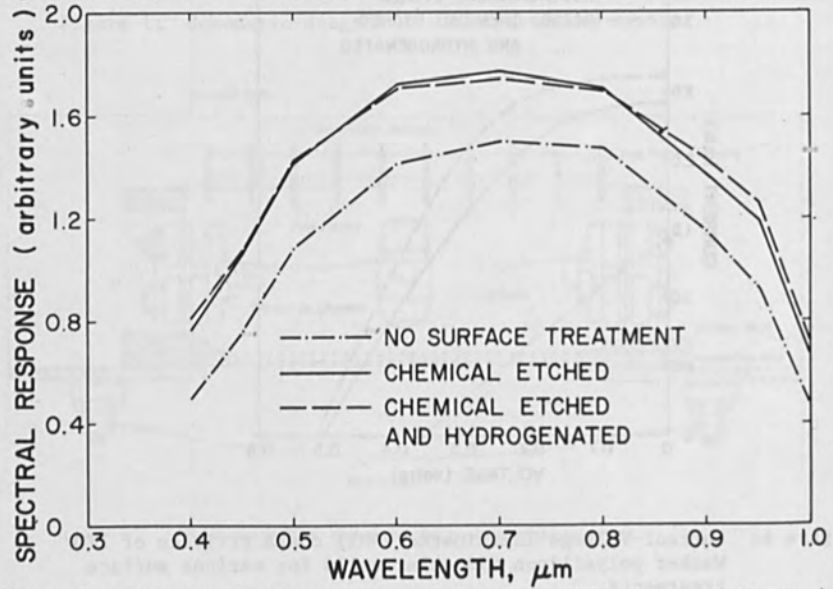

Figure 6: Relative Spectral response of solar cells shown in Figure 4.

GASEOUS FIELD ION SOURCES FOR SUBMICRON FABRICATION

Gary R. Hanson and Benjamin M. Siegel
National Research and Resource Facility for Submicron Structures
and
School of Applied and Engineering Physics
Clark Hall, Cornell University, Ithaca, N.Y. 14853

ABSTRACT

A gaseous field ion source (GFIS) of very high angular current density has been developed. H_2^+ ion beams of 2-20na have been obtained subtended within half-angles of 7-10mr at 5-6kV. The emitter tip is operated at cryogenic temperatures, $\lesssim$ 20°K for H_2 and ~40°K for A in an UHV system to avoid contaminating gases that affect the stability of the ion currents. High long term stability is demonstrated with fluctuations of less than ±2% over periods of hours. An energy analyzer that has been installed in the system to measure the energy width of the beam is described. The characteristics and potential advantages of this gaseous field ion source are compared with the liquid metal ion source, and ion beam lithography based on the GFIS is also compared with electron beam lithography.

INTRODUCTION

Field ionization has been studied extensively since E. Müller first invented the field ion microscope (1). Most of the basic studies have been directed toward elucidating the physical processes involved, observing crystalline surface and defect structures of solids using the field ion microscope (2,3). Previous attempts to produce focussed gaseous ion probes with high current density have been disappointing. Levi-Setti and his group have developed a proton microscope using a hydrogen field ion source but they report only ~10^{-14} amps in their focussed probe (4). Orloff and Swanson describe a hydrogen field ion probe system (5) using a gaseous field ionization source from which they measured an angular current density of 1.0μa/sr (6). Both of these systems cool the field emitter tips to liq. N_2 temperatures and operate at fields which produce a mixture of H_2^+ and H^+ with an energy spread in the beam of ~4eV.

More recently we have reported on a gaseous field ionization source from which we have measured angular current densities as high as 60μa/sr (7). This angular current density is greater than that obtained from Ga liquid ion sources (8). Using hydrogen we have measured ion beam currents of 2 to 20 nanoamps into half-angles of 7 and 10mrad., giving angular currents of ~10 to 60μa/sr. These

high angular currents are obtained by operating a processed tungsten tip at liq. He temperatures under carefully controlled conditions of the gas supply. The field ionization pattern is observed on a channel plate image intensifier (CEMA) and an adjustable aperture is moved into the beam to subtend the desired angle and allow measurement of the beam current passing through the aperture. A number of developments, measurements and observations have been made since that publication was submitted and they are reported here. See Fig. 1.

Stability of H_2^+ Ion Source.

Measurements have been made on the stability of the field ion beam. By carefully controlling 1) the gas flow to the space around the emitter tip from which it is differentially pumped, 2) the temperature of the tip and 3) the voltage between the tip and cathode a very steady beam current is obtained. Fig. 2. shows fifteen minute segments of the current recorded over a period of one hour. Fig. 2a. is the trace of the current recorded from an H_2^+ ion beam giving 2.0na within a 7.8×10^{-3}rad. half angle. The angular divergence subtended by the 40μm aperture that defined the beam was determined from the geometry of the system by measuring the distance between the aperture and the intensifier screen and the diameter of the shadow cast on the screen by the defining aperture when illuminated from the emitter tip. This very steady beam current is obtained by carefully adjusting the parameters that determine the current characteristics of the ion beam. A steady flow of H_2 is required to the cathode cap which is differentially pumped through a 1.0mm aperture in the cathode, the tip is kept at a constant temperature of ≈20°K, and the stabilized voltage between the tip and cathode is set just past the value that gives the maximum beam current. After ~15 minutes of continuous operation some small, very slow fluctuations, about ±2% set in. This behaviour is illustrated by the trace shown in Fig. 2b. which is a continuation of the measurement of current from the same beam illustrated in Fig. 2a. By a slight adjustment of the voltage and the alignment of the defining aperture, the extremely steady ion current illustrated in the trace shown in Fig. 2c. is obtained. The beam current increased slightly with these adjustments to $I_b = 2.2 \times 10^{-9}$ amp into a half-angle of 7.8mr, giving an angular current density $\frac{dI}{d\Omega} \simeq 12$μamp/sr. The low frequency flicker noise usually associated with gaseous field ionization at liq. N_2 temperature is not observed with the source at liq. He temperature. At the lower temperature the supply to the emitting sites is by surface diffusion of the physisorbed gas and this field enhanced process gives a very steady supply in a clean system. Gaseous contamination can be a source of instability causing flicker noises of a few percent and sudden jumps in current of 10-20%. A baked, leak free, UHV system is needed to obtain the very stable performance that has been observed.

Our preliminary observations of argon ion beams indicate that at the higher temperatures at which maximum A^+ ion beam currents are obtained, i.e. ~40°K, contamination has a much greater effect on the stability and character of the field ionization pattern. There are large shifts in the ionization sites and considerable flickering in the pattern.

Processing of Emitter Tips.

The procedures used for processing the emitter tips to obtain high angular currents also require a clean, baked UHV system. Field evaporated end forms produce the large, smooth areas required to obtain a high supply of H_2, however in this end form, ion emission is distributed over a large area of the field emitter. Our observations indicate that the ideal emitter configuration would be one which has a large, atomically smooth area over which neutrals are accommodated with only a localized area or site where the field is enhanced sufficiently to ionize the physisorbed neutrals. Thermal annealling of the <110> oriented tips was used to produce such a configuration, consisting of a flat surface on the (110) face with random disorder at the edges of this face. By adjusting the voltage to produce a critical field at some of the atomic sites at this edge, a few high current emitting sites were obtained. 1-2 nanoamps were emitted into 7mr half-angles from a few of these atomic sites, giving angular current densities, $\frac{dI}{d\Omega} \geq 10\mu a/sr$ (7).

A similarly annealled tip with a defect provided a source that emitted 20na into 10mr half-angle from an area of a few atomic dimensions to produce a beam $\frac{dI}{d\Omega} \geq 60\mu a/sr$. Brady has processed a <100> oriented tungsten tip to obtain a microsite on the <100> axis. With this tip a coaxial beam of ~10na within a 10mr half angle ($\frac{dI}{d\Omega} \simeq 30\mu a/sr$) has been obtained (9).

Energy Analyzer.

The energy width of the ion beam is an important parameter that will determine the chromatic aberration figure obtained when the beam is focussed to a probe with electrostatic lenses. Under the condition that we have been operating, using hydrogen, we believe that we have a single ion species, H_2^+. We obtain maximum current and operate at a field of $\simeq 1.5V/\text{Å}$. Jason et al. have reported that under these low fields only H_2^+ is produced by field ionization with no field dissociation to produce H^+ (10). Hanson measured an energy spread of ~1eV in the H_2^+ beam using low pressures (11). We expect that a similar low energy spread obtains in the higher current beams that we have produced. However, it is important to measure the

actual energy width of the beam. It is possible that space charge or coulombic interactions will introduce a broadening in the beam energy.

A retarding energy analyzer has been built and is now mounted in the gaseous field ion system. A schematic cross-section of the five electrode energy analyzer is shown in Fig. 3. The design is based on the data from Soa (12) who determined the characteristics of three element lenses. Simpson (13) has used this data to construct an energy analyzer with two immersion lenses, the first retarding, the second reaccelerating. We have followed his basic concept, choosing parameters to fit the particular conditions desired for our system. The analyzer has been constructed to titanium electrodes and "Macor" machinable ceramic for the insulators. All parts were machined to high tolerance (± 0.0001") and brazed into a single unit using a single active brazing method developed here (14). The 0.070" hole in the central retarding plane electrode was made using a spark cutter after the whole unit was assembled. After brazing, the apertures in all the electrodes were found to be coaxial within ± 0.0001". The first and final electrodes are kept at cathode potential and the bias electrodes and the retarding plane electrode can be biased at different voltage ratios to move the focal point of the retarding lens so that it produces either a focussed or parallel beam at the central retarding electrode. The lens has been designed for the mode of operating in which the field emitter and the retarding plane are conjugate object-image planes. For this case the energy resolution, $\Delta E/E$, is determined by the Abbe sine condition, being $\sim 8 \times 10^{-5}$ for a beam half angle of 10mr and $\sim 4 \times 10^{-5}$ for a half angle of 7mr. This sensitivity should allow the energy to be measured to a few tenths of an eV and will be more than adequate to determine the energy width of the beam and to investigate the possible influence of space charge upon the beam.

DISCUSSION

Comparison of the Gaseous and Liquid Metal Field Ion Sources for the Fabrication of Submicron Structures.

There has been a great deal of recent interest in liquid metal ion (LMI) sources, evidenced by the three papers presented on the subject in this volume (15-17). Liquid metal ion sources have been investigated as far back as the 1960's but it is only in the past few years that there has been an increased interest in LMI sources, their characteristics, the physical mechanisms involved and their potential application, particularly for the fabrication of submicron structures and devices (18-24). Swanson, et al. (8) have investigated the properties of a liquid gallium ion source, reporting gallium ion beams of angular current densities of $\sim 20 \mu a/sr$ with a minimum energy spread of 4.5eV. They found that increased fields will produce gallium ion

beams with ~40μa/sr but, unfortunately, have an increased energy spread of ~20eV. Focussing these beams requires electrostatic ion optics and because of the large energy spread, the minimum beam diameter will be set by chromatic aberration. These investigators (8) set a lower limit of ~550Å diameter for the spot size at 55kV with a beam current of ~1na. This chromatic aberration limited probe diameter is calculated assuming a virtual Gaussian source diameter of 150Å, the use of a three element, asymmetric electrostatic lens designed to have a minimum chromatic aberration coefficient and the source operated to have an energy spread of 6eV. They calculate that this source would provide a current density of ~38amp/cm^2 in a 0.1μm focussed spot having a brightness ~3.3x10^6 amp/cm^2/sr at 55kV.

Seliger, et al. (23) have described a scanning ion probe system using a liquid gallium ion source with which they have produced probes focussed to spots 0.1 to 0.5μm in diameter with currents of 0.12 to 3.0na subtending half-angles of 1.2 to 6mrad. The current varied as angle squared, while the probe diameter varied as α (to be expected for chromatic aberration limited optics) so they obtained a constant current density of 1.5A/cm^2 in the focussed probes. Thus, for the 0.1μm diameter probe at 57kV an "effective" source brightness of 3.3x10^6 amp/cm^2/sr is obtained. The 0.1μm diameter probe was used to ion etch 0.1μm lines in a 400Å thick gold film (23). Focussing the beam to a line image, they were also able to ion etch 400Å lines in the gold film.

The H_2^+ ion beams with currents of 20na and an angular current density, $\frac{dI}{d\Omega} \simeq 60\mu a/sr$ that we have obtained should focus to a 0.1μm diameter probe with a current density of ~250amp/cm^2 or a 500Å diameter probe with ~1x10^{3}amp/cm^2. These high current densities could be realized with good electrostatic ion optics unless there are strong coulombic effects that cause energy broadening in the beam. Given an energy width of ~1eV in the beam, the aberration limited, effective brightness of our source should be >1x10^{9}amp/cm^2/sr at 57kV. There are several advantages that can be expected with the higher brightness GFI source compared to the LMI source in the fabrication of submicron structures.

1) The H_2^+ ion source with an effective source brightness of some 100 times greater than that available from the liquid metal sources, could be focussed to smaller spot diameters with higher current density and smaller angular divergence. Deflection aberrations are a function of the angular divergence of the probe and thus the high brightness gaseous probe could be scanned over larger fields with greater current densities allowing more rapid scanning rates than the ions from the liquid metal sources.

2) H_2^+ ions could be used to expose thicker resists for high resolution lithography at very rapid rates with moderate ion energies.

Since the total beam current is larger from the LMI source, it is possible that the LMI sources could give larger beam currents than the gaseous source focussed to probes with diameters ≈0.5μm. However, the actual realization of higher current densities with this probe diameter will depend on the aberrations in the system and must be demonstrated experimentally.

3) Rare gas A^+ ions (also Kr^+ and Xe^+) or reactive O_2^+ or N_2^+ ions could be used directly to fabricate submicron structures by ion sputter etching without introducing atomic contaminants that would be difficult to anneal out. The sputtering rates could be high enough for fabricating VLSI at practical rates. It will be necessary to experimentally determine the actual sputtering rates that can be realized and to investigate the effects of the high current densities on the materials used in electronic devices. Extrapolating from existing data on ion milling and sputter etching obtained with large diameter beams may be misleading and experiments must be carried out to obtain the data necessary for evaluating the feasibility of direct etching at submicron dimensions.

4) There is an area in which the liquid metal field ion sources could very usefully complement the high brightness gaseous ion sources. In the fabrication of electronic devices substitutional doping of semiconductors, e.g. groups IIIA or VA elements implanted in Si, plays a very important role in determining the characteristics of the devices.

Comparison of Ion Beam Lithography with Electron Beam Lithography.

Electron beam lithography is well developed and is being used for the fabrication of microstructures in a number of laboratories. There is instrumentation available for producing submicron structures. Various approaches such as vector scan, shaped beam and raster scan are being used or developed. The subject has been reviewed by Broers (24). For our purposes the present state of the art and the potential developments using field emission sources will be described very briefly to afford a basis for comparison of electron beam lithography with the potentials of ion beam lithography.

The principal limitations in electron beam lithography are, 1) the relatively high exposures required by the high resolution resists such as PMMA and 2) the limitations on resolution caused by the backscattering of electrons from thick substrates. The proximity effect that occurs because of the backscattering of electrons sets a lower dimensional limit of ~0.1μm on structures that can be produced on thick substrates with electron beam lithography (25). Complex computer control of the beam exposure is required to minimize this effect (26). Probe diameters of ~250Å are used to write 0.1μm lines in vector scan systems, since multiple passes are used

to obtain the pattern configurations and the varying exposures desired (27). PMMA requires exposures of between 10^{-4} and $10^{-5}C/cm^2$ to obtain satisfactory development of the resist. The best electron source now in use is the LaB_6 thermionic emitter with a brightness of $\sim 10^6 A/cm^2/sr$. Brightness sets the limit of the ultimate speed with which patterns can be written in resists by being a measure of both the current density in the focussed spot and the angular divergence of the beam which sets the deflection aberrations. However, in current instrumentation the digital electronic control of the scanning system sets a practical limit. Much brighter field emission sources ($\beta \simeq 10^8 amp/cm^2/sr$) (28) will undoubtedly be available soon. Bell and Swanson (29) have studied the characteristics of T-F emitters and their results indicate that stable, very high intensity electron beams with angular currents of >1ma/sr could become available. Shaped beam systems give promise of faster throughput for electron beam lithography (24,25). But it is not at all clear at this stage in the development of these systems that they can be used efficiently and to advantage at dimensional levels of 0.5μm and smaller. Very high beam currents are required and space charge and coulomb interactions limit their capability when they are compared with the vector scan system in the 0.1μm to 0.5μm range.

The H_2^+ field ion source that we have developed should produce ion current densities when focussed into probes in the submicron range that could make writing with ion lithography processes faster than electron beam lithography at 0.5μm and smaller. Since resists such as PMMA are 50 to 100 times more sensitive to ions than electrons (30) and our ion source has produced beams with 20na of ion current into aperture angles of 10mrad., the equivalent electron beam current required would be some 1 to 2μamps for equal writing speeds. The LaB_6 thermionic source cannot be expected to give these currents with probe diameters of less than ~0.2μm and while the high intensity field emission sources may give calculated currents in the submicron region, the coulomb interactions may become very important and may well limit the current densities that can be realized. Of course, a very large advantage of ion beam lithography would be that there are no proximity effects for which exposure corrections must be made in electron beam lithography. Karapiperis and Lee (31) have already demonstrated 400Å structures and spacings using H^+ ion exposures of PMMA and thus clearly, structures ≤0.5μm could be written with ion probes without the complicated, time consuming correction of exposures. The final development and experimental characterization of submicron probes from both the gaseous field ion source and the field emission source will be required to obtain a comparative evaluation of their application in the lithographic processes in the submicron range.

This work was supported as a program of the National Research and Resource Facility for Submicron Structures under the National Science Foundation: Grant 77-09688.

REFERENCES

1. E.W. Müller, Z. Physik 131, 136 (1951).
2. R. Gomer, Field Emission and Field Ionization (Harvard Univ., Cambridge, 1961).
3. E. Müller and T.T. Tsong, Field Ion Microscopy (Elsevier, N.Y., 1969).
4. R. Levi-Setti, "Proton Scanning Microscopy: Feasibility and Promise," Proc. 7th Ann. SEM Sym. ed. O. Johari (IIT Res. Inst. Chicago, 1974) p.125.
5. J. Orloff and L.W. Swanson, "Fine Focus Ion Beams with Field Ionization," J. Vac. Sc. and Tech. 15, 845 (1978).
6. J. Orloff and L.W. Swanson, "Angular Intensity of a Gas-Phase Field Ionization Source," J. Appl. Phys. 50, 6026 (1979).
7. G.R. Hanson and B.M. Siegel, "H_2 and Rare Gas Field Ion Source with High Angular Current," J. Vac. Sc. and Tech. 16, 1875 (1979).
8. L.W. Swanson, G.A. Schwind, A.E. Bell and J. Brady, "Emission Characteristics of Gallium and Bismuth Liquid Metal Field Ion Sources," J. Vac. Sc. and Tech. 16, 1864 (1979).
9. J. Brady, G.R. Hanson and B.M. Siegel, "Reproducible Localization of the Ionization Site in the Gaseous Field Ion Source," Proc. 9th Int. Conf. on Electron and Ion Beam Sc. and Tech. (St. Louis, 1980).
10. A. Jason, B. Halper, M.G. Inghram and R. Gomer, "Field Ionization from H_2 Layers," J. Chem. Phys. 52, 2227 (1970).
11. G.R. Hanson, "Dissociative Field Ionization of H_2 and HD," J. Chem. Phys. 62, 1161 (1975).
12. E.A. Soa, "A Systematic Investigation of Electrostatic Immersion Objectives," Jenaer Jahrbuch I 115 (1959).
13. J.A. Simpson, "Design of Retarding Field Analyzers," Res. Sc. Inst. 32,1283 (1961).
14. G.R. Hanson, Metal-Ceramic Bonding Technique, Patent Pending.
15. Y. Kuk, R.J. Culbertson and T. Sakurai, "Atom-Probe Study of Ga Ion Beams from a Point Source," 9th Int. Conf. on Elec. and Ion Beam Sc. and Tech. (St. Louis, 1980).
16. L.W. Swanson, A.E. Bell, G.A. Schwind and J. Orloff, "A Comparison of the Emission Characteristics of Liquid Ion Sources of Gallium, Indium and Bismuth," 9th Int. Conf. on Elec. and Ion Beam Sc. and Tech. (St. Louis, 1980).
17. R.W. Vahrenkamp, V. Wang, J.W. Ward and R.L. Seliger, "Liquid Metal Ion Sources Using Alloyed Materials," 9th Int. Conf. on Elec. and Ion Beam Sc. and Tech. (St. Louis, 1980).
18. V.E. Krohn and G.R. Ringo, "Ion Sources of High Brightness Using Liquid Metal," Appl. Phys. Lett., 27, 479 (1975).
19. R. Clampitt, K.L. Aitken, D.K. Jefferies, "Intense Field Emission Ion Source of Liquid Metal," J. Vac. Sci. and Tech. 12, 1208 (1975).
20. R. Clampitt and D.K. Jefferies, "Miniature Ion Sources for Analytical Instruments," Nucl. Inst. and Meth. 149, 739 (1978).

21. B.W. Colby and C.A. Evans, Jr., "Electrohydrodynamic Ionization Mass Spectrometer," Anal. Chem. 45, 1884 (1973).
22. R. Gomer, "On the Mechanism of Liquid Metal Electron and Ion Sources," J. Appl. Phys. (in press).
23. R.L. Seliger, J.W. Ward, V. Wang and R.L. Kubena, "A High Intensity Scanning Ion Probe with Submicrometer Spot Size," Appl. Phys. Lett. 34, 310 (1979).
24. A.N. Broers, "A Review of High Resolution Microfabrication Techniques," Proc. Int. Electron Device Conf. (IEEE), 1978.
25. A.N. Broers, "Current State of the Art of Microstructure Fabrication," Proc. of the NSF Workshop on Opportunities for Microstructure Science, Engineering and Technology at Airlie House, Nov. 19-22 (1978) p.17.
26. M. Parikh, "Proximity Effect Corrections in Electron Beam Lithography," Proc. 8th Int. Conf. Elec. and Ion Beam Sci. and Tech., ed. R. Bakish (Elect. Chem. Soc., Princeton 1978) p.382.
27. A.J. Speth, A.D. Wilson, H. Kem and T.H.P. Chang, "Electron-Beam Lithography Using Vector-Scan Techniques," J. Vac. Sci. and Tech. 12, 1935 (1975).
28. H.P. Kuo and B.M. Siegel, "A High Brightness High Current Field Emission Electron Probe," Proc. 8th Int. Symp. Electron, and Ion Beam Tech., ed. R. Bakish (Electro. Chem. Soc., Princeton, 1978) p.3.
29. A.E. Bell and L.W. Swanson, "Total Energy Distribution of Field Emitted Electrons at High Current Density," J. Appl. Phys. (in press).
30. M. Komuro, N. Atoda and H. Kawakatsu, "Ion Beam Exposure of PMMA Resist," Proc. 24th Ann. Meet. Japan Soc. Appl. Phys. - 1977(J); H. Kawakatsu personal communication.
31. L. Karapiperis and G.A. Lee, "400Å, High-Aspect-Ratio Lines Produced in PMMA by Ion-Beam Exposure," Applied Phys. Lett.

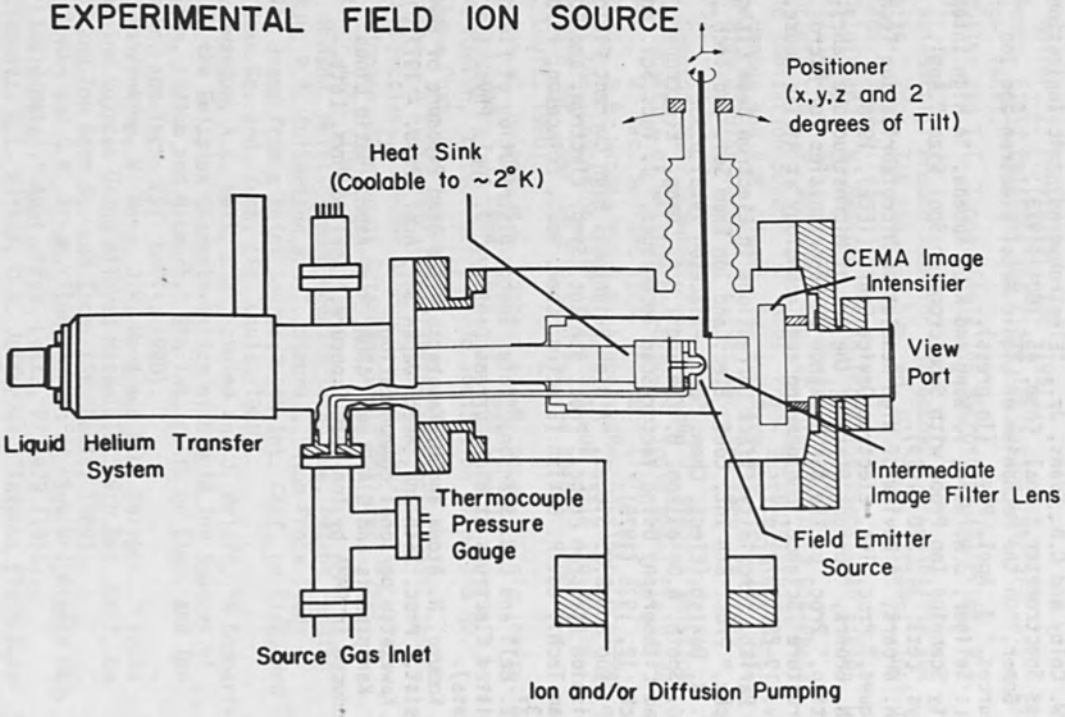
EXPERIMENTAL FIELD ION SOURCE
Positioner
(x,y,z and 2
degrees of Tilt)
Heat Sink
(Coolable to ~2°K)
CEMA Image
Intensifier
View
Port
Liquid Helium Transfer
System
Thermocouple
Pressure
Gauge
Intermediate
Image Filter Lens
Field Emitter
Source
Source Gas Inlet
Ion and/or Diffusion Pumping

Fig. 1.

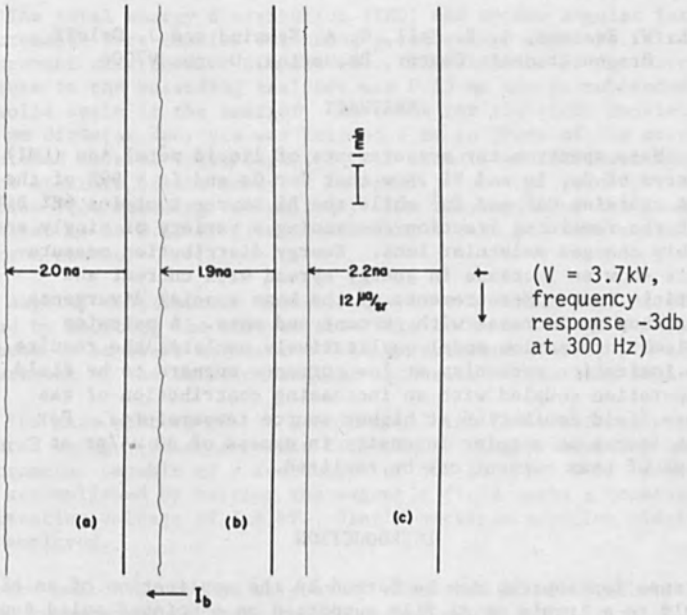

Fig. 2.

Photograph of chart recording showing hydrogen ion current subtended within a 7.8mr half-angle measured vs. time. 2a. Current during initial 15 minute period. 2b. Current during later 15 minute period showing periodic fluctuations ±2%. 2c. Current after slight repositioning of aperture in the ion beam and adjusting the voltage.

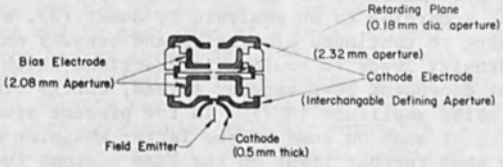

Fig. 3. Intermediate Image Filter for Energy Analysis.

A COMPARISON OF THE EMISSION CHARACTERISTICS OF LIQUID ION SOURCES OF GALLIUM, INDIUM AND BISMUTH

L. W. Swanson, A. E. Bell, G. A. Schwind and J. Orloff
Oregon Graduate Center, Beaverton, Oregon 97006

ABSTRACT

Mass spectrometer measurements of liquid metal ion (LMI) sources of Ga, In and Bi show that for Ga and In > 99% of the beam contains Ga^+ and In^+ while the Bi source contains 60% Bi^+ with the remaining fraction containing a variety of singly and doubly charged molecular ions. Energy distribution measurements show an increase in energy spread with current and particle mass. Measurements of the beam spacial divergence also show an increase with current and mass. A pairwise coulomb interaction model qualitatively explains the results. The ionization mechanism at low currents appears to be field evaporation coupled with an increasing contribution of gas phase field ionization at higher source temperatures. For each source an angular intensity in excess of 30 μA/sr at ~ 15 μA of beam current can be realized.

INTRODUCTION

Intense ion sources may be formed by the application of an electric field to a liquid metal film supported on a pointed solid support of 5 to 10 μm radius. The geometric stability of the liquid cone is provided by the balance of the electrostatic and surface tension forces when the cone half angle is 49.3° (1). Measurement of the energy distribution and deficit at low total currents (1 to 10 μA) suggest field evaporation with an increasing contribution of gas phase field ionization at higher currents as the ionization mechanism (2,3).

In a previous study using the liquid metal source in the electron emitting mode it was found that the cone elongation and concomitant rapid increase in field emission led to a pulsed mode emission (4). The much slower moving heavy ions lead to the rapid build up of a positive charge density in front of the emitting tip which lowers the electric field and, according to an analysis by Gomer (5), stabilizes the cone with respect to continued elongation and runaway emission. The high current density leads to coulomb interactions which are manifested by a current dependent beam angular spread, energy broadening and unusually low noise amplitude (6,7). In the present study we investigate the effect of mass on some of the latter emission characteristics in order to shed further light on the beam coulomb interactions and emission characteristics.

EXPERIMENTAL APPROACH

The total energy distribution (TED) and source angular intensity measurements were carried out using a focussing, meshless filter lens arrangement described by Simpson (8). The diameter of the entrance aperture to the retarding analyzer was 0.13 mm and it subtended a 6.0 μsr solid angle at the emitter. An extractor electrode consisting of a 10 mm diameter aperture was located 1 mm in front of the emitter and biased several volts negative with respect to the downstream entrance aperture of the analyzer in order to prevent secondary electron emission from reaching the emitter. The resolution of the analyzer was estimated to be 0.15 eV from measurement of the TED from a field electron source.

Angular distribution measurements of the source current were performed by mounting the emitter structure on an x-y stage. This allowed the beam to be swept across the 0.13 mm aperture thereby providing a measurement of the emission angular intensity versus beam angle.

The mass spectra of the liquid metal ion (LMI) sources were measured using a Hitachi-Perkin Elmer RMU-7 single focussing mass spectrometer capable of a resolution of 600 at m/e = 500. Mass scans were accomplished by varying the magnetic field using a constant accelerating voltage of 3.6 kV. Single particle counting electronics were employed.

The emitters used in this study consisted of electrochemically etched tungsten or nichrome points coated with liquid films of Ga, In and Bi. The details of the source structure are described elsewhere (6). Emitter temperature was controlled by resistive heating and measured by monitoring the resistance of the 0.18 mm diameter W filament to which the emitter was spot welded.

RESULTS

Mass Spectra

Table 1, which summarizes the relative intensities of the various mass species for the Ga, In and Bi sources, shows that the M^+ species is the major one in each case at a total current I_T of 10 μA. As will be shown, the energy spread ΔE of the ions is not only current dependent, but also dependent on ionic charge ne and mass m. Thus, it is important to measure the total area under each mass peak rather than peak height when determining relative abundance ratios since $\Delta E = (\Delta m/m)E$. This leads to a differing degree of broadening of the various mass peaks as shown in Fig. 1 for the various Bi species. Because the mass scale in Fig. 1 is the voltage due to a Hall effect probe in the swept magnetic field, the mass scale is nonlinear. Nevertheless, the relative energy broadening determined from the full width half maximum (FWHM) of the mass peaks (corrected for the

nonlinear Hall voltage probe) versus m/ne was found to vary in the following fashion:

$$M_3^+ > M_2^+ > M^+ > M_5^{++} > M_3^{++} > M^{++}$$

In each case the mass peaks were observed to broaden with increasing value of I_T and the doubly charged entity of each mass gave a narrower FWHM than the corresponding singly charged specie. This latter effect was observed by other workers using an Au LMI source (9).

A limited study of the variation of the various mass species with temperature T and I_T is summarized in Tables 2 and 3. From these results we are able to conclude that the ratios

$$\frac{M_n^+}{M_n^{++}} \text{ and } \frac{M_{n+1}^+}{M_n^+} \text{ for } n > 1$$

are, for the most part, independent of I_T and T. On the other hand, M_n^+/M^{++} decreases with increasing I_T and decreasing T. The temperature dependence of M^+/M^{++} was not determined. These results support the notion put forth previously (3) that the species M_n^+ and M^{++} (for $n > 1$) are formed by a common mechanism involving a temperature dependent volatilization of the M_n species followed by gas phase field ionization. In view of its narrow energy spread the species M^{++} is formed by a field evaporation mechanism while the M^+ species is believed to be formed primarily by a field evaporation process and secondarily by volatilization followed by field ionization. The foregoing mechanisms can be described in terms of the rate constants for field evaporation $k_{FE}(F,T)$ and field ionization $k_{FI}(F)$ where F is the applied field strength. At the very high field strengths, believed to be the case for the LMI source, the temperature dependence of field evaporation is very low, thus

$$k_{FE}(F,T) \sim k_{FE}(F)$$

and similarly for field ionization

$$k_{FI}(F) \sim k_{FI}$$

Thus

$$I_M^+ = k_{FE}^+(F) + k_{FI}^+ P_M(T)\alpha(F) \quad (1)$$

$$I_M^{++} = k_{FE}^{++}(F) \quad (2)$$

$$I_{M_n}^{m+} = k_{FI}^{m+} P_{M_n}(T)\alpha(F) \quad (n > 1) \quad (3)$$

where $\alpha(F)$ is the field enhancement factor of the supply function due to field-polarization attraction and P(T) is the vapor pressure of M_n.

Thus, the ratio $I_{M_n^{m+}}/I_M^{++}$ (for $n > 1$) is expected to increase with T as observed in Table 2 for $I_{Ga_2}^{+}/I_{Ga_3}^{++}$ and I_{Ga}^{++}/I_{Ga}^{++} since

$$\frac{I_{M_n^{m+}}}{I_{M++}} = \frac{k_{FI}P(T)\alpha(F)}{k_{FE}^{++}(F)} \quad (n > 1) \tag{4}$$

and the numerator will increase with T due to the P(T) term. In contrast,

$$\frac{I_{Ga_2}^{+}}{I_{Ga_3}^{+}} \sim \frac{P_{Ga_2}(T)}{P_{Ga_3}(T)}$$

is not expected to exhibit a significant temperature dependence, as observed in the Table 2 results, provided the heats of vaporization for Ga_2 and Ga_3 are approximately the same. Similarly, the current independence of the Eq.(4) ratio can be predicted if one assumes that the current increase, which occurs by increasing the source voltage, is due to an increase in F. Since both the numerator and denominator on the right side of Eq.(4) increase with F the ratio is not expected to vary greatly over the limited range of I investigated as observed in the Table 3 results. By similar reasoning using Eqs.(1) and (3) and assuming $k_{FE}^{+}(F)/k_{FE}^{++}(F)$ has negligible variation with F and that $\alpha(F)/k_{FE}^{++}(F)$ decreases with increasing F, one can account for the current (i.e. F) dependence of Bi^{+}/Bi^{++} in Table 3.

Energy Distribution

Figs. 2 and 3 show typical TED curves as functions of I_T for the Ga and Bi LMI sources. The TED's for all ionic species are superimposed in these results; however, the M^{+} species will dominate all of the TED results. The FWHM values of the TED for the three sources are summarized in Fig. 4 as a function of the axial angular intensity. The Figs. 2 and 3 results show that the TED FWHM values not only increaase with I_T but also display a significant shift ΔE_p of the TED curves toward higher energy with increasing I_T. This effect is more pronounced with increasing mass.

The FWHM values increase significantly with mass at both constant I_T and angular intensity $I(\Omega)$ as shown in Fig. 5. A summary of the empirical findings of the effect of I_T, m and ne on the FWHM values ΔE_F can be given as follows:

$$\Delta E_F \propto \frac{m^g I^h}{(ne)^k} \tag{5}$$

In addition, as shown in Figs. 2 and 3, an energy shift ΔE_p of the TED

curve toward higher energy occurs according to

$$\Delta E_p \propto I^{\ell}\, m^{p} \tag{6}$$

where the exponents in both Eqs.(5) and (6) are positive.

A simple model involving coulomb-coulomb interaction was developed which qualitatively predicts the empirical findings of Eqs.(5) and (6). The model is shown in Fig. 6 where two charged, in line particles 1 and 2 are accelerated in a concentric sphere electric field from a spherical cathode of radius r_o and applied field F_o. Neglecting image potential interactions the forces f_1 and f_2 on the two particles are

$$f_1 = m\ddot{x}_1 = \frac{neF_o r_o^2}{x_1^2} + \frac{k(ne)^2}{(x_1 - x_2)^2} \tag{7}$$

$$f_2 = m\ddot{x}_2 = \frac{neF_o r_o}{x_2^2} - \frac{k(ne)^2}{(x_1 - x_2)^2} \tag{8}$$

where $k = 1/(4\pi\varepsilon_o) = 9 \times 10^9$ (in MKS units). The above equations of motion can be integrated as follows to give the energy change ΔE_1 and ΔE_2 for particles 1 and 2 that occurs due to the mutual coulomb terms (last terms) in Eqs.(7) and (8):

$$\Delta E_1 = k(ne)^2 \int_{\delta_o}^{x_\ell} \frac{dx_1}{\delta^2} \tag{9}$$

$$\Delta E_2 = -k(ne)^2 \int_{r_o}^{x_\ell} \frac{dx_2}{\delta^2} \tag{10}$$

where δ_o is the initial spacing of the particles and x_ℓ, the upper limit of integration, is taken so that no further change in ΔE_1 or ΔE_2 occurs on further increase of x_ℓ. Inorder to integrate Eqs.(9) and (10) it is necessary to solve the differential equations (7) and (8) to obtain a relationship between the particle positions and in the interparticle spacing $\delta = x_1 - x_2$. This was done numerically using a 4th order Runga-Kutta method with a step size that varied from .01 r_o to .01 x_ℓ. A cubic spline fit to the solutions yielded a set of $\delta(x)$ relationships that allowed a piecewise integration of Eqs.(9) and (10) to be performed (10). Negligible error was introduced by terminating the integration at $x_\ell \sim 1$ m.

The results of the model predictions are given in Fig. 7 where the energy spread $\Delta E_F = |\Delta E_1| + |\Delta E_2|$ and the energy shift $\Delta E_p = (|\Delta E_1| - |\Delta E_2|)/2$ are plotted vs current for several m/e ratios. The current I in Fig. 7 was calculated according to

$$I = \frac{ne}{\tau_2}$$

where τ_2 was the time for particle 2 to travel the distance δ_o from the emitter.[2] Because of the in-line particle constraint of the model the absolute values of the current have only relative significance. Nearly all of the qualitative features of the experimental results are predicted by the Fig. 7 summary. For example, the empirical findings of the effects of m, ne and I_T on ΔE_F and ΔE_P summarized in Eqs.(5) and (6) are all confirmed by the two particle model. An interesting result of the model predictions, which is verified by experimental findings is the asymmetrical broadening of the TED. That is, the leading particle of the pair undergoes a larger increase in kinetic energy than the decrease incurred by particle 2. This effect, which increases with both m and I and decreases with increasing value of ne, leads to an asymmetrical TED shape and a shift to smaller energy deficits (i.e. larger kinetic energy).

Interestingly, according to Fig. 7, the energy spread for Li^+ is identical to that of Bi^{++} in the range of current indicated. The model clearly confirms the experimental findings that smaller m and larger ne lead to significantly reduced energy spread due to the coulomb interactions.

Beam Broadening

Fig. 8 illustrates the typical variation of emission intensity (in current/solid angle) with beam angle. A similar result was measured for In and Bi sources except that a larger beam spread was observed for a specific current. Thus, the beam spacial divergence increases with both I_T and m. This result is summarized in Fig. 9 where the beam divergence, in terms of the FWHM values of the Fig. 8 curves, is plotted versus m at two values of I_T. The spacial divergence of the Bi LMI source is nearly double that of the Ga source at a specific current.

The beam divergence can easily be predicted qualitatively from the Fig. 6 two particle model when the particles are launched side by side with increasing lateral spacing and varying ne and m values. In addition, a continuous charge density model using a Gauss' law approximation was also employed to analyze the diverging beam results. In each case the models predicted the qualitative dependence of beam divergence on I_T and m observed in this study. Interestingly, the continuous charge model predicted the space charge divergence of a Bi beam made up of the following mass and charge combinations to decrease at constant I_T as

$$Bi_3^+ > Bi_2^+ > Bi_5^{++} > Bi^+ > Bi_3^{++} > Bi^{++}$$

Curiously, this is nearly the same order of the experimentally determined decrease in energy broadening mentioned earlier and underscores

the similarity of the coulomb interactions that lead both to spacial beam divergence and energy broadening.

As a result of beam broadening the maximum achievable axial angular intensity at any current is less for ions of increasing mass. Even with these limitations, angular intensities in excess of 30 μA/sr at $I_T \cong 15$ μA can be obtained from each of these LMI sources.

CONCLUSIONS

The results of this investigation point to the increasing importance of pairwise coulomb interactions with beam current and particle mass. These interactions are manifested by an increased energy and spacial divergence of the beam and place certain limits on the optical quality of the LMI sources in terms of axial angular intensity and chromatic effects. The Fig. 4 results show the increase in energy spread for Ga, In and Bi to be 5, 14 and 21 eV respectively at an angular intensity of 20 μA/sr. Assuming the source size to be < 1000 Å, the source brightnesses at the aforementioned energy spread values is an impressive > 1×10^5 A/sr cm^2. Thus, a small source acceptance half angle of 4 mrad in order to reduce chromatic aberration still allows 1 nA of beam current to be realized.

ACKNOWLEDGEMENTS

This work was carried out under a grant from the M. J. Murdock Charitable Trust Foundation. The authors benefited by computer calculations of the energy spread by Mr. Dale Larson and Dr. C. H. Hinrichs.

REFERENCES

1. G. I. Taylor, Proc. Roy. Soc. (London) A280, 383 (1964).
2. L. W. Swanson, G. A. Schwind and A. E. Bell, J. Appl. Phys. (in press).
3. R. J. Culbertson, G. H. Robertson, and T. Sakurai, J. Vac. Sci. and Technol. (in press).
4. L. W. Swanson and G. A. Schwind, J. Appl. Phys. 49, 5655 (1978).
5. R. Gomer, Appl. Phys. 19, 365 (1979).
6. L. W. Swanson, G. A. Schwind, A. E. Bell and J. E. Brady, J. Vac. Sci. and Technol. (in press).
7. L. W. Swanson, G. A. Schwind and A. E. Bell, Scanning Electron Microscopy, Vol. I (SEM Inc., AMF O'Hare, Ill., 1979) p. 45.
8. J. A. Simpson, Rev. Sci. Inst. 32, 1283 (1961).
9. P. Sudraud, C. Colliex and J. van de Walle, Le J. Phys. Lettres 40, L207 (1979).
10. T. N. Greville, J. Siam, Numer. Anal. (Ser B) 1, 53 (1964).

TABLE 1

Relative amount of the various mass species at I_T = 10 μA for the Ga, In and Bi liquid metal ion sources.

Ga^+	~ 1*	In^+	1	Bi^+	1
Ga^{++}	2.2×10^{-3}	In^{++}	1.9×10^{-5}	Bi^{++}	.023
Ga_2^+	9.0×10^{-3}	In_2^+	2×10^{-6}	Bi_2^+	.21
Ga_3^+	3.6×10^{-3}			Bi_3^+	.24
				Bi_3^{++}	.15
				Bi_5^{++}	.025

*Measurement of the relative amount of Ga^+ is only approximate in this study due to a limit on the dynamic range of the detection electronics during these measurements.

TABLE 2

Variation of mass peak area ratios with source temperature at I_T = 10 μA

T(K)	$\frac{Ga_2^+}{Ga^{++}}$	$\frac{Ga_3^+}{Ga^{++}}$	$\frac{Ga_2^+}{Ga_3^+}$
300 K	4.2	1.6	2.6
361 K	6.0	2.1	2.9
432 K	22	9.7	2.3

TABLE 3

Variation of mass peak area ratios with I_T for Ga at 303 K and Bi at 525 K

I_T(μA)	$\frac{Ga_2^+}{Ga^{++}}$	$\frac{Ga_3^+}{Ga^{++}}$	$\frac{Ga_3^+}{Ga_2^+}$	$\frac{Bi^+}{Bi^{++}}$	$\frac{Bi_2^+}{Bi^{++}}$	$\frac{Bi_3^{++}}{Bi^{++}}$	$\frac{Bi_2^+}{Bi_3^+}$	$\frac{Bi_2^+}{Bi_3^+}$	$\frac{Bi_3^+}{Bi_3^{++}}$
5	5.8	4.9	.84	51	22	15	1.5	0.56	2.0
10	4.2	1.6	.39	20	8.4	6	1.4	0.87	1.6
14	6.5	2.2	.32	-	-	-	-	-	-
18	4.0	1.6	.30	14	7.1	4.6	1.5	-	-

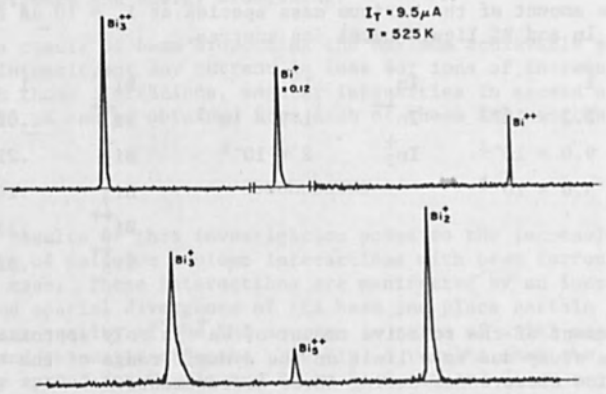

Fig. 1. Typical mass spectrum of the LMI Bi source. The mass scale is nonlinear.

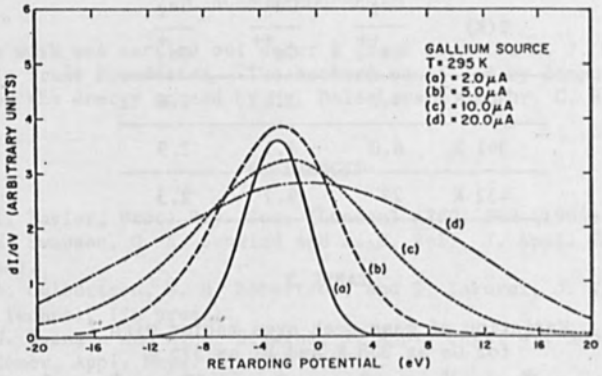

Fig. 2. Curves of the TED for the Ga LMI source at the indicated values of total current.

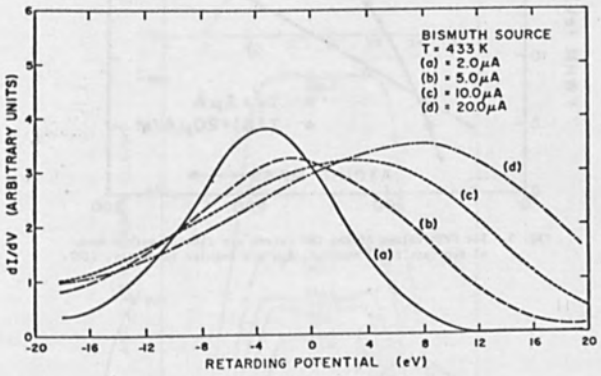

Fig. 3. Curves of the TED for the Bi LMI source at the indicated values of total current.

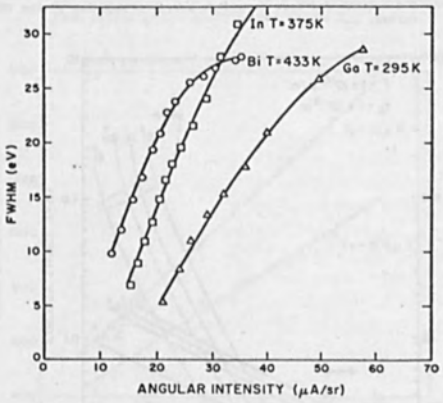

Fig. 4. The FWHM values of the TED curves are plotted versus angular intensity for the indicated LMI sources.

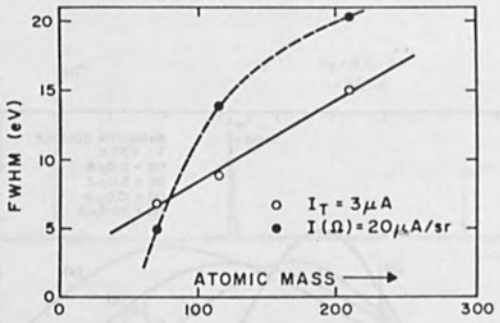

Fig. 5. The FWHM values of the TED curves are plotted versus mass at constant total current, I_T, and angular intensity, I(Ω).

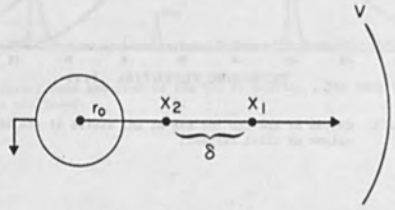

Fig. 6. Diagram of the in line, two-particle model used to estimate the current and mass dependent energy broadening of the TED curves.

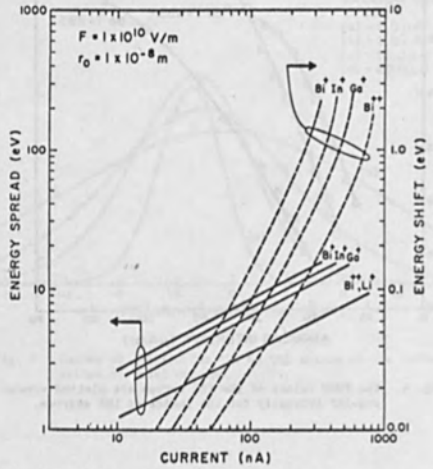

Fig. 7. Plot of the energy broadening ΔE_B and shift ΔE_P due to the pairwise coulomb interaction based on the Fig. 6 model. Calculations were made at the indicated values of F_o and r_o.

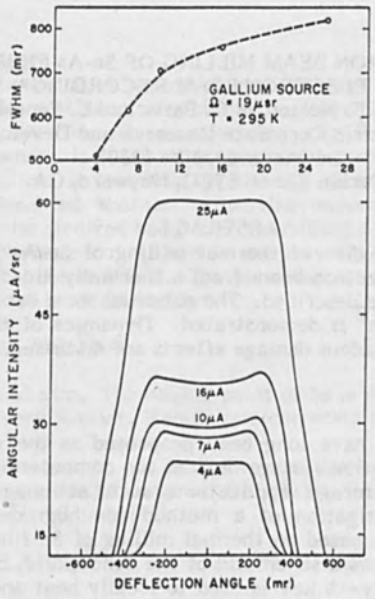

Fig. 8. Lower curves show the angular current intensity vs beam angle (0 is the emitter apex direction) at the indicated total source current I_T for Ga. The upper curve shows the FWHM values of the lower curves versus I_T.

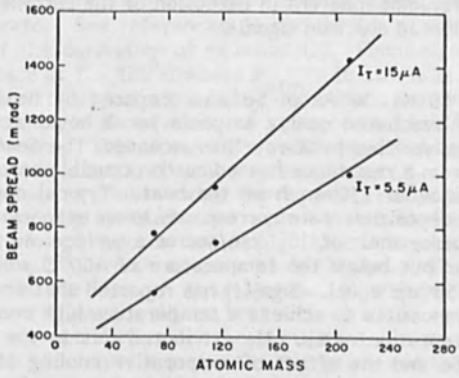

Fig. 9. The FWHM values of the beam angular divergence values versus mass for the Ga, In and Bi LMI sources at the indicated currents.

ELECTRON BEAM MILLING OF Se-As FILMS FOR ELECTRON BEAM RECORDING*

G.E. Possin, J.F. Norton, H.G. Parks and L. Veneklasen**
General Electric Corporate Research and Development
Schenectady, NY 12301
**Perkin Elmer ETEC, Hayward, CA

ABSTRACT

Experimental studies of thermal milling of Se-As films using a high power 0.2μm focused electron beam from a thermally aided oxygen processed field emission source are described. The potential for a data recording density in excess of 10^9 bits/cm^2 is demonstrated. Dynamics of the milling process and low beam current readout damage effects are discussed.

Introduction

Electron beams have long been propoosed as the writing mechanism for high density information storage devices for computers and for other high capacity information storage applications such as image recording. We describe here an investigation of a method for high density storage and retrieval of information based on thermal milling of Se films on silicon diode detectors. Figure 1 shows a schematic of the concept. A high power focused electron beam of energy ~4 keV is used to locally heat and evaporate a thin layer of Se-As film. The presence of written holes can be detected by the sane electron column operating at a lower current, through the induced current signal generated in a planar np junction which forms the substrate for the thin Se layer. This readout method has very high gain and low noise and avoids many of the problems inherent in detection of the surface structure by secondary or backscattered electron signals.

Sample Preparation

An alloy of 13 wt. % As in Se was prepared by heating the pure elements in a sealed evacuated quartz ampoule for 8 hours at 300°C. The alloy composition was verified by X-ray fluorescence. The Se-As films were vacuum evaporated from a resistance heated carbon crucible onto silicon diode substrates at a distance of 150mm from the boat. Typical deposition rates were 30 Å/sec. This deposition rate corresponds to an evaporation rate from the surface of the source melt of 10^{-3} cm/sec or a surface melt temperature ~300°C which is near but below the temperature of 400°C where the vapor pressures of As and Se are equal. Sigai(1) has reported that for dilute (0.5% As) alloys it is was impossible to achieve a temperature high enough to obtain equal As and Se evaporation rates. He attributed this to the poor thermal conductivity of the Se and the effect of evaporative cooling of the surface. Arsenic was chosen as a component of the films because it stabilizes the amorphous Se against crystallization (2-6). We observed that some of our films prepared from lower As concentration alloys crystallized if stored in a laboratory environment. The higher As content films as well as some of the lower content films have been stable for more than 1 year both in air and vacuum.

Properties of Selenium

Se was chosen as a prototype material for high resolution thermal milling because of a combination of desirable properties. It has a low boiling temperature and low thermal conductivity. It can be deposited in thin amorphous films whose lack of structure is consistent with the goal of 0.1 micron resolution, and it is stable in air and vacuum. In this section we summarize the reported thermal properties important for constructing a detailed model of the electron beam thermal milling process.

The vapor pressure of As and Se are very similar (1,7,8). As is about a factor of 10 less than Se at 200°C. The pressures are identical at 450°C. The Se vapor pressure can be described by:

$$\log P = 5.6 - 5376^{\circ}K/T \qquad (1)$$

where P is in units of atm. The boiling point of Se is 690°C. Since the As and Se pressures are very similar, Raoult law corrections for the As component will be neglected.

The evaporation rate can be determined from the vapor pressure using an argument originally due to Langmuir (ref. 9, p. 17). The evaporation flux J_v in g-atoms/cm^2 sec is given by(10):

$$J_v = \alpha' f P/(2\pi MRT)^{1/2} \qquad (2)$$

where M is the molecular weight, R = 1.987 cal/g-atom°K, f = 1.554 cal$^{1/2}$cm^{-2} atm^{-1} sec^{-1} is a conversion factor and α' is a sticking or condensation fraction = 1 for liquid to vapor transitions. The derivation of equation (2) assumes no interference from the evaporated material. Also Se may partially evaporate as Se_2 or more complex molecules. Both of these effects can reduce the evaporation rate. See references 11 and 12 for a critical discussion of the limitations of the derivation of equation (2). From equations (1) and (2) the evaporation rate at T = 920°C where P_{atm} = 10 atm is 24 cm/sec.

The heat of vaporization $(\Delta H_v)^{atm}$ can reduce the evaporation rate due to evaporative cooling. We have used a value of 14.3 kcal/g-atom for the liquid to vapor transition. This is consistent with reported handbook values (13,7). ΔH_v can also be related to the vapor pressure (ref. 9, p. 740). This yields 24.6 kcal/g-atom which is almost twice the reported values and indicates that the liquid Se is primarily in equilibrium with a molecular form Se_2. To estimate the effect of heat of vaporization on high speed evaporation of Se, consider a cube of Se $(0.1\mu m)^3$ which evaporates in 0.1μsec. This required 3.25×10^{-5} watts to provide the heat of vaporization. As will be seen to maintain this volume of material near a silicon heat sink at 900°C requires $\sim 5 \times 10^{-4}$ watts. Hence, heat of vaporization can be significant for evaporation many times faster than 0.1μsec depending upon the degree of heat sinking. For bulk Se the power required to maintain the same 0.1μm volume at 900°C is about 10^{-4} watts.

Table I summarizes the reported or recommended values for the thermal conductivity at 40°C of amorphous Se or As-Se alloys. We have used a value of K = 0.005 watts/cm°K.

TABLE I
THERMAL CONDUCTIVITY OF BULK As Se
(Amorphous Alloys) at 40°C

At % As	watts/cm-sec	Reference
0	3.0×10^{-3}	14
10	3.3	14
20	3.6	14
30	3.4	14
40	4.0	14
40	2.0	15
40	3.0	16
40	7.0	17, 18
20(?)	1.4	19
0	7.9	20
0	5.6 (20°C)	20

Milling Model

We have formulated a model for the evaporated thickness of the Se film as a function of the dwell time of a focused electron beam. Approximate 1 and 2-dimensional solutions of the heat flow equation are used to calculate the surface temperature of the film. The transition between the two approximations occurs where they both predict the same surface temperature. The 1-dimension limit assumes a beam power density of $P = P_T/(\pi a_1^2)$ where P_T is the total beam power including a 20% backscattered electron correction,

$$a_1 = (0.67 R_G + b)/2 \qquad (3)$$

b = the beam e^{-1} spot diameter, and R_G = the Grün range for Se. TheGrün range (21,22) is $R_G = (\beta/\rho) E^{1.75}$ where E is the beam energy in keV, ρ the mass density = 4.38/cm^3 and $\beta = 4.28 \times 10^{-6}$ g/cm^2. The 1-dimensional thermal model includes the effect of beam penetration through the Grün energy loss function (22) and assumes the silicon substrate has ∞ thermal conductivity. The 2-dimensional approximation is based on a solution by Goldenberg(23) for a uniformly heated hemisphere of radius a_2 in a semi-infinite medium. The temperature at the center of the heated surface is

$$T(0) = 3P_T/4\pi K a_2 \qquad (4)$$

where we approximate a_2 by $a_2^2 = 0.5R_G(0.67R_G + b)$. This approximation is based on analysis of experiments on lateral electron beam scattering(24, 25). We have found that even in the transition region bewtween these two approximate solutions where the electron beam spot size and electron range are comparable to the film thickness the temperature calculations are within 20% of exact numerical model calculations(26). This is certainly adequate for a model whose primary purpose is to predict functional dependences and trends. Determination of the incident beam power density to better than 25% is difficult because of problems in determining beam spot size.

Both limiting models predict thermal response times $\tau = d^2/k$ where the thermal diffusivity, $k = K/C_p = 4 \times 10^{-3}$ cm^2/sec and d is a characteristic thickness. d = 0.64 times the film thickness for the 1-dimensional limt and a_2 for the 2-dimensional limit). Again these response times are in substantial agreement with the exact numerical solutions. For a typical case considered here, with a film thikcnesses of 0.07μm the maximum e^{-1} response time is 5×10^{-9} sec. Hence the film surface will be within 2% of its equilibrium temperature (in the absence of evaporation) in 20 nsec or less.

The milling depth is determined as a function of time by numerically integrating equation (2) using the surface temperature predicted by the thermal model after adjustment of the film thickness for any milled loss of Se due to evaporation. The effect of heat of vaporization is included as a power loss, assuming the rate of Se film vaporization is uniform over the entire heated radium (a_1 or a_2). Since the rate of evaporation at the edge of the heated area is slower, this will overestimate the effect of heat of vaporization. The time response is included through a factor $1-\exp(-t/\tau)$ multiplying the equilibrium surface temperature. This is a reasonable approximation to the true time response. Exact numerical calculations (26) indicate this underestimates the rate of approach to equilibrium. No attempt is made to calculate the effect of Se removal on the thermal constant since the time constant is so short compared to the experimental conditions of interest. Significant amounts of Se are not removed before several thermal time constant.

Figure 2 shows some typical results of the milling model. Considered is a 4 keV electron beam with a 1/e spot diameter of 0.2μm, a beam current of 200, 400 or 800 nA incident on a 0.07μm thick Se film on a silicon substrate. The solid curves are the full model simulation. The dotted curves indicate the effect of ignoring thermal time constant effects (i.e. assuming that the film reaches full equilibrium temperature instantaneously). The thermal time constant τ for these cases was 5 nsec. The dashed curves show the effect of assuming the heat of vaporization is zero. Note that except for the highest beam current, the effect of thermal time response and heat of vaporization is negligible. Even for the highest beam current only about 60% of the Se film can be evaporated. This is due to the strong heat sinking effect of the silicon substrate. The maximum surface temperature reached for the 400 nA beam is 940^{o}C around 16nsec and for the 800nA beam 1210^{o}C around 9 nsec. The reason the maximum temperature is not reached at the same time and is not linear in beam current is because of the power loss due to heat of vaporization. If the Se did not evaporate, the equilibrium surface temperature for the 4nA case would be 1010^{o}C.

Diode Substrates

The readout signal is generated by the induced current in the np junction substrates. The reading beam voltage must be chosen low enough to prevent electron scattering during reading from degrading the spatial resolution of the readout signal. For 0.1 m resolution the electron range should be less than 0.1 m or a beam energy of 4 keV for Se. This requies diodes with high electron beam gain at low beam penetrations. The diodes used in this study are similar to large area planar diodes described previously(27). These diodes convert 80% of the electron-hole pairs generated by a 4 keV electron beam into diode signal. We have found that the diode process described in ref.

27 can be modified to use an As^+ implant fluence of $10^{16}cm^{-2}$ without significantly affecting the diode gain. This results in a N^+N layer sheet resistance of 500 ohms/square. For 1.5x1.5 cm diodes with N^+ contacts only on the perimeter and no metal grid the frequency response is in excess of 20 MHz. As we have discussed previously (28) readout of digital data patterns from such diode substrates provides signal to rms noise ratios of better than 15:1 with beam currents of 1 to 10 nA. This is suitable for low error rate data recovery. The principal advantages of diode readout are, the high gain low noise signals, the insensitivity to small irregularities in surface structure which can affect secondary and backscattered electron detection and the freedom to design the electron optical system without a requirement for an above substrate detection device. The readout method depends upon the variations in diode gain due to electron beam induced changes in Se fim thickness. Figure 3 shows the diode gain at 4 keV versus Se film thickness. This based upon the experimentally determined electron beam induced diode gain versus beam energy and the assumption that the electron beam energy loss versus depth is a piecewise Grun function scaled by the Grun ranges for Se and Si. This figure also assumes that the Se film is uniform in thickness over several spot diameters or electron ranges so that lateral electron beam scattering is unimportant. Figure 3 provides a convenient method for presenting the results of the milling experiments in terms of Se thickness instead of diode signal.

Electron Column

The electron column used for the writing experiments is a thermally oxygen processed field emission source (29) with an electrostatic gun lens and scaled down ETEC auto scan objective lens. The gun design and operation are similar to those reported previously(30). For the writing experiments the column was operated at 4 keV and beam currents 400 nA. An objective lens focal length of 8 mm was used which corresponds to a working distance from the center of the slightly reinterant objective lens. The spot size was determined by measuring the transmitted current past a sharp gold grid edge. Apertures were used to prevent both forward and backscattered electrons from entering the secondary electron detector. The measured spot size at 250 nA was typically .20μm defined as the 12 to 88% rise aprt of the transmitted signal. If the beam is gaussian this corresponds to 50% of the total beam current within the measured spot size. At 800 nA the measured beam spot diameter is 0.35μm. These spot sizes are corrected by 0.05 m for the resolution limit of the detector. The beam is blanked electrostatically using a single set of plates near the gun. The blanking plate is driven directly by a 10V, single ended pulse from programmable pulse generator (E & H 1504). The deflection coils are driven directly by two programmable DAC's (HP 59501A). Beam blanking times less than 10 nsec are possible in the high current mode because of the small beam diameter (~500μm) at the final aperture which also serves as the beam blanking aperture. The programmable instruments are controlled using the IEEE 488(1975) bus and a TEK 4051 controller.

Results

Figure 4 shows a secondary electron and diode signal micrograph of a typical written pattern. The diode signal micrograph is obtained by intensity modulating the display with the induced current diode signal. Bright areas

correspond to areas of thinner Se. The written pattern consists of a single array of 25 written dots repeated twelve times at two different array sizes. The beam dwell times are .16, .28, .40, .6, 1.1 and 2.1μsec for each group of six in ascending order from left to right. The resolution pattern is a 5x5 array of equally spaced written holes with a single bit in the center unwritten. The 25th dot is a single written hole well separated from the 5x5 array. The scope traces on the right hand side are the diode readout signal from single line scans across the centers of the 5x5 arrays as indicated. A major scope division corresponds approximately to a diode signal of about 100 times beam current.

If digitally encoded data were recovered by a threshold detection technique, the difference in signal level between the central unwritten bit and the isolated written bit would be useful modulated signal (31). As can be seen for all but the shortest writing times, and both bit spacings this difference in signal is positive and corresponds to a signal of about 100 times beam current. Figure 5 shows these signal amplitudes plotted as remaining Se thickness versus bit spacing. The conversion of diode signal to Se thickness was discussed previously and provides a convenient method for presenting the experimental results independent of the reading beam voltage or diode properties. The reading beam current was 0.25 nA. Figure 3 can be used to convert the Se thicknesses back to diode gain or diode signal if desired. Note that for writing pulse widths $> 1\mu$sec the resolution begins to degrade even at 0.4μm spacing. For the shorter pulse widths the degradation becomes significant at 0.25μm spacing. The measured spot size was 0.25μm under these conditions. There is some beam energy out to a spot diameter of about 0.5μm. Hence the degradation of resolution at 0.25μm and the dependence on beam dwell time at 0.4μm spacing is understandable. The reduced writing depth for the isolated written dots at 0.65μm spacing is probably due to a small change in beam current or focus. Smaller beam sizes would be necessary to explore the fundamental resolution limits of the Se film.

Figure 6 shows the measured Se milled depth versus beam pulse time for three beam currents. The spot sizes varied from about 0.25 to 0.35μm between the low and high current conditions. Note the surprising lack of any thermal milling below 0.1μsec. The solid line indicates the thickness of the unwritten Se film. Writing pulses between 0.01 and 0.1μsec gave no detectable writing. Careful examination of diode and secondary signals from the pulsed areas indicated no change in the film thickness or surface topography. We feel confident that thickness changes of more than 25Å would have been detected. These results are at complete variance with the predictions of the milling model. Figure 7 compares one set of experimental results with the milling model prediction. The milling depths at times longer than 0.5 sec are well predicted by the model. The dotted curve indicates the effect of subtracting a latency time of 100 nsec from the time scale of the milling model prediction.

This latency cannot be explained by an anomalously long thermal time constant. A thermal time consant of 100 nsec would be required but this would not produce the abrupt onset of milling at 100nsec as observed. The surprising feature of this behavior is the complete lack of any milling out to about 100 nsec and then an almost explosive removal of the film. We believe that the latency is due to the retardation of the evaporation of the Se by a thin layer of contaminant. Based on estimated bulk diffusion constants only about 10Å of contaminant would be required to significantly reduce the

evaporation rate.

The contaminant layer cannot be Se or As oxides because these are unstable at temperatures far below 1000°C. It is probably a carbon layer created or augmented by the irradiation of the electron beam. The carbon layer is eventually cleared by a complex hydrodynamical mechanism driven by surface tension gradients. Se melts at 220°C and hence there is a large and deep pool of molten material under the electron spot. We have modeled this convective like flow and find fluid circulation times ~100nsec in agreement with the observed latency times. Because the viscosity of Se at its melting point is about 10 times larger than typical liquid metals, the fluid circulation times are much long than for typical liquid films of comparable thickness. We will discuss this phenomena in more detail in a following publication.

Three types of electron beam damage have been observed during low current (<1 nA) readout of our Se films. One type can be seen in figure 4 near the digit 5. These are small pits about 0.4μm in diameter and 0.02μm deep (as inferred from the diode signal). They have been observed to appear spontaneously during early read scans of unwritten fims. Before their appearance there are no artifacts in the secondary or diode images. We believe they are micro explosions due to pressure generated by electron beam decomposition of small amounts of organic contaminants, probably pump oil, captured during the evaporation of the films. The generation of these defects seems to stop after a total electron beam readout fluence of 10^{16} e/cm^2 and typically 10^5 cm^{-2} are observed. Figure 8 shows the second and third type of damage observed. The two vertical lines (length 60μm) were scanned for the indicated times and beam currents. Two effects are observed. First is the expected electron beam induced contamination layer, probably due to decomposed pump oil. This tends to decrease the diode signal because of the increased film thickness and appears black on the secondary micrograph because of its low secondary emission. Second the Se film desorbs because of the electron beam ionization. This effect is widely observed in other materials (32). This causes the bright line in the diode micrograph. The damaged lines consist of a depressed Se surface due to ionization induced description, partially obscured and covered by the carbon contamination layer. The effect of the contamination is to obscure the much greater loss of Se from the surface. Repetition of the same type of experiment in a high vacuum (10^{-9} Torr) Auger system indicates that 10^{15} e/cm^2 at 5 keV will remove 0.01μm of Se from a clean surface. The rapid desorption of Se is not surprising considering the low binding energy of Se. The heat of vaporization of Se is low, about 0.5 ev/atom. The surface tension of Se is also low indicating weak surface binding. We have observed that a thin 0.005μm film of sputtered gold decreases the rate of Se desorption by at least a factor of 100. Such Au coated films can be written by thermal milling. They have the same milling behavior and milling rate. They appear to be superior to a pure Se-As film because of the reduced sensitivity to electron beam damage. This would explaing why Mee did not report electron beam desorption of Se from his Se-As-Au films(33). The only problem noted with electron milling of the Au coated films is the formation of the gold particles. These particles are ~700Å in diameter and produce gain reductions of ~100 at 4 kev. This could result in errors during readout. Possibly thinner gold layers would be equally effective.

Summmary and Conclusions

We have investigated the suitability of thermal milling and diode readout of Se-As films for electron beam recording of information. Potential for bit spacings of 0.25 μm or 1.6×10^9 bits/cm^2 were demonstrated. Using the diode readout method, readout rates in excess of 10 MBits/sec should be possible.

A latency effect limiting the thermal milling time of thin Se films to $\gtrsim$ 100 nsec was discovered. This is believed to be due to a thin surface contamination layer, probably carbon, which retards the evaporation of the Se until a surface tension driven convective flow clears the surface. This will be a physical limit to the writing speed in this electron beam memory system.

Pure Se-As films develop two types of defects in addition to the expected carbon contamination layer. These are the appearance of small crater like depressions, and the ionization induced loss of Se during low current density electron beam scanning. The second effect can be reduced at least several orders of magnitude by a thin gold layer on the Se film.

*Work supported by the Defense Advanced Projects Research Agency through the Air Force Avionics Laboratory

REFERENCES

1. A.G. Sigai, "Open Boat Evaporation of Low Arsenic-Selenium Alloys," J. Vac. Sci. and Tech., 12, pp. 753-77, 1975.
2. H.P.D. Lanyon, "Crystallization and Viscosity of Vitreous Selenium," in Int'l Symp. on the Physics of Selenium and Tellurium, ed. W. Charles Cooper, Pergamon Press 1969.
3. R.A. Fortland, J. Appl. Phys., 35, p. 1558, 1960.
4. J. Neyhart, Phot. Sci. Eng. 10, p. 126, 1966.
5. M.B.I. Janjua, J.M. Toguri, and W.C. Cooper, Can. J. Phys., 49, p. 475, 1971.
6. W. Charles Cooper and R.A. Westbury, "The Structure of Selenium," in Selenium, ed. Ralph A. Zingaro and W. Charles Cooper, Van Nostrand Reinhold Co., New York 1974.
7. CRC Handbook of Chemistry and Physics, 48 Edition (Chemical Rubber Co., Cleveland, Ohio), 1967.
8. Handbook of Tables for Applied Engineering Science, Chemical Rubber Co., Cleveland, Ohio.
9. Saul Dushman, Scientific Foundations of Vacuum Technique, 2nd Edition John W. Wiley and Sons, 1972.
10. Joseph F. Dettorre, Thomas G. Knorr and Elton H. Hall, "Evaporation Process," in Vapor Deposition, ed. Carrol F. Powell, Joseph H. Oxley and John M. Blocher, Jr., John Wiley and Sons, pp. 62-101, 1966.
11. Raymond J. Ackermann, Robert J. Thorn and George H. Winslow, "Some Fundamental Aspects of Vaporization," in The Characterization of High-Temperature Vapors, ed. John L. Margrave, John Wiley and Sons, pp. 427-452, 1967.
12. IBID Appendix A by Richard E. Honig, pp. 475-494.
13. C.J. Smithells, Metals Reference Book, 5th ed. Butterworths 1976 p. 186.
14. Masaaki Kuriyama, "Thermal Conductivities of As-Se Glasses," pp. 302-3, 1975.

15. I.A. Rozov, A.F. Chudnovskii, and V.F. Kokorina, Sov. Phys. Semicond. 1, p. 969, 1968.
16. Richard Flasck and Howard K. Rockstad, "The Thermal Conductivity of Some Chalcogenide Glasses," J. of Non-Crystalline Solids, 12, pp. 353-6, 1973.
17. B.T. Kolomiets, L. Payasova, and L. Stourac, Sov. Phys.-Solid State 7, p. 1285.
18. L. Stourac, B.T. Kolomiets, and V.P. Silo, Czech. J. Phys. B18, p. 92, 1968.
19. Handbook of Military Infrared Technology, ed. William L. Wolfe, US Government Printing Office, p. 331, 1965.
20. Thermophysical Properties of Matter, Vol. 1, Y.S. Touloukian, Cy. Ho. eds. - IFI/Plenum, NY 1970.
21. A.E. Grun, "Lunieszenz-photometrische Messungen der Energieabsorption im StrahlungSfeld von Elektronenquellen Eindimensionaler Fall in Luft," Z. Naturforsch, 12A (1957).
22. T.E. Everhart and P.H. Hoff, "Determination of Kilovolt Electron Energy Dissipation vs. Penetration Distance in Solid Materials," J. Appl. Phys. 42 (1971) pp. 5837-5846.
23. A.H. Goldenberg, "A Problem in Radial Heat Flow," Brit. J. Appl. Physics, 2, pp. 233-37, 1951.
24. A. Cohn and G. Caledonia, "Spatila Distribution of the Fluorescent Radiation Emission Caused by an Electron Beam," J. Appl. Phys. 41 pp. 3767-3775, 1970.
25. G.E. Possin and J.F. Norton, "Spatial Distribution of 5 and 10 Kilovolt Electron Beam Ionization in Solids," Proc. 8th Ann. SEM Symp. O. Johari and I. Corvin (ed.) IIT Res. Inst., Chicago 1975, pp. 457-464.
26. P.V. Gray, unpublished.
27. G.E. Possin and C.G. Kirkpatrick, "Recombination in Heavily Doped Planar Diodes," J. Appl. Physics, 50, 3478-83 (1979).
28. W.C. Hughes, C.Q. Lemmond, H.G. Parks, G.W. Ellis, G.E. Possin and R.H. Wilson, "A Semiconductor Nonvolatile Electron Beam Addressed Mass Memory" Proc. IEEE 63, 1230, 1975.
29. L.H. Veneklasen and B.M. Siegel, J. Appl. Phys., Vol. 43, No. 4, April 1972.
30. L. Veneklasen, N. Yew, and J. Wiesner, Proceedings of the 8th International Conference on Electron and Ion Beam Science and Technology, Seattle, Washington, May 1978.
31. G.E. Possin, Bit Packing Density of the BEAMOS Target, J. Appl. Phys., 48, pp. 5245-61, 1977.
32. T.E. Madey and J.T. Yates, Jr. "Electron-Stimulated Desorption as a Tool for Studies of Chemsorption: A Review" J. Vac. Sci. and Tech. 8, p. 525-55 (1971).
33. P.B. Mee, "Observations of Electron-Beam-Induced Thermal Effects in Amorphous $Se_{80}As_{20}$ and $Se_{64}As_{16}Au_{20}$, Thin Solid Films, 26, p. 227-41, 1975.

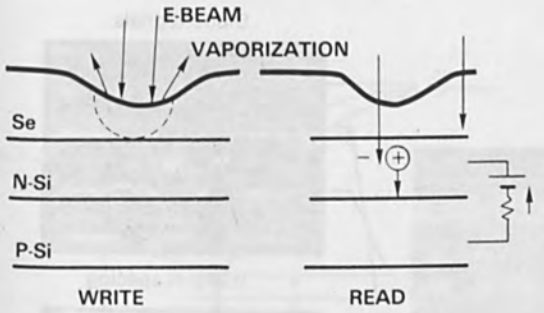

Fig. 1 - Electron beam thermal milling and readout.

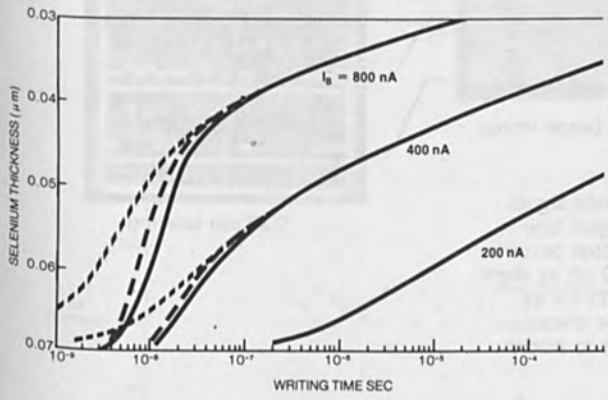

Fig. 2 - Calculated milled depth of a selinium film versus beam dwell time per spot. Spot size is 0.2 m, beam voltage 4 keV. Initial Se film thickness 0.07 m. Dotted line shows the effect of ignoring the initial thermal transient and the dashed line the effect of ignoring heat of vaporization.

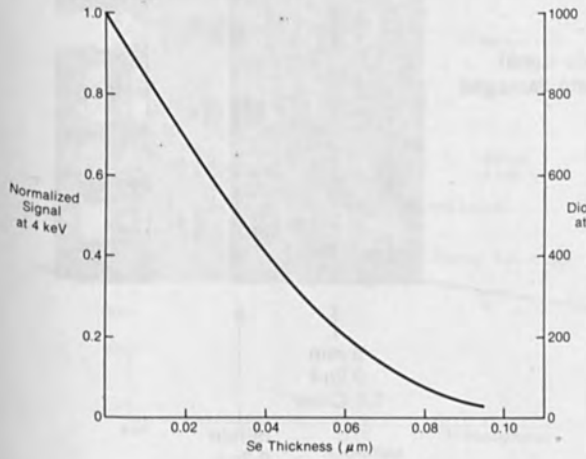

Fig. 3 - Diode gain (signal current/beam current) at 4 keV versus Se thickness. Based on experimentally measured diode response versus beam voltage and Grun energy loss function.

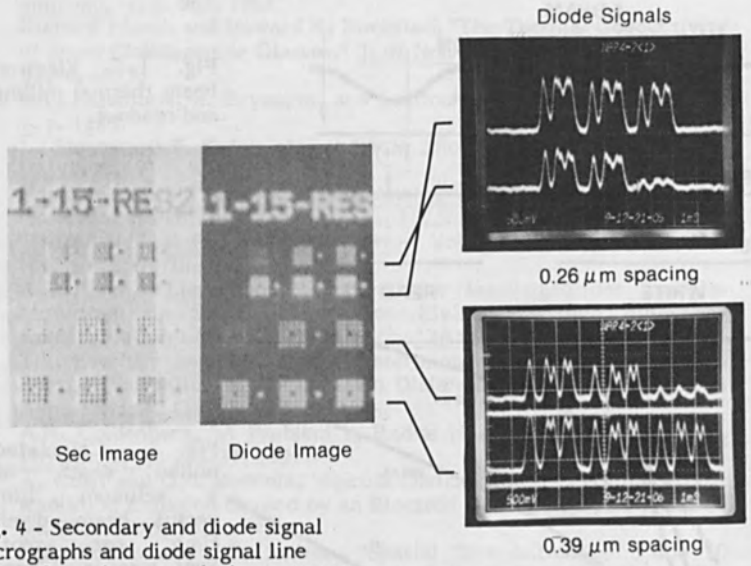

Fig. 4 - Secondary and diode signal micrographs and diode signal line scans of a written resolution pattern. Writing beam current 400 nA at 4keV. Reading beam current 0.25 nA at 4 keV. Direction of scope traces are reversed with respect to micrographs.

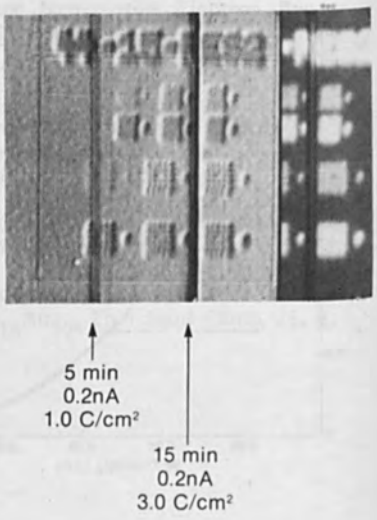

Fig. 8 - Secondary and diode signal micrograph of electron beam damaged lines on Se film.

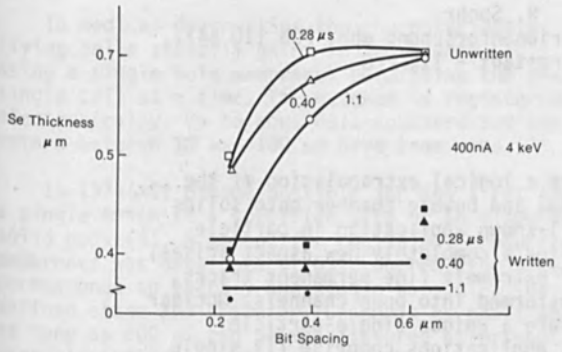

Fig. 5 - Reduced resolution data from figure 4.

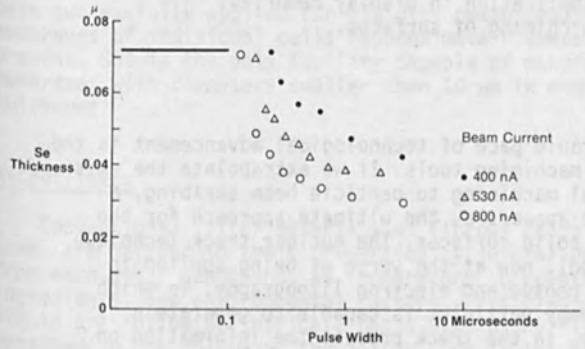

Fig. 6 - Thickness of residual Se film at bottom of milled hole versus beam dwell time for three different writing beam currents at 4 keV.

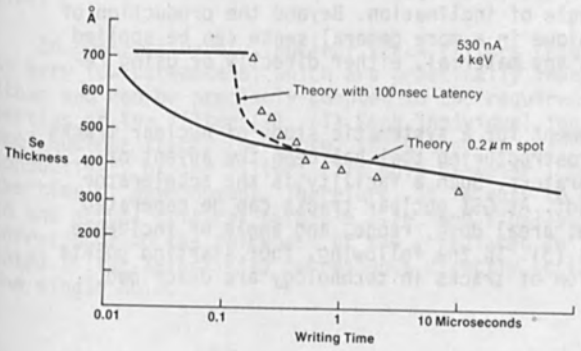

Fig. 7 - Comparison of milled depth to milling model for 530nA data of figure 6.

HEAVY ION NUCLEAR TRACKS - AN EMERGING TECHNOLOGY

R. Spohr
Gesellschaft für Schwerionenforschung mbH, POB 110 541,
D-6100 Darmstadt - 11, FRG

Abstract

Nuclear tracks are a logical extrapolation of the principles of cloud and bubble chamber onto solids. Besides their well-known application in particle detection, in solids a completely new aspect arises, the generation of extremely fine permanent tracks, which can be transformed into open channels. Nuclear tracks are therefore a unique single-particle structuring tool. Applications comprise (I) single hole membranes for particle counting and sizing, (II) manufacture of microfilters with very uniform hole sizes, (III) modification of magneto-optic materials for application in display memories, and (IV) micromachining of surfaces.

Introduction

One measure for the rapid pace of technological advancement is the steady refinement of our machining tools. If we extrapolate the existing trend from mechanical machining to particle beam scribing, a single particle technique appears as the ultimate approach for the shaping and machining of solid surfaces. The nuclear track technique (1) is actually such a tool, now at the verge of being applied in practice. In contrast to photon and electron lithography, in which only the interaction of many particles is capable to generate a permanent material change, in the track process the information on number, nuclear charge, energy, and direction of single particles is maintained. Nuclear tracks are thus capable to produce holes of uniform size, length, and angle of inclination. Beyond the production of discrete holes, the technique in a more general sense can be applied for the shaping of almost any material, either directly or using replica techniques.

One necessary requirement for a systematic study of nuclear tracks as a single-particle microstructuring tool has been the advent of powerful heavy ion accelerators. Such a facility is the accelerator UNILAC (2) at GSI Darmstadt. At GSI nuclear tracks can be generated with defined beam isotope, areal dose, range, and angle of incidence in virtually any material (3). In the following, four starting points for a practical utilization of tracks in technology are described.

Single Hole Membranes

In medical diagnostics the characterisation and sorting of single living cells steadily gains in importance. This goal is achieved, using a single hole membrane, permitting the passage of only one single cell at a time. The passage is registered either optically or electronically. Up to now, cell counters and sorters with hole diameters between 10 and 100 μm have been used.

In 1977, it became possible for the first time to generate at will a single track at a specified site of an elsewhere completely virgin solid body (4). A method for convenient production of single hole membranes was developed at GSI, whereby the single hole (Fig. 1) corresponds to exactly one single particle. The single hole has a well defined shape and diameter. Channels as small as 10 nm in diameter and as long as 200 μm can be manufactured at present. This unique single particle application illuminates the concept of the nuclear track technique as the finest possible tool.

In blood rheology such single hole membranes of 5 μm diameter have been successfully applied for rigidity measurements of red blood cell membranes of individual cells (approximate diameter 8 μm) (4-6). At present, GSI is the only facility capable of manufacturing single hole membranes with diameters smaller than 10 μm in membranes of sufficient thickness.

Microfilters

Conventional filter materials as fibrous felts or open-porous foams are defined in their properties by several parameters, which are from each other dependent, as temperature, concentration of various ingredients, and environmental factors. Particles suspended in the liquid are following intricate paths within the filter and finally are retained in the volume of the filter. The filter transmission function is broad and not well suited for classification of microscopic particles.

In contrast hereto, nuclear track filters (Fig. 2) are determined by very few parameters, which are practically independent from each other and can be precisely adapted to the required transmission properties of the filter (7): (I) Each individual ion generates exactly one nuclear track. Therefore, it is easy to adjust the throughput conductivity of the filter; (II) Hole diameter increases linearly with the time of development. Therefore, it is easy to adapt the hole size to the actual critical particle size. And finally, (III) Hole length corresponds to the thickness of the irradiated foil. Therefore, the total filter selectivity corresponds directly to the selectivity of the single hole.

Due to the statistical distribution of the original nuclear tracks on the filter surface, multiple holes of larger cross sections occur. This leads to a mutual dependence of two of the originally independent parameters : Hole size and areal density of tracks. The influence of multiple holes on filter properties has been investigated in computer simulation using square holes (8) and compared with image analysis of etched nuclear tracks in mica (9). An upper limit for the transmission of particles of given size is given by the "areal transmission function" T_S (Fig. 3). Only at very high "nominal porosity" P (defined as the product of areal track density, N, and single hole area, S_1), uncommon to conventional filters, the influence of multiple holes on transmission properties becomes important. For thick filters this influence can be minimized using irradiations under different angles.

Nuclear track filters using fission fragments from a nuclear reactor are available since 1972 (10). This is the first example of a commercial use of single atomic particles as a structuring tool. At GSI heavy ions up to ten times the range of fission fragments are available at present, making nuclear track filters with hundredfold increased strain-yield possible. The applied ion beam technique enables in addition the manufacture of almost parallel arrays of holes (cf. Fig. 2).

Magneto-Optic Memories

Iron garnets were originally conceived and developed for use in bubble memories, where high domain wall mobility is a requirement. For application as an optical memory it was necessary to divide the film into an array of discrete magnetooptic islands.

In a wider scope, nuclear tracks can be used for modification of solid state properties, imposing a structural change on a submicroscopic level. Bubble memories represent a good case for studying this feature of the nuclear track technique. Thereby, nuclear tracks act as very efficient pinning centers (Fig. 4), thereby drastically reducing the domain wall mobility by more than a factor 100 (11-15). In this simple way a new magneto-optic material with high resolution is created for use in erasable optical memories with display capability.

Heavy Ion Lithography

In solid state technology more and more components have to be packed onto smaller and smaller areas. Maintaining simultaneously critical cross sections of conductors becomes a problem in planar technology using either photons, x-rays, or electrons. Thereby, high lateral resolution is not anymore a sufficient condition. Much more stress has to be placed on obtaining better control over depth profiling. Any further progress will depend on the capability of the applied technique to stop at a precisely defined depth.

In contrast to other techniques, heavy ions possess this feature (16-17). Only heavy particles are subject to a quasi-continuous energy loss on their trajectory and thus, come to a hold at precisely defined depth. Range and angular straggling are of the order of only a few percent, in contrast to either photons, x-rays, or electrons where an equivalent term for "range" can be only defined rather arbitrarily as a gross property of many particles, via the exponential law of extinction. Therefore, by using heavy ions, deep structures with high steepness of the edges can be achieved directly (Fig. 5).

Application of heavy particles has another inherent advantage over x rays and electrons. Due to the very high specific energy loss of heavy ions, an almost unlimited number of different materials can be used quasi as photoresists. Therefore, the resist coating step in silicon technology can be replaced by a simple oxidizing step leading to a "resist" layer of much better defined thickness. Even pure silicon can be track-sensitized using heavy ion irradiation and transforming the inscribed information into structure during a later selective etching process (Fig. 6).

A final virtue of heavy ions as a structuring tool in comparison to x-ray sources resides in the existence of very bright ion sources. Parallel heavy ion beams of high intensity can be achieved using conventional ion optical systems. Heavy ion lithography can be directly applied to small accelerators and low energy implanters. At 1 mA beam current a sample throughput of 1 m^2/sec. can be achieved.

REFERENCES

(1) R.L. Fleischer, P.B. Price, and R.M. Walker: "Nuclear Tracks in Solids. Principles and Applications", Univ. of Calif. Press, Berkeley (1975).

(2) N. Angert, Ch. Schmelzer: "UNILAC, the Accelerator Facility for Heavy Ions of the GSI", Kerntechnik, 19, 57-66 (1977).

(3) R. Spohr: "Nuclear Track Irradiations at GSI", Nuclear Tracks (accepted for publication February 27, 1980).

(4) H. Kiesewetter, K. Mussler, H. Schmid-Schönbein, B. Genswürger, R. Spohr: "Messung der Verformbarkeit roter Blutzellen mit Hilfe einer Einlochmembran", GSI Annual Report 1977, p. 141.

(5) H. Kiesewetter, K. Mussler, P. Teitel, U. Dauer, H. Schmid-Schönbein, R. Spohr: "New Methods for the Measurement of Red Cell Deformation Ability", Symposium on Blood Rheology, Glasgow, Sept. 27. - 28., 1979.

(6) H. Kiesewetter, U. Dauer, K. Mussler, H. Schmid-Schönbein,

R. Spohr: "Rigidtiy Measurements in Individual Red Cells", Hemorheology et Pathologie Symposium European, Nancy, Oct. 1979.

(7) C. Riedel, R. Spohr: "Möglichkeiten und Grenzen bei der Herstellung von Kernspurfiltern aus Glimmer", Ber. der Bunsenges. Phys. Chem. 83, 1165-1168 (1979).

(8) C. Riedel, R. Spohr: "Statistical Properties of Etched Nuclear Tracks, I. Analytical Theory and Computer Simulation", Radiation Effects 42, 69-75 (1979).

(9) C. Riedel, R. Spohr: "Statistical Properties of Etched Nuclear Tracks, II. Experiment and Filter Design", Radiation Effects (accepted July 27, 1979).

(10) Nuclepore Corporation, 7035 Commerce Circle, Pleasanton, California 94566, USA.

(11) J.-P. Krumme, I. Bartels, B. Strocka, K. Witter, Ch. Schmelzer, R. Spohr: "Pinning of 180° Bloch Walls at Etched Nuclear Tracks in LPE-Grown Iron Garnet Films", J. Appl. Phys. 48, 5191-5196 (1977).

(12) H. Heitmann, C. Fritzsche, P. Hansen, J.-P. Krumme, R. Spohr, K. Witter: "Influence of Irradiation with High Energetic Ions on Storage Properties of Magneto-Optic $(Gd,Bi)_3$ $(Fe,Ga)_5$ O_{12} Expitaxial Films", J. Magnetism and Magnetic Materials 7, 40-42 (1978).

(13) P. Hansen, H. Heitmann: "The Influence of Nuclear Tracks on the Magnetic Properties of a $(Gd,Bi)_3$ $(Fe,Ga)_5$ O_{12} Garnet Film", Phys. Rev. Letters 43, 1444-1447 (1979).

(14) H. Heitmann, P. Hansen, K. Witter, R. Spohr: "Influence of Nuclear Tracks on the Coercivity of Single Crystalline $(Gd,Bi)_3$ $(Fe,Ga)_5$ O_{12} LPE Garnet Films", J. Magn. Magn. Mat. 10, 97-99 (1979).

(15) B. Strocka, G. Bartels, R. Spohr: "Lattice Strain in Garnet Single Crystals Caused by High Energy Heavy Ion Irradiation", Appl. Phys. 21, 141-149 (1980).

(16) B.E. Fischer, R. Spohr: "Heavy Ion Microlithography - A New Tool to Generate and Investigate Submicroscopic Structures", Nucl. Instr. and Meth. 168, 241-246 (1980).

(17) B.E. Fischer, R. Spohr: "Heavy Ion Lithography", Contribution to "Microcircuit Engineering '79 - Microstructure Fabrication", 25-27. September 1979, RWTH Aachen; Proceedings: Inst. of Semiconductor Electronics, p. 349-357 (1979).

---

*Courtesy: P. Tischer, Siemens AG, Munich, FRG

FIGURE CAPTIONS

Fig. 1: Single hole for use in single hole cell counting apparatus (4-6). Hole diameter 5.0 µm, hole length 45 µm. Material: 50 µm thick Hostaphan BN 50 (Kalle, Wiesbaden, FRG). Irradiation: One single ^{136}Xe ion of 4.7 MeV/nucleon. Development: 70 min in ⅓ 6n NaOH + ⅓ H_2O + ⅓ Methanol at 40° C. Observation: Scanning electron microscope.

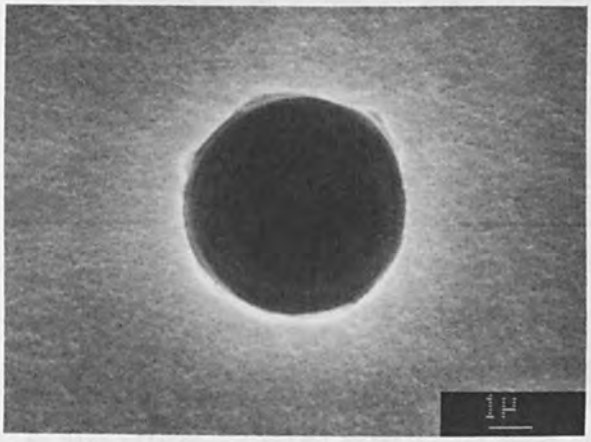

Fig. 2: Nuclear track filter manufactured with high energy heavy ions. Hole diameter 0.7 µm, hole length 49 µm. Material: 50 µm thick Hostaphan BN 50 (Kalle, Wiesbaden, FRG). Irradiation: 1.6 x 10^7 cm^{-2} ^{136}Xe ions of 4.7 MeV/nucleon. Development: 42 h 99 % 1n NaOH + 1 % Tickopur R33 (Brinkmann Instrumentenbau GmbH, Mannheim FRG) at 40° C. Observation: Scanning electron microscope.

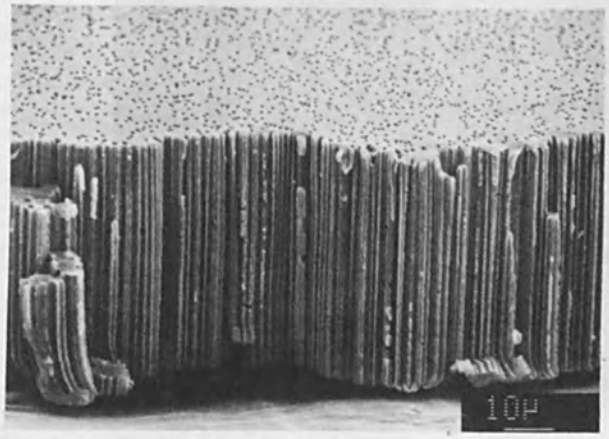

Fig. 3: Areal transmission function T_S, defined as fraction of holes with larger area than S, representing an upper limit for the actual transmission function. Points: Image analysis (9). Lines: Computer simulation (8).

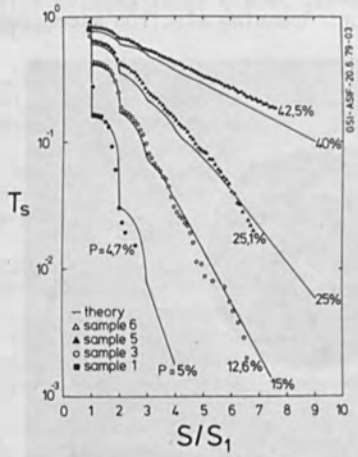

Fig. 4: Pinning of magnetic domain walls by etched nuclear tracks. Model experiment. Material: Epitaxial $(Gd,Bi)_3(Fe,Ga)_5O_{12}$ garnet film. Irradiation: 3×10^6 cm^{-2} Xe ions of 1.4 MeV/nucleon. Development: 3 h ⅓ HNO_3 + ⅓ CH_3COOH + ⅓ H_2O at 80° C. Observation: Light microscope, Faraday contrast using polarized light.

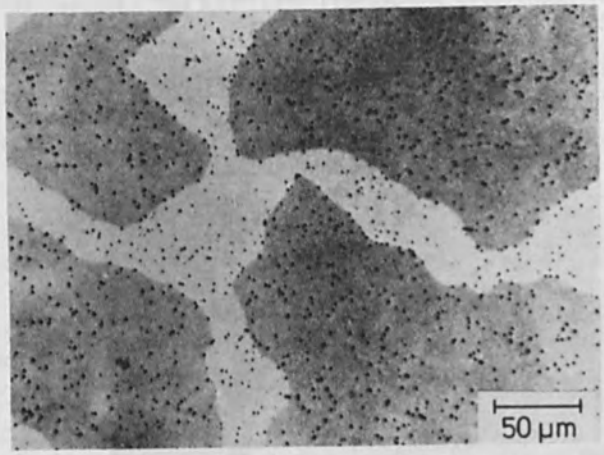

Fig. 5: Heavy ion lithogram of metal mask* inscribed into high resolution photoresist. Material: Polymethyl metacrylate (PMMA) layer on silicon substrate*. Irradiation: 3 x 10^{12} argon ions per cm^2 at 720 keV particle energy. Distance between metal mask and photoresist was approximately 1 mm. Development: 10 min methyl isobutyl keton plus isopropanol 1:3. Observation: Scanning electron micrograph of cross section.

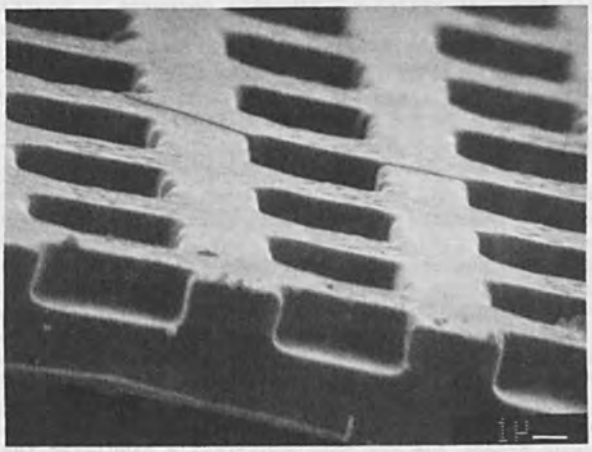

Fig. 6: Bare silicon - a resist material for heavy ion lithography. Mask*: Self-supporting metal mask. Resist*: Bare silicon, (111) orientation. Irradiation: 7 x 10^{13} argon ions per cm^2 at 720 keV particle energy. The distance between the mask and the silicon was approximately 1 mm. Development: 10 sec Sirtl etch (CrO_3-HF-H_2O), a dislocation sensitive etching medium. Observation: Scanning electron microscopy.

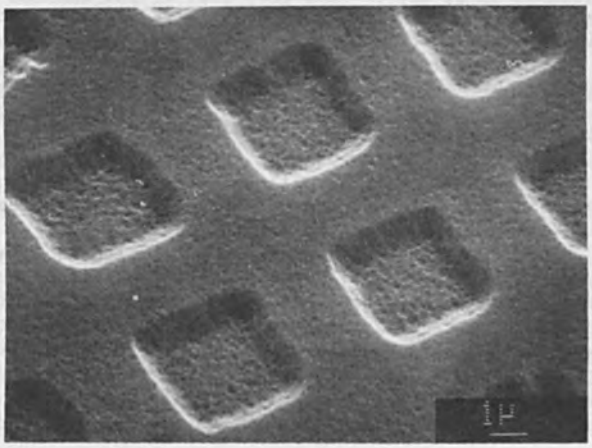

*Courtesy: P. Tischer, Siemens AG, Munich, FRG

THEORETICAL ANALYSIS OF THE MAIN FEATURES OF AN ELECTRON GUN FOR ANNEALING IMPLANTED SILICON LAYERS

G.Lulli

Istituto di Fisica, Università di Bologna
Via Irnerio 46, Bologna, ITALY

P.G.Merli, M.Vanzi

LAMEL-CNR, Via Castagnoli 1, Bologna, ITALY

ABSTRACT

Thermal effects from irradiation of a Silicon wafer with electron beams of 30keV and different current densities ($0.5A/cm^2 \leq I \leq 10A/cm^2$) have been considered. Numerical solution of the heat conduction equation gives the beam parameters (current density, diameter, exposure time) suitable to produce the solid phase epitaxy of an implanted layer. An outline of a proper electron-optical apparatus is given, too. A plane cathode triode gun has been numerically simulated taking into account space charge and thermal velocity spread effects. A column with two magnetic lenses focuses the spot on the specimen. The spot diameter comes out to be independent of the last aperture size, which can be used to regulate current density.

1. INTRODUCTION

The use of electron beams as a thermic tool is a well stated technique in material processing. The high power density which can be produced, the easy control of the beam, the possibility of generating quite different effects on the workpiece by proper selection of beam parameters together with the processing speed, are the basis of the great development of this technique(1).
Recently, thermal treatments based on the use both of energy pulses, obtained from electron beams as well as from coherent or incoherent light, and scanned continuous laser or scanned electron beams, have found interesting applications in semiconductor technology (2,3).
The most important refer to the annealing of implanted layers, grain growth in polycristalline semiconductors, fabrication of ohmic contacts. Among these methods for thermal treatment the use of electron beams is attracting growing interest because, compared to the techniques based on the use of coherent or incoherent light, it has the following advantages (4): 1) absorption of energy more predictable and less dependent on uncontrollable variables, such as doping density, than absorption of energy from light beams, 2) ability to define pro-

cess depth, 3) ability to process large areas and control process uniformity.
There is then the tendency to extend the capabilities of electron beams as a thermic tool to semiconductor technology. The papers published on this subject are mainly related to the annealing of implanted semiconductors. The apparatuses used for electron irradiation are pulsed generators or scanning systems. The latter are generally got from electron guns for melting or scanning electron microscopes, both suitably modified.
In spite of the interesting results obtained in both cases the peculiarities of experimental apparatuses make theoretical interpretation of the results difficult. In fact both the lack of monochromaticity in pulsed systems and the use of multiscanning methods make the exact evaluation of thermal effects complicated.
On this ground, in order to completely recover the possibilities of controllable thermal treatment, we decided to evaluate the characteristics of an apparatus conceived with the main purpose of annealing implanted layers. We refer to this specific field given the interest it has in solar cell technology, where the introduction of these methods appears more promising in view of the increased speed of the processes and lower production costs.
In a previous work (5) thermal effects produced by electron beams of different energies ($5keV \leq E \leq 30keV$) and different current densities ($1A/cm^2 \leq I \leq 10^3 A/cm^2$) perpendicularly impinging on the surface of a Si specimen have been simulated. They show that, in order to have a liquid phase epitaxy without enlarging the doping profile, it is necessary to work at high current densities ($I \simeq 10^3 A/cm^2$) and at a low value of the energy ($E < 10keV$). In fact, at high current density specimen heating occurs in a "quasi-adiabatic" way; then the temperature profile in the sample is determined by the energy loss profile in the sample itself. As a consequence, the liquid layer has always a thickness determined by the distance l_{sm} between the surface and the inner position of maximum energy loss (see fig.1). l_{sm} is an increasing function of E so that only for small values of energy is it possible to have a liquid layer with a thickness comparable to that of the doped stratus and, consequently slight diffusion of dopant.
The epitaxial regrowth in solid phase does not involve enlargement of the doping profile and may be obtained with a wide choice of values of I and E. Then we chose to examine an apparatus suitable for solid phase regrowth. Besides, as the current density required for solid phase epitaxy is a decreasing function of energy, we resolved to consider a system working at 30keV and able to operate in a single scan mode.
In paragraph 2, through a numerical simulation of thermal effects, current densities, exposure times and beam diameters are estimated. Paragraph 3 presents the main features of an electron gun meeting the requirements resulting from paragraph 2 and obtained by numerical simulation. They regard the geometry of the electrodes, the grid potentials, diameter and shape of the cross-over, divergence of the beam. In paragraph 4 are described the characteristics of the electron-optical column which transfers the required current densities onto the

specimen.

2. NUMERICAL SIMULATION OF TEMPERATURE DISTRIBUTION: DETERMINATION OF BEAM PARAMETERS

In order to have information on the beam parameters required to cause solid phase epitaxy it is necessary to know the regrowth time t of a layer of thickness λ as a function of temperature. t is normally defined by a relation of the type: $t=\lambda/v_o \exp(-E_a/kT)$ where k is the Boltzmann's constant and T the absolute temperature. v_o and E_a are two constants which are not univocally defined by all researchers. Avoiding consideration of the problem, we have reported in fig.2 the regrowth times as a function of temperature for a layer 100 nm thick according to two different evaluations which have been assumed as extreme. The curves t_1 and t_2 refer to the estimates of v_o and E_a reported in references (6) and (7) respectively.
The one-dimensional heat equation has been numerically solved using a Crank-Nicolson method (8), keeping account of the temperature dependence of the thermal conductivity and heat capacity while, regarding the spatial distribution of energy loss by the electrons (the heat source), data obtained by the Monte-Carlo method have been adopted. Two different boundary conditions have been assumed: a) specimen thermally insulated, i.e. no heat dissipation either from the lower or the upper surface; b) no surface radiation, and lower specimen surface having good thermal contact with a substrate kept at a constant temperature of 300°K. In both cases specimen thickness has been assumed equal to 300μm. The following current densities have been considered: I=10, 3, 1, 0.5A/cm^2. In fig.3 a),b),c),d) surface temperature as a function of time is reported. The beam is switched off at a time t_E immediately prior to the beginning of melting (melting temperature of Si equal to 1685°K) and is reported in the figures. In the insert of each figure is drawn the spatial distribution of temperature at the time t_E. The continuos lines refer to results obtained with the boundary condition a), and the dashed ones with the boundary condition b). It may be observed that the effect of the different boundary conditions on surface temperature is revealed for $I \leq 1$A/cm^2 only. Then, in order to have the same surface temperature boundary condition b) involves a larger exposure time.
The dashed line at constant temperature t=1600°K evidences time τ, which the specimen spends at a temperature higher than 1600°K. Comparing with the data reported in fig.2 it is possible to deduce that for $I \leq 1$A/cm^2 $\tau > t_2 > t_1$, while for higher current densities $t_1 < \tau < t_2$. For I=10A/cm^2 $\tau \simeq t_1$. Then, operating with current densities $I \leq 1$A/cm^2 it is certainly possible to induce specimen heating for a time proper to the epitaxial regrowth in solid phase.
It should be noted that the time τ may be increased by using an exposure time larger than t_E. In this case the specimen may remain at the melting temperature for an additional time Δt depending on the melting heat, on the energy loss from the beam in unit time and, after switching off the beam, from the rate of release of the stored heat.
In fig.4 are reported the times necessary to complete the melting of a

layer 100nm thick: Δt_M layer centered on the energy loss peak, Δt_S surface layer. Δt_S has been evaluated neglecting conductivity between layers so that it is overestimated and melting of the surface can be considered to occur at a time $t+\Delta t_M < t_M < t+\Delta t_S$.
Since, in order to avoid enlarging of the doping profile, melting of the specimen surface must be avoided, time Δt can be considered as the maximum error in the exposure time that can be tolerated by the apparatus. It should be said that $\Delta t/t$ becomes very small decreasing current density.
The one-dimensional approximation may be qualitatively justified assuming the diameter of the electron beam interacting with the specimen to be larger than the penetration depth of heat on the time scale of interest. This point has been quantitatively defined in reference (9). According to the calculations reported by the authors the length $4\sqrt{a^2 t}$ where a^2 is the thermal diffusivity, represents the minimum radius of a circular source such that solution of heat equation in one dimension may constitute a satisfactory approximation of the three-dimensional case. Assuming thermal diffusivity at ambient temperature $a^2 = 0.946$ cm^2/sec it is possible to deduce the values of the radius r reported in Tab.1. As a^2 is a decreasing function of temperature this evaluation of beam radius is over-estimated as can be seen from the spatial distribution of temperatures in figs.3 a),b). In the same table the values of the current are reported.
On summarizing, as a result of numerical computation, values of the beam parameters suitable for solid phase epitaxy have been obtained. These features are close to those of an electron gun for melting. However, in agreement with the comments made on fig.4, it is opportune to foresee some features typical of a scanning electron microscope, like accurate measurement of current density, beam diameter (using the edge scan method) and exposure time.

3. NUMERICAL ANALYSIS OF THE ELECTRON GUN

3.1 Outline of the method

The numerical method used to analize the theoretical features of a triode gun with plane electrodes is that described by Weber (10). Numerical simulation is built up to take into account the aberrations due to thermal transversal emission velocities and space charge. Relativistic and self-induced magnetic field effects are neglected, because the aim of the present computation is to analyse 30keV guns.
At first Laplace's equation is solved numerically with a successive over-relaxation method in the mesh points of a square grid. Emission current is calculated using Child's law in a very thin region in front of the cathode. The total beam is divided into annular beamlets, each one generated by rotation around the axis of symmetry of an elementary "gaussian beamlet" Gaussian beamlets are centered around trajectories that start from the cathode with no transverse velocity. Their behaviour is described by two differential equations, derived from the electron distribution function in phase space, that give the width variation of beamlets around their trajectories. A system is built up with these

equations and the differential equations of motions for the trajectories.The system is solved with a fourth order Runge-Kutta method. Then the space charge in the mesh points of the grid is calculated from the beam current distribution. Space charge terms are introduced, resolving the Poisson's equation now to determine new potentials at the mesh points. This procedure is carried on till the variation of emission current from one cycle to the other falls below a certain tolerance. In our computations this tolerance is about 4% if the required error on the potentials is less than 1%. The convergence is reached with a strongly dumped oscillation in a maximum of 5-6 cycles if a proper underrelaxation is applied to the electric field at the cathode.

3.2 Results

Figures 5, 6, 7 show the main features of a triode gun calculated with the method described above.
Accelerating voltage is of 30 kV; the results shown refer to a grid electrode voltage of -800 V, and a cathode emission temperature of 2900°K. Fig.5 shows the gun geometry, with a sketch of some equipotential lines and of two calculated trajectories. The dashed region L represents the emission area. The difference in the points at which trajectories cross the axis is due to spherical aberration. Beam divergence at the exit of the gun is $\alpha_0 = 10^{-1}$ rad. Total emission current density of the gun is i = 40 mA. The curve of fig.6 represents the emission current density at the cathode. Maximum cathode loading is 2.3 A/cm^2 on the axis. The computation program calculates also crossover characteristics. Fig.7 shows the current density distribution at the crossover. The "hollow" form is due to space charge effects. From the distribution of fig.7 we can deduce a crossover diameter $\phi \simeq 350$ um. Comparing the current supplied by this electron gun with the data reported in table 1 the impossibility of working with $I \leq 1 A/cm^2$ is evident. In order to increase τ, i.e. the time the specimen spends at a temperature higher than 1600°K, it would be necessary to operate at a lower current density. Yet the beam diameter required by the one-dimensional approximation imposes a higher current value. To this end studies on new types of gun with a larger emission surface are in progress.

4. OUTLINE OF THE ELECTRON-OPTICAL COLUMN

A suitable projection system must allow accurate regulation of diameter and current density on the final spot. This cannot be done by a single lens system, because both excitation and aperture of the lens affect diameter and current density of the spot. The simplest set that can be useful is a two-lens system. In fact the focused image of the source can be produced at various magnifications, and, when in focus, the spot size is independent of the last aperture. So, this aperture can be used to regulate beam current without affecting the diameter of the irradiated area.
The electrical and mechanical characteristics of the apparatus have to be carefully chosen in order to avoid excessive beam divergence and

consequent intensity losses in some working conditions.
A simple scheme is reported in fig.8: it takes into account beam divergence and the finite source size, while the lenses are supposed thin. From the source, size ϕ and with current density I_o, the beam propagates with divergence α_o as far as L_1 lens at a distance a. On this lens, the beam diameter is:

$$D_1 = \phi + 2a\alpha_o$$

and the current density:

$$I_1 = I_o/(1+2a\alpha_o/\phi)^2$$

A first aperture can be used on this lens to clean the beam. Its diameter has to be $d_1 \simeq D_1$. From lens L_1 to lens L_2 (separated by a distance b) the beam converges to an intermediate image of the source, and then diverges from the image to the last lens. If the final screen has a distance c from L_2, and a total magnification M is selected, the beam diameter on L_2 can be expressed as:

$$D_2 = b\phi/a + 2c\alpha_o/|M|$$

and the current density as:

$$I_2 = I_1(d_1/D_2)^2$$

If an aperture d_2 is placed on the L_2 plane, the focused final image is unaffected; in fact:

$$D = |M|\phi$$

but the current density depends on M and d_2 according to:

$$I = I_o d_2^2/(D_2 M)^2$$

For numerical determination of these parameters, some practical conditions have to be considered. c has to be large enough to allow wide scan areas with small deflection angles in order to minimize the defocalization effect of the magnetic deflection system, which is intended at the output of L_2. At the same time, c must not give too large a value for D_2. Furthermore the focal lengths:

$$f_1 = ab/(a+b+c/M) \qquad f_2 = bc/(b+c+Ma)$$

have to be positive and defined within a reasonable range. Taking account of these indications many solutions can be found. A typical one meeting the requirements of Tab.1 is reported in the following scheme:

column geometry

a = 30 mm b = 50 mm c = 100 mm

electron-optical data

	$I = 10A/cm^2$ $M = 0.3mm$	$I = 3A/cm^2$ $M = 0.8mm$	$I = 1A/cm^2$ $M = 2.2mm$
M	0.86	2.32	6.29
f_1	7.64mm	12.18mm	15.64mm
$d_1=D_1$	6.35mm	6.35mm	6.35mm
f_2	28.44mm	22.77mm	14.76mm
D_2	23.8mm	9.2mm	3.76mm
d_2	9.8mm	5.5mm	3.5mm

The diameter of the lenses has to be greater than d_1 for L_1 and greater than the maximum value of d_2 for L_2. Ordinary symmetrical magnetic lenses will fit these figures in the low part of their excitation range. As an example, considering lenses with a ratio of gap width to bore diameter S/D = 0.2 (11), and working at 30keV, the following scheme gives a possible set of lens parameters:

	L_1	L_2
R	3.5mm	5.5mm
S	1.4mm	2.2mm
N	3500	3000
I_{max}	296mA	307mA
I_{min}	208mA	215mA

where R is the lens radius, S the gap width, N the number of windings and I the excitation current. The low values of the required excitations indicate that the thin lens approximation can be an appreciable one. Moreover, owing to the large values of the beam diameter the aberration contributions can be ignored.

5. CONCLUSIONS

Numerical solution of the heat conduction equation allows evaluation of the electron beam parameters suitable for production of solid phase epitaxy in Silicon implanted layers. The first results concerning the numerical analysis of electron guns show that it is possible to fit these figures using a simple triode gun. However, more work has to be done on this subject in order to find a geometry able to supply higher

currents with small divergence and a not too inhomogeneus current distribution in the cross-over.
Concerning the electron-optical column the greater flexibility of a two lens system has been stated. Many geometries are possible with performances of magnetic lenses which appear easy to obtain.
Two important problems are still to be considered: 1) the plan of the deflection system; 2) the way to perform accurate measurements of beam current and beam diameter. However, on the basis of the great experience in this sector, their solution does not appear difficult.

REFERENCES

1. H.K.Steigerwald, Proceedings of Eight International Conference on "Electron and Ion Beam Science and Technology", ed. by R. Bakish, The Electrochemical Soc. Inc., p.594,(1978)

2. Proceedings of "Laser-Solid Interactions and Laser Processing-1978", ed. by S.D.Ferris, H.J.Leamy and J.M.Poate, American Institute of Physics, New York, (1979)

3. Proceedings of "Laser Effects in Ion Implanted Semiconductors", ed. by E.Rimini, Istituto Nazionale di Struttura della Materia, Università di Catania, Italy,(1978)

4. A.R.Kirkpatrick, A.C.Greenwald, L.A.Minnucci and R.G.Little, in ref.(2) p.475

5. P.G.Merli, Optik, in press

6. D.H.Auston, J.A.Golovchenko, A.L.Simons, R.E.Slusher, F.R.Smith, C.M.Surko and T.N.C.Venkatesan, in ref.(2) p.11

7. J.W.Mayer and P.T.Clogston, in ref.(3) p.1

8. D.U.Von Rosenberg, "Methods for the Numerical Solution of Partial Differential Equations", American Elsevier Publishing Company Inc., New York, (1969)

9. R.Meharabian, S.Kou, S.C.Hsu and A.Munitz, in ref.(2) p.129

10. C.Weber,"Laplace's and Poisson's Equations. Numerical Solution", in "Focussing of Charged Particles",ed.by A.Septier, Mc Graw-Hill, New York, p. 46, (1967)

11. A.B.El-Kareh and J.C.J.El-Kareh, "Electron Beams, Lenses, and Optics", Academic Press, New York and London, (1970)

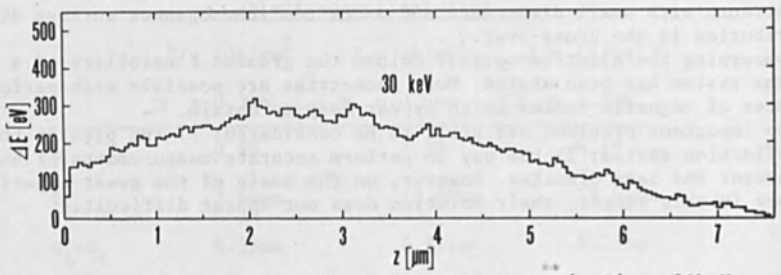

Fig.1 Energy loss E, in eV/layer per electron, in Si at 30keV. Calculations have been done using layers 50nm and 100nm thick. The distance l_{sm} is in this case nerly 2.5um.

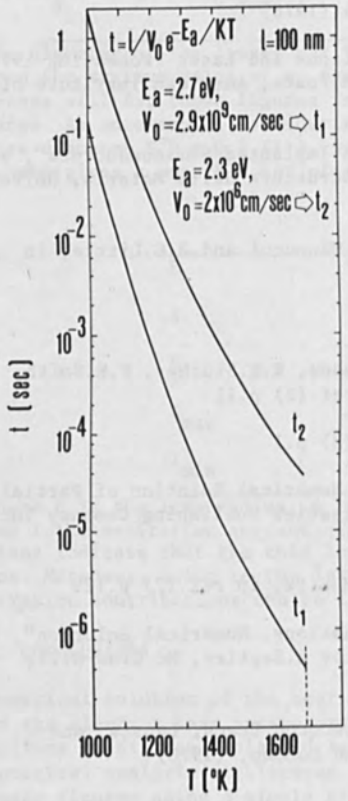

Fig.2 Regrowth velocity in solid phase as a function of temperature according to the data reported in ref. 6 (t_1) and ref. 7 (t_2)

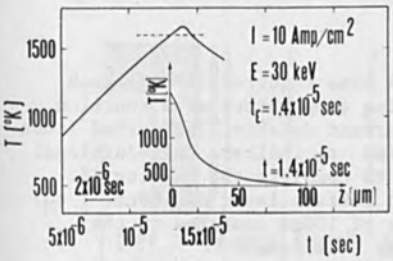

Fig. 3 a)

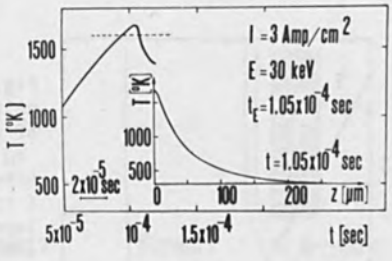

Fig. 3 b)

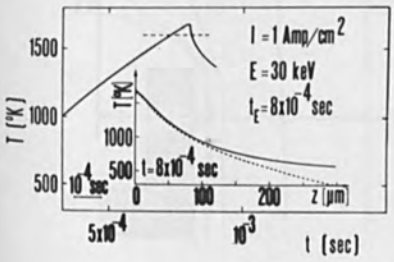

Fig. 3 c)

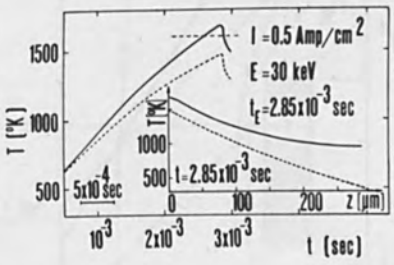

Fig. 3 d)

Fig. 3 Surface temperature as a function of time and (in the insert) spatial distribution of temperature at a time t_E immediately prior to the beginning of melting in a Si wafer irradiated with electrons of 30keV for different values of current density: a) 10A/cm^2, b) 3A/cm^2, c) 1A/cm^2, d) 0.5A/cm^2. The continuous lines refer to a sample thermally insulated, while the dashed ones to a specimen in good thermal contact with a substratum kept at T = 300°K.

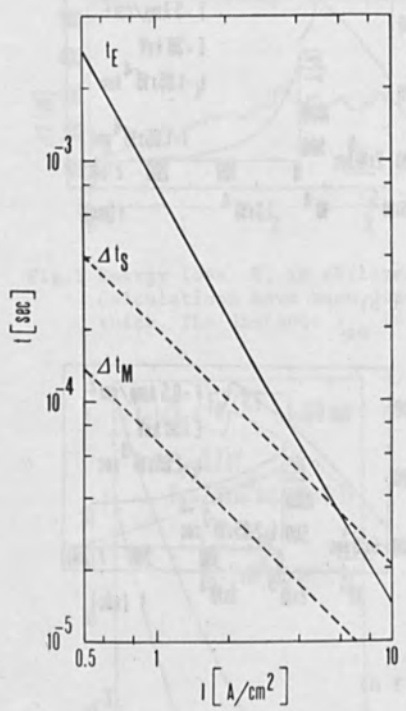

Fig.4 Time required (t) to reach melting temperature as a function of current density. The dashed lines t_M and t_S indicate the additional time to complete the melting of: (t_S) surface layer of 100nm, (t_M) layer of 100nm centered on the energy loss peak.

I (A/cm²)	t_E (sec)	$r=4\sqrt{a^2 t}$ r (mm)	i (mA)
0.5	2.85×10^{-3}	2.1	68
1	8×10^{-4}	1.1	38
3	1.05×10^{-4}	0.4	15
10	1.4×10^{-5}	0.15	7

Tab.1 Exposure time, radius and current of the beam,for different values of I, resulting from the numerical simulation.

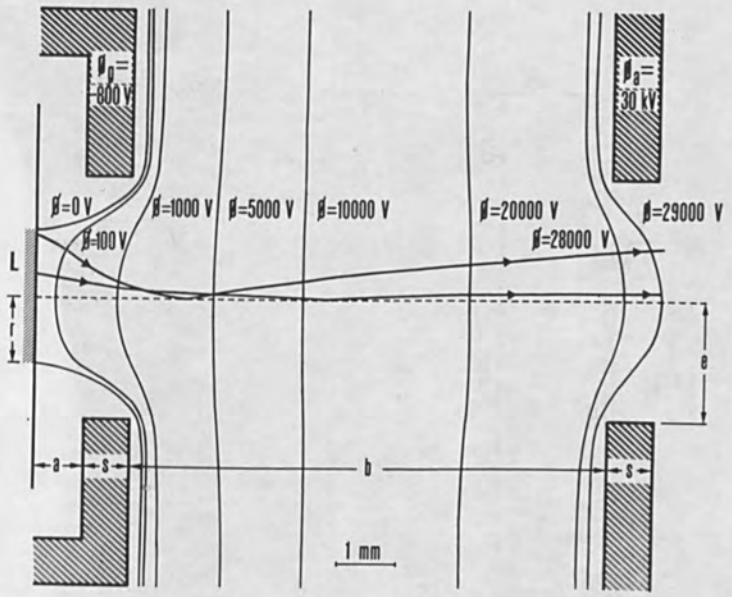

Fig.5 Geometrical configuration of the gun with a sketch of some equipotentials and of two calculated trajectories. a = 0.8mm, S = 0.8mm, b = 8mm, e = 2mm, r = 1.2mm.

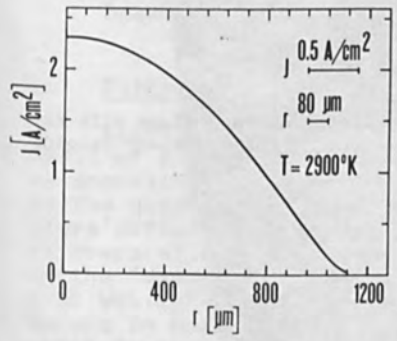

Fig.6 Emission current density distribution.

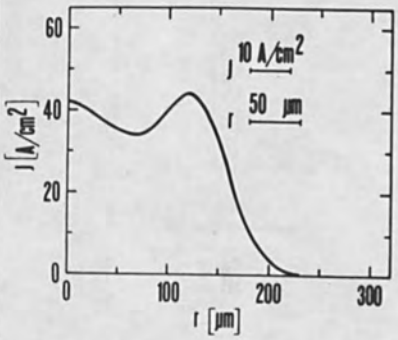

Fig.7 Current density distribution at the crossover.

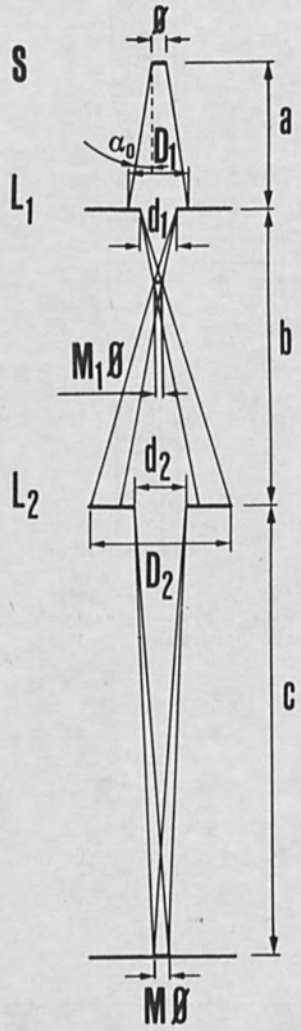

Fig.8 Sketch of the column with ray tracing for crossover imaging.

SOME RESULTS OF HIGH POWER EB GUNS IN INDUSTRIAL APPLICATIONS

Schiller, S., Foerster, H., Wenzel, B., and von Ardenne, A.
Manfred von Ardenne Research Institute, Dresden / GDR

Abstract

Electron guns in a power range of 60-1,200 kW represent the latest state of the art. To produce and guide such a high power to the point of action over a path of up to some meters in a low-loss manner it was necessary to utilize new effects. One of them is magnetic gas focusing where the magnetic field produced by the beam causes a self-focusing action. The other effect, the socalled displacement action, is evoked by the high power density due to vigorous overheating of the vapor or gas within the beam region. Based on this knowledge, a type series of high power electron guns has been developed and built by the Manfred von Ardenne Research Institute of Dresden / GDR which are now being used in many countries; e.g., USSR, USA, Japan and GDR. A report is given on practical experience in industrial use of these guns, in particular, with respect to melting and evaporation. In our opinion these guns will give a fresh impetus to high power electron beam technology.

1. Introduction

Electron guns of 30-1,200 kW now have found a wide field of industrial application in such vacuum techniques as annealing, melting and evaporation of metals. Referred to the quantity of the stock to be handled, energy expenditure differs widely. For heat treatment of strip-steel it is comparatively low. In the case of melting it depends on the fusion point of the stock and covers a range of 1-50 $kWh \cdot kg^{-1}$. With evaporation, however, the additional demand in heat of evaporation increases energy expenditure still further; i.e., by a factor of 20-50. Based on an hourly capacity of some tons for annealing and remelting, and on rates of up to some hundred kilograms for evaporation, guns with ratings in the order of 1,200 kW have to

be used (1, 2).

Continuous annealing, remelting and evaporation of metals requires the use of guns that give a high power during many hours of operation. High productivity is characteristic of these continuous processes so that any outage results in high scrap cost. Hence, gun reliability is of prime importance whilst, under this aspect, initial and maintenance costs play a minor role only.

In vacuum metallurgy constructional elements and process-inherent influence factors determine the reliability of the gun. Either pressure bursts or continuous actions of residual gas or vapor may occur in the working chamber which are likely to interrupt the power supply if they cause a pressure increase in the beam generating chamber of the gun. This is why adequate pressure decoupling between beam generating chamber and working chamber becomes a must in high power guns. Closely related to this basic requirement is the need for a comparatively high operating pressure in the working chamber where the gun still has to work to full satisfaction. Moreover, beam guidance must allow a programmed power density distribution on work site. As a consequence, a beam of high power density has to be passed over a long distance in the working chamber through both residual gas and vapor. Experience with high power guns has shown that all these requirements are met to satisfaction by axial guns where the beam generating system is pumped down separately. Designs of this type have been brought to maturity and are now used in plants with power requirements above 30 kW almost exclusively. Moreover, existing high power transverse guns are increasingly replaced by axial guns.

2. Beam Generation and Guidance

There are various characteristic phenomena in high power guns that must be duly considered and utilized in an axial system to ensure proper beam generation and guidance. These phenomena shall be briefly dealt with below (see Figure 1) (3).

Efficient beam generation aims at the proper shaping of a bundle of rays with high power density and homocentricity. In practice, this objective is realized by a specialized geometric array of solid cathode, focusing electrode and anode as well as by a matched acceleration voltage. For this, some particular conditions in high power guns must be duly considered.

An essential condition is the presence of ions that are produced within the complete region of beam shaping and guidance. Ions in the beam shaping region are accelerated towards the solid cathode due to the high voltage applied. But this results in strong and irregular sputtering of the solid cathode so that its emitting surface undergoes a steady change during the whole cathode life. The rather large beam diameter in the anode region and the short distance between cathode and anode are other factors that render beam guidance more difficult.

To obtain a well guided and highly efficient beam it is therefore mandatory to utilize several phenomena during beam guidance in a directed manner. Compensation of negative space charges of the beam electrons through ions substantially reduces the divergence of the beam. This action is supported by the effect of magnetic gas focusing. Thus all electrons having an incline of their trajectories towards the beam axis below the socalled critical angle of magnetic gas focusing will stay within the beam region. In addition, the high temperature of the ion gas produced in the beam displaces both residual gas and vapor emitted by the beam. This displacement effect inhibits a possible ingress of residual gas or vapor through the beam guidance tube into the beam generating chamber and thus reduces the tendency to arc-overs. In spite of the generally high vapor pressure and residual gas pressures in the order of 1 Pa within the working chamber the utilization of magnetic gas focusing and displacement action evoked by beams of high power density allows the creation of long-range beams. As a consequence the guns can be mounted to the working chamber at any desired location. It has been shown that the displacement effect reduces beam widening at high power densities caused by residual gas and vapor scattering to an extent which proves to be fully adequate for technological processes. Displacement due to the beam further diminishes the unwanted coating of structural elements in the gun near the beam (e.g., parts of the deflection system). This is why constant deflection conditions can be maintained over long operating periods. The build-up time of a gas-focused beam is so short that all hitherto implemented technological processes with high sweep rates turned out to be free from defocusing effects. Irrespective of the sweep rate a focal spot of high power density is thus available on work site which allows to program the power density distribution on the stock with respect to time and location.

3. Characteristic Parameters of High Power Guns

In the development of high power guns with ratings from 5 kW to 1,200 kW it is necessary to take into account those interactions between beam, residual gas and vapor that govern the laws of beam guidance. Listed in the table on Figure 2 are high power guns with sequential power ratings developed for various applications in annealing, melting and evaporation.

With these guns a differentiated power density distribution can be obtained over large areas with respect to time and location due to low-loss beam guidance even in case of high residual gas pressures in the working chamber and high vapor pressures of up to 100 Pa above work site (4).

It should be pointed out, however, that proper beam guidance through magnetic gas focusing and displacement actions is linked up with power densities greater than 20 $kW \cdot cm^{-2}$.

Such a power density is obtained by matched acceleration voltage and geometry of the beam guidance system for all these high power guns. Pressure decoupling between working chamber and beam generating system in the order of 10^2 is obtained by separate pumping-down of beam generating system and intermediate chamber. Thus even high acceleration voltages cannot result in additional high voltage flash-overs in the beam generating system.

In connection with wide sweep angles and a long beam path, programming with respect to time and location allows to cover a large processing area as well as several work sites. This permits almost free selection of the mounting site of high power guns and superior flexibility in plant design.

With continuous plants for long operating times the prospective working hours of the gun are of significance as a parameter which mainly depends on the cathode life. Cathode life is the period between installation and removal of the cathode within which the beam has been actually produced. Shown in Figure 3 is the cathode life distribution of a 250-kW high power gun used in an EB melting furnace of 250 kW. Investigated were 63 cathodes during 4 years of three-shift melting operation. Since the cathodes are usually exchanged in the course of preventive maintenance prior to an actual failure, the number of melt interrupts due to cathode failure can be kept below 1 %.

The statistically determined mean cathode life is about 200 hours. In addition, it emerges from statistical investigations that premature dismantling of the cathode owing to malalignment during gun installation or mechanical deformation caused by material defects is as low as 2.5 %. Cathodes have to be replaced if proper beam generation and guidance cannot be maintained so that the gun becomes overloaded due to the power lost in the flow resistances. However, actual gun operation in practice has shown that such overloads never occur on a sudden but gradually increase during a time of 10 to 20 hours. With operating times much greater than 20 hours it is now common usage to monitor the beam in the gun by means of additional devices.

Plotted in Figure 4 is the thickness distribution of condensed vapor deposits at the beam entrance region of the working chamber which bears witness of the reliability of high power guns. Because of the discussed displacement effect the deposits on the deflection system are also reduced to a minimum so that stable deflection conditions are maintained over long operating times.

4. Actual Design and Industrial Application of High Power Guns

The design of high power guns with ratings of 80 kW, 250 kW and 1,200 kW is illustrated in Figure 5. The most frequent application will be found in melting furnaces fitted with one gun that operate according to the following principle: Melting off the rod, dripping into a crystallizer and keeping the melt in the crystallizer in liquid state for refining and ingot formation. As an example, Figure 6 shows a 250-kW EB furnace for melting titanium ingots.

As far as high-capacity plants, extended processing areas and long operating times are concerned, feasibility studies should be made to decide whether the use of one high power gun or of several medium-power guns will be more profitable with respect to the costs accruing from a possible scrap. With increasing operating time the failure rate of gun components rises also. To render the failure probability of large plants very low in spite of this trend it is common usage to employ several guns with programmable control devices; an advantage especially for process control in case of damage. The project of a melting furnace with forehearth for producing steel ingots of up to 150 tons described in (5) makes use of 8 guns for melting in the forehearth and for keeping the melt in the crystallizer

in liquid state. Since the production of sound ingots must be ensured over long continuous melting times of more than 100 hours even in the case of a failure, the system must be programmed in such a manner that melting continues in the forehearth and crystallizer regions should one of the guns be at fault.

Of course, auxiliary devices for gun operation become more complex in the higher power range. To reduce attendance and maintenance times of the gun — i.e., to extend the useful operating time — all auxiliary devices of the gun have been integrated in the latter and are mounted to the working chamber as a detachable unit. Shown in Figure 7 is a 1,200-kW high power gun engineered according to this principle. This EH 1200/500 high power gun is now being used to equip melting furnaces for large steel ingots of up to 100 tons (6).

5. Summary

Beam generation and guidance in high power guns entails phenomena the founded knowledge and directed use of which is a prerequisite to the development of reliable gun designs. With due consideration to these phenomena, high power guns have been upgraded since they entered the scene about 20 years ago. In our days, advances in gun design brought about such a perfection that it is not the gun which determines the process any longer. As a rule, guns now are to be selected according to the process in question. To comply with this need, a series of high power guns with overlapping ratings from 30 kW to 1,200 kW is now made available.

Principal applications of high power guns are such industrial vacuum processes as annealing, melting and evaporation of metals.

Axial guns not only allow easy programming of the power density with respect to time and location, low-loss penetration of high residual gas and vapor pressures but also ensure top reliability in service which, in turn, permits continuous operation for about 100 hours and more.

Theoretical knowledge and experience gathered by experiments, development work and practice now have paved the road for developing guns with beam powers of up to several thousand kilowatts.

References

1. Schiller, S.; Foerster, H.; Jaesch, G.: Elektronenstrahlanlagen für die Metallurgie. LEW-Nachrichten No. 13/15

2. Schiller, S.; Lenk, P.; Foerster, H.; Jaesch, G.; Kuehn, G.: Bedampfen von Bandstahl mit Elektronenstrahlen als Produktionsverfahren. Die Technik 30 (1975) No. 1, pp 20-23, No. 2, pp 100-106

3. Schiller, S.; Jaesch, G.; v. Ardenne, A.: On the Effects of Gas/Vapor and Plasma on High Power Electron Beam Generation and Guidance. 8th Int. Conf. on Electron Beam and Ion Beam Science and Technology, Seattle/Washington, USA (1978)

4. Schiller, S.; Heisig, U.; Panzer, S.: Electron Beam Technology. J. Wiley (in Print)

5. Schiller, S.; Foerster, H.; Jaesch, G.: Electron Beams for Metallurgical Processes in Vacuum. 6th Int. Vacuum Metallurgy Conf. on Special Melting and Metallurgical Coatings, San Diego USA 1979

6. Dolbenko, E.T.; Dub, W. S.; Chotin, W. A.; Lambrecht, J.; Foerster, H.; Werner, K. H.: Zur Perspektive des Elektronenstrahlschmelzens bei der Erzeugung schwerer Blöcke. Paper (4 A/25) presented on World Electrotechnical Congress, Moscow 1977

Illustrations

Phenomena

- Ions in the anode region accelerated towards the cathode
- Electron beam (EB) which fills the anode bore almost completely
- Short distance between cathode and anode
- Space-charge compensation of beam electrons
- Magnetic gas focusing of EB
- Displacement of residual gas and vapor through EB
- Residual gas and vapor scattering of EB

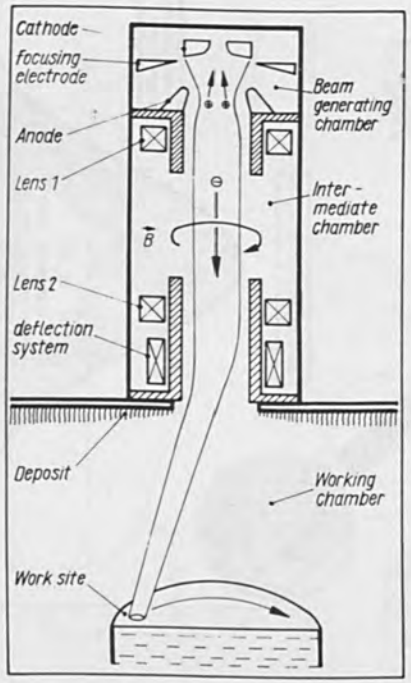

Consequences

- Irregular sputtering of the cathode; steep inclines of electron trajectories towards the system-axis
- Large aperture aberration of anode bore, poor homocentricity of the beam
- Large dispersive action of the anode bore
- Inhibition of beam divergence caused by intrinsic space charges of the beam electrons
- High pressure decoupling between beam generating- and working chamber; minimized hazard of high voltage arc-overs in the beam generating chamber; electron trajectories with only slight inclination towards the system-axis stay within EB
- Pronounced reduction in deposit thickness on constructional components near EB; long-range EB; almost freely selectable gun mounting site on the working chamber, stable deflection conditions over a long processing time
- Energy absorption and focal spot enhancement of EB in residual gas and vapor; suitable selection of acceleration voltage and EB power density

Fig. 1 Beam generation and guidance in high power guns

High power gun	EH 30	EH 80	EH 250	EH 600	EH 1200	
Beam power	5...30	10...80	30...250	100...600	200...1200	kW
Max. acceleration voltage	20	30	30	40	50	kV
Beam diameter at entry into working chamber	6	7	16	22	35	mm
Max. deflection angle	± 45	±22	±35	±35	±35	°
Length of beam path in the working chamber at a pressure $p \leq 10^{-1}$ Pa	1,5	2	2	2,5	3	m
Max. possible working pressure in working chamber	0,5	5	1	1	1	Pa

Fig. 2 Type series of high power guns and performance parameters

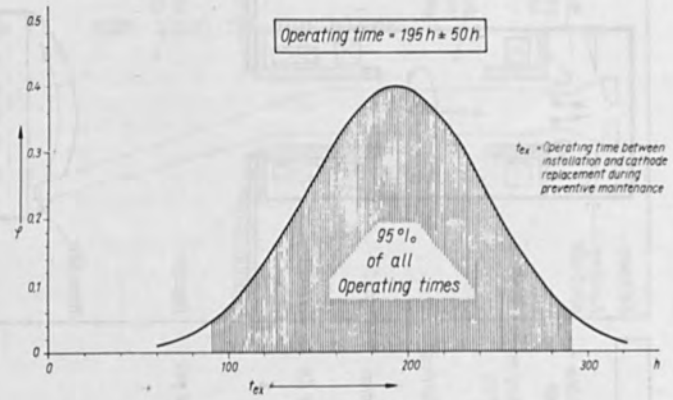

Fig. 3 Cathode life distribution of EH 250/30 High Power Guns $\varphi(t_{ex})$
(Observation period: 4 years in thress-shift operation: Qty of investigated cathodes: 63)

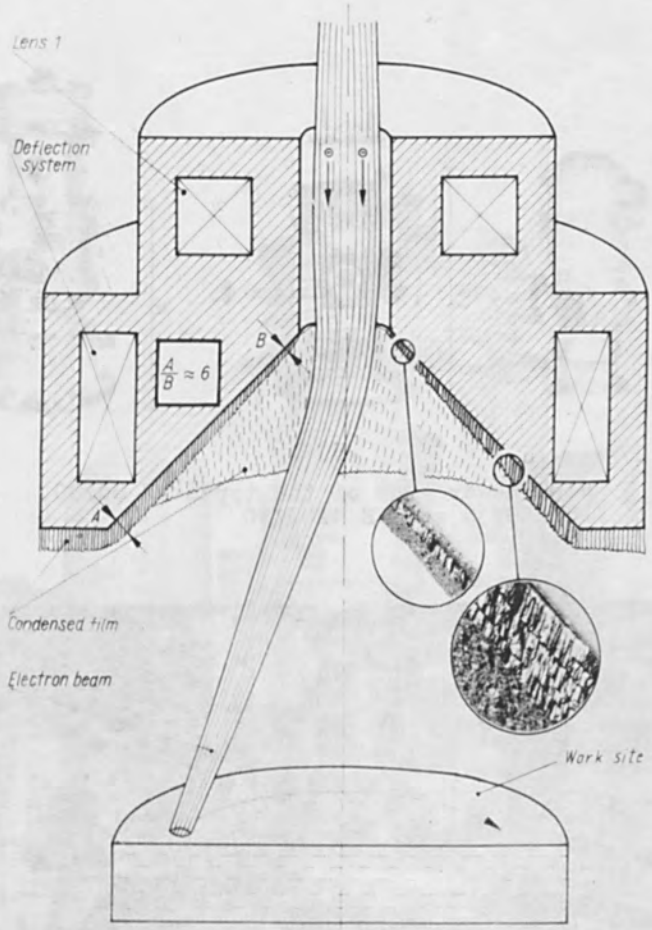

Fig. 4 On the vapor displacement through high power electron beams at the beam entrance zone of the working chamber

(Deposited layer in an EH 1200/50 Gun after 40 hours melting time)

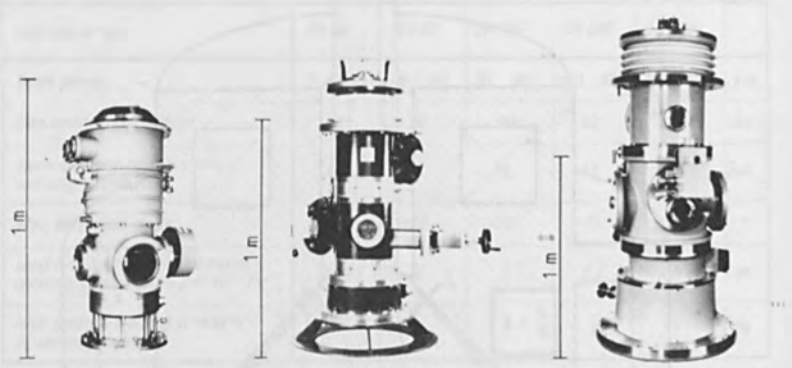

Fig. 5 High power guns of the types EH 80/30, EH 250/30 and EH 1200/50

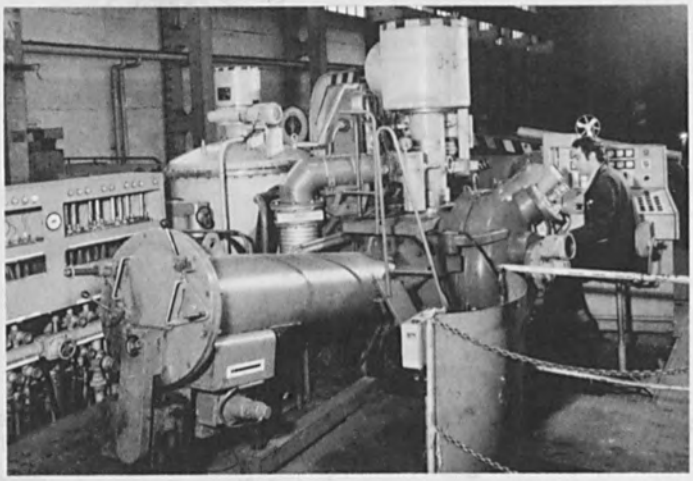

Fig. 6 EMO 250 EB melting furnace for remelting of titanium

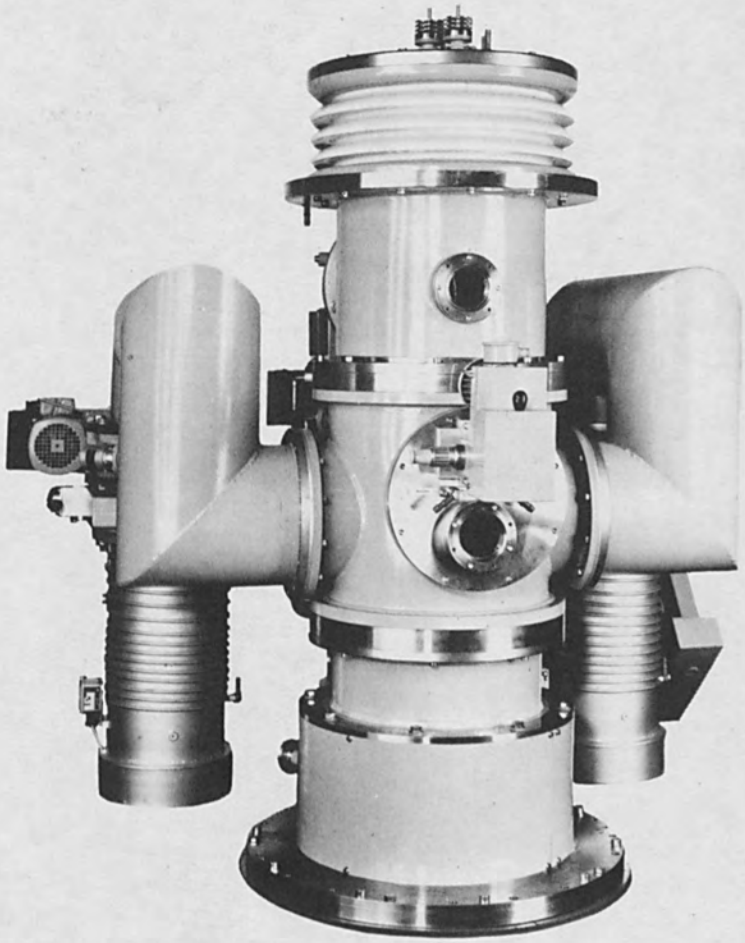

Fig. 7 KEH 1200/50 gun block